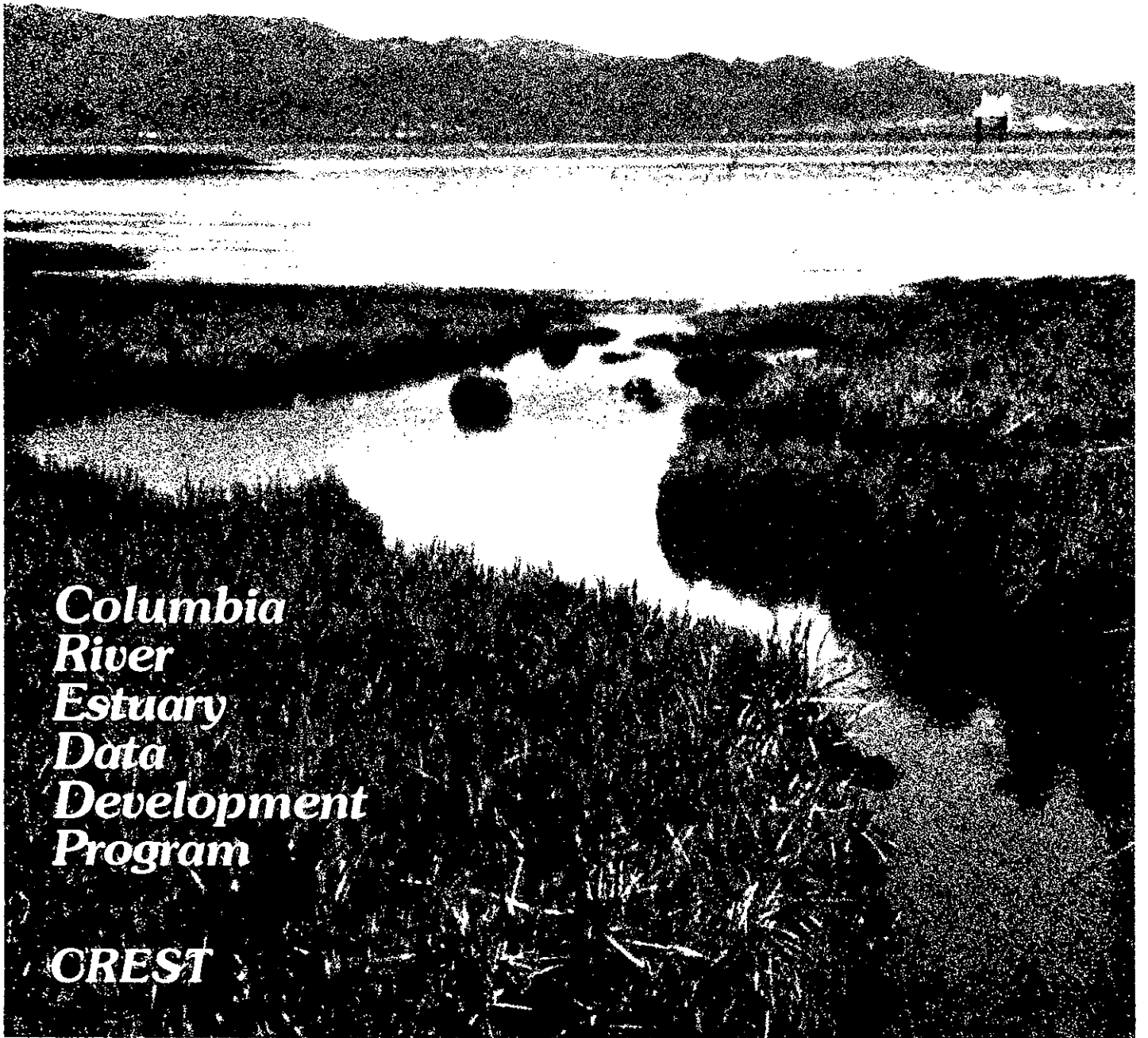


# HYDRODYNAMIC MODELING OF THE COLUMBIA RIVER ESTUARY



*Columbia  
River  
Estuary  
Data  
Development  
Program*

**CREST**

Final Report on the Simulation Work Unit  
of the Columbia River Estuary Data Development Program

HYDRODYNAMIC MODELING OF THE  
COLUMBIA RIVER ESTUARY

(two volumes)

Contractor:

Science Applications, Inc.  
4900 Water's Edge Drive, Suite 255  
Raleigh, N. C. 27606

Principal Investigator:

Peter Hamilton  
Science Applications, Inc.  
4900 Water's Edge Drive, Suite 255  
Raleigh, North Carolina 27606

April 1984

AUTHOR

Peter Hamilton

## PREFACE

### The Columbia River Estuary Data Development Program

This document is one of a set of publications and other materials produced by the Columbia River Estuary Data Development Program (CREDDP). CREDDP has two purposes: to increase understanding of the ecology of the Columbia River Estuary and to provide information useful in making land and water use decisions. The program was initiated by local governments and citizens who saw a need for a better information base for use in managing natural resources and in planning for development. In response to these concerns, the Governors of the states of Oregon and Washington requested in 1974 that the Pacific Northwest River Basins Commission (PNRBC) undertake an interdisciplinary ecological study of the estuary. At approximately the same time, local governments and port districts formed the Columbia River Estuary Study Taskforce (CREST) to develop a regional management plan for the estuary.

PNRBC produced a Plan of Study for a six-year, \$6.2 million program which was authorized by the U.S. Congress in October 1978. For the next three years PNRBC administered CREDDP and \$3.3 million was appropriated for the program. However, PNRBC was abolished as of October 1981, leaving CREDDP in abeyance. At that point, much of the field work had been carried out, but most of the data were not yet analyzed and few of the planned publications had been completed. To avoid wasting the effort that had already been expended, in December 1981 Congress included \$1.5 million in the U.S. Water Resources Council (WRC) budget for the orderly completion of CREDDP. The WRC contracted with CREST to evaluate the status of the program and prepare a revised Plan of Study, which was submitted to the WRC in July 1982. In September, after a hiatus of almost one year, CREDDP work was resumed when a cooperative agreement was signed by CREST and the WRC to administer the restructured program and oversee its completion by June 1984. With the dissolution of the WRC in October 1982, the National Oceanic and Atmospheric Administration (NOAA) assumed the role of the WRC as the federal representative in this cooperative agreement.

CREDDP was designed to meet the needs of those groups who were expected to be the principal users of the information being developed. One such group consists of local government officials, planning commissions, CREST, state and federal agencies, permit applicants, and others involved in planning and permitting activities. The other major anticipated user group includes research scientists and educational institutions. For planning purposes, an understanding of the ecology of the estuary is particularly important, and CREDDP has been designed with this in mind. Ecological research focuses on the linkages among different elements in the food web and the influence on the food web of such physical processes as currents, sediment transport and salinity intrusion. Such an ecosystem view of the estuary is necessary to

predict the effects of estuarine alterations on natural resources.

Research was divided into thirteen projects, called work units. Three work units, Emergent Plant Primary Production, Benthic Primary Production, and Water Column Primary Production, dealt with the plant life which, through photosynthesis and uptake of chemical nutrients, forms the base of the estuarine food web. The goals of these work units were to describe and map the productivity and biomass patterns of the estuary's primary producers and to describe the relationship of physical factors to primary producers and their productivity levels.

The higher trophic levels in the estuarine food web were the focus of seven CREDDP work units: Zooplankton and Larval Fish, Benthic Infauna, Epibenthic Organisms, Fish, Avifauna, Wildlife, and Marine Mammals. The goals of these work units were to describe and map the abundance patterns of the invertebrate and vertebrate species and to describe these species' relationships to relevant physical factors.

The other three work units, Sedimentation and Shoaling, Currents, and Simulation, dealt with physical processes. The work unit goals were to characterize and map bottom sediment distribution, to characterize sediment transport, to determine the causes of bathymetric change, and to determine and model circulation patterns, vertical mixing and salinity patterns.

Final reports on all of these thirteen work units have been published. In addition, these results are integrated in a comprehensive synthesis entitled The Dynamics of the Columbia River Estuarine Ecosystem, the purpose of which is to develop a description of the estuary at the ecosystem level of organization. In this document, the physical setting and processes of the estuary are described first. Next, a conceptual model of biological processes is presented, with particular attention to the connections among the components represented by the work unit categories. This model provides the basis for a discussion of relationships between physical and biological processes and among the functional groups of organisms in the estuary. Finally, the estuary is divided into regions according to physical criteria, and selected biological and physical characteristics of the habitat types within each region are described. Historical changes in physical processes are also discussed, as are the ecological consequences of such changes.

Much of the raw data developed by the work unit researchers is collected in a magnetic tape archive established by CREDDP at the U.S. Army Corps of Engineers North Pacific Division Data Processing Center in Portland, Oregon. These data files, which are structured for convenient user access, are described in an Index to CREDDP Data. The index also describes and locates several data sets which were not adaptable to computer storage.

The work unit reports, the synthesis, and the data archive are intended primarily for scientists and for resource managers with a scientific background. However, to fulfill its purposes, CREDDP has developed a set of related materials designed to be useful to a wide

range of people.

Guide to the Use of CREDDP Information highlights the principal findings of the program and demonstrates how this information can be used to assess the consequences of alterations in the estuary. It is intended for citizens, local government officials, and those planners and other professionals whose training is in fields other than the estuary-related sciences. Its purpose is to help nonspecialists use CREDDP information in the planning and permitting processes.

A detailed portrait of the estuary, but one still oriented toward a general readership, is presented in The Columbia River Estuary: Atlas of Physical and Biological Characteristics, about half of which consists of text and illustrations. The other half contains color maps of the estuary interpreting the results of the work units and the ecological synthesis. A separate Bathymetric Atlas of the Columbia River Estuary contains color bathymetric contour maps of three surveys dating from 1935 to 1982 and includes differencing maps illustrating the changes between surveys. CREDDP has also produced unbound maps of the estuary designed to be useful to resource managers, planners and citizens. These black-and-white maps illustrate the most recent (1982) bathymetric data as contours and show intertidal vegetation types as well as important cultural features. They are available in two segments at a scale of 1:50,000 and in nine segments at 1:12,000.

Two historical analyses have been produced. Changes in Columbia River Estuary Habitat Types over the Past Century compares information on the extent and distribution of swamps, marshes, flats, and various water depth regimes a hundred years ago with corresponding recent information and discusses the causes and significance of the changes measured. Columbia's Gateway is a two-volume set of which the first volume is a cultural history of the estuary to 1920 in narrative form with accompanying photographs. The second volume is an unbound, boxed set of maps including 39 reproductions of maps originally published between 1792 and 1915 and six original maps illustrating aspects of the estuary's cultural history.

A two-volume Literature Survey of the Columbia River Estuary (1980) is also available. Organized according to the same categories as the work units, Volume I provides a summary overview of the literature available before CREDDP while Volume II is a complete annotated bibliography.

All of these materials are described more completely in Abstracts of Major CREDDP Publications. This document serves as a quick reference for determining whether and where any particular kind of information can be located among the program's publications and archives. In addition to the abstracts, it includes an annotated bibliography of all annual and interim CREDDP reports, certain CREST documents and maps, and other related materials.

To order any of the above documents or to obtain further information about CREDDP, its publications or its archives, write to CREST, P.O. Box 175, Astoria, Oregon 97103, or call (503) 325-0435.

## FOREWORD

The research reported in the following two volumes was funded primarily by CREDDP in two parts. The first part of the study employed the U. S. Army Corps of Engineers Waterways Experiment Station Implicit Flooding Model (WIFM). Thanks are due to Lee Butler of WES for supplying the original code for WIFM. The second part of the study, which was performed after CREDDP restarted in 1982, consisted of the modification of a depth-dependent channel model and its application to the estuary. This second study would not have been carried as far as it has without additional support from the Portland District Corps of Engineers in the form of a contract to Science Applications, Inc. (Contract Number DACW57-83-M-1703). Thanks are due to Dave Askren and Steve Chesser of the Portland District for their interest and support.

Throughout the study, data was supplied to this work unit from the Currents work unit investigators. David Jay is especially thanked for providing carefully edited data files in a uniform format from a number of different sources. Thanks are also due to the staff members of Science Applications, Inc., Raleigh, N. C. for their help in many aspects of this program.

## EXECUTIVE SUMMARY

This final report of the simulation work unit of CREDDP consists of two volumes. The first volume presents the results of applying a two-dimensional tidal-storm surge model to the Columbia River Estuary. This study was completed in September 1981. The second volume presents the results of applying a depth-dependent, laterally averaged channel model in a specially developed multi-channel form to study the salinity and depth-dependent hydrodynamics of the estuary. This study occupied all of the second phase of the program during 1983.

The purpose of the study was to use modern hydrodynamic models to simulate the tidal and tidal-residual circulation of the estuary and to assist in determining the physical processes responsible for the major circulation modes of the estuary. This study is the only CREDDP work unit to use comprehensive models to simulate and predict processes occurring in the estuary. It is recommended that these reports be read along with the CREDDP Current work unit report: "Circulatory Processes in the Columbia River Estuary" (Jay 1984) in order to arrive at a comprehensive picture of the circulation and the physical oceanography of the estuary.

Volume I discusses the application of the U. S. Army Corps of Engineers Waterways Experiment Station Implicit Flooding Model (WIFM) to the Columbia River Estuary. WIFM is a two-dimensional model employing the depth-integrated equations of momentum conservation and continuity. It has a number of special features including provision for sub-grid scale barriers, and the flooding and dewatering of grid cells with changing water levels. The model was forced by tidal elevations offshore and at Eagles Cliff at the head of the estuary. The tidal elevations and depth mean currents simulated by the model agreed well with tide gauge and current meter data obtained by the Corps of Engineers during their March 1978 field program. The maps of current vectors showed that the tidal currents were largely constrained by the channels though substantial currents could occur over the sand banks. The model was used in series of experiments to determine possible effects of the wind on the non-tidal flow. Since the model includes a portion of the inner shelf off the river mouth, upwelling and downwelling lowering and raising of sea level by longshore winds was approximately simulated. It was found that strong longshore winds were effective in changing water levels within the estuary and altering the distribution of residual currents but the changes predicted were small compared with the amplitude of the tidal elevations and currents.

Volume II contains the results from the multi-channel model. The model was developed using as a basis previous channel models developed by Hamilton (1975, 1976) Blumberg (1975), Elliott (1976) and Wang and Kravitz (1980). The model solves, by time-stepping finite difference methods, the laterally averaged equations of along-channel momentum and salt conservation and continuity. The model thus includes the important vertical dimension and is able to calculate currents, salinity and elevations as functions of time, depth, and along-channel position. The extension of the model to multiple interconnecting channels allows the complex channel topography of the Columbia River Estuary to be

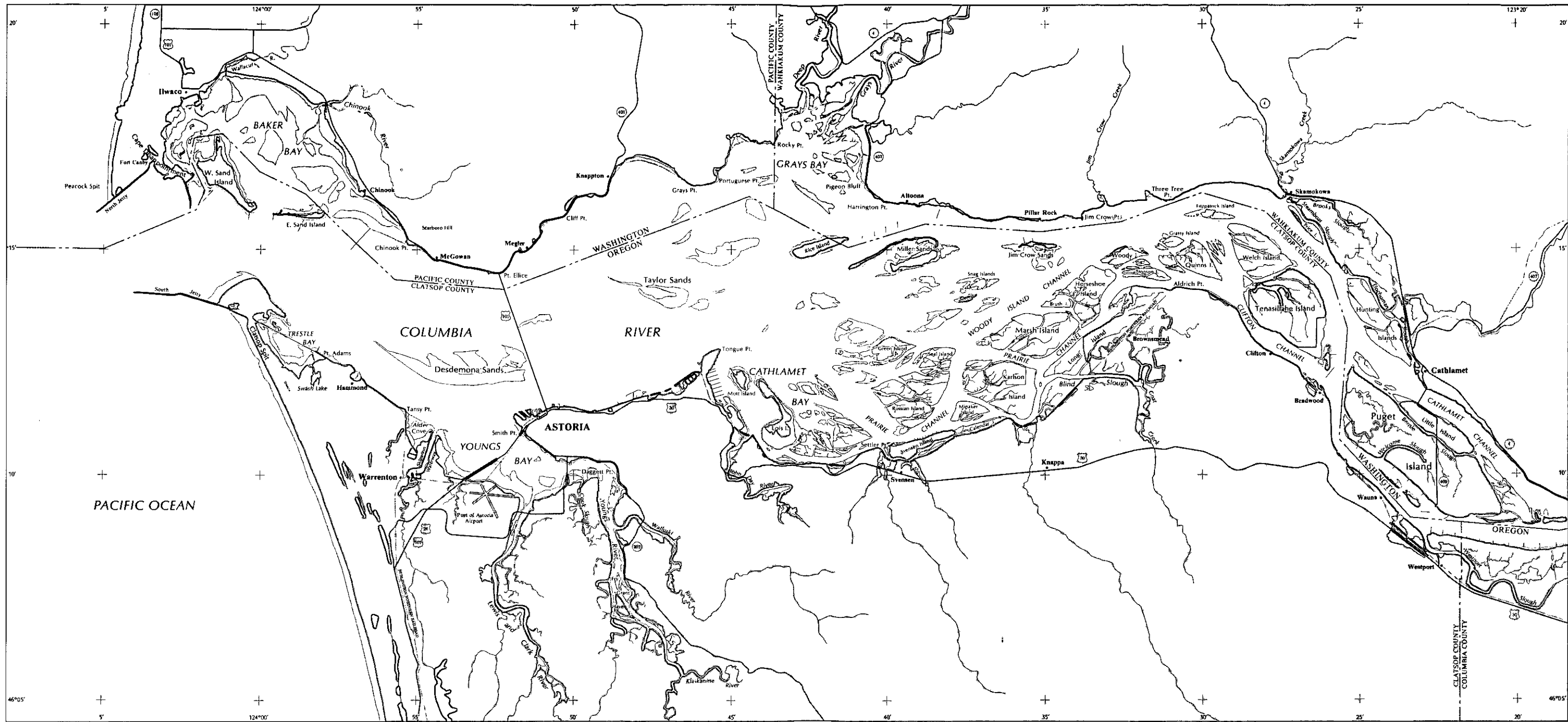
efficiently schematized. It is found that simulations of horizontal currents and tidal elevations are almost as good as the WIFM results even though the horizontal grid was much more sparse than the WIFM rectangular grid. Inclusion of a relatively fine resolution depth grid ensures that the vertical exchange processes of mixing and advective fluxes as well as the combined interaction of current shear and stratification are taken into account in determining the salinity field and interaction of the salinity field with the currents. These important processes are excluded from depth-integrated models. Other features of the model include the provision for interchannel exchanges of water and salt across sandbanks when the water level exceeds the crest of the sandbank, a numerical advection scheme which minimizes numerical dispersion, and an efficient semi-implicit numerical method.

Two periods with extensive data from the CREDDP and NOS field programs are simulated: a 10-day period of low flow in October 1980 and a 60-day period of high flows in May and June of 1981. The latter includes a freshet which peaked at about 15,000 m<sup>3</sup>/s. The reproduction of the observed current and salinity time series is good for both periods, establishing the model's ability to reproduce the main features of the circulation under two different riverflow forcings. The stratification and salinity intrusion differences between neap and spring tide caused primarily by increased vertical mixing on the spring tides are simulated as well as the differences in the salinity intrusion characteristics between the North Channel and the Main Navigation Channel. Mean circulations revealed intermittent weak upstream bottom density-current flows as being more prevalent on neap than spring tides. The intermittency is suspected to arise from non-linear tidal residual effects due to shoals and constrictions in the channels.

The model was then used to predict the circulation and salinity intrusion for a constant riverflow of 2,000 m<sup>3</sup>/s. Historical riverflow records have shown that prior to dam construction on the upper Columbia River, such low riverflows have occurred very occasionally. The main result is that the Cathlamet Bay Channels would only expect a small rise in salinity, to generally less than 5 ‰, if such an event occurred in the future.

As part of a desire to assess the impact of dredging and jetty construction on the hydrodynamics of the estuary, the model was used to predict the circulation that existed for the bathymetry of 1868. The model was reconfigured to represent the different channel networks of the estuary at that time. Three runs were performed for riverflows of 12,000, 4,000, 2,000 m<sup>3</sup>/s. The results show that despite the generally shallower channel depths, the tidal flows were stronger than today and with more asymmetric floods and ebbs in the major channels. Residual flow also greatly favors the North Channel rather than Astoria Channel west of Tongue Point. This results in increased salinity intrusion for all riverflows compared with the present day. The Astoria Channel is predicted to be more saline for low riverflows than the North Channel, which is opposite to that found today. The very low riverflow case showed that Cathlamet Bay would have been quite saline on presumably rare occasions, with some areas showing salinities greater than 10 ‰. The other feature of the salinity field not observed today is the

presence of strong well-mixed vertical fronts over the major interior bars of the estuary at river end of the salt intrusion, particularly at high tide. These predictions are not intuitively obvious and show the value of a comprehensive model to simulate estuarine conditions not encountered or not measured.



# Columbia River Estuary

Scale 1:160,000



Map produced in 1983 by Northwest Cartography, Inc.  
 for the Columbia River Estuary Data Development Program

-  Shoreline (limit of non-aquatic vegetation)
-  Intertidal vegetation
-  Shoals and flats
-  Lakes, rivers, other non-tidal water features
-  Major highways
-  Cities, towns
-  Railroads
-  Other cultural features

The Columbia River Estuary

HYDRODYNAMIC MODELING OF THE  
COLUMBIA RIVER ESTUARY

VOLUME I

TWO-DIMENSIONAL SIMULATIONS OF THE  
TIDE AND WIND-FORCED FLOW

## TABLE OF CONTENTS

	<u>Page</u>
LIST OF FIGURES	v
LIST OF TABLES	vii
1. INTRODUCTION	1
2. METHODS	3
2.1 THE MODEL	3
2.2 THE DATA	5
2.3 INITIAL CONFIGURATION OF THE MODEL	5
3. RESULTS AND DISCUSSION	11
3.1 RESULTS FROM TIDAL SIMULATIONS	11
3.2 COMPARISON WITH DATA	18
3.2.1 Tidal Heights	18
3.2.2 Currents	24
3.3 HARMONIC ANALYSIS OF MODEL RESULTS	35
3.4 RIVERFLOW AND WIND FORCING EXPERIMENTS	41
4. SUMMARY	55
LITERATURE CITED	57

## LIST OF FIGURES

	<u>Page</u>
1. Computational cell definition.	4
2. Chart of the Columbia River Estuary with positions of tide gauges (B) and current meter moorings (T) from the March 1978 CE measurement program.	6
3. The finite difference grid overlaid on a map of the estuary. Heavy solid lines show land/water boundaries or exposed barriers and dashed lines show the positions of submerged or overtopping barriers.	7
4. Perspective views of the model bathymetry.	9
5. Map of depth-mean current vectors and contours of water levels for the times stated.	13
6. Map of depth-mean current vectors and contours of water levels for the times stated.	14
7. Map of depth-mean current vectors and contours of water levels for the times stated.	15
8. Map of depth-mean current vectors and contours of water levels for the times stated.	16
9. Map of depth-mean current vectors and contours of water levels for the times stated.	17
10. Volume transports per unit width ( $\text{ft}^2/\text{s}$ ) and elevations (ft) for the indicated hours and tides.	19-20
11. Observed water level with means removed for the indicated tide gauges (solid line).	21
12. Observed water level with means removed for the indicated tide gauges (solid line).	22
13. Observed water level with means removed for the indicated tide gauges (solid line).	23
14. Observed currents (solid line) and computed depth-mean currents (dashed line) for the indicated stations.	25-26
15. Observed currents (solid line) and computed depth-mean currents (dashed line) for the indicated stations.	27-28

16.	Observed currents (solid line) and computed depth-mean currents (dashed line) for the indicated stations.	29-30
17.	Observed currents (solid line) and computed depth-mean currents (dashed line) for the indicated stations.	31-32
18.	Observed currents (solid line) and computed depth-mean currents (dashed line) for the indicated stations.	33-34
19.	Co-range and co-phase lines for $M_2$ tide.	38
20.	Co-range and co-phase lines for $K_1$ tide.	39
21.	The principal axes of the tidal ellipses for the $M_2$ and $K_1$ tide.	40
22.	Current vectors and water levels for 7 m/s wind directed at the indicated degrees.	44
23.	Current vectors and water levels for 7 m/s wind directed at the indicated degrees.	45
24.	Current vectors and water levels for 7 m/s wind directed at the indicated degrees.	46
25.	Water levels at tide stations B1 through B10 for runs 8 through 13 where the time-series have been joined together.	47
26.	U and V components of depth-mean currents for grid cells corresponding to mooring T1 - T7 for runs 8 through 13.	48
27.	U and V components of depth-mean currents for grid cells corresponding to mooring T8 through T12 for runs 8 through 13.	49
28.	Hourly water level records from tide gauges B1 through B8.	51
29.	Hourly water level records from tide gauges B9 and B10 both filtered (solid) and nonfiltered (dashed).	52
30.	Volume Transports per unit width ( $\text{ft}^2/\text{s}$ ) and elevations (contour labels in ft scaled by 1000) for the riverflow run 8.	53

LIST OF TABLES

	<u>Page</u>
1. Comparison of the simulated and observed $M_2$ tidal constituents.	36

## 1. INTRODUCTION

Simulation studies performed for the Columbia River Estuary Data Development Program (CREDDP) during the period 1980-1984 fall into two parts. The first part (1980-1981) applied a two-dimensional, vertically integrated, tidal/storm-surge model to the estuary to simulate in time and space the distribution of water levels and depth mean currents that are produced by ocean tides and local wind forcing. Results of this first numerical modeling study are presented in Volume I of this report. The second part (1983-1984) involved the development and application of a depth-dependent, laterally-averaged channel model that includes salinity as well as currents and water levels as simulated variables. This second model is better suited to modeling the salt intrusion processes, including the vertical mixing and vertical current shears, and therefore simulates most of the important hydrodynamics of the Columbia River Estuary. This second model was used also to simulate circulation in 1863 before the North and South Jetties were constructed and the main Navigation Channel was dredged. This depth-dependent model was sufficiently successful that it was used exclusively in the simulation studies in 1983-1984 rather than performing more refined studies with the two-dimensional horizontal model. The development and exercise of the depth-dependent channel model was aided considerably by additional funding from the Portland District, Corps of Engineers under a contract with Science Applications, Inc. (SAI). The results of this second model are given in Volume II of this Final Report.

The investigation, reported in this volume, is essentially a preliminary model study of the horizontal tidal and wind driven flows. The vertically integrated model is capable of more sophisticated and detailed simulations of horizontal flows in the estuary by the use of smaller grid spacings and selectively refined grids. These studies were not performed because it was felt that more useful information would be obtained from the channel model simulations, particularly on salinity intrusion processes, than would be gained by refining the horizontal tidal simulations given the level of funding available. Due to the timing of the two model studies, different datasets were used for calibration and verification. In 1981 neither the CREDDP Currents work unit data nor the 1980-81 bathymetry were available; therefore, U.S. Army Corps of Engineers current meter and tide gauge data were used from March 1978. The channel model studies of 1983 required salinity data and the more comprehensive CREDDP and National Ocean Survey (NOS) data were used in preference.

The two modeling studies should be regarded as complementary, even though they were performed as essentially separate projects. The horizontal model (Volume I) has a finer horizontal grid spacing than the channel model and thus is able to give more detail on the horizontal distribution of the current fields. It is also better suited to describe the effects of wind-induced coastal upwelling and downwelling on the sub-tidal currents and water levels. The channel model allows investigation of the salinity intrusion for neap and spring tides under varying riverflows.

Taken together, these two models give a comprehensive picture of the tide, riverflow, and wind-forced circulation in the estuary which, incidentally, is much less costly than the exercise of a three-dimensional model with a grid fine enough to resolve properly the processes occurring in the estuary. These reports should be read in conjunction with Jay (1984), which discusses the results of the physical oceanographic field program and analysis of data.

The Columbia River Estuary is characterized by a large tidal range (about 2 m at neap, and 4 m at spring tide) and very large fresh-water flows (4,000 - 15,000 m<sup>3</sup>/s). The tide at the mouth is a mixed type with a prominent diurnal as well as the usual dominant semi-diurnal constituents. This type of tide produces two low and two high waters a day of differing heights. The large fresh water flows combined with strong but variable tidal mixing result in a salt intrusion with large horizontal and vertical salinity gradients, which can vary from almost a salt-wedge to vertically homogeneous. During the low flow season (fall), with riverflows averaging about 4,000 m<sup>3</sup>/s, salinity can intrude as far as Altoona, with the higher salinities greater than 5 ‰, generally downstream of Tongue Point. There is marked difference in the salinity intrusion length and stratification between neap and spring tides for low freshwater flows (Jay 1984). The major stratification is greater and the salinity intrusion longer for neap tides, as against spring tides. At high freshwater flows (8,000 - 12,000 m<sup>3</sup>/s), which occur in spring and early summer due to snow melt in the Cascades, the salt intrusion is generally downstream of Astoria and does not show as much variability between neap and spring tides as for low flows. The salinity is maintained in the lower estuary primarily by tidal dispersion (Hughes and Rattray 1980; Jay 1984). The interaction of the tidal currents and salinity gradients produces an upstream flux of salt which counteracts the downstream advection of salt by the riverflow. Analyses by Jay (1984) and the results of the channel model (Volume II) indicate that mean density current flows, characteristic of many partially mixed estuaries, are not important for the salt balance of the Columbia River Estuary.

## 2. METHODS

### 2.1 THE MODEL

The numerical model used during this portion of the study is the Waterways Experiment Station Implicit Flooding Model (WIFM) originally developed by Butler (1980) and extensively used for various Corps of Engineers (CE) projects around the country. A description of the equations and numerical method as well as the results from CE projects are presented in Butler (1980). A rather more detailed description of essentially the same model, including setting up the input data, is given by April and Raney (1980) in their report on the application of WIFM to Mobile Bay and Mississippi Sound.

The numerical model solves the long-wave hydrodynamic equations for water level and depth-mean velocity on a finite-difference grid. The solution technique is an alternating direction, implicit two-level, finite-difference time-stepping scheme. Features of the model include a flexible rectangular grid using piecewise continuous functions to independently map the two Cartesian coordinate directions (x,y). This feature allows increased resolution of selected parts of the grid and decreased resolution of less important areas relative to the basic grid increments ( $\Delta x$ ,  $\Delta y$ ). This feature was not employed because of the preliminary nature of the study and the desire to model all regions of the estuary with the same resolution.

The model also allows inundation or drying of grid elements or cells with rising and falling water levels. Thus, areas within estuaries which dry at low water (such as Desdemona Sands) or are flooded at high water (such as wetlands) can be accommodated by the model. The numerical algorithm for flooding areas is similar to that of Reid and Bodine (1968).

The final feature of the model is the use of sub-grid barriers. Such barriers are defined along cell faces and are of three types: exposed, submerged, and overtopping. Exposed barriers are handled by simply specifying no-flow conditions across the appropriately flagged cell faces. Submerged barriers are simulated by controlling flow across cell faces with the use of a time-dependent frictional coefficient. The term "overtopping barrier" is used to distinguish barriers which can be submerged during one phase of the simulation and totally exposed during another. Actual overtopping is treated by using a broad-crested weir formula to specify the proper flow rate across the barrier. Water is transferred from the high to low side according to this rate. Once the barrier is submerged (or conversely exposed), procedures as described for submerged barriers (or exposed) are followed.

The sub-grid barriers were most useful for the Columbia River Estuary simulations, as the grid is relatively coarse and small islands, jetties, and sandbanks were approximated by exposed and overtopping barriers along appropriate cell faces.

The principal adjustable parameter is the bed friction and here the conventional Chezy formulation is used

$$\{ T_{bx}, T_{by} \} = \frac{g (U^2 + V^2)^{1/2}}{C^2 d^2} \{U, V\} \quad (1)$$

where:  $T_{bx}$ ,  $T_{by}$  represents the bottom stresses in the x, y direction, respectively;

- U, V are the vertically integrated transports per unit width in the x, y direction, respectively;
- g is the acceleration due to gravity;
- d is the total depth of water; and
- C is the Chezy coefficient.

The model allows C to vary in space according to depth and bed composition. The Chezy coefficient is related to the Manning roughness factor, n, by

$$C = \frac{2.21}{n} d^{1/6} \quad (2)$$

where d is in meters, and  $C^2$  has the dimensions of  $m/s^2$ . The basic grid element or computational cell is shown Figure 1. The conventional boundary conditions are no normal flow at a land-water boundary specified along a cell face, and water surface elevation or flow rates given as a function of position and time at open boundaries. The model in its present version excludes the non-linear inertial terms in the momentum equations, and there are no lateral friction terms.

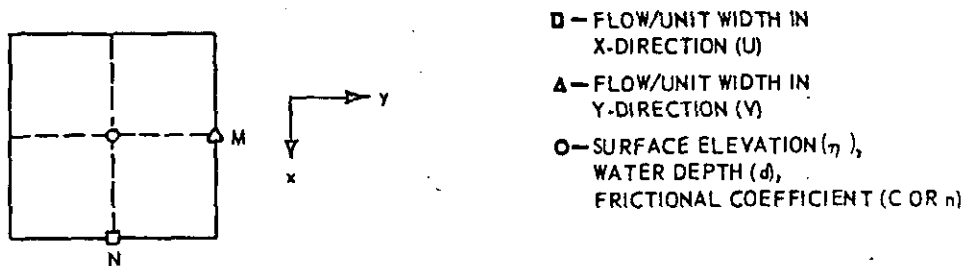


Figure 1. Computational Cell Definition.

The neglect of the non-linear inertial terms in the momentum equation is possibly an important omission if tidal residual circulations are studied. The depth dependant model of Volume II does include the inertial terms and they are found to modify the depth dependant tidal residual flows over a version of the model without inertial terms. However, in a depth integrated model inertial terms are expected, from scaling considerations, to have only minor effects on the depth mean residual flows compared with the dominant riverflows.

Further studies employing vertically integrated models to calculate tidal residual flows should probably include the inertial terms. Tidal residual flows were not calculated from the tidal simulations in this preliminary study.

## 2.2 THE DATA

The data used to calibrate the model derive from a U. S. Army Corps of Engineer field study in 1978. Figure 2 shows the positions of the tide gauges and current meter moorings, and their designations. The majority of the current meter moorings had one ENDECO current meter at mid-depth, but a few moorings in the deeper channels had an upper meter (1.5m from the surface) and a near-bottom meter (1.5m above the bottom). These are stations T1, T2, T5, and T11 (Figure 2). The period when the maximum number of instruments were recording data was March 19 to April 4, 1978, thus providing a good synoptic data set of approximately 16 days. The current meters were actually in the water for about a month, beginning March 9, 1978; unfortunately the crucial tide gauge at Jetty A (B2) was not working until March 19, 1978. The upstream boundary of the Model is the Eagle Cliff tide gauge (B10) at River Mile (RM) 55.5.

The data were supplied to the Simulation work unit, from the CREDDP currents work unit investigator Mathematical Sciences Northwest. For the period above, data were not available from the Hungry Harbor (B5) and Altoona (B7) tide gauges nor from mooring T3. Tide gauge data was supplied in the form hourly water level heights and the current meter data, which was recorded as speed and direction at 30 minute intervals, was resolved into east (U) and north (V) components with a 3-hour Lanczos filter to remove high frequency noise and then low pass filtered.

## 2.3 INITIAL CONFIGURATION OF THE MODEL

The model was configured for the estuary by overlaying a rectangular grid on NS(y) and EW(x) axes over the chart of the estuary. The portion of the grid overlaying the CREDDP map is given in Figure 3. The grid cell dimensions ( $\Delta x$ ,  $\Delta y$ ) = 1.52 km. The grid extends seaward of the mouth by 6 grid cells to give the total number of grid points as 50 x 15. The heavy lines on Figure 3 denote the boundary of the land areas. In explicit models using the long wave equations (i.e., Reid and Bodine 1968). The time step,  $\Delta t$ , is restricted by the Courant-Friederich-Lewys condition for free gravity waves, namely

$$\Delta t \leq \Delta x / (gH)^{1/2} \quad (3)$$

where H is the maximum depth. In alternating direction implicit (ADI) methods, the explicit condition on the time step is eliminated, however too large a time step can result in substantial phase errors. A generally accepted criteria for ADI methods is that the time step should not exceed about 5 times the explicit criterion (3). Therefore, to comply with this restriction a time step of 3 minutes was used for all simulations reported in the following sections.

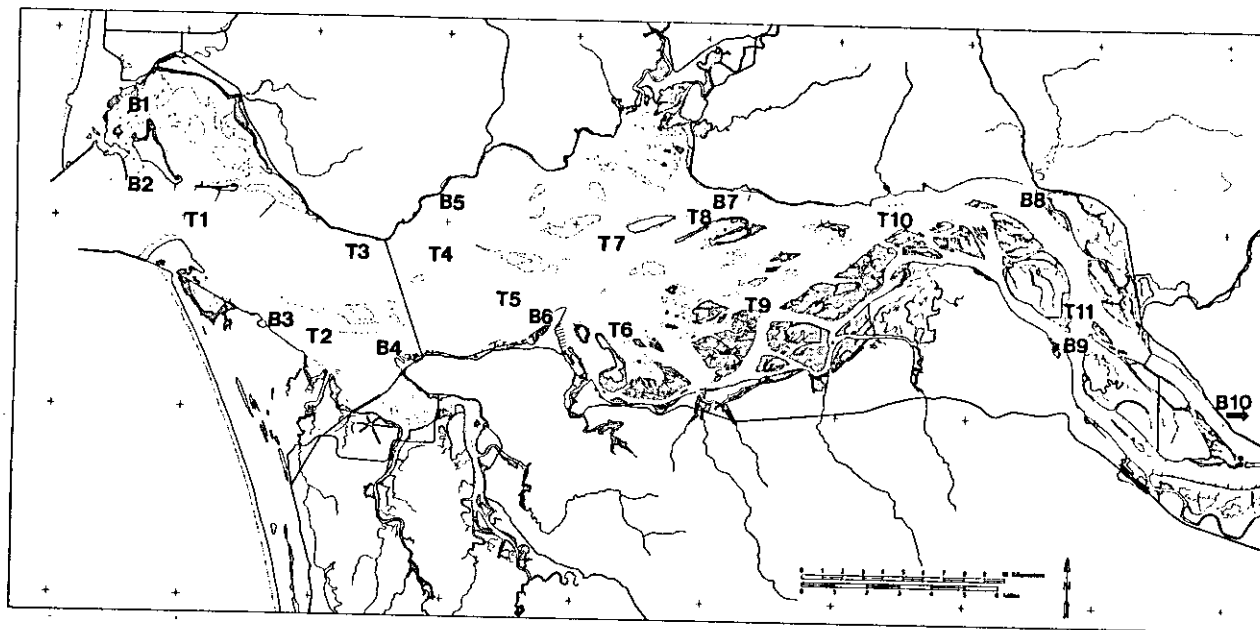
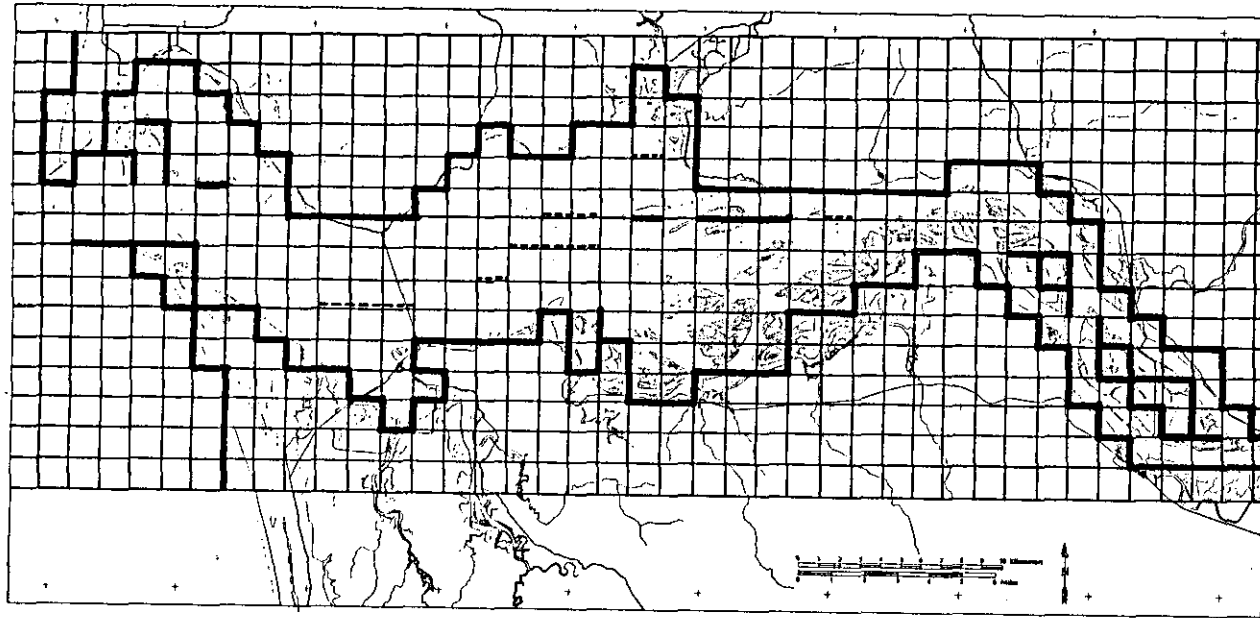


Figure 2. Map of the Columbia River Estuary with positions of tide gauges (B) and current meter moorings (T) from the March 1978 CE measurement program.



7

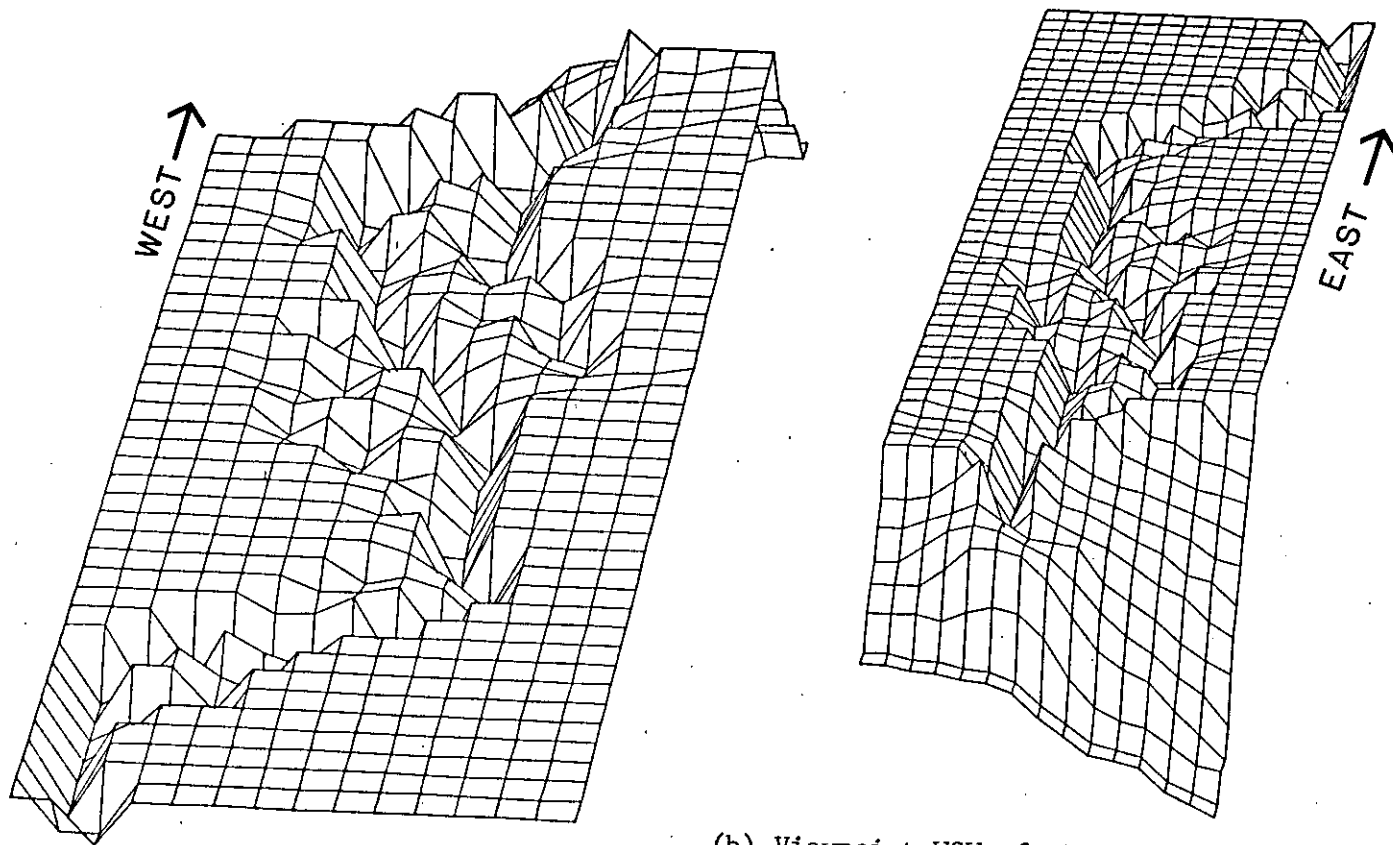
Figure 3. The finite difference grid overlaid on a map of the estuary. Heavy solid lines show land/water boundaries or exposed barriers and dashed lines show the positions of submerged or overtopping barriers.

The model was calibrated by adjusting the friction coefficients by the use of (2). Manning's n ranges from 0.015 to 0.024, with the low value in the deeper water of the continental shelf and the deep entrance channel and the high value representing the shallow waters at the head of the bays. Average values in the main body of the estuary are generally 0.018 or 0.020. The latter value was also used in the Baker Bay numerical model of Roberson et al. (1980). During the calibration of the present model, it was found that reproducing the tidal wave was fairly insensitive to the friction coefficient in deep water, but required sufficient friction in the shallow bays to give the correct tide ranges.

The depths used in the model are taken directly from NOAA charts 18521 and 18523 by overlaying the grid and taking a weighted average of the depths in each cell. The weighting is rather subjective but favors the deeper water depths. As grid element sizes are reduced and finer resolution results, this procedure becomes less subjective and thus more accurate. Evidently, at 1.52 km resolution, complex systems of islands and channels such as occur in Cathlamet Bay are poorly resolved and the simulations of flows are not likely to be accurate in these shallow regions. However, the simulation of the tidal elevations is quite good and implies that as long as the storage volume of the peripheral bays is reasonably represented in the model, the dynamics of the tidal wave are primarily controlled by the deep main channels. The chart depths are the result of surveys taken in 1959, and it is well known that the topography of the estuary has changed considerably in some areas since then. Another problem using chart depths is that the heights above the datum of drying sand banks and flooding wetlands are not indicated. Present day bathymetry from the 1980-1981 depth surveys by the CE and CREDDP should be used for future studies involving increased resolution tidal modeling. These latter bathymetric data, were utilized in the simulation studies reported in Volume II. For the results reported here, the sandbanks and wetlands were set to the MLLW datum. The zero datum level in the model simulations is the mean tide level, 4 ft or 1.22m above the chart datum (MLLW). Two perspective views of grid bathymetry are shown in Figure 4. The model grid extends from 9.1 km offshore of the North Jetty to the Eagle Cliff tide gauge (RM 55.5).

The submerged, exposed and overtopping barriers used to represent small islands, sand banks, and jetties are shown in Figure 3. Exposed barriers are represented by solid, heavy lines and submerged or overtopping barriers by dashed lines along cell faces. Thus, the barrier to cross channel flow between the Main and North channel caused by Desdemona Sands is represented in the model by a submerged barrier. These model barriers are important for the success of the simulations since the help to channelize the flow in certain regions of the estuary.

The input boundary conditions for the tidal simulations consist of the observed water levels at Jetty A, which are backed off to the seaward boundary using the free gravity wave speed,  $(gd)^{1/2}$ . It was found that allowing no phase differences in the input elevations along the seaward boundaries produced reasonable simulation within the estuary. This procedure may not produce the correct tidal currents on the nearshore continental shelf; however, it does produce the correct tide



(a) Viewpoint ENE of the grid looking down. This view emphasizes the eastern channel systems.

(b) Viewpoint WSW of the grid looking east. This view emphasizes the topography of the continental shelf and the estuary entrance channels. Level areas represent land reduced to the mean tide level datum of the model.

Figure 4. Perspective views of the model bathymetry.

levels at Jetty A, except for a small amplification, and seems to produce more realistic phasing of the currents in the entrance channel than if the tidal elevation boundary condition were applied at the end of the entrance jetties. The latter situation was used for the early model runs. The upstream boundary condition is the input of measured water levels at Eagle Cliff (B10) as a function of time. A more proper boundary condition would be to specify the riverflow; however, tidal influence in the Columbia River extends to the Bonneville Dam which is also the major source of fresh water flow. To adequately model the upstream system, a one-dimension channel model of the river channel (e.g. McDowell and Prandle, 1972) would need to be spliced into the eastern side of the grid at Eagle Cliff. Specifying the water level as a function of time at Eagle Cliff from observations gives a good representation of the tide in the estuary, but due to the uncertainty in datums between Jetty A and Eagle Cliff and the accuracy of the tide gauge measurements (probably about  $\pm 2$  cm), the tidal mean slope between the upstream and seaward boundary is not precisely known; thus calculated tidal mean flows do not necessarily correspond to Bonneville flows. It is apparent from the tidal simulations that in the channels east of the Skamokawa tide gauge (B8) the residual mean flows are too small. In Volume II a riverflow boundary condition is used along with a procedure to limit the length of the upriver channels and still produce the correct tidal elevations in the main channels of the estuary. Future model studies with WIFM should adapt the upstream boundary condition to specifying the riverflow as a function of time as suggested above. Specifying elevation boundary conditions at both the mouth and the river end of the estuary can sometimes lead to problems of free surface waves set up by initial transients being reflected from the boundaries and not escaping from the model domain. This phenomenon was not observed in any of the Columbia River simulations and the lack of any problems of this type is probably due to the strong frictional dissipation in the system.

### 3. RESULTS AND DISCUSSION

#### 3.1 RESULTS FROM TIDAL SIMULATIONS

Results are presented for the simulation of the tide for a total of  $7\frac{1}{2}$  days beginning at 0600 hours (PST) March 19, 1978, ( $t=0$ ). The initial conditions are level water surface and zero velocity everywhere. The input tide gauge records at Jetty A and Eagle Cliff were adjusted slightly from the measurements for the first 2 hours to accommodate the initial conditions. A number of runs (approximately 10-15), usually of 60 hours duration, were made during the initial investigation and calibration of the friction coefficients; however, results will be presented only from the calibrated model.

The water levels and depth-mean currents are shown every three hours between  $t=33$  and  $t=60$  hours and thus cover a 25 hour tidal cycle (Figures 5-9). In these figures, a vector with multiple shafts indicates that the speed is equal to the shaft length multiplied by the number of shafts. The vector scale for single and multiple-shaft arrow is given in the lower right hand corner of the plot. Water level contours are solid when positive and dashed when negative. The zero datum is mean tide level at Jetty A. In studying these results, it should be noted that the observed tide at Eagle Cliff lags the tide at Jetty A by about  $2\frac{1}{2}$  hours, indicating that the tide wave is of predominantly progressive character with tidal elevations and velocities along the channel axis being approximately in phase. However, in the Astoria reach and the Cathlamet Bay region the tidal wave has also some of the characteristics of a standing wave and the phase lags between tidal elevations and velocities are between  $0^\circ$  and  $90^\circ$ . Jay (1984) discusses the nature of the tidal wave using a simple analytical model. Major points from the results are summarized below.

#### 33 hours (Figure 5)

Maximum ebb velocities are shown at the mouth as the water level approaches lower low water. The tide is still weakly flooding at Eagle Cliff. Note how the ebb flows in the main body of the estuary split and recombine according to the complex system of channels; i.e. between Woody Island channel and the Main channel in the Cathlamet Bay region, between the complex system of channels between Grays Bay and Tongue Point, and the joining of the north and south main channels at the entrance to Baker Bay.

#### 36 hours (Figure 5)

Flood flows are beginning at the mouth as the water level begins to rise. Note that higher current speeds are seen on the shallower south side of the entrance channel than in the deeper north side. The currents are also beginning to flood on the sand banks and north channel system between Baker Bay and Grays Bay, whereas currents are still ebbing in the main (south) channel, west of Tongue Point. The tide is at low water in western Cathlamet Bay.

39 hours (Figure 6)

The tide is now flooding everywhere west of Skamokawa, with close to maximum velocities at the mouth. Notice the substantial water level slope of 0.40m between the mouth and Grays Bay. In the upper estuary, the flow is weakly ebbing at Eagles Cliff, but note that the flood has begun in the shallow Clifton Channel on the west side of Tenasillahe Island, while flows in the main channel on the east side of the island are nearly zero.

42 hours (Figure 6)

At the mouth, the water level is at high water. Flooding flows are in evidence throughout the estuary and the channel systems are fairly well delineated. There is an eddy circulation in the entrance channel, with the currents flowing west along the south jetty and east in the deeper part of the channel on the north side.

45 hours (Figure 7)

Ebb flows are now established over most of the western part of the estuary, and the flows are similar to those shown 12 hours previously (at 33 hours) in Figure 4, though a little earlier in the flood. Note that the flows change from flood to ebb in the vicinity of Tenasillahe Island produces a clockwise circulation around the island.

48 hours (Figure 7)

The water level at the mouth is now rising from low water (-0.45m at Jetty A; there is a substantial diurnal inequality in the tide records at this stage of the spring-neap cycle). The current patterns shown are at a similar stage of the tide relative to low water as the 36-hour circulation relative to lower-low water. Note the similarity of flow patterns with generally weaker currents at 48 hours than at 36 hours.

51 hours (Figure 8)

The tide at the mouth is rising and the strongly flooding currents are similar to those at 39 hours, though 51 hours is relatively closer to higher-high water than 39 hours is to high water, so the currents are a little weaker at the latter time.

54 hours (Figure 8)

This figure shows the early part of the fall of water levels at the mouth from higher-high water to lower-low water and is similar to that at 42 hours. Flow is weakly flooding in the main channels of the western estuary, though ebb flows are still in evidence over the major sandbanks. The clockwise circulation is again established in the entrance channel at the mouth. It is approximately higher-high water in eastern Cathlamet Bay. Baker Bay circulation is interesting, generally showing flow out of the Bay to join the flooding tide in the main channels. An anticlockwise circulation is set up between Chinook Point and Sand Island in the eastern part of the Bay.

57 hours (Figure 9)

The ebb is now very strong over most of the main body of the estuary as lower-low water is approached, and the patterns are similar to those shown at the approach of low water at the mouth at 45 hours. The flows

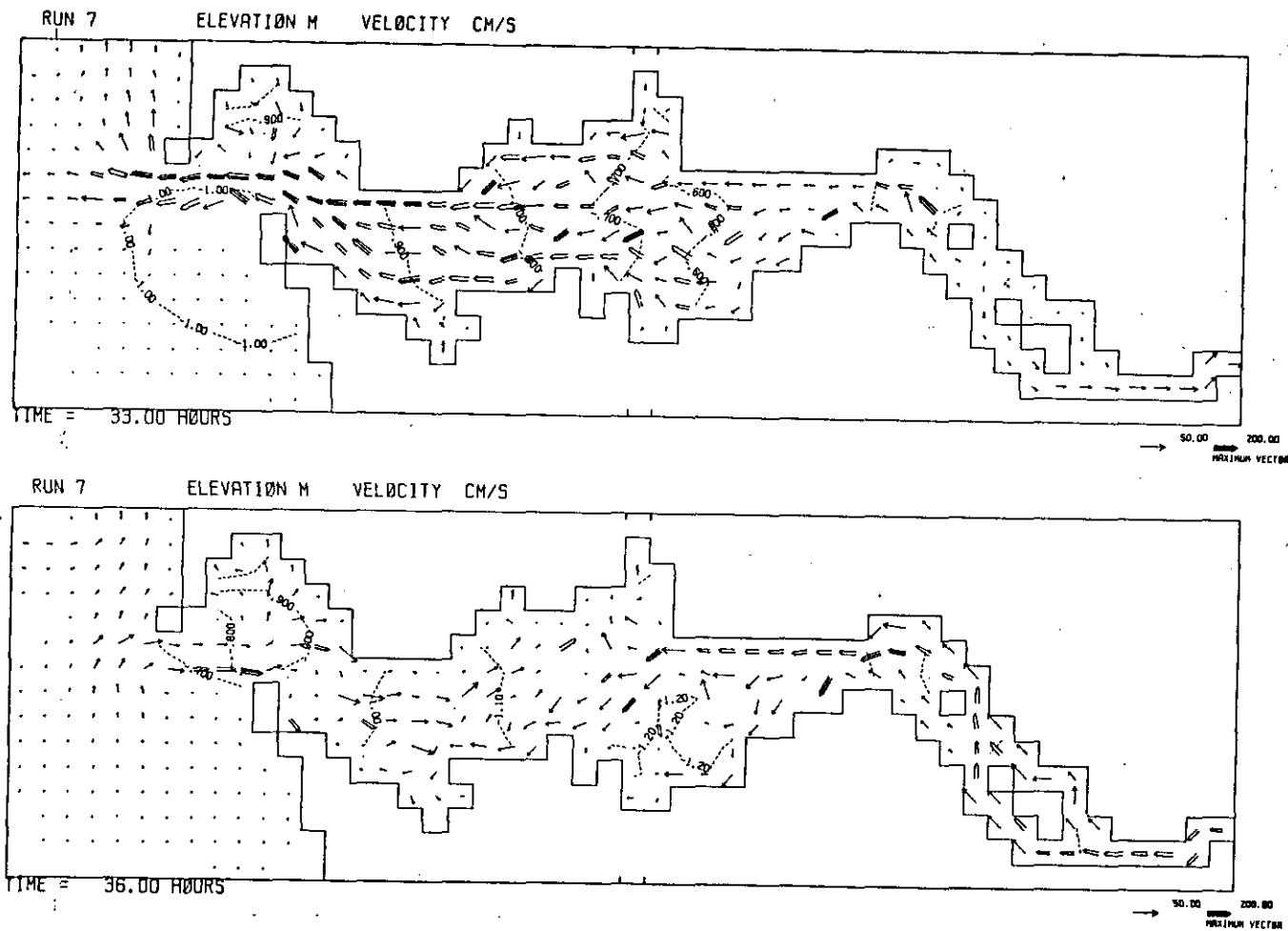


Figure 5. Map of depth-mean current vectors and contours of water levels for 33 and 36 hours.

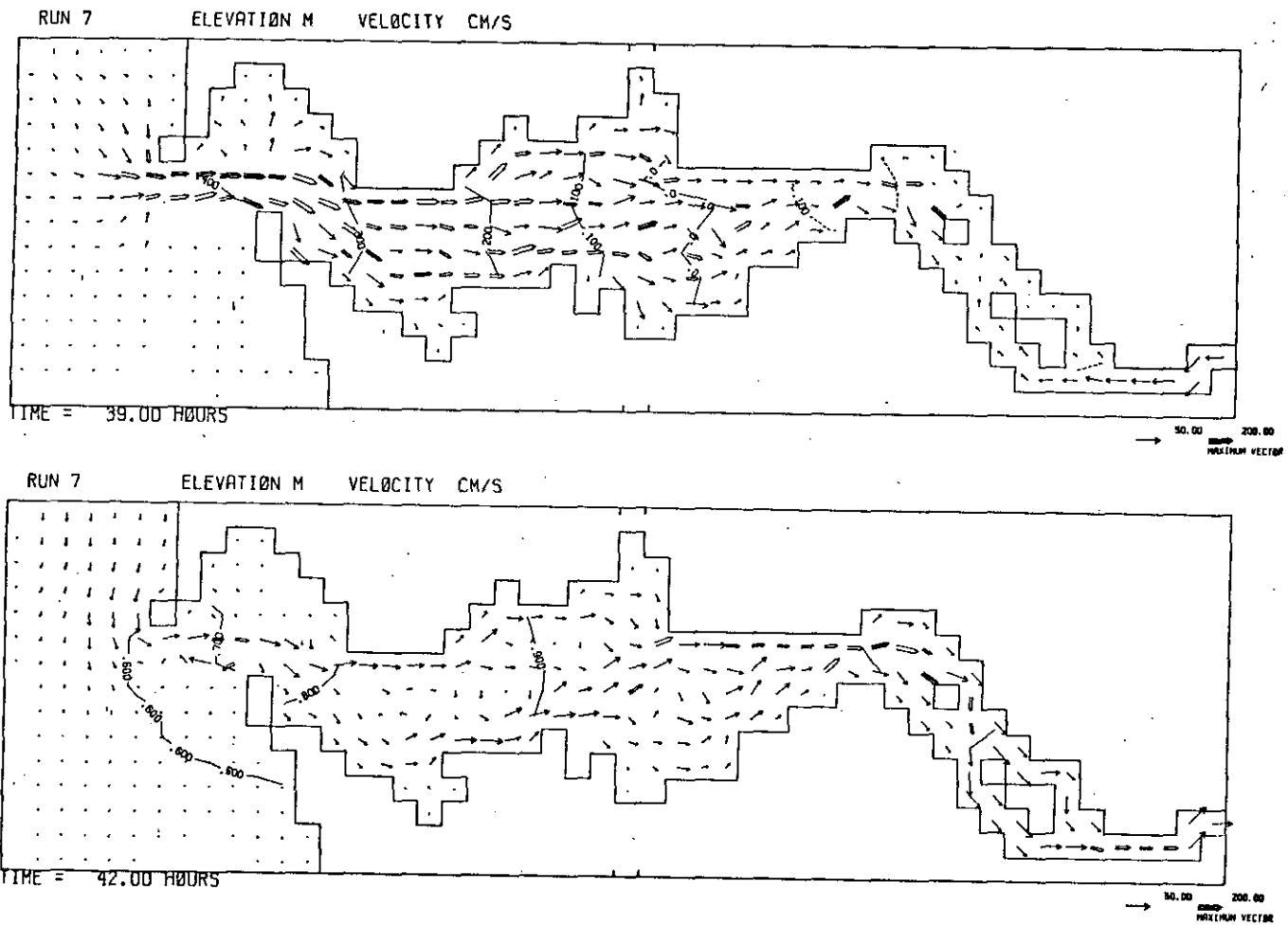


Figure 6. Map of depth-mean current vectors and contours of water levels for 39 and 42 hours.



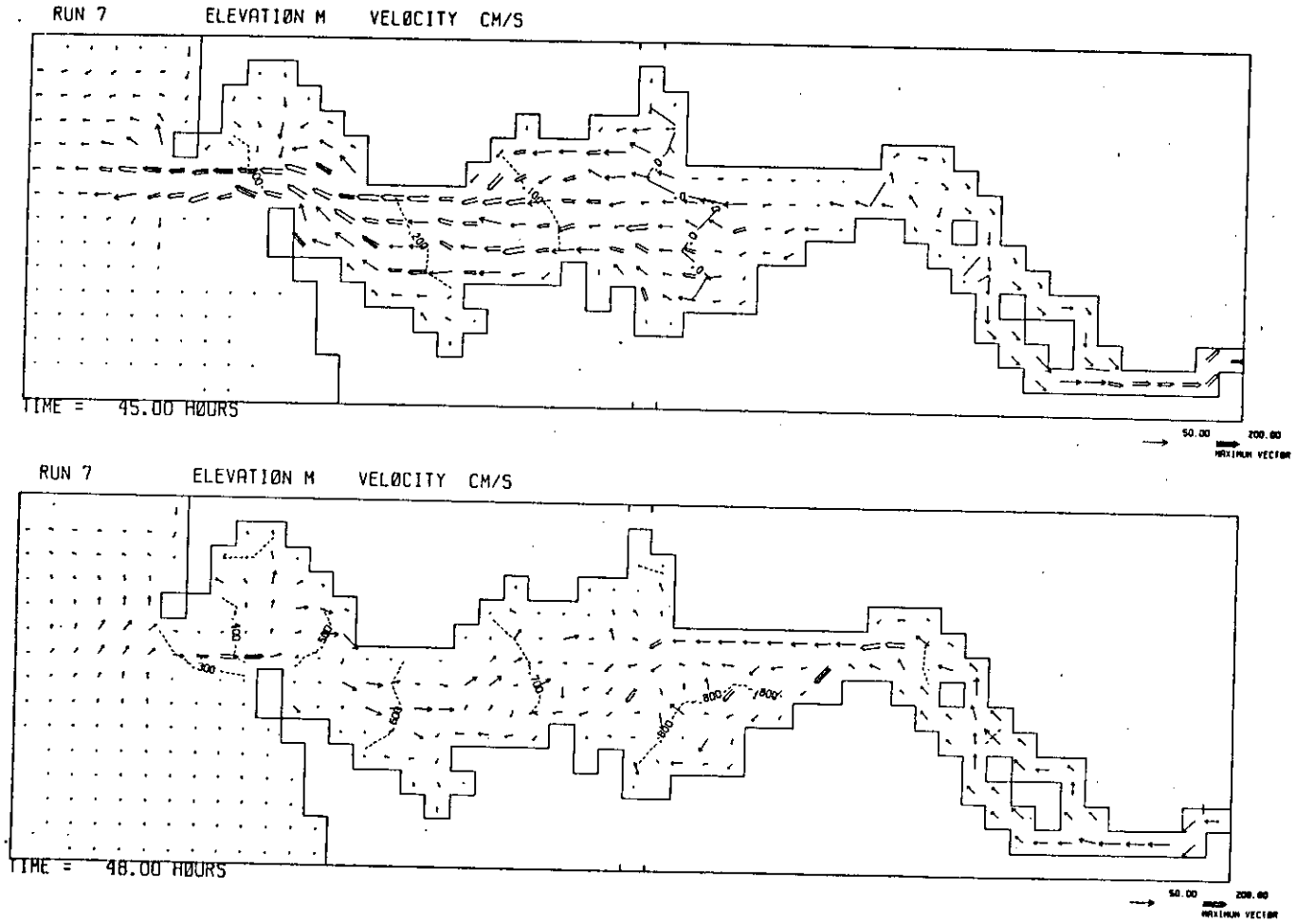


Figure 7. Map of depth-mean current vectors and contours of water levels for 45 and 48 hours.

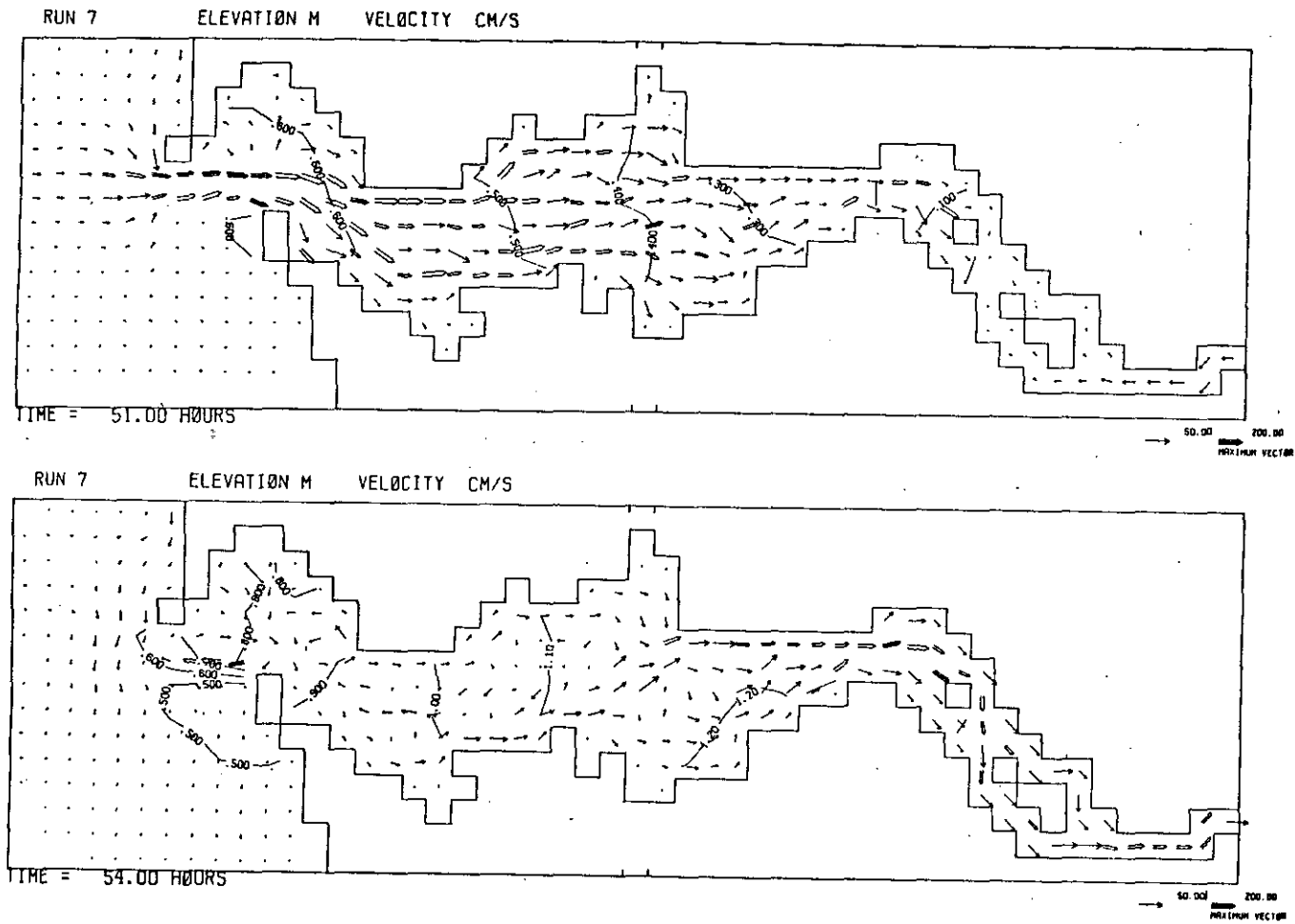


Figure 8. Map of depth-mean current vectors and contours of water levels for 51 and 54 hours.



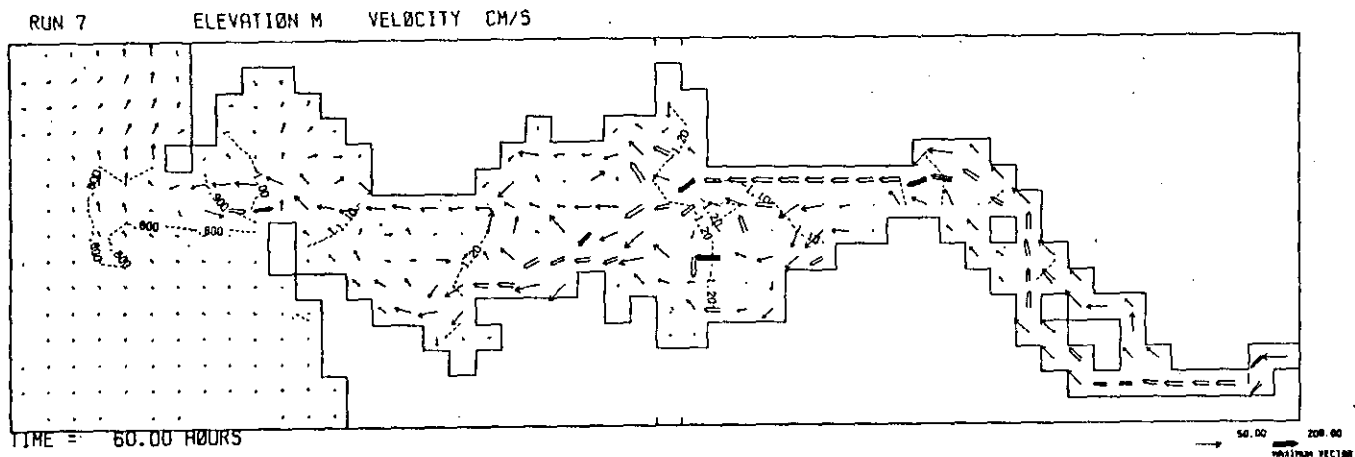
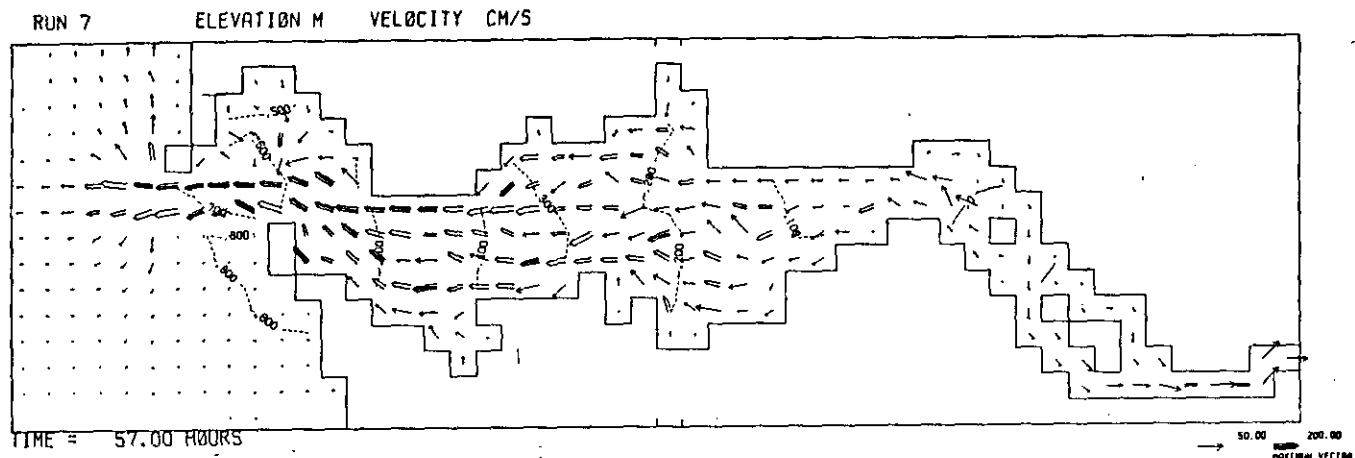


Figure 9. Map of depth-mean current vectors and contours of water levels for 57 and 60 hours.

are also in different directions in two channels on either side of Tenasillahe Island.

#### 60 hours (Figure 9)

At 60 hours, ebb is now well established in the eastern estuary and the main channel as far as Astoria. Current patterns are confused in Grays and Cathlamet Bays. In Baker Bay, the weak ebb appears to be partially feeding inflow into the bay. While a weak ebb continues in the deep entrance channel, a strong flood is apparent along the channel side of the south jetty.

The descriptions above have attempted to highlight some aspects of the tidal circulation in the Columbia River Estuary. The main result of studying the circulation patterns is the an appreciation of spatial variability of currents in the many different channels, shallow regions, and around islands at different tidal stages. The complex circulations in the bays are not well resolved with this grid, and studies of these regions using finer resolution grids are needed. A more quantitative discussion of tidal amplitudes and phases is given below in Section 3.3.

The maps of current vectors are useful for accessing the strength of the currents at various stages of the tide. However, it is also useful to determine the volume transports in order to determine where the major conveyance of volume occurs. Figure 10 shows the volume transports per unit width for each cell (i.e., to obtain volume transports the vector magnitudes should be multiplied by  $\Delta x$ ), corresponding to maximum flood and ebb at mouth. It is evident that the major volume flows occur in the deeper channels. The North Channel (Chinook Point to Megler) has larger tidal volume transports through the Navigation Channel off Astoria. This difference (about a factor 2 at the Astoria-Megler Bridge ) will be shown to be important for salt intrusion processes in Volume II. The peripheral bays have very small transports. An exception is the Grays Bay channel connecting Harrington Point with the North Channel at Point Ellice. In the entrance channel, the majority of the volume transport is on the north side of the channel for both ebb and flood. These results indicate that the estuary could be schematized by a channel network which would account for the majority of the tidal volume transports even though the sandflats and other shallow areas would be neglected.

### 3.2 COMPARISON WITH DATA

#### 3.2.1 Tidal Heights

The accuracy of the tidal simulations can be assessed by comparison with the CE data. Figures 11, 12, and 13 show the simulated tide over a period of  $7\frac{1}{2}$  days plotted on the same axes as the data from the tide gauges. The time series are obtained from the model output for the nearest grid point to the appropriate tide gauge. Means are removed from the data to remove the discrepancies due to the varying datum levels. In all these comparison figures (11-18), the ordinate axis on the lowest plot applies to all the other plots above it. The horizontal axis on each plot correspond to the center of the ordinate axis.

19

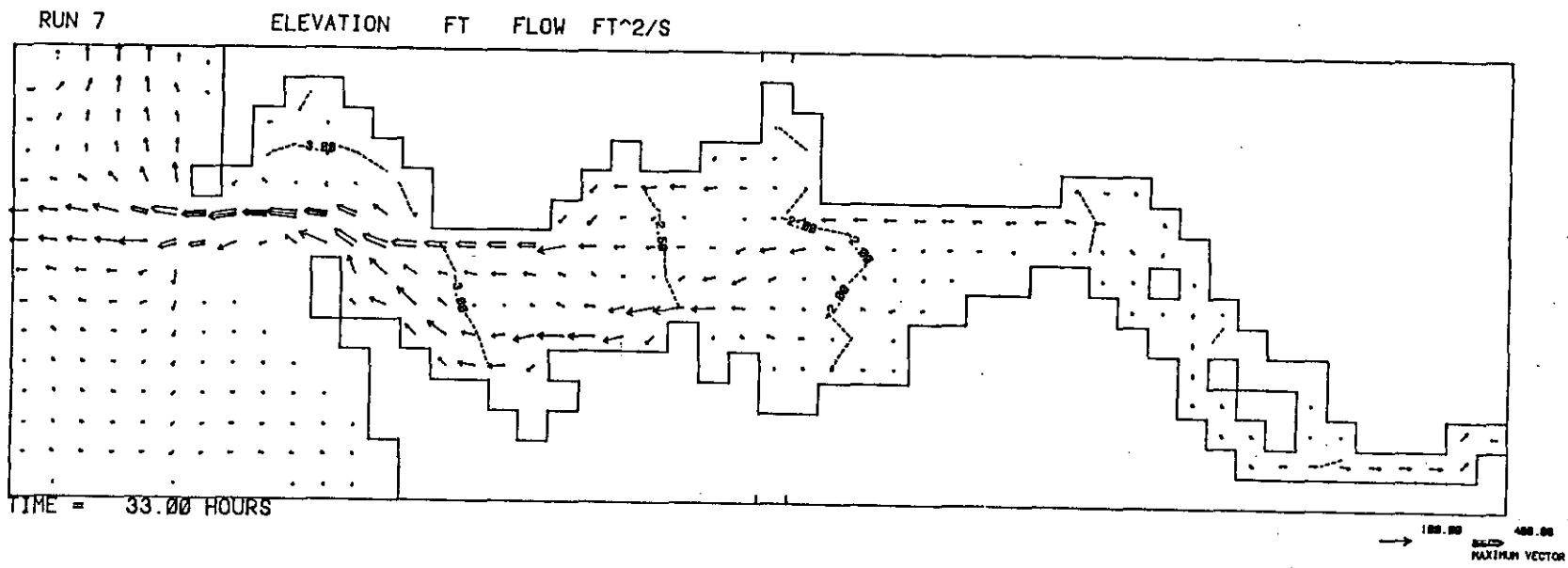


Figure 10a. Volume transports per unit width (ft<sup>2</sup>/s) and elevations (ft) for 33 hours (ebb tide).

20

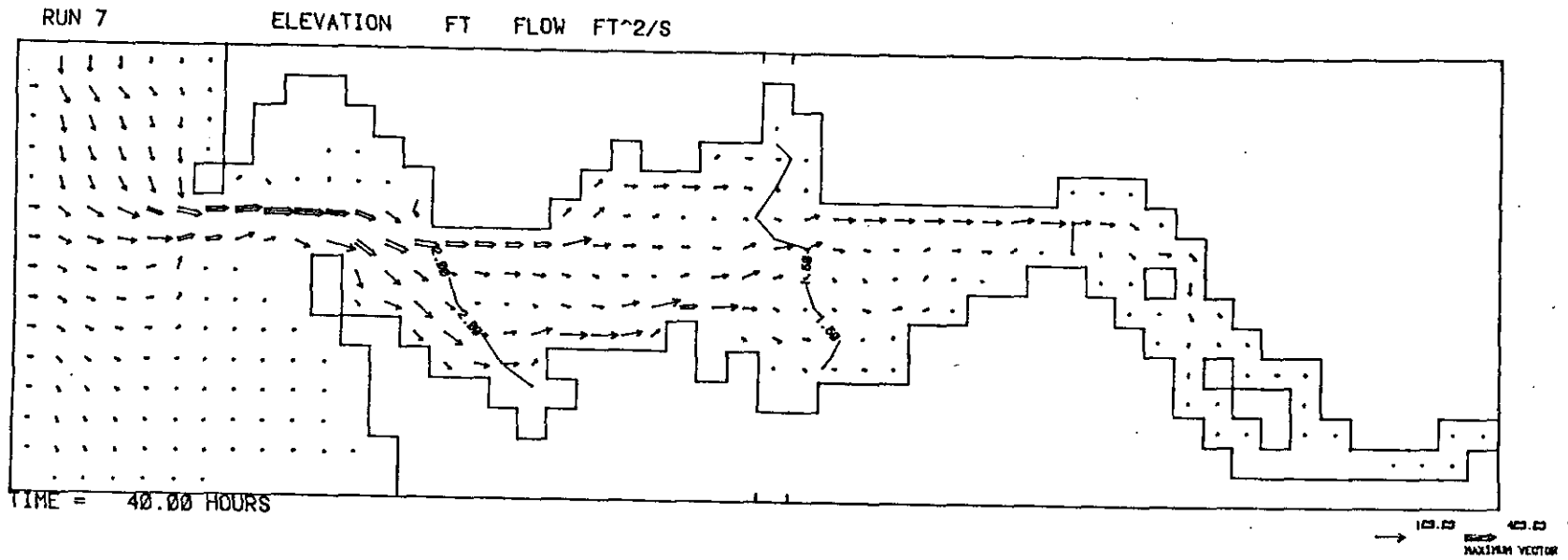
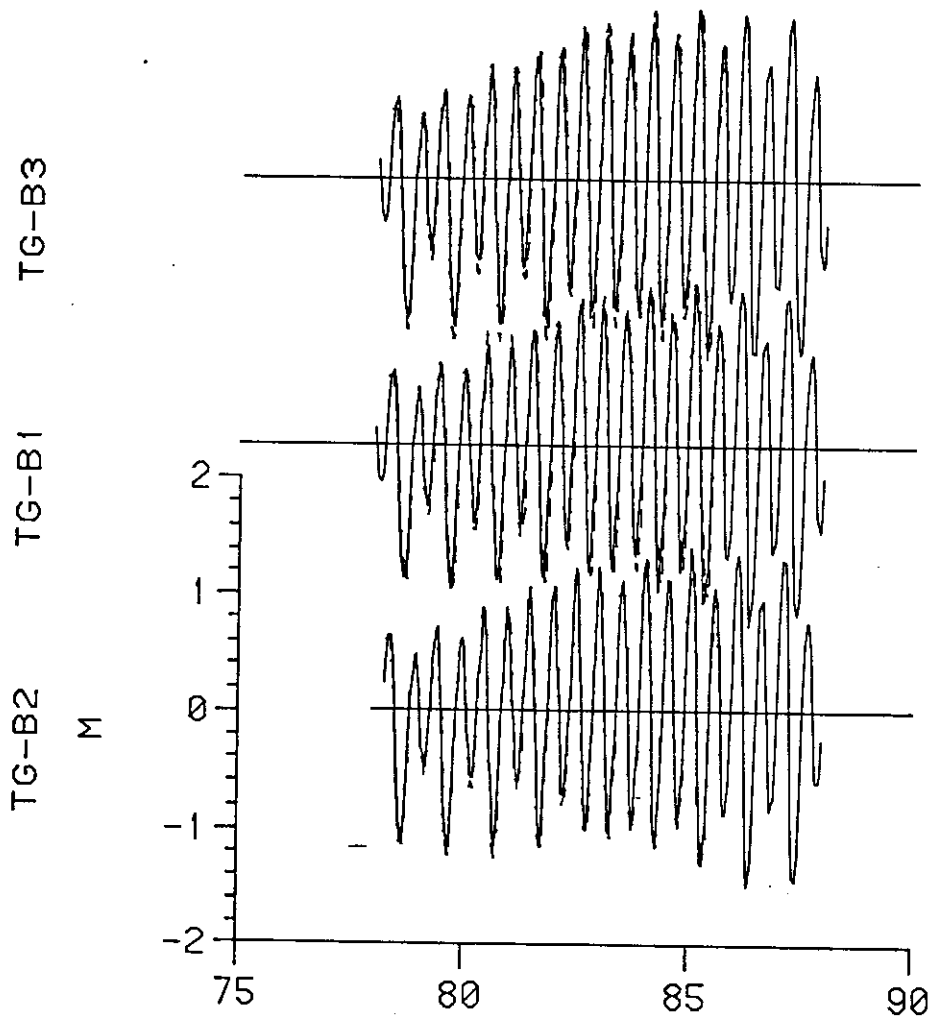
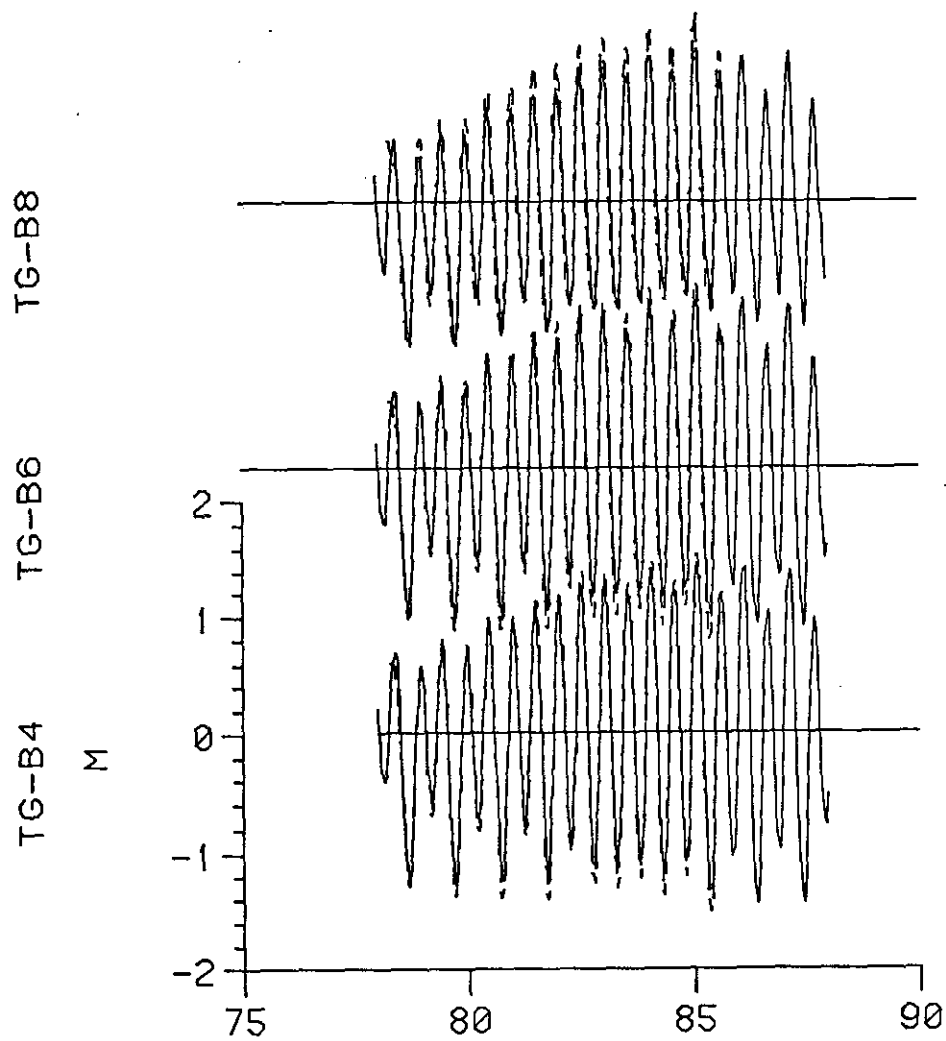


Figure 10b. Volume transports per unit width (ft<sup>2</sup>/s) and elevations (ft) for 40 hours (flood tide).



JULIAN DAYS 1978  
 DAY 75 IS 3/16/1978 U-COMPONENT

Figure 11. Observed water level with means removed for the indicated tide gauges (solid line). Superimposed are the computed water levels from the nearest grid point to the gauge (dashed line).



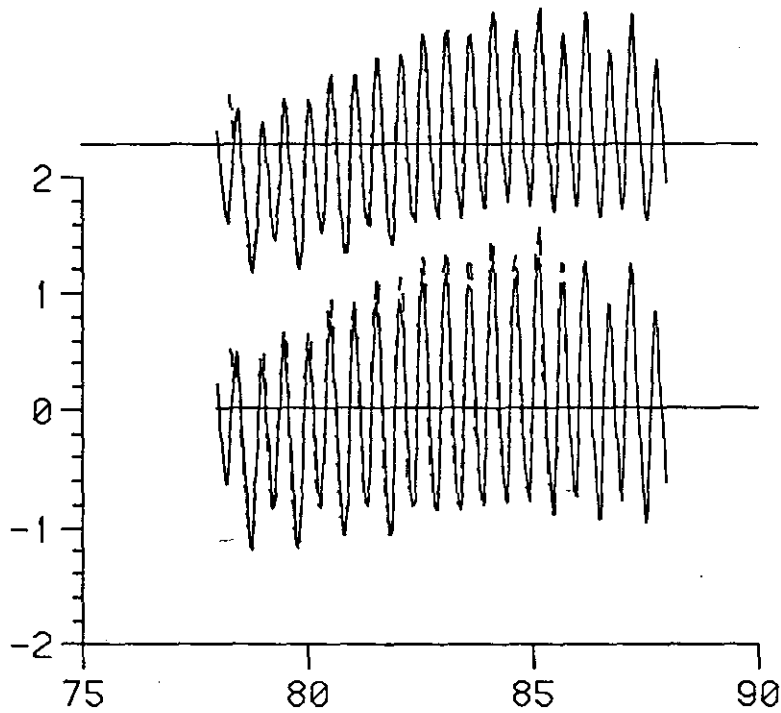
JULIAN DAYS 1978  
 DAY 75 IS 3/16/1978 U-COMPONENT

Figure 12. Observed water level with means removed for the indicated tide gauges (solid line). Superimposed are the computed water levels from the nearest grid point to the gauge (dashed line).

TG-B10

TG-B9

M



JULIAN DAYS 1978

DAY 75 IS 3/16/1978 U-COMPONENT

Figure 13. Observed water level with means removed for the indicated tide gauges (solid line). Superimposed are the computed water levels from the nearest grid point to the gauge (dashed line).

Comparison of simulated tide record at Jetty A (B2) with the data shows that the procedure for backing the tide record off to the seaward boundary for the input boundary conditions succeeds fairly well, with the phases at Jetty A being accurate, but with small amplification of the signal being observed. The Ilwaco tide gauge (B1) in Baker Bay shows good agreement (Figure 11), except for some phase error where the observation precedes the simulation at low tide. NMFS Pier tide gauge (B3) record is well reproduced, as is the record at Astoria (B4, Figure 12) where there is slight overshoot at high and low water.

Proceeding up estuary, the Tongue Point and Skamokawa gauges, B6 and B8, respectively, show good phase agreement between observed and simulated records with the simulation low waters slightly preceding the observations. The Bradwood gauge (B9) simulated record is a little better than B8, and of course the Eagle Cliff gauge is used as an input boundary condition, so the correspondence in Figure 11 is exact.

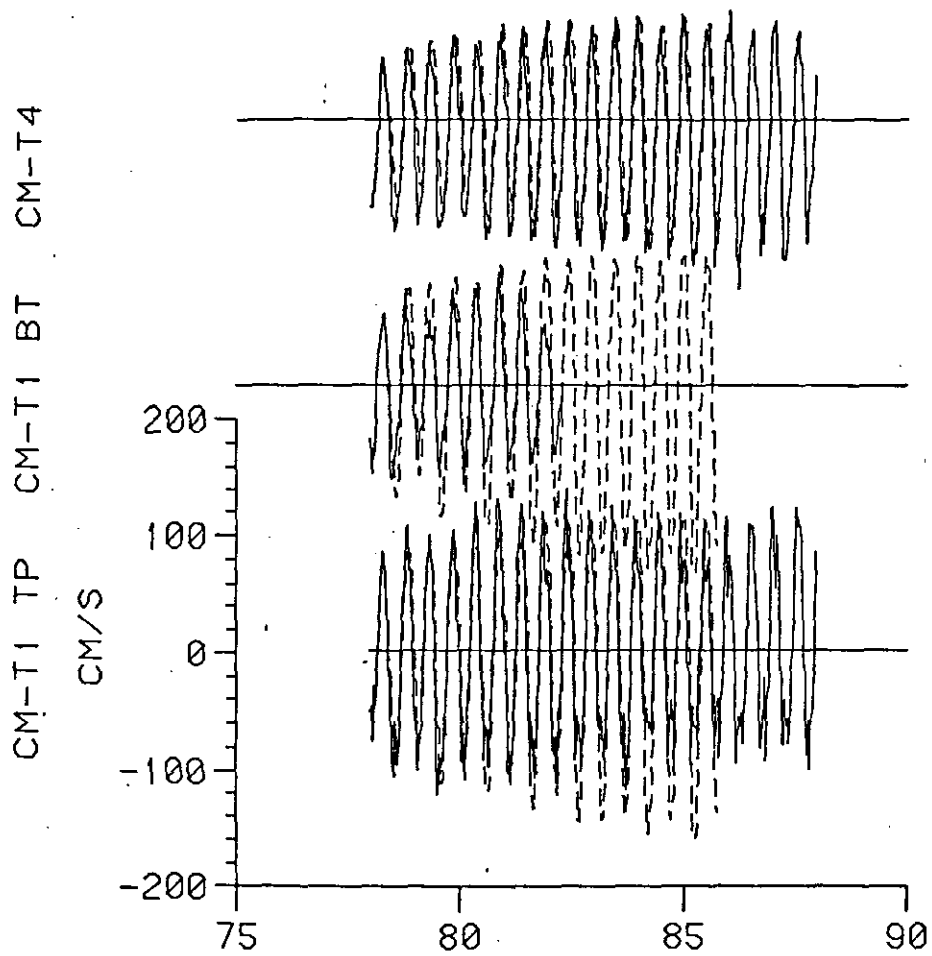
A general observation on the water level records is that there are the strong diurnal inequalities in the lower estuary which diminish upstream, but also change during the spring-neap cycle, being relatively more prominent at neaps than at springs.

### 3.2.2 Currents

Comparisons of simulated current records and observations are shown in Figures 14-18, where U component refers to EW or x direction, with x positive to the east, and V refers to NS or y direction, with y positive to the north. In construction of the simulated time series from the model output, both U and V are averaged over adjacent cell faces to produce a value at the center of the cell which is closest to the current meter station. The simulated currents are depth-averaged currents which represent flow through a cell face which has width of 1.52 km. These simulated currents are being compared to point measurements made by a current meter, usually at mid-depth; therefore some discrepancies are to be expected, and agreement is not expected to be as good as with observed and simulated water level time series. Also, the comparison is being made for NS and EW components and not with axes aligning with the channels.

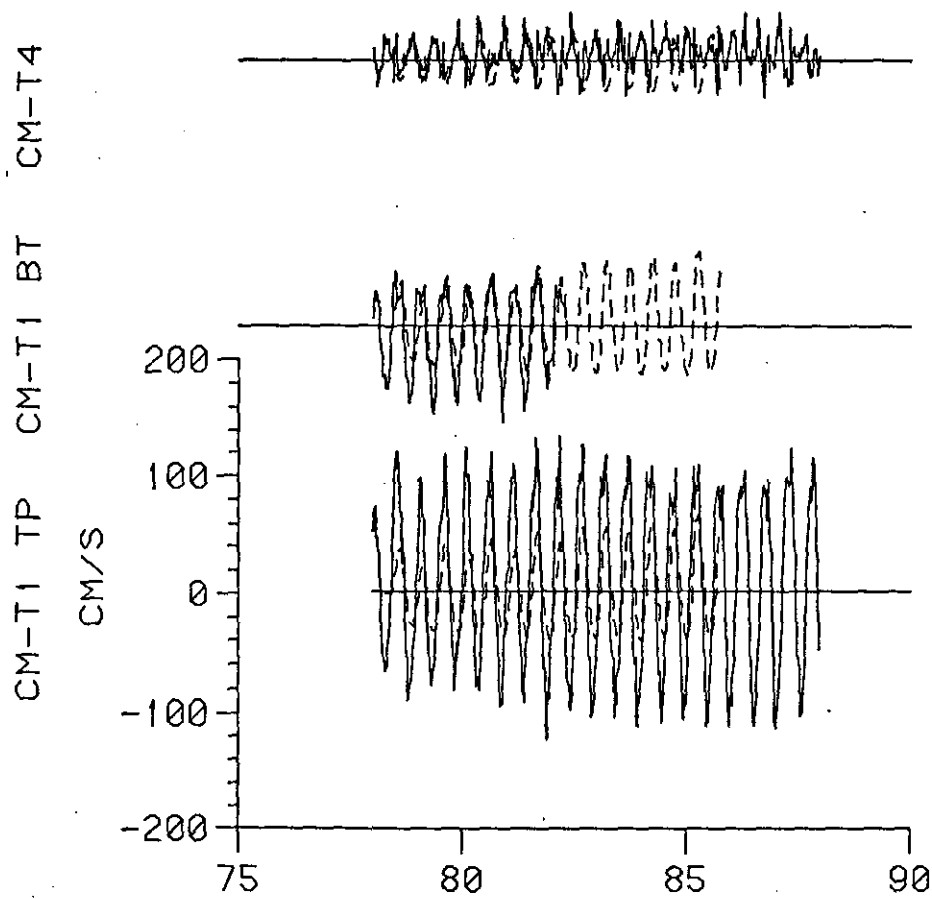
Figure 14 shows the comparison for stations T1 (Little Sand Island) and T4 (Cliff Point). Current magnitudes compare quite well, with differences between U and V component magnitudes in the T1 surface comparison being probably due to differences in the principal axes of measured and simulated currents. The depth-mean simulated currents at T1 compare fairly well in phase with both surface and bottom meters, indicating that phasing differences between top and bottom are small for tidal currents and the depth-mean representation is a reasonable approximation. At both T1 and T4, the measured peak ebb and flood velocities slightly precede the simulated peak currents.

Station T7 (Tansy Point, south main channel) shows better agreement in phase between simulation and observations than at T1, but the peak magnitudes are not in as good agreement at the surface meter. The depth-mean current is in quite good agreement with the T2 bottom meter.



JULIAN DAYS 1978  
 DAY 75 IS 3/16/1978 U-COMPONENT

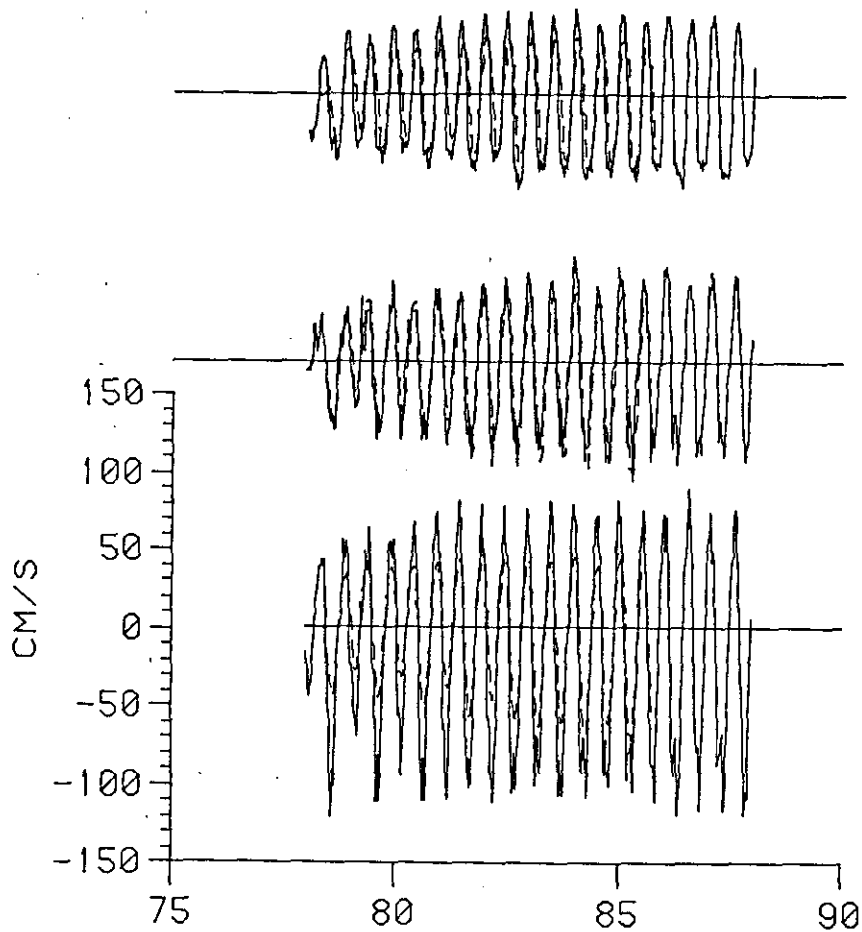
Figure 14: Observed currents (solid line) and computed depth-mean currents (dashed line) for the indicated stations. U component refers to x or E direction.



JULIAN DAYS 1978  
 DAY 75 IS 3/16/1978 V-COMPONENT

Figure 14b. Observed currents (solid line) and computed depth-mean currents (dashed line) for the indicated stations. V component refers to y or N direction.

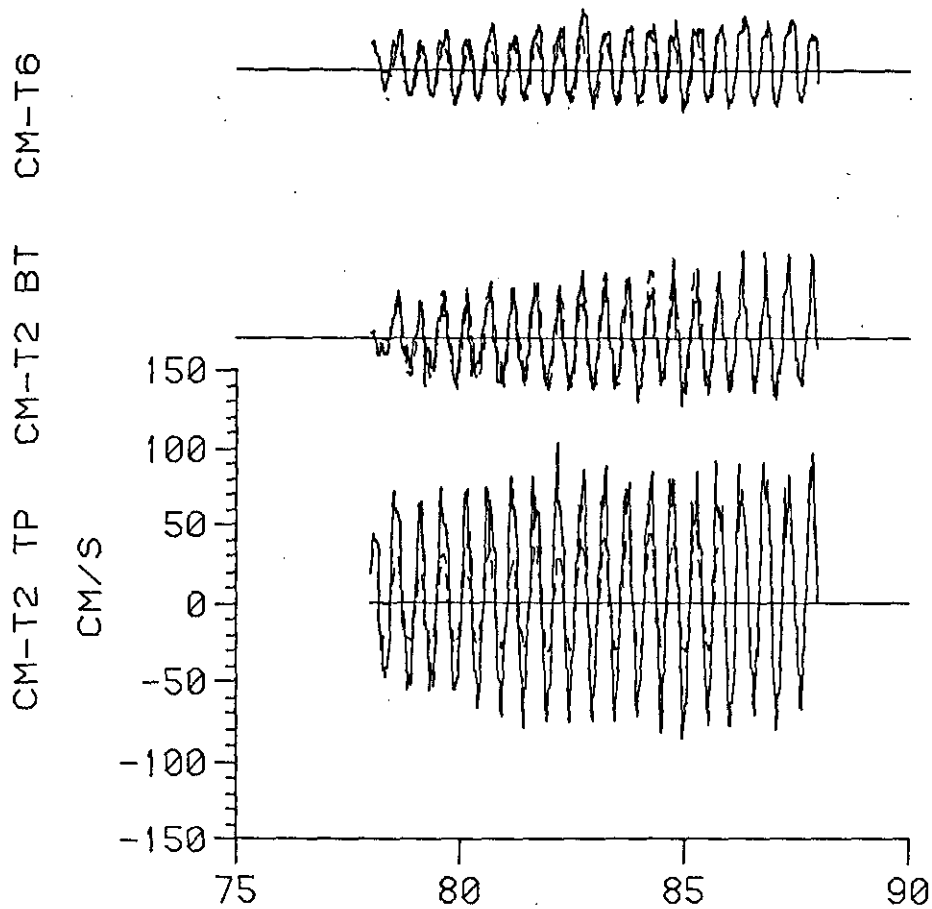
CM-T2 TP CM-T2 BT CM-T6



JULIAN DAYS 1978

DAY 75 IS 3/16/1978 U-COMPONENT

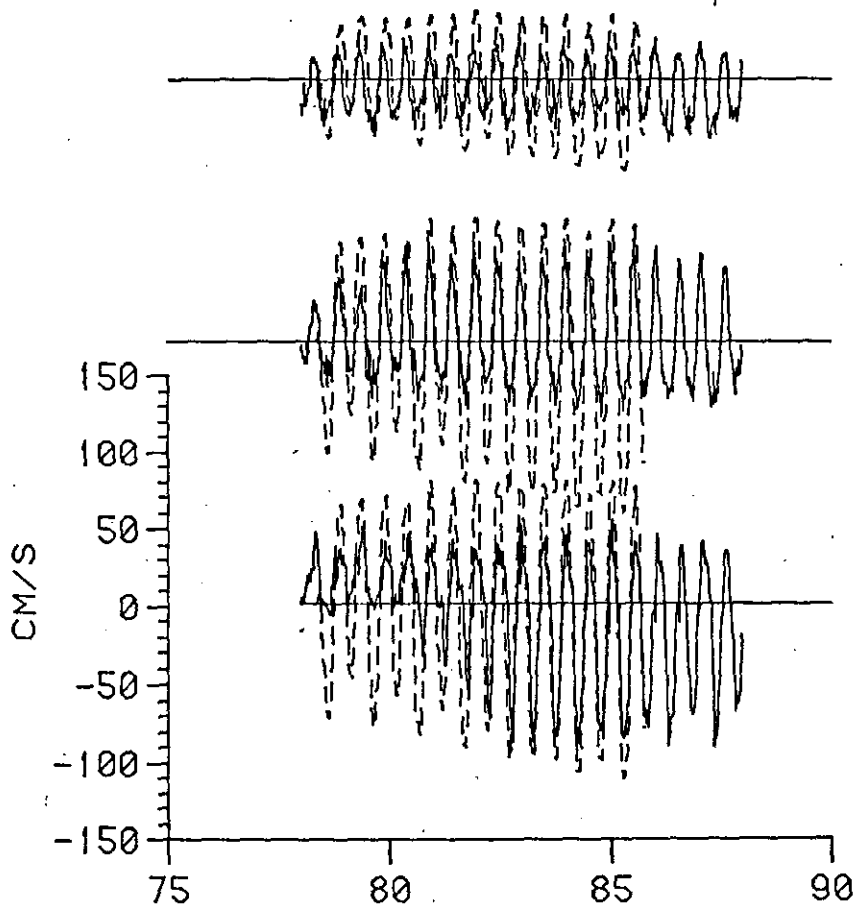
Figure 15a. Observed currents (solid line) and computed depth-mean currents (dashed line) for the indicated stations. U component refers to x or E direction and V component to y or N direction.



JULIAN DAYS 1978  
 DAY 75 IS 3/16/1978 V-COMPONENT

Figure 15b. Observed currents (solid line) and computed depth-mean currents (dashed line) for the indicated stations. U component refers to x or E direction and V component to y or N direction.

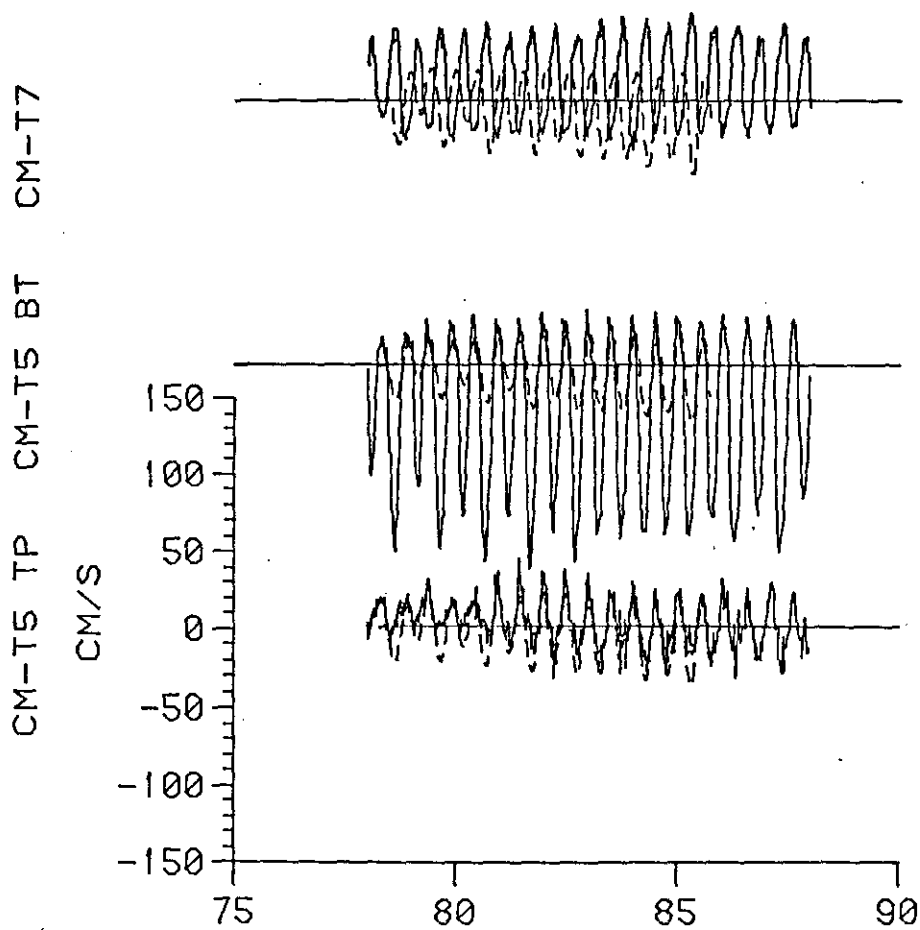
CM-T5 TP CM-T5 BT CM-T7



JULIAN DAYS 1978

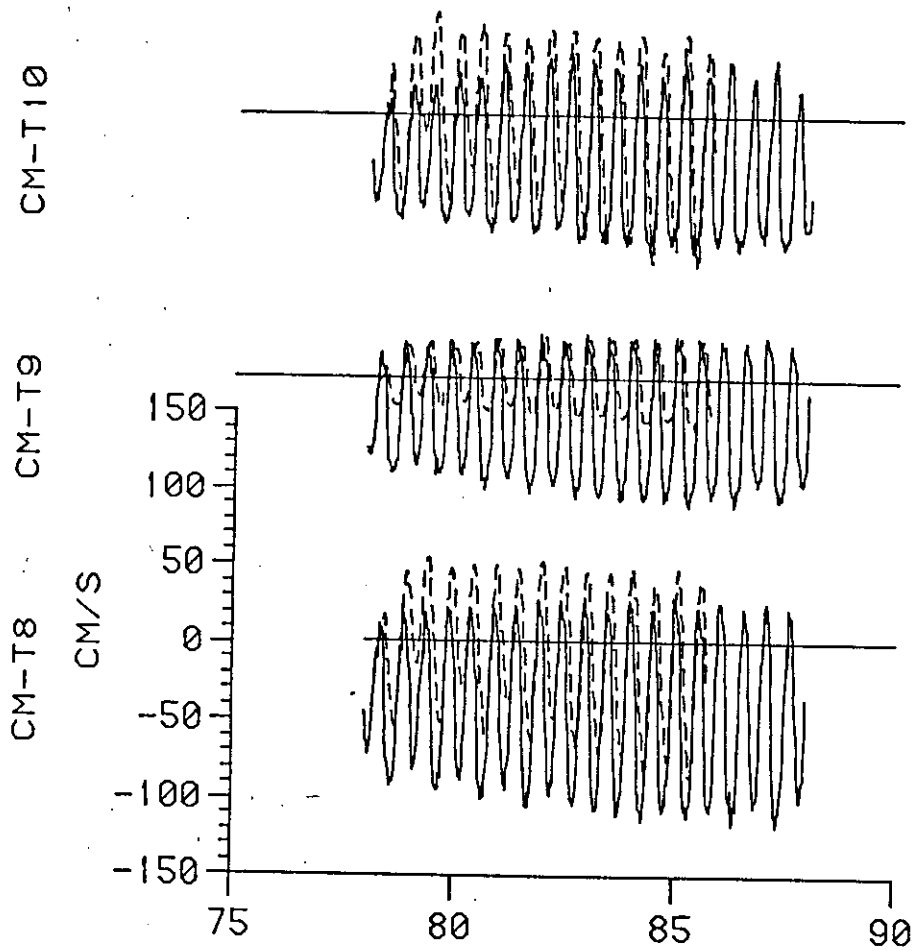
DAY 75 IS 3/16/1978 U-COMPONENT

Figure 16a. Observed currents (solid line) and computed depth-mean currents (dashed line) for the indicated stations. U component refers to x or E direction and V component to y or N direction.



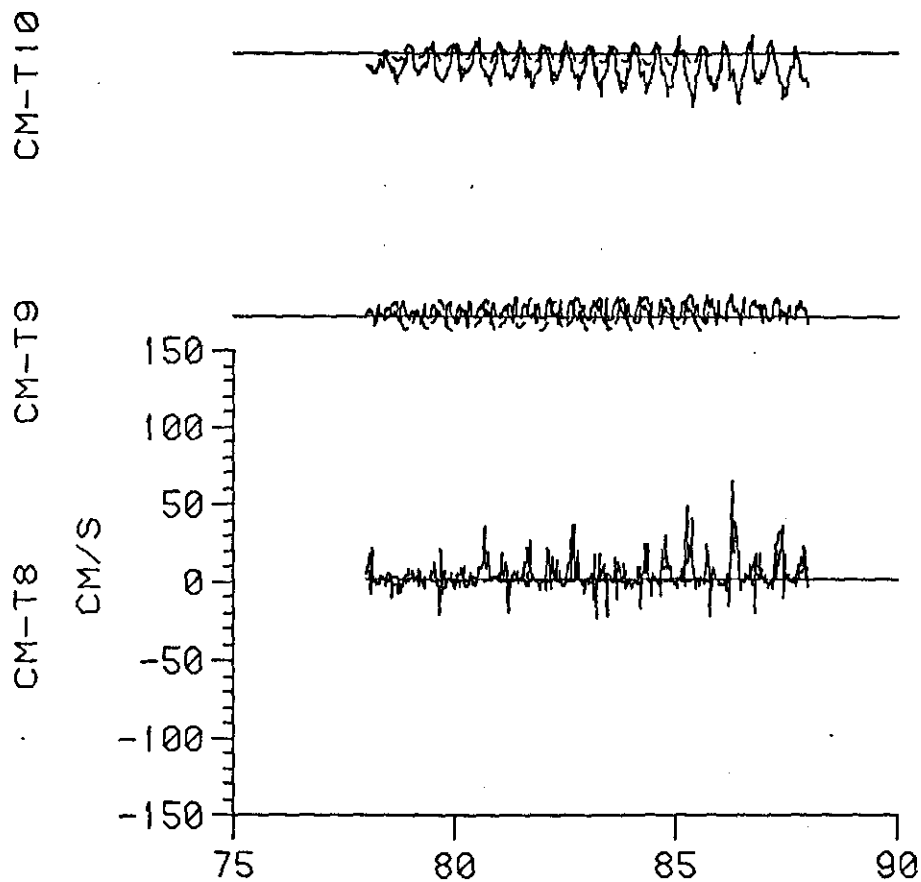
JULIAN DAYS 1978  
 DAY 75 IS 3/16/1978 V-COMPONENT

Figure 16b. Observed currents (solid line) and computed depth-mean currents (dashed line) for the indicated stations. U component refers to x or E direction and V component to y or N direction.



JULIAN DAYS 1978  
 DAY 75 IS 3/16/1978 U-COMPONENT

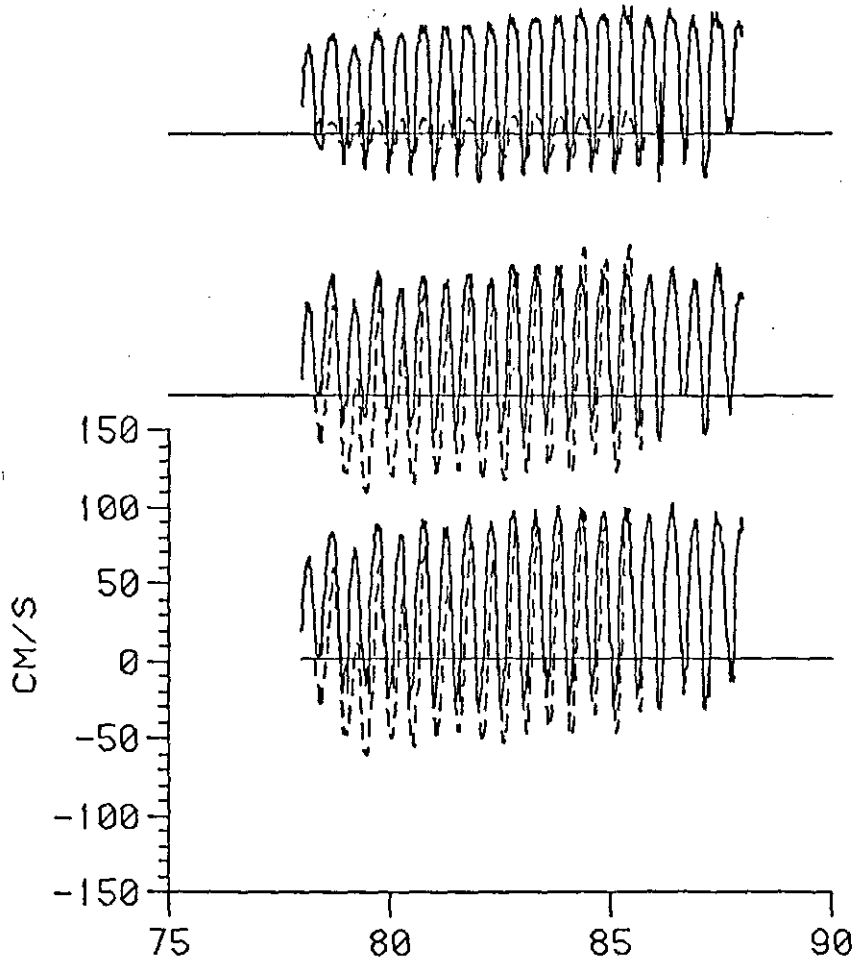
Figure 17a. Observed currents (solid line) and computed depth-mean currents (dashed line) for the indicated stations. U component refers to x or E direction and V component to y or N direction.



JULIAN DAYS 1978  
 DAY 75 IS 3/16/1978 V-COMPONENT

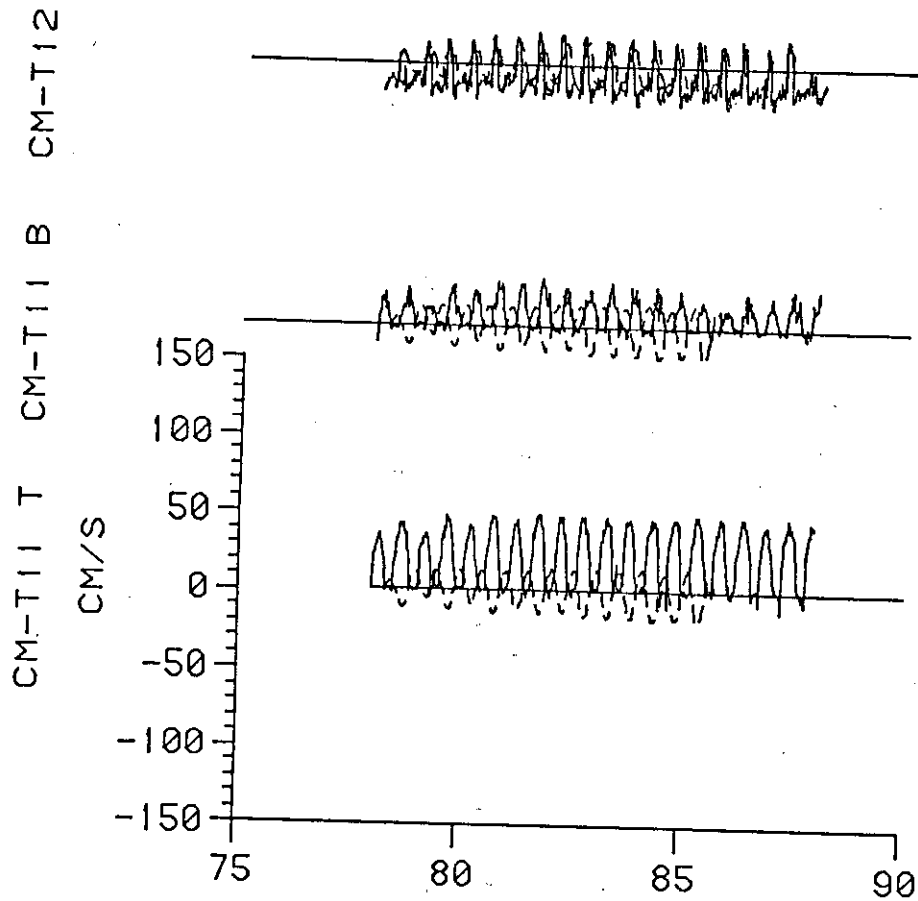
Figure 17b. Observed currents (solid line) and computed depth-mean currents (dashed line) for the indicated stations. U component refers to x or E direction and V component to y or N direction.

CM-T11 T CM-T11 B CM-T12



JULIAN DAYS 1978  
DAY 75 IS 3/16/1978 V-COMPONENT

Figure 18a. Observed currents (solid line) and computed depth-mean currents (dashed line) for the indicated stations. U component refers to x or E direction and V component to y or N direction.



JULIAN DAYS 1978  
 DAY 75 IS 3/16/1978 U-COMPONENT

Figure 18b. Observed currents (solid line) and computed depth-mean currents (dashed line) for the indicated stations. U component refers to x or E direction and V component to y or N direction.

Observations and simulation agree well for the mid-depth meter in the Cathlamet Bay North Channel and station T6 (Figure 15), though again the observations slightly lead the simulated currents. Station T9 in the Woody Island Channel, also shows good phase agreement (Figure 17), though the magnitudes do not agree as well. However, this lack of agreement between observation and simulation is probably due to the inadequate grid resolution of the Cathlamet Bay bathymetry.

The stations in the main channel (T5, T7, T8 and T10) show varying degrees of agreement for the simulation, the best being at T10 for amplitude and T5 for phase. The large pulses of negative V velocity on the ebb tide are difficult to explain as they are approximately perpendicular to the channel. Current meter station T7 is positioned where there are influences from a number of secondary channels, so lack of agreement is not too surprising (Figure 16). The currents at T8 and T10 start to show the influence of the riverflow in the negative displacement of the observed current curves.

The current meter record at the junction of the Clifton channel and the main channel at the southern tip of Tenasillahe Island is poorly simulated again because of poor resolution of the grid (Figure 18). The current meter levels at T11 in the main channel have much better amplitude, though the ebb peaks (V component) are more skewed in the simulation than the observations. Again there are very small phase differences between surface and bottom observations.

Comparison of the 7½ day simulation with the CE observations indicates generally good agreement, with some room for improvement in amplitude and phases between Cathlamet Bay and Puget Island. It is likely that the deeper channels in this region should have a little more frictional dissipation for a closer agreement with the observations, though the grid resolution and inaccurate bathymetry may also be important.

### 3.3 HARMONIC ANALYSIS OF MODEL RESULTS

One quantitative measure of the model results presented above is to compare amplitudes and phases of observed and simulated tidal elevations and currents. The harmonic method extracts, from time series of hourly observations, the amplitudes and phases of constituents at tidal frequencies. The number of tidal constituents resolved depends primarily on the length of the time series. The amplitudes and phase of the constituents whose frequencies are determined from astronomical criteria, are determined from least square fitting of sine waves to the demeaned observations. The tidal harmonic analysis programs of Foreman (1977, 1978), which are based on the methods of Godin's treatise (Godin, 1972), were used in this study similarly to Jay (1984) for the current meter and tidal height analyses performed for the CREDDP Current Studies work unit.

The model runs described above produced 7½ day long time series of elevations and two components of current velocity for all grid cells which were not land. These time series were harmonically analyzed and the results are given in Table 1. The amplitudes and phases of the

Table 1  
Comparison of the Simulated and Observed  $M_2$  Tidal Constituents

	Model Results				Observations			
	Elevation		Depth Mean Currents		Elevation		Mid-Depth Currents	
	Amplitude (m)	Phase (Degrees)	Amplitude (cm/s)	Phase (Degrees)	Amplitude (m)	Phase (Degrees)	Amplitude (cm/s)	Phase (Degrees)
Navigation Channel								
RM 0	0.93	12.85	139.4	324.3	0.79	6	130	314 ± 10
RM 3	0.97	18.56	159.3	332.4	0.83	11	130	319 ± 10
RM 5	1.02	24.79	91.8	322.8	0.87	15	120	324 ± 10
RM 10	1.08	31.78	53.7	343.4	0.94	23	80	334 ± 5
RM 15	1.10	38.55	80.5	1.9	0.96	31	90	349 ± 1
RM 20	1.12	46.56	45.9	14.1	0.94	40	80	354 ± 2
RM 25	1.07	58.49	61.8	46.4	0.91	48	70	4 ± 1
RM 30	1.07	58.49	66.1	46.4	0.87	57	70	14 ± 1
RM 35	0.98	65.71	49.7	63.4	0.80	64	-	-
RM 40	0.93	71.99	39.0	83.0	0.72	73	-	-
North Channel								
RM 5 (Sand Isle)	1.03	28.02	107.7	336.2	0.87	15	140	319 ± 15
RM 12 (Bridge)	1.06	35.69	106.2	335.8	0.95	26	140	329 ± 5
RM 15 (Knappton)	1.10	38.76	95.6	327.4	0.96	31	120	339 ± 2

\*Phase is in Greenwich angles, time zone = PST.

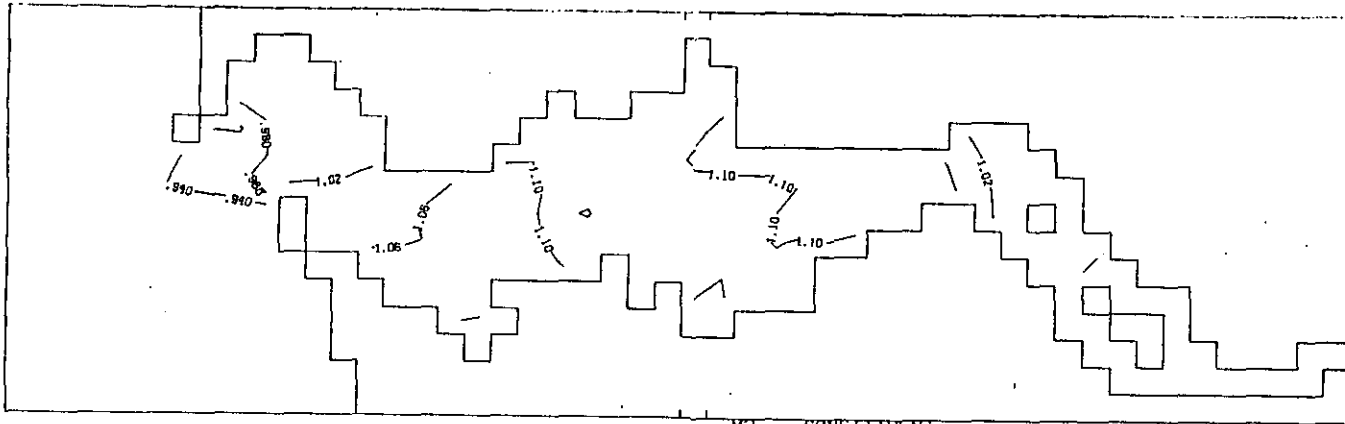
simulated currents and elevations are given as functions of river mile along the main Navigation Channel and along the North Channel between Little Sand Island and Knappton. Positive currents are directed upriver. The dominant  $M_2$  constituent (period 12.42 hours) is the only constituent well resolved by the short length of the model runs. The amplitude and phases of the tidal elevations and currents are taken from Jay (1984; sections 3.1 and 3.4). All available data were used to construct  $M_2$  amplitudes and phases as a function of River Mile for both the Navigation and North Channels. The bounds on the observed current phases are not error bounds but an indication of the top and bottom phase differences relative to the mid-depth values at the stations. Bottom currents lead the surface currents in the salt intrusion region. The simulated  $M_2$  tidal elevation amplitudes are larger than observed partly because the  $7\frac{1}{2}$  day period analyzed favors large spring tides. However, part of the difference is due to the small amplification of the tidal wave propagating across the model shelf region. Phase error at Jetty A is about  $6^\circ$  or 12 minutes which is almost within the error of the analysis method (Jay 1984). The observed and simulated tide amplifies and decays at about the same rate with maximum amplitudes occurring between RM 15 and 20. Phase differences between elevations and currents range from  $49^\circ$  at the mouth to about  $12^\circ$  at RM-30 for the simulation, whereas mouth phase differences are about  $52^\circ$  and at RM-30 about  $44^\circ$  for the observations. The change from a mixed standing-progressive tidal wave in the lower estuary (phase differences between  $0-90^\circ$ ) to a more progressive wave (phase differences near  $0^\circ$ ) occurs at a more western section of the estuary in the model than in the observations. This may be due to using an elevation boundary condition at Eagle Cliff and possible partial reflection of the computed tidal wave that may occur there.

To summarize the tidal wave characteristics calculated by the model the amplitude and phases for the  $M_2$  and  $K_1$  (period 23.93 hours) elevations are contoured in Figures 19 and 20. The co-range lines or contours of constituent amplitude and co-phase lines are shown in the plot. The phases are Greenwich phases relative to Pacific Standard Time (PST).

The semi-diurnal tide (the  $M_2$  constituent) dominates the tidal records and the contour plot of the amplitude and phase lines (Figure 19) show the partially progressive nature of the  $M_2$  tide. Amplification occurs between the mouth and the Grays Bay - Cathlamet Bay section and decreases from this point to Eagles Cliff ( $6^\circ$  of phase difference represent a time difference of 12.42 minutes). At the mouth, there are relatively large amplitude and phase changes occurring in the region of the South Jetty, indicating that applying a boundary condition with no cross-channel phase differences at the mouth may lead to some errors in this region.

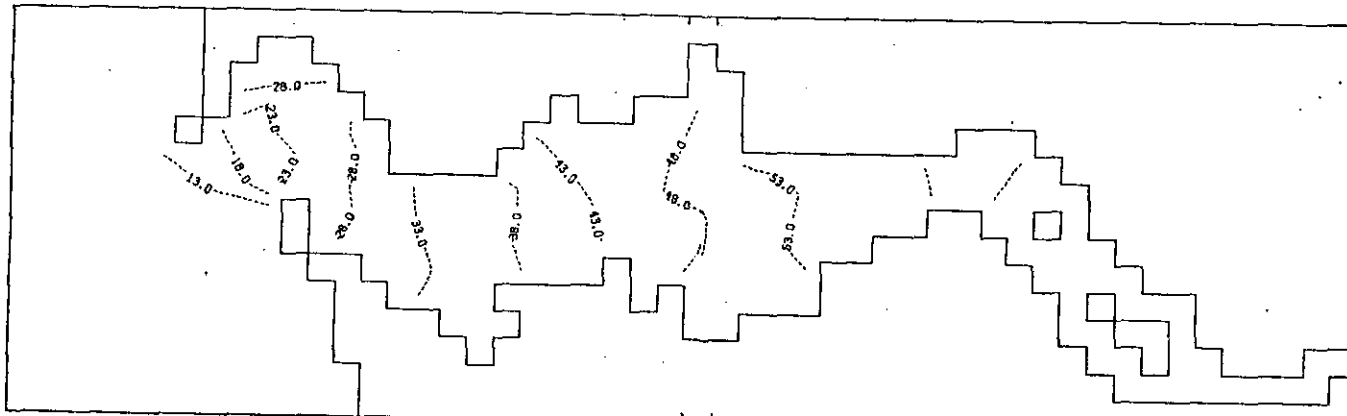
The  $K_2$  constituent results are not very accurate due to the short length of the model run. However, it is worth showing the results as an indication that the diurnal tidal wave behaves rather differently from the semi-diurnal tide. The  $K_1$  constituent amplitudes and phases (Figure 20) again show that this constituent progresses at a similar speed to the  $M_2$  ( $3^\circ$  phase difference = time difference of 11.97 minutes), but in

RUN 7.16.17



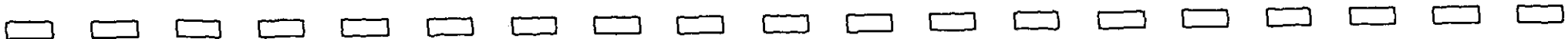
M2 CONSTITUENT  
TIDAL AMPLITUDE (M)

RUN 7.16.17



M2 CONSTITUENT  
TIDAL PHASE (DEG)

Figure 19. Co-range and co-phase lines for M2 tide. Result of harmonic analysis of simulated water levels.



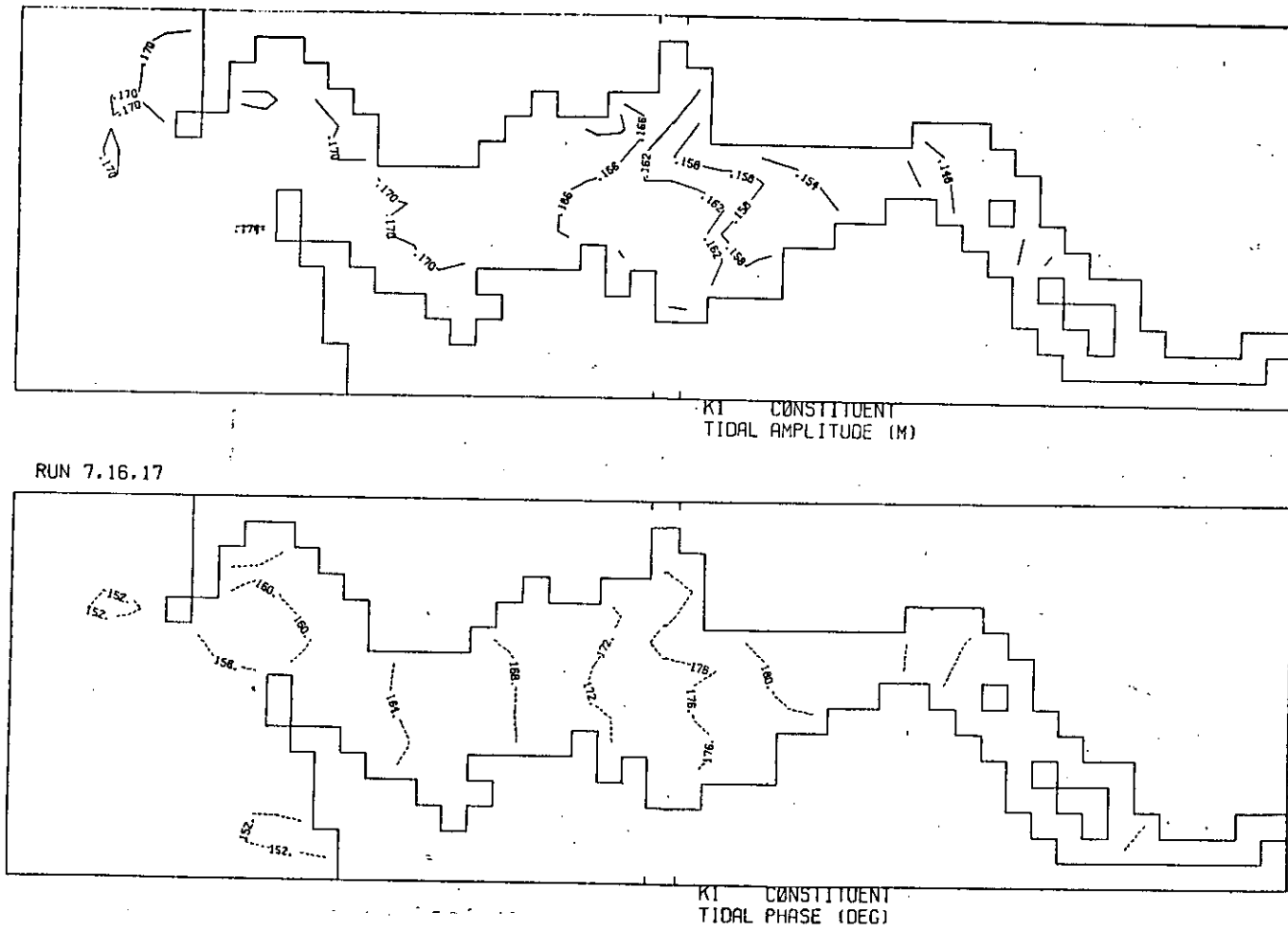
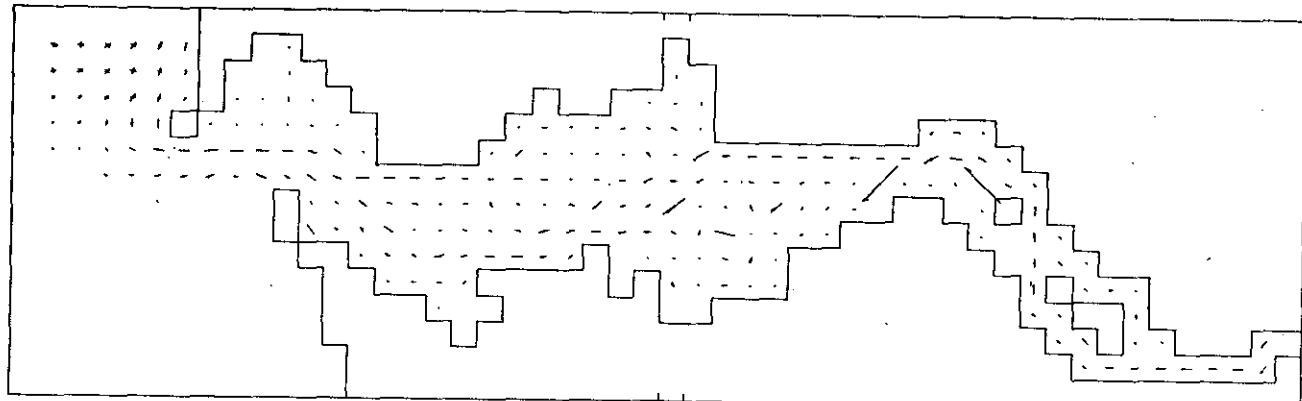


Figure 20. Co-range and co-phase lines for K1 tide.

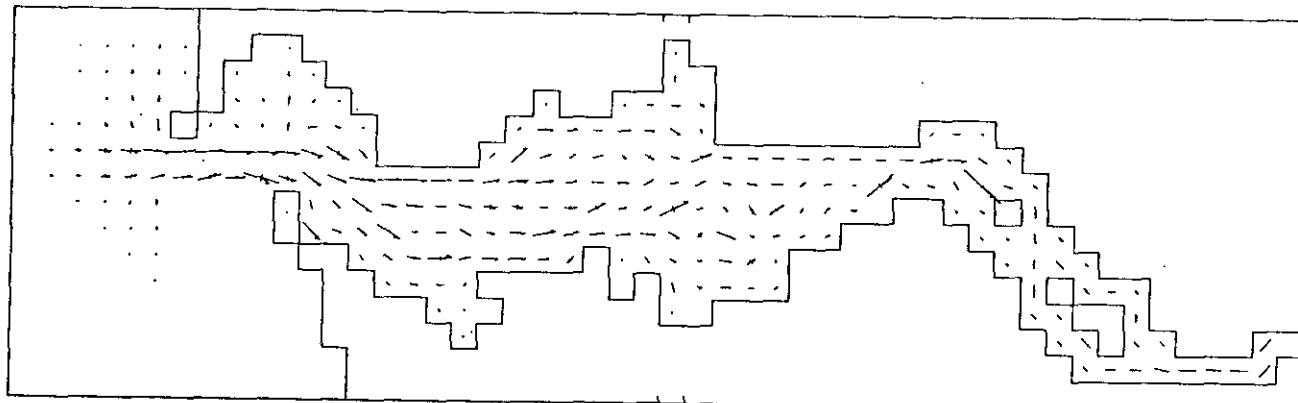
RUN 7.16.17



K1 CONSTITUENT  
CURRENT ELLIPSES (CM/S)

100.00  
MAXIMUM VECTOR

RUN 7.16.17



M2 CONSTITUENT  
CURRENT ELLIPSES (CM/S)

500.00  
MAXIMUM VECTOR

Figure 21. The principal axes of the tidal ellipses for the M2 and K1 tide. Result of harmonic analysis of simulated depth-mean currents.

this case the amplitudes uniformly decrease in the up-estuary direction. There is a relatively more rapid decrease in amplitude and a more rapid phase change in the Grays Bay - Cathlamet Bay region. Therefore, a possible model for the tidal response in the lower estuary is a mixed progressive-standing (current-elevation phase differences between  $0^\circ$  and  $90^\circ$ ) wave which partially reflects where the estuary narrows towards Skamokawa. The partial interference with the reflected wave is constructive, leading to amplification for the  $M_2$  and destructive for the  $K_1$ . Upstream of Skamokawa the transmitted wave is almost purely progressive with phase differences between currents and elevation being close to zero.

The currents are similarly analyzed, and axes of the  $M_2$  and  $K_1$  constituent tidal ellipses are shown in Figure 21. These give some idea of the energy of tidal currents as a function of position in the estuary and also the principal axes of the flow. Some parts of the estuary (e.g. the Clifton channel off the northern tip of Tenasillahe Island) show relatively larger amplitude currents than at surrounding grid points, thus these regions may be subject to increased erosion and sediment transport due increased bottom stresses and dispersion due to large horizontal velocity shears.

#### 3.4 RIVERFLOW AND WIND FORCING EXPERIMENTS

One of the most important uses of a circulation model is to study responses of the estuary to different types of forcing. In the sections above the most energetic motions, which are due to the tide, have been examined. However, the circulation due to the riverflow, which is a major component of tidal mean circulation, and circulations due to wind-forcing over the estuary and over adjacent shelf waters, are important as well, particularly for transport studies. Riverflow and wind driven circulation are difficult to study using observations alone, because current meter data are dominated by the strong tidal signal; therefore, a series of experiments were run with no tidal inputs to examine riverflow and circulations driven by constant winds.

The open boundary conditions are that constant riverflow is specified at the head (Eagle Cliff), while at the seaward boundary a radiation condition, modified by a normal flux condition, is applied. The latter condition allows free gravity waves to pass through the boundary with little reflection, and the normal flux condition allows water to pass through the boundary.

The formulation is

$$Z = \frac{U \cdot n}{(gd)^{1/2}} \text{ and } \frac{\partial U}{\partial n} = 0 \quad (4)$$

where:

U is the flow vector,  
 n is the unit normal, directed away from the water body, and  
 Z is the sea surface elevation

This boundary condition is much more satisfactory than the more usual  $Z = 0$ , in that spurious oscillations are less persistent, and the system reaches a steady state much faster. Note that these riverflow case boundary conditions are completely different from the tidal case discussed previously, where the elevations at the boundaries were specified as functions of time and the radiation condition (4) was not used.

The initial conditions for the riverflow run (run 8) are water levels set to zero everywhere and an annual average riverflow of 7,350  $m^3/s$  (25,9064 cfs), which produces a depth-mean velocity of 66 cm/s at Eagle Cliff. The riverflow is the annual average flow for the period 1970-1982 (Jay 1984). This initially imposed flow takes  $3\frac{1}{2}$  hours to reach ocean, which gives some indication of the mean flow transport time for the lower estuary. The estuary reaches steady state in about  $1\frac{1}{2}$  days, and the results for  $t=2\frac{1}{2}$  days are shown in Figure 22. It is noted these are depth-mean flows, and in reality salinity effects would be expected to modify the flows in the salt intrusion region. The Coriolis effect causes the flow to turn northwards after exiting the estuary.

This steady state riverflow circulation at  $t=60$  hours is now used as the initial condition for the wind experiments. At  $t=60$  hours, a wind of constant speed and direction is applied to the whole water body, including the shelf waters, and the model run to steady state. Results are presented for  $t=120$  hours,  $2\frac{1}{2}$  days after applying the wind stress. A typical time scale for wind fluctuations in the Pacific Northwest is 1-2 days (Hickey and Hamilton 1980). The wind speed used is 7 m/s which gives a wind stress of 2.8 dynes/cm<sup>2</sup> (coefficient of friction = 0.00475). In summer, the wind systems are dominated by the North American High and the prevailing wind is directed towards the south along the coast of the Pacific Northwest. In winter and spring, the weather is dominated by low pressure systems moving eastwards over the northeastern Pacific. Average winds in the winter tend to be directed towards the northeast. The circulations are discussed by run number below.

Run 8: Riverflow alone. (Figure 22)

The currents are seaward at all points with stronger flows in the channels. Note the substantial flows in the Cathlamet Bay channels and around Harrington Point into Grays Bay. At the Astoria bridge, there is more volume flow through the north channel than the south channel.

Run 9: Wind stress directed towards the south. (Figure 22)

On the shelf, southward currents are generated, typical of wind driven upwelling flow. There is an associated set down at the estuary mouth of 2 cm which is communicated all the way to Skamokawa. In the estuary the wind stress acts more directly causing a set down of water levels in the northern bays and relative set ups on the southern shore, particularly in Cathlamet Bay. The effect is to reverse the current directions, compared to Run 8, on the eastern sides of Grays Bay and Baker Bay, and to reduce the flow in the northern main channels between Grays Bay and Baker Bay at the expense of increased flow in the southern main channel.

The eddy-like circulation occurring on the southern seaward boundary of the shelf region is probably an anomalous circulation caused by the boundary conditions. Moving the seaward boundary to twice the distance offshore produces a similar eddy but with a shift in position indicating that it is an effect of the boundary conditions.

Run 10: Wind stress directed towards the east. (Figure 23)

In this case, the wind produces a weak southerly circulation on the shelf with only small change in water level at the mouth over the no-wind case (Run 8). However, within the estuary the effect is dramatic, with a raising of water levels throughout the estuary inducing a 20cm rise at Eagle Cliff. The along-estuary water slope is steepened over the no-wind case. The effect on the currents shows the outflows in the channels in the western estuary are intensified by up-estuary flows in the shallow regions. Currents are confused in Cathlamet Bay and there is southeasterly flow along the eastern shore of Baker Bay. There is also flow into the estuary on the shallow south side of the entrance channel.

Run 11: Windstress directed towards the north (Figure 23)

This is the opposite case to Run 9, with strong northward currents on the shelf and a set up of water level at the coast, which is seen in all water levels as far as Skamokawa. In the estuary, there is strong north-south cross-estuary slope which tends to generate northward flow out of the southern bays. There is an increase of flow in the northern main channels at the expense of weaker flows in the southern main channel.

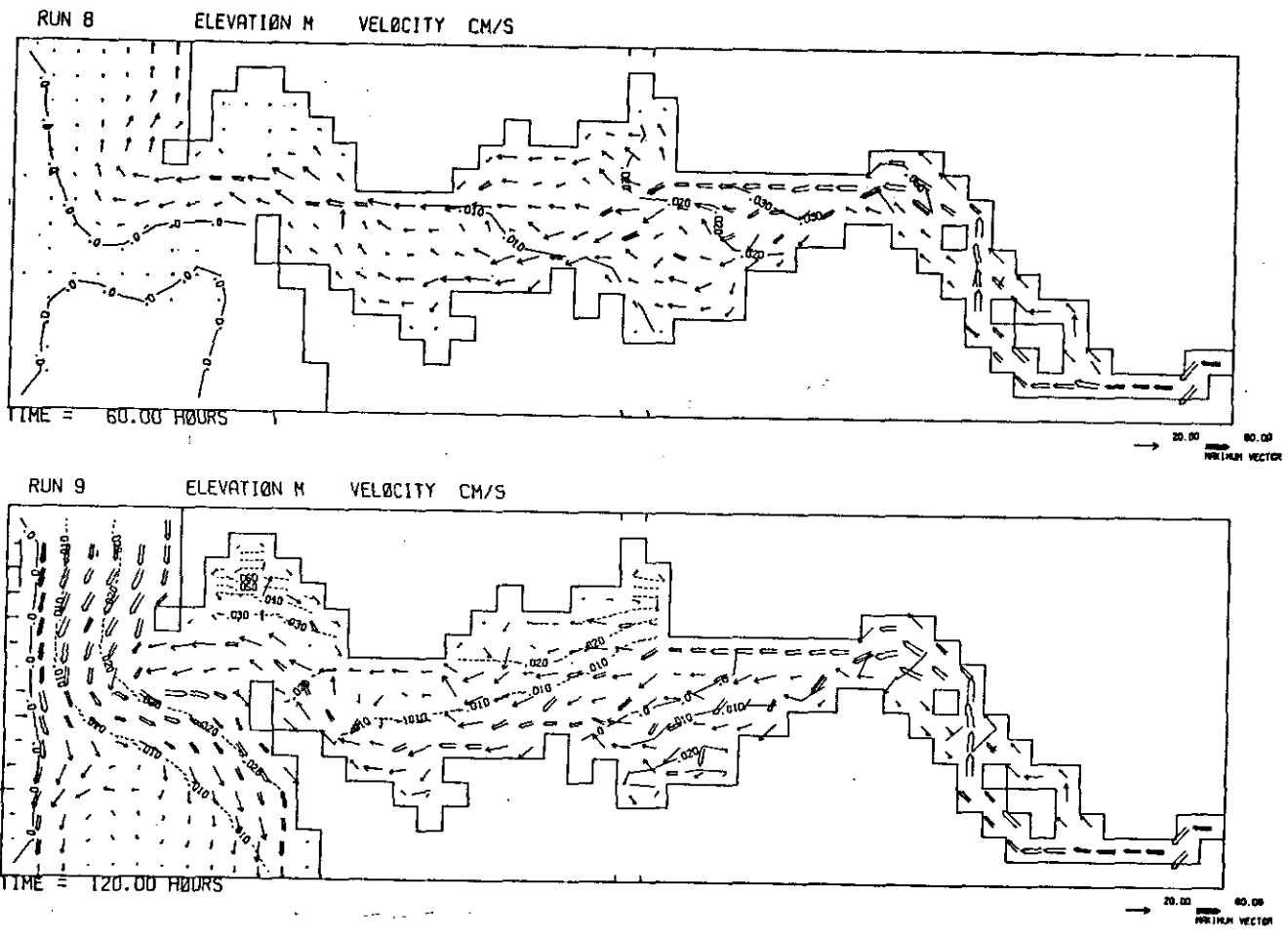
Run 12: Windstress directed towards the west (Figure 24)

This is opposite to Run 10, and water has been driven out of the estuary resulting in a fall in water level of about 20cm at Eagle Cliff and a negative up-estuary water level slope. There are strong westward flows over the sand banks and northwest or northward flow on the eastern sides of the north bays. Flows are generally stronger on the south side of the estuary, including the southside of the entrance channel.

Run 13: Windstress directed towards the northeast (Figure 24)

This case is included because it is the direction of prevailing winds in winter. The circulations show characteristics of both runs 10 and 11. The set up at the coast due the northward component of the wind is again seen as far as Skamokawa, but the easterly component also raises the water level of the estuary. An increase of 17 cm is seen at Eagle Cliff. There is inflow on the south side of the entrance channel and northeastward flow over the major sandbanks.

As an aid to interpreting these results in terms of time series records, Figures 25-27 show time-series derived from the model runs for positions corresponding to the tide gauges and current meter stations. In these figures, the first 2½ days corresponds to Run 8, the second 2½ days to Run 9, etc.. The boundaries between runs are obvious from sharp impulsive changes in the records. The short-period oscillations (period ~ 18 hours) seen primarily in the riverflow case (8) and the east and west wind cases seems to be a natural seiche period for the estuary.



77.

Figure 22. Top panel: map of depth-mean current vectors and water level height contours (conventions the same as Figure 5) for steady state riverflow of 7350 m<sup>3</sup>/s. Bottom panel: current vectors and water levels for 7 m/s wind directed 180° after 60 hours of wind.



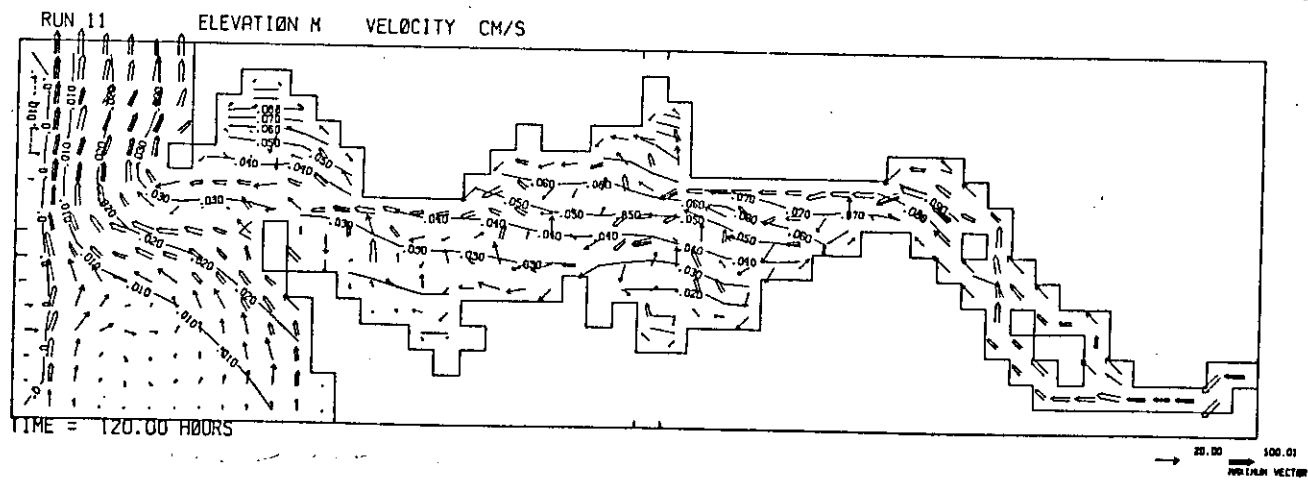
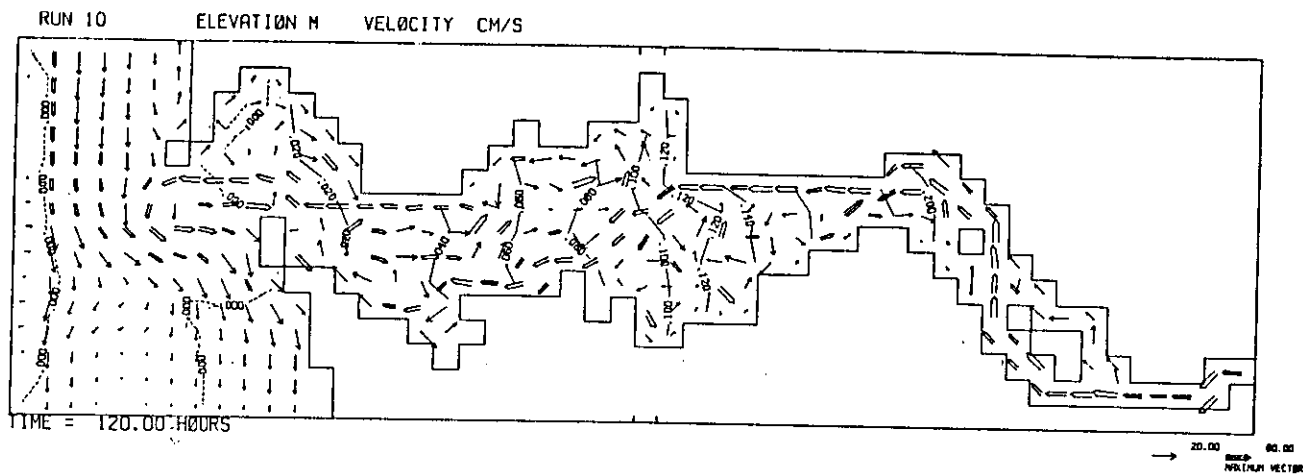


Figure 23. (Top panel) current vectors and water levels for 7 m/s wind directed  $090^{\circ}$ ; -----  
 (Bottom panel) 7 m/s wind directed  $0^{\circ}$ .

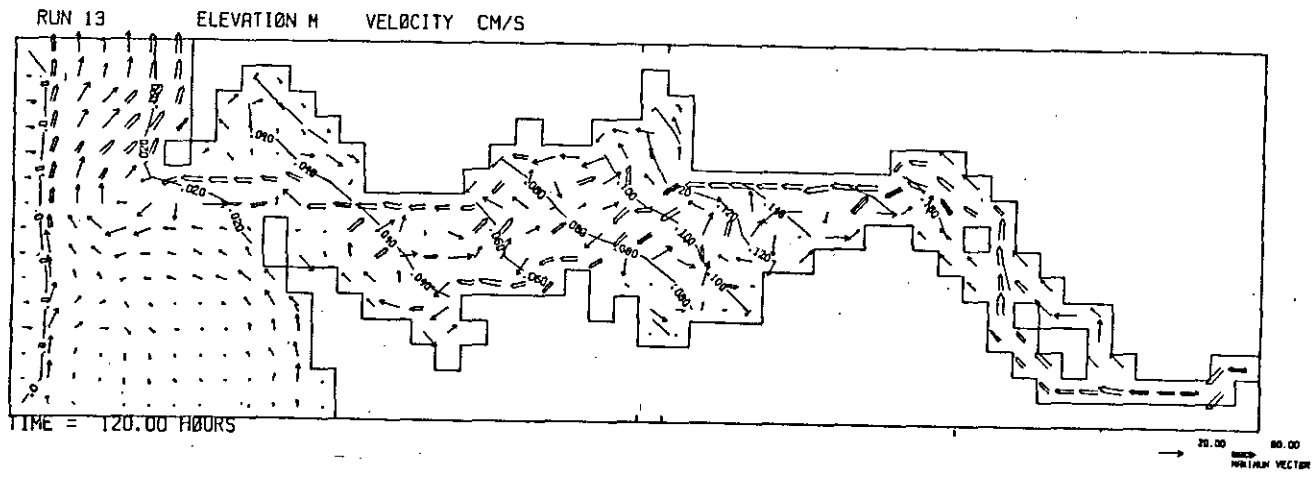
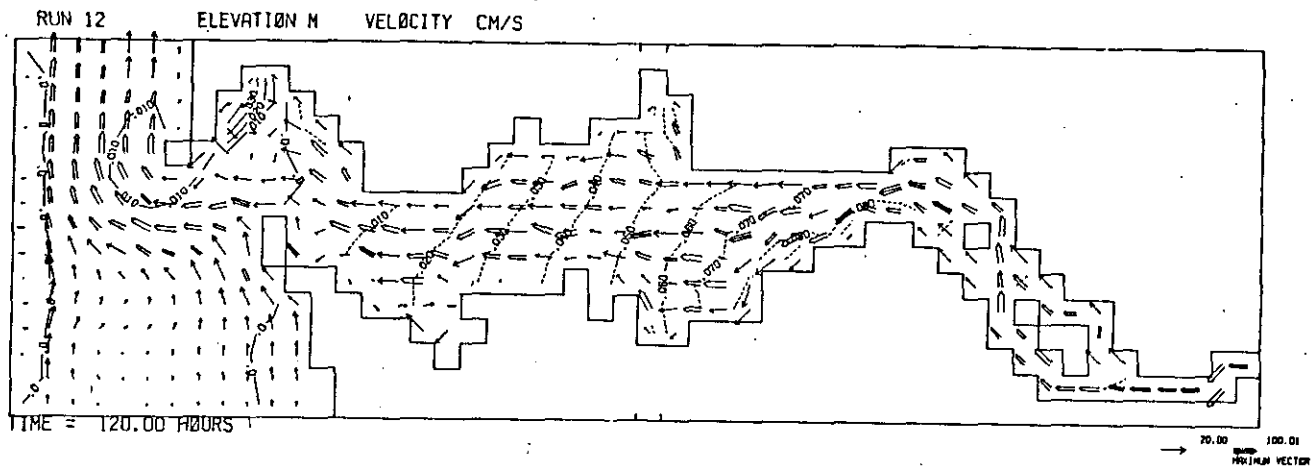
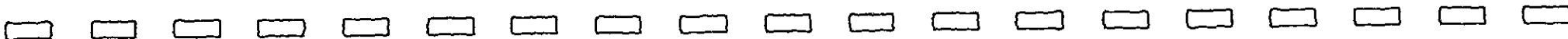
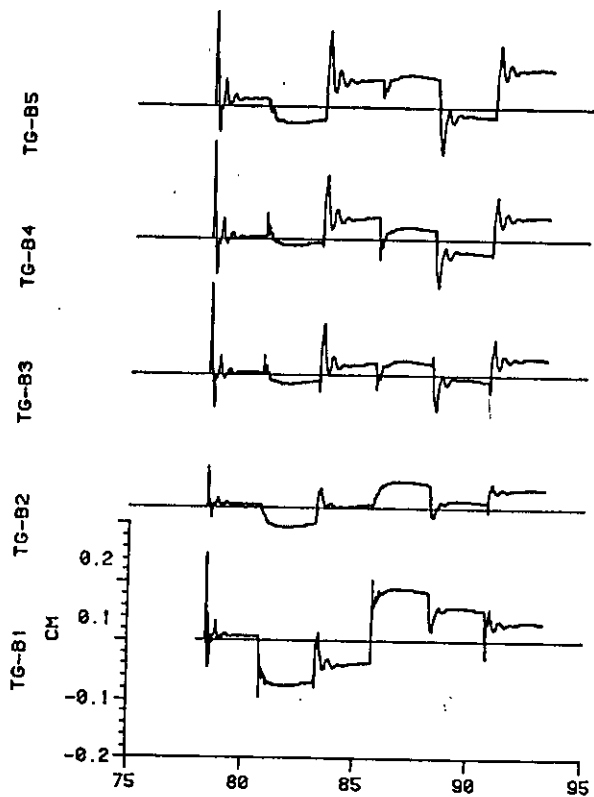
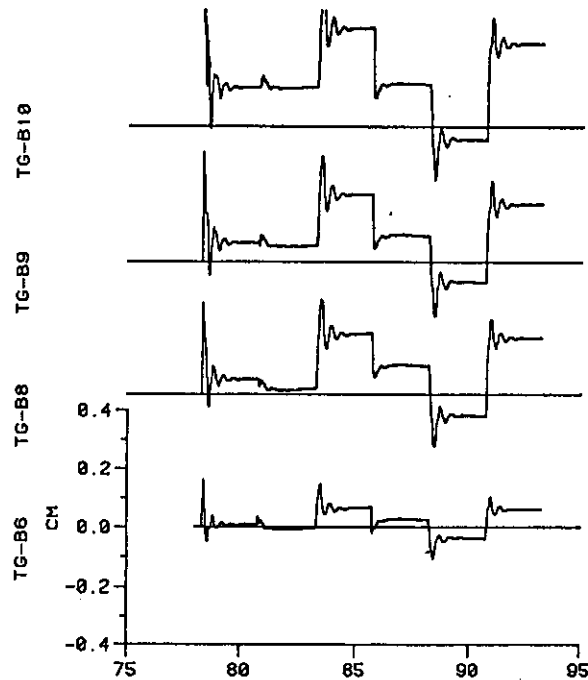


Figure 24. (Top panel) Current vectors and water levels for 7 m/s wind directed 090°;  
 (Bottom panel) 7 m/s wind directed 0°.





JULIAN DAYS 1978  
 DAY 75 IS 3/16/1978 U-COMPONENT



JULIAN DAYS 1978  
 DAY 75 IS 3/16/1978 U-COMPONENT

Figure 25. Water levels at tide stations B1 through B10 for runs 8 through 13 where the time-series have been joined together.

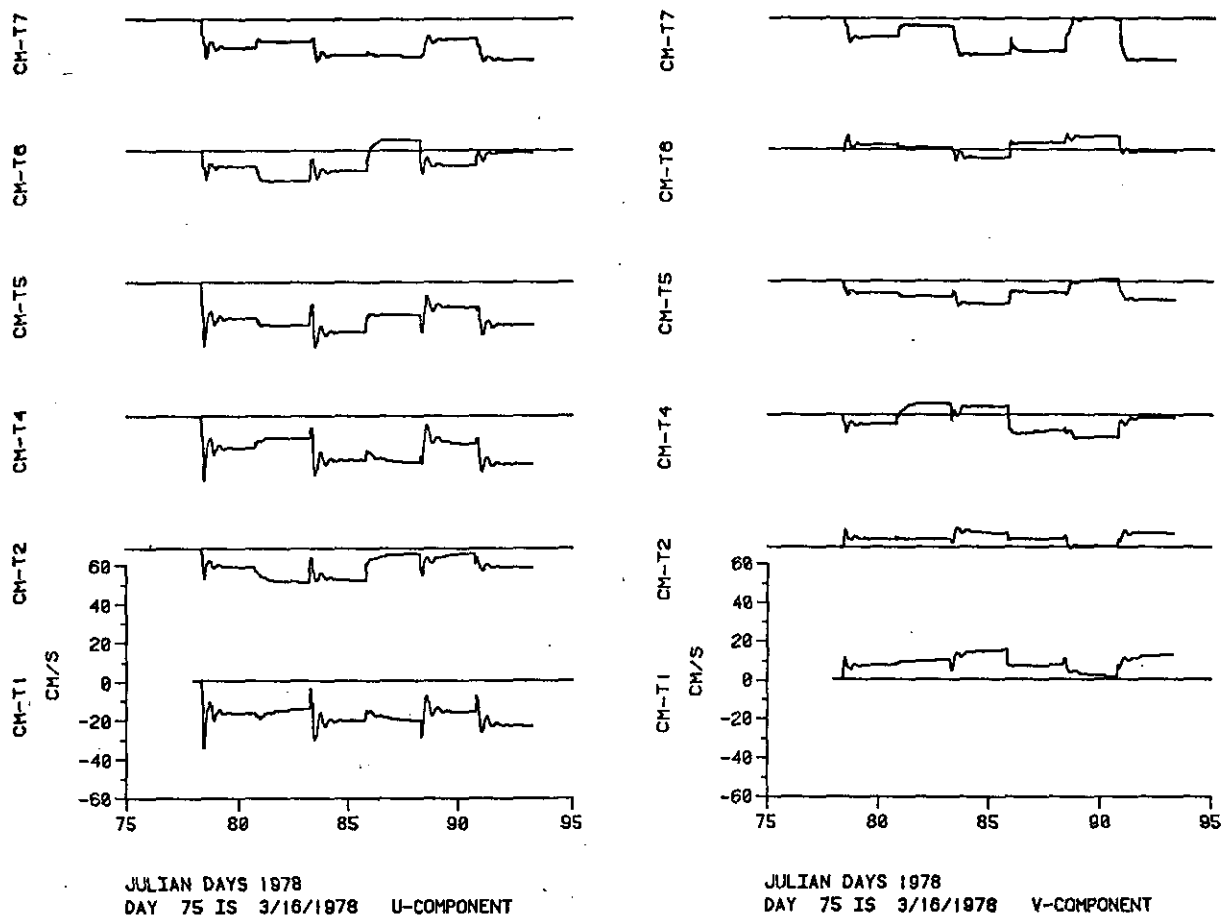


Figure 26. U and V components of depth-mean currents for grid cells corresponding to mooring T1 - T7 for runs 8 through 13.

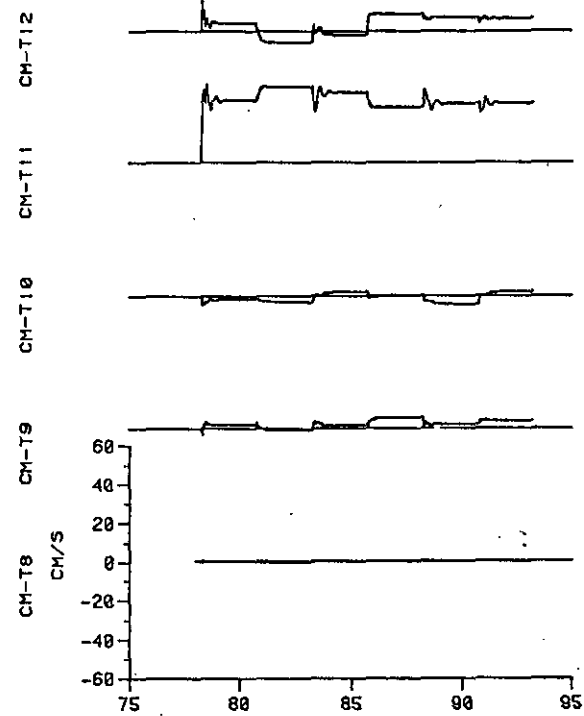
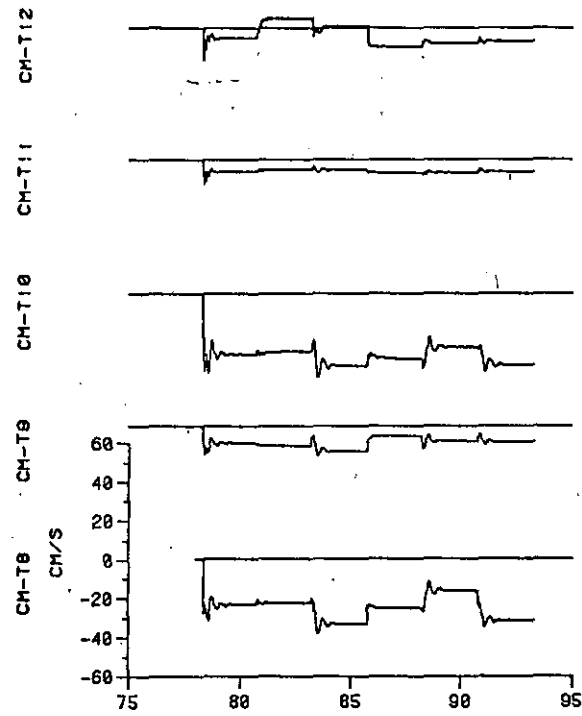


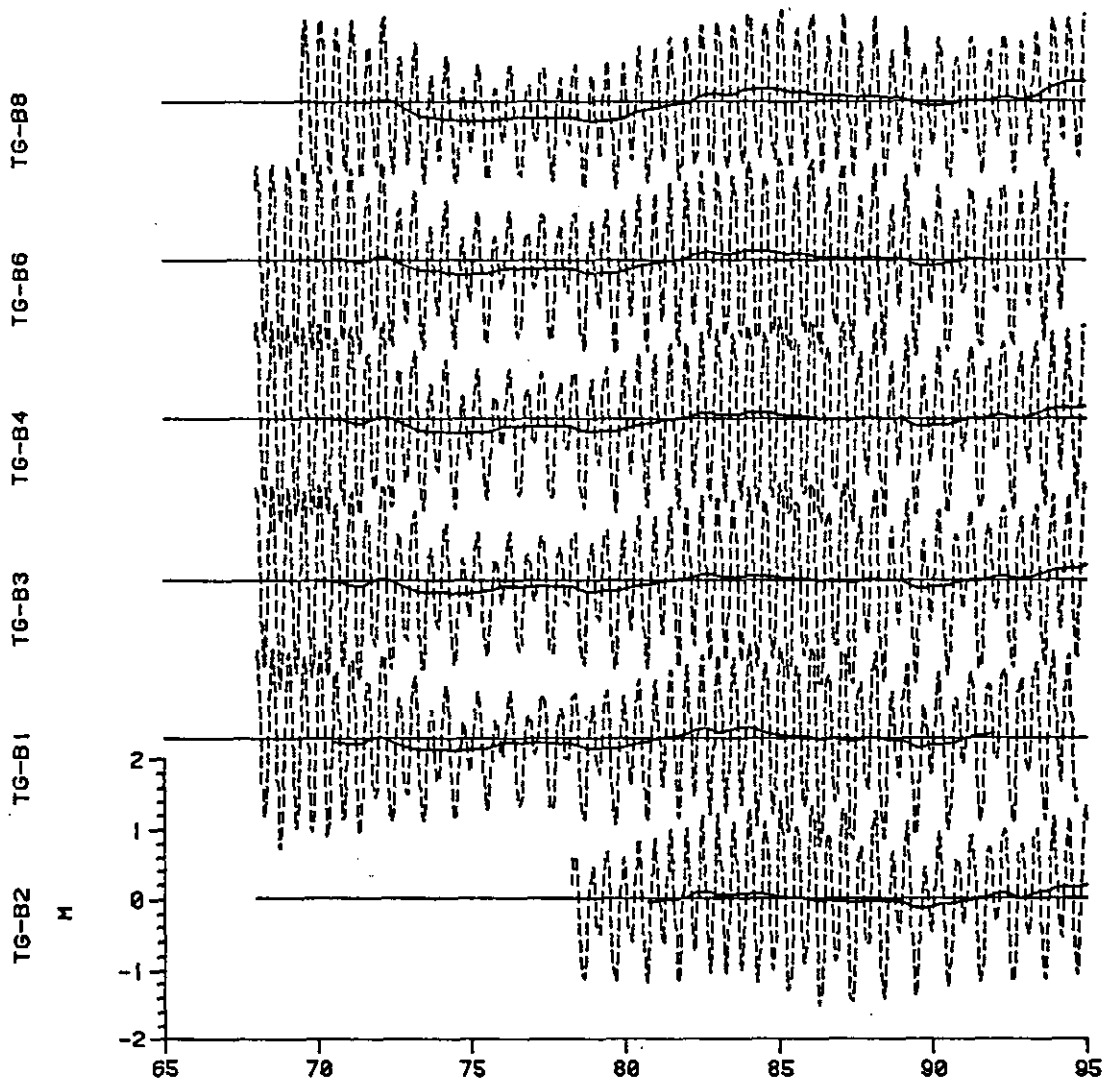
Figure 27. U and V components of depth-mean currents for grid cells corresponding to mooring T8 through T12 for runs 8 through 13.

Figures 28 and 29 show the records from the tide gauges (low-pass filtered records which removes the tidal fluctuations), along with a stick plot of the wind from Astoria airport. It can be seen that low-frequency fluctuations occur approximately in phase throughout the estuary and reflect sea level variations at the mouth which in turn are similar to along-coast winds. Thus, the simple experiments described above can be used as tools to interpret the data.

The conclusions from the wind-forced and riverflow experiments ran without the tide are primarily that wind-forced currents produce only small changes in predominant riverflows in the deep channels. These flows are very small compared with maximum ebb or flood currents due to the tide. However, it can be concluded that wind-driven upwelling and downwelling circulations on the adjacent shelf are effective in lowering and raising mean water levels throughout the estuary by approximately 5-20 cm. Strong winds may possibly be associated with increased exchanges of water masses between the estuary and the shelf by promoting residual inflows on the south side of the entrance channel. This type of flow, however, may be considerably modified by the salinity field, and the increased inflow may be restricted to the lower layers of the salt intrusion. The model also indicates that residual flows in the shallow peripheral bays may be strongly effected by winds. This may be of importance for the productivity of these shallow areas since increased win-driven mean flows will tend to promote exchanges of material between the deep channels, where high turbidity and strong turbulence inhibit production, and the shallow areas.

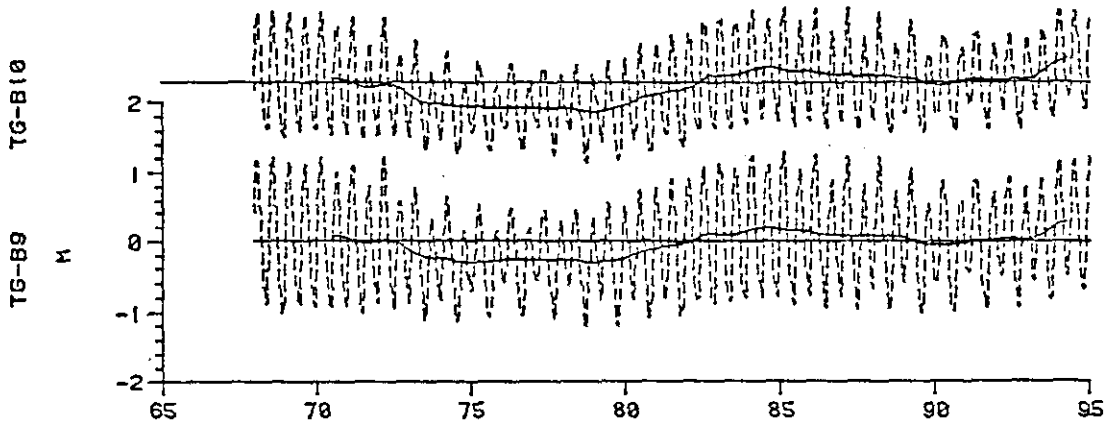
Finally, to show the distribution of riverflow within the estuary without wind, the volume transports for run 8 are given in Figure 30. It clearly shows that majority of the riverflow is restricted to the major channels. Between Harrington Point and Astoria, the riverflow is partly diverted from the Navigation Channel to the North Channel through the small channels across Grays Bay, Taylor Sands and Eastern Desdemona Sands. This is partly compensated for by the flow through Woody Island Channel which rejoins the Navigation Channel at Tongue Point producing increased volume transports there. Thus, at the Astoria-Megler Bridge, the riverflow volume transports are approximately equally divided between North and Navigation Channels.

It would be worthwhile to study depth mean residual flows in the presence of tides in order to estimate the relative effects of tidal residual flows versus wind-induced flow and riverflows. The model would need to be modified to include the non-linear terms and boundary conditions appropriately modified. Lack of funding and changes of priorities as new information on the circulation of the estuary became available prevented further studies with this two-dimensional model.

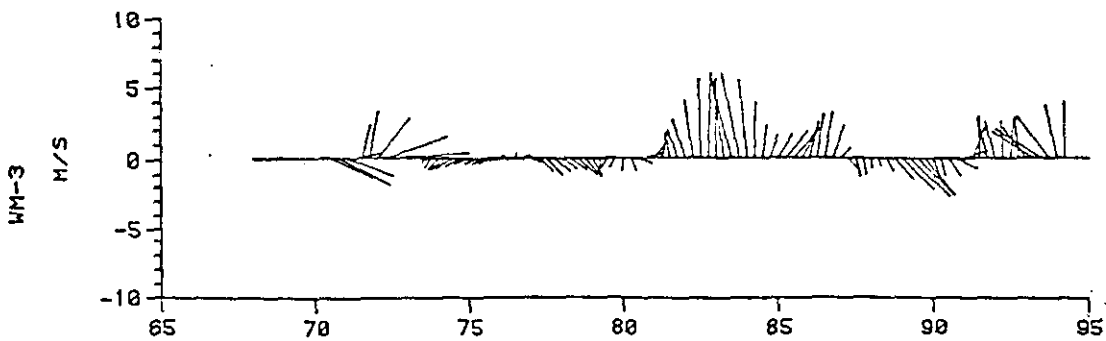


JULIAN DAYS 1978  
 DAY 65 IS 3/ 6/1978 U-COMPONENT

Figure 28. Hourly water level records from tide gauges B1 through B8. Data are unfiltered (dashed) and 40 hour low-pass filtered (solid).

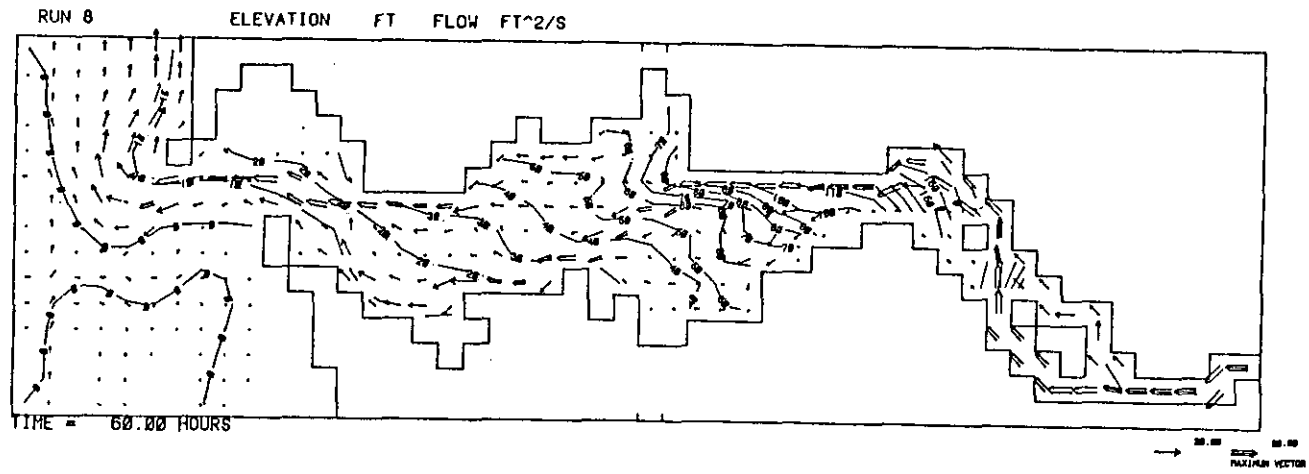


JULIAN DAYS 1978  
 DAY 65 IS 3/ 6/1978 U-COMPONENT



JULIAN DAYS 1978  
 DAY 65 IS 3/ 6/1978

Figure 29. Hourly water level records from tide gauges B9 and B10 both filtered (solid) and nonfiltered (dashed). Corresponding stick plot of low-pass filtered winds. Record from Astoria Airport (Figure 2).



53

— Figure 30. Volume Transports per unit width ( $\text{ft}^2/\text{s}$ ) and elevations (contour labels in ft scaled by 1000) for the riverflow run 8.

#### 4. SUMMARY

This first part of the simulation study of the circulation of the Columbia River Estuary made use of two-dimensional vertically integrated tidal-storm surge model (WIFM). The model was configured to include a small area of the shelf adjacent to the mouth and extended upriver to RM 55 (Eagle Cliff). A uniform grid of 1.52 x 1.52 km cells was used; and, extensive use of subgrid scale barriers was made to incorporate sandbanks and small islands into the relatively coarse grid.

The model was calibrated by simulating the tidal heights and flows and adjusting the bottom friction coefficients until satisfactory agreement was achieved. The model was forced by the observed tidal elevations at Jetty A, backed off to the seaward boundary, and at Eagle Cliff. A study of the ebb and flood flows showed that the majority of the conveyance of volume transport occurs in the relatively narrow, deep channels, principally the main Navigation Channel and the North Channel. The North Channel, off Chinook Point, has about twice the volume transports at maximum flood and ebb than the Navigation Channel off Youngs Bay. The simulated tide was further studied and compared with observations by harmonically analyzing the currents and water levels. The dominant  $M_2$  constituent showed good amplitude and phase agreement with the observations. The  $M_2$  tidal wave showed amplification between the mouth and Tongue Point and then decay upriver. The diurnal  $K_1$  tide decayed landward of the mouth though it had the same phase speed in the lower estuary as the  $M_2$  constituent. The  $M_2$  depth-mean currents lead elevations by about  $45^\circ$  in the lower estuary, but this phase difference decreases to almost  $0^\circ$  upriver of Skamokawa. This change in character of the  $M_2$  tide from a mixed standing-progressive wave in the lower estuary to an almost purely progressive wave upriver along with amplification of tide in the lower estuary is interpreted as being caused by partial reflection of the wave where the estuary rapidly narrows at Skamokawa which causes only the progressive part of the wave to be transmitted and dissipated in the upriver sections of the estuary.

The second part of this volume was concerned with simulating wind-induced and riverflow circulations when the tide is neglected. Wind-forced flows are much smaller than the tidal flows and the riverflows. Neglect of the tide allows wind forced flows to be more easily studied. Strong winds blowing parallel to the coast induce raising and lowering of coastal sea-level along with associated downwelling and upwelling shelf circulations. These coastal sea-level effects are shown to be effective in raising and lowering sea-level throughout the estuary. Local winds over the estuary have lesser effects of water levels except in the peripheral Bays, where strong winds may be expected to have large effects on the residual circulations. Thus storms may be effective in transporting water borne material from the bays into the deeper channels where they would be rapidly flushed from the system. The riverflow volume transports showed that between Harrington Point and Astoria there is a diverting of flow across Taylor Sands and eastern Desdemona Sands channels and through the Grays Bay channels into the North Channel such that at the Astoria-Megler Bridge the North Channel and the Navigation Channel have

approximately equal volume flows. The system of channels favored by the riverflow is clearly delineated in this plot (Figure 30), which further supports the idea that the majority of the flow in the estuary is well channelized and the extensive flats of the estuary do not have an important dynamical role and can be considered as high water volume storage areas.

In some respects, the studies reported in this volume could be considered as a preliminary application of a two-dimensional tidal-storm surge model to the estuary. The hiatus in the program and the subsequent reconsideration and redirection of the modeling studies into investigating salinity intrusion processes, which necessarily requires a depth dependent model, were responsible for the preliminary nature of this first part of the investigation. Nonetheless, the tidal modeling was valuable in that it showed that the laterally averaged channel model of Volume II would reasonably represent the two-dimensional horizontal flows of the estuary as far as tidal and riverflows were concerned. The investigation of the effects of wind on residual flows in the estuary, particularly in the Bays, was most efficiently performed using WIFM and is not considered in the next volume.

Thus, recommendations for tidal modeling in the estuary using WIFM includes:

- 1) Extension of the river channel at the eastern boundary of the model so that a riverflow boundary condition may be used instead of a tidal elevation condition.
- 2) Inclusion of the non-linear inertial terms so that non-linear tidal residual flows may be calculated.
- 3) Successive refinements of the grid, perhaps using the flexible grid option of the model to produce higher resolution flows and better resolution of the bathymetry.
- 4) Detailed simulations of the flows in the peripheral bays by using a fine resolution mesh with flexible grid spacing for the bays embedded in a coarse grid of the whole estuary so that accurate boundary conditions are employed for the bay model boundaries.

#### LITERATURE CITED

- April, G.C., and Raney, D.C. 1980. Hydrodynamics of Mobile Bay and Mississippi Sound. Sea Grant Report BER 247-112, MASGP-79-020. University: University of Alabama.
- Butler, H.L. 1980. Evolution of a numerical model for simulating long-period wave behavior in ocean-estuarine systems. Hamilton, P., and Macdonald, K.B. eds. Estuarine and Wetland Processes. New York: Plenum Press.
- Foreman, M.G.G. 1979. Manual for Tidal Heights Analysis and Prediction. Pacific Marine Science Report 77-10. Victoria, B.C.: Institute of Ocean Sciences, Patricia Bay.
- Foreman, M.G.G. 1979. Manual for Tidal Currents Analysis and Prediction. Pacific Marine Science Report 78-6. Victoria, B.C.: Institute of Ocean Sciences, Patricia Bay.
- Godin, G. 1972. The Analysis of Tides. Toronto: University of Toronto Press.
- Hickey, B.M., and Hamilton, P. 1980. A Spin-up Model as a Diagnostic Tool for Interpretation of Current and Density Measurements on the Continental Shelf of the Pacific Northwest. J. Phys. Oceanogr. 10: 12-24.
- Hughes, F.W. and M. Rattray, Jr. 1980. "Salt Flux and Mixing in the Columbia River Estuary." Estuarine and Coastal Marine Science. 10, 479-493.
- Jay, D. 1984. "Circulatory Processes in the Columbia River Estuary. Final CREDDP Report, CREST, Astoria OR.
- McDowell, D.M., and Prandle, D. 1972. Mathematical Model of the River Hoogly. J. Wat. Harbors Div. ASCE 98, WW2: 226-242.
- Reid, R.O., and Bodine, B.R. 1968. Numerical Model for Storm Surges in Galveston Bay. J. Wat. Harbors Div. ASCE 94, WW1: 33-57.
- Roberson, J.A.; Copp, H.D.; Naik, B. 1980. Mathematical Model of Circulation in Baker Bay, Washington/Oregon. Tech. Rept. HY-4/80. Pullman: R.L. Albrook Hydraulics Laboratory, Dept. of Civil and Environmental Engineering, Washington State University.

HYDRODYNAMIC MODELING OF THE  
COLUMBIA RIVER ESTUARY

VOLUME II

TWO-DIMENSIONAL SIMULATIONS OF THE  
VERTICAL CIRCULATION

## TABLE OF CONTENTS

	<u>Page</u>
LIST OF FIGURES	v
LIST OF TABLES	xi
1. INTRODUCTION	1
1.1. ESTUARINE CIRCULATION IN THE COLUMBIA RIVER ESTUARY	1
2. METHODS AND MATERIALS	3
2.1. THE MODEL	3
2.1.1. Boundary Conditions	4
2.1.2. Channel Networks	5
2.1.3. Sandbank Overtopping	7
2.1.4. The Finite Difference Method	9
2.1.5. Programming Considerations	12
2.1.6. Initialization	12
2.2. APPLICATION OF THE MODEL TO THE COLUMBIA RIVER ESTUARY	13
2.2.1. The Data Base	16
2.3. CALIBRATION AND VERIFICATION	23
2.3.1. Tidal Calibration	23
2.3.2. Vertical Eddy Coefficient Formulation	29
2.3.3. Current and Salinity Comparisons	30
3. RESULTS AND DISCUSSIONS	57
3.1. SIMULATIONS	57
3.1.1. Introduction	57
3.1.2. Tidal Circulation	57
3.1.3. Tidal Analysis	88
3.1.4. The Effects of Tide and Riverflow on Mean Circulations	109
3.1.5. Extreme Low Flow Simulations	185

3.2.	SIMULATION OF THE 1868 ESTUARY	212
3.2.1.	Introduction	212
3.2.2.	Neap and Spring Tides	217
3.2.3.	Riverflows	284
3.2.4.	Conclusions	345
4.	SUMMARY	349
	LITERATURE CITED	353

## LIST OF FIGURES

	<u>Page</u>
1. Sketch of a branching channel network.	6
2. Sketch of the cross-sections of two channels with lateral transport of water across a connecting sandbank.	8
3. Arrangement of computational variables in a grid cell.	10
4. The channels and grid cells used for the schematization of the estuary.	15
5. (a) Tide gauge (diamonds) and current meter moorings (stars) deployed during the 1980 CREDDP field study.	18
(b) Tide gauge (diamonds) and current meter moorings (stars) deployed during the Spring 1981 National Ocean Survey field study.	21
6. Observed (solid) and simulated (dashed) tidal heights for the indicated stations for the October 1980 low-flow period.	24
7. (a-d) Observed (solid) and simulated (dashed) tidal heights for the indicated stations for the Spring 1981 high-flow period.	25 - 28
8. (a-h) Observed (solid) and simulated (dashed) salinity and current time-series for the indicated meters for the October 1980 low-flow period.	31 - 38
9. (a-e) Observed (solid) and simulated (dashed) along-channel current time-series for the indicated meters for the May 1981 high-flow period.	41 - 45
10. (a-d) Observed (solid) and simulated (dashed) salinity current time-series for the indicated meters for the May 1981 high-flow period.	47 - 50
11. (a,b) Observed (solid) and simulated (dashed) along-channel time-series for the indicated meters for the June 1981 high-flow period.	51 - 52
12. (a,b) Observed (solid) and simulated (dashed) salinity time-series for the indicated meters for the June 1981 high-flow period.	53 - 54
13. (a-i) Channel 1, neap tide period, currents and salinities (m/s and ‰), low riverflow.	61 - 69
14. (a-i) Channel 2, neap tide period, currents and salinities (m/s and ‰), low riverflow.	70 - 78

	<u>Page</u>
15. (a-i) Horizontal volume transport vectors ( $m^3/s$ ) for neap tide and low riverflow.	79 - 87
16. (a-i) Channel 1, spring tide period, currents and Salinities (m/s and $^{\circ}/\infty$ ), low riverflow.	89 - 97
17. (a-i) Channel 2, spring tide period, currents and Salinities (m/s and $^{\circ}/\infty$ ), low riverflow.	98 - 106
18. (a,b) Horizontal vectors averaged over a neap tide plotted on the estuary chart.	110 - 111
19. (a-c) Channel 1, neap tide period (Fall, 1980).	113 - 115
20. (a-c) Channel 2, neap tide period (Fall, 1980).	116 - 118
21. (a-c) Channel 4, neap tide period (Fall, 1980).	119 - 121
22. (a-c) Channel 7, neap tide period (Fall, 1980).	122 - 124
23. (a-c) Channel 1, spring tide period (Fall, 1980).	125 - 127
24. (a-c) Channel 2, spring tide period (Fall, 1980).	128 - 130
25. (a-c) Channel 4, spring tide period (Fall, 1980).	131 - 133
26. (a-c) Channel 7, spring tide period (Fall, 1980).	134 - 136
27. (a-c) Channel 1, neap #1, (Spring, 1981).	138 - 140
28. (a-c) Channel 2, neap #1, (Spring, 1981).	141 - 143
29. (a-c) Channel 1, spring #1 (Spring, 1981).	144 - 146
30. (a-c) Channel 2, spring #1 (Spring, 1981).	147 - 149
31. (a-c) Channel 1, spring #2 (Spring, 1981).	150 - 152

	<u>Page</u>
32. (a-c) Channel 2, spring #2 (Spring, 1981).	153 - 155
33. (a-c) Channel 1, neap #2 (Spring, 1981).	157 - 159
34. (a-c) Channel 2, neap #2 (Spring, 1981).	160 - 162
35. (a-c) Channel 1, neap #3 (Spring, 1981).	163 - 165
36. (a-c) Channel 2, neap #3 (Spring, 1981).	166 - 168
37. (a-c) Channel 1, spring #3 (Spring, 1981).	169 - 171
38. (a-c) Channel 2, spring #3 (Spring, 1981).	172 - 174
39. (a-b) Channel 1, 15-day mean; (c-d) Channel 2, 15-day mean.	176 - 179
40. (a-b) Channel 1, 15-day mean; (c-d) Channel 2, 15-day mean	180 - 183
41. (a-c) Channel 1, neap tide period, riverflow = 2,000 m <sup>3</sup> /s.	188 - 190
42. (a-c) Channel 2, neap tide period, riverflow = 2,000 m <sup>3</sup> /s.	191 - 193
43. (a-c) Channel 4, neap tide period, riverflow = 2,000 m <sup>3</sup> /s.	194 - 196
44. (a-c) Channel 7, neap tide period, riverflow = 2,000 m <sup>3</sup> /s.	197 - 199
45. (a-c) Channel 1, spring tide period, riverflow = 2,000 m <sup>3</sup> /s.	200 - 202
46. (a-c) Channel 2, spring tide period, riverflow = 2,000 m <sup>3</sup> /s.	203 - 205
47. (a-c) Channel 4, spring tide period, riverflow = 2,000 m <sup>3</sup> /s.	206 - 208
48. (a-c) Channel 7, spring tide period, riverflow = 2,000 m <sup>3</sup> /s.	209 - 211

	<u>Page</u>
49. The channels and grid cells used for the schematization of the 1868 estuary.	214
50. Cross-sections of bathymetric for 1982 and 1868 between indicated points (see Figure 5a).	215
51. (a,b) Horizontal vectors averaged over a neap tide plotted on the 1868 estuary chart.	218 - 219
52. (a-i) Channel 1, neap tide period, currents and salinities (m/s and ‰).	221 - 229
53. (a-i) Channel 2, neap tide period, currents and salinities (m/s and ‰).	230 - 238
54. (a-i) Channel 3, neap tide period, currents and salinities (m/s and ‰).	239 - 247
55. (a-i) Horizontal volume transport vectors (m <sup>3</sup> /s) for neap tide and low riverflow.	248 - 256
56. (a-i) Channel 1, spring tide period, currents and salinities (m/s and ‰), low riverflow.	257 - 265
57. (a-i) Channel 2, spring tide period, currents and salinities (m/s and ‰), low riverflow.	266 - 274
58. (a-i) Channel 3, spring tide period, currents and salinities (m/s and ‰), low riverflow.	275 - 283
59. (a-c) Channel 1, neap tide period (historical bathymetry, riverflow = 12,000 m <sup>3</sup> /s).	284 - 287
60. (a-c) Channel 2, neap tide period (historical bathymetry, riverflow = 12,000 m <sup>3</sup> /s).	288 - 290
61. (a-c) Channel 3, neap tide period (historical bathymetry, riverflow = 12,000 m <sup>3</sup> /s).	291 - 293
62. (a-c) Channel 1, spring tide period (historical bathymetry, riverflow = 12,000 m <sup>3</sup> /s).	294 - 296
63. (a-c) Channel 2, spring tide period (historical bathymetry, riverflow = 12,000 m <sup>3</sup> /s).	297 - 299
64. (a-c) Channel 3, spring tide period (historical bathymetry, riverflow = 12,000 m <sup>3</sup> /s).	300 - 302
65. (a-c) Channel 1, neap tide period (historical bathymetry, riverflow = 4,000 m <sup>3</sup> /s).	303 - 305

	<u>Page</u>
66. (a-c) Channel 2, neap tide period (historical bathymetry, riverflow = 4,000 m <sup>3</sup> /s).	306 - 308
67. (a-c) Channel 3, neap tide period (historical bathymetry, riverflow = 4,000 m <sup>3</sup> /s).	309 - 311
68. (a-c) Channel 1, spring tide period (historical bathymetry, riverflow = 4,000 m <sup>3</sup> /s).	312 - 314
69. (a-c) Channel 2, spring tide period (historical bathymetry, riverflow = 4,000 m <sup>3</sup> /s).	315 - 317
70. (a-c) Channel 3, spring tide period (historical bathymetry, riverflow = 4,000 m <sup>3</sup> /s).	318 - 320
71. (a-c) Channel 1, neap tide period (historical bathymetry, riverflow = 2,000 m <sup>3</sup> /s).	321 - 323
72. (a-c) Channel 2, neap tide period (historical bathymetry, riverflow = 2,000 m <sup>3</sup> /s).	324 - 326
73. (a-c) Channel 3, neap tide period (historical bathymetry, riverflow = 2,000 m <sup>3</sup> /s).	327 - 329
74. (a-c) Channel 6, neap tide period (historical bathymetry, riverflow = 2,000 m <sup>3</sup> /s).	330 - 332
75. (a-c) Channel 1, spring tide period (historical bathymetry, riverflow = 2,000 m <sup>3</sup> /s).	333 - 335
76. (a-c) Channel 2, spring tide period (historical bathymetry, riverflow = 2,000 m <sup>3</sup> /s).	336 - 338
77. (a-c) Channel 3, spring tide period (historical bathymetry, riverflow = 2,000 m <sup>3</sup> /s).	339 - 341
78. (a-c) Channel 6, spring tide period (historical bathymetry, riverflow = 2,000 m <sup>3</sup> /s).	342 - 344

LIST OF TABLES

	<u>Page</u>
1. Channel Names	14
2. Model Parameters	17
3. (a) October 1980 CREDDP Data	19
3. (b) Spring 1981 NOS Data	22
4. Model Runs and Analysis Periods	58
5. (a) Tidal Elevations and Transports	107
5. (b) Tidal Constants, Surface and Bottom Currents and Salinities	108
6. Channel Names for 1868 Bathymetry	213

## 1. INTRODUCTION

Volume I of this report described the simulation of the tide using the Waterway's Experiment Station Implicit Flooding Model (WIFM). Tidal flows are the dominant process in the Columbia River Estuary, and it has been shown (Jay 1984) that the changes in tidal amplitude between spring and neap can profoundly alter the salinity field and the tidal mean circulation by changing the intensity of the mixing processes. Hughes and Rattray (1980) showed that, similar to other coastal plain estuaries, vertical mixing and vertical variations of salinity and along-channel currents are the most important processes in determining the tidal mean salt balance and thus the mean salinity field. Lateral variability of the mean salinity, residual, and tidal currents seems to be of secondary importance for the salt balance, at least as regards the major deep channels (Hughes and Rattray, 1980). The studies using WIFM gave a great deal of information on tidal currents, but because of the neglect of the vertical dimension, WIFM cannot address the simulation of the salinity field or of the density current circulation and the vertical tidal current shears with which the salinity is coupled. Therefore, to investigate these important aspects of the circulation of the estuary, a model which divides the estuary into a number interconnected channels was devised. For each channel, the three-dimensional equations are laterally averaged and integrated in time, using a numerical formulation similar to the laterally-averaged depth-dependent single-channel model developed by Hamilton (1975, 1976). The Columbia River Estuary is also characterized by sandflats and marshlands, which are submerged at high tide and exposed at low. The flow over these sandflats between channels is included in a manner similar to that of the WIFM.

The multiple-channel model formulation, the application of the model to the Columbia River Estuary, and the calibration and verification of the model are given in Section 2. The model results for high and low riverflows, and the historical bathymetry simulations are given in Section 3. The latter section describes the application of the model to the estuary, with the shoreline configuration and bathymetry of 1863 compiled from historical records by Northwest Cartography, Inc. (CREDDP 1983). The circulation and salinity distribution for this pre-dredging era is investigated and allows some inferences as to the physical oceanography of the estuary during that era compared with present day conditions. This section illustrates the power of the model to make predictions of past and future conditions and is, in fact, the only quantitative way that such predictions can be made, if field data do not exist for the simulated period.

### 1.1 ESTUARINE CIRCULATION IN THE COLUMBIA RIVER ESTUARY

This section contains a brief review of some of the important physical processes governing the circulation in the Columbia River Estuary. Greater detail on the physical oceanography of the estuary can be found in the CREDDP Currents work unit report (Jay 1984). A review of the theoretical aspects of estuarine circulation is given by Hamilton and Rattray (1978), and a review of recent developments in

characterizing the turbulent mixing in highly stratified estuaries is given by Gardner et al. (1981).

Salinity intrusion in estuaries is governed by a number of complex factors. Fundamentally, the salinity distribution is caused by the mixing of ocean and fresh water. Horizontal and vertical mixing of salt and brackish water is determined by the tidal currents, stratification, bottom roughness and topographic effects. The longitudinal salinity distribution is the primary cause of the depth-dependent density current circulation, which in turn influences the vertical and horizontal salinity fields by advection. The tidal-mean density-current circulation consists of upstream flow in the lower, more saline layer with seaward flow in the upper, less saline layer. The density current circulation is a strong function of depth and vertical turbulent mixing. This latter fact explains why the salinity intrusion is governed primarily by the tidal currents, and vertical mixing in the deep main channels of the Columbia River, and also why the residual tidal mean circulation is such a strong function of tidal amplitude. On neap tides the energy for vertical mixing is less, and the main channels of the Columbia become more stratified, which causes the density-current circulation to be relatively stronger and thus the salt to intrude further up the estuary in the lower layer. However, despite the importance of the longitudinal salinity gradients in determining mean flow, the main mechanism in determining the mean salinity field is the interaction of the tidal flows and mixing with the vertical and horizontal time-varying salinity gradients.

Jay (1984) gives a discussion based on observations of the variability of the stratification and associated current profiles for different sections of the estuary and at different stages of the tide for the low-flow October 1980 period. The estuary showed almost salt wedge behavior at the end of the flood tide near Tongue Point, which was quickly eroded during the following ebb. In the North Channel, however, the salinity stratification more closely resembles a strongly stratified, partially-mixed estuary on both ebb and flood. During strong spring tides in the navigation channel near Hammond, the water column becomes vertically homogeneous.

At the mouth of the estuary, strong stratification is seen on the ebb tide, accompanied by an almost linearly sheared current profile in the upper part of the water column with a weak reversal of the current in the lower one-third of the water column. There is evidence of a moderate density current in the entrance region for neap tides and much weaker mean flows for the spring. Therefore, it can be seen that the model has to encompass extremes of stratification and mixing as well as large tidal ranges, strong currents, and topographical complexity. The model described below is able to simulate most of the major physical processes reasonably well and to produce a quantitative simulation of the circulation that agrees quite well with available data.

## 2. METHODS AND MATERIALS

### 2.1. THE MODEL

The two-dimensional time and depth-dependent numerical model used in this project is essentially an improvement and modification of the single-channel model developed by Hamilton (1975, 1976). Some of the improvements are based on the estuary models of Blumberg (1975), Elliot (1976) and Wang and Kravitz (1980). To simplify the description of the model, the single-channel version will be presented and then the modifications, to include a network of interconnecting channels, will be given.

For a single channel, the equations of continuity, momentum and salt conservation are averaged across the width of the channel, so that the variables are functions of depth, time and position along the longitudinal axis of the channel. The mathematics of the averaging, with the approximations involved, are given in detail in Elliot (1976). The equations of the model, using the Boussinesq approximation for a narrow channel of variable width and depth, are:

#### Continuity:

$$b \zeta \frac{\partial \zeta}{\partial t} + \frac{\partial U}{\partial x} = 0 \quad (1)$$

$$bw = - \frac{\partial}{\partial x} \int_{-h}^{\zeta} b u dz \quad (2)$$

#### Momentum Conservation:

$$\begin{aligned} \frac{\partial u}{\partial t} + \frac{1}{b} \frac{\partial}{\partial x} (buu) + \frac{1}{b} \frac{\partial}{\partial z} (buw) = -g \frac{\partial \zeta}{\partial x} - g \int_{-h}^{\zeta} \frac{\partial \rho}{\partial x} dz \\ + \frac{1}{b} \frac{\partial}{\partial z} (bN_v \frac{\partial u}{\partial z}) - \frac{k_s |u|u}{b} (1 + (db/dz)^2)^{1/2} \end{aligned} \quad (3)$$

$$\begin{aligned} \frac{\partial U}{\partial t} + \int_{-h}^{\zeta} \frac{\partial}{\partial x} (buu) dz + \int_{-h}^{\zeta} \frac{\partial}{\partial z} (buw) dz = \\ -gA \frac{\partial \zeta}{\partial x} - \frac{g}{\rho} \int_{-h}^{\zeta} b \int_{-h}^{\zeta} \frac{\partial \rho}{\partial x} dz' dz + b_{\zeta} \tau_s - b_h \tau_b \\ - \int_{-h}^{\zeta} k_s |u|u (1 + (db/dz)^2)^{1/2} dz \end{aligned} \quad (4)$$

#### Salt Conservation:

$$\begin{aligned} \frac{\partial (bs)}{\partial t} + \frac{\partial}{\partial x} (bus) + \frac{\partial}{\partial z} (bws) \\ - \frac{\partial}{\partial x} (bK_h \frac{\partial s}{\partial x}) - \frac{\partial}{\partial z} (bK_v \frac{\partial s}{\partial z}) = 0 \end{aligned} \quad (5)$$

where: x and z are coordinates in the plane of the undisturbed water surface, with z directed vertically upward and x along the longitudinal axis of the channel,

and, where:

- t = time
- $\zeta$  = elevation of the water surface above the undisturbed plane ( $z = 0$ )
- u, w = velocity components in the x and z directions, respectively
- $\rho$  = density of water
- s = salinity
- h = depth, a function of x only
- b = channel width, a function of x and z
- $b_{\zeta}, b_h$  = channel widths at  $z = \zeta$  and  $z = h$ , respectively
- U = volume transport through a channel section, defined by  $U = \int_{-h}^{\zeta} budz$
- A = cross-sectional area of channel, defined by  $A = \int_{-h}^{\zeta} b dz$
- $K_h, K_v$  = vertical and horizontal eddy diffusion coefficients, respectively
- $N_v$  = vertical eddy viscosity coefficient
- $\tau_s, \tau_b$  = surface wind stress and bottom stress, respectively, directed along x
- g = acceleration due to gravity
- $k_s$  = sidewall friction coefficient

The last terms in (3) and (4) represent the frictional effects of the channel sides. The formulation is due to Blumberg (1975) and is discussed also in Elliott (1976). Density is given as a function of salinity by a linear equation of state,

$$\rho = \rho_0 (1 + as) \quad (6)$$

where  $\rho_0$  is the density of fresh water and  $a = 7.5 \times 10^{-4}$ . SI units are used throughout this volume.

### 2.1.1 Boundary Conditions

At the free surface,  $z = \zeta$ , the along-channel wind stress is prescribed, and there is no salt flux through the free surface. At the bottom,  $z = -h$ , salt flux normal to the bottom is zero, and bottom stress is given in terms of bottom current. These conditions are given by:

$$K_v \frac{\partial s}{\partial z} = 0 \text{ at } z = \zeta \quad (7)$$

$$K_v \frac{\partial s}{\partial z} + K_h \frac{\partial s}{\partial x} \frac{\partial h}{\partial x} = 0 \text{ at } z = -h \quad (8)$$

$$\tau_s = -N_z \frac{\partial u}{\partial z} \text{ at } z = \zeta \quad (9)$$

$$\tau_s = c\rho_a |W| W_x / \rho_o$$

where  $\rho$  = density of air

$c^a$  = wind stress coefficient

$W$  = component of wind directed along  $x$

$W^x$  = magnitude of wind vector

$$\tau_b = -N_v \frac{\partial u}{\partial z} = k |u_b| u_b \quad (10)$$

where  $u_b = u(x, -h, t)$  at  $z = -h$ , and  $k$  = bottom friction coefficient.

At the river end of the estuary,  $x = L$ , the volume flow,  $Q$ , is given as a function of time using available riverflow data (Jay 1984), thus:  $u$  is independent of  $z$  and given by:

$$u = Q/A \quad (11)$$

and the salinity is zero, thus;

$$s = 0 \quad \text{at } x = L. \quad (12)$$

At the mouth of the estuary ( $x = 0$ ), the tidal elevation is given as a function of time

$$\zeta(0, t) = \zeta_o(t), \quad (13)$$

and the salinity is specified as a function of depth and time

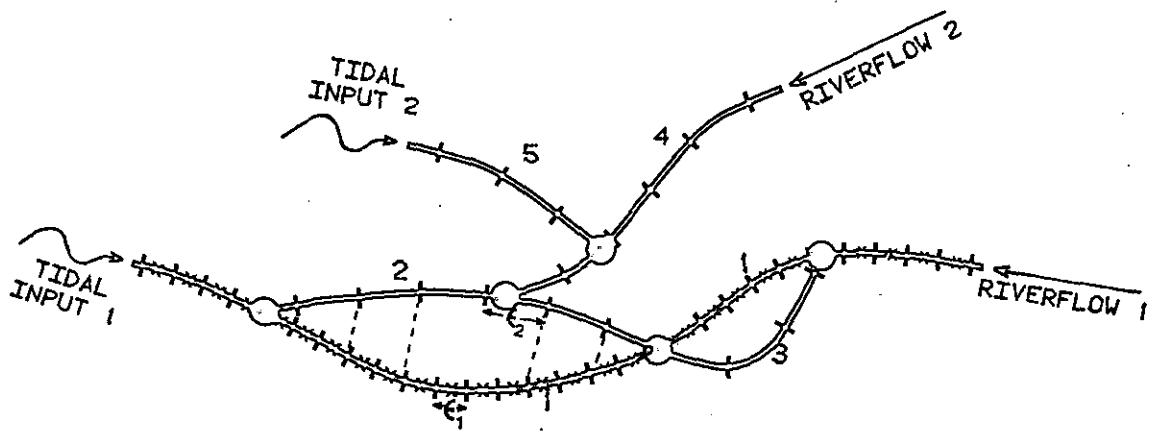
$$s(o, z, t) = S(z, t). \quad (14)$$

Equation (5) is modified at the mouth so that (14) applies only when  $u$  is positive, i.e. for flooding currents. On an ebb tide,  $u < 0$ , salinity is determined by (5) using upwind advection, so that upstream salinities determine the boundary values. Note that the geometry of the channel is specified relative to the level surface  $z = 0$ , which is not necessarily the chart datum, therefore, bottom slope terms often encountered in one dimensional tidal models (Jay 1984) are implicitly accounted for by the formulations above.

### 2.1.2. Channel Networks

The model is organized into a number of channels that interconnect at nodes. A sketch of a plan view of an estuary, consisting of a number of branching channels with two freshwater sources and two entrance channels, is given in Figure 1.

At all grid points, except at channel junctions, Equations (1) through (5), along with surface and bottom boundary conditions, apply.



| Elevation grid points      ○ Channel junctions  
 X Transport grid points    - - - Across-sandbank connections

Figure 1. Sketch of a branching-channel network.

At junctions, the equations of continuity (1) and (2) and salt conservation (5) are altered to take into account volume and salt fluxes from up to two side channels. Thus (1) becomes

$$b_{\zeta} \frac{\partial \zeta}{\partial t} + \frac{\partial U}{\partial x} + \frac{\partial V}{\partial y} = 0 \quad (15)$$

where V is the volume transports from the side channels and y is the cross (main) channel coordinate. Equation (2) is modified similarly. The salt conservation equation becomes

$$\begin{aligned} & \frac{\partial (bs)}{\partial t} + \frac{\partial (bus)}{\partial x} + \frac{\partial (bvs)}{\partial y} + \frac{\partial (bws)}{\partial z} \\ & - \frac{\partial}{\partial x} (bK_h \frac{\partial s}{\partial x}) - \frac{\partial}{\partial y} (bK_h \frac{\partial s}{\partial y}) - \frac{\partial}{\partial z} (bK_v \frac{\partial s}{\partial z}) = 0 \end{aligned} \quad (16)$$

where v is the depth-dependent velocity of the side channels. Note U and v are the same as U and u of the side channels. The along-channel momentum equations (3) and (4), which determine U and u, do not need to be modified, as they are vector equations which contain only x derivatives of  $\zeta$  and s. Hence, the determination of V in (15) is calculated from the cross-channel momentum equation which is the same as the along-channel momentum equation (4) for the side channel. Apart from the junction modifications, the equations for each channel are solved just as if it were a single channel with the boundary conditions given by  $\zeta$  and s at the junctions for the beginning or end of each secondary channel. Thus, for example, in Figure 1 the equations for Channel 1 are solved first for a given time-step, and the solutions for  $\zeta$  and s at the junctions with Channel 2 are used as boundary conditions for the solutions for Channel 2, and so on until the equations have been solved for all the channels. The solution method is described briefly below.

### 2.1.3. Sandbank Overtopping

The channels of the Columbia River often are separated by extensive shallow sand flats or low-lying marsh land. At high water these areas are often flooded and at low water exposed. In the latter case there is a barrier between the channels, whereas in the former case there can be transport of water and salt across the barrier from one channel to another.

The model has been developed so that lateral transports between channels are allowed when the water level on one side or the other exceeds the height of the crest of the bank or barrier. The formulation used is very similar in many respects to the treatment of overtopping sub-grid barriers in the two-dimensional (horizontal) tidal-storm surge WIFM model (Butler, 1980). Lateral over-barrier connections between channels are indicated by dotted lines on the sketch (Figure 1); a cross-section view is given in Figure 2. The over-barrier transports are assumed to occur across cell faces which are parallel to the main channel axis and centered midway between elevation grid points.

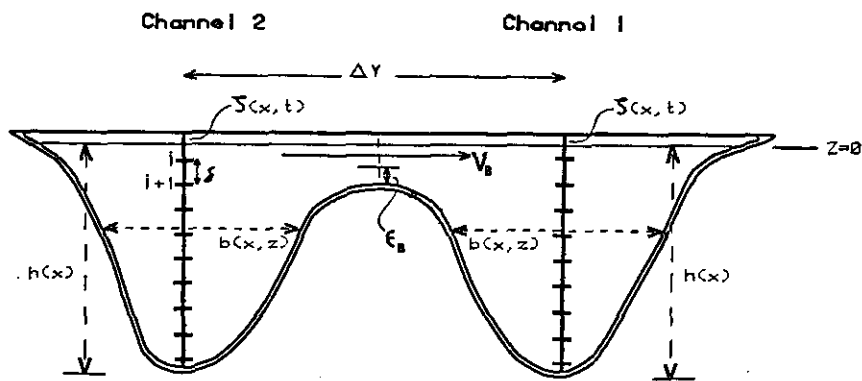


Figure 2. Sketch of the cross-sections of two channels with lateral transport of water across a connecting sandbank.

Three cases can be distinguished:

1) The water level on both sides of barrier is below the crest of the barrier. In this case,

$$V_B = 0 \quad (17)$$

where  $V_B$  is the volume transport across the barrier.

2) The water level on one side but not the other exceeds the crest height by a small increment,  $\epsilon_b$ . Water is transferred to the lower side at a rate given by the broad-crested weir formulae (Butler, 1980). where:

$$V_B = \pm f_B A_B (gd_B)^{1/2} \quad (18)$$

where  $f_B$  is a barrier friction coefficient and  $A_B$  is the cross-sectional area defined by the length of the barrier crest ( $L_B$ ) in a grid cell and the depth of the water ( $d_B$ ) above the crest ( $A_B = L_B d_B$ ).

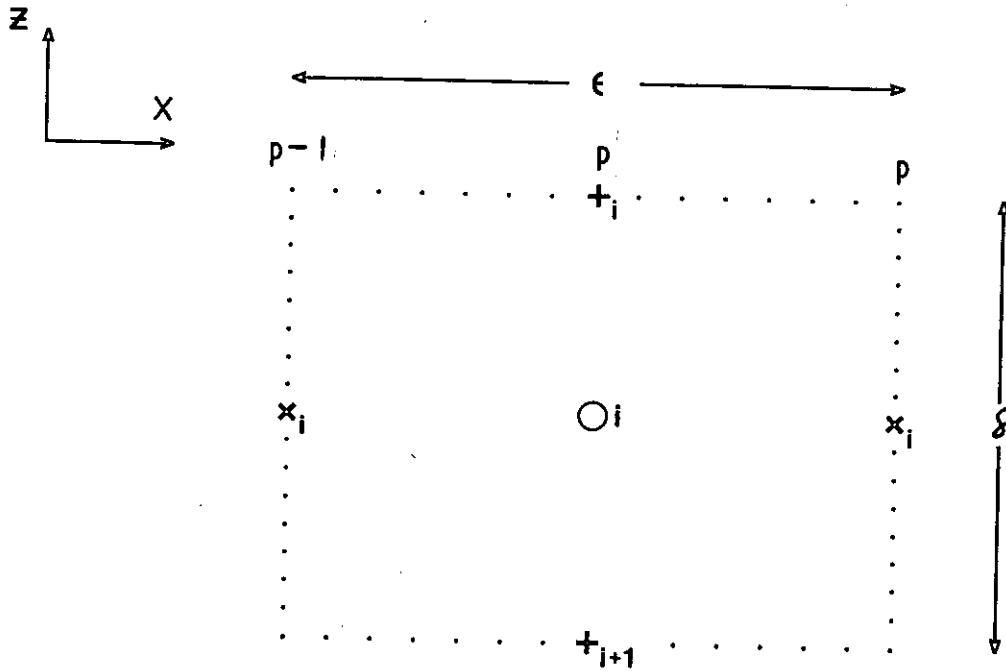
3) If the water level on both sides of the barrier is greater than  $\epsilon_B$ , then the momentum equation is solved for  $V_B$ . Thus

$$\frac{\partial V_B}{\partial t} = -gA_B \frac{\partial \zeta}{\partial y} - g \frac{L_B}{\rho} \frac{\zeta}{d_B} \frac{\zeta}{z} \frac{\partial \rho}{\partial y} dz' dz - L_B \frac{k|V_B|V_B}{A_B^2} + L_B \tau_{ys} \quad (19)$$

where  $y$  is the axis direction approximately normal to the center lines of the two channels (or a set of channels if there is more than one barrier), and  $\tau_{ys}$  is the wind stress in the direction of the  $y$ -axis. The continuity equation (5) is modified in a manner similar to (15), with  $V_B$  replacing  $V$ . An assumption is made that the current velocities over the crest are uniform with depth. Thus salt transport over the crest is accounted for with an equation similar to (16), with  $v$  replaced by  $V_B/A_B$ . This facility is important for efficient schematization of the Columbia River Estuary because of its large shoal areas. Considerable volume transports can occur over these shoals as was illustrated in the WIFM results of Volume I.

#### 2.1.4. The Finite Difference Method

The numerical method is an adaption of the methods described in Hamilton (1975, 1976), with improvements based on the semi-implicit shelf model of Hamilton and Rattray (1978) and the models of Blumberg (1975), Elliott (1976) and Wang and Kravitz (1980). The basic grid cell and arrangement of variables is given in Figure 3. The vertical spacing,  $\delta$ , is the same for all channels; but the horizontal spacing,  $\epsilon$ , can vary between channels, though it is fixed for any particular channel. The grid is arranged in a vertical plane corresponding to the longitudinal section down the center line of the channel and is fixed in space. The free surface moves up and down through the grid, with determination of the position of the grid points closest to the surface being performed every time step. The implementation is essentially the



- Salinity point,  $S_{i,p}$
- + Vertical velocity point,  $W_{i,p}$
- × Horizontal velocity point,  $U_{i,p}$
- $\epsilon, \delta$  Horizontal and vertical grid spacing
- $X, z$  Horizontal and vertical coordinates
- $p$  Column number
- $i$  Vertical cell number

Figure 3. Arrangement of computational variables in a grid cell.

same as Hamilton (1975). The method uses forward and backward one-step time differences and central differences in space on a staggered grid. It also uses Equations (1) and (4) in a semi-implicit scheme to solve for volume transports,  $U$ , and free-surface elevations,  $\zeta$ , similar to Hamilton (1976) and Wang and Kravitz (1980). This method removes the Courant-Friederich-Lewys (CFL) criterion based on the free gravity wave-speed as a restriction on the time-step. Channel junctions,  $V$ , and cross-barrier transports,  $V_B$ , in (15) are treated explicitly in this calculation. The semi-implicit equations are inverted for each channel individually, and the updated value of  $\zeta$  at a junction is used as a boundary value for a secondary channel. This imposes a restriction on the network; that is a channel must begin and end on a lower-numbered channel (see Figure 1). Of course, any channel can begin or end at an estuary mouth or end at a river.

The solution of equations (19) and (15) for the barrier flows are carried out similarly, using a one time-step, semi-implicit scheme after  $\zeta$  and  $U$  and have been stepped forward. The scheme is essentially the stabilizing correction scheme illustrated by Butler (1980) as one of the solution methods for WIFM. The distance between elevation grid points on either side of the barrier is taken as  $\delta$  (Figure 2) in the finite difference form of (19). Thus, Equation (19) is advanced a time step semi-implicitly, and then  $\zeta$  is corrected for the relevant grid points using (15).

Equations (1), (4), (15), and (19) can be solved as a one-dimensional network if the frictional stresses are made functions of  $U$  and  $\rho = 0$ . Thus, to save computer time, upstream of the salt intrusion the model is reduced to a one-dimensional channel model for  $U$  and  $\zeta$ , with  $\tau_b = k|U|U/A^2$  and  $U/A$  replacing  $u$  in the side-friction term. Thus for the Columbia River the Upriver Channel and the Cathlamet Channel are one-dimensional (see Section 2.2).

The depth-dependent equations of conservation of salt and momentum, (3) and (5), are explicit except for a Crank-Nicholson (Roach 1972) implicit treatment of the vertical eddy diffusion terms. This removes another, severe restriction on the time step. In explicit schemes,  $\Delta t < \delta^2/N_v$ . If  $N_v$  is large or  $\delta$  small, instabilities will occur for time steps exceeding this criterion. The Crank-Nicholson scheme eliminates this restriction, which could be easily violated if  $N_v$  is a function of the flow variables. The sum of the finite difference version of the depth-dependent momentum equation (3) over the water column reduces to (4) to ensure correct integral conservation of momentum. The salt conservation equation (5) is in conservative form, and the advection terms are the principle non-linear terms, along with bottom friction, in the model equations. Since the Columbia River is dominated by tidal currents and salt balance is maintained principally by tidal advection (Jay 1984), it is important to use accurate finite difference analogues to these non-linear terms. Recent developments in finite difference methods for the two-dimensional advection equation now allow a reasonably accurate calculation of advection of a solute without the previous drawbacks of strong implicit numerical diffusion in low order upwind schemes, or noise in the form of ripples, negative values or overshoots, in high-order schemes. The

method used in the model is due to Smolarkiewicz (1983). This is a two-step method in which the first step is a conventional upwind scheme followed by an anti-diffusive step that reverses the implicit numerical diffusion of the first step. Its advantages are low diffusion, positive definiteness and freedom from  $2\Delta x$  noise or ripples. The method is efficient in computer time compared with methods producing similar accuracies. In an earlier version of the Columbia River model, the Flux Corrected Transport Method of Zalesak (1979), as implemented by Smolarkiewicz (1982), was used. This method did not produce as satisfactory a result as the present method, since it diffused the horizontal salinity gradients, which masked the neap-spring effect on the salt intrusion length. The stability of the scheme is given by the Courant condition, where  $((u \Delta t / \Delta x)^2 + (w \Delta t / \Delta z)^2)^{1/2} \leq 2^{-1/2}$ . This is the major restriction on the time step for the complete solution of all the equations of the model. There is also a weak condition involving bottom friction, but it is not usually restrictive in this estuary, compared with the Courant condition. The conventional upwind advection scheme is used for the y derivative terms in (16) at junctions or for salt transport across sandflats and for all the horizontal advection terms at horizontal boundary grid points (estuary mouth) when the tide is ebbing.

#### 2.1.5. Programming Considerations

The multi-channel, semi-implicit, two-dimensional (2-D) estuary model has been coded in FORTRAN 77 for SAI/Raleigh's Gould 32/27 32-bit super-minicomputer. Advantage has been taken of modern structured programming techniques available with FORTRAN 77. The variables, which are functions of x and t only, are stored in one-dimensional (1-D) arrays containing the horizontal grid values for all channels. The beginning and end points of the channels and their connection points with other channels within the 1-D array are stored in pointer arrays, using techniques similar to those of the storage of sparse matrices. The depth-dependent variables are stored in similar 2-D arrays, with the first dimension being the depth and the second corresponding to the 1-D horizontal arrays.

The program writes output to magnetic tape for fixed intervals (usually 1 hour) for further statistical processing. The calculations can be stopped and restarted on any given day. Boundary condition data are read in from time series files, if required, and linearly interpolated to the model time step. The program has not been documented due to funding limitations; therefore, it is not available through CREDDP. The model output data is stored in binary form on magnetic tape which can be read only on a Gould 32 series computer. Copies of output data tapes can be obtained from the author.

#### 2.1.6. Initialization

To start the time-stepped solutions to (1)-(5), the variables must be initialized. The model runs described below were initialized from a state of rest with all transports and velocities equal to zero at  $t=0$ . The free surface elevation was assumed to be at mean tide level ( $z=0$ ) at all grid points. Thus the initial conditions are:

$$\zeta = u = w = U = V = V_B = 0 \text{ for all } x \text{ and } z \text{ at } t = 0. \quad (20)$$

Riverflow is imposed at the ends of the required channels and, to lessen the possibility of shock waves, the elevation at mouths is linearly interpolated over the initial 6-hour time period ( $t = 0$  to 6 hours) before following the true tidal signal. For the Columbia River network, riverflow imposed at the head of the estuary takes about 3 hours to reach the mouth.

Experience has shown that salinity calculations should not be started until the tidal velocities have stabilized (Hamilton, 1975). Therefore, the salinities are initialized to a high tide distribution at least one day after the start of the tidal calculations. During this initial period, salinities are held constant. This procedure allows the tidal velocities to be established and a density-current circulation to be generated before salinity is advected and mixed by the currents and turbulence. The salinity field is initialized from observed data (primarily from the conductivity sensors of the current meters) using linear interpolation between observation points.

## 2.2 APPLICATION OF THE MODEL TO THE COLUMBIA RIVER ESTUARY

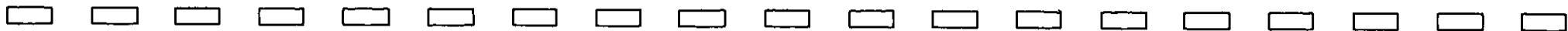
The schematization of the Columbia River into 12 channels is shown in Figure 4. Horizontal grid spacings were chosen to resolve the channels adequately and to mesh with the junction points. The cell numbers are at elevation (salinity and vertical velocity) grid points, and the small stars on the cell boundaries are at transport (horizontal velocity) grid points. At both these types of points, the cross-sections are plotted using the isobath contours given on a detailed bathymetric 1:20,000 chart provided by Northwest Cartography, Inc. The widths are digitized at 2 m intervals from the mean tide level (taken to be 1.22 m (4 ft) above the MLLW datum of the chart). The depths are taken to be the deepest part of the cross-section. The channel names are given in Table 1. Channels 11 and 12 are one-dimensional. Channel 1 will be referred to often as the Navigation Channel.

Tidal and salinity boundary conditions are applied at grid point 1, channel 1 and riverflow boundary conditions are applied at the river ends of channels 1, 10, and 12. The riverflows added together from channels 1 and 12 equal the daily cumulative riverflow estimated for Astoria from USGS records (Jay 1984). Channel 12 riverflow is held constant at 2,000 m<sup>3</sup>/s and channel 10 at 10 m<sup>3</sup>/s. The average riverflow for the ten-day October 1980 period simulated below is 4,046 m<sup>3</sup>/s, with a minimum of 3,313 and a maximum of 4,474 m<sup>3</sup>/s. The 60-day spring 1981 riverflows average to 10,120 with a minimum of 6,210 and a maximum of 15,910 m<sup>3</sup>/s.

The tidal boundary condition at the mouth was obtained from the hourly, 3-hour, low pass filtered, tidal height time-series at Jetty A (TG-N1 or TG-1), with the record mean removed. The salinity boundary conditions were originally taken from two Aanderaa current meter records at 7 and 15 m below MLLW at Station CM-2S. The data were from the October 1980 CREDDP data set, and station CM-2S corresponds to elevation grid point 2 in channel 1. The data at every time-step were

Table 1. Channel Names

<u>Channel Number</u>	<u>Name</u>	<u>Total No. Points</u>	<u>Horizontal Grid Spacing (km)</u>
1	Main-Astoria (Navigation Channel)	40	3
2	North Chinook-Taylor Sands	8	3
3	Taylor Sands	3	3
4	North - Praire - East Woody Island	11	2.5
5	John Day - South	5	3
6	Woody Island West	4	2.25
7	Grays Bay	6	3.5
8	Prairie - Clifton	7	3
9	Fitzpatrick Island	3	2.6
10	Youngs Bay	5	3
11	Cathlamet - East Puget Island	5	3.5
12	Upriver-Tidal	<u>15</u>	3.5
	Total	112	



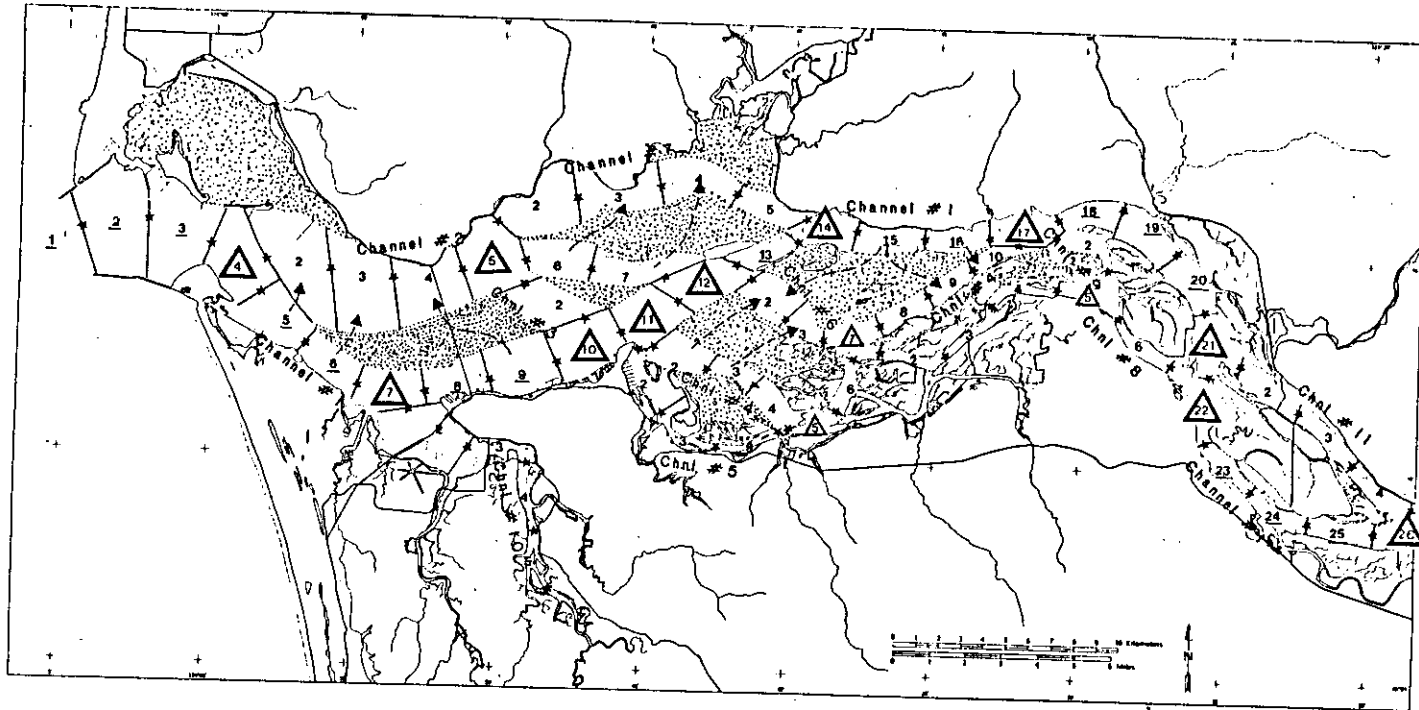


Figure 4. The channels and grid cells used for the schematization of the estuary. Grid cell number gives the position of elevation points, a star is the position of a transport point. Triangles denote channel junction grid points. Dashed arrows denote across barrier inter-channel connections.

linearly interpolated through the water column from the surface to 15m. Below 15 m the salinity was held constant at the 15 m value. However, it was found during the experimentation stage that holding the mouth salinity profile constant in time made very little difference to the results. Since adequate salinity boundary data were not available for the June 1981 period simulated, a time-variant linear profile varying from 32 ‰ at the surface to 32.2 ‰ at the bottom was used for the mouth boundary condition for all the simulations discussed below. Note that this boundary condition operates only for positive or flooding mouth currents.

The model parameters are given in Table 2. The bottom friction parameters were varied a little in the upper reaches of channel 1 to improve the simulation of the tidal wave. The main parameter affecting the salinity distributions are the vertical eddy coefficients of viscosity and diffusion,  $K_v$  and  $N_v$ . The formulas used for these parameters will be discussed separately below.

Two periods are simulated, for which data are available for direct comparison. The first is the October 1980 CREDDP field study, which is a low riverflow period with maximum salinity intrusion. October 16, 1980, 0800 hours, Pacific Standard Time (PST) corresponds to  $t = 0$  for the model runs. The model was run for a 10-day period. The initialization of salinity corresponds to values recorded by CREDDP current meter moorings at 0900, October 17, Model time - day 2: 01 hours, 25 hours after  $t = 0$ . The initial salinity values were held constant over the first 25 hours of the model simulation. The second period is a high flow period between May 5 and July 3, 1981 (60 days). The first 20 days have relatively constant riverflow of 7,500 m<sup>3</sup>/s, followed by a large freshet, which peaks at 15,910 m<sup>3</sup>/s on June 10. The freshwater flow then slowly reduces to 7,500 m<sup>3</sup>/s on July 1. Initialization at  $t = 0$  corresponds to 00 hours PST, May 5, 1981. The salinity corresponds to interpolation of values measured by the current meters at 0300 hours, May 6, which corresponds to high tide at the mouth. The salinity was held constant for the first 27 hours of the model simulation. Therefore, the simulations include a typical low-flow period, a high-flow period and the response of the model to a large freshet. The model was calibrated by choosing the formulation and adjusting the constants in the eddy coefficient equations for the October 1980 period. The spring 1981 simulations were performed with no further adjustments, and thus the predictive ability of the model can be assessed from the National Ocean Survey (NOS) 1981 data. A complete 10-day simulation of the full depth-dependent model of the 12-channel network required a little under two hours of CPU time on the Gould 32/27.

### 2.2.1. The Data Base

The period of the October 1980 CREDDP field study was chosen initially for simulation because of the existence of synoptic time-series data for verification and calibration. The usable data derive from eight current meter moorings, six with more than one meter, and six tide gauges. The current meter moorings are shown as stars and the tide gages as diamonds on Figure 5a. Names used in the discussion

Table 2. Model Parameters

Total number of horizontal grid points		112
Total number of vertical grid points		18
Vertical grid spacing, $\delta$		2 m
Time step		6 minutes
Friction Coefficients		
	Bottom	$k$ 0.0025
	Side	$k_s$ 0.0020
	Barrier	$k_B$ 0.0025
		$f_B$ 0.1
		$\epsilon_B$ 0.1 m

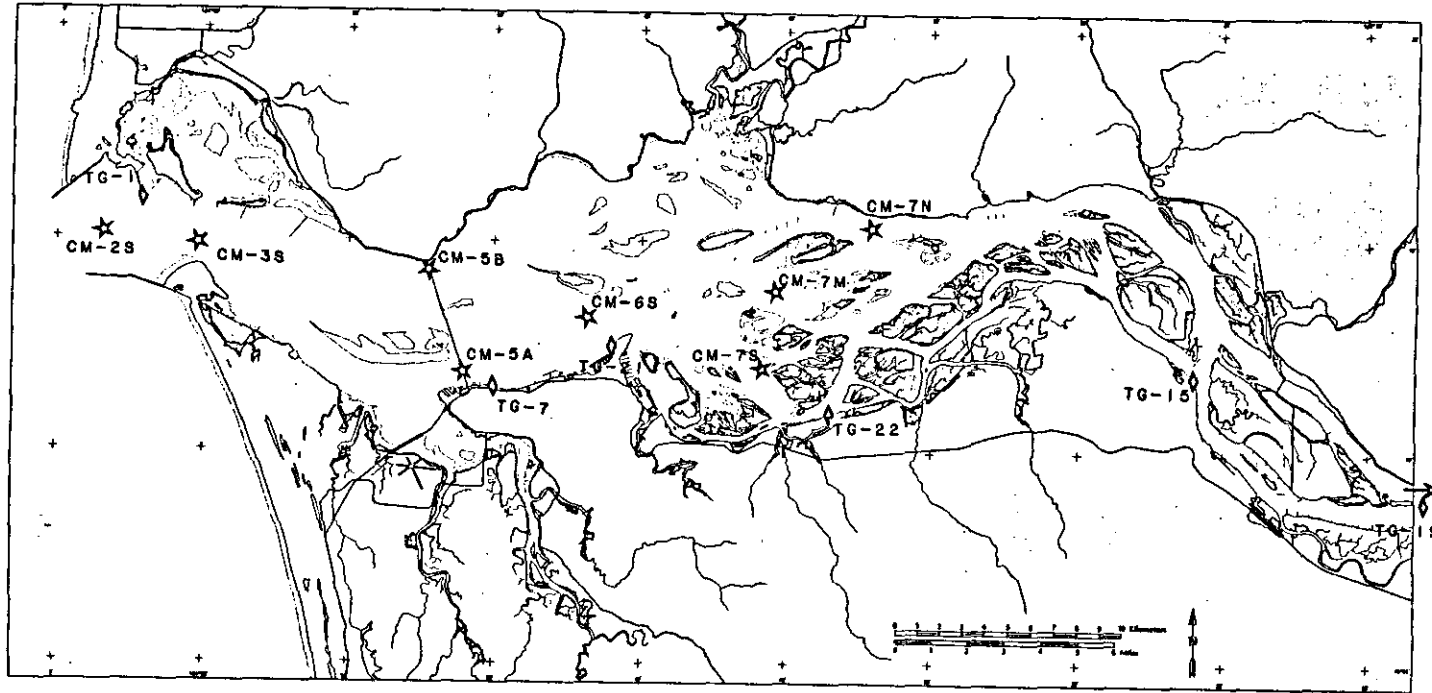


Figure 5a. Tide gauge (diamonds) and current meter moorings (stars) deployed during the 1980 CREDDP field study.

Table 3a. October 1980 CREDDP Data.

<u>CREDDP ID</u>	<u>Station Type</u>	<u>Variables<sup>1</sup></u>	<u>Model Channel #</u>	<u>Grid #</u>	<u>Depth<sup>2</sup> (m)</u>
CM-2S	Current Meters	U, S	1	2	6 (T) 16 (B)
CM-3S	Current Meters	U, S	1	3	12 (T) 18 (B)
CM-5A	Current Meters	U, S	1	8	2 (T) 10 (B)
CM-5B	Current Meters	U, S	2	3	6 (T) 12 (M)
CM-6S	Current Meters	U, S	1	10	8 (T) 12 (M)
CM-7N	Current Meters	U, S	1	14	6 (T) 10 (M)
CM-7S	Current Meters	U, S	4	3	4 (T)
CM-7M	Current Meters	U, S	6	2	4
TG-1	Tide Gauge Jetty-A	E	1	1	---
TG-7	Tide Gauge Astoria Warf	E	1	8	---
TG-1	Tide Gauge Tongue Point	E	1	11	---
TG-15	Tide Gauge Bradwood	E	1	22	---
TG-19	Tide Gauge Beacon 76	E	1	27	---
TG-22	Tide Gauge Svensen Island	E	4	5	---

<sup>1</sup>Variables U=Along Channel Current  
S=Salinity  
E=Tidal Elevations

<sup>2</sup>T=Top  
M=Middle  
B=Bottom

are shown on the place names map immediately preceding Volume I. The CREDDP identification is used. Table 3a shows the stations used, and channel and grid numbers of the corresponding model grid points (see Figure 4). The time series data have been filtered with a three-hour low pass (3-HLP) Lanczos filter, to remove high frequency noise, and decimated to 60-minute intervals. The main disadvantage of these data is the sparseness of spatial coverage, particularly in the secondary channels. Also, the majority of the top current meters are 5 m below MLLW, so the upper part of the water column is not sampled except at CM-5A. Current meters CM-5A and CM-5B were attached to the piers of the Astoria-Megler Bridge and thus are subject to distortion of the flow by the bridge piers. It is suspected that flooding currents may be undersampled and ebbing currents oversampled, as the current meter mounts were on the east or upriver side of the piers. The position of CM-7S may not be correct, as the indicated depth of the meter is deeper than the chart water depth at its supposed position. For the comparisons with model current data, the observed currents were rotated so that the u-component axis was parallel to the major axis of the  $M_2$  tidal ellipse, which in general was parallel to the channel axis. The sense of the axis was such that positive currents were directed in the same direction as the channel axis (i.e. usually upstream).

The National Ocean Survey (NOS) staged an extensive field program in the estuary in 1981. One of the best periods for synoptic coverage by tide gauge and current meter moorings west of Tongue Point is the high flow period in May and June of 1981. This data base is described by Jay (1984) and used to analyse the high flow circulation in the estuary. From the modeler's point of view, the NOS data provide an independent check of a calibrated model for riverflows ranging from 2-3 times the October 1980 riverflows. Therefore, the ability of the model to predict the high flow circulation and salinity distribution can be assessed, and thus the strengths and weaknesses of the model are more clearly delineated. The positions of tide gauge and current meter stations are given in Figure 5b with the CREDDP identification. Table 3b shows the stations used and the channel and grid numbers of the corresponding model grid points. Limitations of the data include lack of coverage of the mouth region and variation between deployments in the nominal depths and positions of the meters due to the method of rotating the moorings (usually at two-week intervals). Therefore, there is some uncertainty as to the true depths of the current meters. This fact, along with the high degree of stratifications in the estuary, makes direct comparison of absolute salinity values somewhat difficult. However, the vertical grid points in Table 3b are the best approximation of the average meter-depth during the deployment. They may however vary by  $\pm 2$ m between deployment periods. The NOS data were processed by the CREDDP Currents investigator and supplied in 3-HLP filtered form to this work unit. Current components were rotated into a channel frame of reference based on the major axis of the  $M_2$  tide, in the same manner as for the October 1980 data.

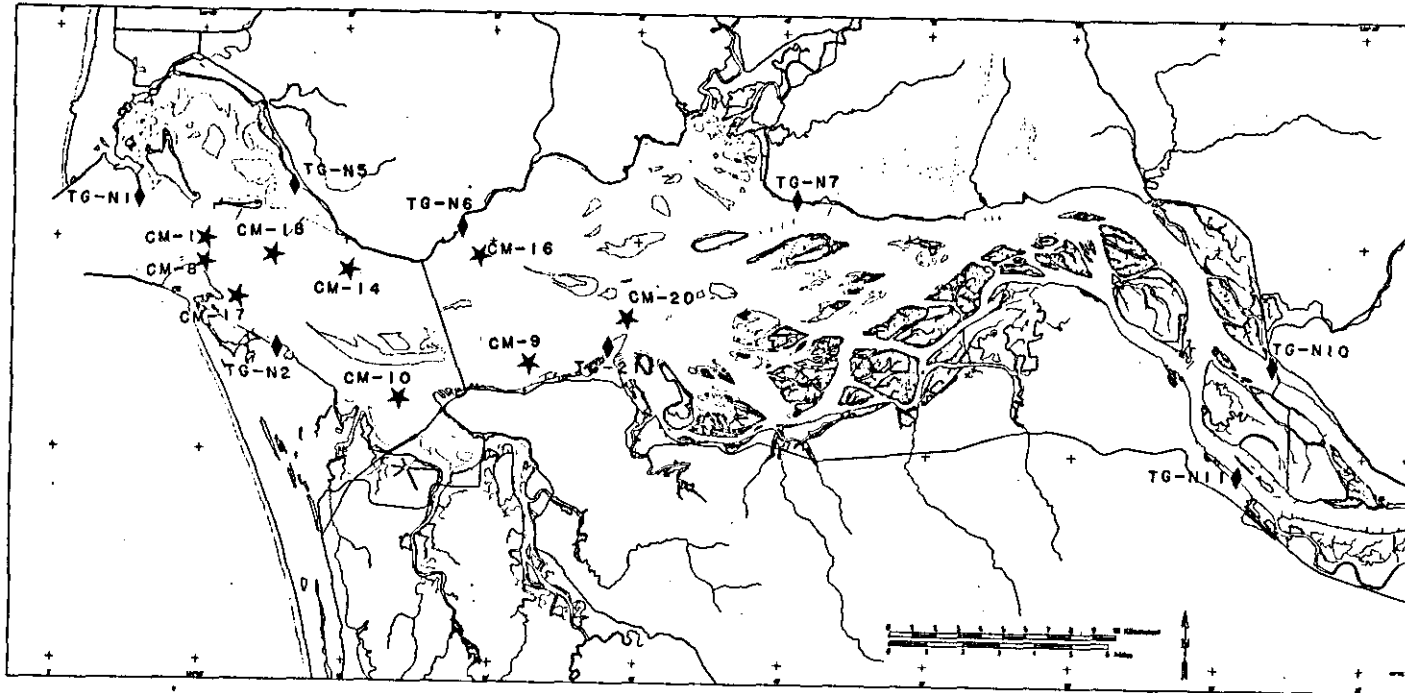


Figure 5b. Tide gauge (diamonds) and current meter moorings (stars) deployed during the spring 1981 National Ocean Survey field study.

Table 3b. Spring 1981 NOS Data

<u>CREDDP ID</u>	<u>Station Type</u>	<u>Variables<sup>1</sup></u>	<u>Model Channel #</u>	<u>Grid #</u>	<u>Depth<sup>2</sup> (m)</u>
CM-8	Current Meters	U, S	1	3	6 (T) 16 (B)
CM-17	Current Meters	U, S	1	4	4 (T) 11 (B)
CM-10	Current Meters	U, S	1	7	7 (M) 13 (B)
CM-9	Current Meters	U, S	1	9	5 (T) 7 (B)
CM-20	Current Meters	U	1	11	4 (T) 14 (B)
CM-1	Current Meters	U, S	2	1	6 (M) 16 (B)
CM-18	Current Meters	U, S	2	2	4 (T) 12 (B)
CM-14	Current Meters	U, S	2	3	8 (M) 11 (B)
CM-16	Current Meters	U, S	2	5	5 (M) 10 (B)
TG-N1	Tide Gauge Jetty A	E	1	2	-
TG-N2	Tide Gauge Fort Stevens	E	1	6	-
TG-21	Tide Gauge Tongue Point	E	1	10	-
TG-N7	Tide Gauge Altoona	E	1	14	-
TG-N11	Tide Gauge Wauna	E	1	23	-
TG-N5	Tide Gauge Chinook	E	2	2	-
TG-N6	Tide Gauge Knappton	E	7	2	-
TG-N10	Tide Gauge Cathlamet Channel	E	11	2	-

<sup>1</sup>Variables U=Along Channel Current  
S=Salinity  
E=Tidal Elevations

<sup>2</sup>T=Top  
M=Middle  
B=Bottom

## 2.3 CALIBRATION AND VERIFICATION

### 2.3.1. Tidal Calibration

The model was first adjusted to reproduce the propagation of the tide for the October 1980 10-day period. The model was used in 1-D mode, neglecting salinities and depth dependence. The method of adjustment was to change the length of the Upriver-Tidal channel so that incoming and reflected waves from the heads of channels 1 and 12 interfere correctly to produce the correct phase and amplitude down-estuary of the junction of these two channels (the junction is at channel 1, grid point 29). The simulation was then checked in 2-D mode (again neglecting salinity), and minor adjustments made to the bottom friction coefficient in the stretch of the Navigation Channel between Tenasillahe and Puget Islands and also in the Clifton Channel ( $k=0.0023$ ). Part of the reason for doing this was so that the friction stability criteria would not be violated in these channels during spring tides.

The results of the final calibration for the October 1980 period are shown in Figure 6. Positions of the gauges are given in Figure 5a. The simulated and observed tidal heights are compared for the indicated tide gauges. The comparison for tide gauge TG-1 is of course exact, since this record is used as the boundary condition. The remaining comparisons in the interior of the estuary show very good phase agreement and only small differences in peak amplitudes. It is noted that the apparent non-tidal effects evident in the observations at Astoria, Tongue Point and Svensen Island, along the central southern shore of the estuary, are due to the pressure gauges sinking into the bottom (Jay 1984). The reproduction the tidal wave can be considered good, having accuracy similar to the WIFM simulations presented in Volume I. A more quantitative comparison using harmonic analysis is given in Section 3.1.3.

The calibrated model was applied with no changes in the values of the parameters to the 60-day June 1981 period. The results from comparing the simulated tidal elevations with the NOS-CREDDP tide gauge records are shown in Figure 7. The positions of the gauges are given in Figure 5b. Note that in these long 1981 time series, there is a fault every 10 days caused by a program error that made the mouth tidal elevation faulty for the first few hours of a restarted run. The 60-day simulation was run in 10-day segments. This has obvious effects for these few hours but appears not to cause any other problems for the rest of the records, including current and salinity presented in the following sections. Lack of funds prevented a rerun of the 60-day simulation for the purpose of removing this fault.

The 1981 tide gauge data has better coverage of the north shore than the 1980 CREDDP data. The simulation of amplitude and phase at all stations is seen to be very good. Since observed riverflows are used, any effects on the tidal amplitudes and phases due to the freshet are also reproduced. It is noted that the underlying low-frequency variability is also well reproduced. Thus, the rise in water level at the up-river gauges TG-N10 and N11 due to the freshet (JD150-170) is

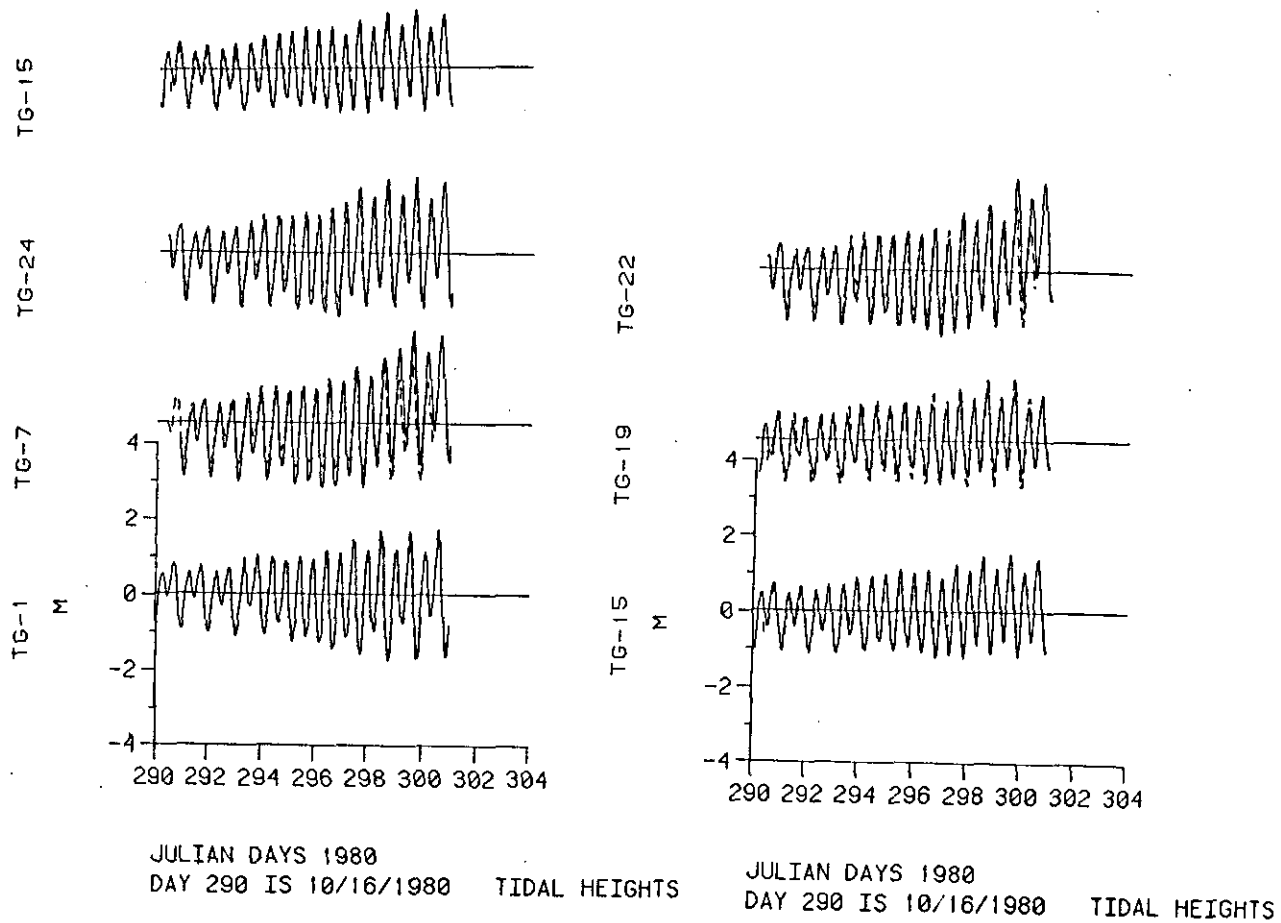


Figure 6. Observed (solid) and simulated (dashed) tidal heights for the indicated stations for the October 1980 low flow period.

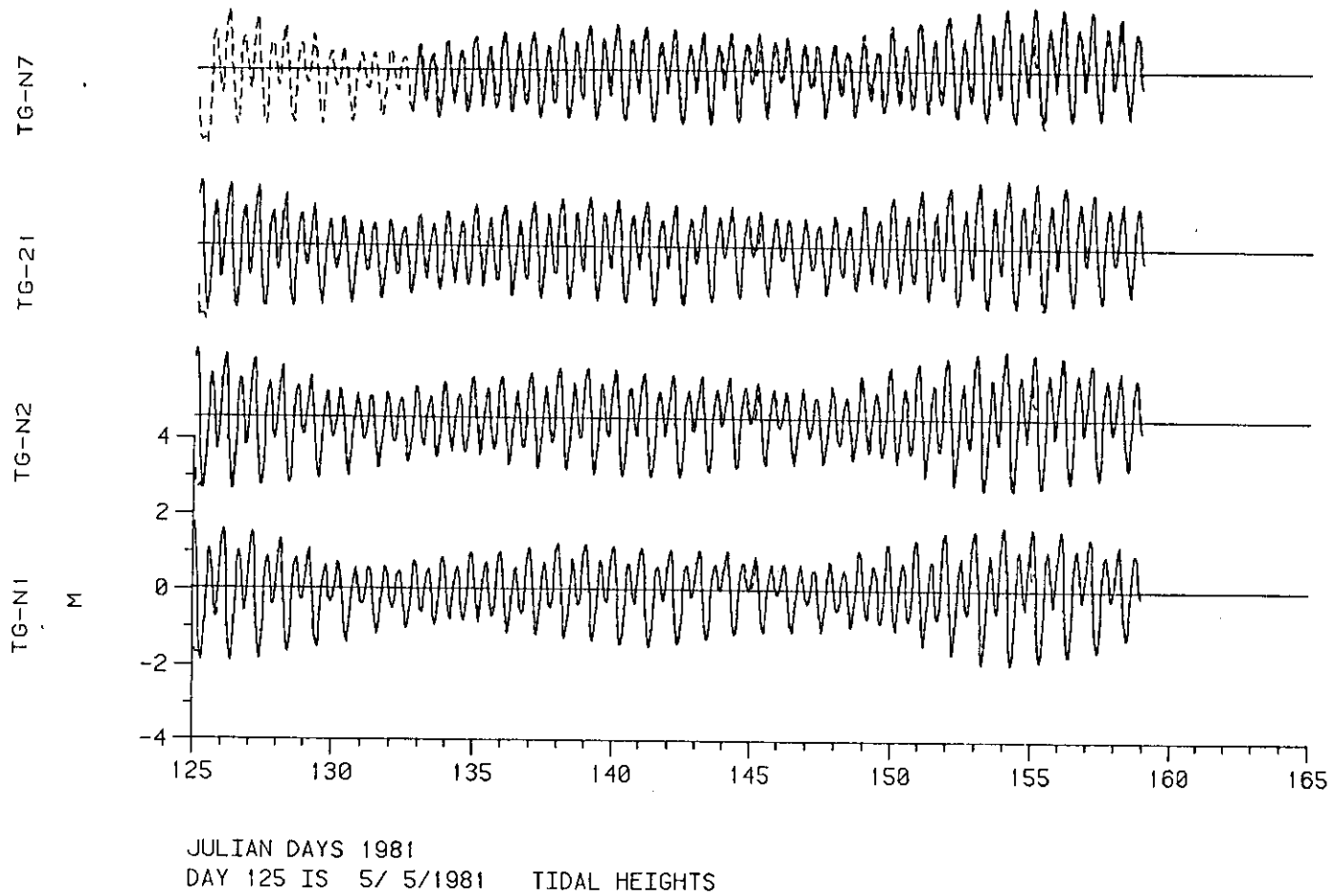


Figure 7a. Observed (solid) and simulated (dashed) tidal heights for the indicated stations for the spring 1981 high flow period.

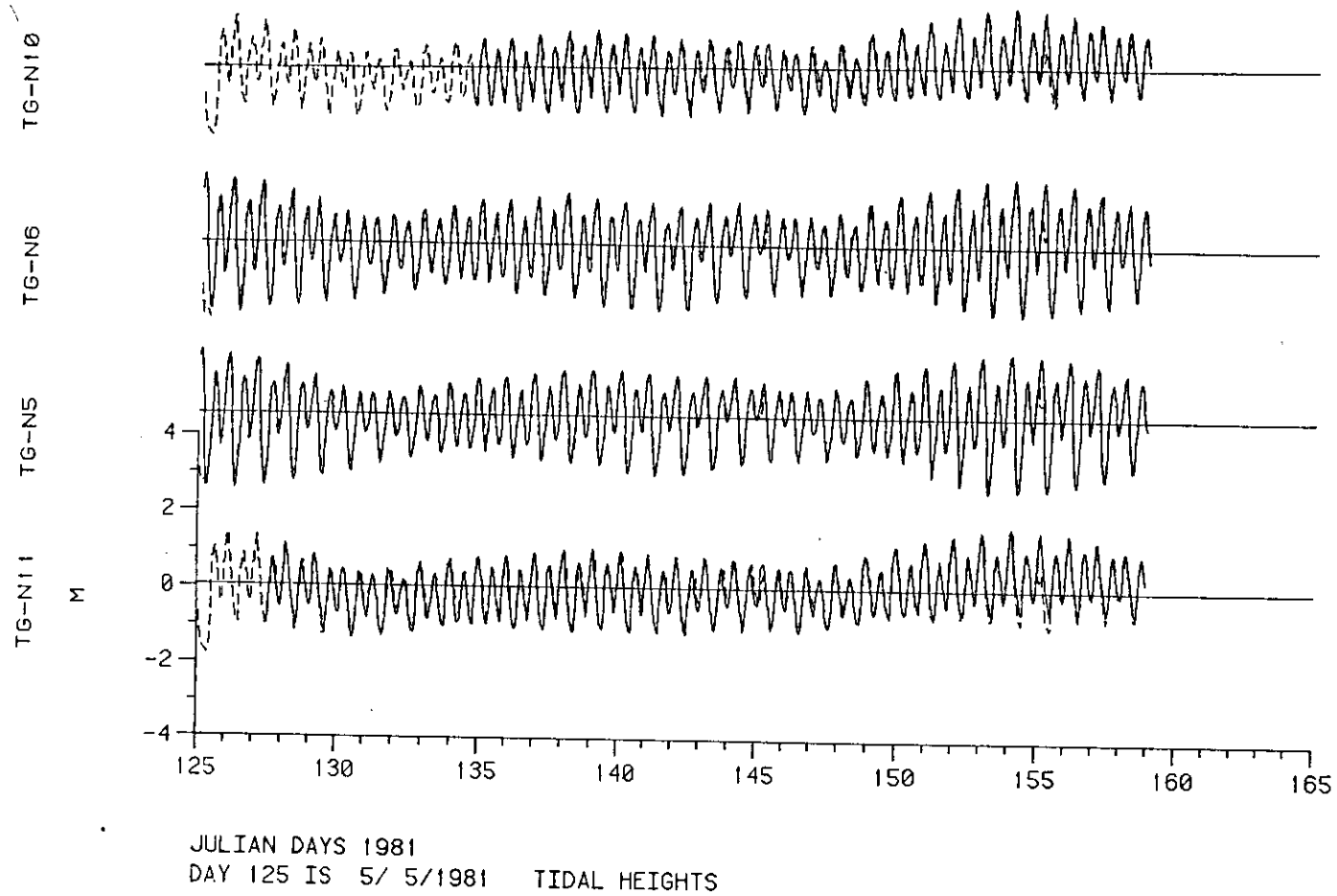


Figure 7b. Observed (solid) and simulated (dashed) tidal heights for the indicated stations for the spring 1981 high flow period.

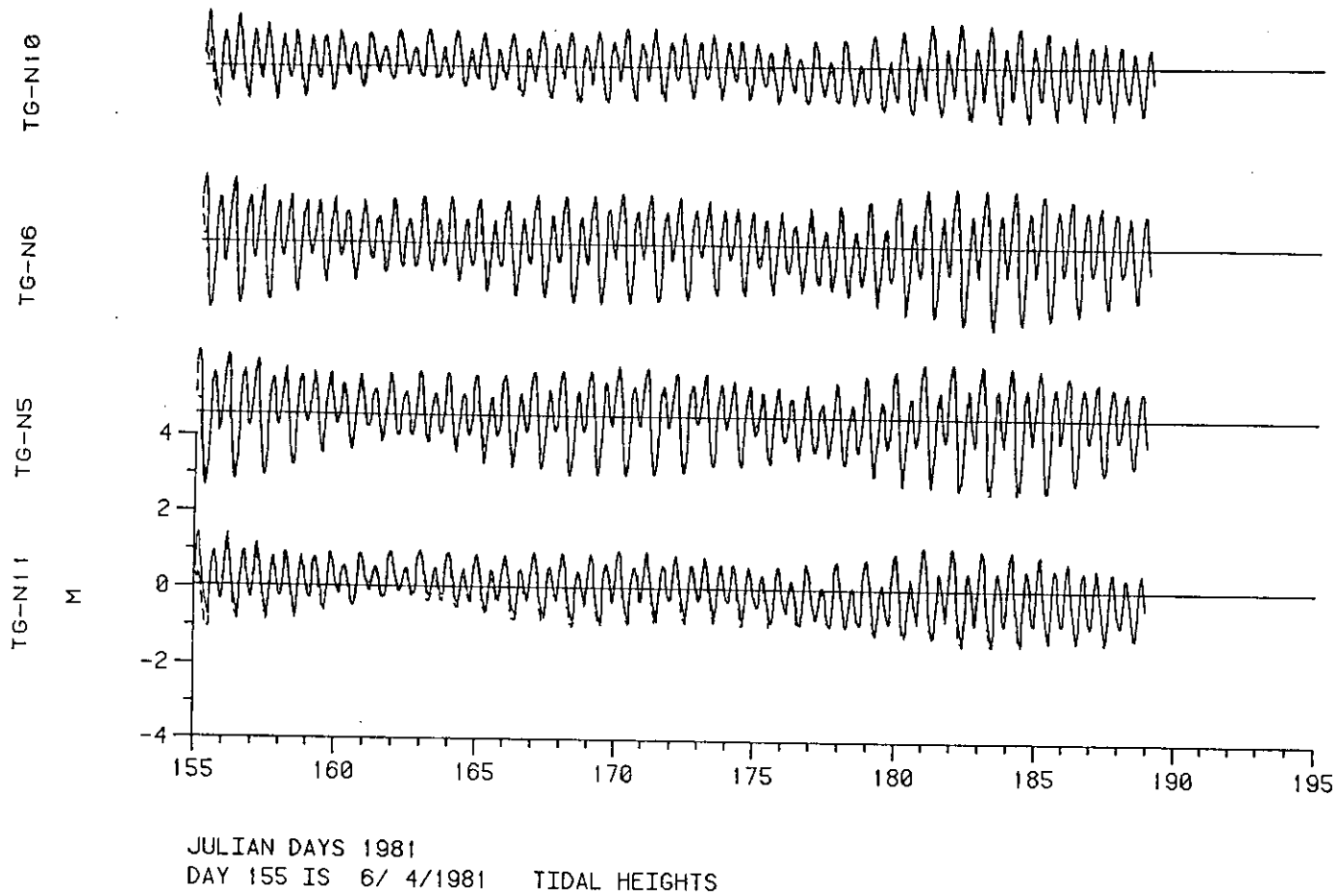


Figure 7c. Observed (solid) and simulated (dashed) tidal heights for the indicated stations for the spring 1981 high flow period.

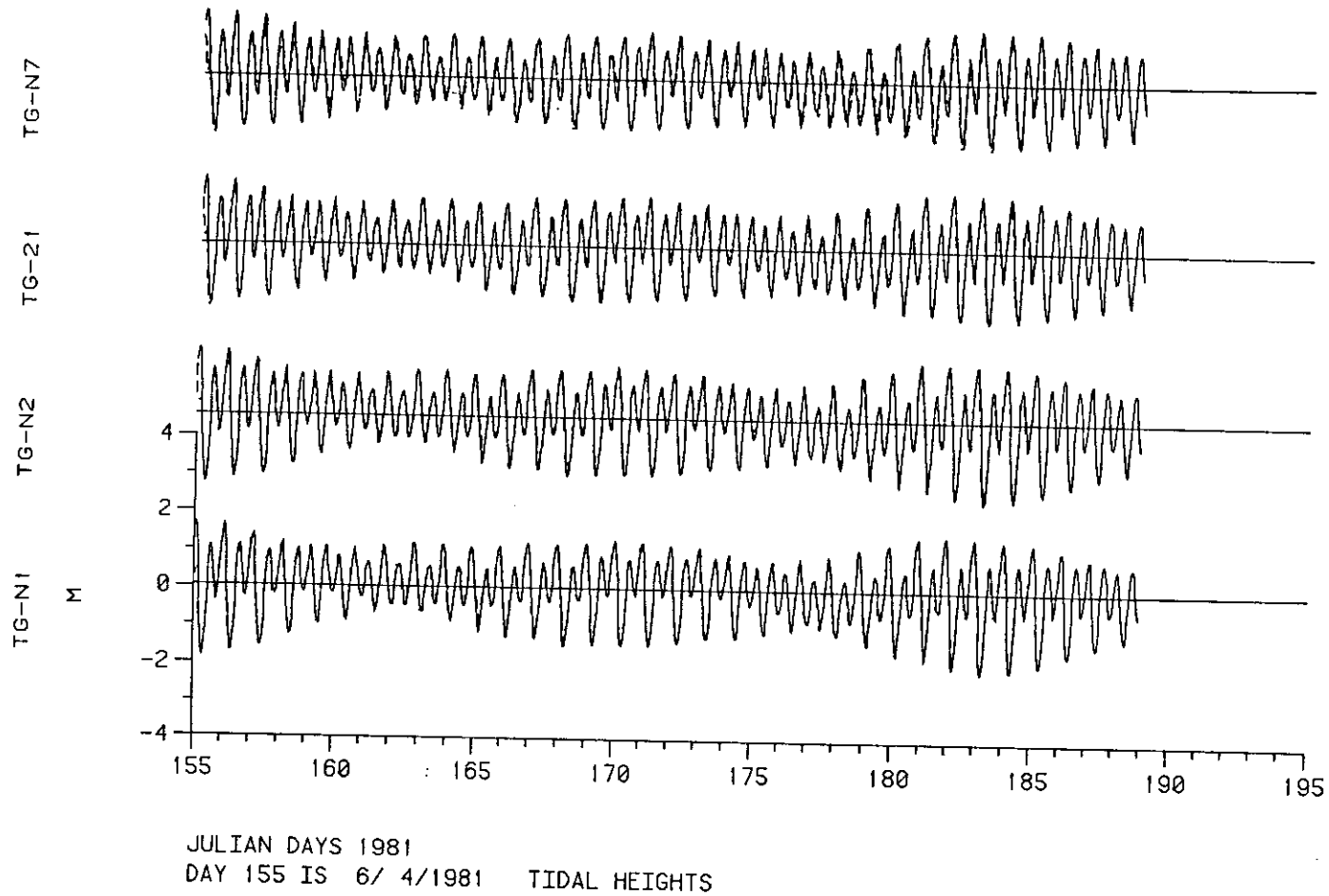


Figure 7d. Observed (solid) and simulated (dashed) tidal heights for the indicated stations for the spring 1981 high flow period.

reproduced. This rise is not observed at the lower estuary gauges. Therefore, the ability of the model to simulate the propagation of the tide to a fairly high degree of accuracy is firmly established by the use of two independent sets of data with greatly differing freshwater flows.

### 2.3.2. Vertical Eddy Coefficient Formulation

The calibration of the model's salinity and currents is most sensitive to the values chosen for  $K_V$  and  $N_V$ . A number of different simulations were performed using a number of different models for these coefficients. The following models were adopted:

$$\begin{aligned} 1) \quad K_V &= 0 \\ N_V &= 10^{-2} \text{ m}^2/\text{s} \end{aligned} \quad (21)$$

$$\begin{aligned} 2) \quad K_V &= K_0 + K_1 (h + \zeta) |U| / A.f(Ri) \\ N_V &= N_0 + N_1 (h + \zeta) |U| / A.g(Ri) \end{aligned} \quad (22)$$

where  $K_0 = 10^{-6}$ ,  $N_0 = 5 \times 10^{-4} \text{ m}^2/\text{s}$

$$K_1 = N_1 = 2.5 \times 10^{-3}$$

and  $f(Ri)$ ,  $g(Ri)$  are the Munk-Anderson (1948) Richardson-number functions.

$$\begin{aligned} f(Ri) &= (1 + 10Ri)^{-1/2} \\ g(Ri) &= (1 + 3.33Ri)^{-3/2} \end{aligned} \quad (23)$$

$$\text{where } Ri = \frac{-g\partial\rho/\partial z}{\rho_o(\partial u/\partial z)^2} \quad (24)$$

$$\begin{aligned} 3) \quad K_V &= K_0 + K_1 16.\eta^2(1-\eta)^2 (h+\zeta) |U| / A.f(Ri) \\ N_V &= N_0 + N_1 16.\eta^2(1-\eta)^2 (h+\zeta) |U| / A.g(Ri) \end{aligned} \quad (25)$$

where  $\eta = (\zeta - z + 0.1) / (\zeta + h + 0.2)$

with  $K_0$ ,  $K_1$ ,  $N_0$ ,  $N_1$ ,  $f(Ri)$  and  $g(Ri)$  defined as above.

The best simulation was obtained with (25), which allows the effects of stratification in suppressing turbulent mixing and assumes that the basic energy for mixing is obtained from the tidal current interacting with the bottom and side boundary layers, and the mixing length is proportional to the square of the distance from the upper or lower boundary. Apart from using the Munk-Anderson Richardson-number functions, the functional form of (25) is similar to the formulation derived by Pritchard (1960) from James River data. The coefficients  $K_1$  and  $N_1$  are taken from Bowden's experiments in a homogeneous tidal current in the Irish Sea. The models described above are discussed in Bowden and Hamilton (1975). A simulation was run with  $K_1$  and  $N_1 = 1.25$

$\times 10^{-3}$ , but the results were not as good.  $K_o$  and  $N_o$  are basically residual values to prevent the estuary from becoming frictionless when  $U = 0$ . The horizontal eddy diffusion coefficient,  $K_h$ , is given the small value of  $10^{-2} \text{ m}^2/\text{s}$  to help smooth slightly the horizontal salinity fields. The effective horizontal mixing in this model is primarily due to cross-channel shear-induced dispersion. The major component of horizontal mixing due to the interaction of vertical shears and stratification is taken directly into account by the model and need not be parameterized. Formulations exist for parameterization of the cross-channel variability component of the along-channel dispersion which Fischer et al., 1979 consider to be important in some estuaries. However, the various formulas give values for  $K_h$  that differ by orders of magnitude. Therefore, in order not to confuse the effects of vertical mixing on the salinity field,  $K_h$  was essentially neglected in these simulations. This neglect is also partly due to the belief that, even in the Columbia River Estuary, advection and vertical exchange process due to advection primarily determine the salinity distribution of the estuary. These assumptions are supported by the salt flux study of Hughes and Rattray (1980) and the CREDDP field data analysis (Jay 1984).

The essentials of the vertical mixing formulations represent the production of energy by the tidal currents interacting with the bottom and side boundary layers and the suppression of this turbulent energy by the effects of stratification. Further sophistication by the use of second order turbulent closure methods (Mellor and Yamada 1983) would greatly increase the complexity and cost of the model. Such approaches have not been applied to complex estuarine circulations and adequately compared with field data. Therefore, such an approach does not seem to be warranted until the adequacy of semi-empirical K-theory in reproducing the salinity and velocity profiles in the Columbia River Estuary has been thoroughly explored.

### 2.3.3. Current and Salinity Comparisons

The time series comparisons for the October 1980 CREDDP current and salinity data and the model simulations for the grid points given in Table 3a are shown in Figure 8. The eddy coefficient formulas used are given by (25) above. It should be noted that the calculated variables are laterally averaged values, whereas the observations are point values; thus some discrepancies should be expected, particularly in the wider channels such as the North Channel.

The horizontal velocities have good phase agreements at all stations. The agreement in amplitude varies from station to station, being very good stations CM-6S and CM-7N but less good at CM-7S (top). It is expected that peak observed velocities would exceed the laterally averaged currents simulated by the model. This is so for all stations except CM-7N, where the observed and simulated peaks are almost equal. The largest amplitude discrepancies occur at stations where the data are suspect for reasons given above (CM-5A, CM-5B, and CM-7S). On the whole, the current comparisons between observations and simulations can be considered good. Therefore, the tidal elevation and tidal currents are well reproduced by the model for the channels in which data are available.

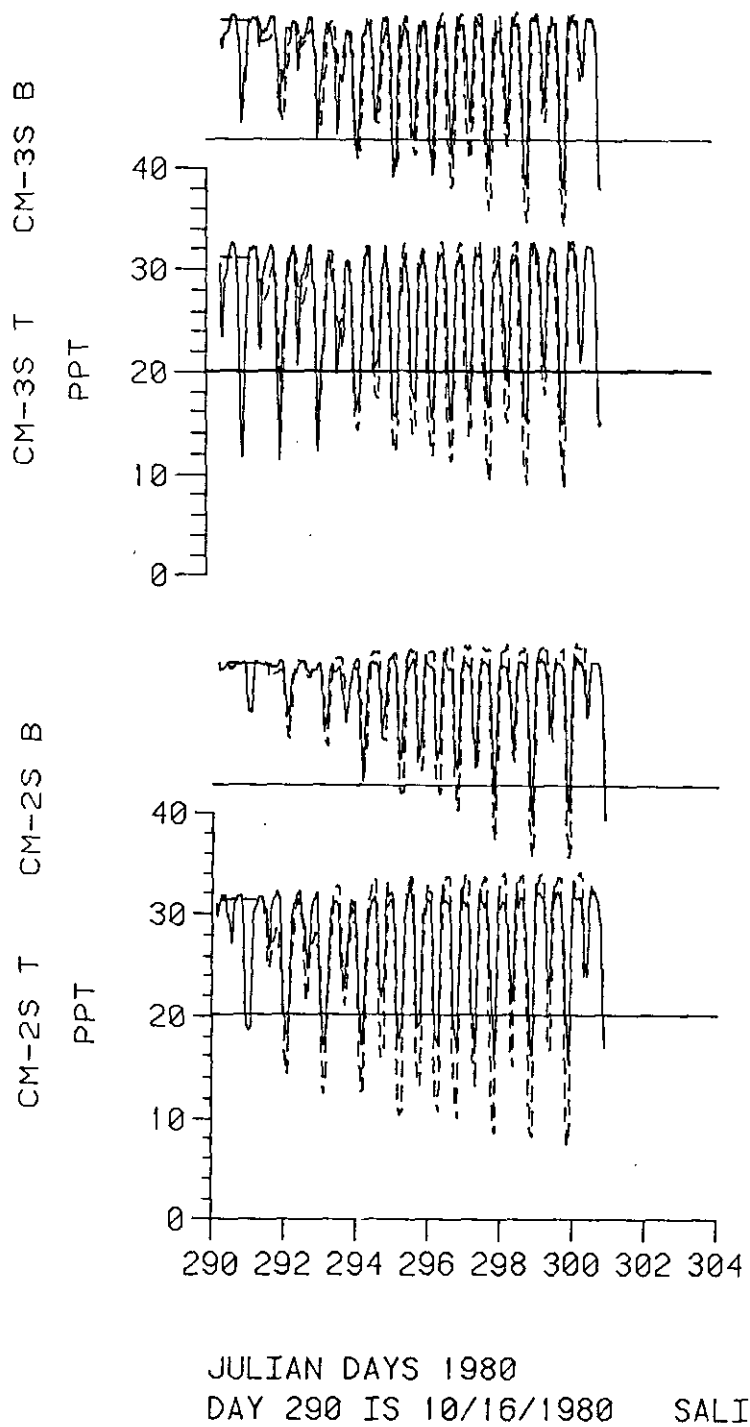
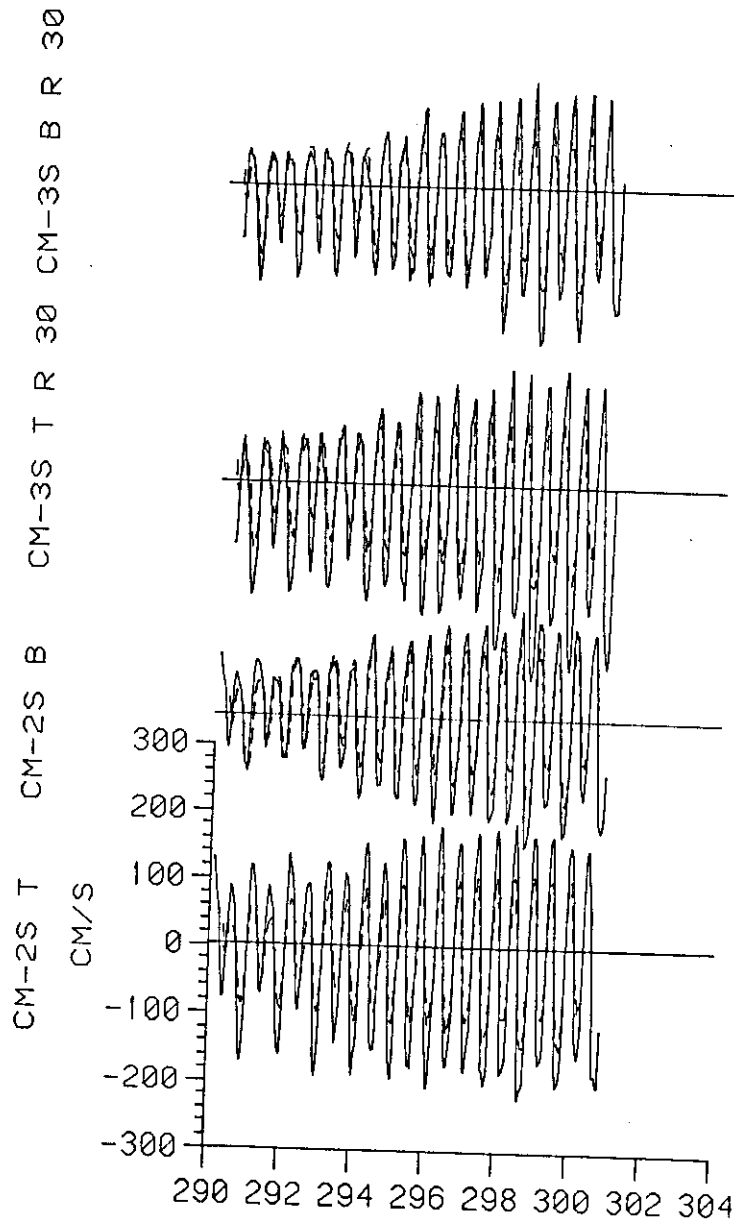
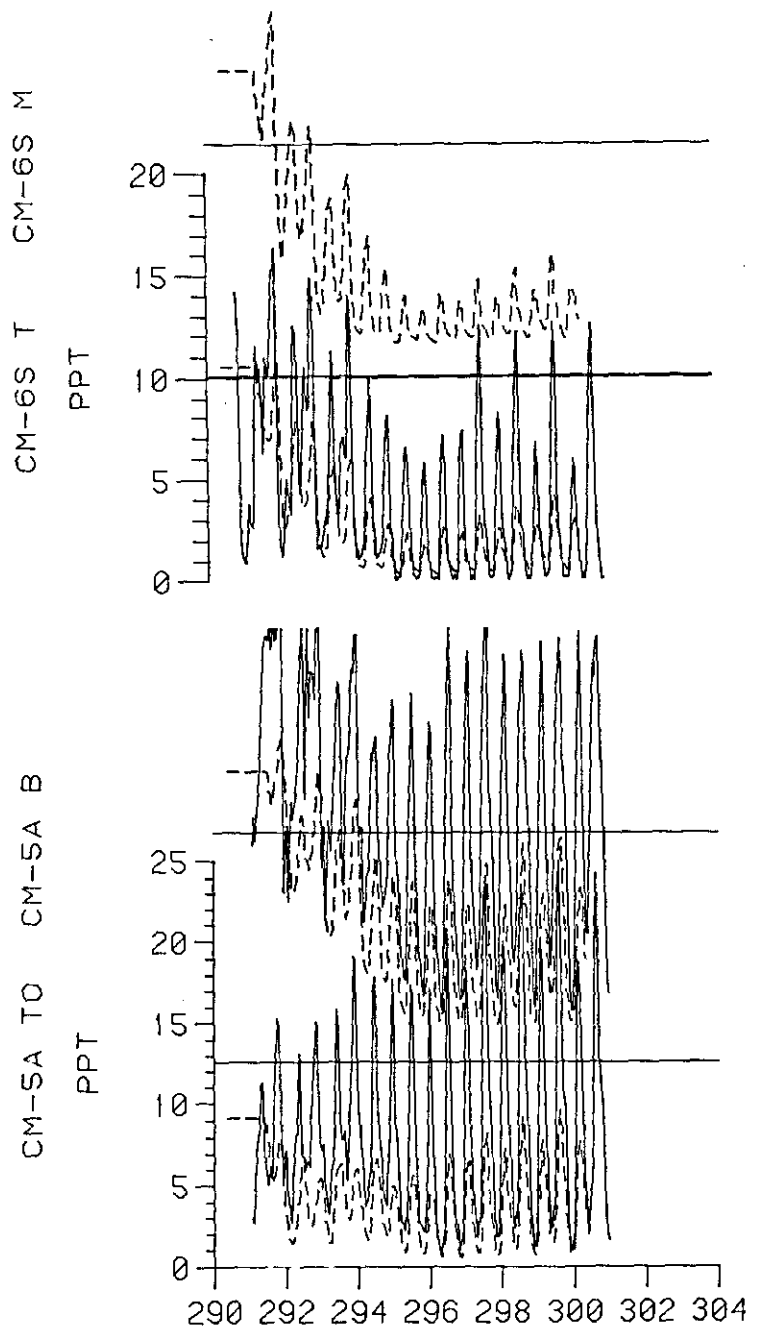


Figure 8a. Observed (solid) and simulated (dashed) salinity time series for the indicated meters for the October 1980 low flow period.



JULIAN DAYS 1980  
 DAY 290 IS 10/16/1980      CURRENTS

Figure 8b. Observed (solid) and simulated (dashed) current time series for the indicated meters for the October 1980 low flow period.



JULIAN DAYS 1980  
 DAY 290 IS 10/16/1980 SALINITIES

Figure 8c. Observed (solid) and simulated (dashed) salinity time series for the indicated meters for the October 1980 low flow period.

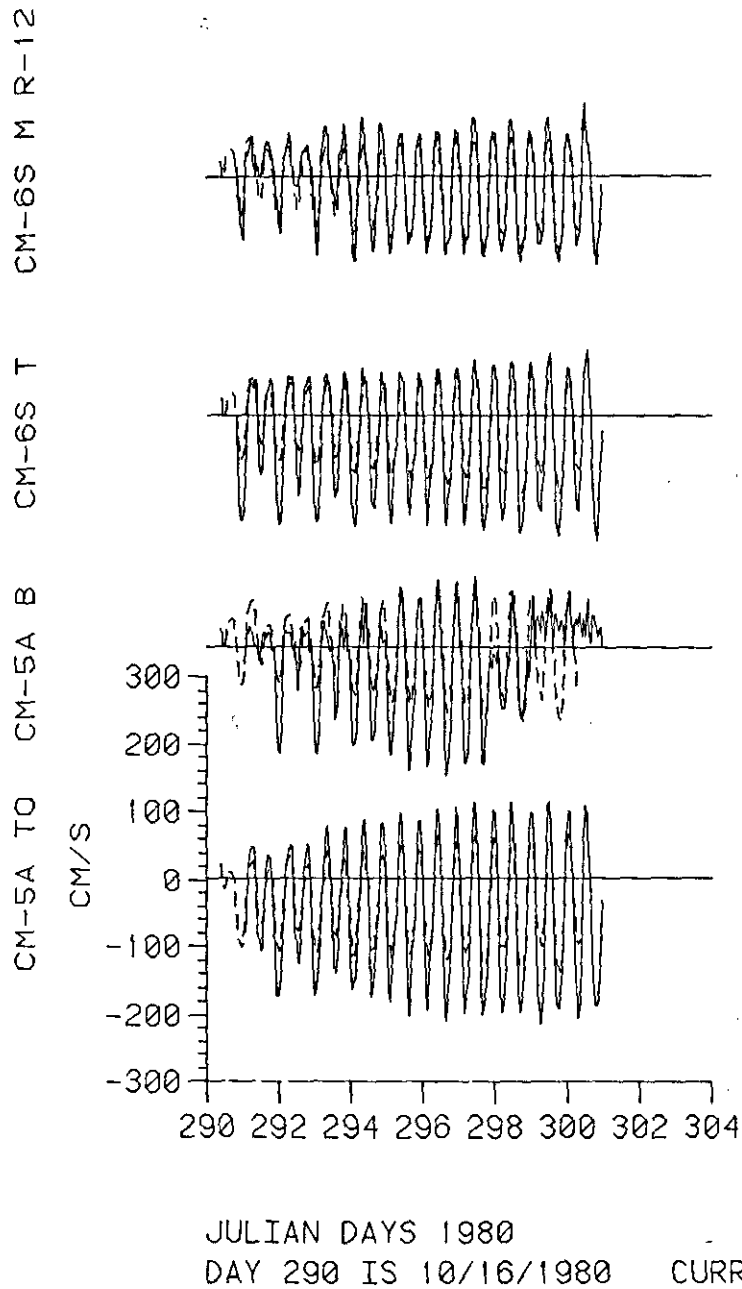
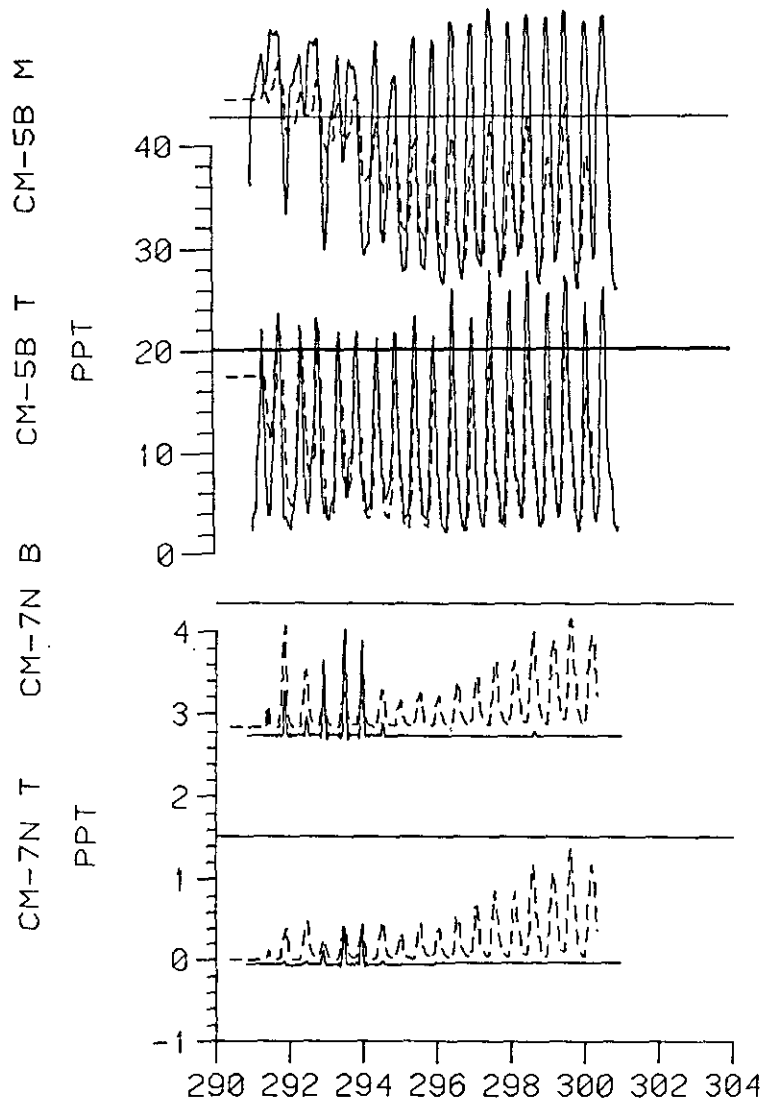
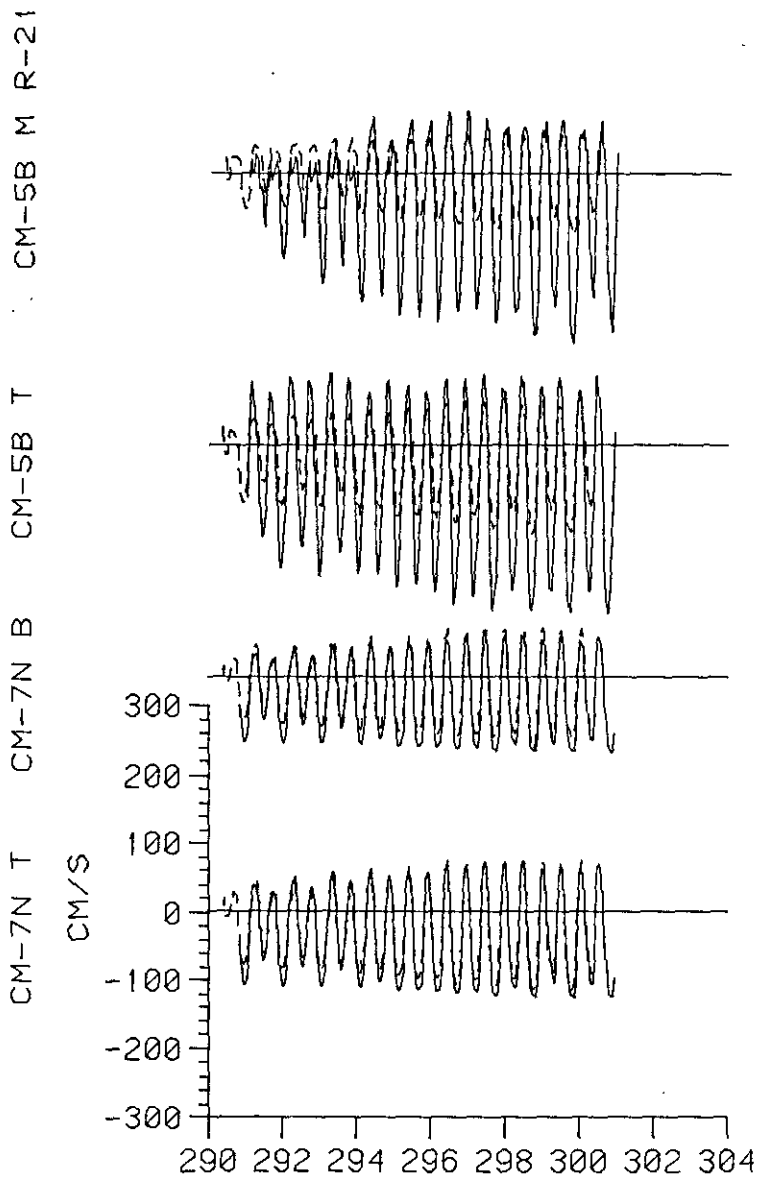


Figure 8d. Observed (solid) and simulated (dashed) current time series for the indicated meters for the October 1980 low flow period.



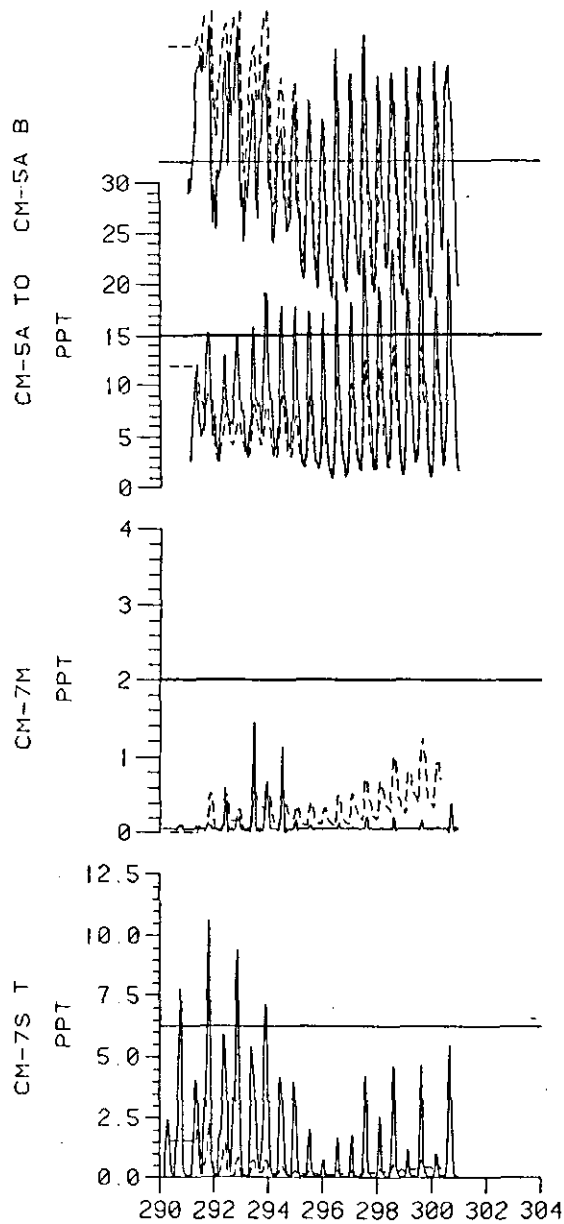
JULIAN DAYS 1980  
 DAY 290 IS 10/16/1980 SALINITIES

Figure 8e. Observed (solid) and simulated (dashed) salinity time series for the indicated meters for the October 1980 low flow period.



JULIAN DAYS 1980  
DAY 290 IS 10/16/1980 CURRENTS

Figure 8f. Observed (solid) and simulated (dashed) current time series for the indicated meters for the October 1980 low flow period.



JULIAN DAYS 1980  
 DAY 290 IS 10/16/1980 SALINITIES

Figure 8g. Observed (solid) and simulated (dashed) salinity time series for the indicated meters for the October 1980 low flow period.

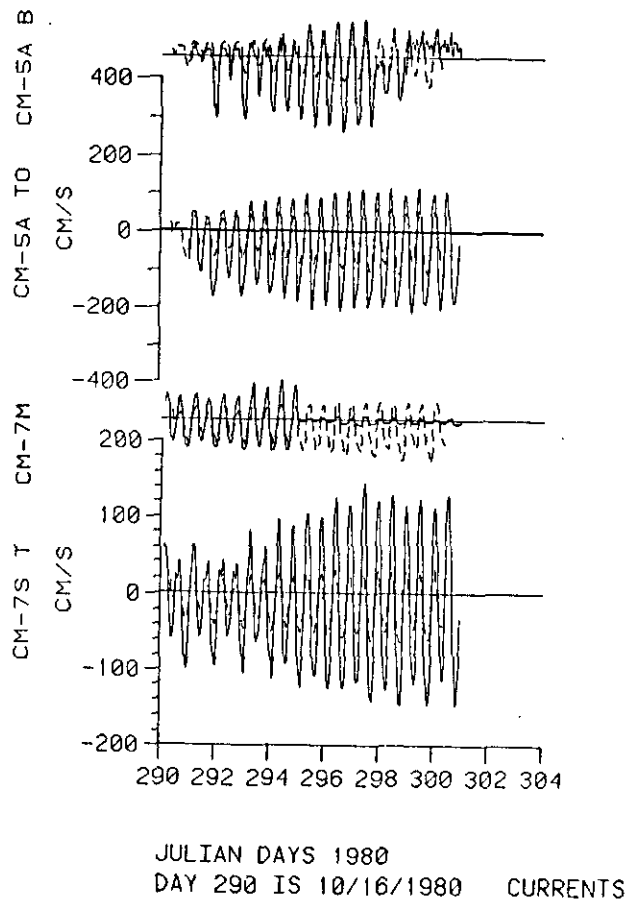


Figure 8h. Observed (solid) and simulated (dashed) current time series for the indicated meters for the October 1980 low flow period.

The salinity comparisons are shown in Figure 8. Stations CM-2S and CM-3S show good agreement for tidal range salinities and mean salinities. This indicates that the mixing formulation provides a reasonable representation of the degree of stratification at most stages of the tide at these near-mouth stations. Farther up the main Navigation Channel at the Astoria and Tongue Point stations (CM-5A and CM-6S), agreement is not quite as good (Figure 8c). The tidal ranges of salinity are smaller than observed, with the Astoria and Tongue Point stations being too fresh. The minimum (low water) salinities are fairly well reproduced. Since the tidal currents (Figure 6b) are well simulated at these sections, the longitudinal salinity gradient must be too small in the simulation compared with the observations, or the salt is not intruding far enough up the Navigation Channel on the flood tide. Figure 8g shows the records at station CM-5A compared with the model simulations at grid point 7 and 2m deeper than the comparisons at grid point 8. In this case (Figure 8g), the apparent comparisons are much better, particularly at the bottom, indicating that indeed the high salinity region is not penetrating quite far enough up the estuary. Cross-sectional plots of the salinity field presented in the next section show that the Youngs Bay- Astoria reach is a region of very strong horizontal and vertical gradients. The subtidal trends of salinity are qualitatively well reproduced, with a decrease in the tidal-mean salinities to about day 296, followed by an increase consistent with increasing amplitudes of the spring tidal currents. Station CM-7N is at the tip of the salt intrusion in the Navigation Channel. Simulated salinities for this station show a similar pattern to the simulation at Tongue Point (CM-6S), indicating that the simulated salt intrusion length is about right for the neap tides at the beginning of the period but shows some salinity values ( $\sim 1$  ‰) not observed in the data at the end of the spring flood tides. There are similar relative differences between observations and simulations for CM-7S and CM-7M in the Cathlamet Bay channels. The more saline station, CM-7S, is similar to CM-6S, and CM-7M is more similar to CM-7N. Data in channel 2 (CM-5B) are more similar to the mouth of the estuary, and salinity ranges and values are reasonably simulated, though again the indications are that model salinities are fresher and the tidal ranges are not as large as observed.

Thus the limitation of the simulation is that the longitudinal salinity gradients in the Astoria-Tongue Point reaches of the navigation channel are underestimated, or the highly saline part of the intrusion does not penetrate far enough in the flood tide. The overall salt intrusion length is quite well reproduced, according to comparisons with upriver stations. Possible physical reasons for these discrepancies are inappropriate mixing formulation in this region, neglect of wind forcing, neglect of the Coriolis effect, underestimation of total riverflow and underestimation of tidal currents in the entrance region. Experiments were tried to investigate the effects of reducing mixing coefficients and applying observed wind stresses. Some very slight improvements occurred applying the wind, but they could not be regarded as significant. Changing  $N_1$  and  $K_1$  to  $1.25 \times 10^{-3}$  did not significantly improve the simulation at stations CM-5A, CM-7N, and CM-7M, but made the agreement worse for the mouth and

channel 2 stations. Coriolis effects could not be included in the model as it is presently formulated, but scale analysis indicated that it is probably not important in an estuary with strong tidal forcing. The riverflow estimates are considered to be good, with an accuracy of + 10%. An increase of 10% would not significantly change the salinity distribution. A more likely reason is the numerical dispersion present in the advection scheme. Earlier versions of the model, which used a simple upwind difference solution and the Zalesak (1979) Flux Corrected Transport (FCT) method, showed similar behavior in the salinity simulations, except that the model salinities showed larger discrepancies at the upriver stations CM-7M and CM-7N, particularly on the spring tides when numerically induced dispersion would be expected to be relatively larger due to the higher velocities. However, neglect of the horizontal dispersion coefficient,  $K_h$ , and the uncertainties of the vertical eddy coefficient formulation<sup>h</sup> should not be discounted, particularly in the mouth region where the salinity ranges are a little large.

Further experimentation with the model showed that the salinity intrusion in the Astoria reach was sensitive to the bottom friction coefficient,  $k$ . It was found that decreasing  $k$  to 0.0011 between the mouth and Astoria and increasing  $k$  to 0.0045 upstream of Tongue Point improved the tidal mean and range of salinities at Astoria, particularly at neap tide. The distribution of  $k$  is similar to the distribution used in the analytical one-dimensional harmonic model of the tide employed by Jay (1984). There is some support from the sediments work unit for small bottom friction coefficients in the entrance channel and large coefficients upstream of Tongue Point since the amplitudes of the sand waves in these regions are small and large respectively. These improved results were obtained for the Portland District of the Corps of Engineers after submission of the draft final report for CREDDP and are not reported in detail herein.

The best independent test of the model's ability to reproduce salinity and current fields is to simulate a period that has a large change in one of the forcing functions compared with the period for which the model was calibrated. This was done using the June 1981 period, for which the riverflow was 2-3 times greater than that for the October 1980 period. The positions of the available NOS current and salinity data are given in Figure 5b, and the comparison grid positions in Table 3b. It is noted that the spacial coverage is quite good west of Tongue Point, where the salinity is restricted during this high flow period. Coverage of the North Channel is also much better than in the October 1980 period. It is reiterated that the model runs for the June period had no change in parameters from the calibrated October simulations. Only the mouth tidal forcing and riverflows were changed using the observed data.

The first 30 days of current observations and the corresponding simulated velocities for the May-June 1981 period are shown in Figure 9. The agreement for the Navigation Channel is good, showing the correct increases and decreases in amplitude between the mouth and Tongue Point. Thus, CM-10 shows lower amplitudes than CM-17 and CM-9 on either side (Figures 9a and 9b). In Channel 2, the upper or

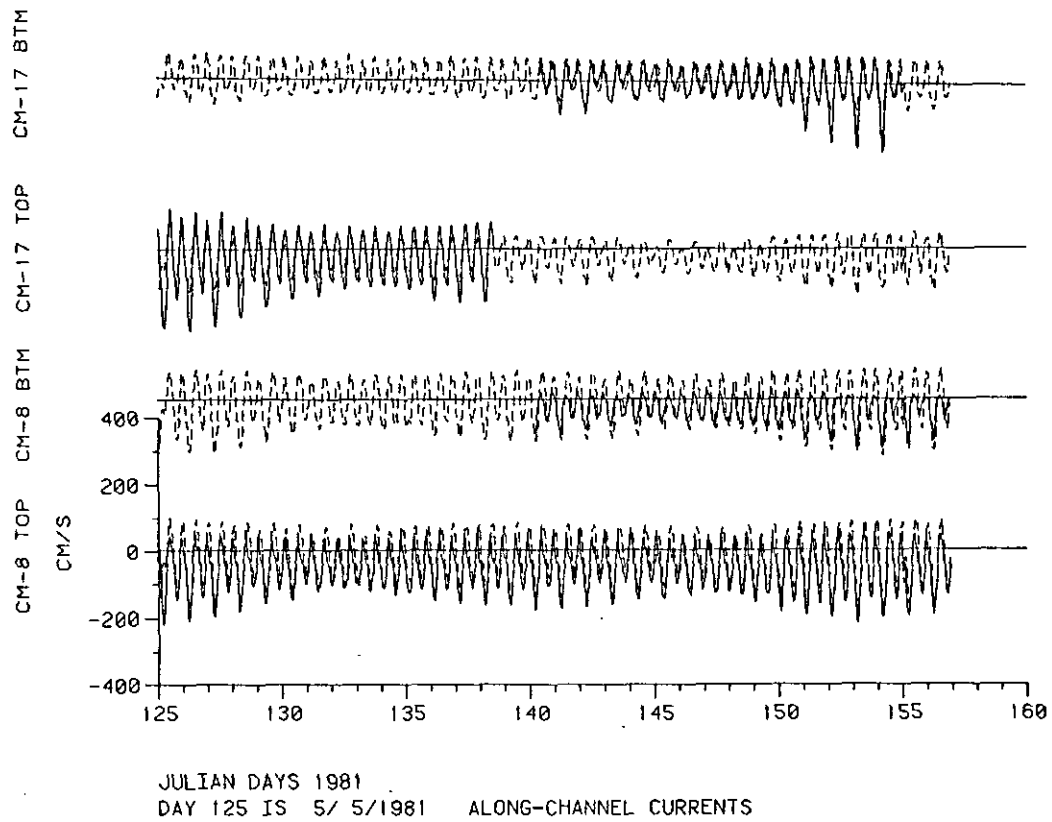


Figure 9a. Observed (solid) and simulated (dashed) along-channel current time series for the indicated meters for the May 1981 high flow period.

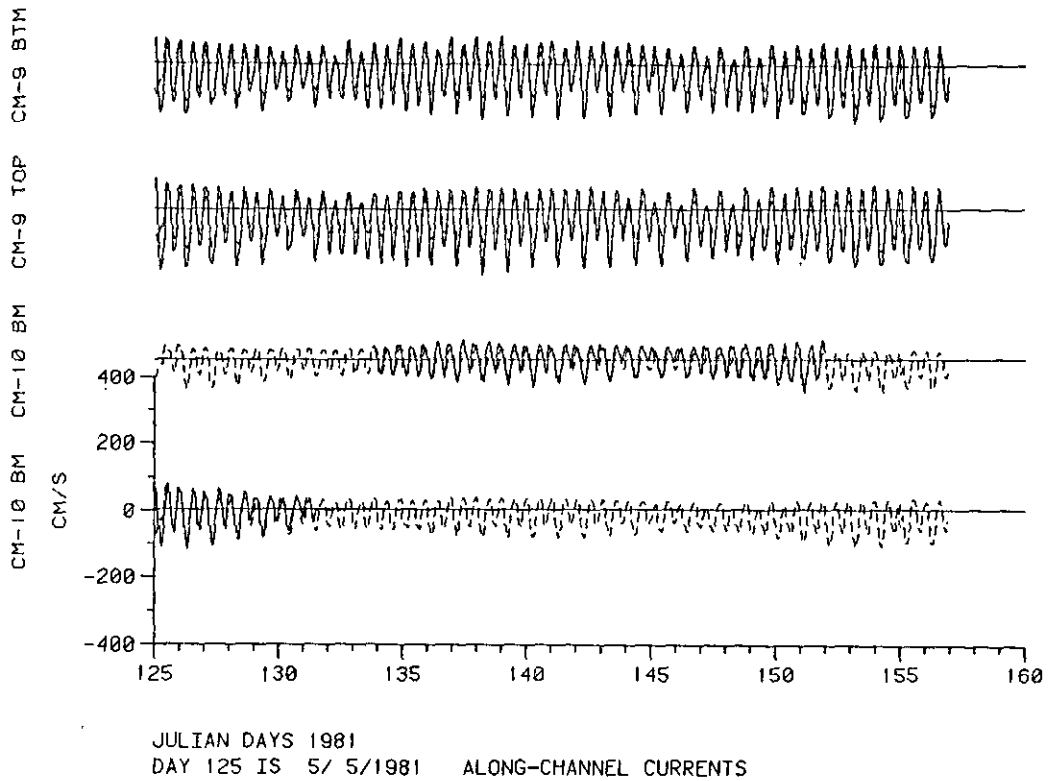


Figure 9b. Observed (solid) and simulated (dashed) along-channel current time series for the indicated meters for the May 1981 high flow period.

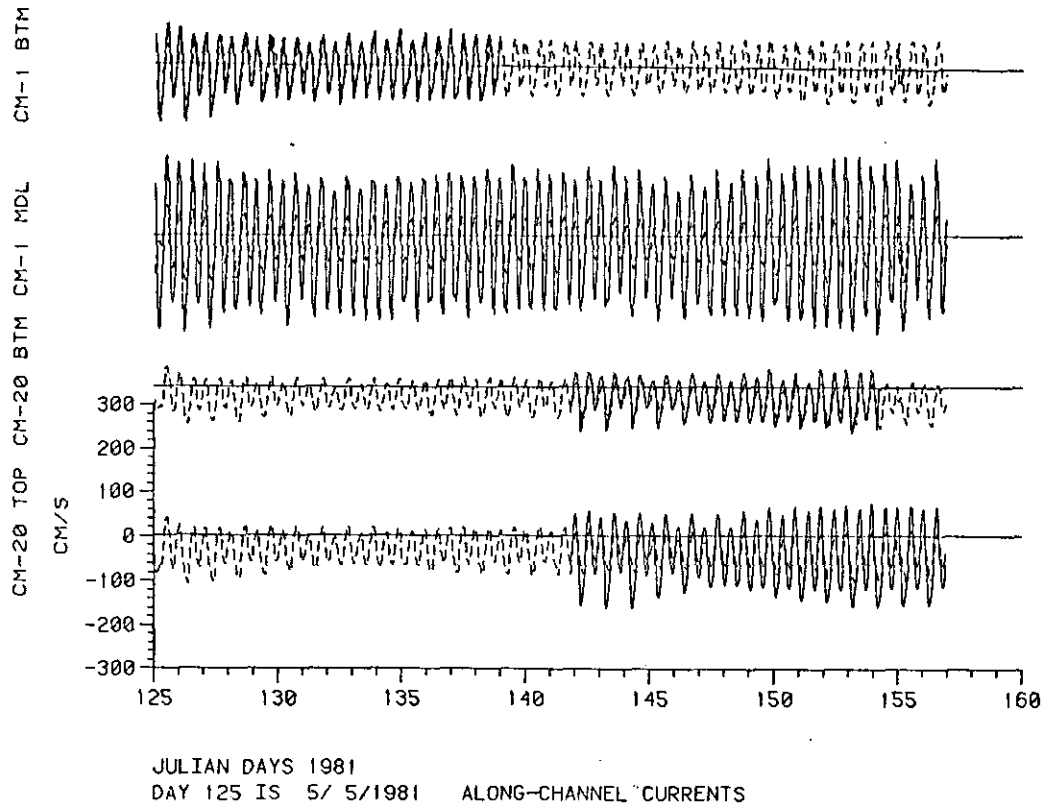


Figure 9c. Observed (solid) and simulated (dashed) along-channel current time series for the indicated meters for the May 1981 high flow period.

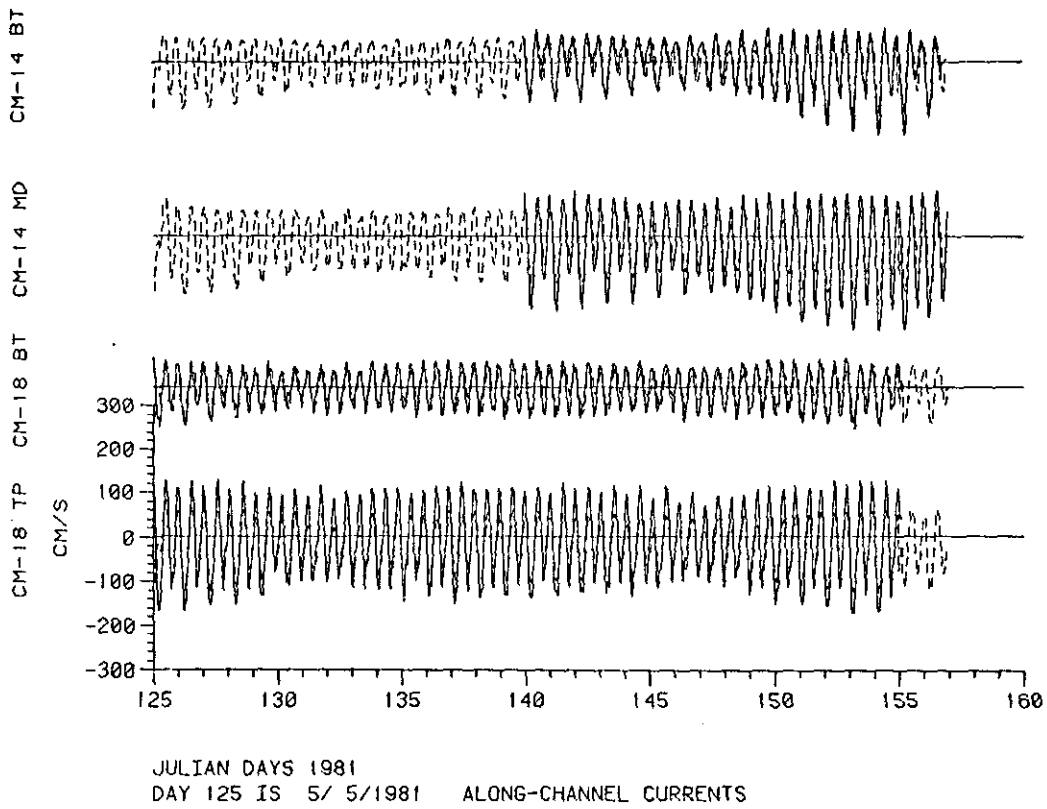


Figure 9d. Observed (solid) and simulated (dashed) along-channel current time series for the indicated meters for the May 1981 high flow period.

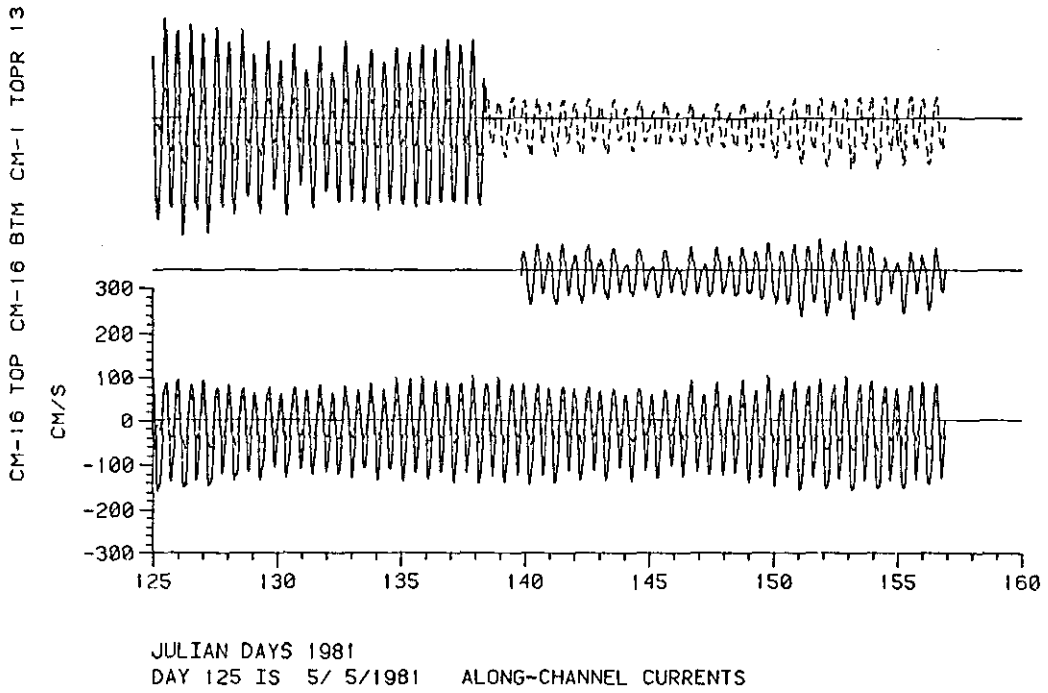


Figure 9e. Observed (solid) and simulated (dashed) along-channel current time series for the indicated meters for the May 1981 high flow period.

mid-depth current meters show larger amplitudes than the model velocities, but bottom velocities are much better simulated. CM-14 shows the best agreement. As in the low flow simulations, agreement between observed and simulated current phases is very good. The better agreement for the Navigation Channel mid-depth meters as against the North Channel meters is probably due to the relatively small width of the former channel. Thus laterally averaged velocities in narrow channels correspond better with point velocities measured by current meters.

The simulated and observed salinity time series for May 1981 are shown in Figure 10. The Navigation Channel shows excellent agreement both for mean salinities, salinity ranges, and phases. The main discrepancies are at the top meter at CM-17 where water is too fresh and at the tip of the salinity intrusion at CM-9 where the lower meter shows higher salinities, particularly at the end of spring floods, than the simulations. In the North Channel the agreement is also good, except at CM-16 where the observations indicate fairly high salinities on flood tides ( $\sim 20$  ‰) whereas the simulation only shows maxima of about 8 ‰. Thus, unlike channel 1, the salinity intrusion is predicted to be a little short in channel 2. It is noted that CM-20 (not shown) is completely fresh in both the observations and the model results.

The response to the freshet is shown in the simulations by a reduction in salinities at CM-14, CM-16, CM-9 and CM-10. This is not the case with the observations, except that ebb minimum salinities seem to become fresher. Therefore the observations show little response to initial stages of the freshet. The second 30 days of the salinity records are shown in Figure 11, which contains the highest riverflows. The model shows salinity reductions at CM-1 that are not reflected by the observations. CM-9 and CM-10 do show salinity decreases, becoming completely fresh, which corresponds to the model simulations. The return of salinity to these stations after the freshet is qualitatively reproduced by the model. Therefore, it seems from the observations that the estuary is able to maintain the salinity against large freshets presumably by increasing horizontal and vertical salinity gradients, which the tidal currents work on to increase the upstream tidal dispersion of salt. The model seems to have some difficulty reproducing this phenomena, probably due to its limited ability to resolve sharp horizontal fronts against numerical diffusion.

The current data corresponding to Figure 11, shown in Figure 12, show the same degree of agreement in Figure 9. The independent test of the calibrated model can be regarded as successful, despite a few discrepancies. It is noted that, despite the difference in response to the freshet between the simulation and the observations, the change in salt intrusion length between the October low flow period and the 1981 high flow period is well reproduced. The high values of salinity at CM-16 in May during flood tides, which are at variance with the model results, are also confirmed to a lesser degree in the October data (CM-5B, Figure 8e). Thus, the salinity content of the east end of channel 2 seems to be underestimated in both periods and may be due to

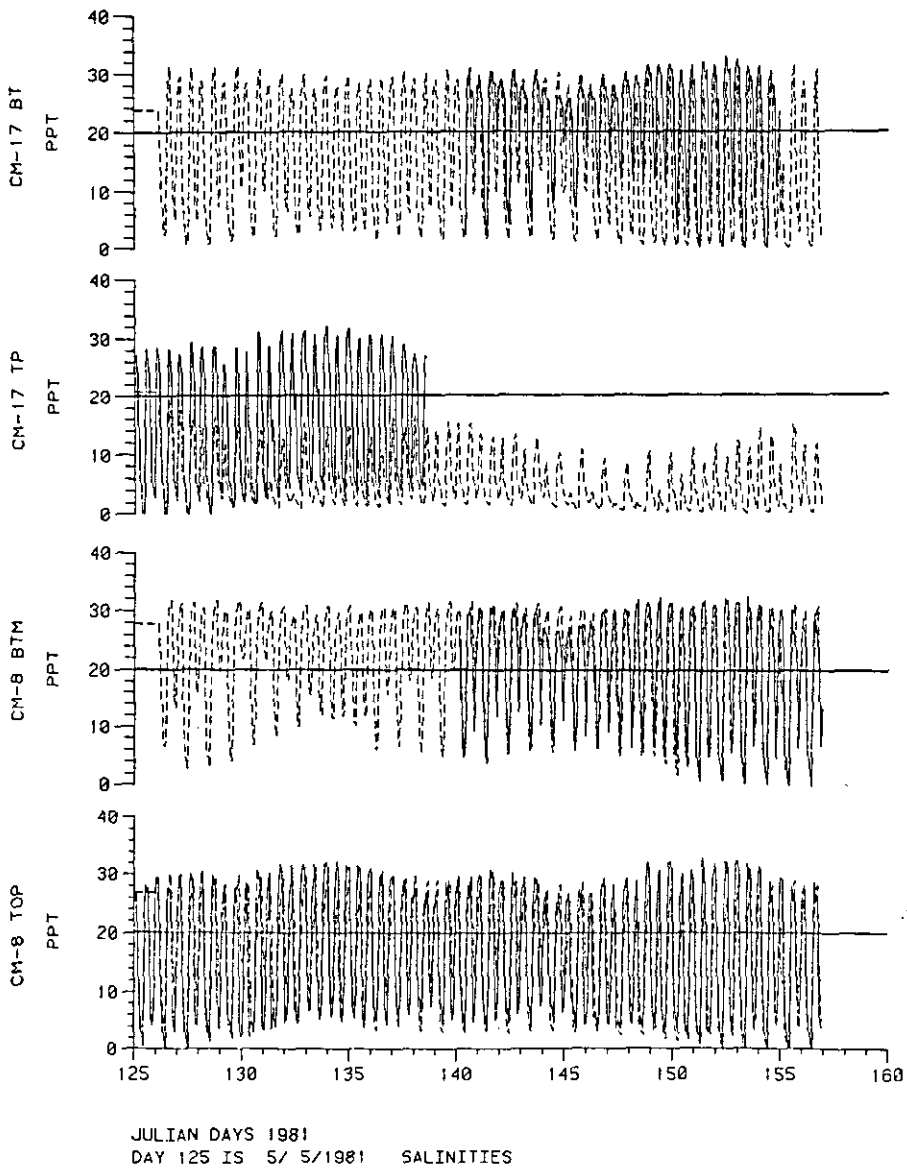


Figure 10a. Observed (solid) and simulated (dashed) salinity time series for the indicated meters for the May 1981 high flow period.

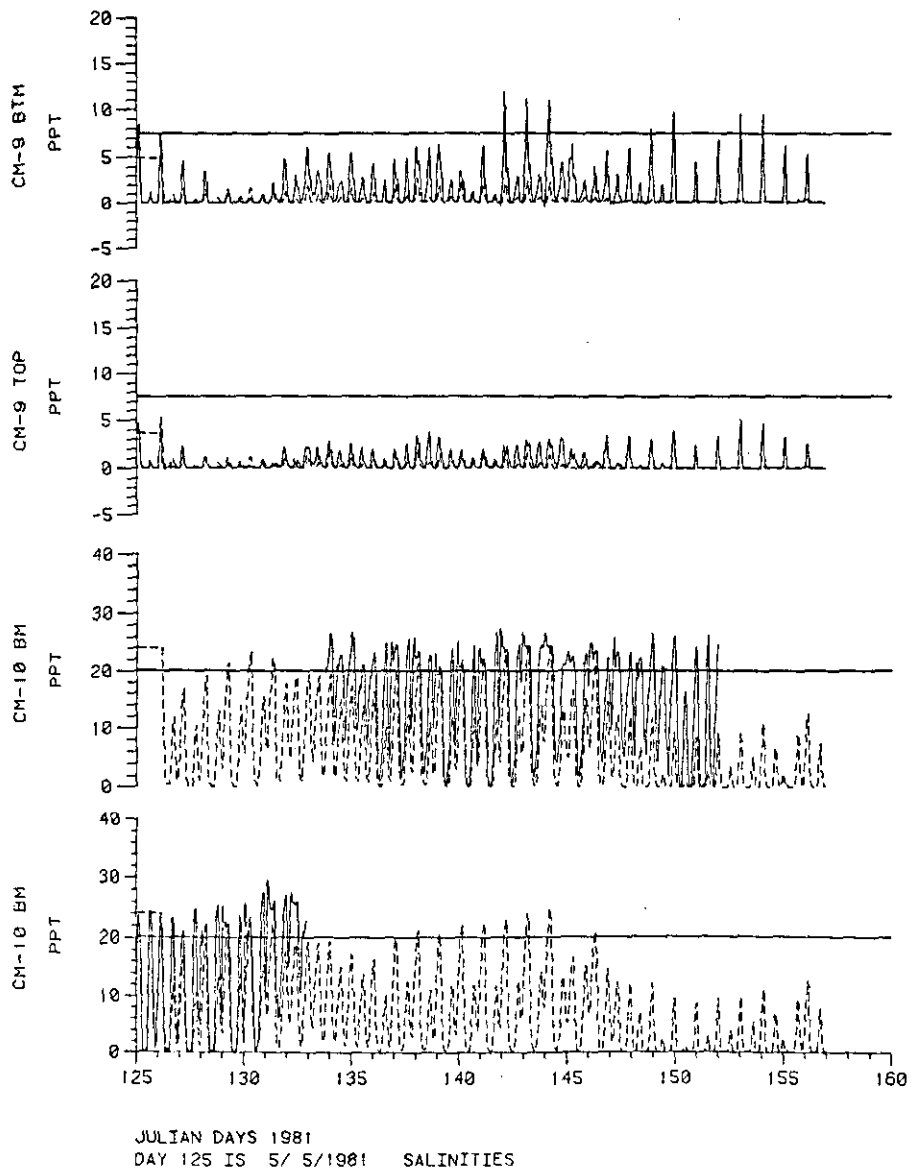


Figure 10b. Observed (solid) and simulated (dashed) salinity time series for the indicated meters for the May 1981 high flow period.

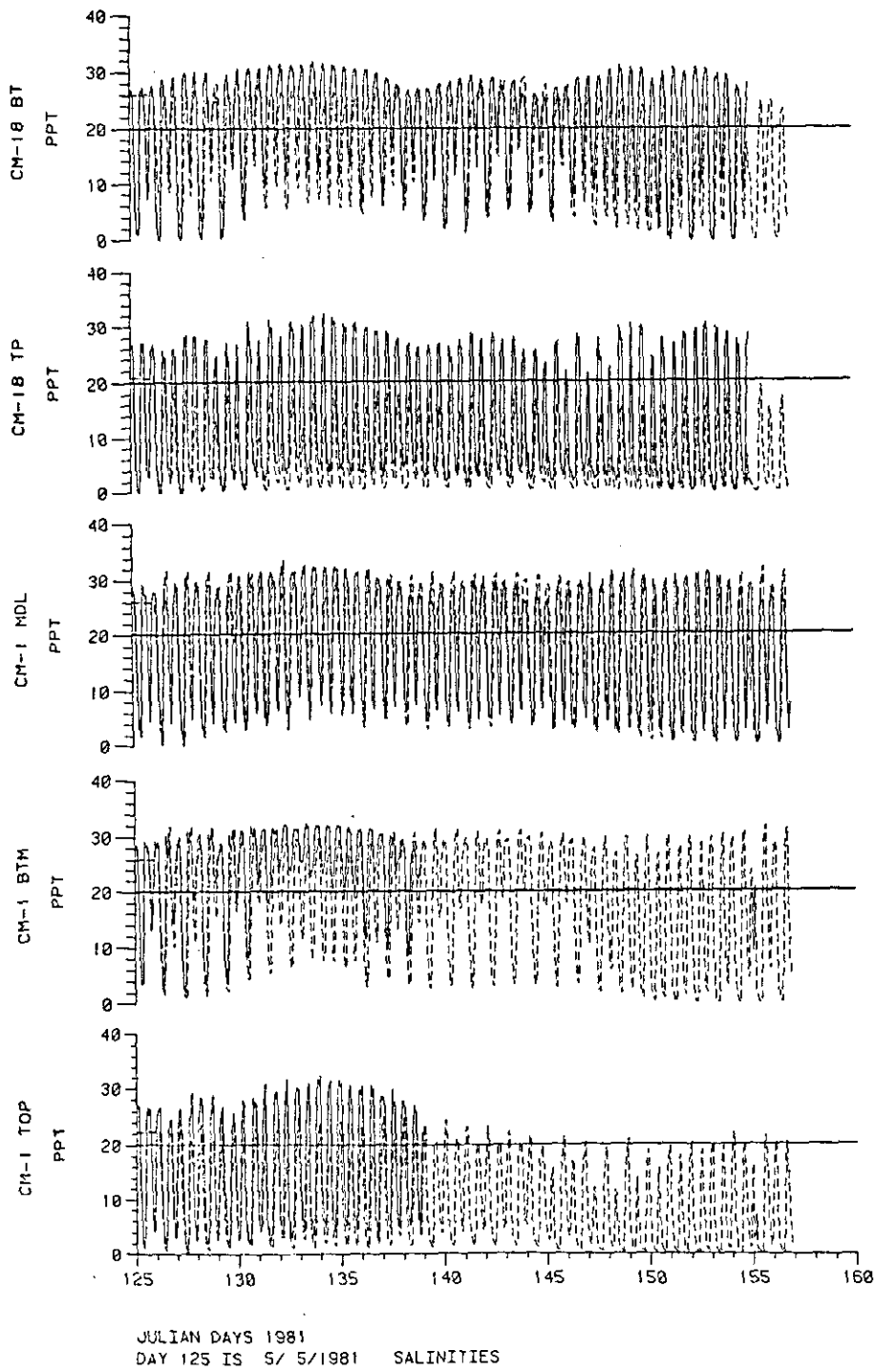
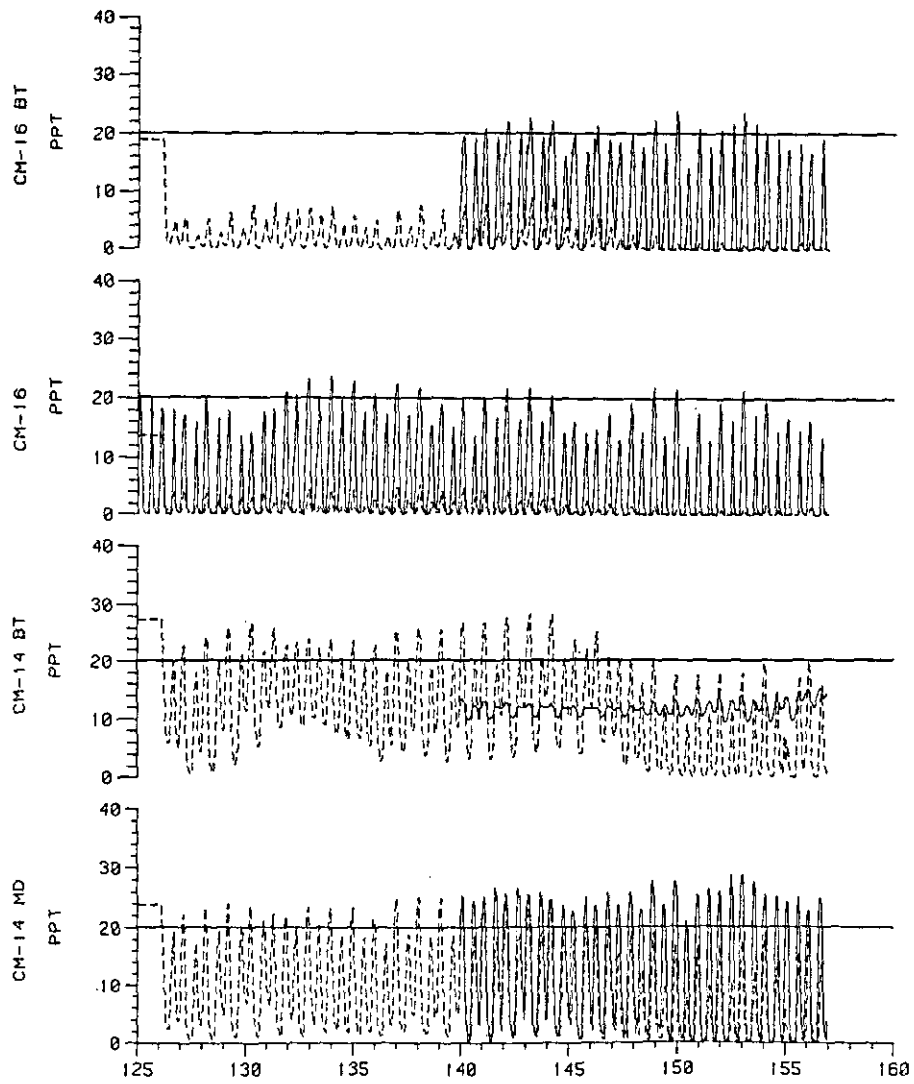
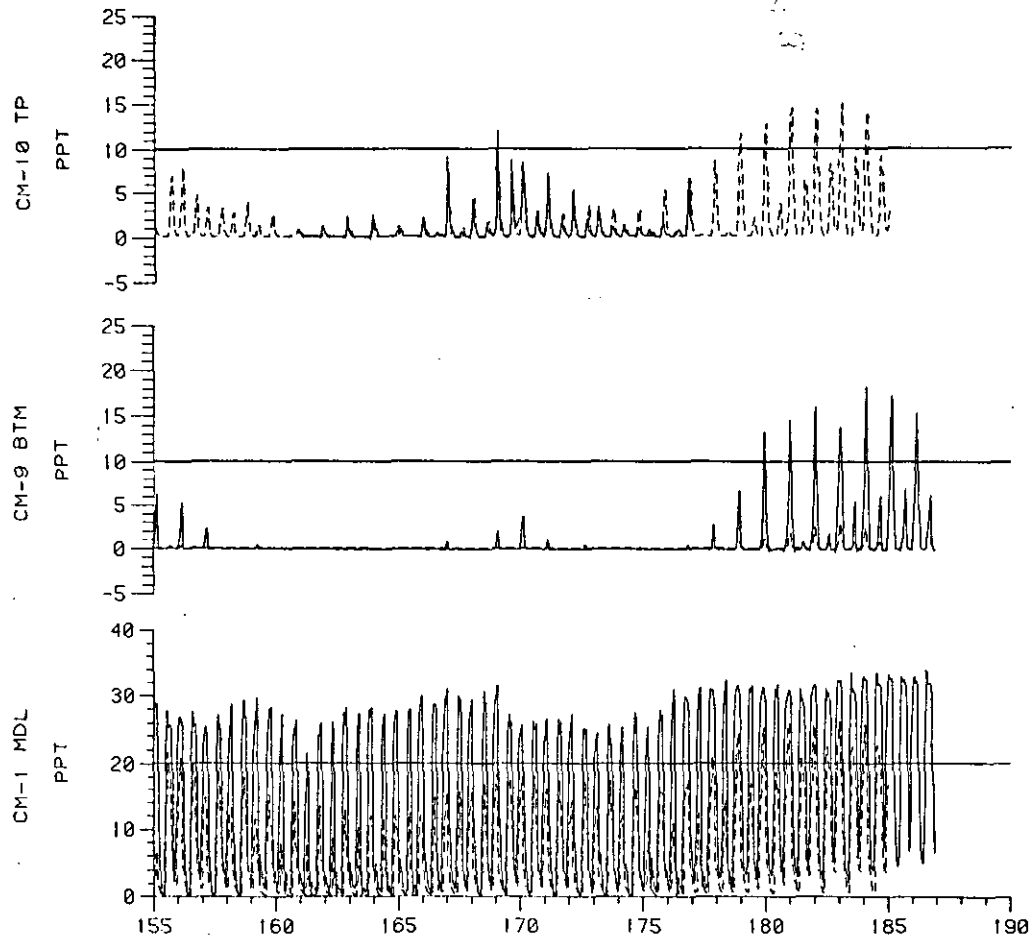


Figure 10c. Observed (solid) and simulated (dashed) salinity time series for the indicated meters for the May 1981 high flow period.



JULIAN DAYS 1981  
 DAY 125 IS 5/ 5/1981 SALINITIES

Figure 10d. Observed (solid) and simulated (dashed) salinity time series for the indicated meters for the May 1981 high flow period.



JULIAN DAYS 1981  
 DAY 155 IS 6/ 4/1981 SALINITIES

Figure 11a. Observed (solid) and simulated (dashed) along-channel current time series for the indicated meters for the June 1981 high flow period.

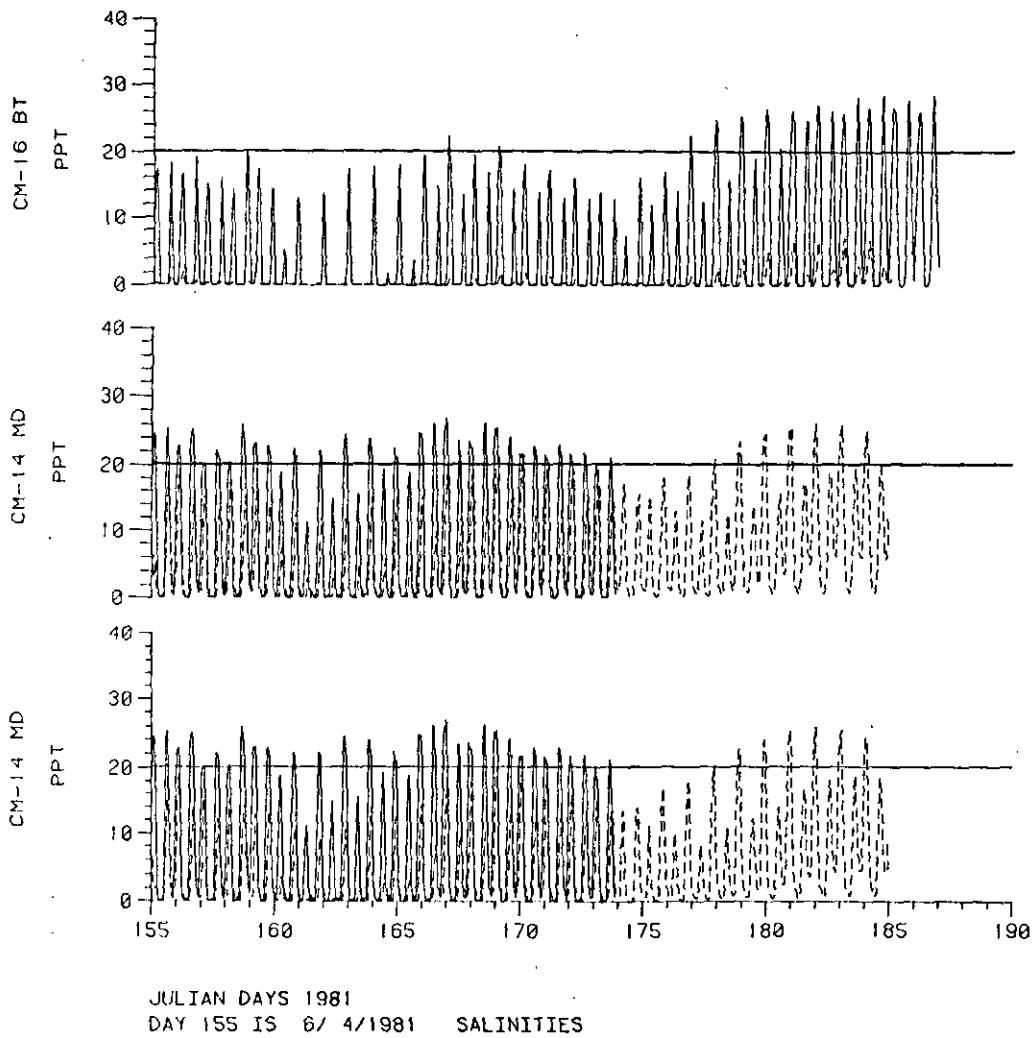
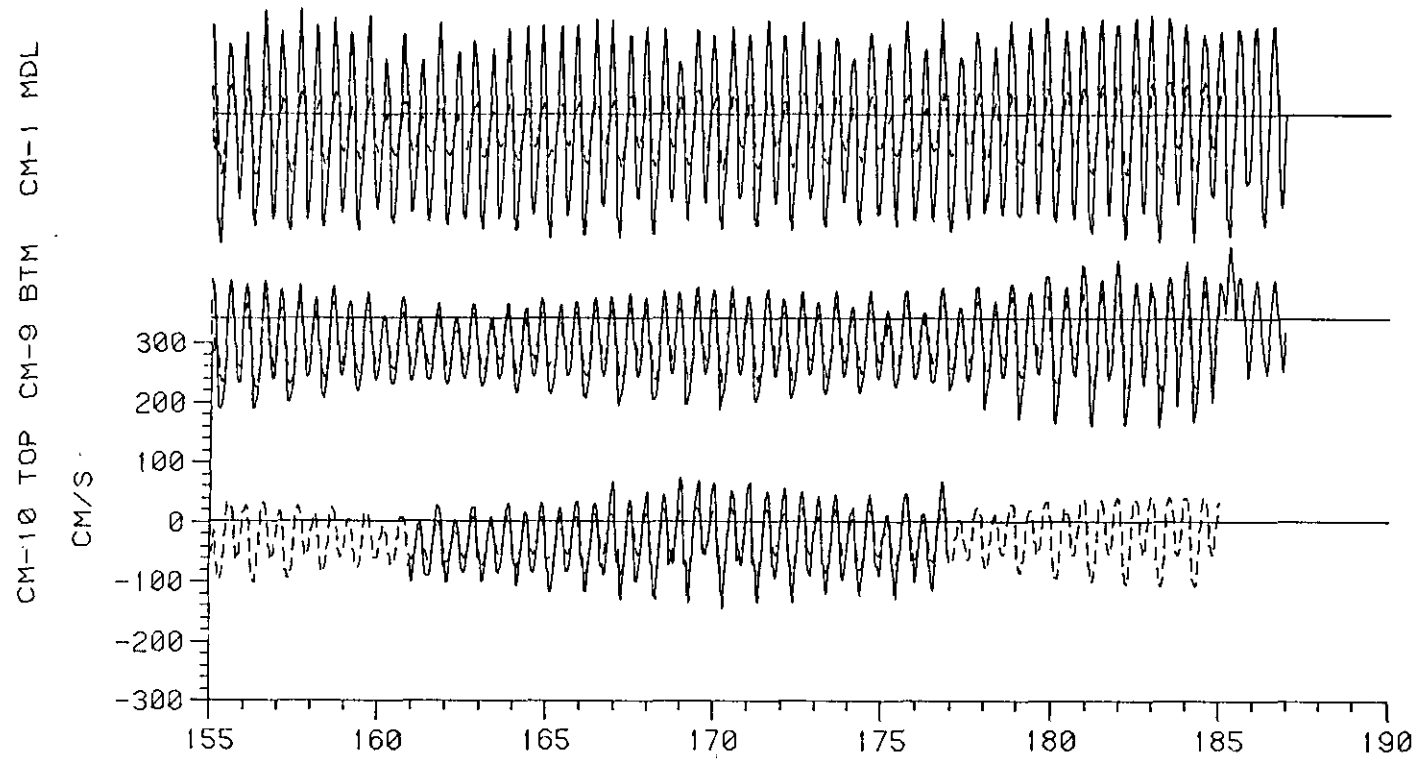


Figure 11b. Observed (solid) and simulated (dashed) along-channel current time series for the indicated meters for the June 1981 high flow period.



JULIAN DAYS 1981  
DAY 155 IS 6/ 4/1981 ALONG-CHANNEL CURRENTS

Figure 12a. Observed (solid) and simulated (dashed) salinity time series for the indicated meters for the June 1981 high flow period.

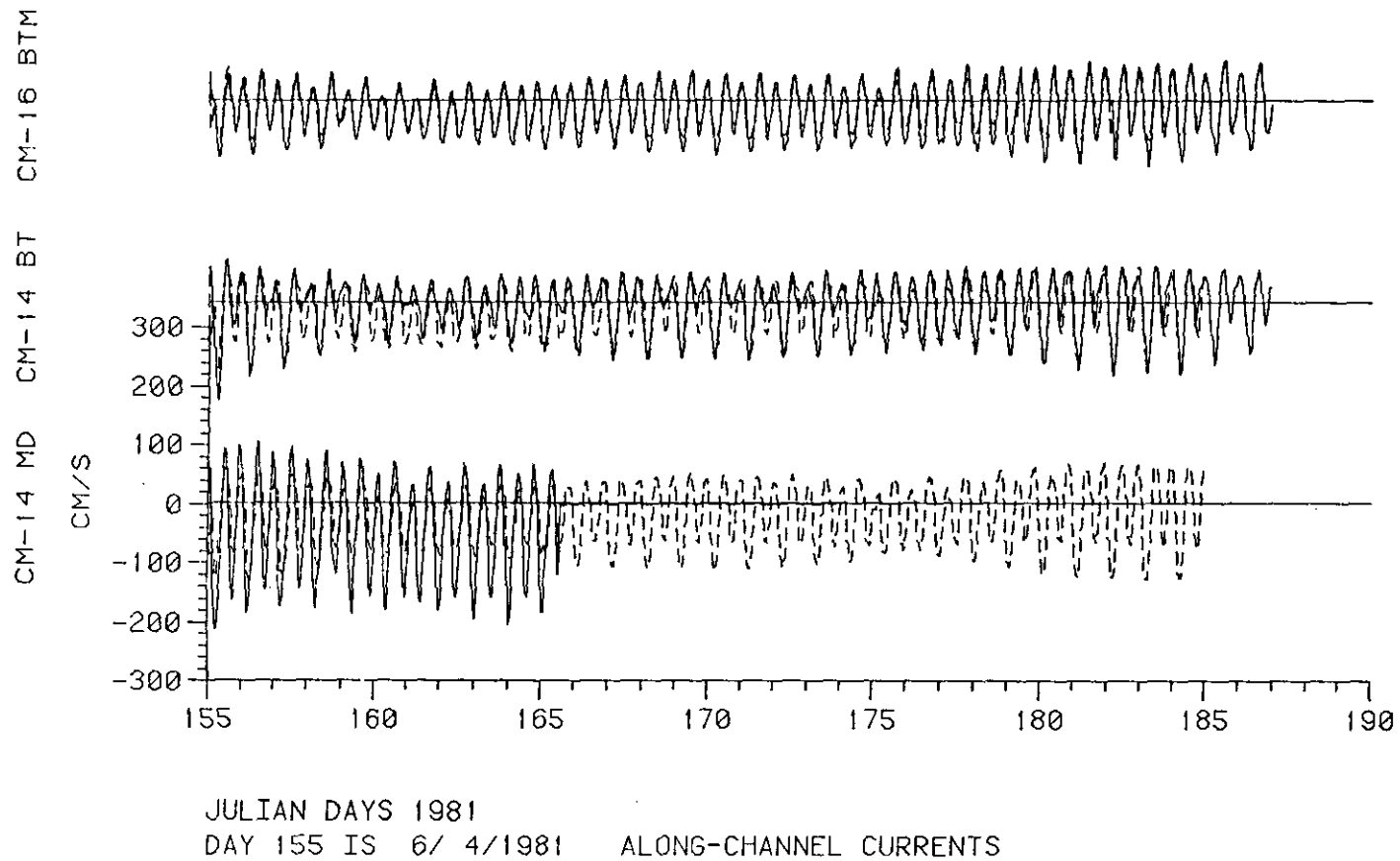


Figure 12b. Observed (solid) and simulated (dashed) salinity time series for the indicated meters for the June 1981 high flow period.



the neglect of cross-channel variability, which would contribute to the upstream salt flux in this wide channel.

On the whole, the calibrated model performed well for the high flow simulations. Therefore, the model can be considered to be adequately verified. The simulation of currents, salinities and tidal heights are probably the best available for this complex estuary. The predictive skill of the model is good and can be used with confidence for channel-deepening studies (performed with an earlier version of the model for the Portland District of the Corps of Engineers (Hamilton 1983).) and for large-scale topographic changes, such as the historical simulation given in Section 3.2.

### 3. RESULTS AND DISCUSSIONS

#### 3.1. SIMULATIONS

##### 3.1.1. Introduction

This section discusses the results of the model simulations for the low flow October 1980 period and the high flow May-June 1981 period, which includes a large freshet. The discussion will be divided into a presentation of the Navigation Channel (channel 1) and the North Channel (channel 2) simulation results. The data analysis (Jay 1984) has shown the importance of the difference between spring and neap tides for low riverflows, not just in terms of the magnitude of the flood and ebb currents but also in terms of the mixing processes that cause the neap tide to be more stratified with a larger salt intrusion length and the spring tide to be less stratified with a shorter intrusion length. The average intrusion length and stratification vary also with magnitude of the riverflow. The ability to model these phenomena is one of the most important results of this study. Where possible, the results of the simulations will be compared with the analysis given in the Currents work unit report (Jay 1984) in order to evaluate the model in terms of the physical processes governing the circulation.

##### 3.1.2. Tidal Circulation

Table 4 shows the model periods and their corresponding data periods, along with daily riverflows, which are used for more detailed analysis. The periods are 50 hours (Two 25-hour tidal periods), corresponding to neap and spring tides for various riverflows observed during the October 1980 and the May-June 1981 data collection periods. For this purpose, the tidal range given in Table 4 is defined to be the difference between maximum and minimum water-levels observed during the 50-hour period at Jetty A.

The instantaneous sections of salinity and velocity field along the axis of channel 1 are shown in Figure 13(a-i). The period encompasses a 25-hour neap tide, starting at high tide at the mouth at day 3: 11 hours. The volume transport tidal signal at the mouth leads the elevation by about  $40^\circ$ , therefore maximum currents at the mouth occur approximately 1 hour and 20 minutes before maximum elevations. The corresponding neap tide velocity and salinity fields for channel 2 are given Figure 14(a-i).

The volume transports for the same times as the longitudinal sections in Figures 13 and 14 are plotted on a map for all the channels and the interchannel sandbank flows. It is instructive to compare these maps with WIFM simulations shown in Figures 4-8 of Volume 1. Generally the directions and magnitude of the flow, which are constrained in the channel model (Figure 15), are well reproduced by the vertically integrated model. The plots are discussed briefly below.

Table 4. Model Runs and Analysis Periods

<u>Run No.</u>	<u>Tide</u>	<u>Dates</u>	<u>Model Time</u>	<u>Riverflow (x10<sup>3</sup> m<sup>3</sup>/s)</u>	<u>Tidal Range (m)</u>
26	Neap	10/18/80:06 h	Day 2: 22 hours	4.30	2.11
		10/20/80:08 h	Day 4: 24 hours		
	Spring	10/24/80:06 h	Day 8: 22 hours	3.88	3.44
		10/26/80:08 h	Day 10: 24 hours		
51	Neap #1	5/9/81: 22 h	Day 5: 22 hours	7.0	2.18
		5/12/81: 0 h	Day 7: 24 hours		
	Spring #1	5/17/81: 22 h	Day 12: 22 hours	7.26	2.59
		5/20/81: 0 h	Day 14: 24 hours		
	Spring #2	5/30/81: 22 h	Day 25: 22 hours	11.50	3.30
		6/2/81: 0 h	Day 27: 24 hours		
	Neap #2	6/8/81: 22 h	Day 35: 22 hours	15.91	2.01
		6/11/81: 0 h	Day 37: 24 hours		
	Neap #3	6/21/81: 22 h	Day 48: 22 hours	12.19	2.43
		6/24/81: 0 h	Day 50: 24 hours		
Spring #3	6/29/81: 22 h	Day 57: 22 hours	7.32	3.48	
	7/2/81: 0 h	Day 59: 24 hours			
51	15-Day Mean	5/10/81: 0 h	Day 6: 0 hours	7.24	-
		5/25/81: 0 h	Day 20: 24 hours		
	15-Day Mean	6/9/81: 0 h	Day 35: 0 hours	13.07	-
		6/24/81: 0 h	Day 50: 24 hours		



High water: Day 3: 11 hours: Figures 13a, 14a and 15a

The flood is well established everywhere. In channel 1 the strongest currents occur near the bottom everywhere salt is present in the water column due to the influence of the horizontal depth-dependent density gradients. In some cases, where the depth shoals abruptly upstream, these stronger currents appear to be channeled in the lower part of the water column. The salinity field shows strong vertical gradients downstream of grid point 8, with a sharp bottom front on the downstream side of the deep hole off Astoria. Channel 2 shows similar features, with the main pycnocline being at mid-depth at the channel mouth and intersecting the bottom at grid point 5 (the Astoria-Megler Bridge). Volume transports in channel 2 are approximately twice those of channel 1, with minimal exchange occurring across Desdemona Sands (Figure 15a). Note that substantial volume flows are diverted from channel 1 into the Cathlamet Bay channels (4 and 6).

Half-Tide: Day 3: 15 hours: Figures 13b, 14b and 15b

Four hours later the tide is ebbing everywhere. In this case, the surface currents are stronger than the bottom currents due to friction and horizontal density gradients. The salinity field is similar to the high tide field, with the bottom front at grid point 7 in channel 1 remaining at the same position. In channel 2 the water is fresher near the surface and saltier near the bottom compared with 4 hours previously. The 1<sup>0</sup>/oo contour is also farther upstream in channel 1 than at high tide. The ebb volume transports are again much larger in channel 2 than in channel 1; this time there is substantial division of flow from channel 1 to channel 2 through the Taylor Sands channel (3) and across bank flow at the east end of Desdemona Sands.

Lower-Low Water: Day 3: 18 hours: Figures 13c, 14c and 15c

The ebb is now past its peak at the mouth, but it is approximately at its peak in the upriver parts of the estuary. The substantial flows out of channel 2 have forced the pycnocline in channel 2, and seaward of grid point 4 in channel 1, downward. This has a tendency to isolate a pool of higher salinity water on the bottom between grid points 4 and 7 in channel 1. The surface water of channel 2 is substantially fresher than the water of this reach of channel 1. The volume transport map is similar to the previous map except that the substantial flows exiting the narrow Welch Island Reach (grid points 16, 17 and 18, channel 1) cause a back flow over the eastern end of Jim Crow Sands between channel 1 and the end of channel 6. This eddy circulation at this channel junction also shows up in the mean flows. The author is not aware of any data that would substantiate such flows off Jim Crow Point.

Half-Tide: Day 3: 21 hours: Figures 13d, 14d and 15d

The flood flow has just begun at the mouth and in channel 2, whereas flow is still ebbing east of Tongue Point. Volume transports in channel 1, between Hammond and Tongue Point, are very small.

Substantial two-layer flows exist between the mouth and Astoria in channel 1. The profiles of velocity and salinity at Station 2 have many similarities with the profiles given by Jay (1984), Figure 5.1, that were taken at a position close to station 2 at the time of the turn between ebb and flood. Note that there is substantial upwelling from the deep hole at grid point 4 into channel 2; this upwelling then partly returns to channel 1 over the west end of Desdemona Sands to grid point 5. The stratification in both channels is between 10-15 ‰ with the high salinities occurring close to the bottom.

Higher-High Water: Day 4: 1 hour: Figures 13e, 14e and 15e

The current and salinity fields resemble those of the high water case 14 hours previously (Figures 13a, 14a and 15a). The channels are not quite as stratified and the current shears are not quite as strong.

Half-Tide: Day 4: 4 hours: Figures 13f, 14f and 15f

This set of figures is again similar to those for the ebb of day 3: 15 hours, except that flows are not as large, since the tide range is not as great. The mixing which occurred on the previous flood still causes the channels to be less stratified.

Low Water: Day 4: 7 hours: Figures 13g, 14g and 15

Again the comparison with day 3: 18 hours shows a great deal of similarity. The currents at this low water are not as large as previously, and the stratification is not as great.

Half-Tide: Day 4: 10 hours: Figures 13h, 14h and 15h

The comparison with day 3: 21 hours shows that flows have higher magnitudes in the lower estuary and lower magnitudes in the upper estuary. Stratification is again similar, with strong stratification being established in the lower water column of the Hammond-Astoria reach. The pycnocline in channel 2 is relatively more sloped than at day 3: 21 hours.

High Tide: Day 4: 12 hours: Figures 13i, 14i and 15i

The final set of figures for this low flow neap tide shows the same patterns as day 3: 11 hours and day 4: 1 hour, with relatively more stratification than day 4: 1 hour but less than day 3: 11 hours. Not surprisingly, the degree of stratification depends upon the tidal range, but there is not a one-to-one correspondence and the effect of mixing over several tidal periods seems to be important in determining mean stratification and salt intrusion length.

The maximum tidal range of about 2m for the above simulation and discussion occurred between day 3: 18 hours and day 4: 1 hour. The spring tide, which occurred between day 9 and 10 of run 26, has a maximum tidal range of about 3.5m and a minimum of 2m. The instantaneous current and salinity sections for channels 1 and 2,

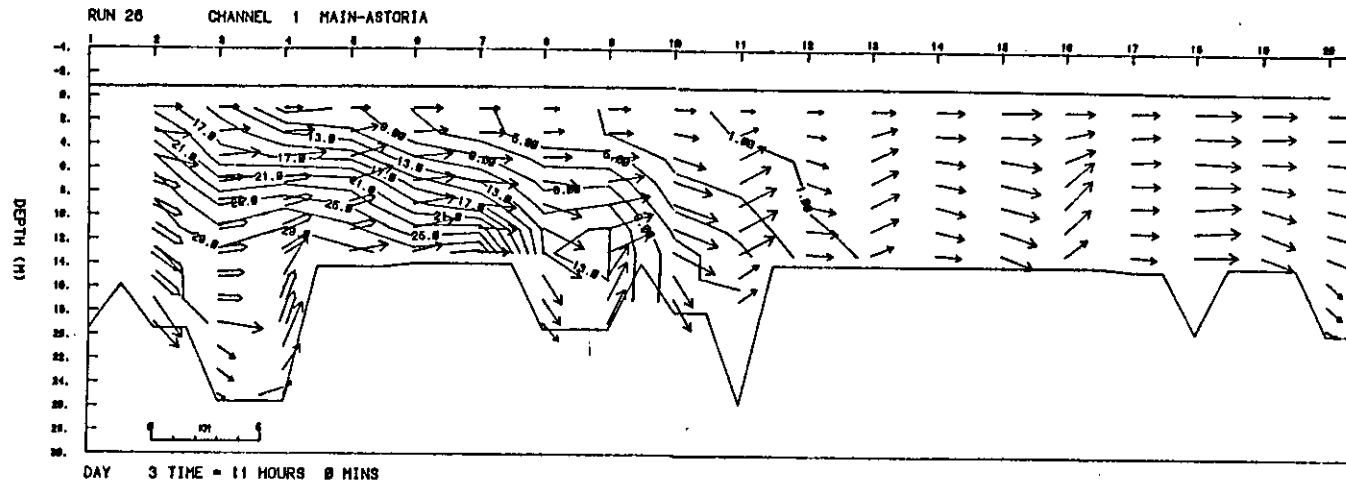
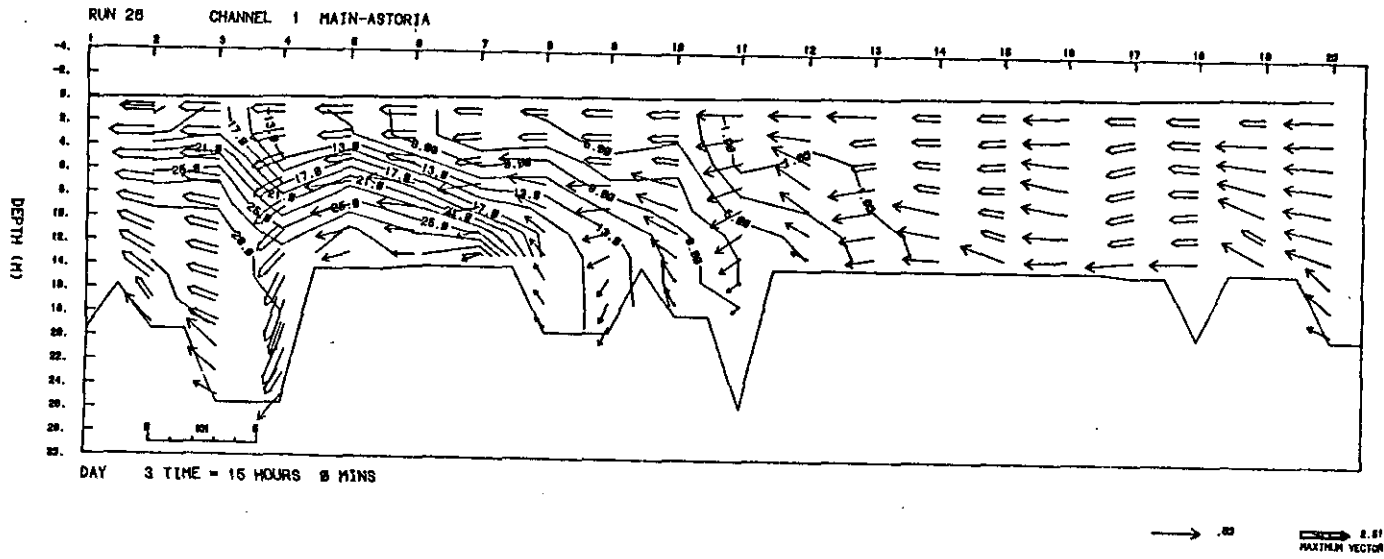


Figure 13a. Channel 1, neap tide period, currents and salinities (m/s and  $^{\circ}/\text{oo}$ ), low riverflow. High water.



62

Figure 13b. Channel 1, neap tide period, currents and salinities (m/s and ‰), low riverflow. Half tide ebb.



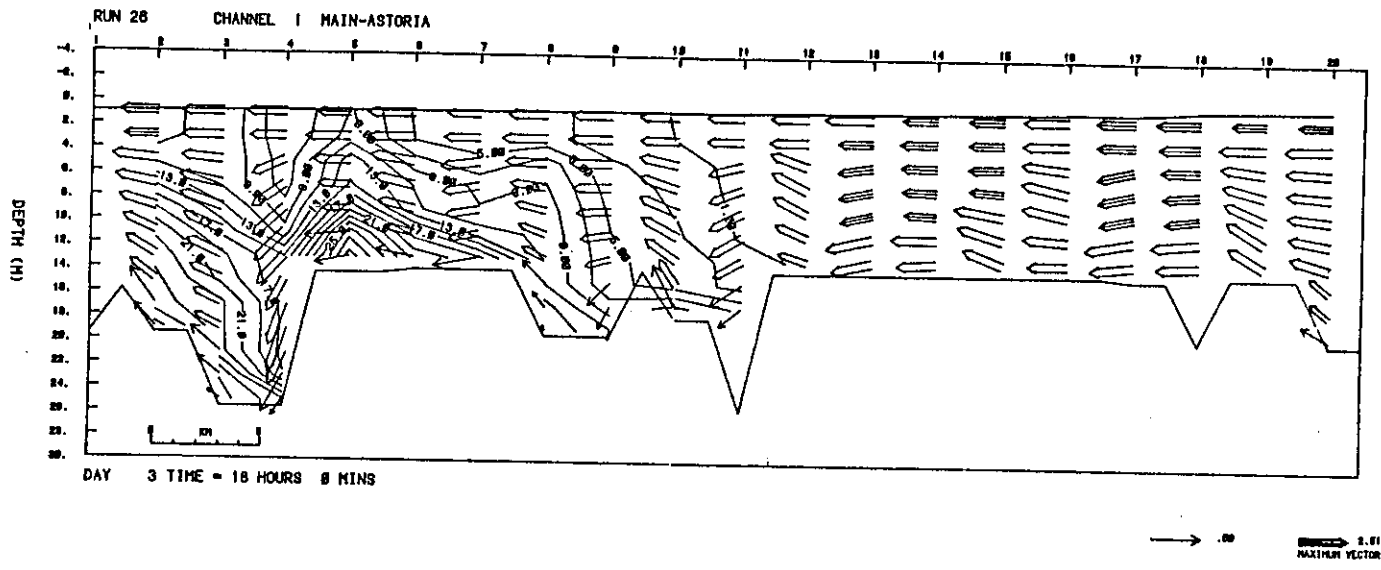


Figure 13c. Channel 1, neap tide period, currents and salinities (m/s and ‰), low riverflow. Low water.

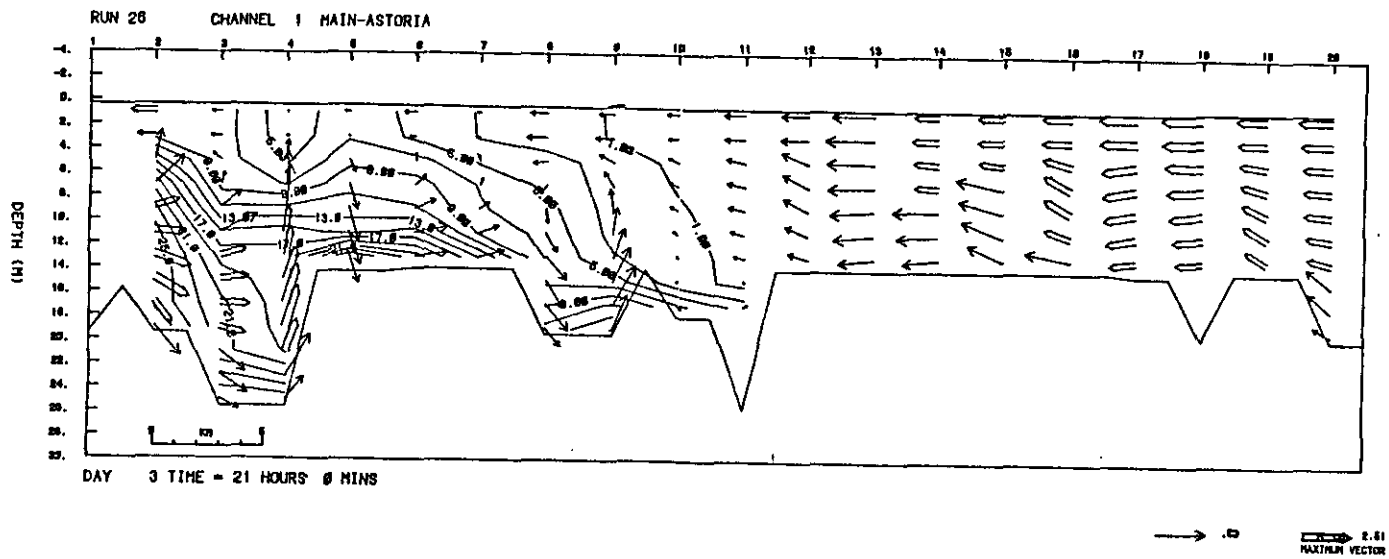
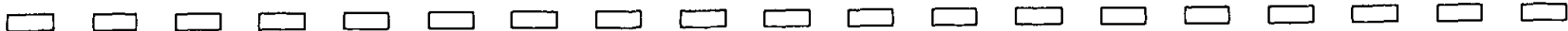


Figure 13d. Channel 1, neap tide period, currents and salinities (m/s and ‰), low riverflow. Half tide flood.



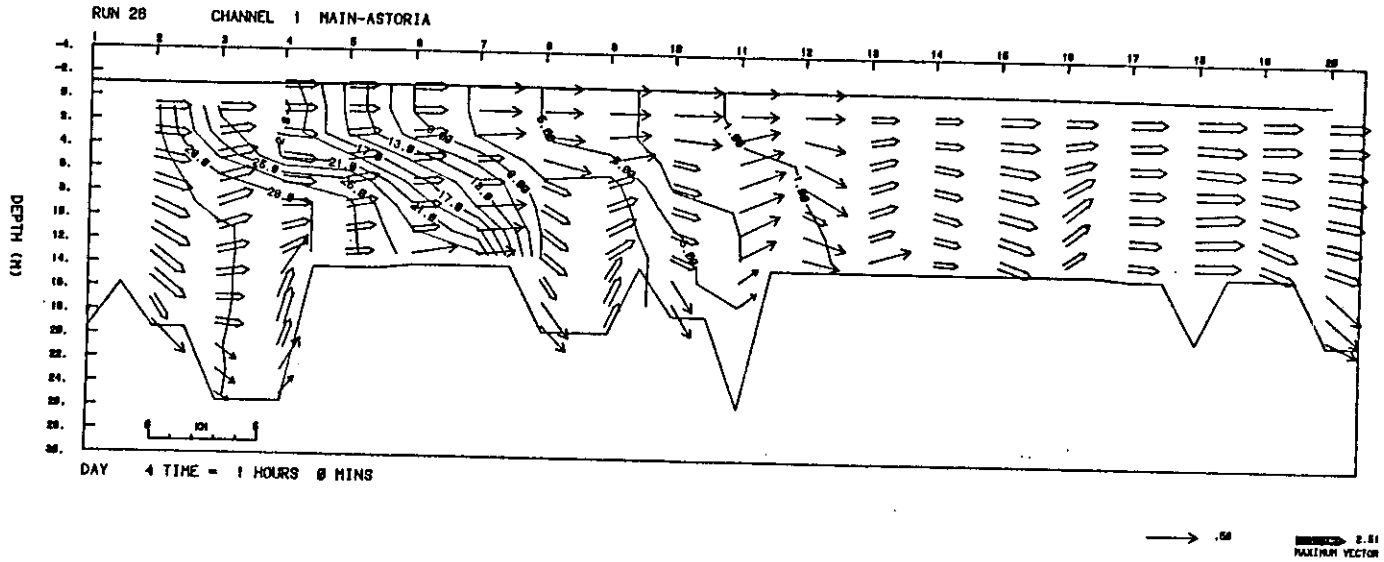


Figure 13e. Channel 1, neap tide period, currents and salinities (m/s and ‰), low riverflow. High water.

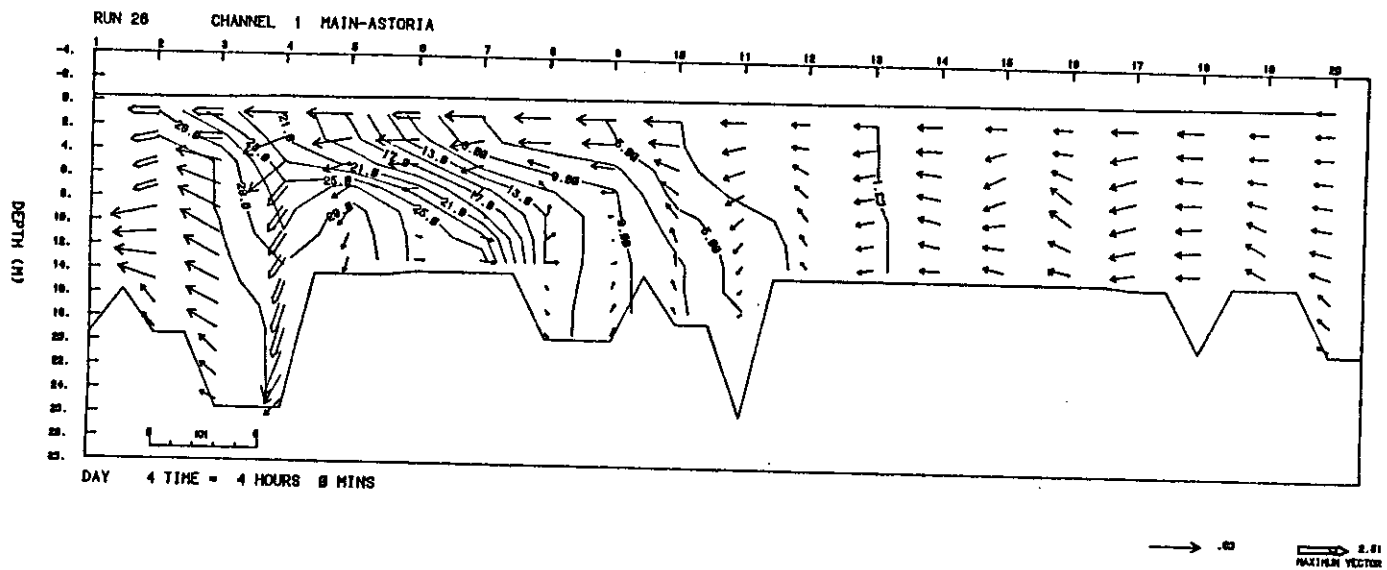


Figure 13f. Channel 1, neap tide period, currents and salinities (m/s and ‰), low riverflow. Half tide ebb.

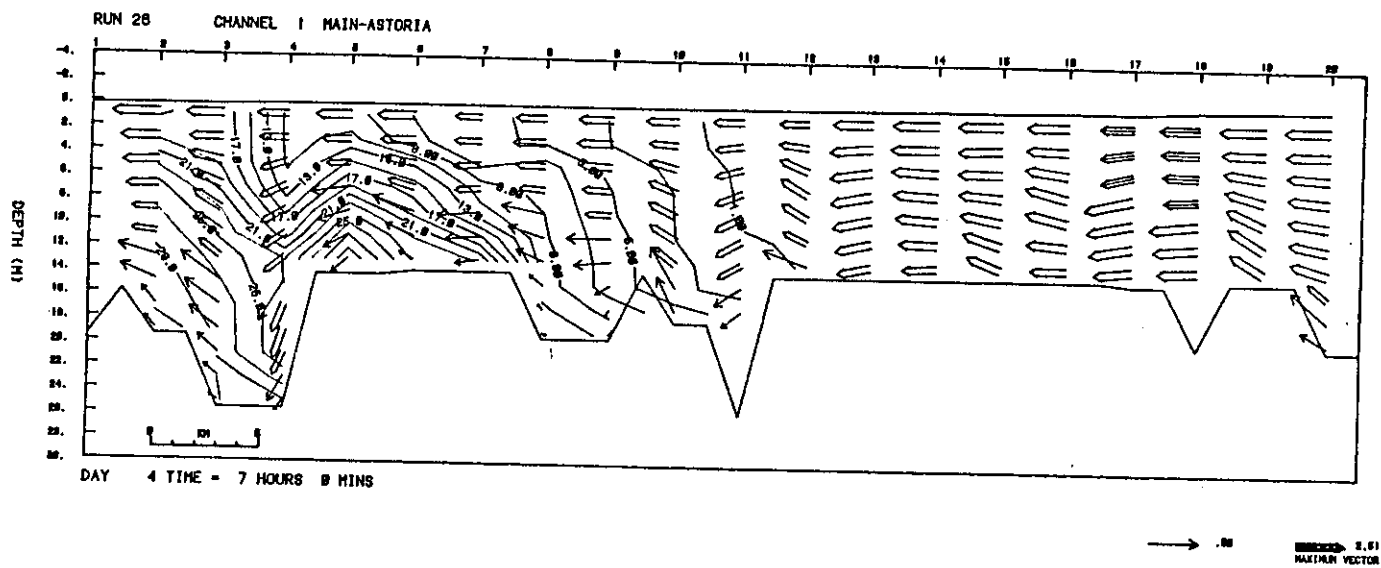


Figure 13g. Channel 1, neap tide period, currents and salinities (m/s and  $^{\circ}/\text{oo}$ ), low riverflow. Low water.

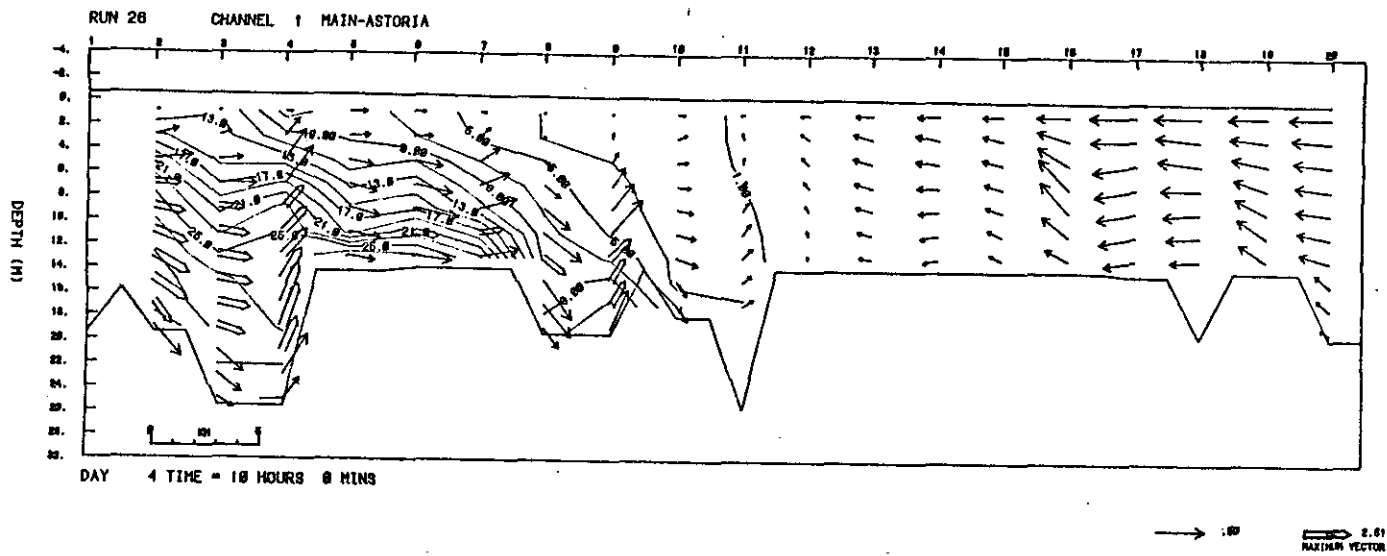


Figure 13h. Channel 1, neap tide period, currents and salinities (m/s and ‰), low riverflow. Half tide flood.

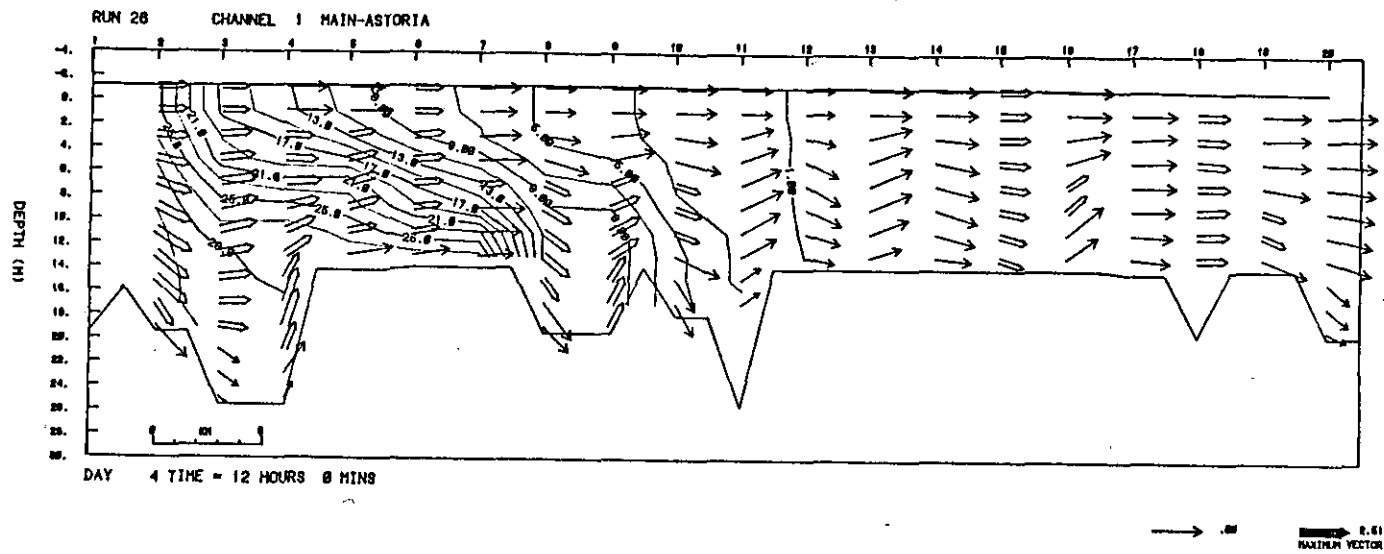


Figure 13i. Channel 1, neap tide period, currents and salinities (m/s and ‰), low riverflow. High water.



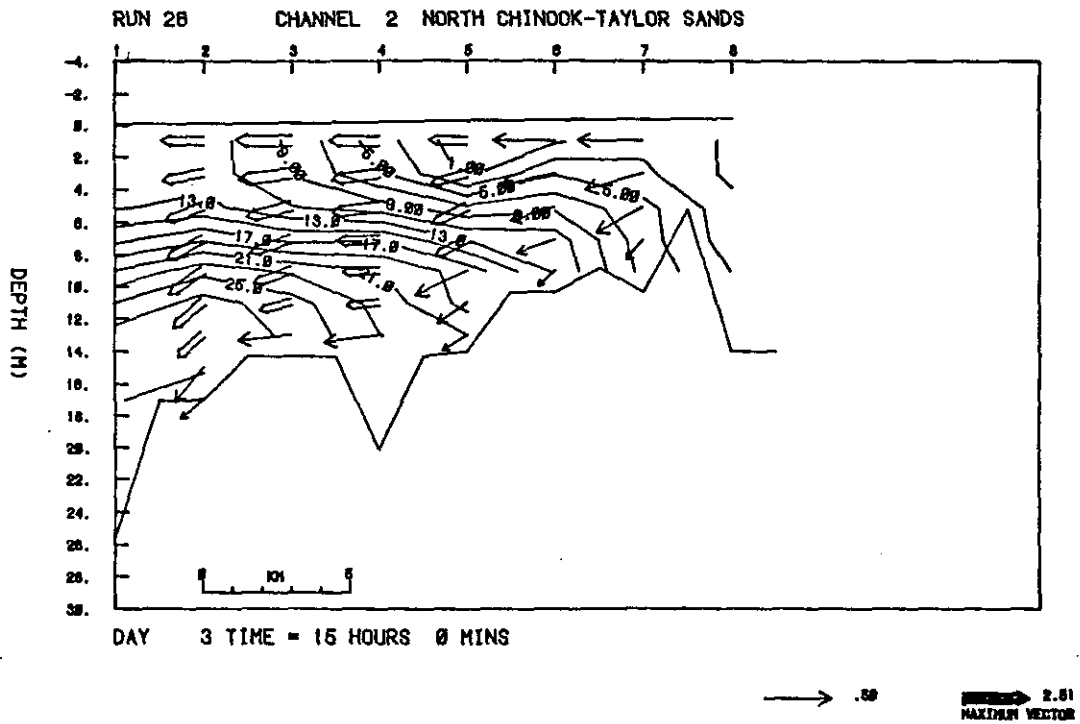


Figure 14b. Channel 2, neap tide period, currents and salinities (m/s and ‰), low riverflow. Half-tide ebb.

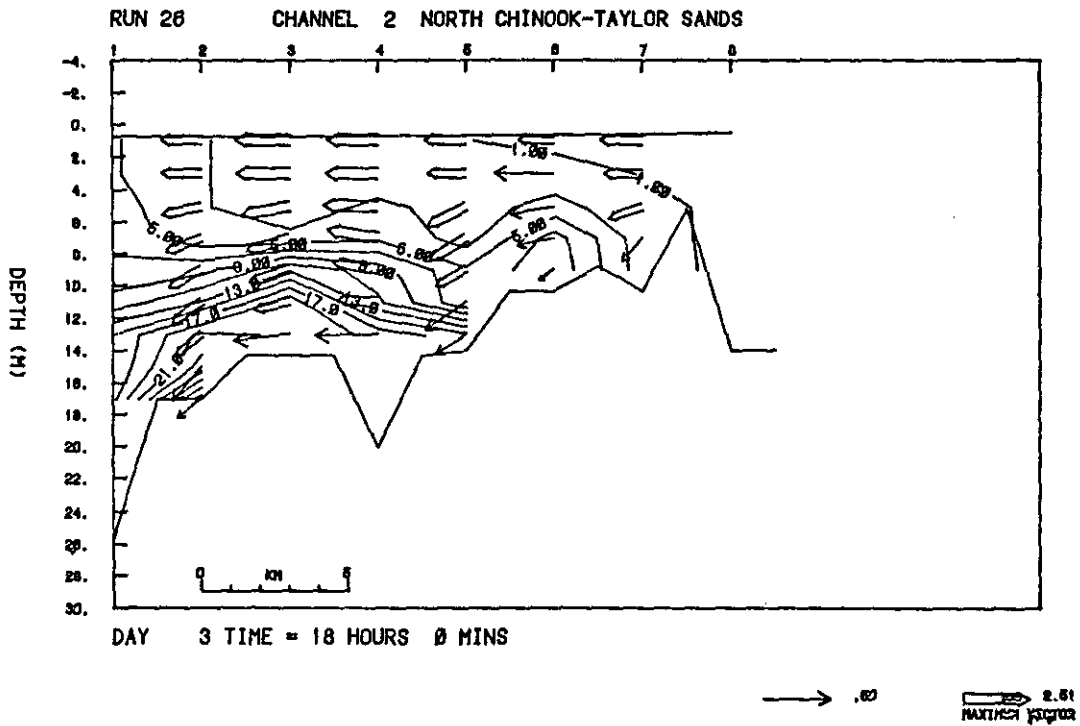
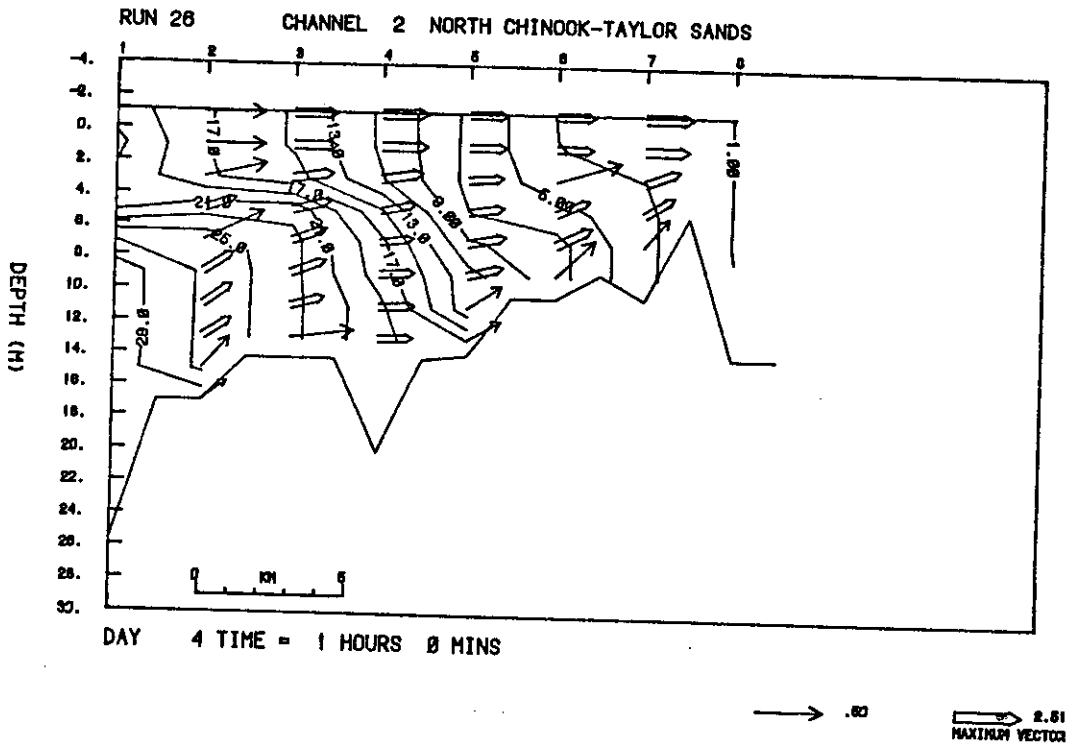


Figure 14c. Channel 2, neap tide period, currents and salinities (m/s and ‰), low riverflow. Low water.





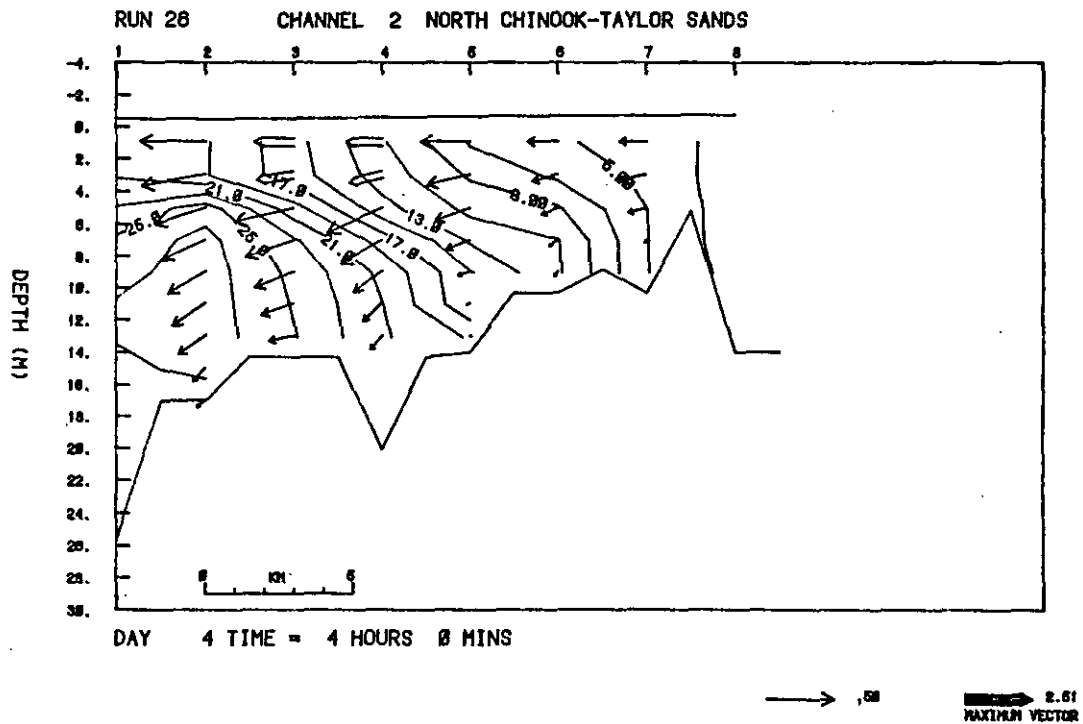


Figure 14f. Channel 2, neap tide period, currents and salinities (m/s and ‰), low riverflow. Half-tide ebb.

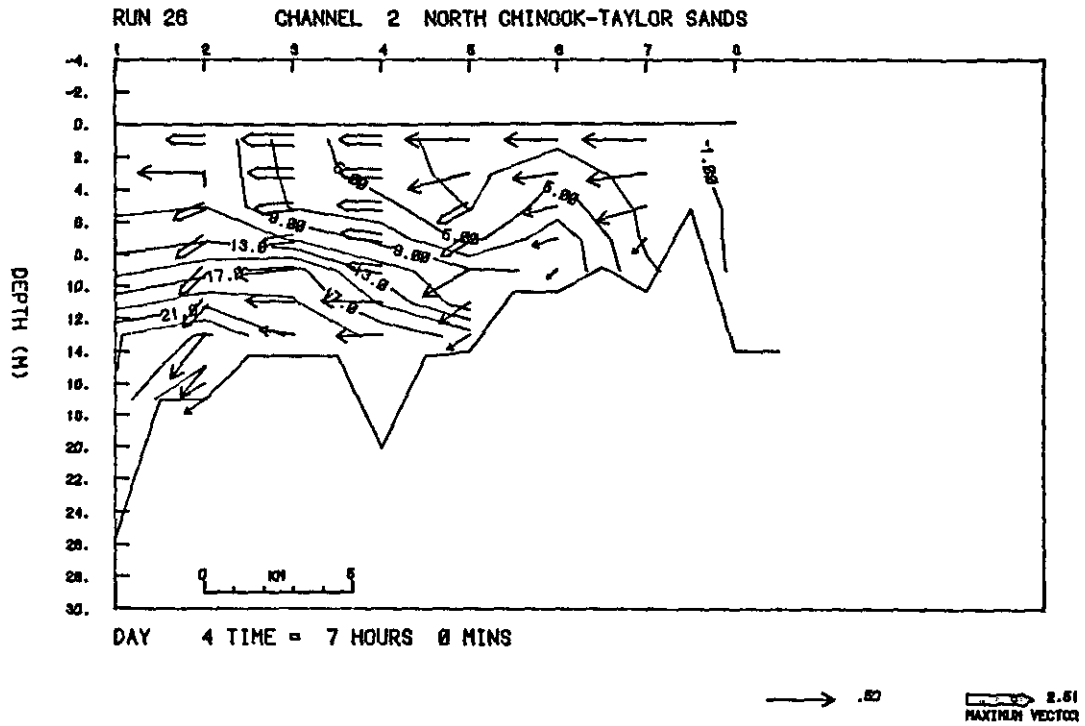


Figure 14g. Channel 2, neap tide period, currents and salinities (m/s and ‰), low riverflow. Low water.

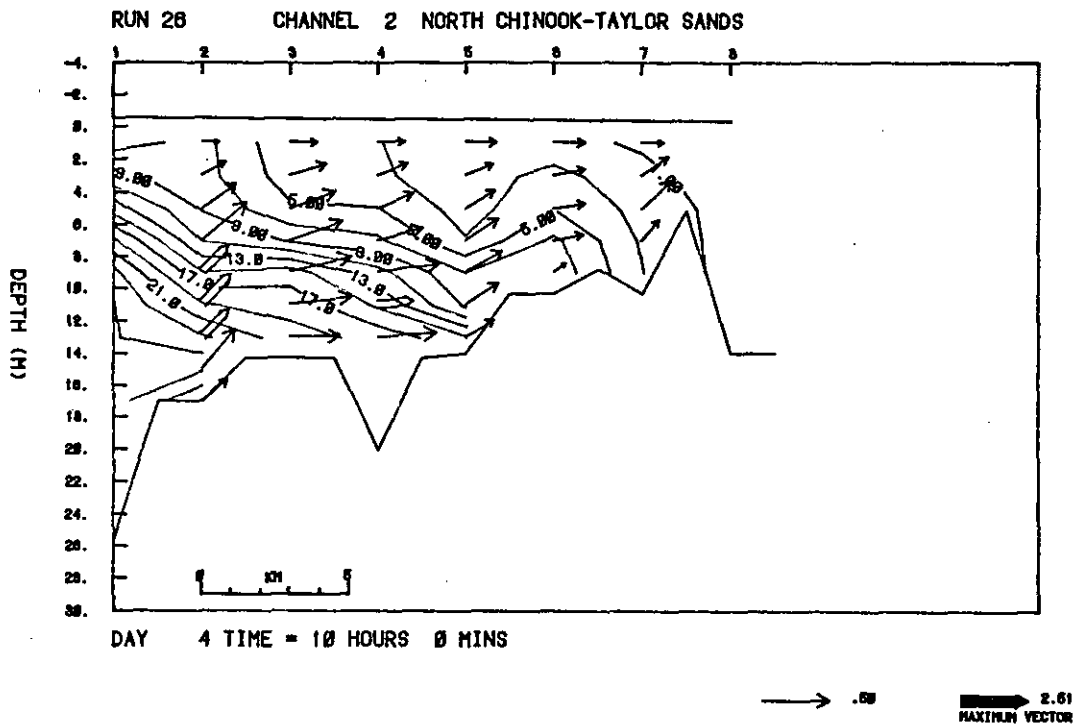
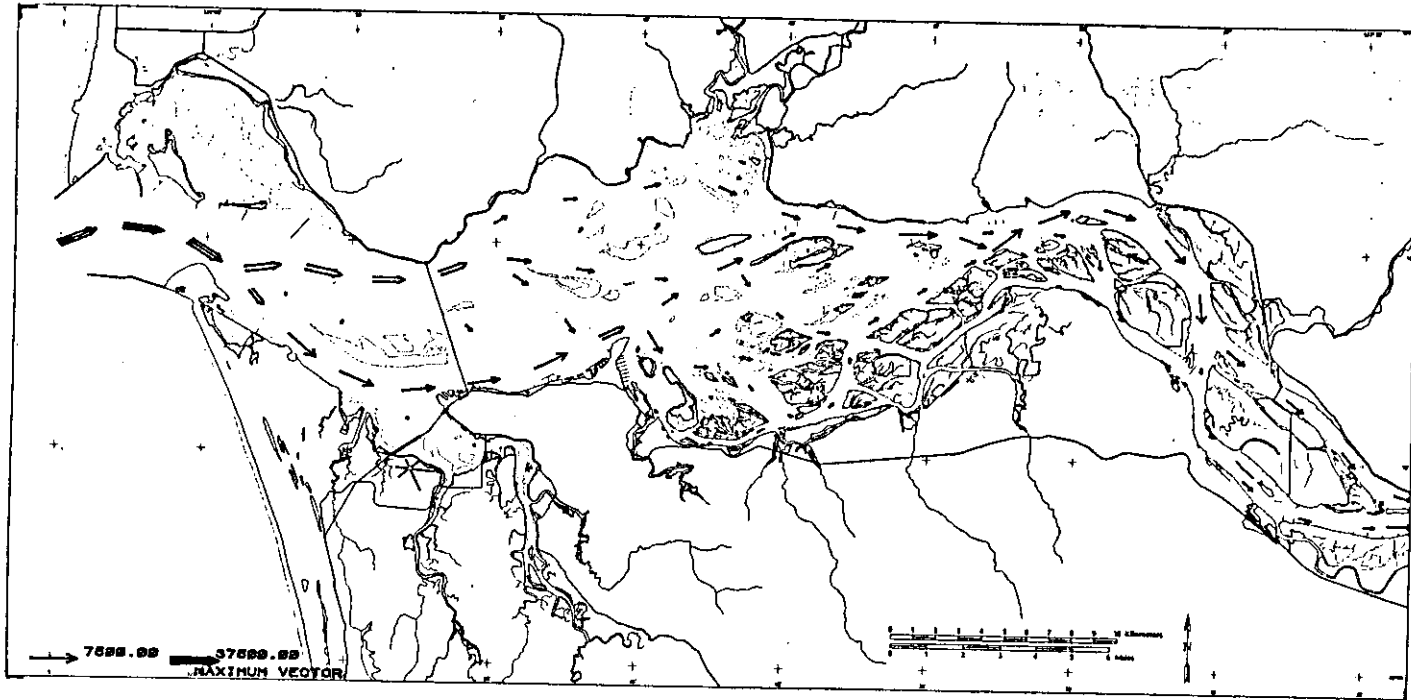


Figure 14h. Channel 2, neap tide period, currents and salinities (m/s and ‰), low riverflow. Half-tide flood.

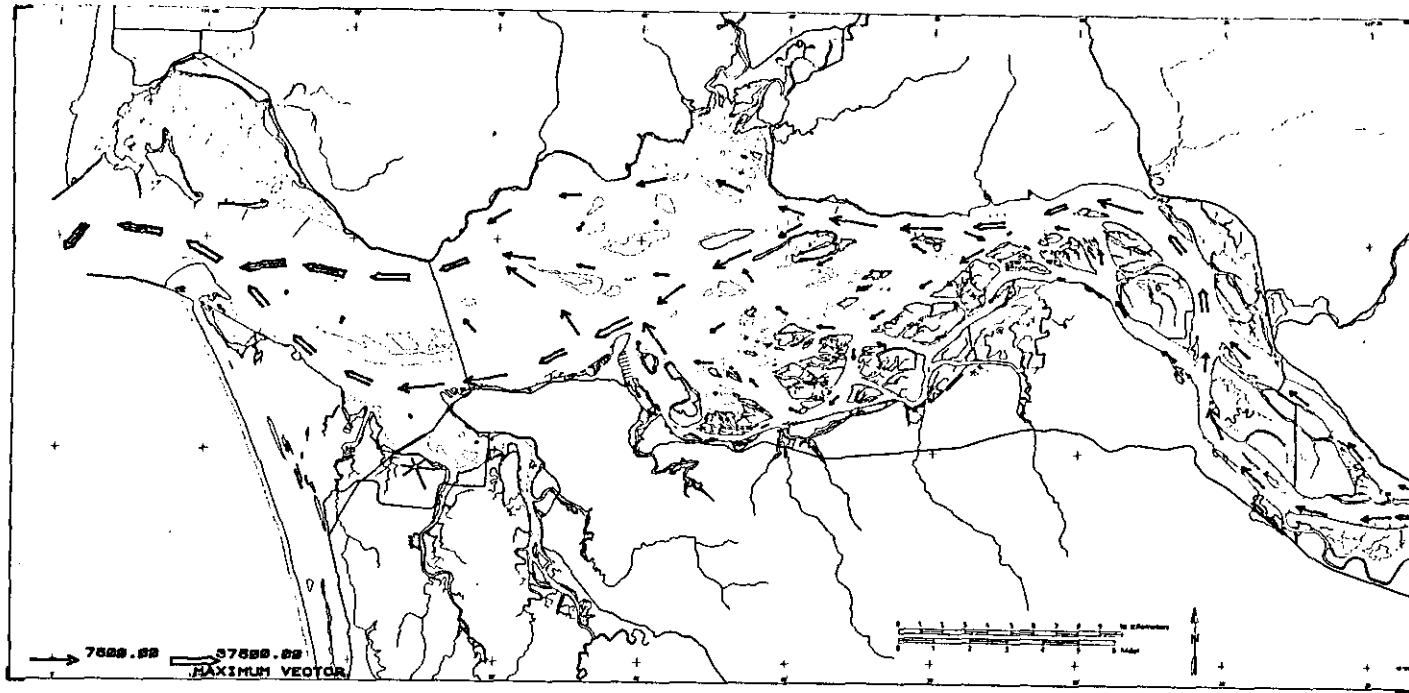




RUN 26

DAY 3 TIME = 11 HOURS 0 MINS

Figure 15a. Horizontal volume transport vectors ( $\text{m}^3/\text{s}$ ) for neap tide and low riverflow. High water.

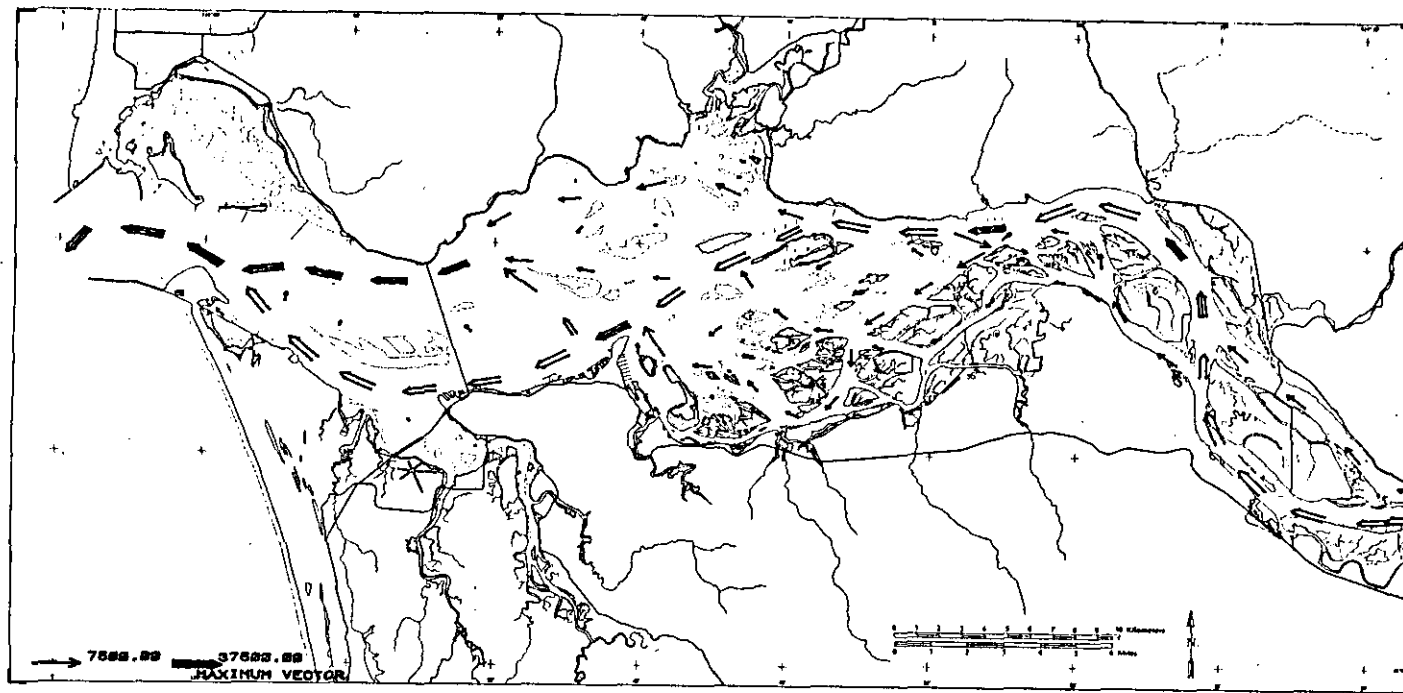


RUN 26

DAY 3 TIME = 15 HOURS 0 MINS

Figure 15b. Horizontal volume transport vectors ( $m^3/s$ ) for neap tide and low riverflow. Half-tide ebb.

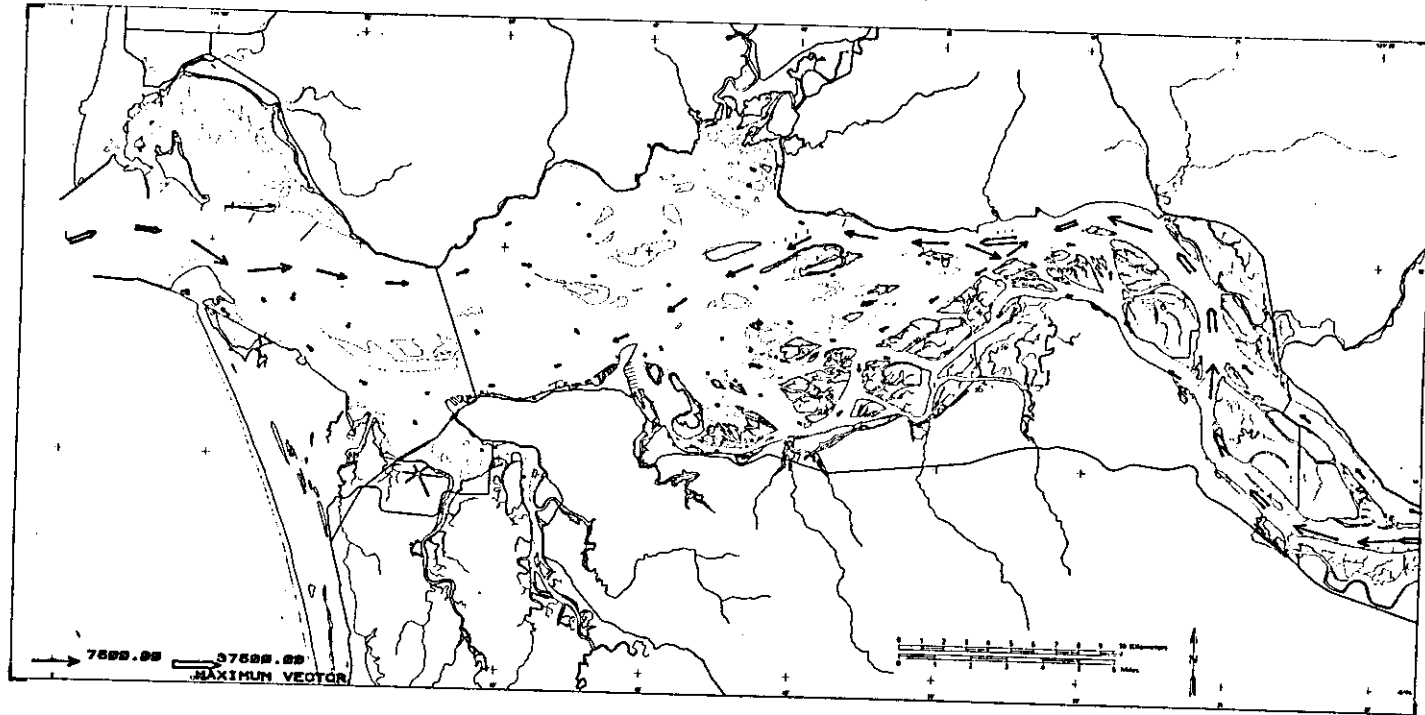




RUN 26

DAY 3 TIME = 18 HOURS 0 MINS

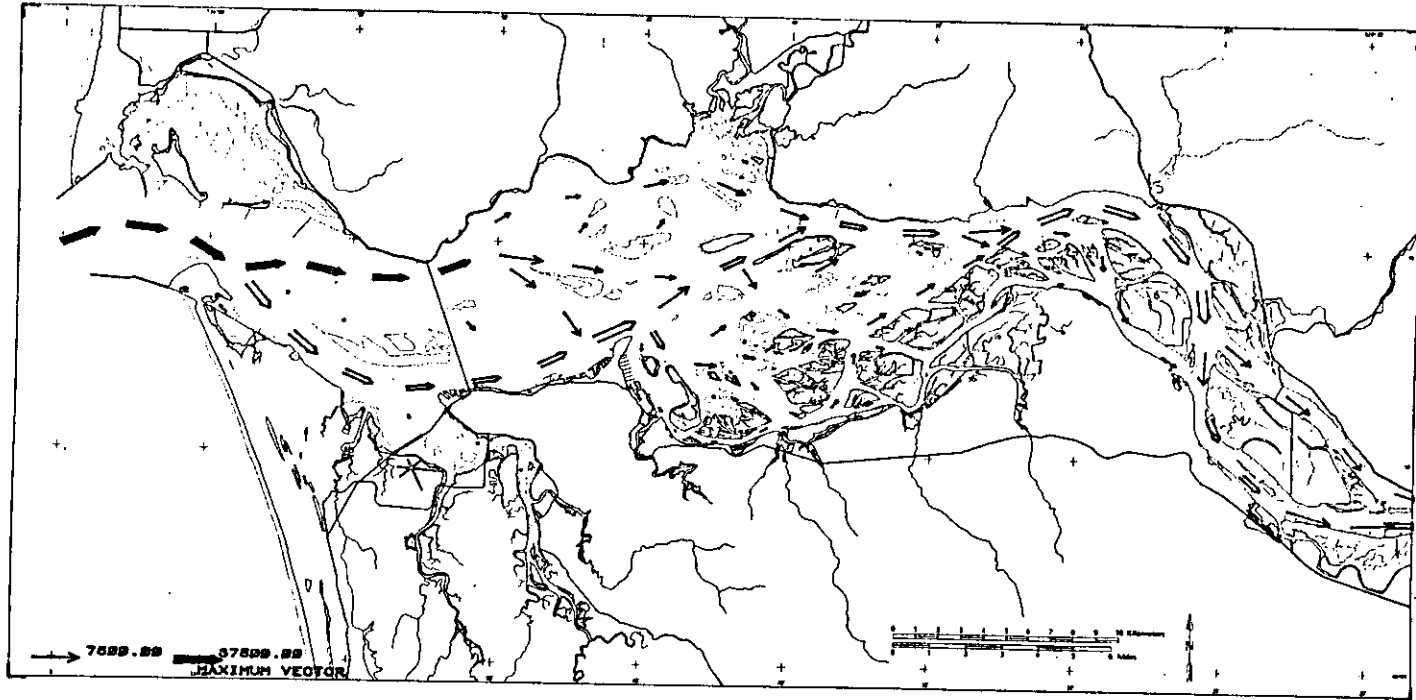
Figure 15c. Horizontal volume transport vectors ( $\text{m}^3/\text{s}$ ) for neap tide and low riverflow. Low water.



RUN 26

DAY 3 TIME = 21 HOURS 0 MINS

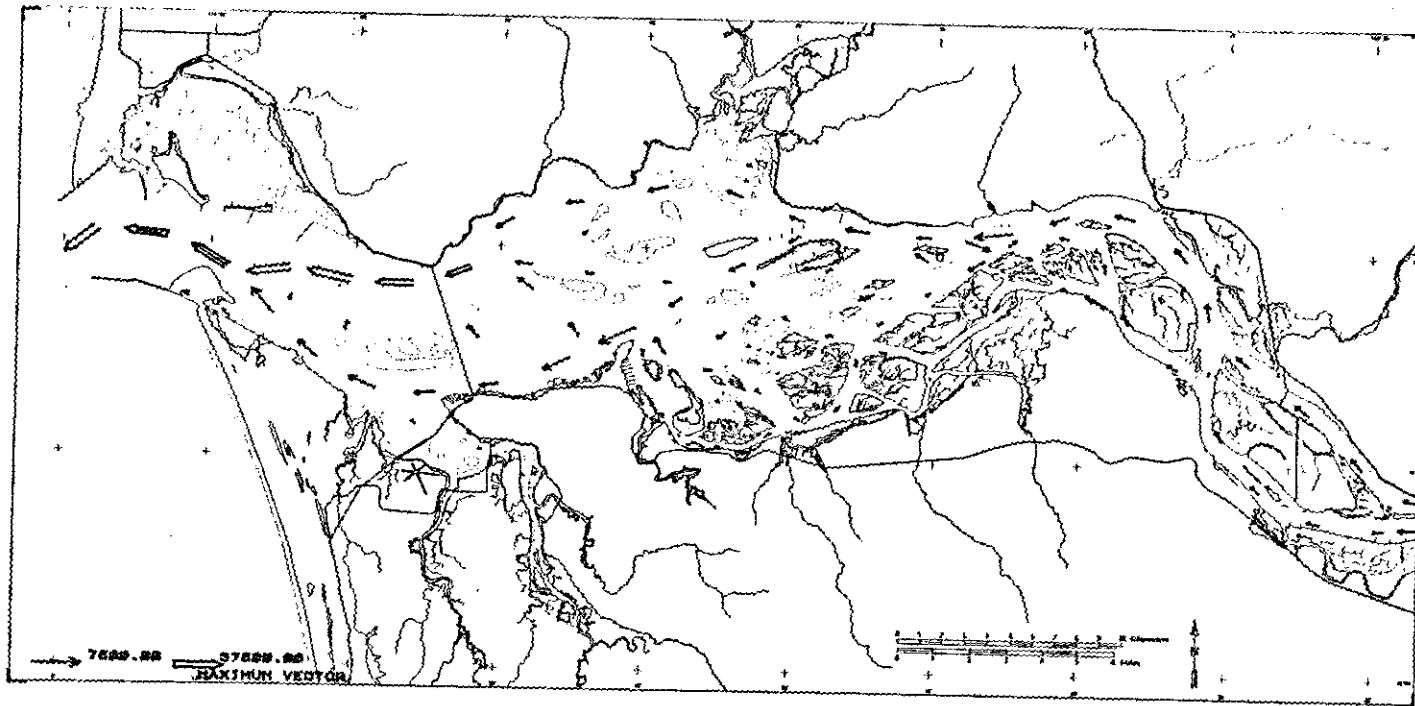
Figure 15d. Horizontal volume transport vectors ( $\text{m}^3/\text{s}$ ) for neap tide and low riverflow. Half-tide flood.



RUN 26

DAY 4 TIME = 1 HOURS 0 MINS

Figure 15e. Horizontal volume transport vectors ( $\text{m}^3/\text{s}$ ) for neap tide and low riverflow. High water.

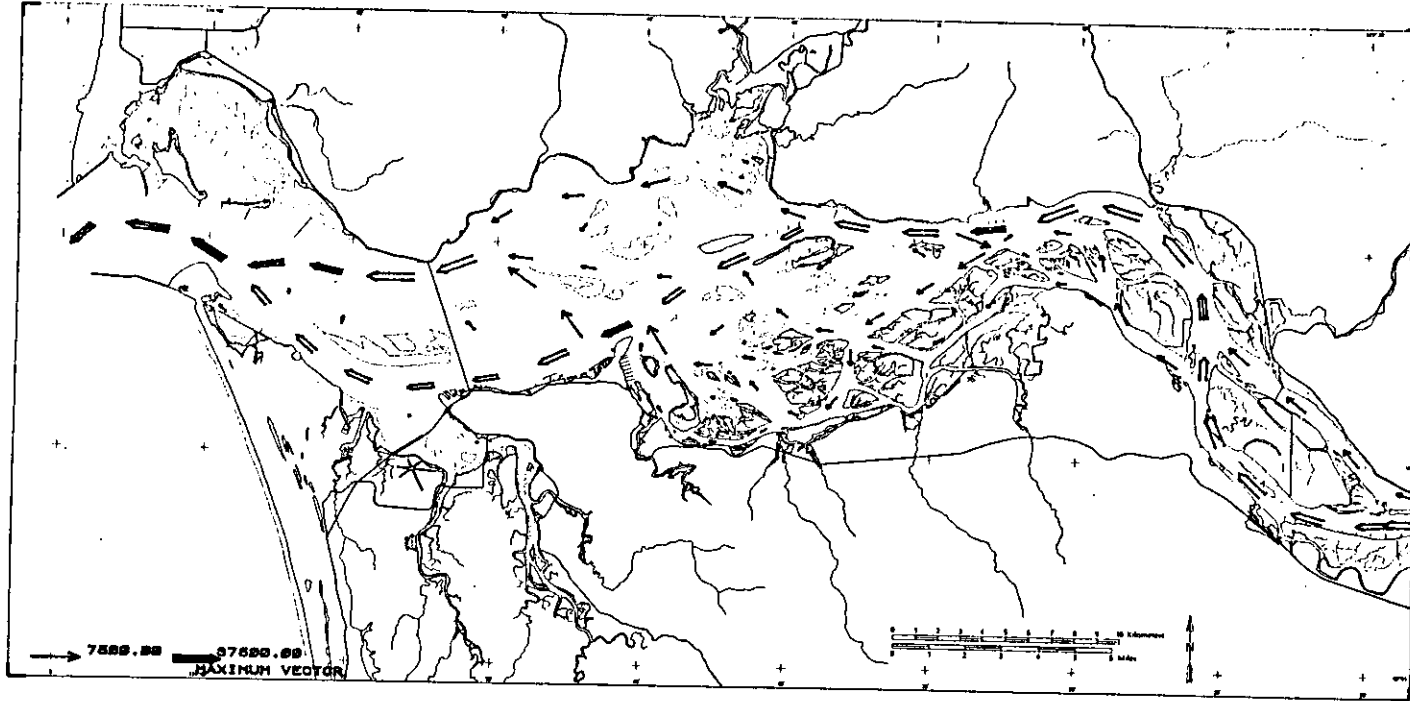


RUN 28

DAY 4 TIME = 4 HOURS 0 MINS

Figure 15f. Horizontal volume transport vectors ( $m^3/s$ ) for neap tide and low riverflow. Half-tide ebb.

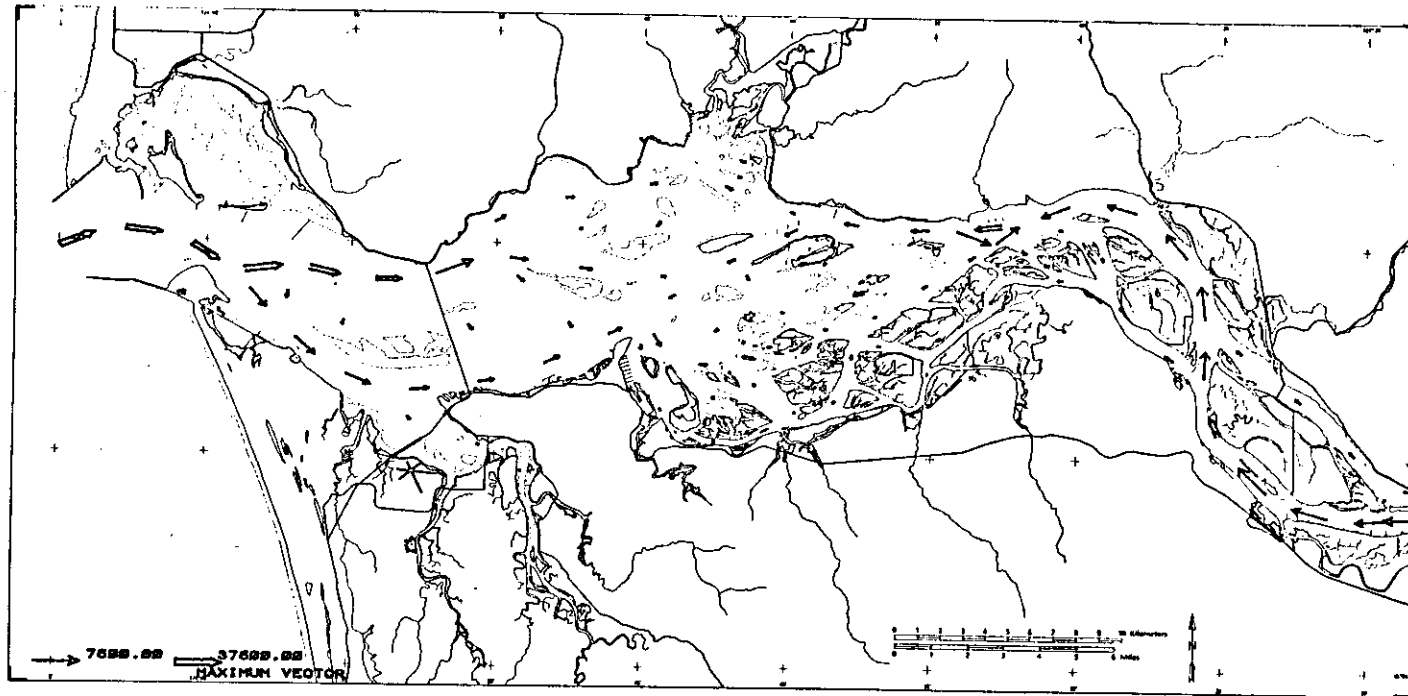




RUN 26

DAY 4 TIME = 7 HOURS 0 MINS

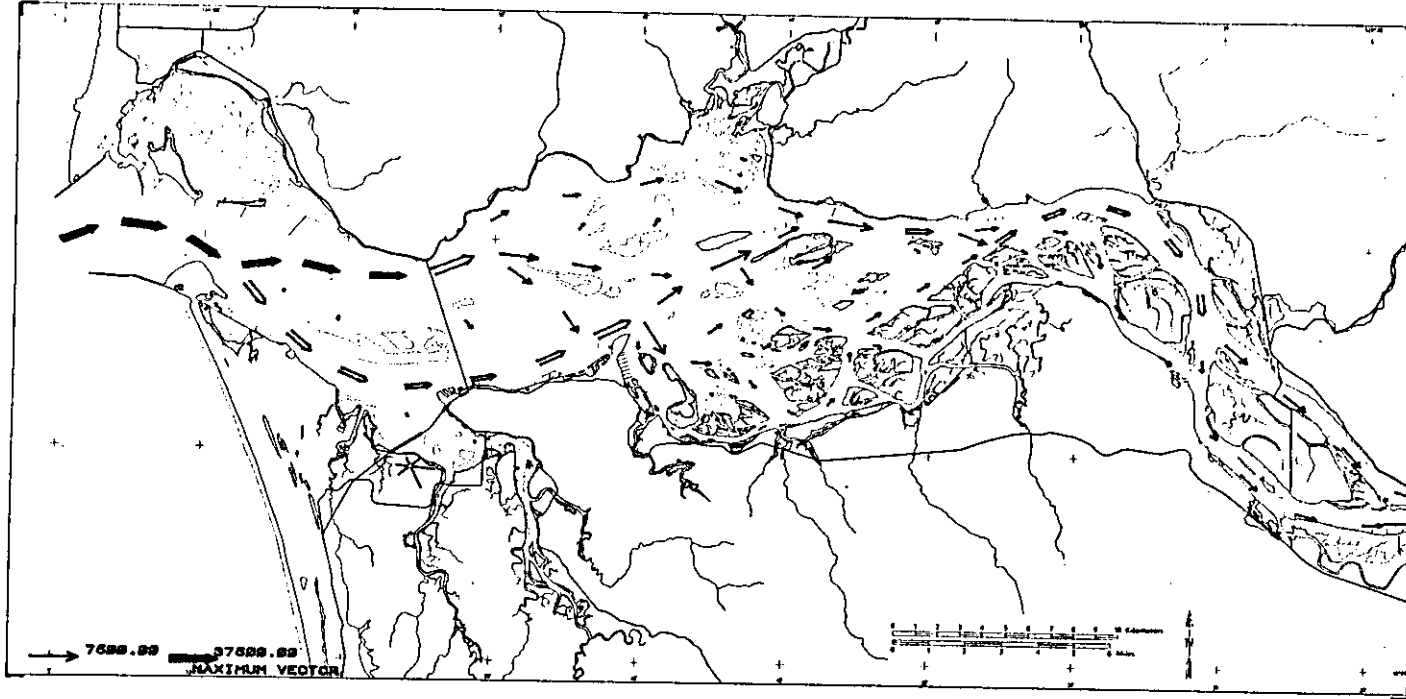
Figure 15g. Horizontal volume transport vectors ( $\text{m}^3/\text{s}$ ) for neap tide and low riverflow. Low water.



RUN 26

DAY 4 TIME = 10 HOURS 0 MINS

Figure 15h. Horizontal volume transport vectors (m<sup>3</sup>/s) for neap tide and low riverflow. Half-tide flood.



RUN 26

DAY 4 TIME = 12 HOURS 0 MINS

Figure 15i. Horizontal volume transport vectors ( $m^3/s$ ) for neap tide and low riverflow. High water.

starting at high water, are shown in Figures 16 and 17 (a-i). The volume transport maps are not shown, as they are very similar to those of Figure 15 except for the relatively larger values. Figures 16 and 17 are in the same high-low water sequence as Figures 13 and 14 and so can be compared directly.

The stronger mixing, less stratification, stronger currents and more uniform current profiles are evident in all these figures. The vertical orientation of the isohalines, particularly during floods, is very striking compared with the horizontal orientation during neap tides. The region upstream of grid point 7 in channel 1 is much fresher than during neap tides; but channel 2, to the contrary, has higher salt content than at high tide during neaps. Tidal excursions of the isohalines are naturally much larger than at neap, and the 1 ‰ isohaline penetrates farther upstream (Figures 16b and 16f) and farther downstream (Figures 16 and 13 g-h) than in the corresponding figures (13b and 13f). Other features are qualitatively similar between the neap and spring simulations, including the tendency for the ebb to be more stratified than the flood and the tendency for an isolated patch of high salinity water to be formed in the Hammond reach of channel 1 at low water due to the outflow of channel 2.

The instantaneous sections for the high flow period neap and spring tides are not shown because they are qualitatively similar to the low flow sections presented above, except for the shorter intrusion length and larger tidal salinity ranges. The differences between low and high flow salinity fields are illustrated in the mean field sections along with the maxima and minima salinity plots given below.

### 3.1.3. Tidal Analysis

A summary of the tidal characteristics of the models is given in Tables 5a and 5b. Table 5a shows the results of tidal analysis of the 60-day spring 1981 simulations for the  $M_2$  and  $K_1$  tide. The analysis programs of Foreman (1979) were used in a similar manner to Volume I and Jay (1984). The tide gauge data was analysed for the same 60-day period or a 60-day period beginning one month later. The  $M_2$  and  $K_1$  amplitudes and phases for the tidal elevation agree quite well. The  $M_2$  amplitudes are smaller than the observations, which is partly due to the glitch the simulation records every 10 days. (Jetty A observed and simulated records should be practically identical.) The model records do not show enough relative amplification of the  $M_2$  tide between Jetty A and Fort Stevens, which may be due to the exclusion of Baker Bay or the values chosen for the frictional coefficient. Further experiments, not reported here, indicate that bottom friction is probably too large in the lower estuary. The depth mean current leads the elevations by about 40-45° for the  $M_2$  constituent and lags the elevations by about 60° for the  $K_1$  constituent. These phase lags compare reasonably with the inferred phase lags from observations using tide gauge and current meter data (Jay 1984).

Table 5b principally describes the phase and amplitude differences between near-bottom and near-surface currents for the same grid points as the elevation and transport analysis. Analysis of salinity records

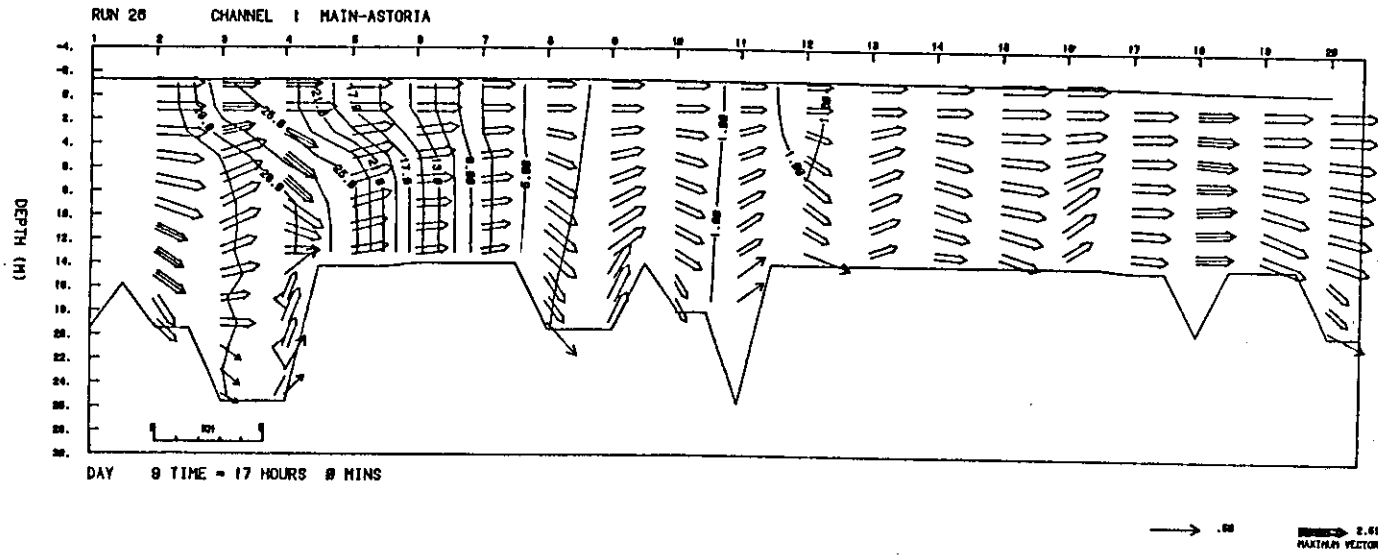


Figure 16a. Channel 1, spring tide period, currents and salinities (m/s and ‰), low riverflow. High water.



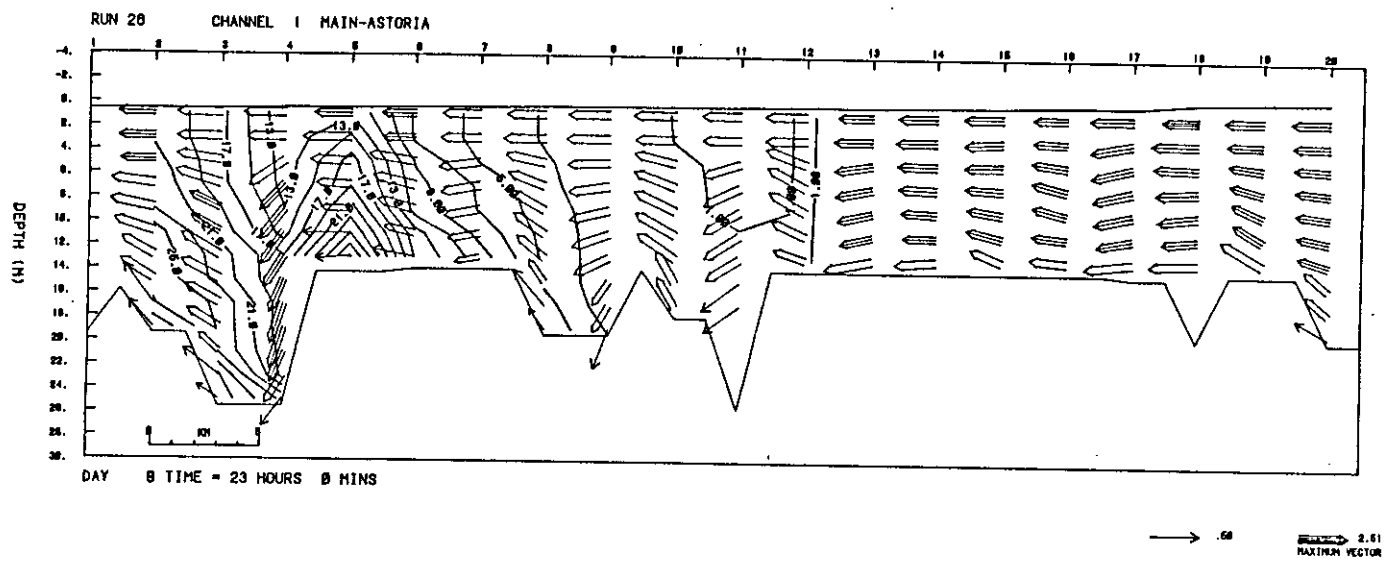


Figure 16c. Channel 1, spring tide period, currents and salinities (m/s and ‰), low riverflow. Low water.

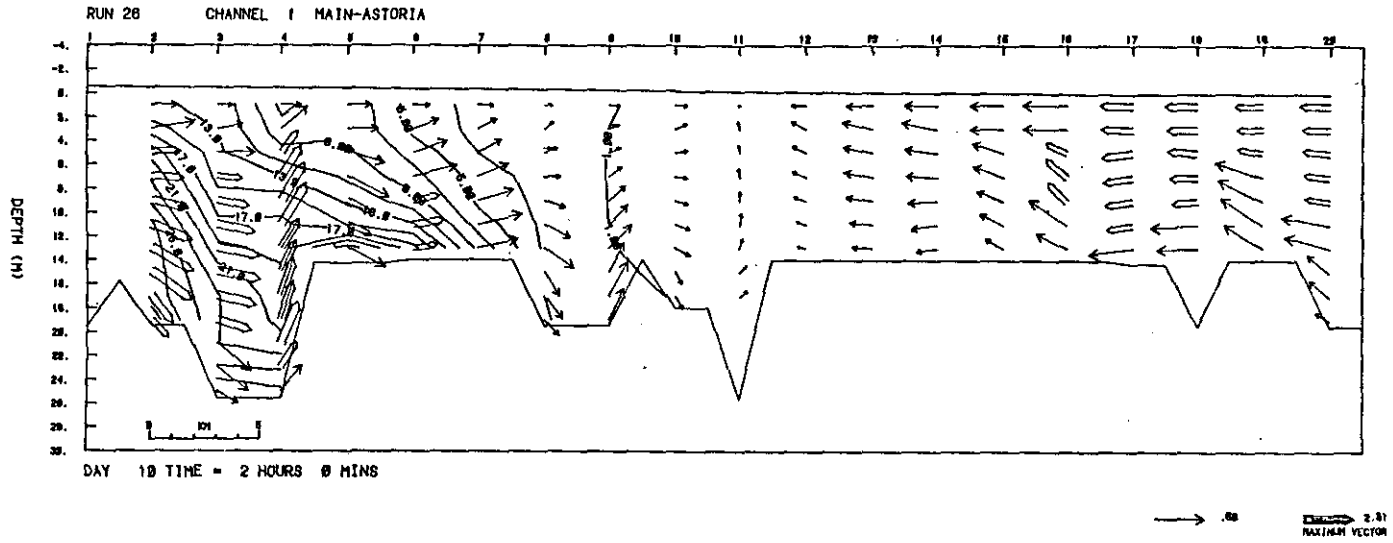


Figure 16d. Channel 1, spring tide period, currents and salinities (m/s and ‰), low riverflow. Half-tide flood.

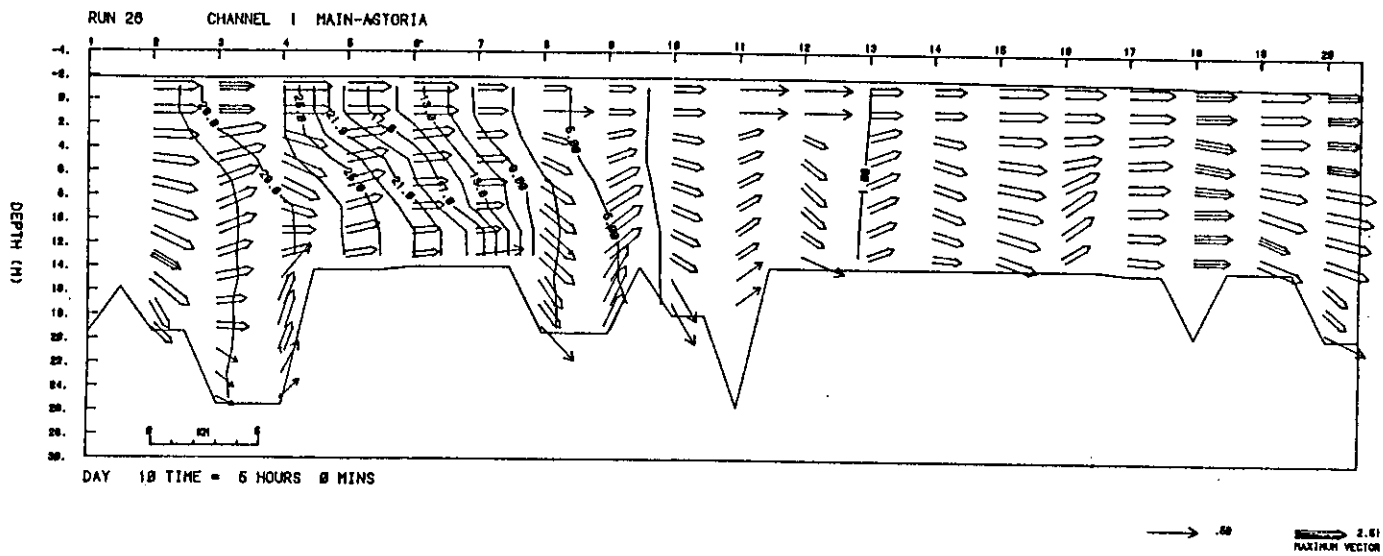


Figure 16e. Channel 1, spring tide period, currents and salinities (m/s and ‰), low riverflow. High water.

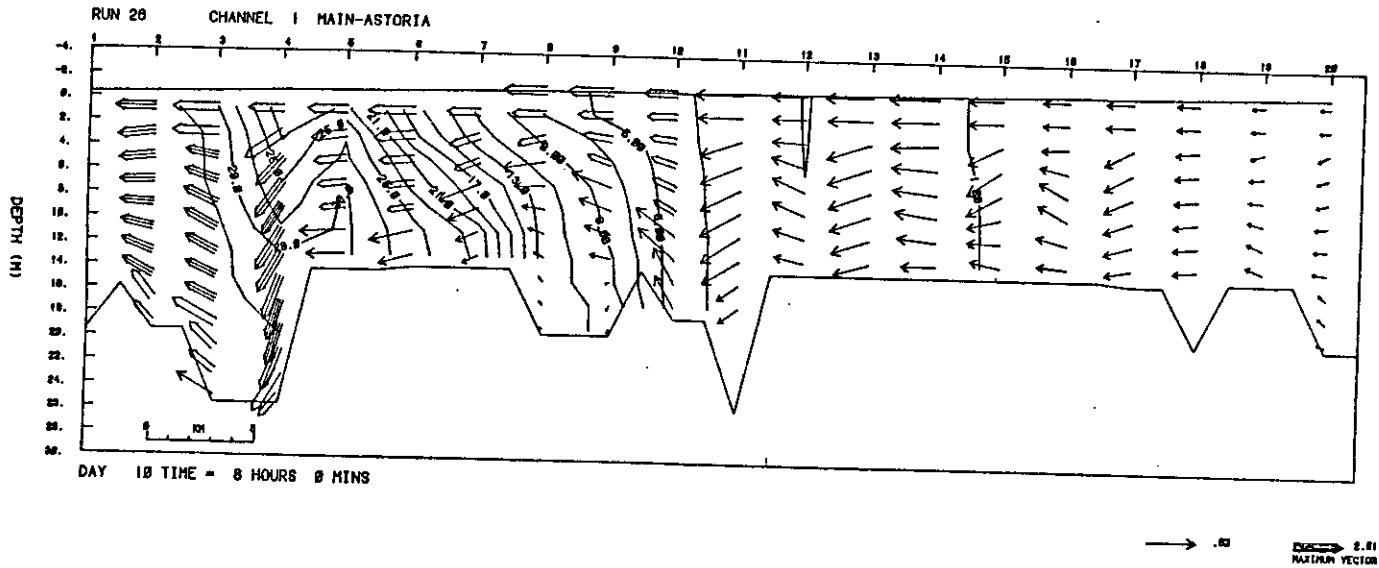


Figure 16f. Channel 1, spring tide period, currents and salinities (m/s and ‰), low riverflow. Half-tide ebb.

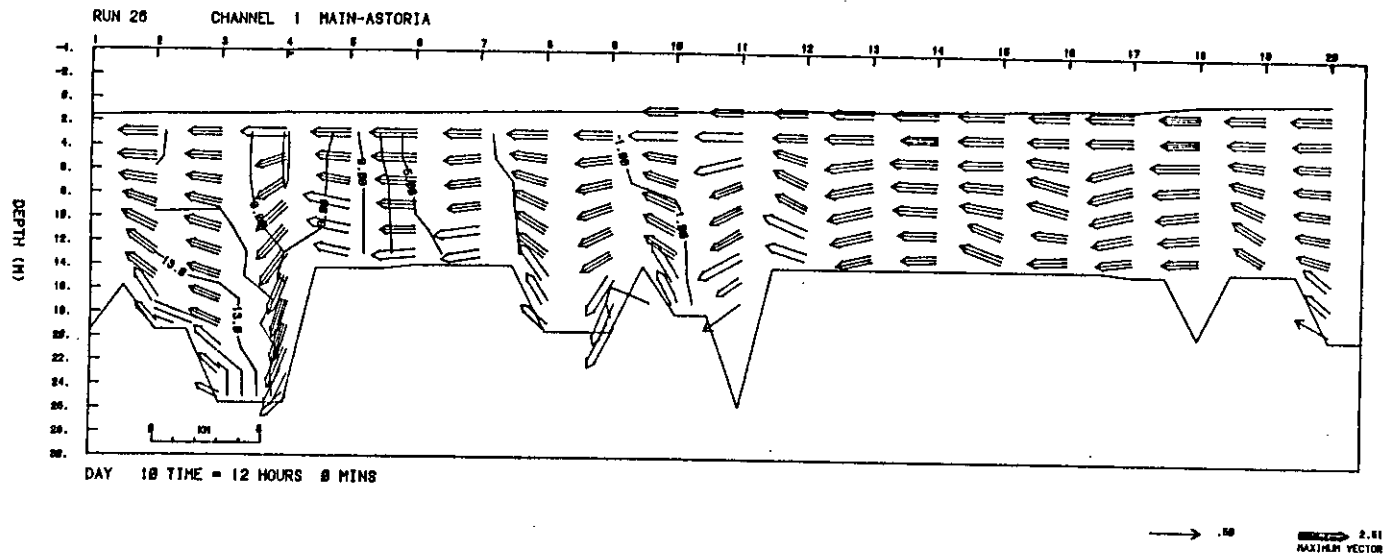


Figure 16g. Channel 1, spring tide period, currents and salinities (m/s and  $^{\circ}/\text{oo}$ ), low riverflow. Low water.

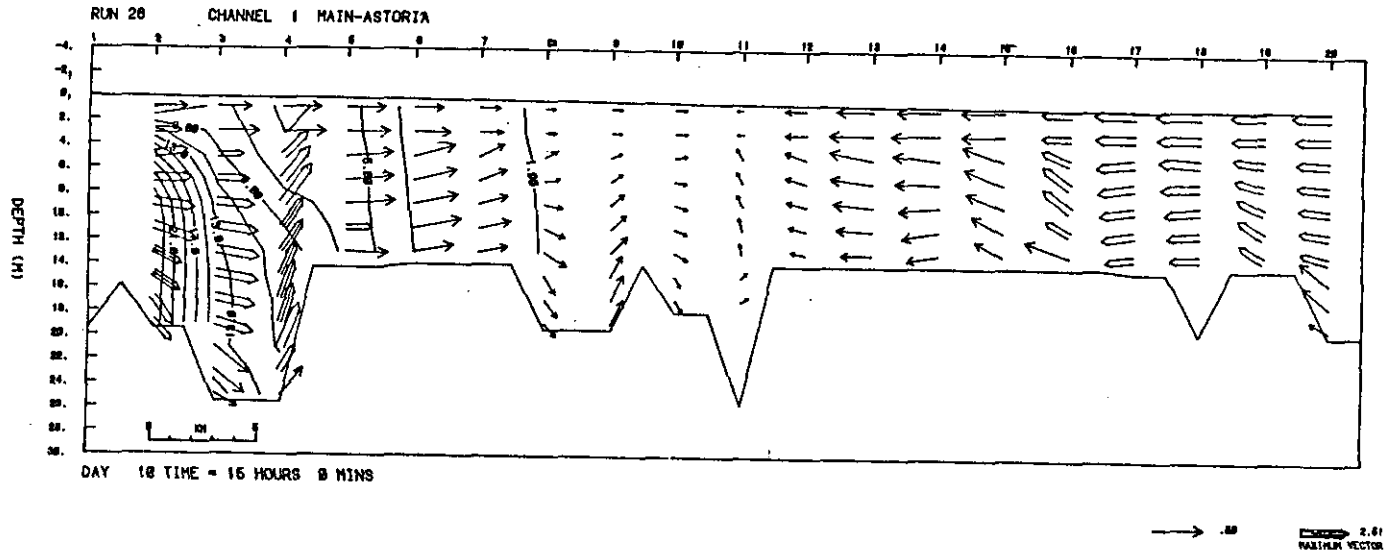


Figure 16h. Channel 1, spring tide period, currents and salinities (m/s and ‰), low riverflow. Half-tide flood.

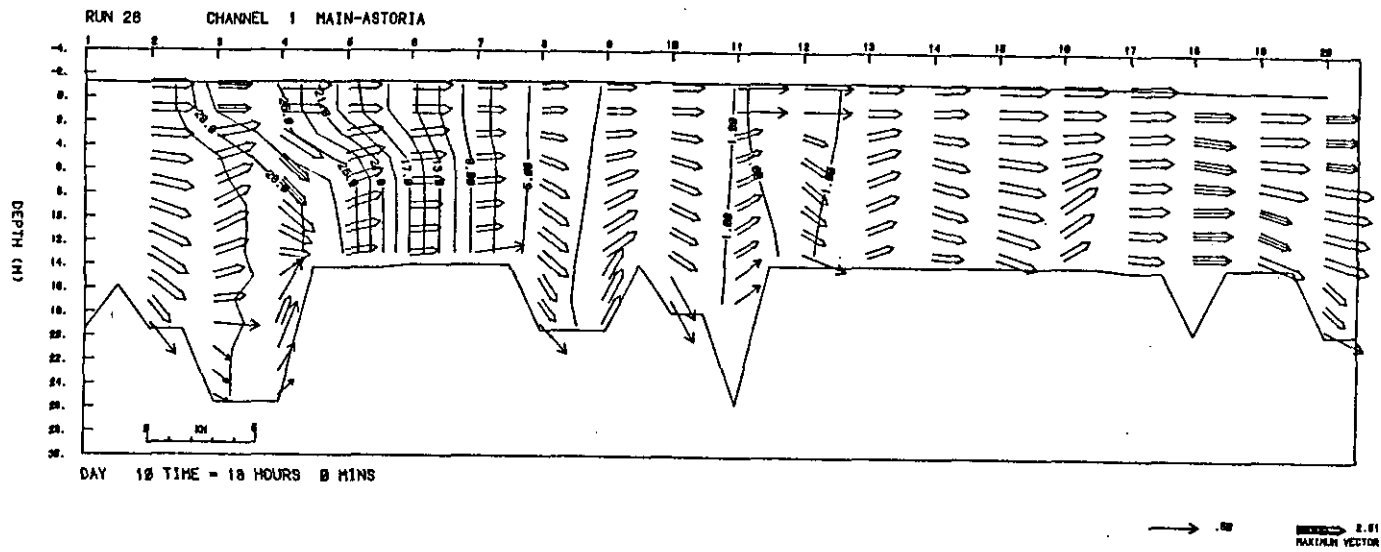


Figure 161. Channel 1, spring tide period, currents and salinities (m/s and  $^{\circ}/\text{oo}$ ), low riverflow. High water.

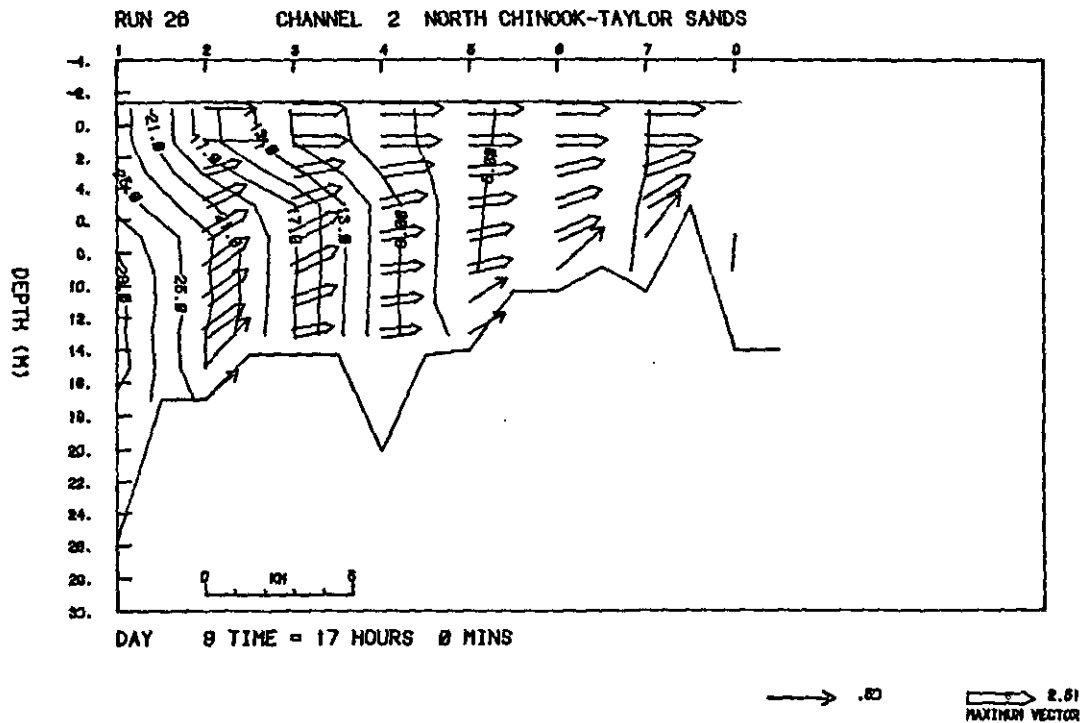


Figure 17a. Channel 2, spring tide period, currents and salinities (m/s and ‰), low riverflow. High water.

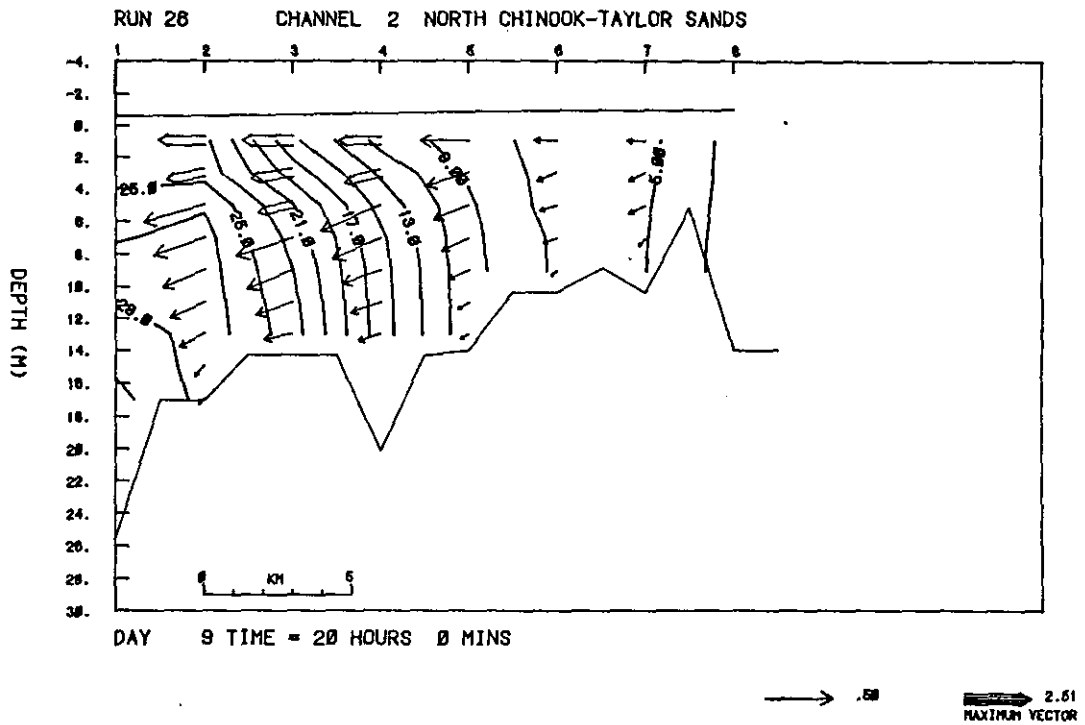


Figure 17b. Channel 2, spring tide period, currents and salinities (m/s and ‰), low riverflow. Half-tide ebb.

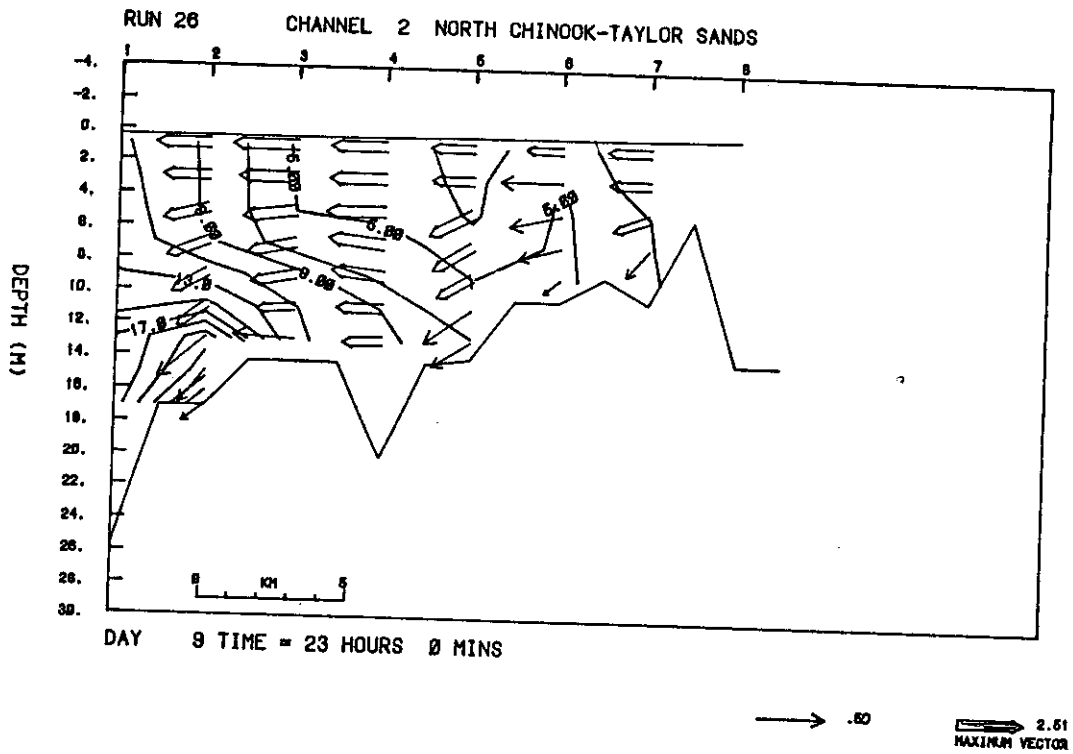


Figure 17c. Channel 2, spring tide period, currents and salinities (m/s and ‰), low riverflow. Low water.

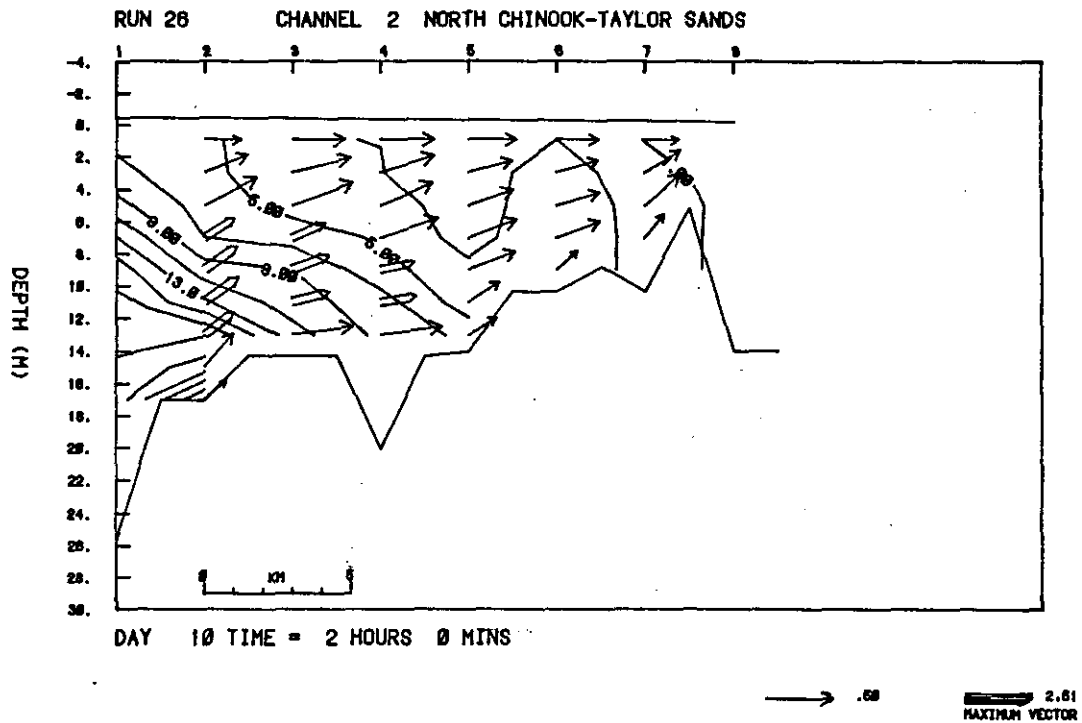


Figure 17d. Channel 2, spring tide period, currents and salinities (m/s and ‰), low riverflow. Half-tide ebb.

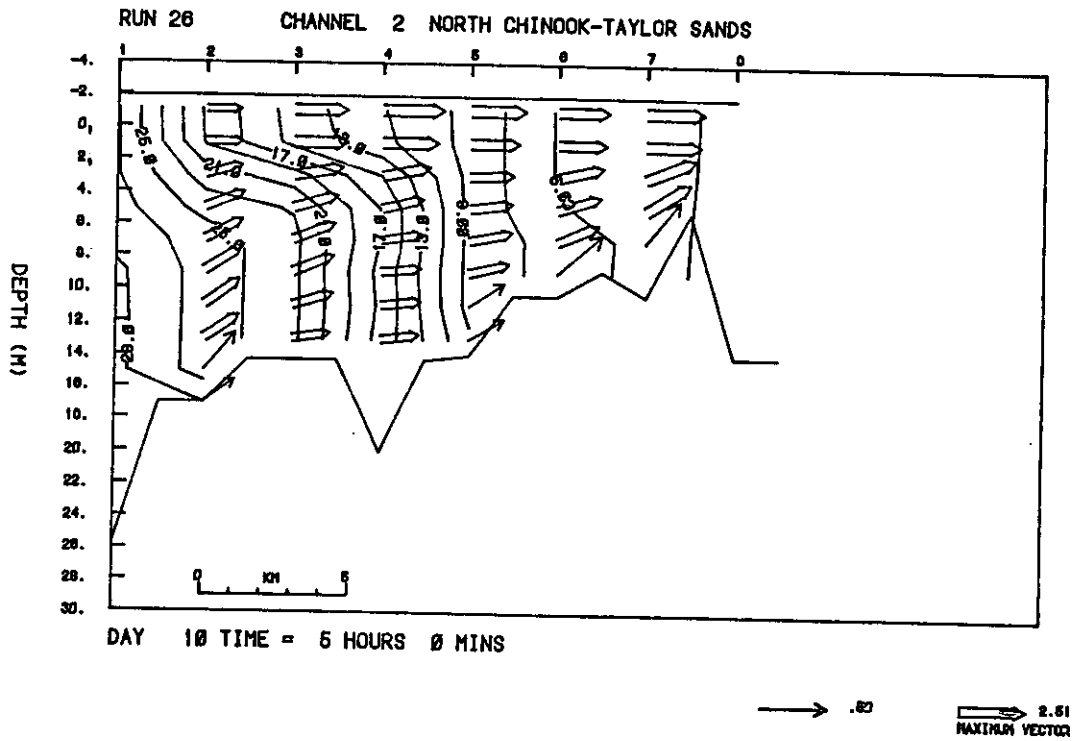


Figure 17e. Channel 2, spring tide period, currents and salinities (m/s and ‰), low riverflow. High water.

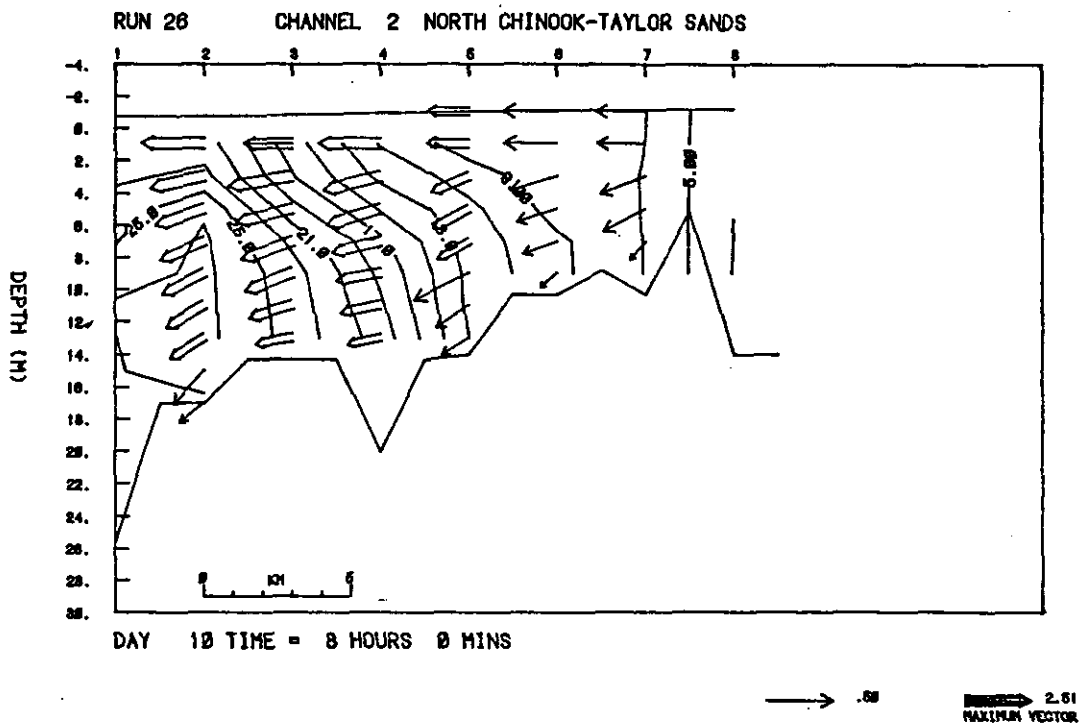


Figure 17f. Channel 2, spring tide period, currents and salinities (m/s and ‰), low riverflow. Half-tide ebb.

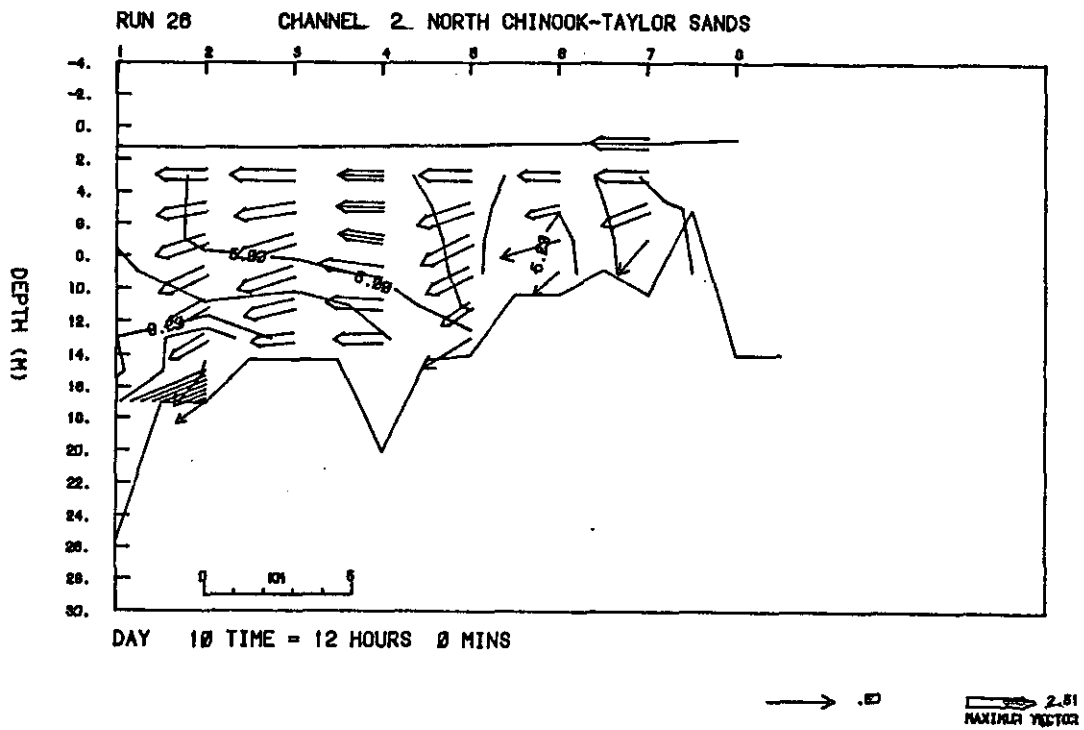


Figure 17g. Channel 2, spring tide period, currents and salinities (m/s and ‰), low riverflow. Low water.

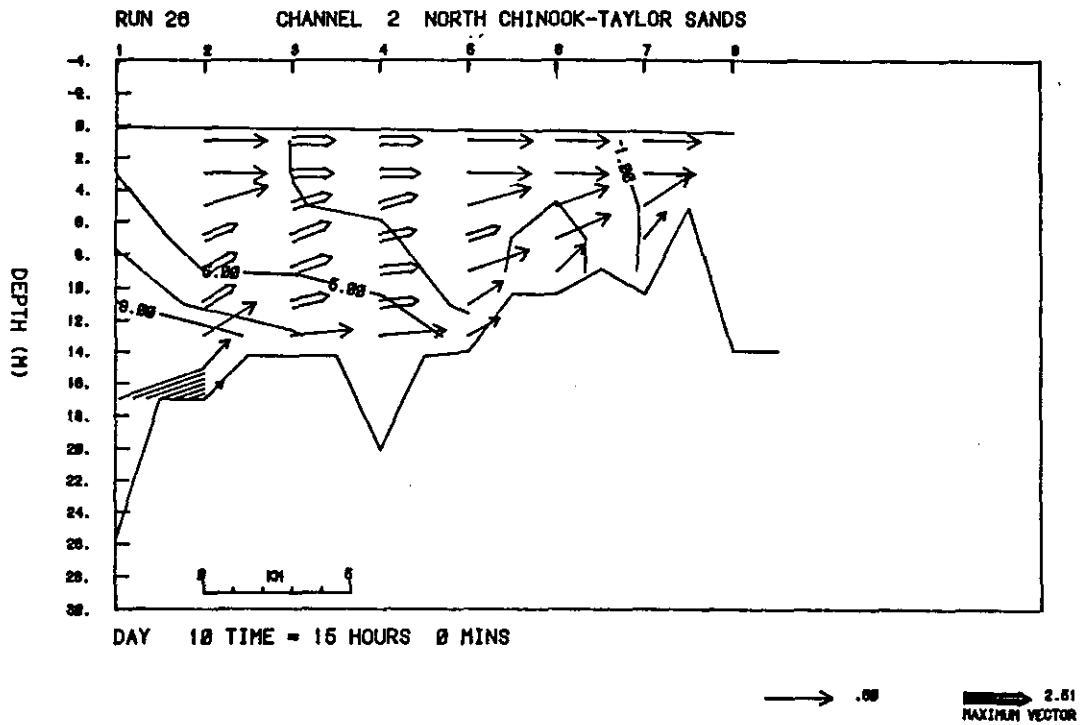


Figure 17h. Channel 2, spring tide period, currents and salinities (m/s and ‰), low riverflow. Half-tide flood.

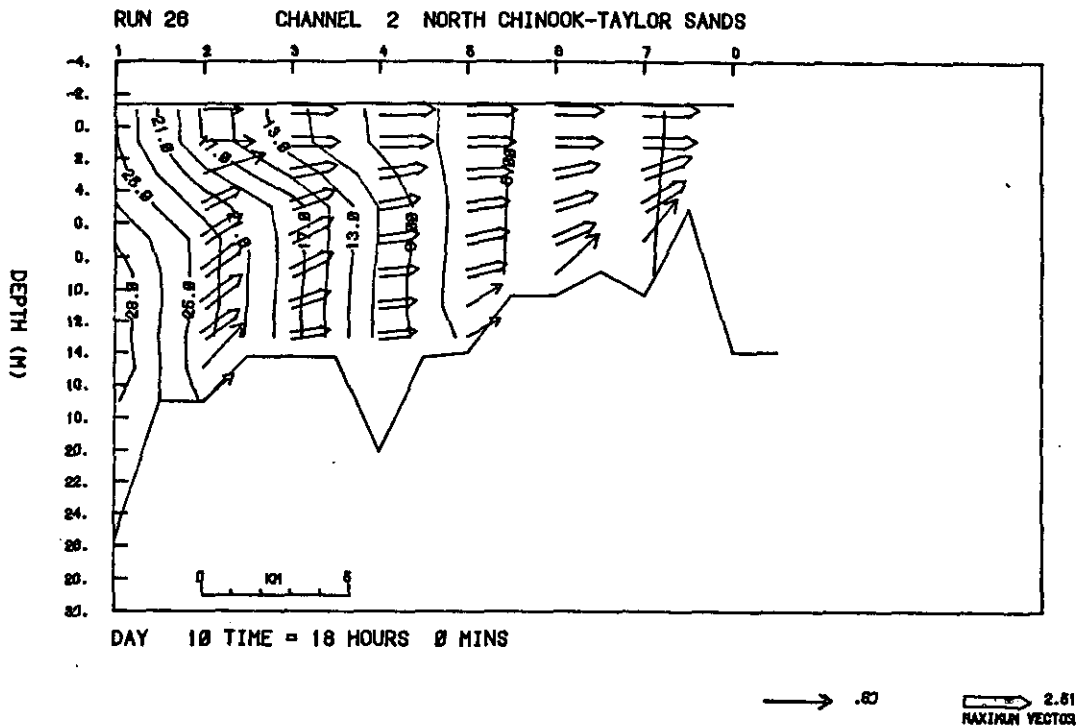


Figure 171. Channel 2, spring tide period, currents and salinities (m/s and ‰), low riverflow. High water.

Table 5a. Tidal Elevations and Transports

<u>Name</u>	<u>Channel No., Grid No.</u>	<u>Elevation</u>		<u>Depth Mean Current</u>		<u>Phase Difference Elevation-Current</u>	<u>Tide Gage Observations</u>	
		<u>Amplitude (m)</u>	<u>Phase</u>	<u>Amplitude (cm/s)</u>	<u>Phase</u>		<u>Amplitude (m)</u>	<u>Phase</u>
<u>M<sub>2</sub> Tide</u>								
Jetty A	1, 2	0.79	14	71	332	42	0.85	11
Fort Stevens	1, 6	0.80	25	58	344	41	0.92	19
Tongue Point	1, 10	0.79	36	52	352	44	0.92	32
Altoona	1, 14	0.74	46	58	11	35	0.86	23
Wauna	1, 23	0.61	85	90	28	57	0.66	77
Chinook Point	2, 3	0.80	24	70	334	50	0.89	15
<u>K<sub>1</sub> Tide</u>								
Jetty A	1, 2	0.46	117	24	55	-62	0.49	116
Fort Stevens	1, 6	0.46	123	22	67	-56	0.49	120
Tongue Point	1, 10	0.44	129	18	68	-61	0.46	128
Altoona	1, 14	0.43	135	17	79	-56	0.42	142
Wauna	1, 23	0.37	155	26	84	-71	0.32	163
Chinook Point	2, 3	0.46	122	23	54	-68	0.49	118

Table 5b. Tidal Constants  
Surface and Bottom Currents and Salinities

Station Channel No. Grid No.	Surface Current		Bottom Current		Phase Difference Bottom-Surface	Surface Salinity		Bottom Salinity		Surface Salinity - Surface Current	Bottom Salinity - Bottom Currents	Salt Flux/Unit Area	
	Amplitude (cm/s)	Phase	Amplitude	Phase		Amplitude	Phase	Amplitude	Phase			Surface	Bottom
<u>M<sub>2</sub> Tide</u>													
1, 2	63	331	76	330	-1	8.2	33	7.2	41	62	71	121	89
1, 6	61	341	48	355	14	1.3	66	6.9	73	85	78	3.5	34
1, 10	51	353	48	352	-1	-	-	-	-	-	-	-	-
1, 14	62	11	43	9	-2	-	-	-	-	-	-	-	-
1, 23	96	29	70	26	-3	-	-	-	-	-	-	-	-
2, 3	76	333	54	343	10	2.2	61	6.7	67	88	84	2.9	19
<u>K<sub>1</sub> Tide</u>													
1, 2	21	53	28	63	10	4.4	90	4.9	101	37	38	37	34
1, 6	22	62	21	86	24	0.8	127	5.7	153	65	67	3.7	24
1, 10	18	68	16	67	-1	-	-	-	-	-	-	-	-
1, 14	20	80	13	72	-8	-	-	-	-	-	-	-	-
1, 23	27	85	20	81	-4	-	-	-	-	-	-	-	-
2, 3	24	51	18	72	21	1.2	114	3.8	155	63	83	6.5	4

in the salt intrusion region are included for completeness. The bottom currents show small phase leads over the surface currents at the freshwater stations. In the salt intrusion region, except for the constituents at the mouth, the surface currents lead the bottom currents due to the influence of the horizontal salinity gradients. The mouth (Jetty A) station shows very small surface-to-bottom phase differences at the  $M_2$  period, with the largest current amplitude occurring at the bottom. In comparing these results to the tidal analyses presented in Jay (1983), it should be remembered that the model currents and salinities are laterally averaged against point measurements by current meters. These WIFM simulations indicate that substantial phase differences occur in the cross-channel direction at the mouth, and the large apparent vertical current phase differences observed at the  $M_2$  period may be a reflection of these cross channel phase differences.

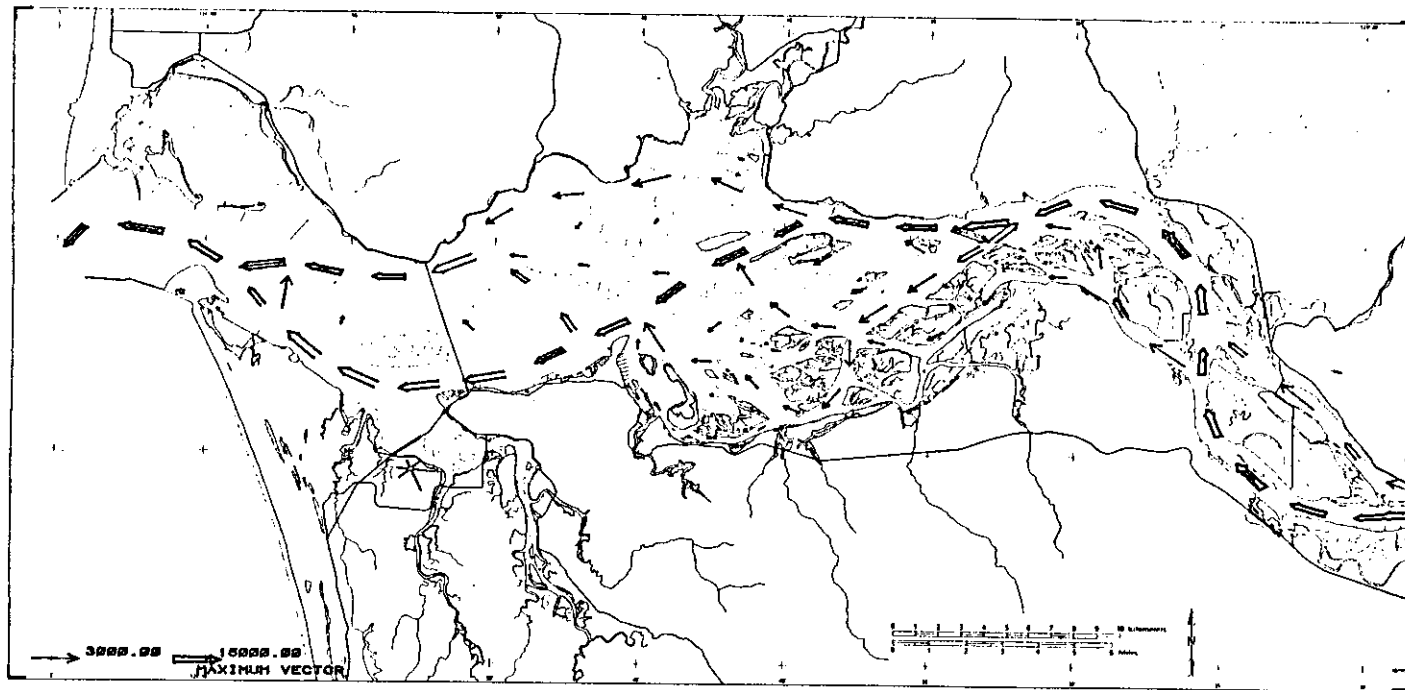
The model currents lead the salinities signals by phase differences less than  $90^\circ$ . This indicates that the oscillatory tidal salt flux is substantial and directed upstream at all analysed stations (Table 5b). Since the larger salinity amplitudes occur in the lower part of the water column, the tidal component of the salt flux will also be concentrated in lower half of the channels. It is noted that a substantial portion of the salinity tidal fluctuations are associated with the  $K_1$  tide; consequently, the tidal salt flux associated with the  $K_1$  components is also a substantial proportion of the total oscillating tidal flux. Salt flux is calculated from:

$$\text{Salt Flux} = \frac{1}{T} \int_0^T u_s = \frac{1}{2} A_u A_s \cos \phi$$

where  $A_u$ ,  $A_s$  are the amplitudes of the salinity current and salinity tidal constituents,  $\phi$  is the phase difference between salinity and current fluctuations, and  $T$  is the tidal period.

#### 3.1.4. The Effects of Tide and Riverflow on Mean Circulations

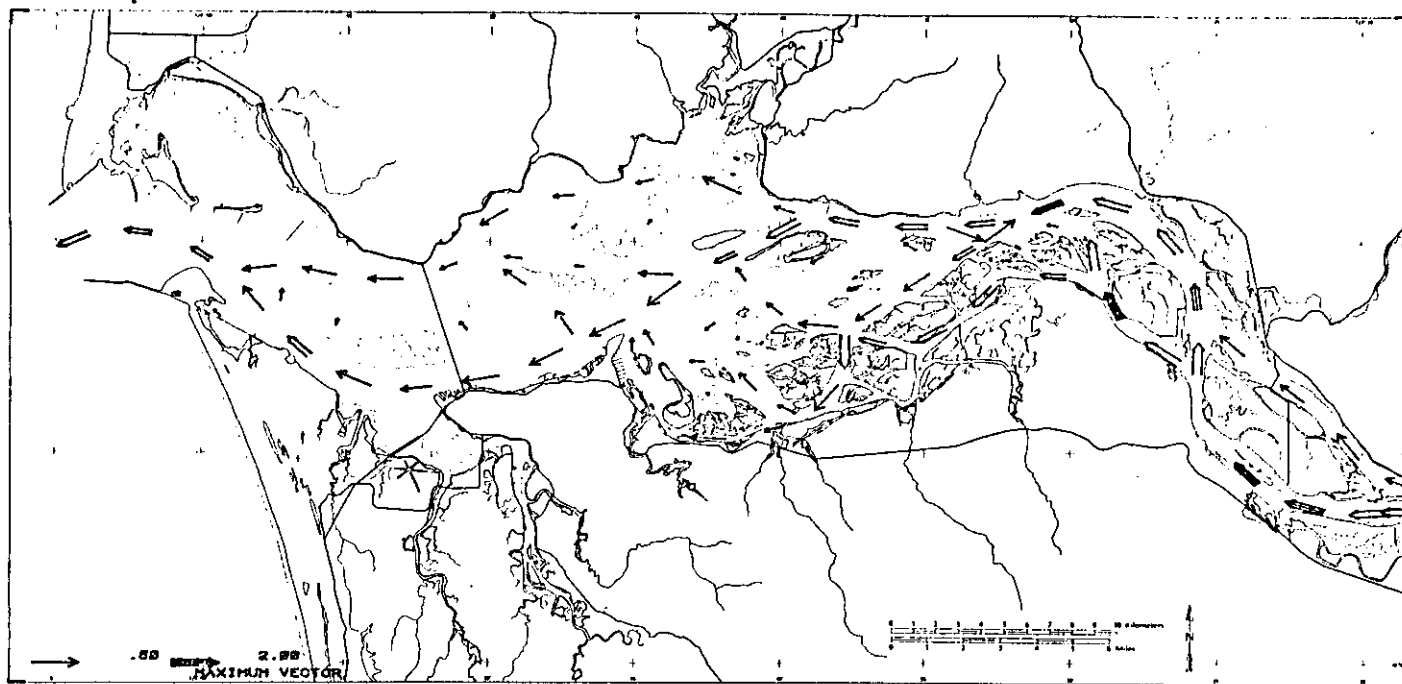
This section summarizes the circulations simulated by the model for the October 1980 and the May-June 1981 period. The periods analysed consist of alternate neap and spring 50-hour periods for which mean salinity and current fields, along with contours of extreme salinities calculated during each period, are presented as sections. The maximum and minimum salinity contours can be regarded as representative of the salinity field at greatest and smallest intrusion into the estuary during the tidal period. They can be compared directly with the similar diagrams derived from current meter observations (Jay 1984). The periods analysed along with daily riverflows and tidal ranges are given in Table 4. In order to place the mean sections in a horizontal context, maps of 50-hour mean volume transports and mean surface currents are given in Figure 18. Except for relative magnitudes of the transport vectors, similar plots for other periods resemble Figure 18 very closely. The vector patterns are quite similar to the riverflow plot in Volume I (Figure 30). The



RUN 51

STOP DAY 28 AVERAGING TIME 50HOURS

Figure 18a. Horizontal vectors averaged over a neap tide plotted on the estuary chart. Volume transports ( $m^3/s$ ).



RUN 51

STOP DAY 28 AVERAGING TIME 50HOURS

Figure 18b. Horizontal vectors averaged over a neap tide plotted on the estuary chart. Surface velocities (m/s).

relatively larger mean volume transports in the North Channel compared with the Navigation Channel is again evident and the transfer of water from the Navigation Channel to the North Channel via the upper end of channel 2, channels 3 and 7 and smaller flows across the Desdomona Sands are also clearly illustrated. The tidal residual eddy off Jim Crow Point shows up clearly, and the relatively high mean velocities in some of the smaller channels of Cathlamet Bay should also be noted.

October 1980, Neap Tide: Figures 19-22

The means for the Navigation Channel show strong stratification and a moderate density current at the mouth, which is suppressed by the outflow of channel 2 at the junction at grid point 4. The density current is re-established between grid points 5 and 9. The density current circulation in channel 2 (Figure 20a) is very weak and confined to the deep channel west of the bridge. The influence of the tidal currents on the residual circulations is also evident in the patchiness of the upstream residual flow. The residual flow observed in these figures is a combination of the effects of density gradients and the effects of the non-linear inertial terms, which are strongly influenced by constrictions and depth changes. Qualitatively, the effects of the non-linear inertial terms in the momentum equation on the residual flow, given by the model, show some of the features of the results of the analytical theory of tidal residual flows for simple channels given by Ianniello (1979, 1981). An earlier version of the model which excluded the inertial terms (Hamilton 1983) did not show the patchiness of the bottom upstream mean flows of Figures 19a and 20a. This supports the interpretation that non-linear inertial effects are largely responsible for such current structures (Ianniello 1979, 1981).

For the neap tide, the salinity mean and extremes for channels 1 and 2 are similar. In channel 7 (Grays Bay), the salinity intrusion is largely confined to west of Grays Point and is nearly completely flushed out at low tide. Similarly, channel 4 shows only a slight influence of the salinity intrusion in the main channel from the region of Tongue Point and is completely flushed out at low tide.

October 1980: Spring Tide: Figures 23-26

The main features of the spring tide (range  $\sim 3.4$  m) as compared with the neap tide (range  $\sim 2.1$  m) are the much weaker stratification, particularly in the Navigation Channel, and the much weaker lower-layer upstream flows at most stations. Note that density current flow is almost nonexistent at the mouth, being strongly overwhelmed by tidal residual flows in the region of the junction of channel 1 and channel 2. Small bottom upstream flows persist upstream of grid point 5, channel 1. The salinity intrusion length of the mean fields as delineated by the  $5$  ‰ contour is much less than the neap tide mean field in channel but not much less than the neap tide mean field of channel 2. Thus the mean salinities for spring tides are higher in channel 2 than in channel 1. There is also a relatively larger tidal excursion of isohalines in channel 2 than in channel 1. These differences in intrusion length and tidal excursions give rise to the  $1$  ‰ isohaline found in a similar position to the neap tide in channel

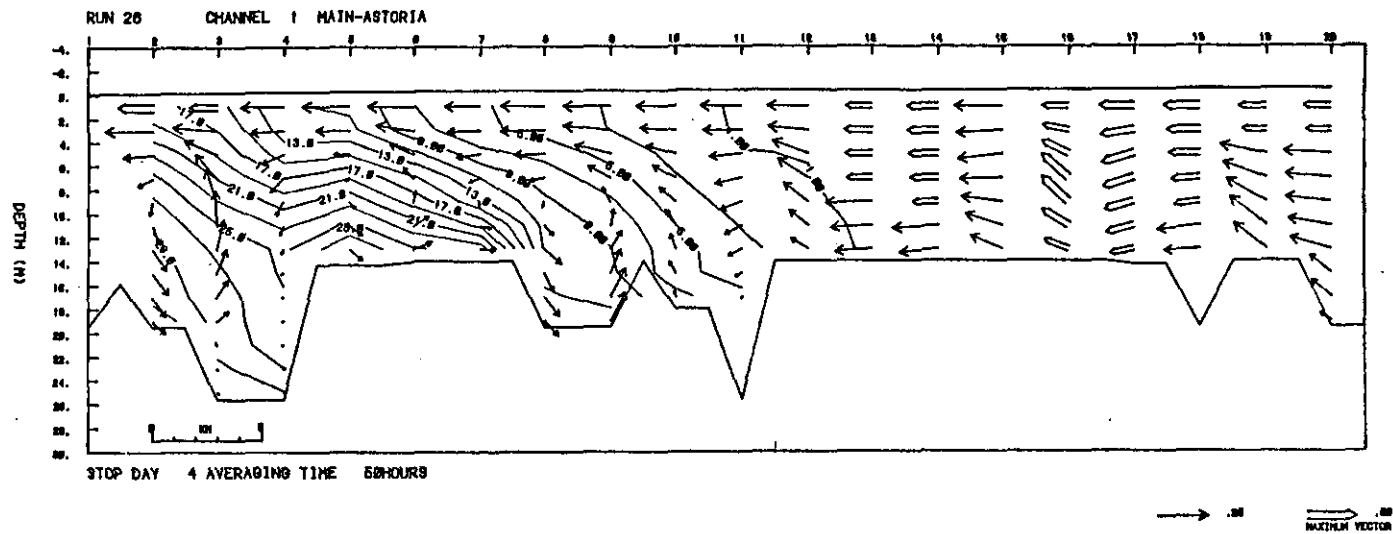


Figure 19a. Channel 1, neap tide period (fall, 1980). Mean currents and salinities (m/s and ‰).

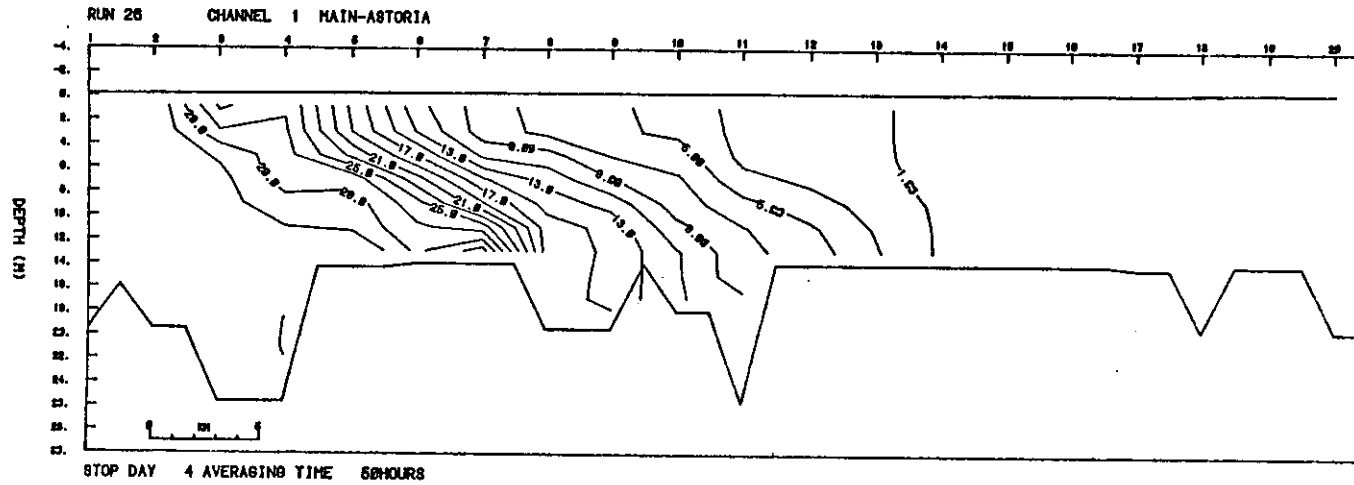


Figure 19b. Channel 1, neap tide period (fall, 1980). Maximum salinities.

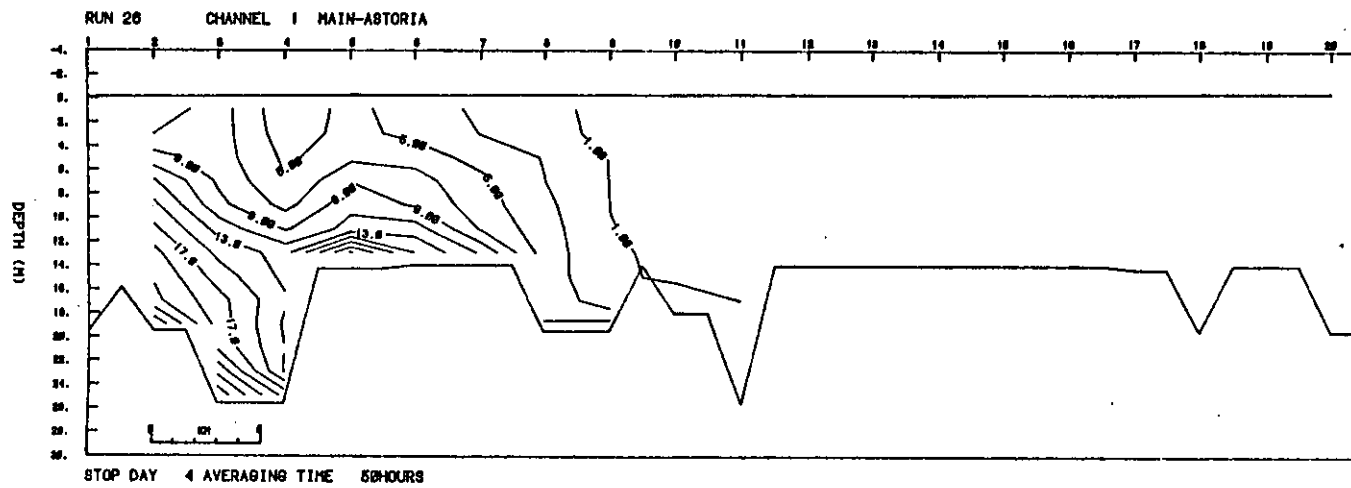


Figure 19c. Channel 1, neap tide period (fall, 1980). Minimum salinities.

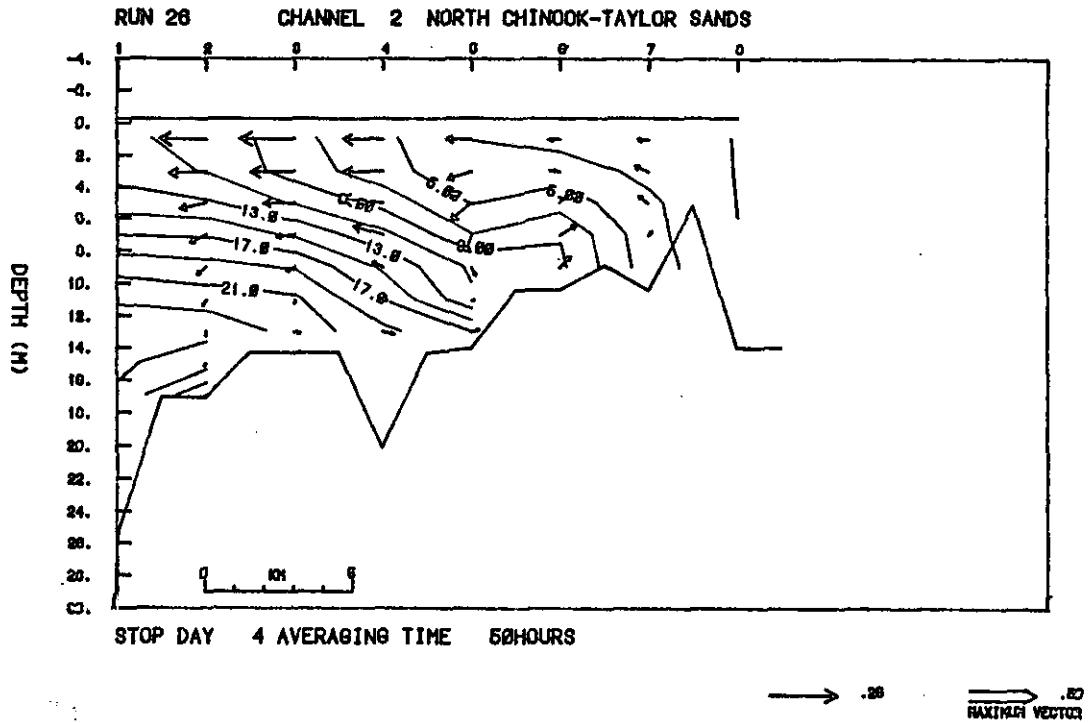


Figure 20a. Channel 2, neap tide period (fall, 1980). Mean currents and salinities (m/s and ‰).

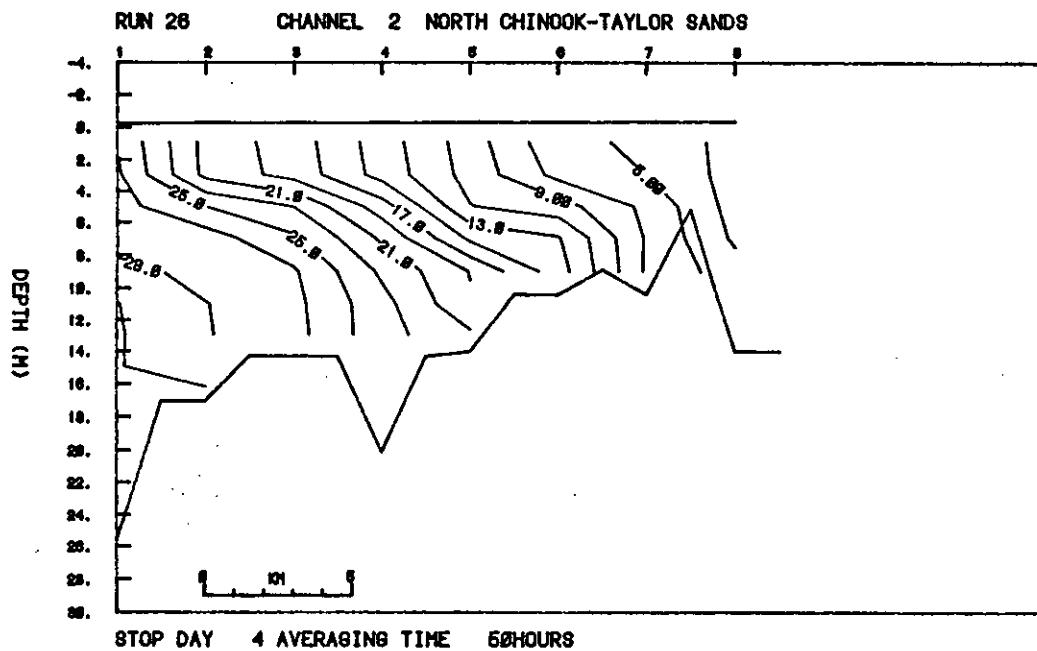


Figure 20b. Channel 2, neap tide period (fall, 1980). Maximum salinities.

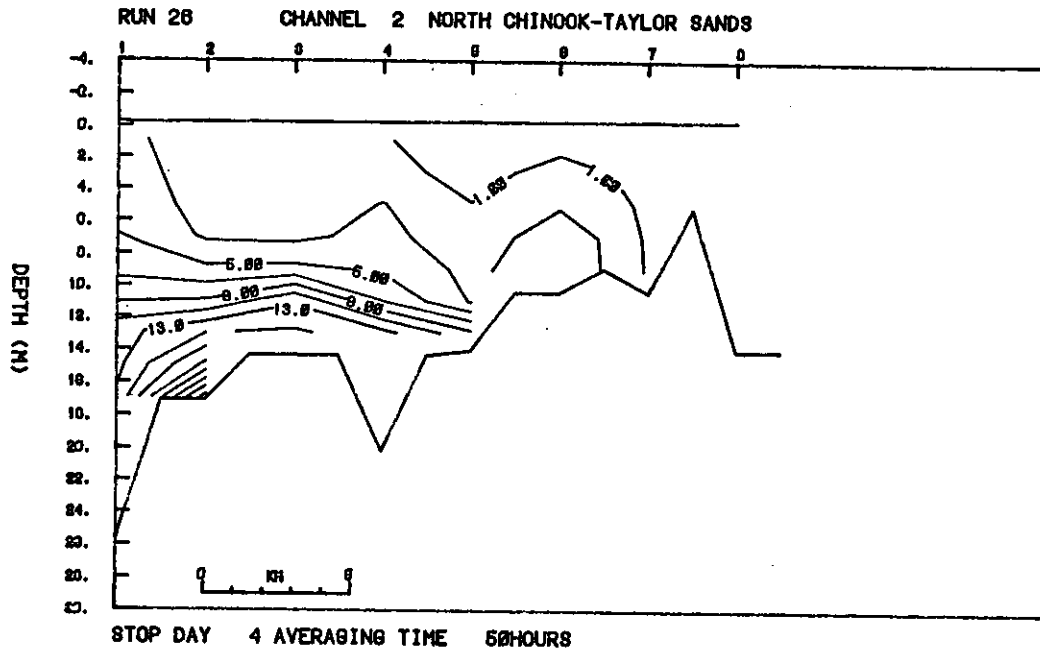


Figure 20c. Channel 2, neap tide period (fall, 1980). Minimum salinities.

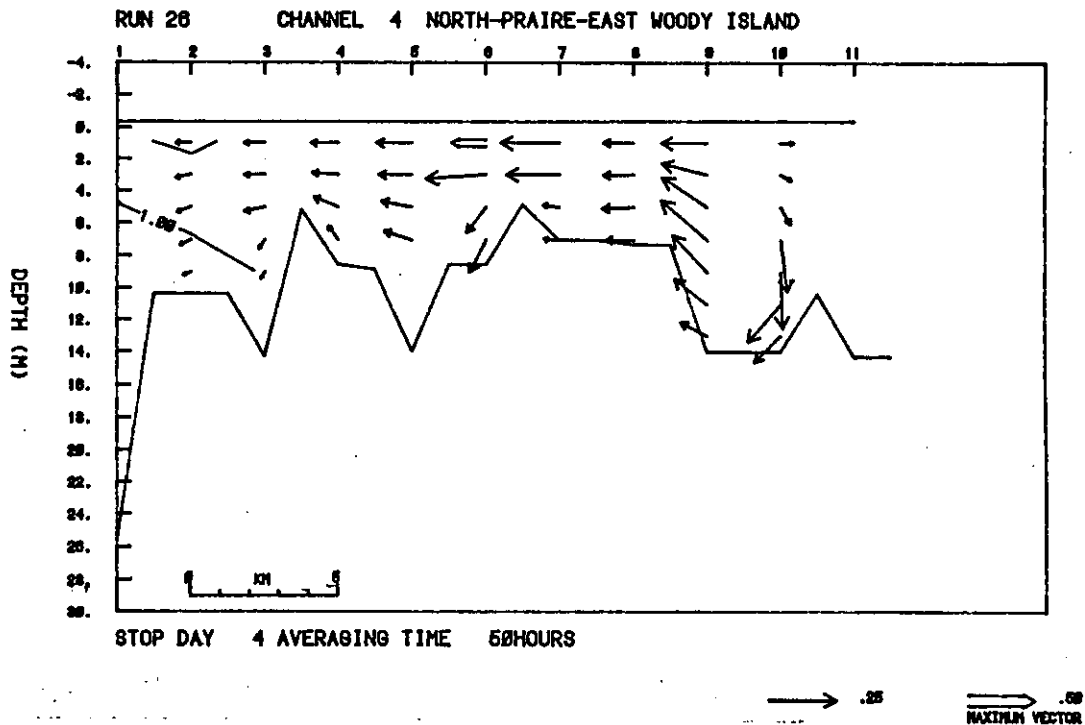


Figure 21a. Channel 4, neap tide period (fall, 1980). Mean currents and salinities (m/s and ‰).

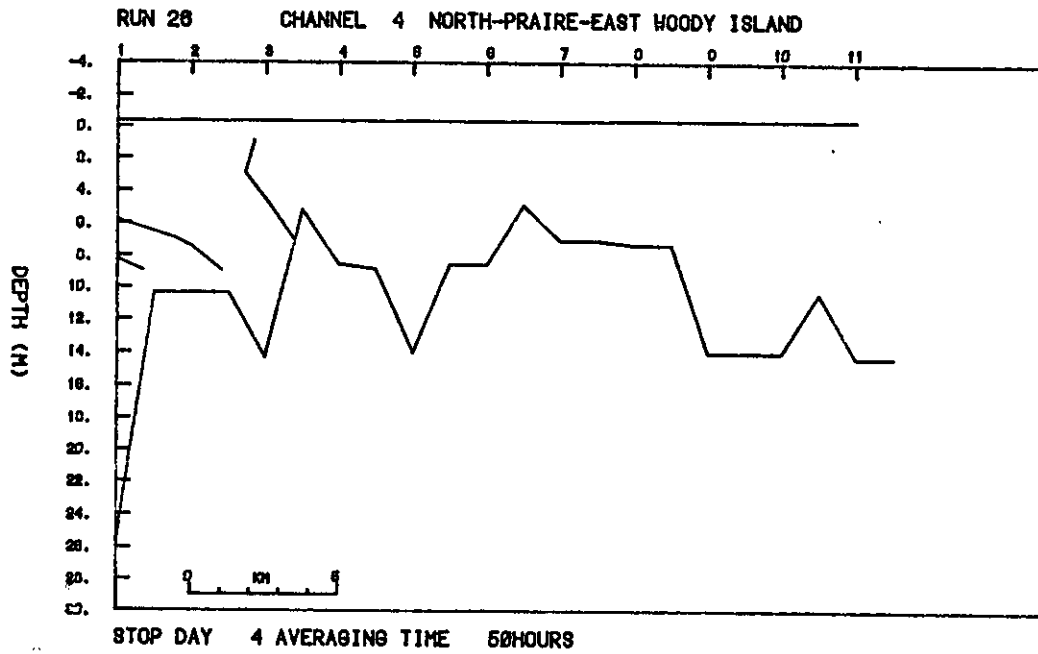


Figure 21b. Channel 4, neap tide period (fall, 1980). Maximum salinities.

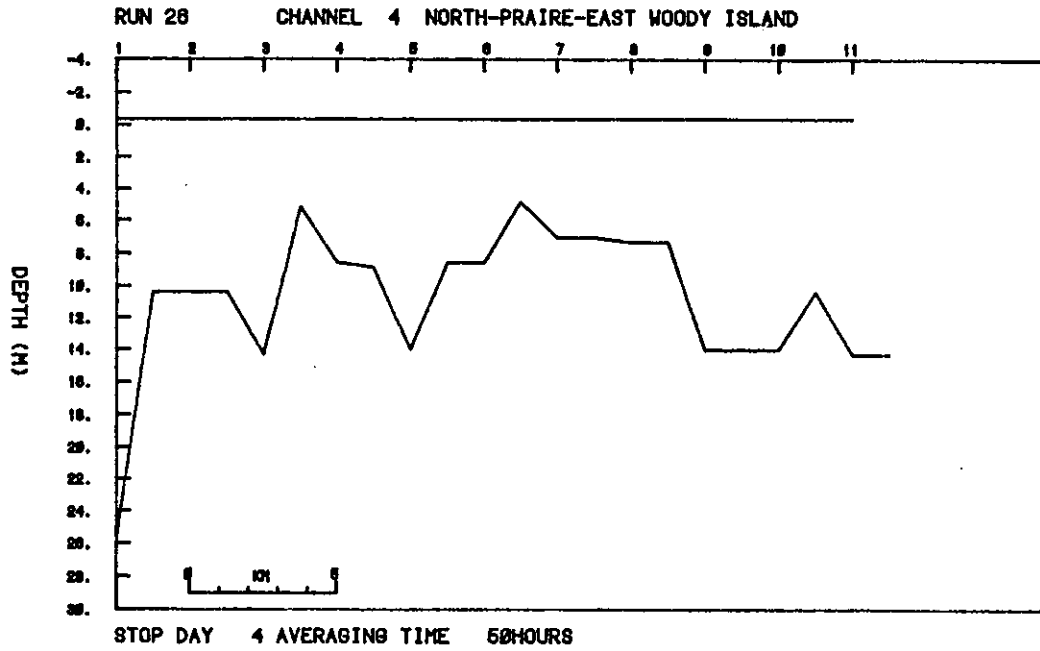


Figure 21c. Channel 4, neap tide period (fall, 1980). Minimum salinities.

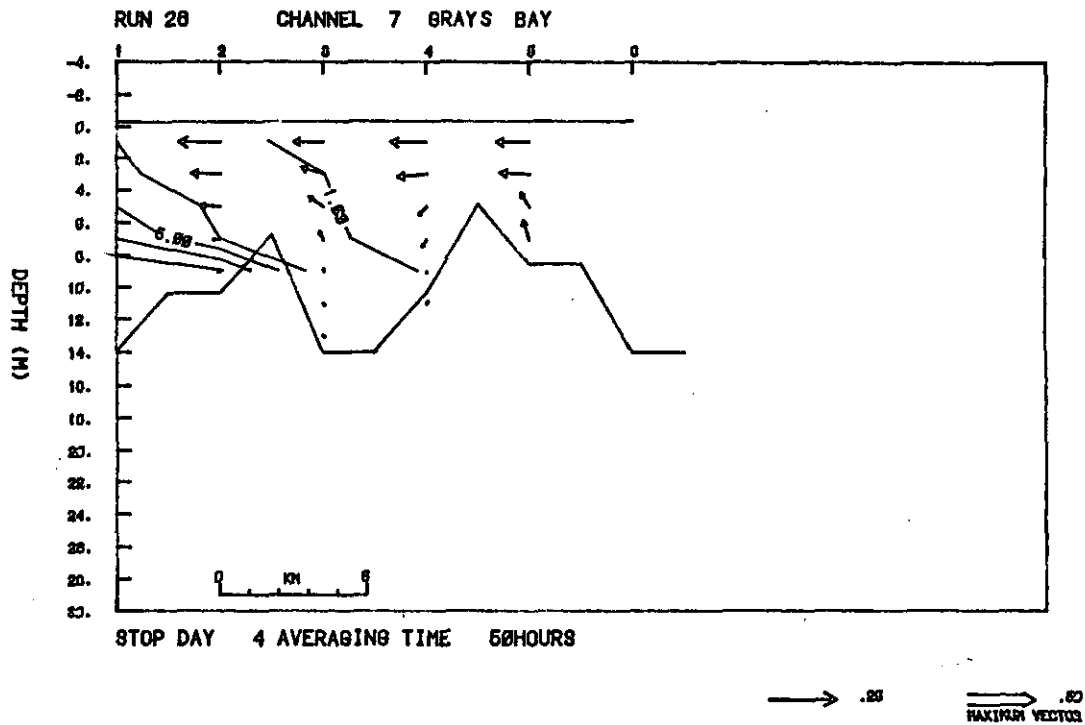


Figure 22a. Channel 7, neap tide period (fall, 1980). Mean currents and salinities (m/s and ‰).

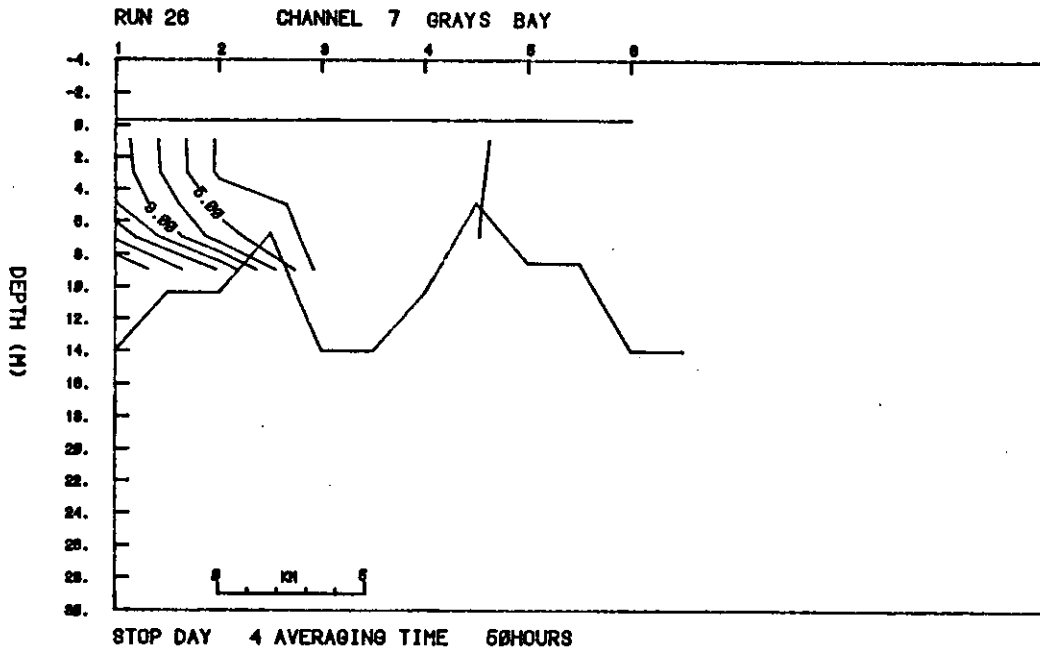


Figure 22b. Channel 7, neap tide period (fall, 1980). Maximum salinities.

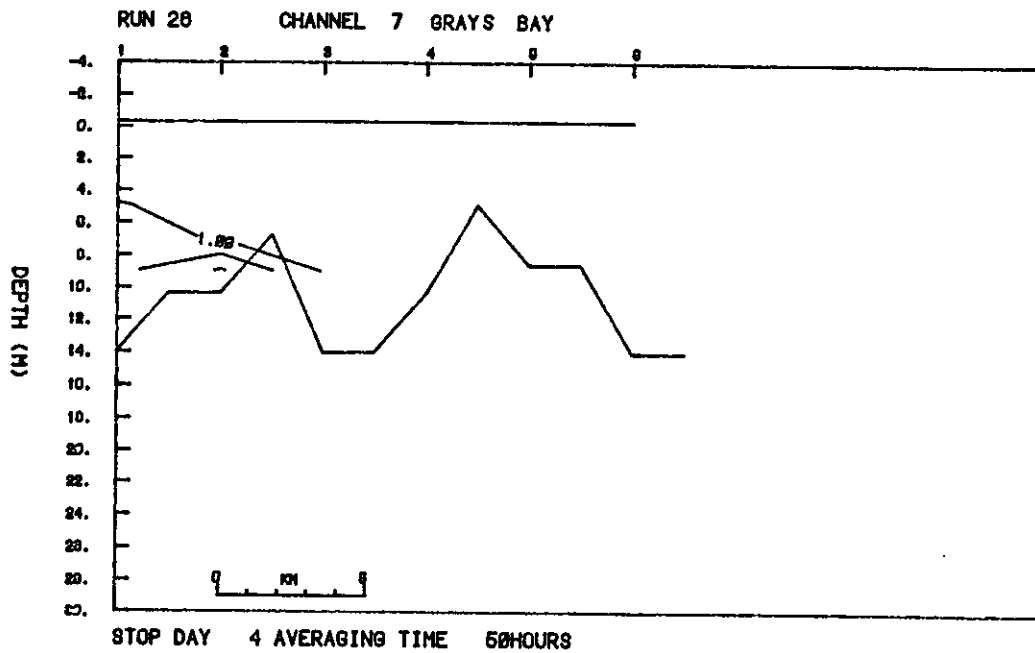


Figure 22c. Channel 7, neap tide period (fall, 1980). Minimum salinities.

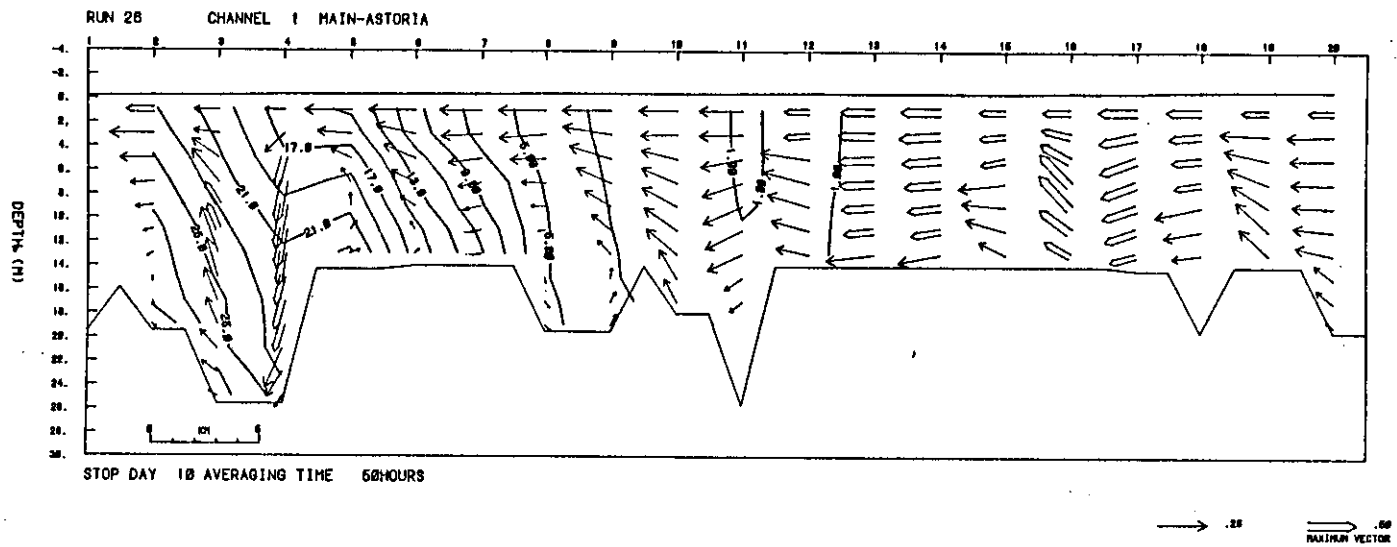


Figure 23a. Channel 1, spring tide period (fall, 1980). Mean currents and salinities (m/s and ‰).

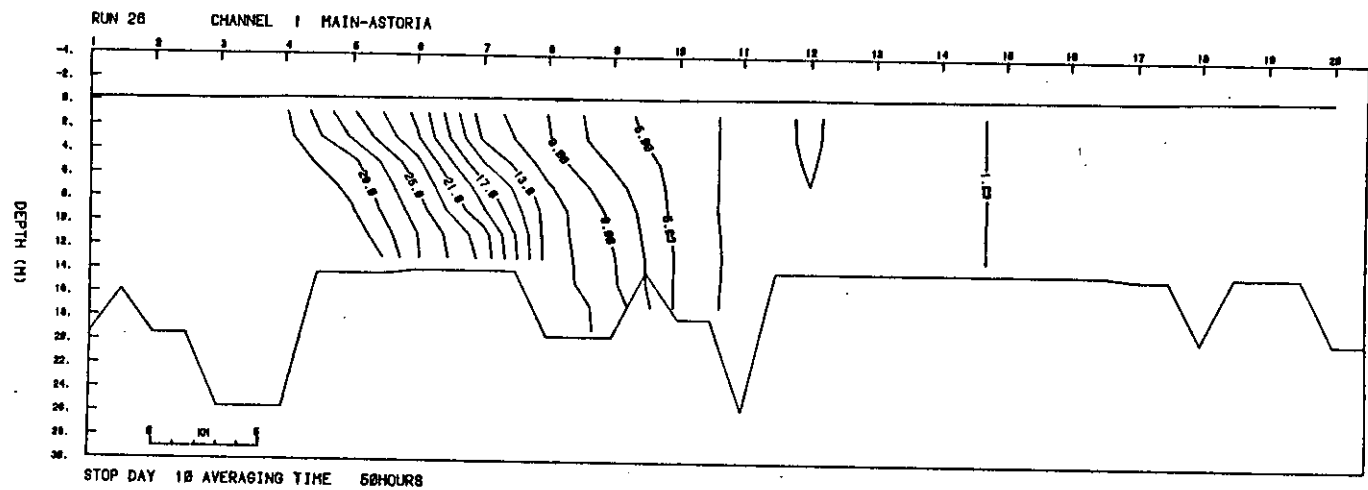


Figure 23b. Channel 1, spring tide period (fall, 1980). Maximum salinities.

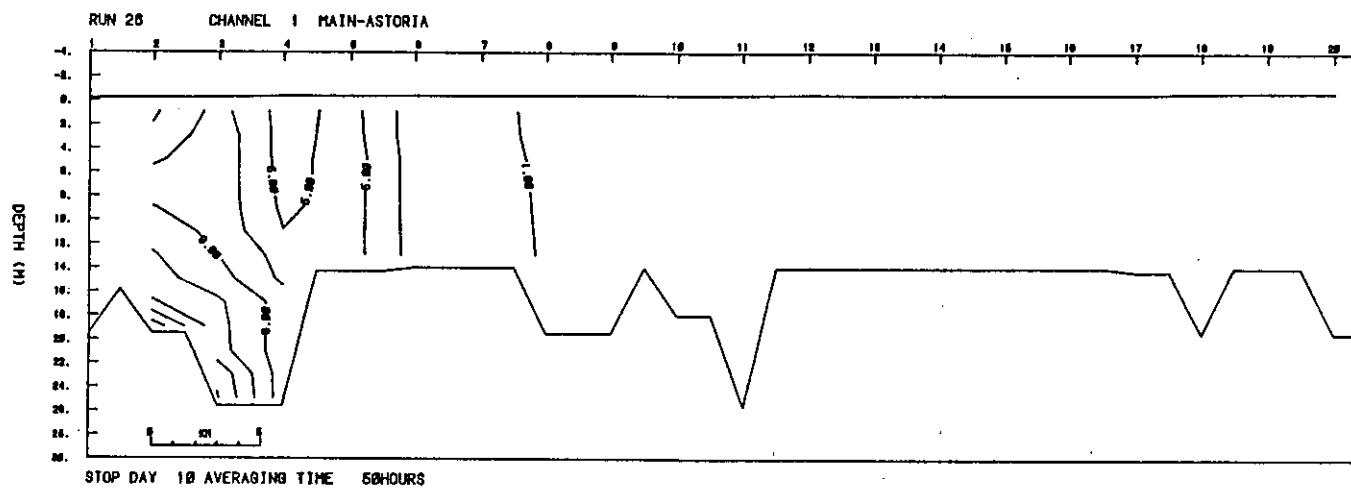


Figure 23c. Channel 1, spring tide period (fall, 1980). Minimum salinities.

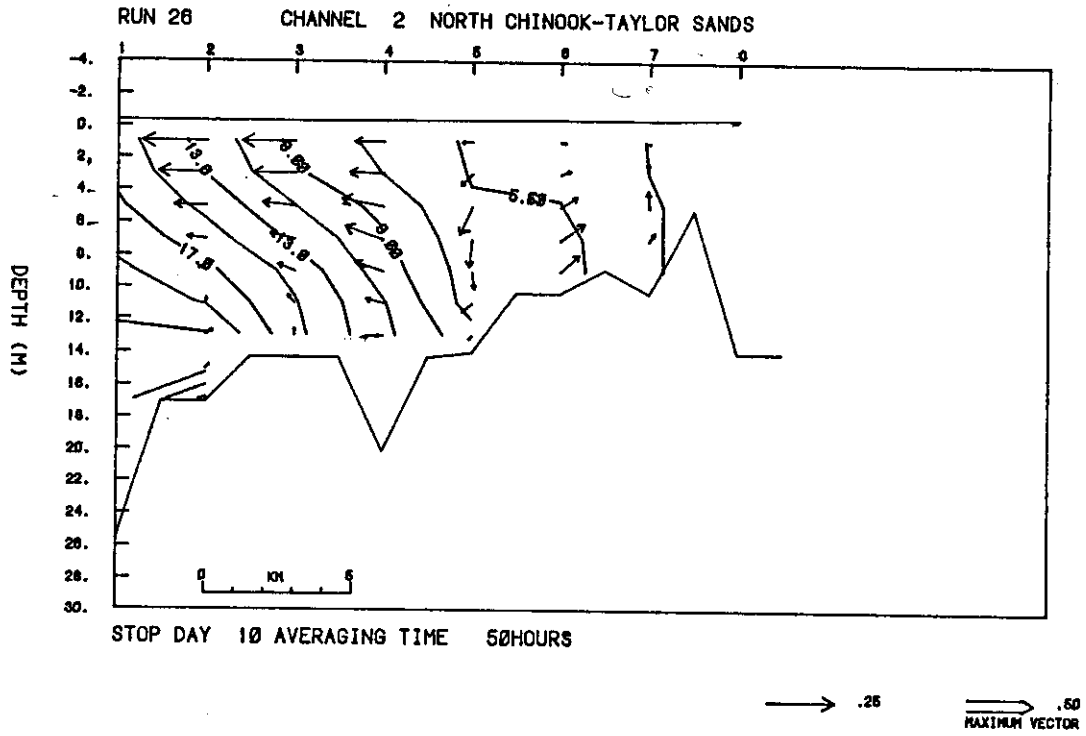


Figure 24a. Channel 2, spring tide period (fall, 1980). Mean currents and salinities (m/s and ‰).

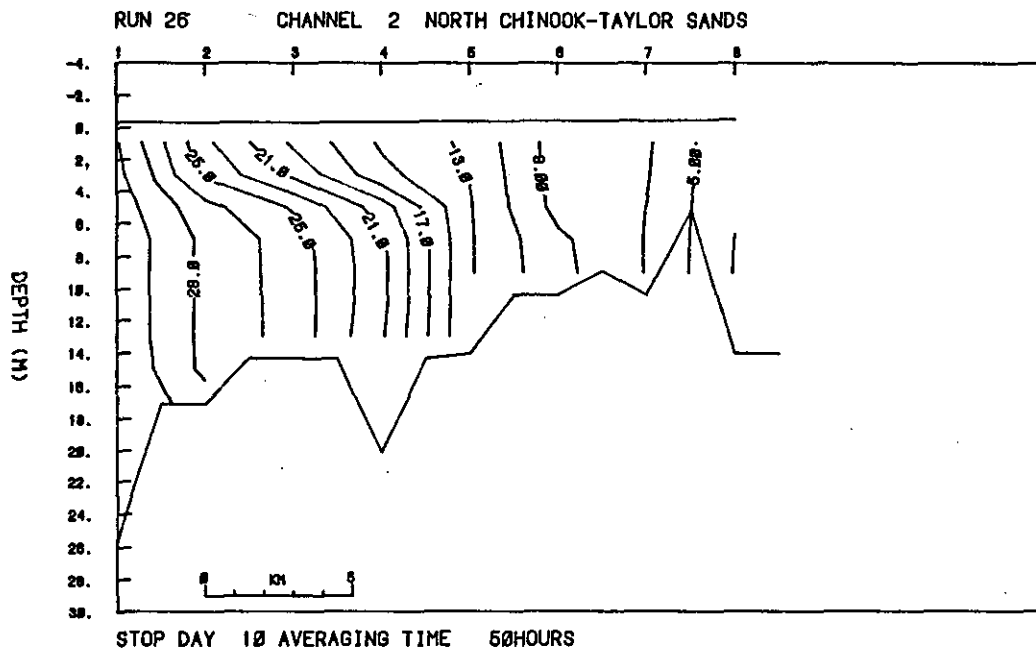


Figure 24b. Channel 2, spring tide period (fall, 1980). Maximum salinities.

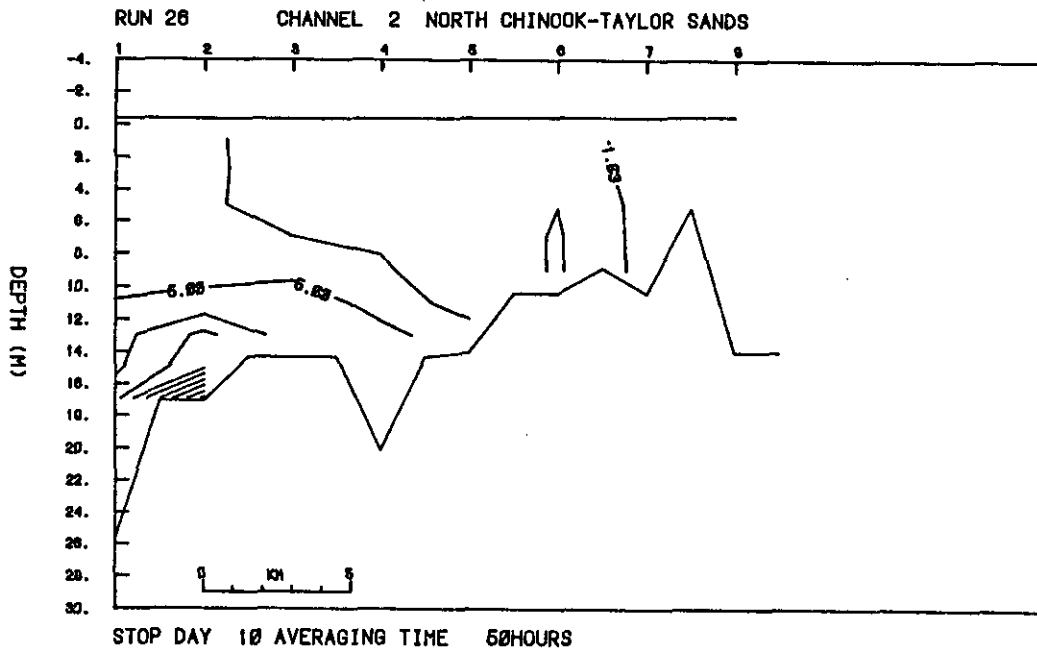


Figure 24c. Channel 2, spring tide period (fall, 1980). Minimum salinities.

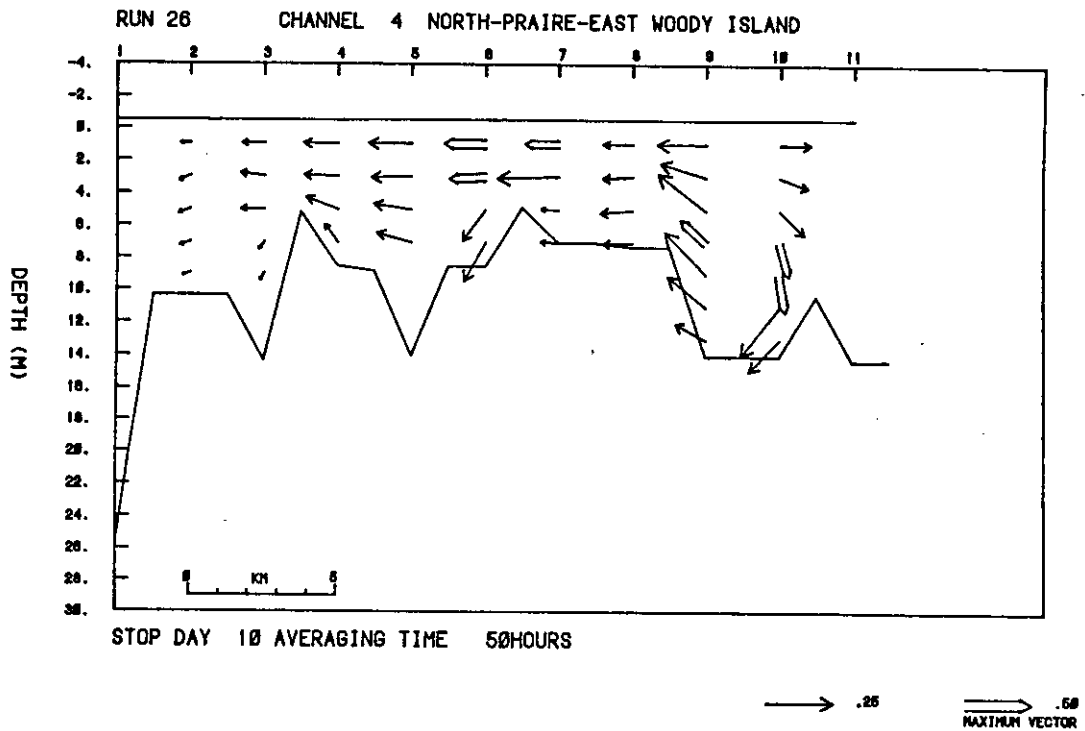


Figure 25a. Channel 4, spring tide period (fall, 1980). Mean currents and salinities (m/s and ‰).

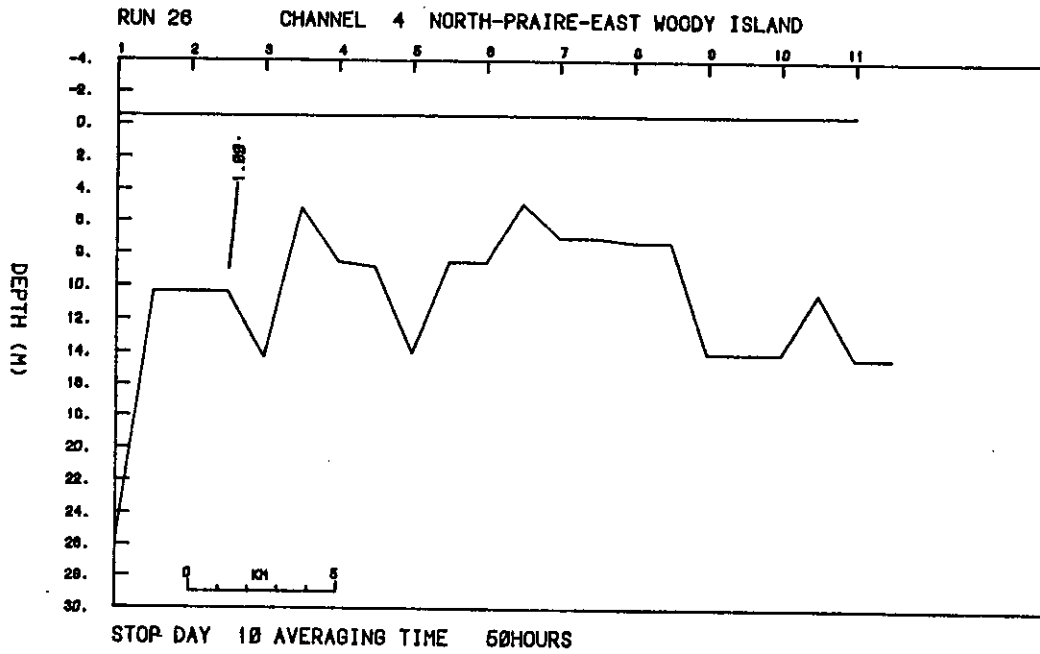


Figure 25b. Channel 4, spring tide period (fall, 1980). Maximum salinities.

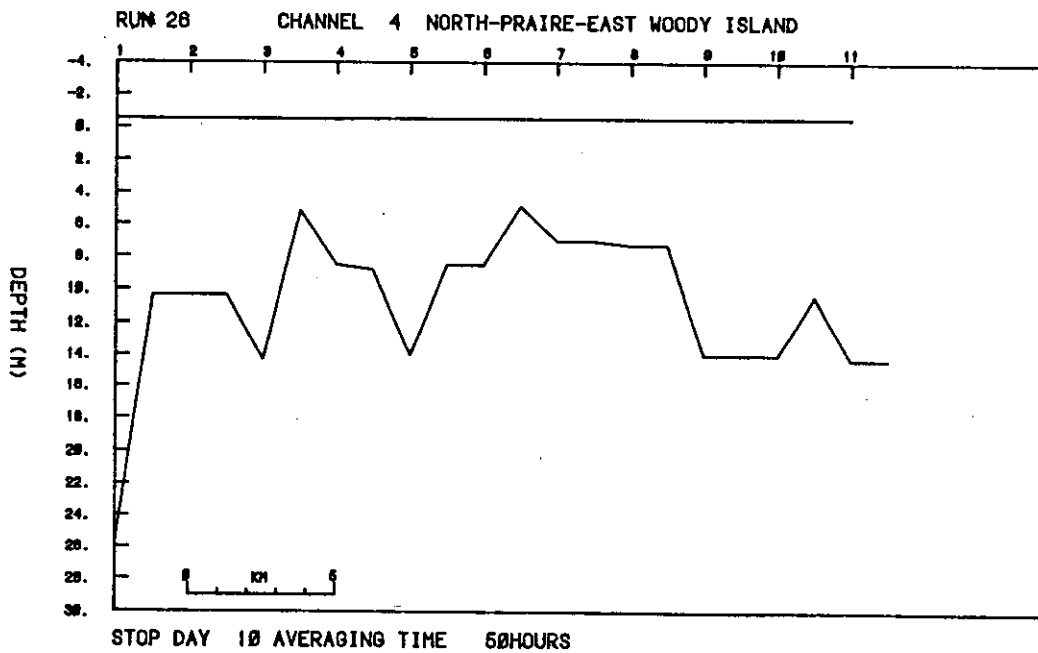


Figure 25c. Channel 4, spring tide period (fall, 1980). Minimum salinities.

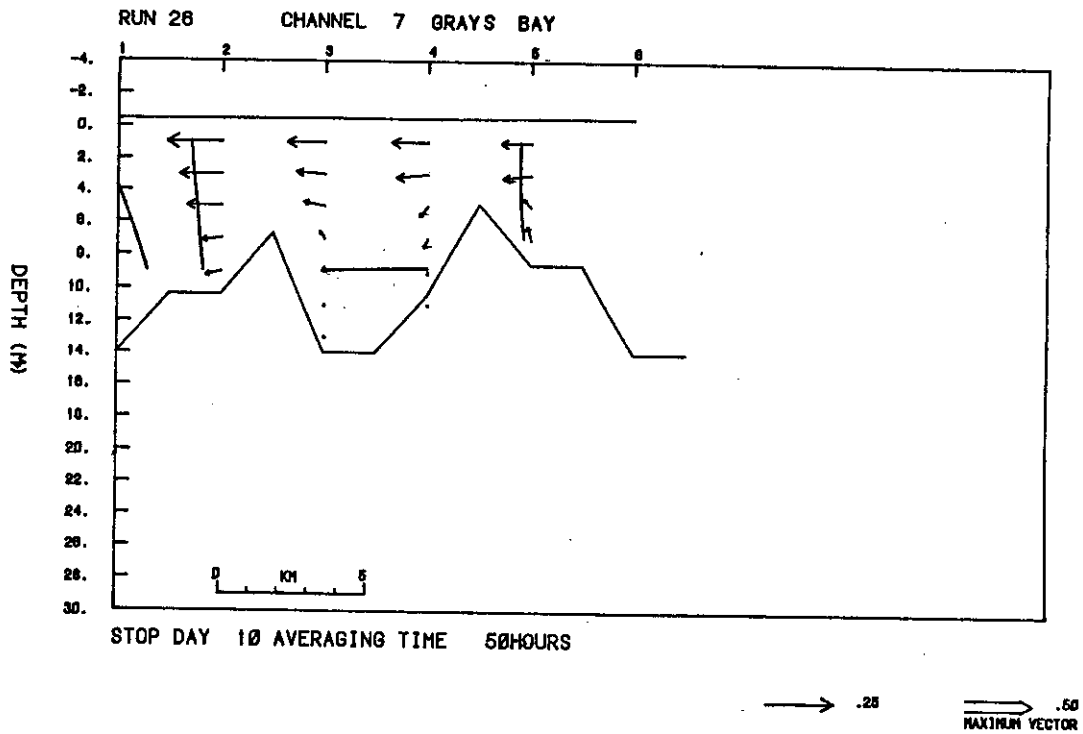


Figure 26a. Channel 7, spring tide period (fall, 1980). Mean currents and salinities (m/s and ‰).

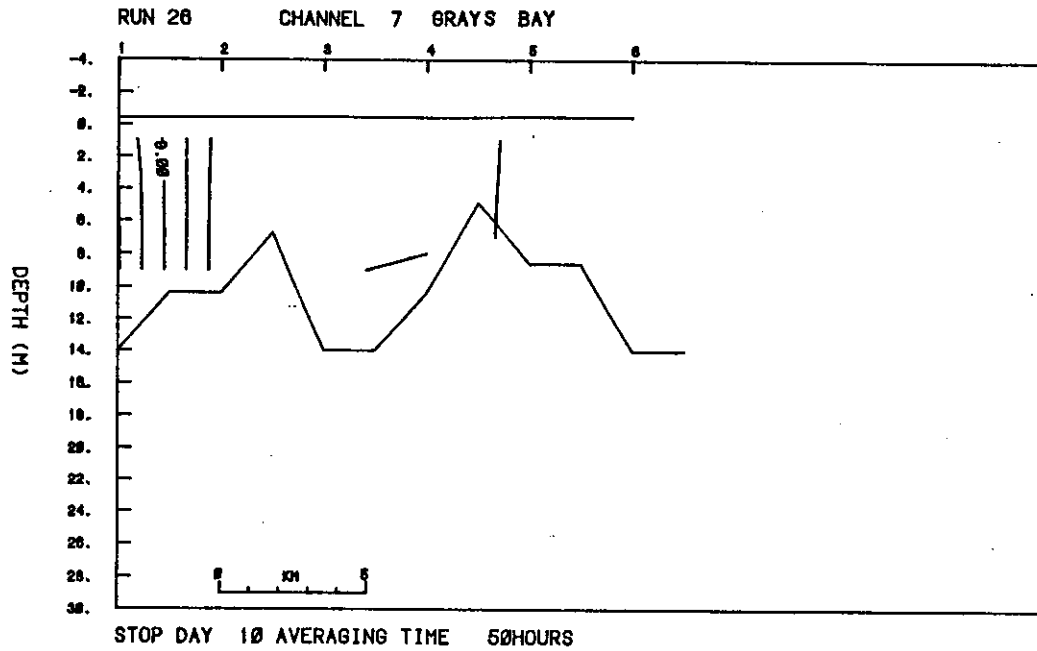


Figure 26b. Channel 7, spring tide period (fall, 1980). Maximum salinities.

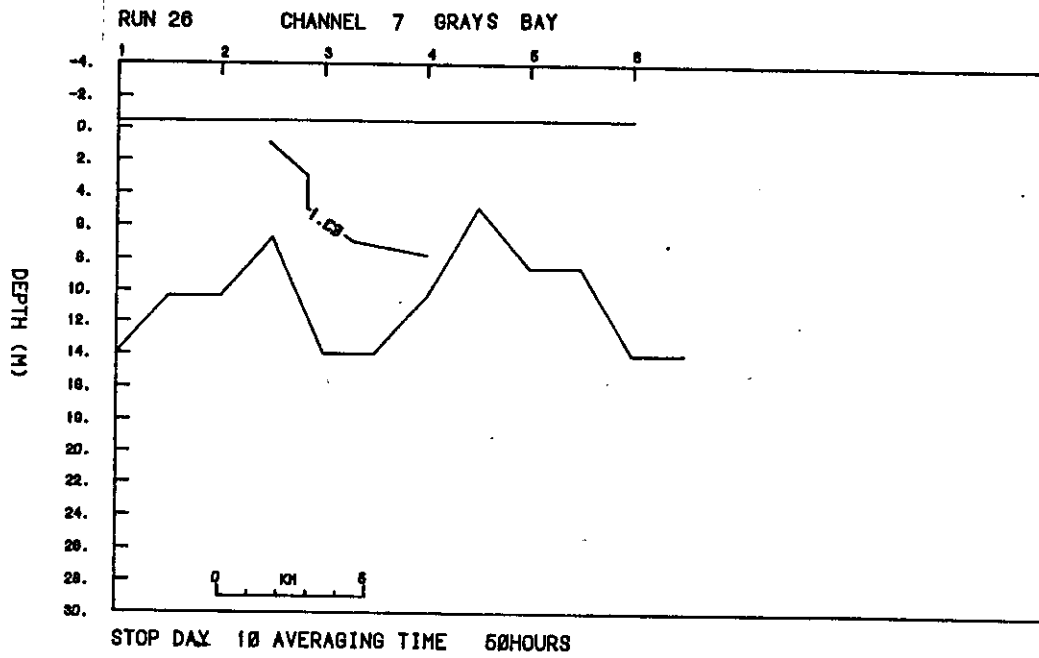


Figure 26c. Channel 7, spring tide period (fall, 1980). Minimum salinities.

1 through the connections of channels 2 and 3 across Taylor Sands with channel 1 at grid points 10 and 12, respectively. The low salinity, low gradient tail of the mean salinity intrusion and maximum isohalines seems to be a feature of the spring tides, which is not so apparent in the neap tides during the low flow period. The difference in the intrusion characteristics means that channel 4 is fresh but channel 7 is a little more salty than for the neap, particularly at high tide. The strong mixing in the relatively shallow depths of channel 7 gives rise to a more vertically mixed and diffuse salinity field in this channel.

Spring 1981: Neap Tide #1: Figures 27 and 28

The first twenty days of the May 1981 simulation are characterized by a fairly constant riverflow of a magnitude nearly twice that of the October 1980 period. Therefore, the first neap and spring periods presented below can be directly compared with the corresponding October tides above (Table 4). Only the sections for channels 1 and 2 are given, since the remaining major channels are completely homogeneous.

The salinity and current fields in channel 1 and channel 2 are very similar to those shown in Figure 19, except for the larger magnitude mean currents. The channels are fresher, with the  $1^{\circ}/\text{oo}$  isoline being at the Astoria-Megler Bridge (8) rather than at Rice Island (12) in channel 1. Upstream lower layer density flows are very similar except that in the Hammond-Astoria reach they do not extend quite as far upstream. The density flows in channel 2 are very similar in both periods, with slightly weaker upstream currents east of the bridge. Not surprisingly, extremes are larger in the salt intrusion region in this period than they are in the fall.

Spring 1981: Spring Tide #1: Figures 29 and 30

This spring tide has only a moderate range (See Figure 7) compared with the spring tide of October 1980, with the consequence that the current and salinity fields are very similar to the neap #1 tide discussed above. This conclusion applies also to the tidal excursion of salinities, a fact largely confirmed by the time series data (Figure 10). The implications are that the tidal range is not large enough to produce the turbulent energy to overcome the stratification maintained by the strong riverflow.

Spring 1981: Spring Tide #2: Figures 31 and 32

This spring tide is comparable in range with the October spring tide. The riverflow increases from  $7,670 \text{ m}^3/\text{s}$  on day 21 to  $12,450 \text{ m}^3/\text{s}$  on day 26, where it remains relatively steady for the next 8 days. The movement of the salinity intrusion downstream from the previous figures is noted. The water column here is still fairly stratified compared with the fall spring tide (Figure 23) but more homogeneous than the previous spring discussed above. Maximum salinity sections are similar to the previous spring except for tighter spacing of the isohalines. The estuary is almost wholly fresh at the end of the ebb.

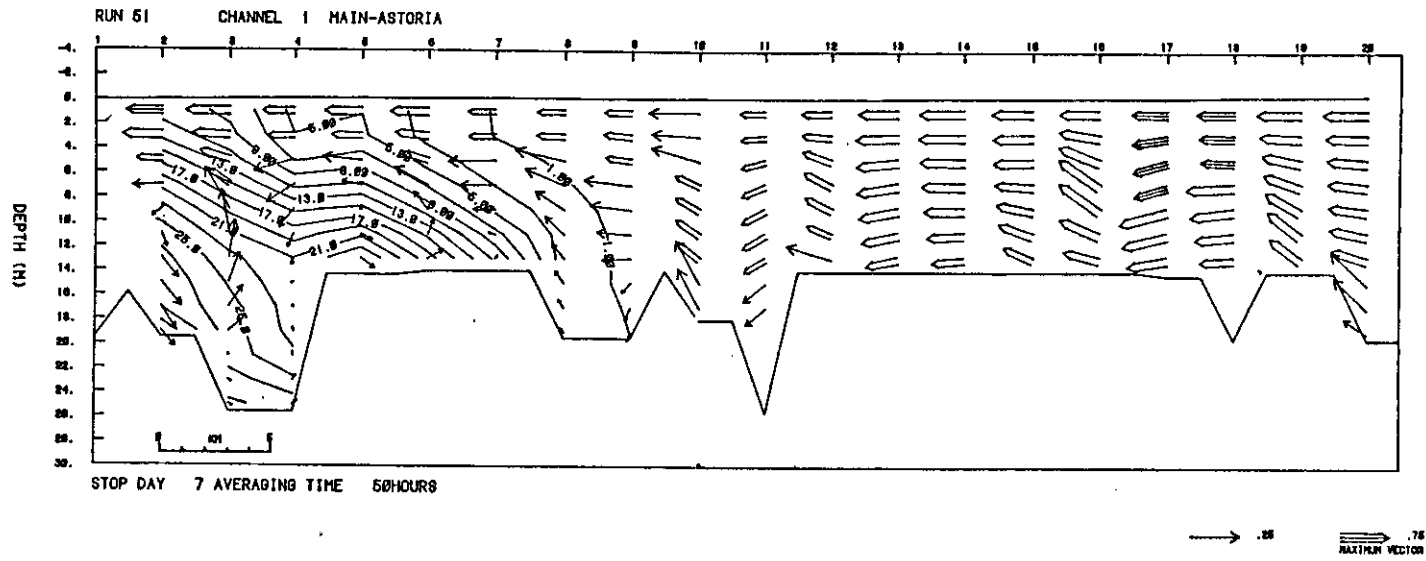


Figure 27a. Channel 1, Neap #1. Mean currents and salinities (m/s and ‰).

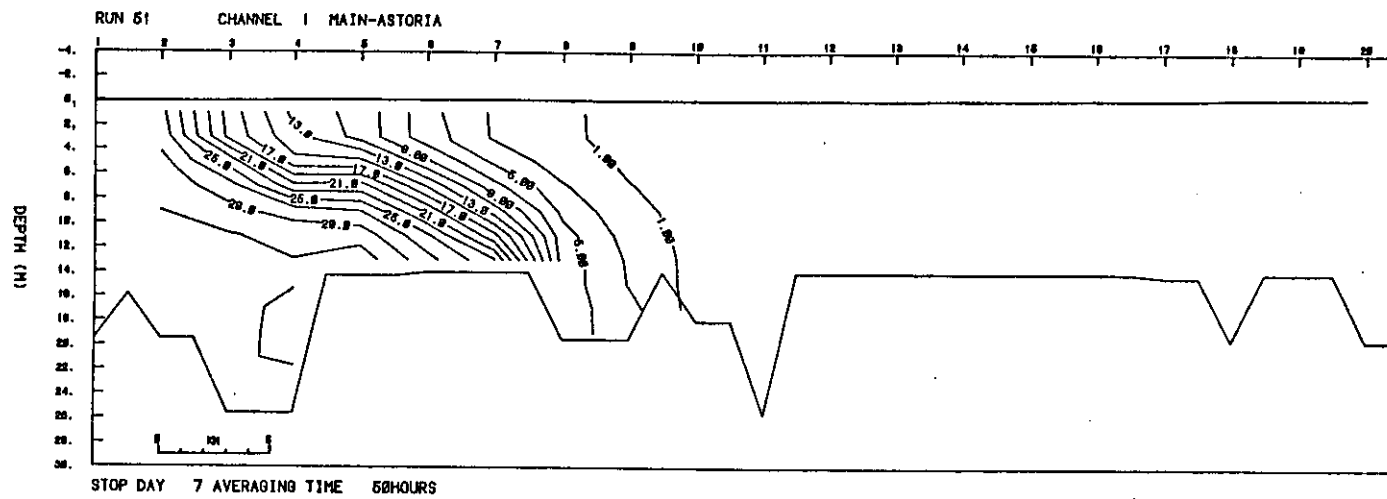


Figure 27b. Channel 1, Neap #1. Maximum salinities.

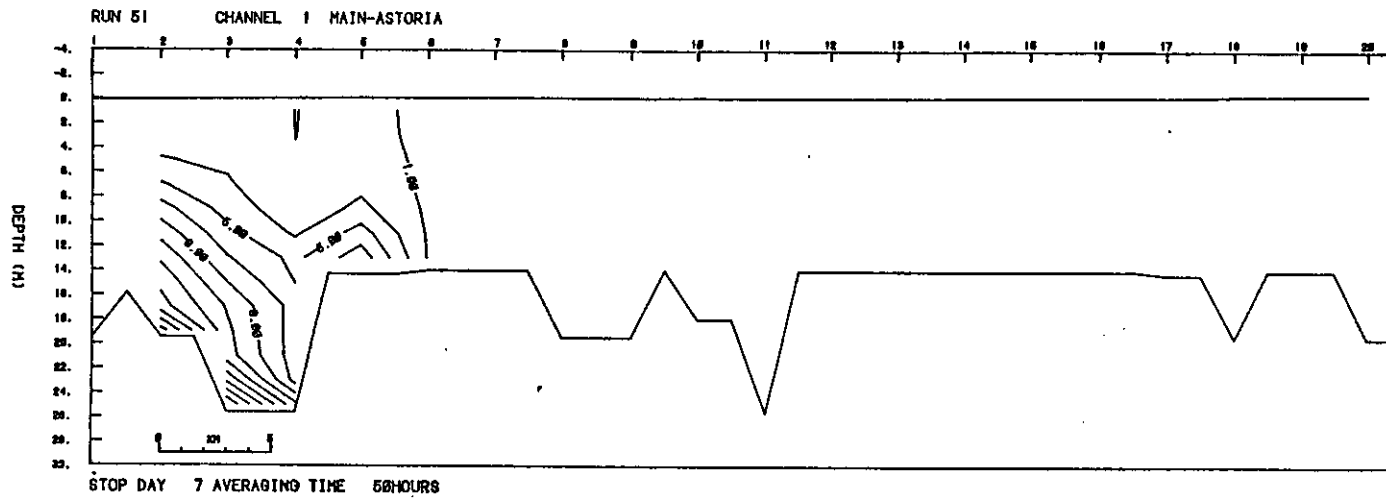


Figure 27c. Channel 1, Neap #1. Minimum salinities.

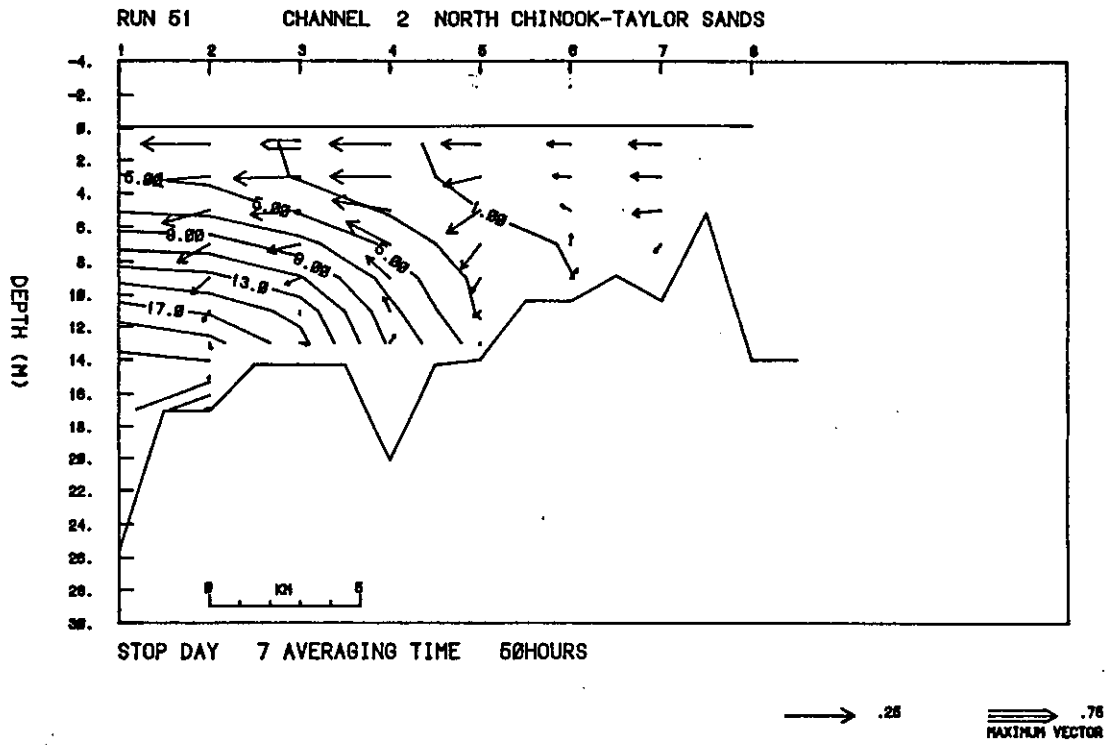


Figure 28a. Channel 2, Neap #1. Mean currents and salinities (m/s and ‰).

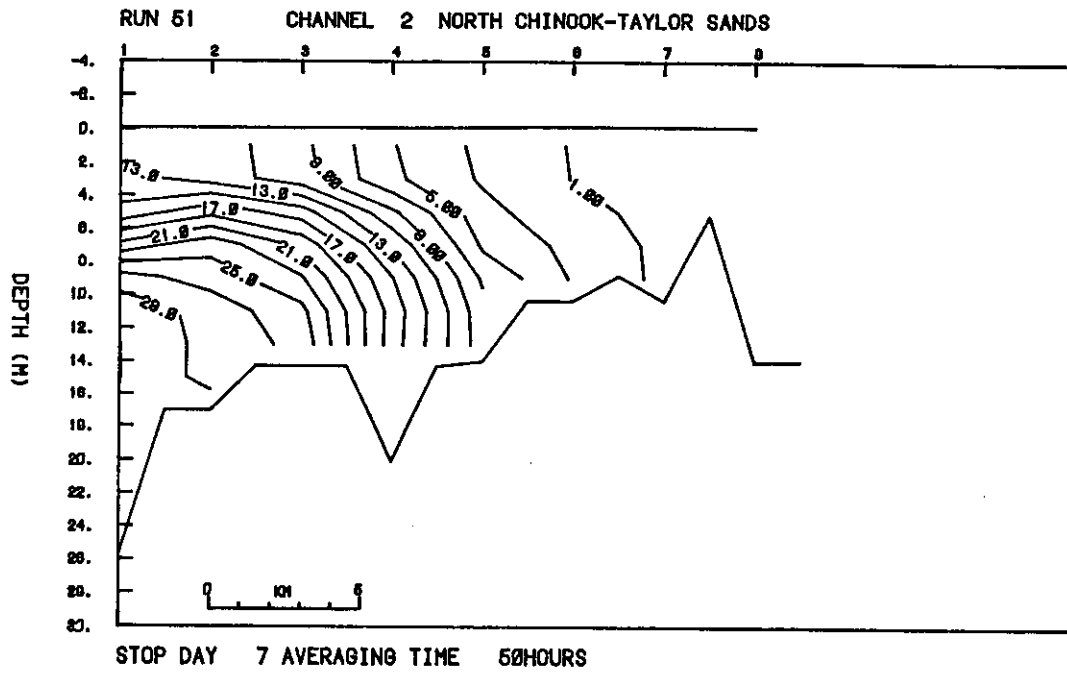


Figure 28b. Channel 2, Neap #1. Maximum salinities.

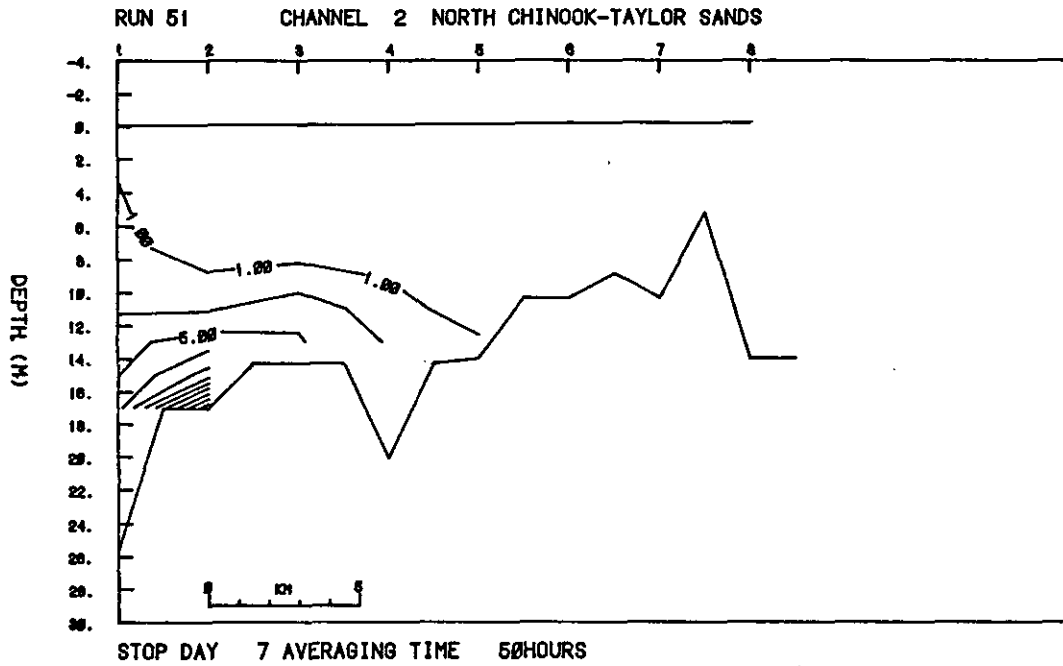


Figure 28c. Channel 2, Neap #1. Minimum salinities.

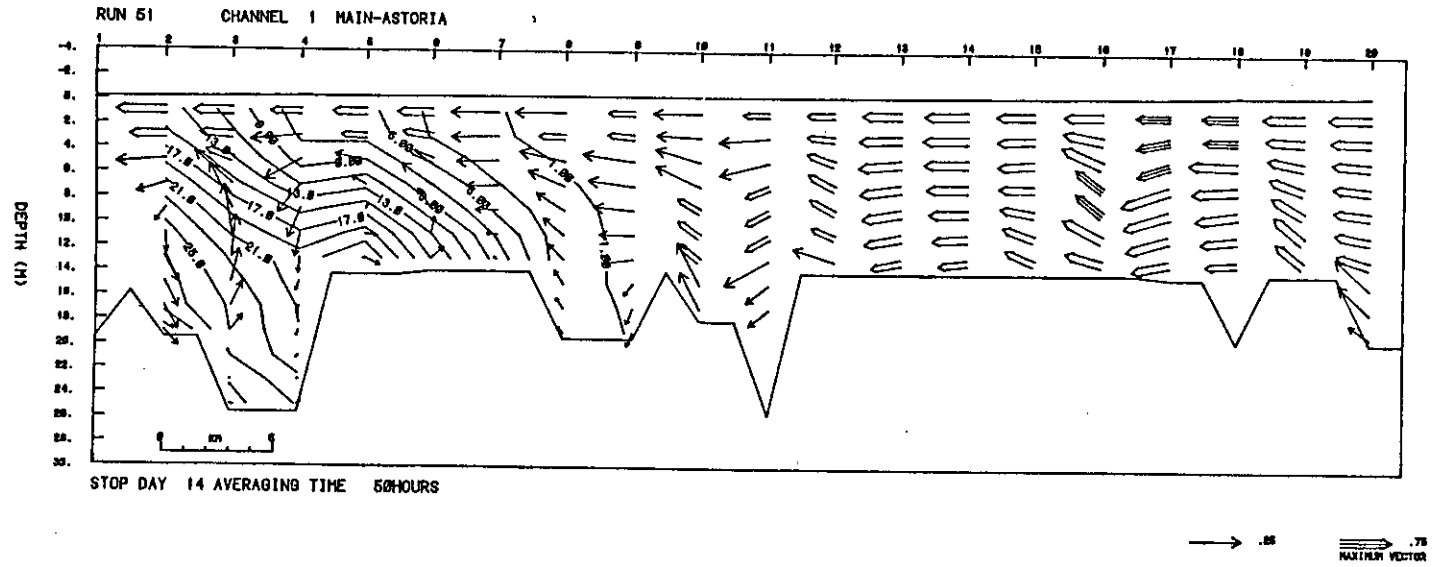


Figure 29a. Channel 1, Spring #1. Mean currents and salinities (m/s and ‰).

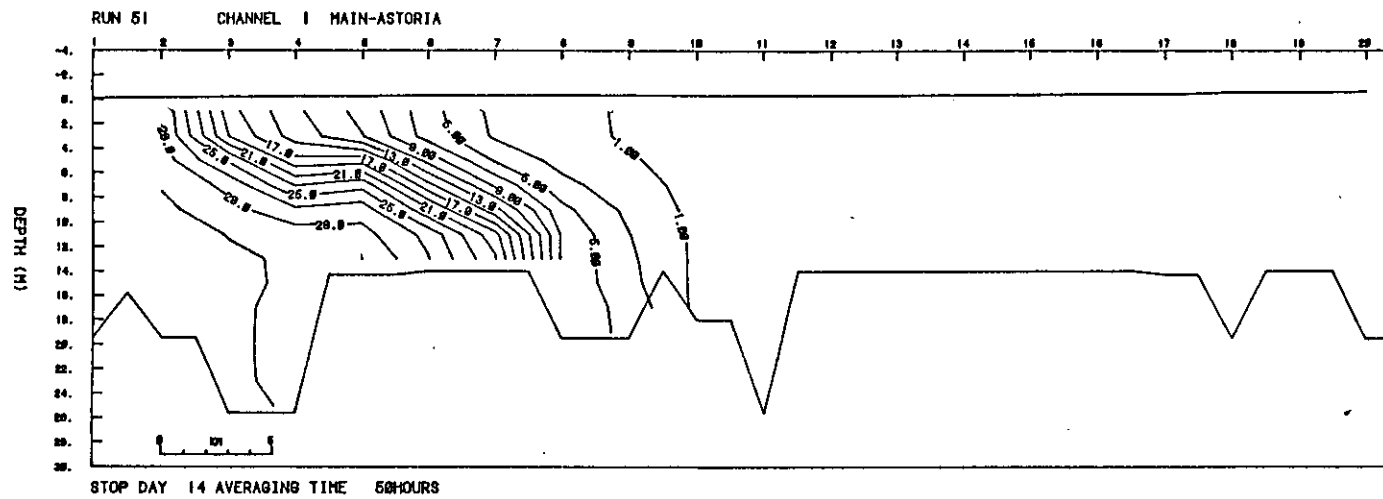


Figure 29b. Channel 1, Spring #1. Maximum salinities.

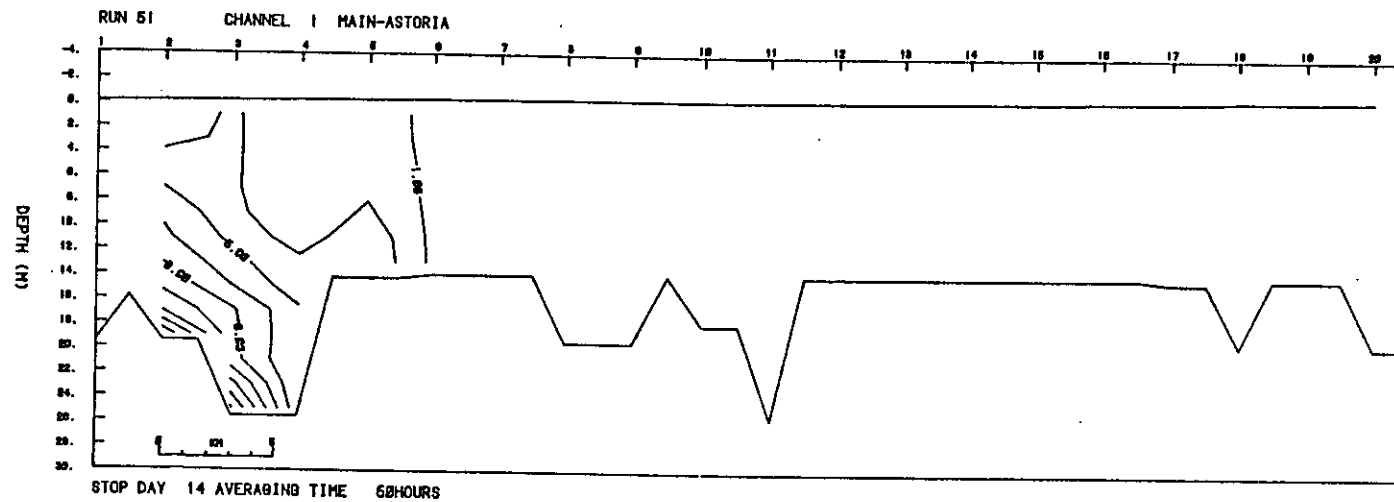


Figure 29c. Channel 1, Spring #1. Minimum salinities.

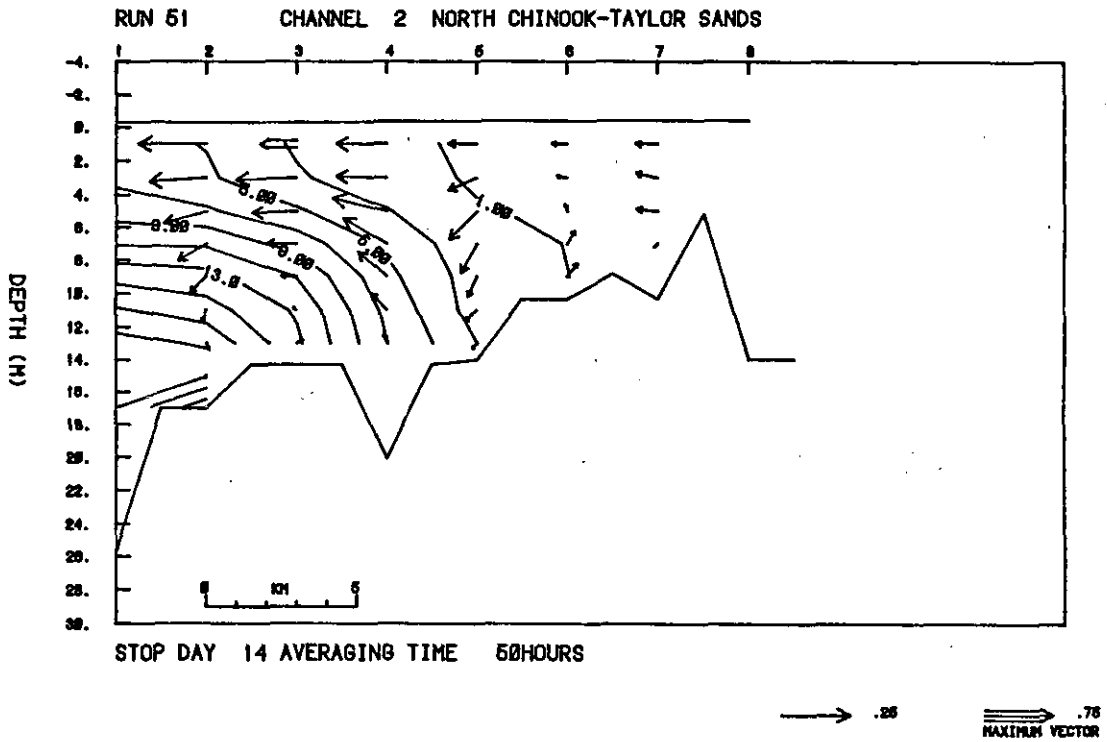


Figure 30a. Channel 2, spring #1. Mean currents and salinities (m/s and ‰).

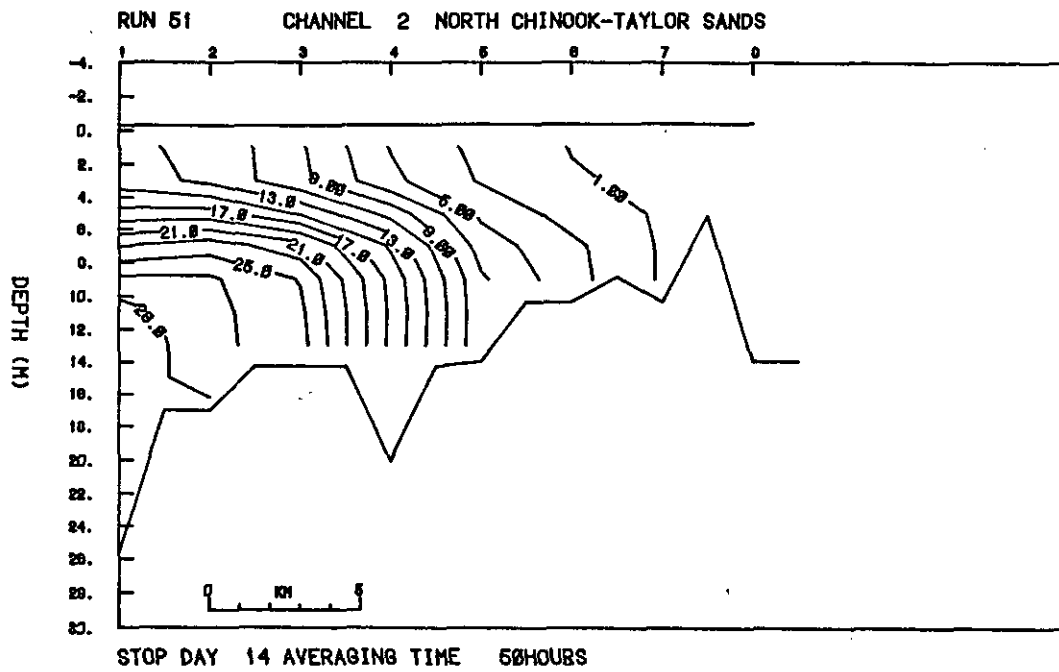


Figure 30b. Channel 2, spring #1. Maximum salinities.

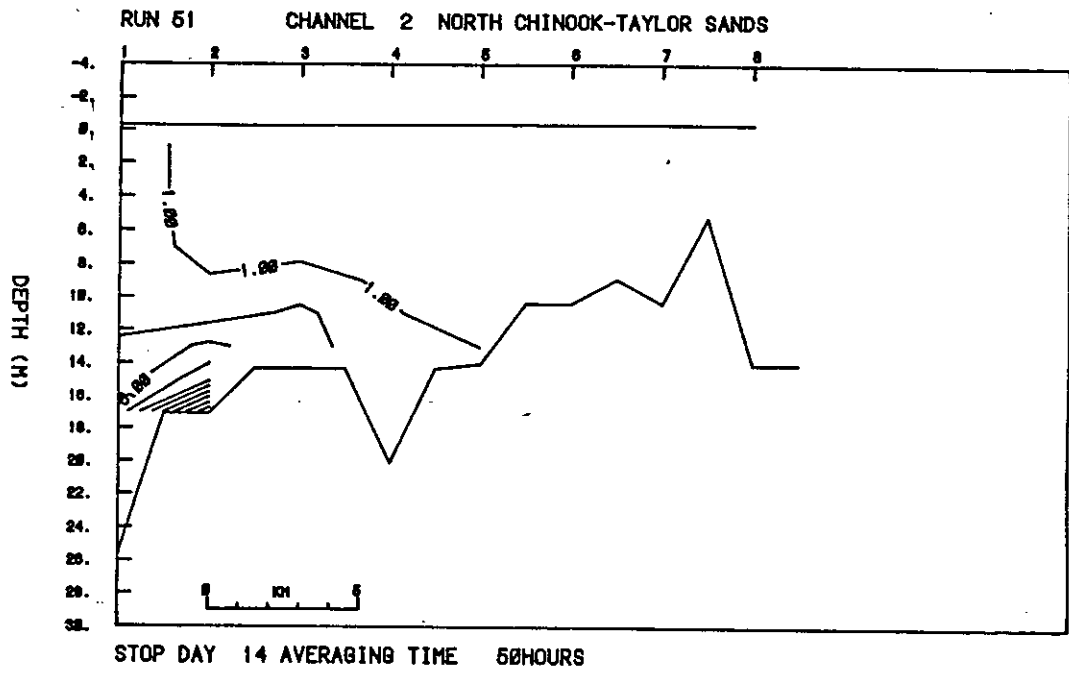


Figure 30c. Channel 2, spring #1. Minimum salinities.

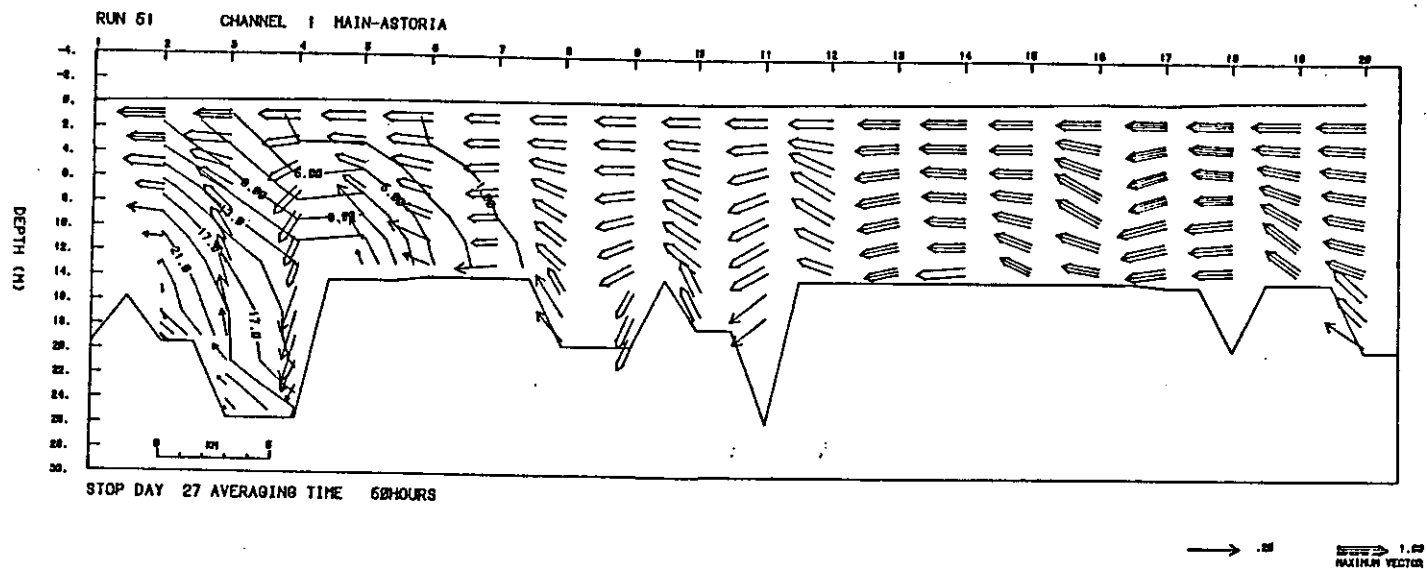


Figure 31a. Channel 1, spring #2 (spring, 1981). Mean currents and salinities (m/s and  $^{\circ}/\text{oo}$ ).

151

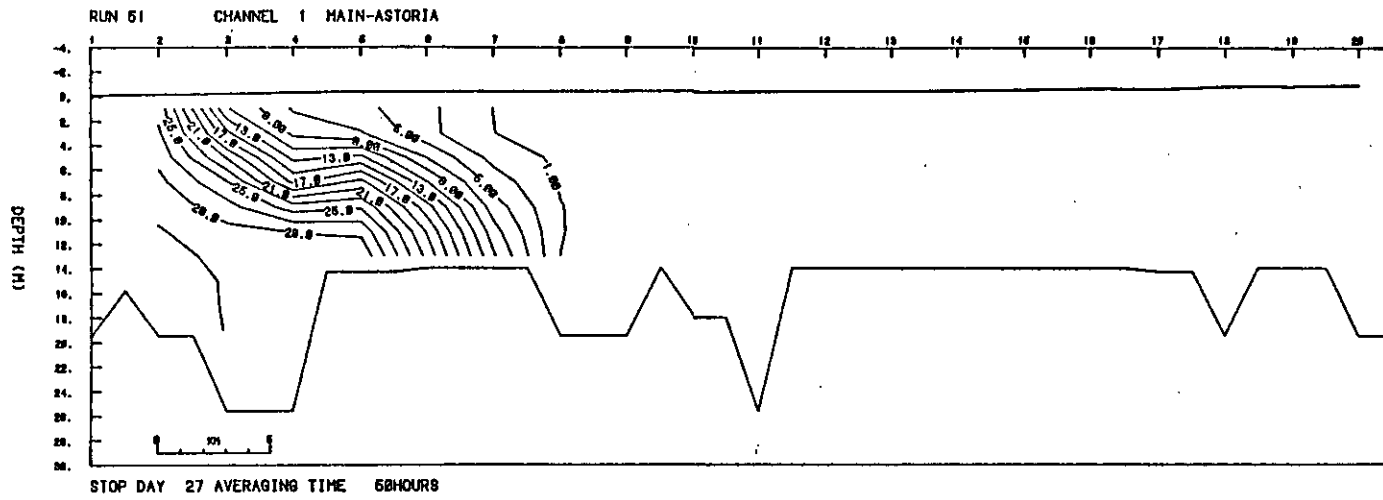


Figure 31b. Channel 1, spring #2 (spring, 1981). Maximum salinities.

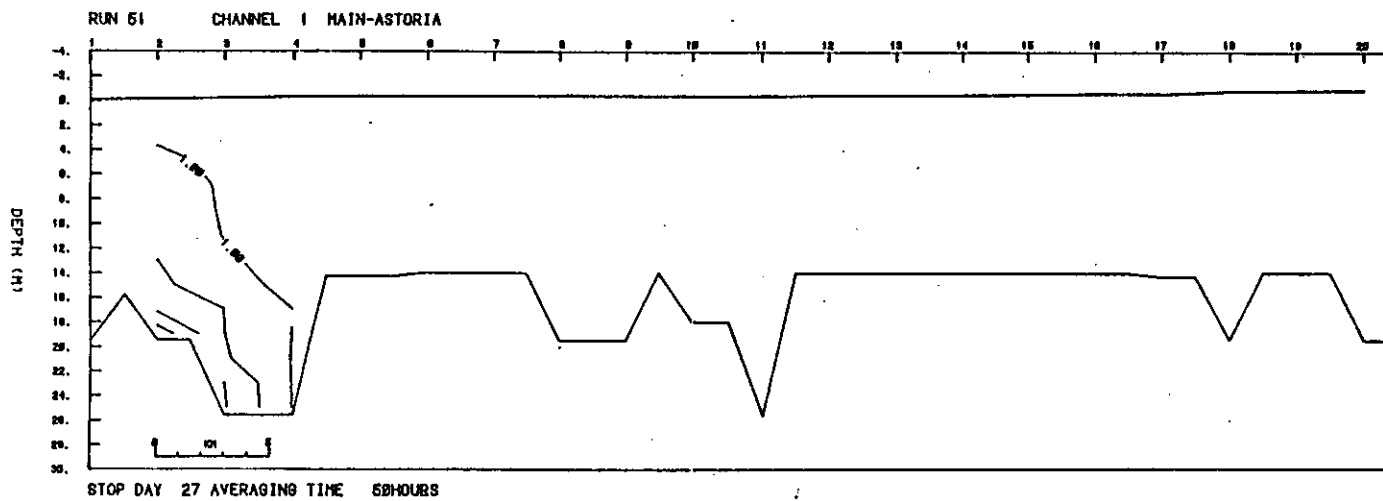


Figure 3lc. Channel 1, spring #2 (spring, 1981). Minimum salinities.

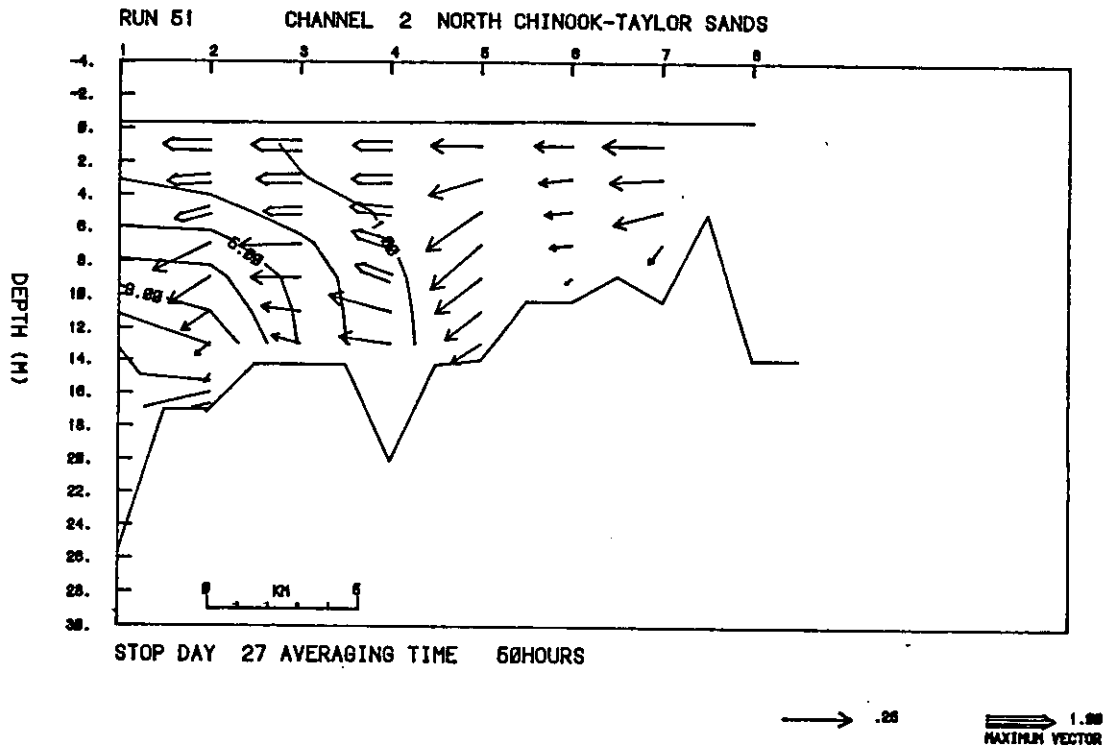


Figure 32a. Channel 2, spring #2 (spring, 1981). Mean currents and salinities (m/s /oo).

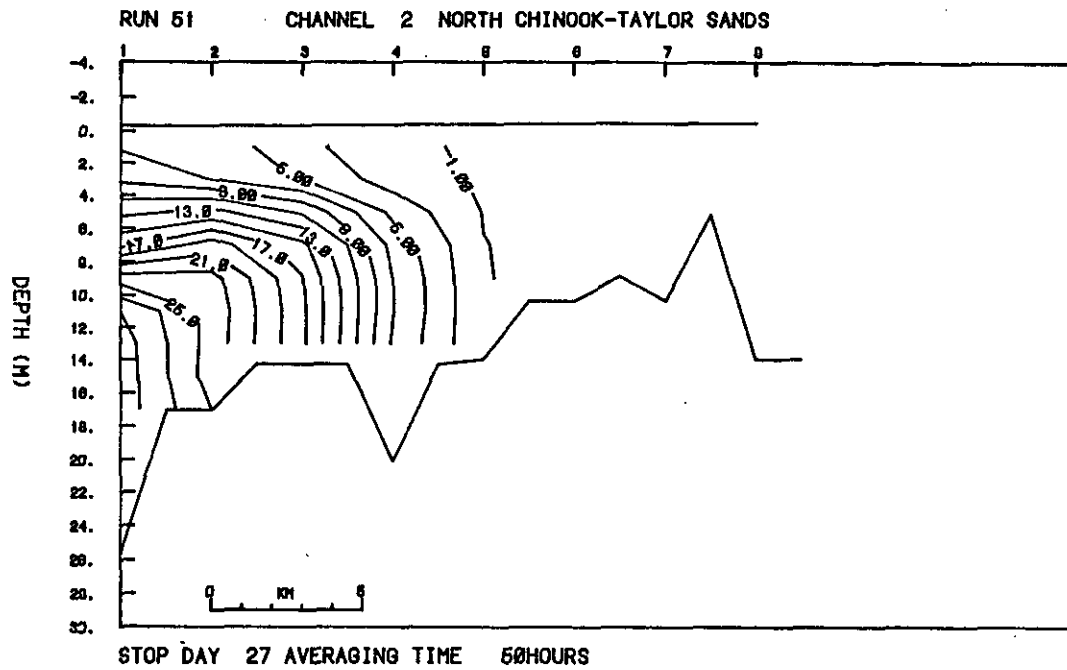


Figure 32b. Channel 2, spring #2 (spring, 1981). Maximum salinities.

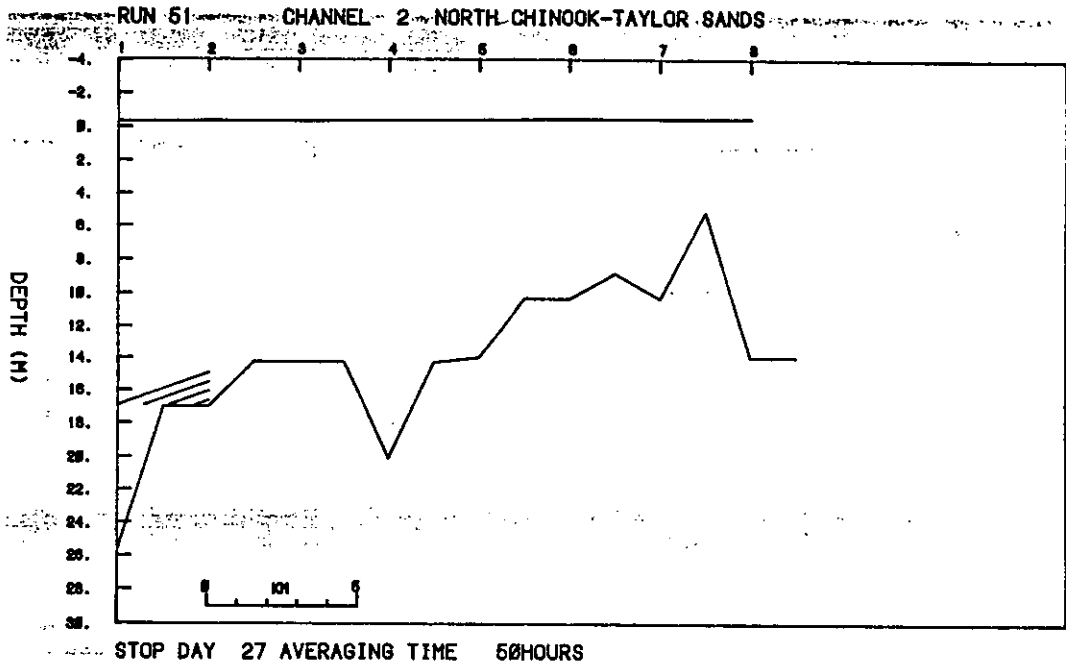


Figure 32c. Channel 2, spring #2 (spring, 1981). Minimum salinities.

Spring 1981: Neap Tide #2: Figures 33 and 34

The second neap tide occurs during a sharp increase in riverflow to the maximum observed during this freshet ( $15,910 \text{ m}^3/\text{s}$ ), about twice the magnitude of the first neap tide. Again, the differences from the previous spring tide are not large. The salinity intrusion has moved farther toward the entrance, and the maximum salinity field in channel 1 no longer shows oceanic salinities over most of the water column at the mouth.

Spring 1981: Neap Tide #3: Figures 35 and 36

After about four days of riverflows greater than  $14 \text{ m}^3/\text{s}$ , the riverflow reduces to about  $12,000 \text{ m}^3/\text{s}$  between days 40-44 and remains reasonably steady until day 50. The neap tide sections for day 50 show that the salinity has moved upstream relative to the previous sections, with greater salinity intrusion at the end of the flood. The Navigation Channel has not quite recovered the mean and maximum salinity fields seen in spring #2, which has a similar riverflow (Figure 31), but the North Channel shows slightly higher salinities than spring #2 (Figure 32).

Spring 1981: Spring Tide #3: Figures 37 and 38

Between neap #3 and spring #3, the riverflow reduces to the same level as at spring #1. Spring #3, however, is an extreme rather than an intermediate tide. The salinity fields are very similar for the means and maximums. There is some indication of stronger mixing than in the spring #2 salinity fields. The minimum salinities are lower than with spring #1, showing the influence of the stronger ebb. A weak density current flow is shown between the mouth and the bridge in the spring #1 results, but not for the stronger spring tides of Figures 37 and 38a.

The conclusions from the model results for fall 1980 and spring 1981 can be summarized as follows:

1. There is a marked spring-neap difference in the salt intrusion length (longer on neap tides), stratification (stronger on neap tides), tidal ranges of salinity (smaller on neap tides), and residual flows (stronger lower layer density flows and weaker tidal residual flows on neap tides) for the low flow period.

2. During the high-flow spring 1981 period, the spring-neap differences are not marked. In fact, spring-neap differences can easily be masked by changes in riverflow. The salt-intrusion length responds rapidly to changing riverflow. If the riverflow increases or decreases over a short period (several days), the salt intrusion length decreases or increases respectively on a daily time scale. If the riverflow remains steady for a period after a large increase, the salt intrusion recovers equilibrium by moving upstream due to tidal advection. This process seems to take about 5-7 days and is most clearly seen in the salinity time series plots (Figures 10 and 11).

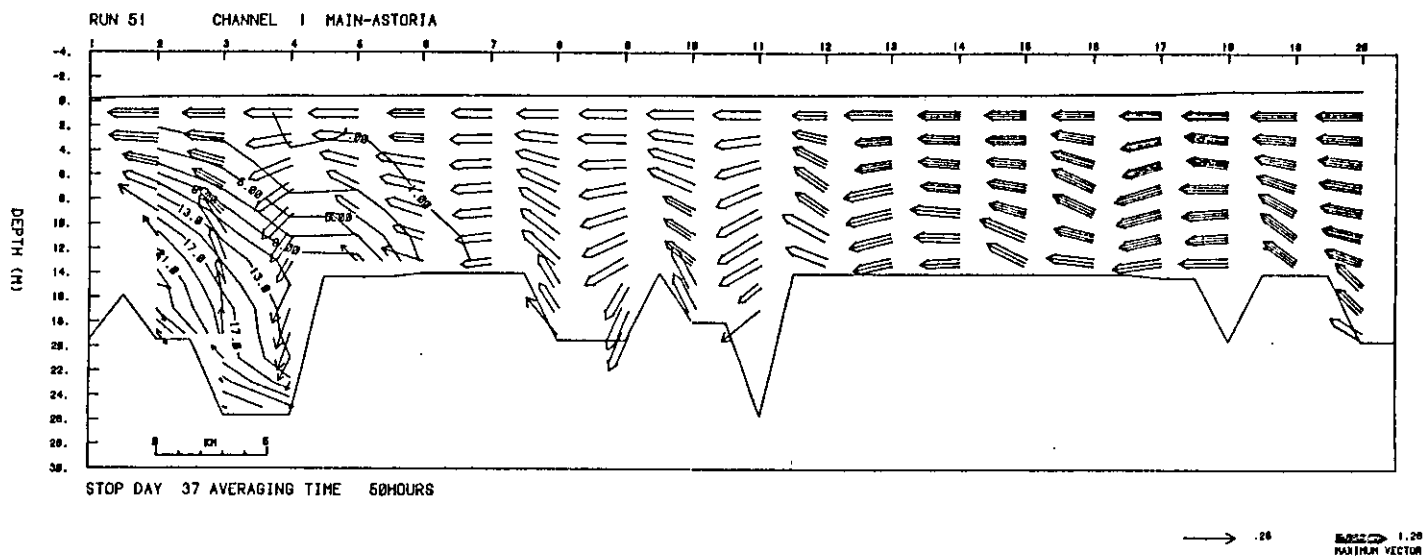


Figure 33a. Channel 1, neap #2 (spring, 1981). Mean currents and salinities (m/s and ‰).

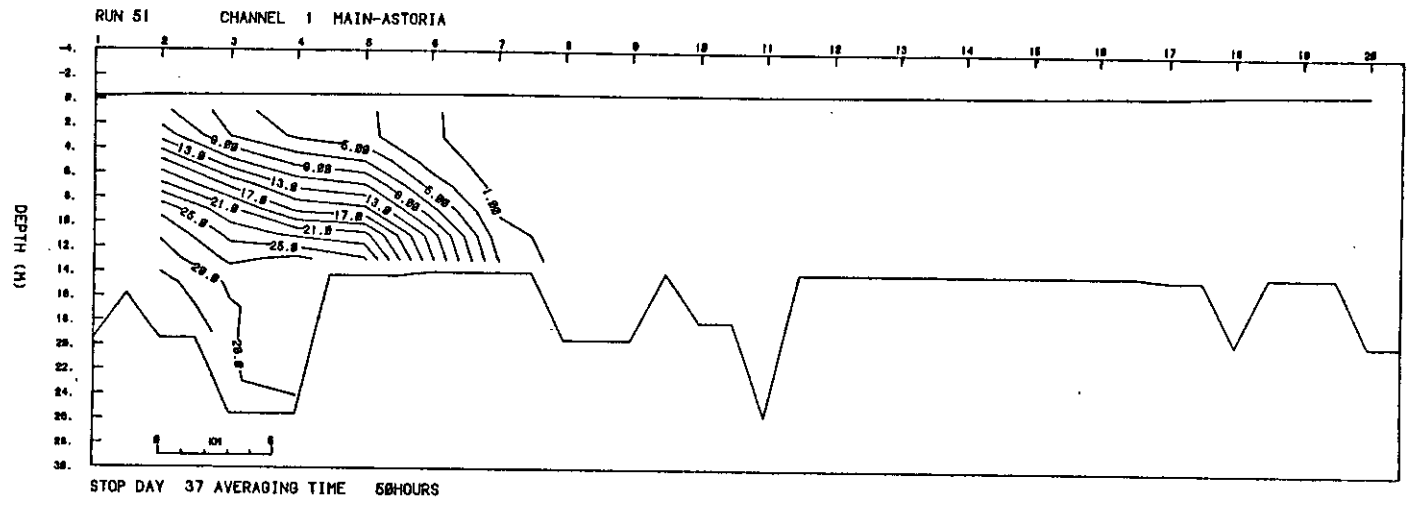


Figure 33b. Channel 1, neap #2 (spring, 1981). Maximum salinities.

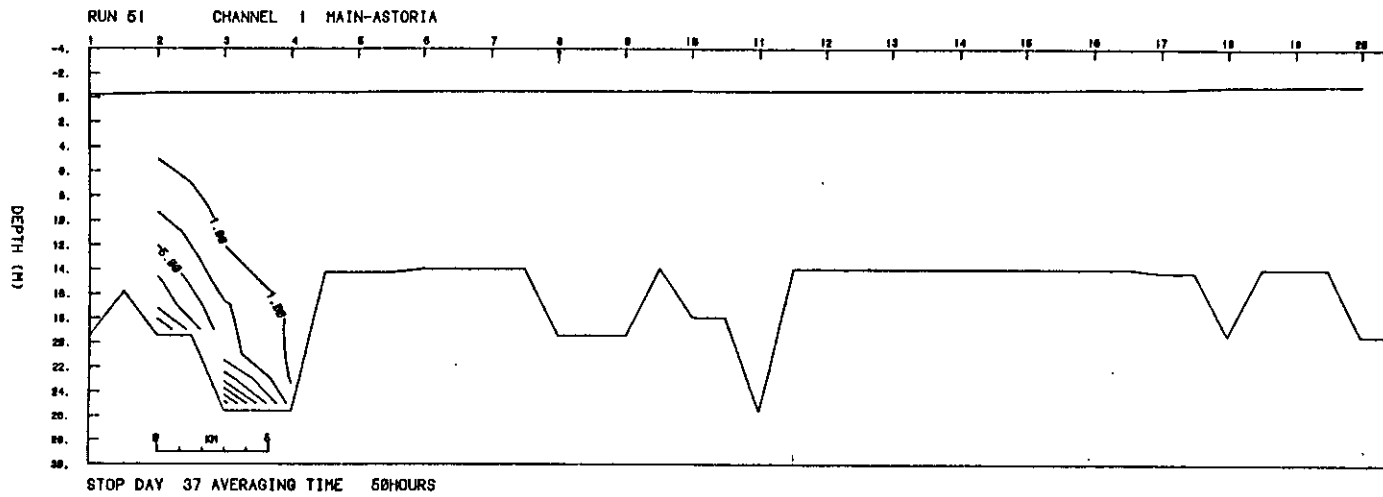


Figure 33c. Channel 1, neap #2 (spring, 1981). Minimum salinities.

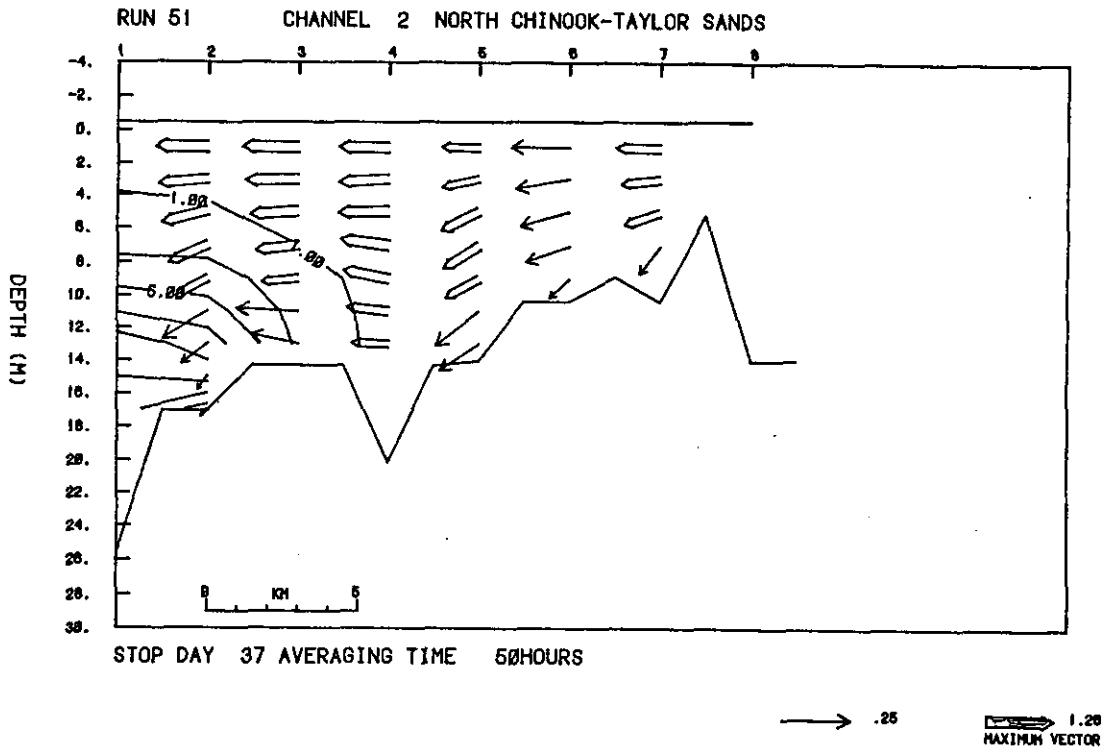


Figure 34a. Channel 2, neap #2 (spring, 1981). Mean currents and salinities (m/s and ‰).

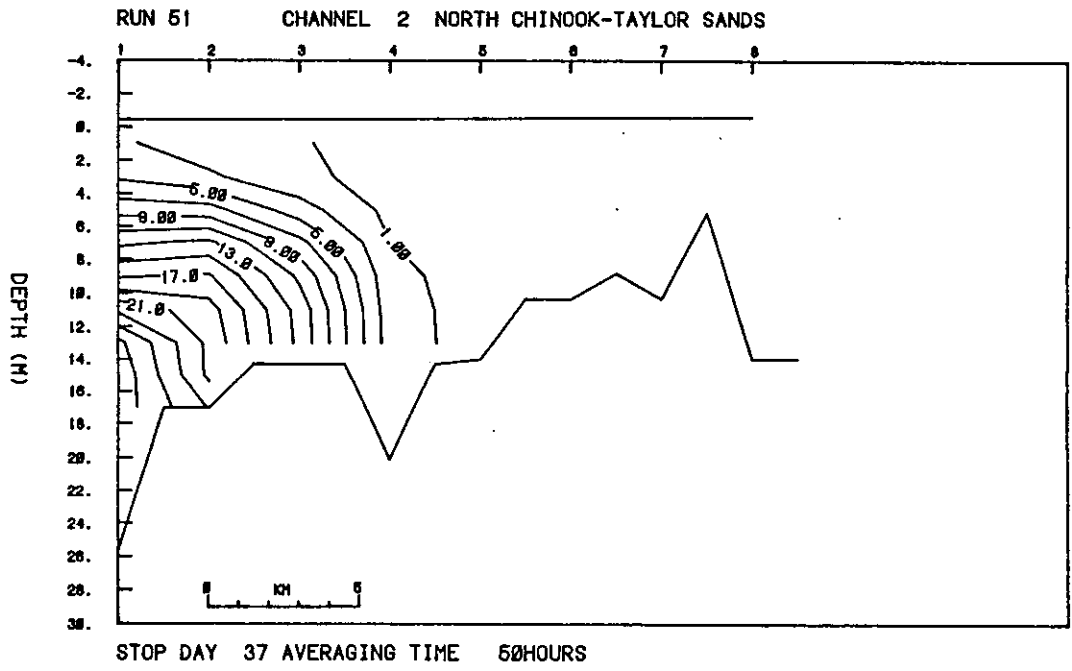


Figure 34b. Channel 2, neap #2 (spring, 1981). Maximum salinities.

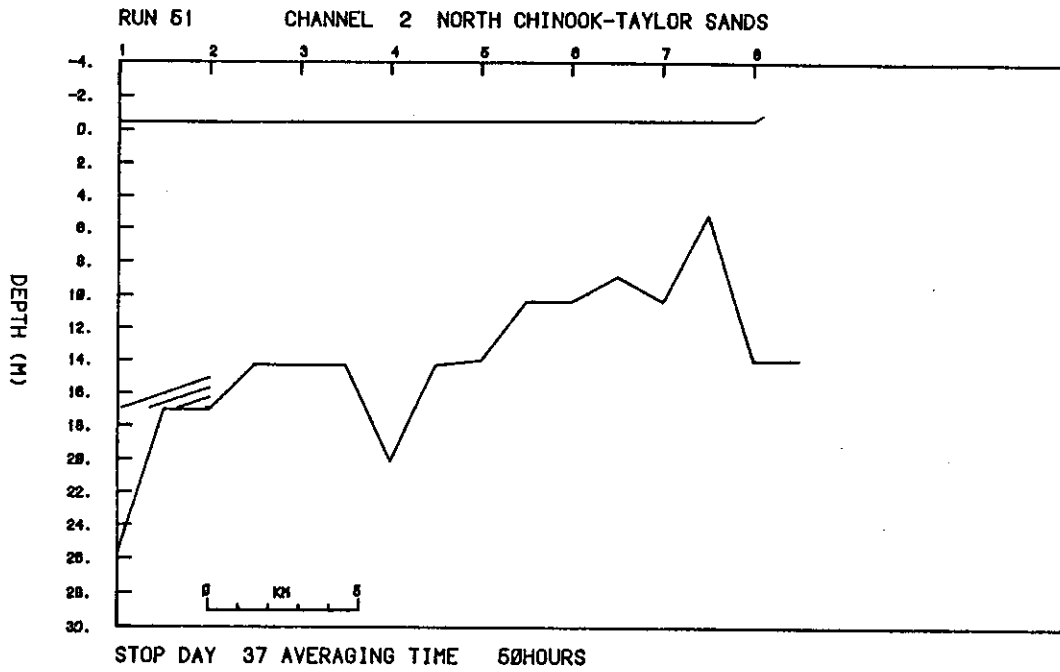


Figure 34c. Channel 2, neap #2 (spring, 1981). Minimum salinities.



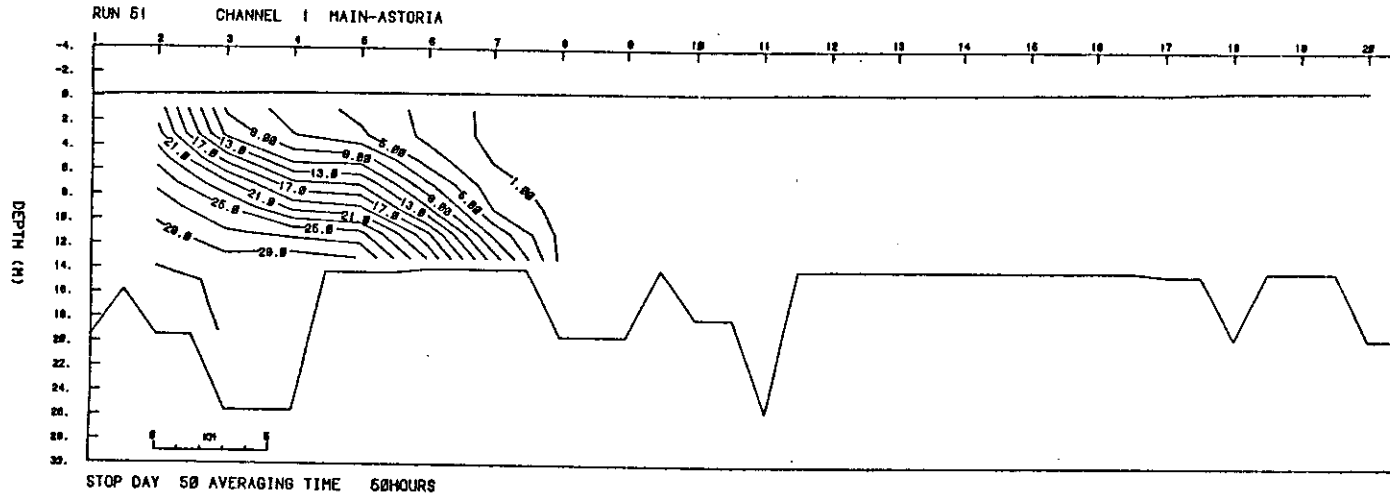


Figure 35b. Channel 1, neap #3 (spring, 1981). Maximum salinities.

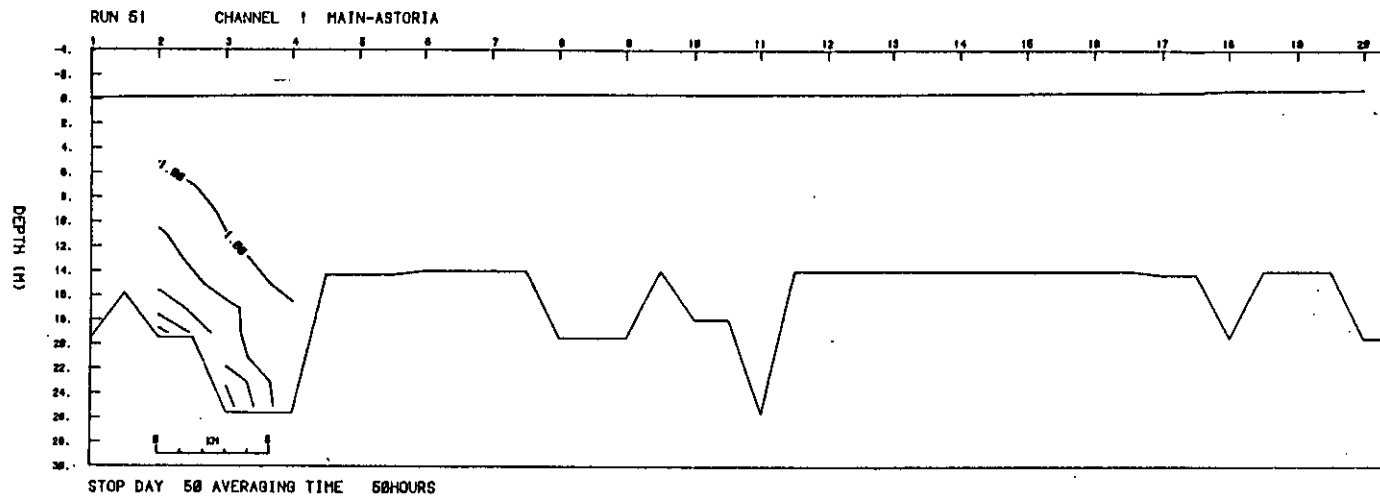


Figure 35c. Channel 1, neap #3 (spring, 1981). Minimum salinities.

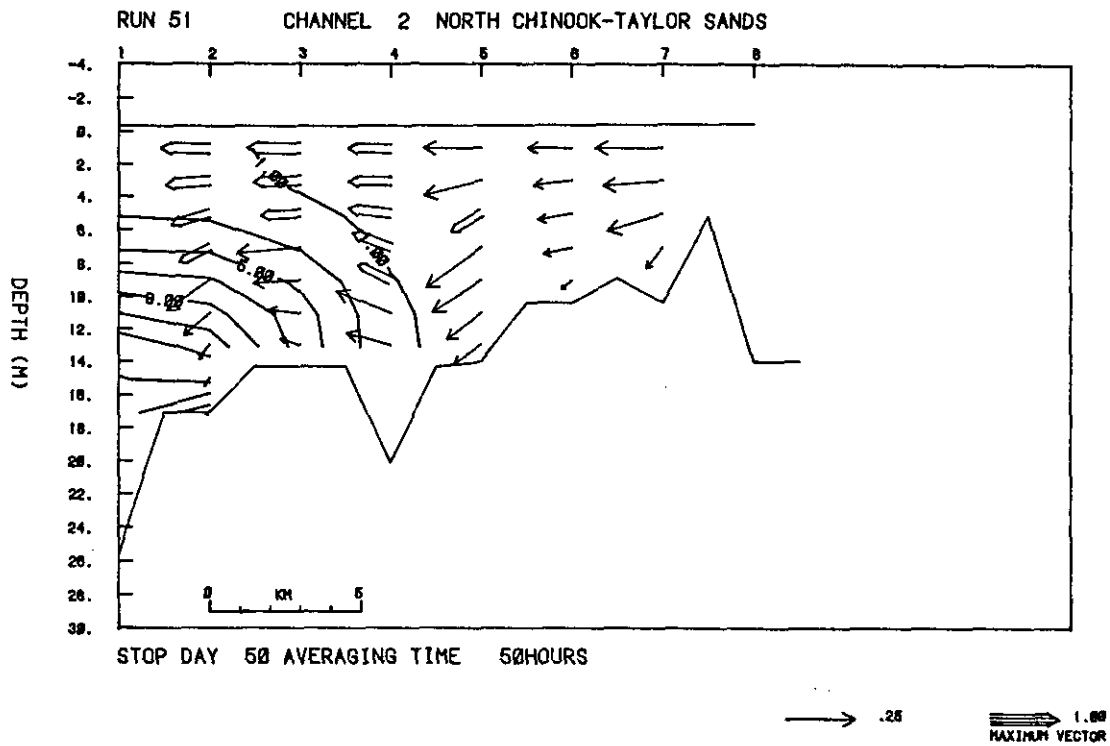


Figure 36a. Channel 2, neap #3 (spring 1981). Mean currents and salinities (m/s and ‰).

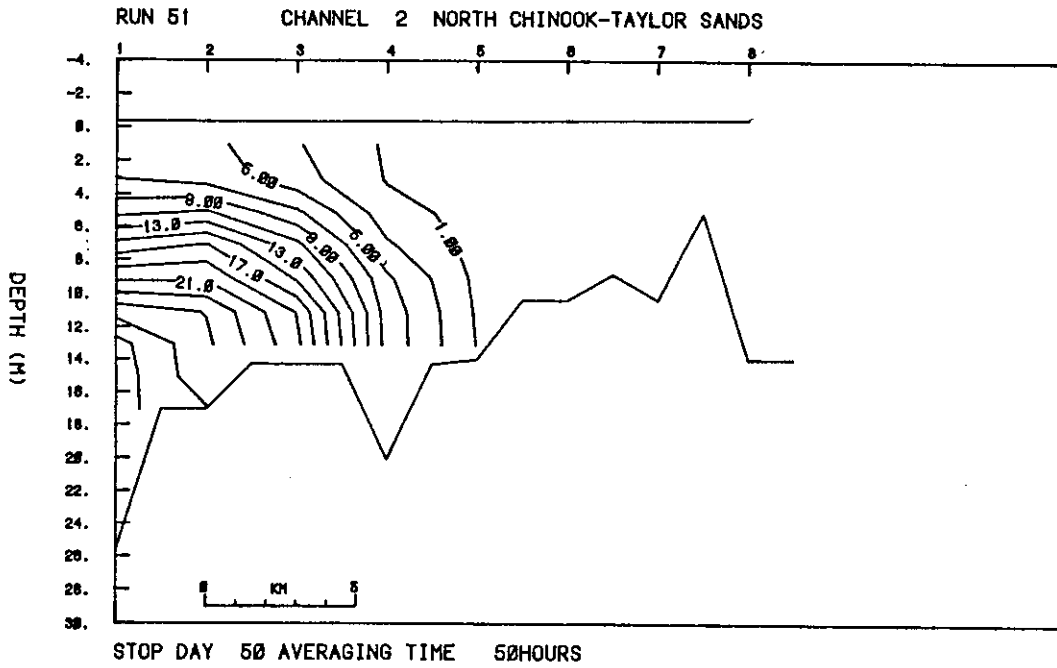


Figure 36b. Channel 2, neap #3 (spring, 1981). Maximum salinities.

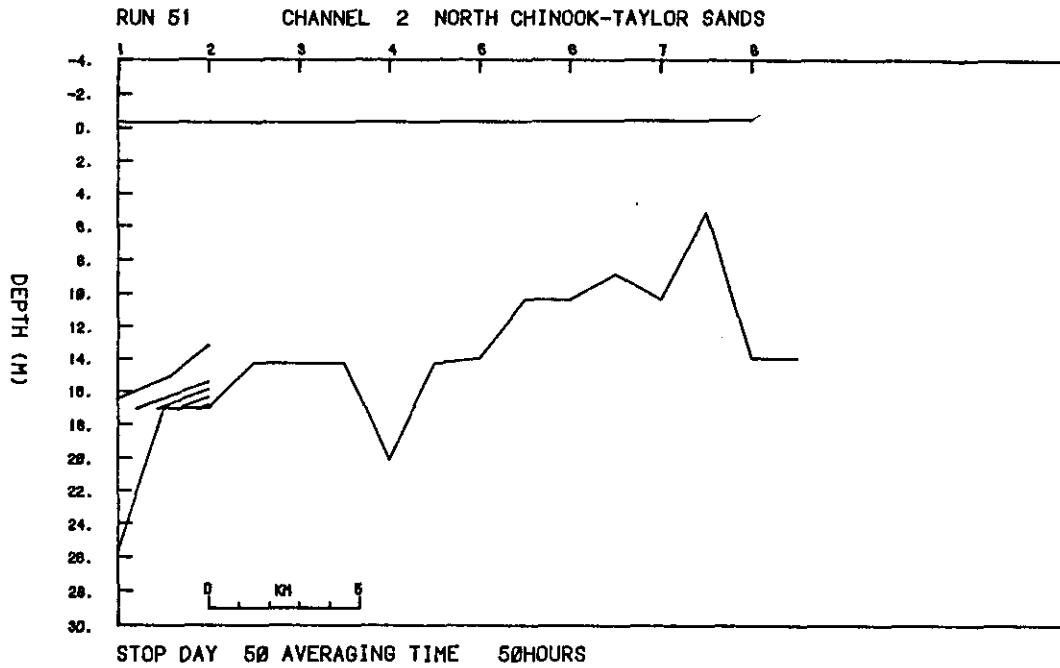


Figure 36c. Channel 2, neap #3 (spring, 1981). Minimum salinities.

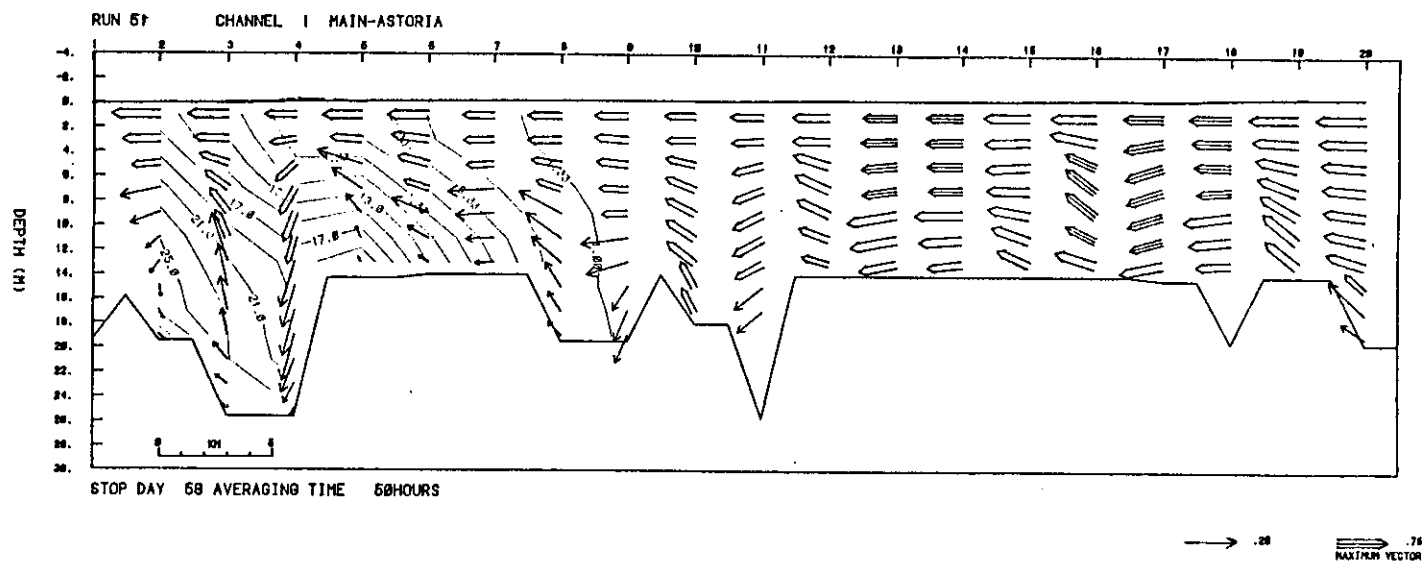


Figure 37a. Channel 1, spring #3 (spring, 1981). Mean currents and salinities (m/s and ‰).

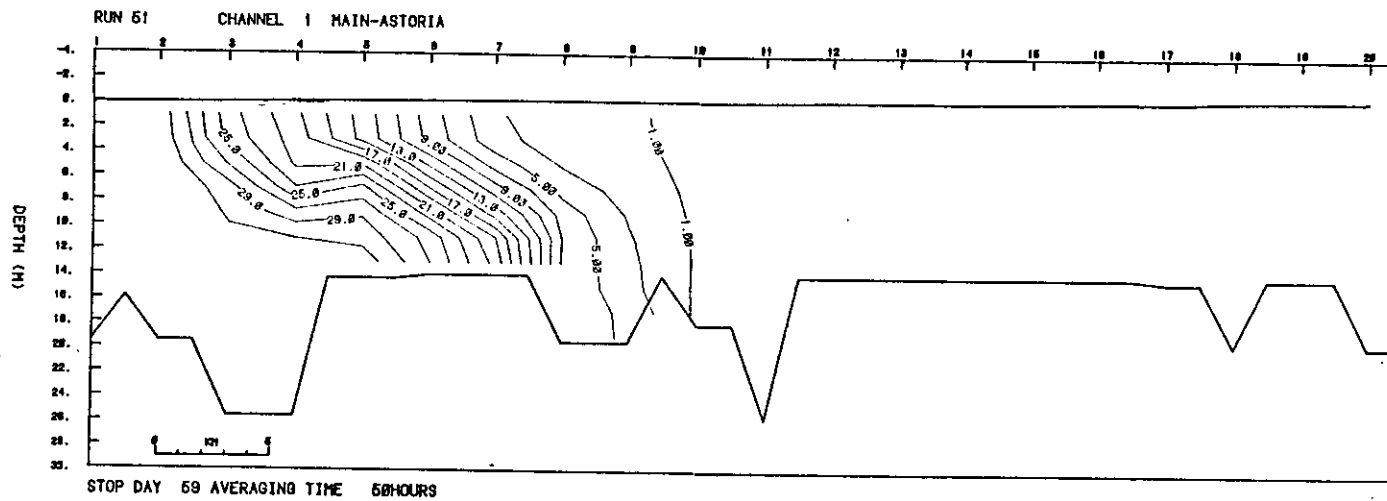


Figure 37b. Channel 1, spring #3 (spring, 1981). Maximum salinities.

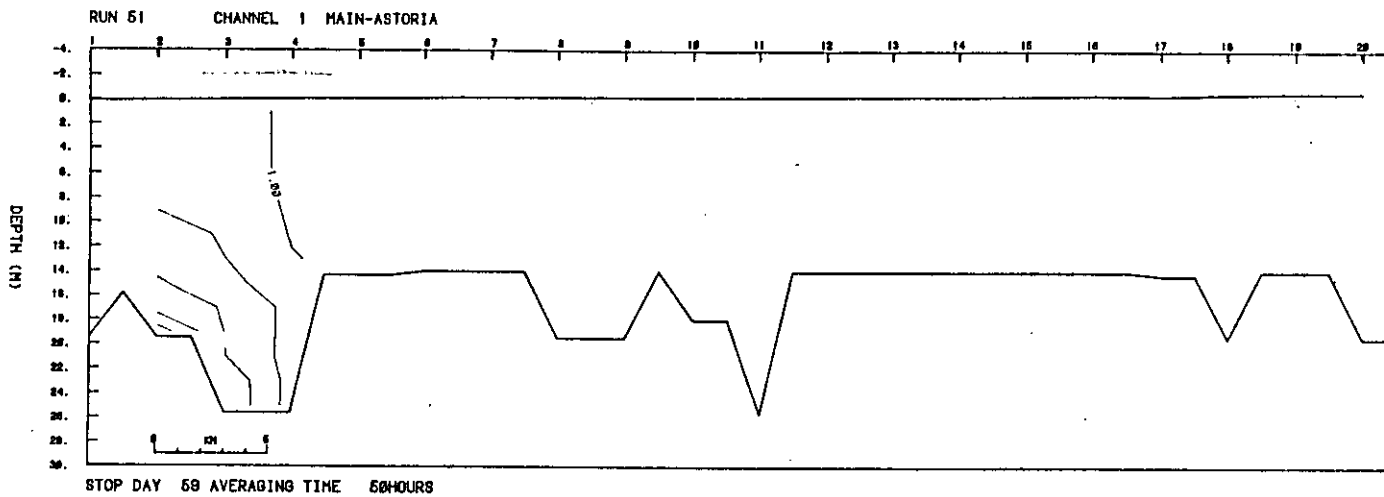


Figure 37c. Channel 1, spring #3 (spring, 1981). Minimum salinities.

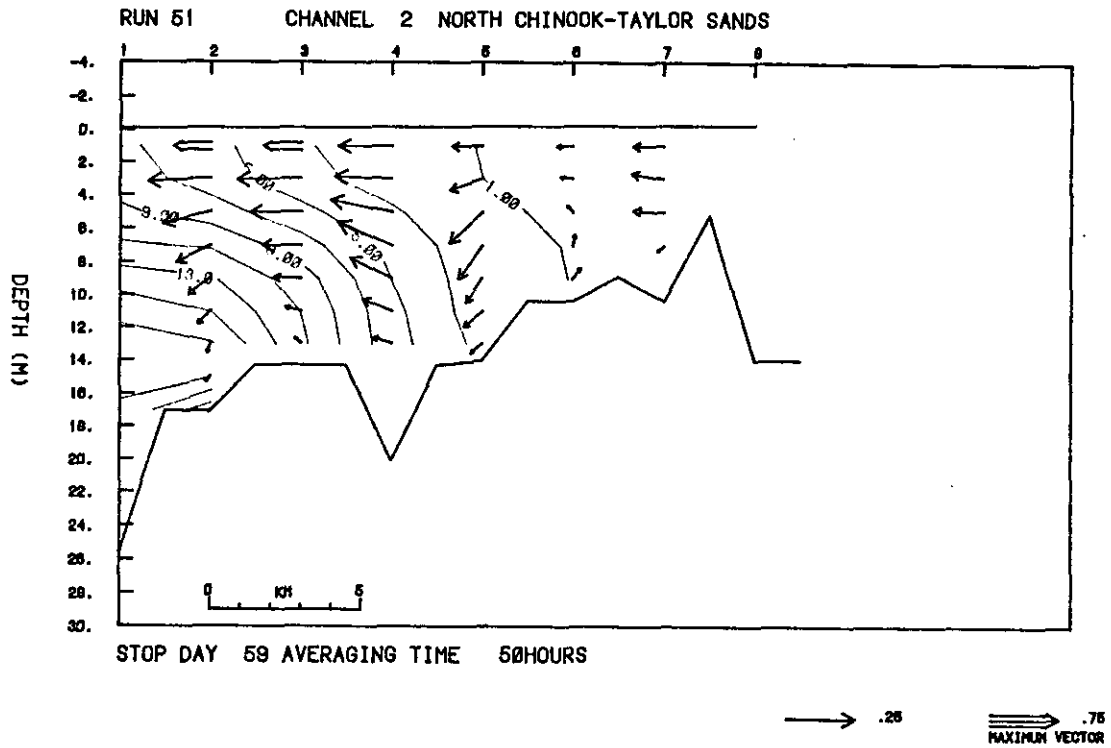


Figure 38a. Channel 2, spring #3 (spring, 1981). Mean currents and salinities (m/s and ‰).

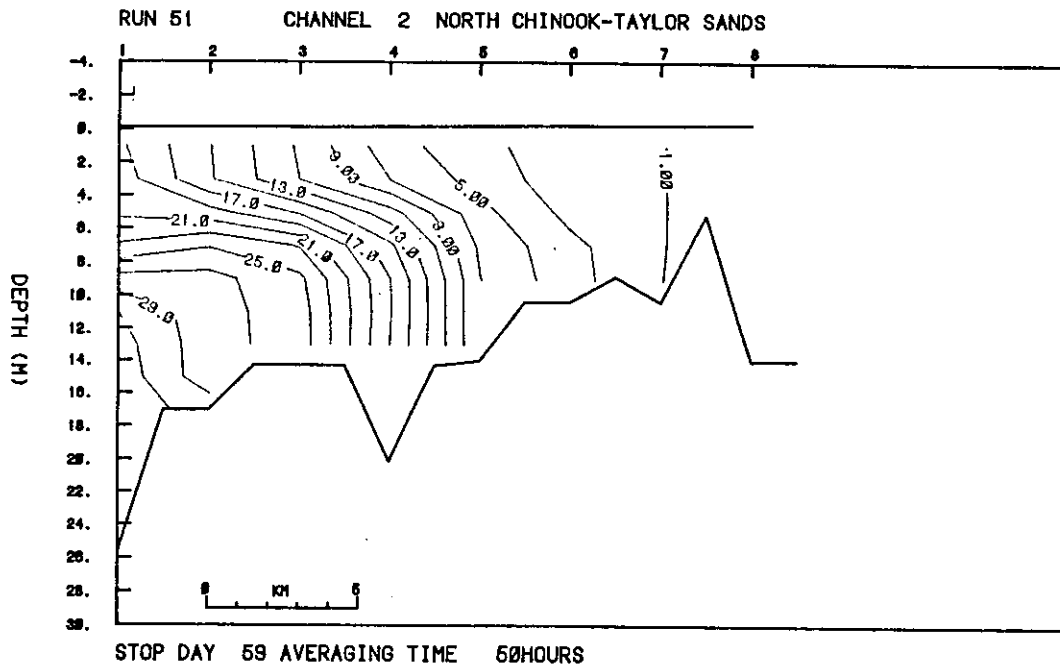


Figure 38b. Channel 2, spring #3 (spring, 1981). Maximum salinities.

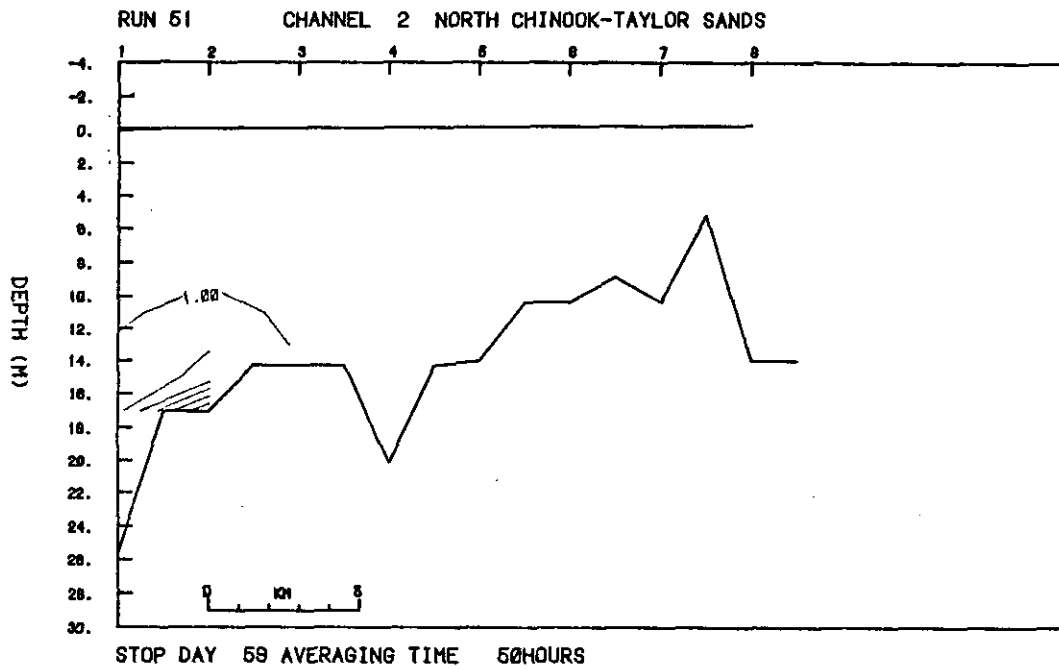


Figure 38c. Channel 2, spring #3 (spring, 1981). Minimum salinities.

To conclude this section, two 15-day periods are presented from the spring 1981 simulation. The two periods have average riverflows that differ by a factor of 2. The 15-day periods contain both neap and spring tides.

In addition to the mean fields, the total mean salt flux has been calculated as follows.

$$\text{Salt Flux} = \frac{1}{T} \int_0^T \int_{z-\delta/2}^{z+\delta/2} \text{busdzdt}$$

The total salt flux is contoured by channel section with positive values representing upstream salt transport. The total salt flux includes both mean flow salt transport and transport due to the cross correlation of the tidal components of  $u$  and  $s$ .

The mean current and salinity fields for channels 1 and 2 (Figures 39 and 40) show obvious similarities with the 50-hour means presented above. The salt intrusion is smaller and the upstream bottom flow is not present for the stronger riverflows (Figure 40). The salt flux sections generally show a two-layer structure consistent with stronger downstream salt flux by the mean flow at the surface than is found at the bottom and a more uniform tidal upstream salt flux throughout the depth. At the junction between the channels (grid number 4, channel 1), there is a larger upstream salt flux into channel 2 than into channel 1. The upstream salt flux is also patchy, with a minimum at grid point 3, channel 1. The salt flux values are lower for the higher riverflows (Figure 40) because the salinity values are lower in the mean and in general throughout the tidal period. The total salt transport calculations, using current meter data for the high flow season for the Clatsop Spit section, are given in Jay (1984) (Figure 6-5a). Based on point measurements, upstream salt flux was calculated to be confined to the North Channel and downstream salt flux confined to the Navigation Channel. This situation is only confirmed by the model to the extent that relatively larger upstream salt flux is calculated for the North Channel than the Navigation Channel. However, model calculations resulting in two-layer opposing total salt fluxes may be a result of the lateral averaging, which is the basis of the model.

The discussion above has been largely descriptive. However, some qualitative conclusions can be drawn concerning physical processes governing the circulation of the estuary. Unfortunately, lack of time and funding have prevented a detailed quantitative evaluation of the individual terms of the governing equations both on an instantaneous and tidal mean basis. This should be performed in order to evaluate the balance of forces and salt balance mechanisms operating at different sections of the estuary. An attempt at quantifying the balances of forces involved in the principal physical processes has been given by Jay (1984) using the CREDDP and NOS observations with some qualitative guidance from the model results.

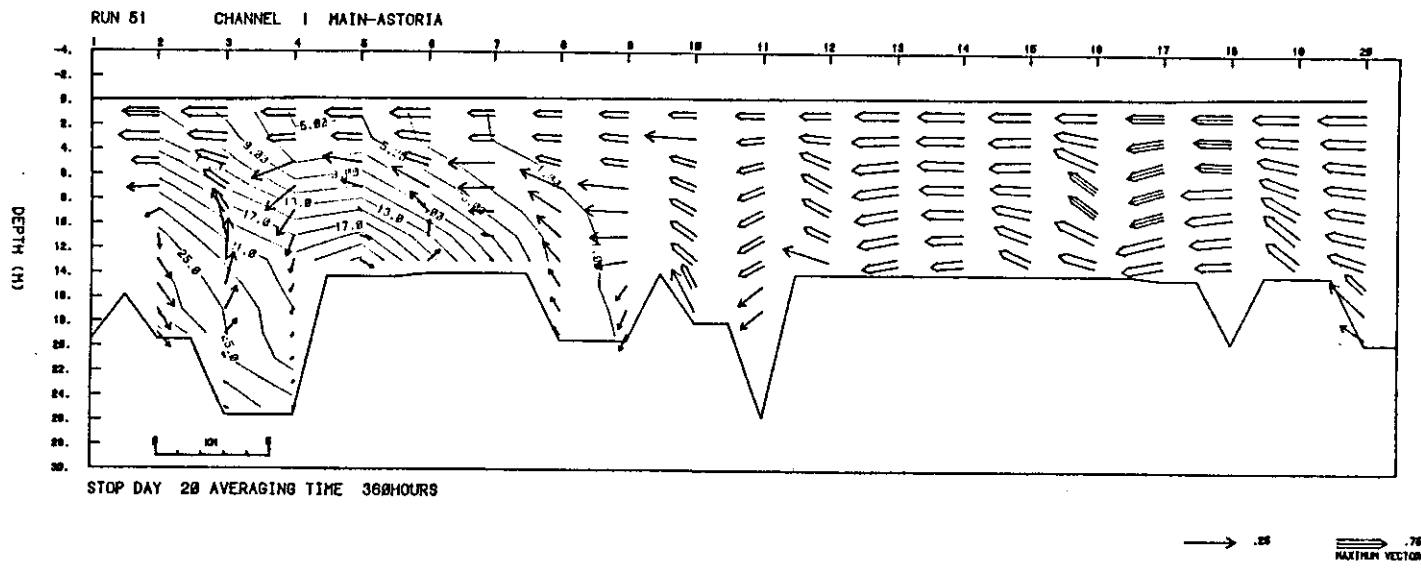
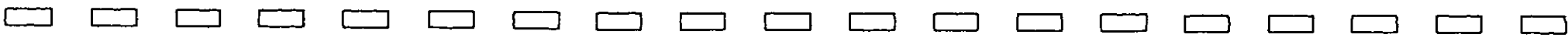


Figure 39a. Channel 1, 15-day mean. Mean currents and salinities (m/s and ‰).



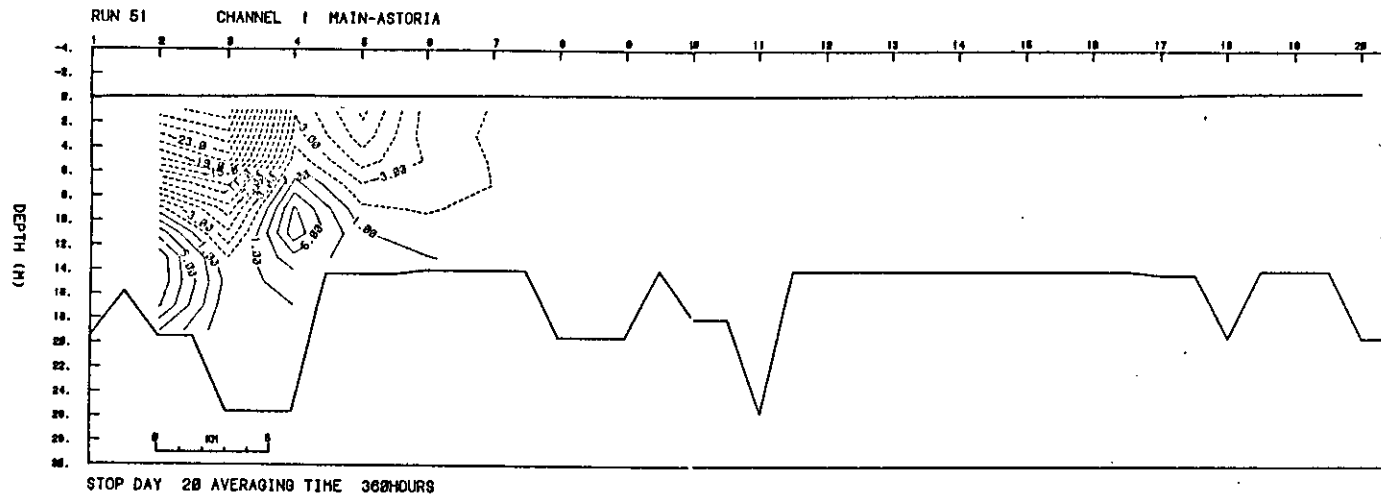


Figure 39b. Channel 1, 15-day mean. Salt flux ( $\text{kg/s} \cdot 10^3$ ).

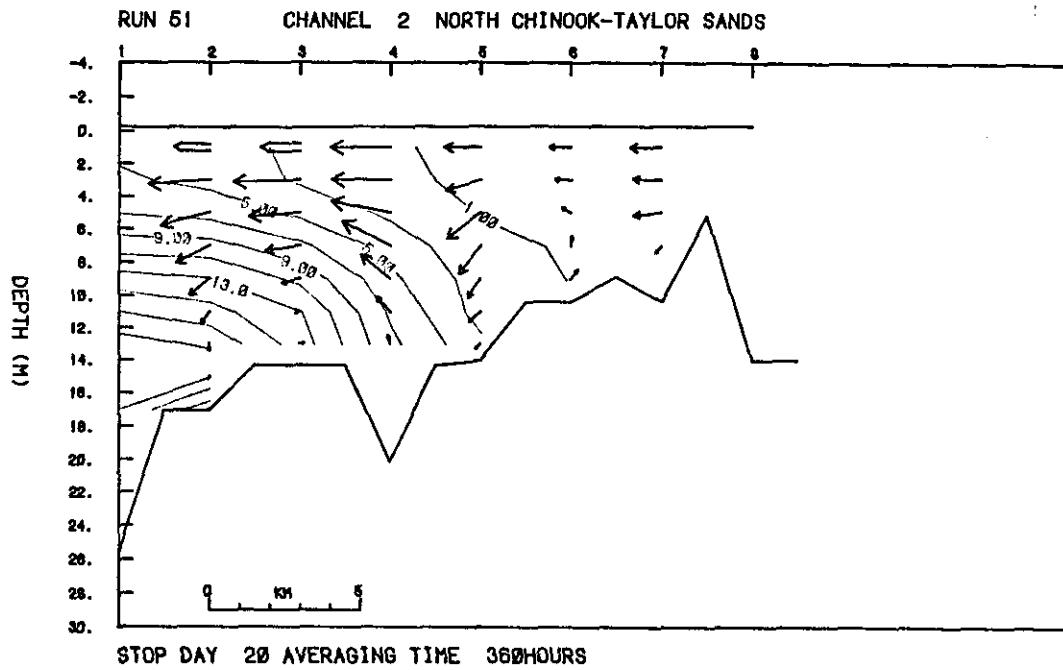


Figure 39c. Channel 2, 15-day mean. Mean currents and salinities (m/s and ‰).

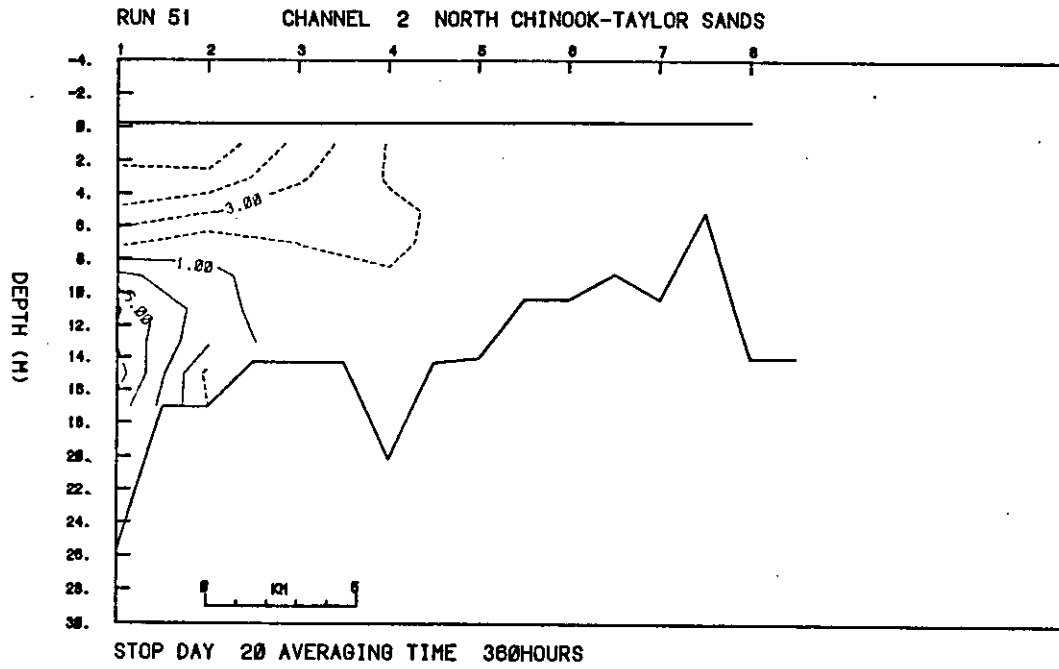


Figure 39d. Channel 2, 15-day mean. Salt flux ( $\text{kg/s} \cdot 10^3$ ).

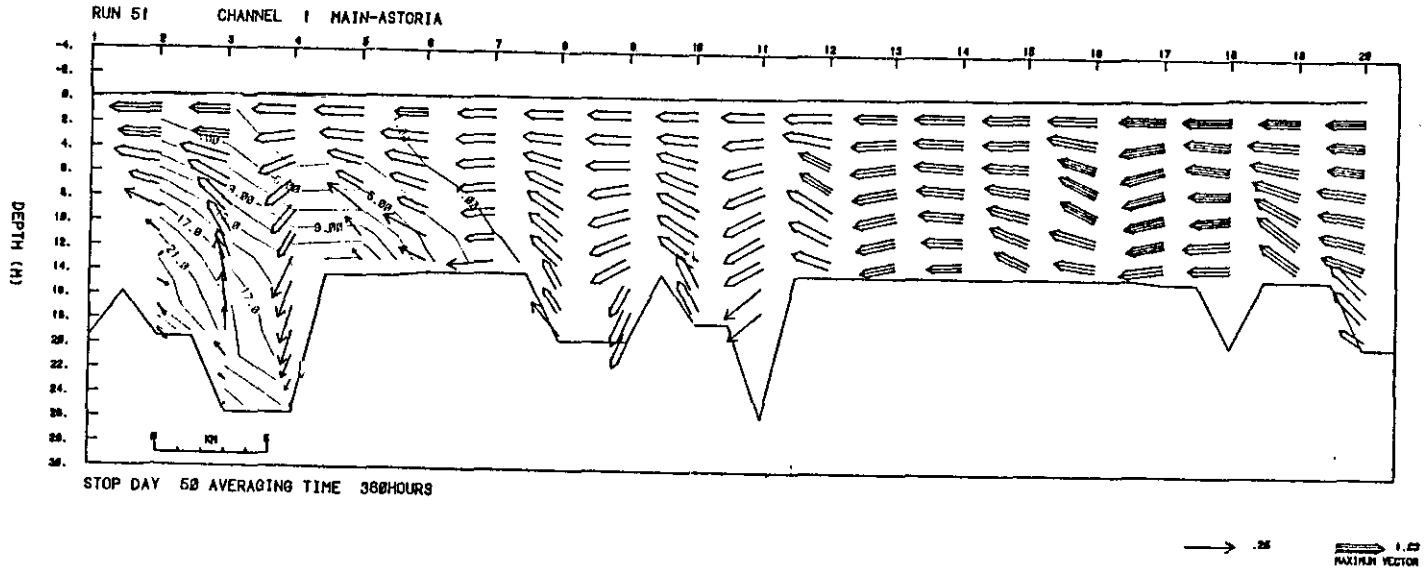


Figure 40a. Channel 1, 15-day mean. Mean currents and salinities (m/s and ‰).



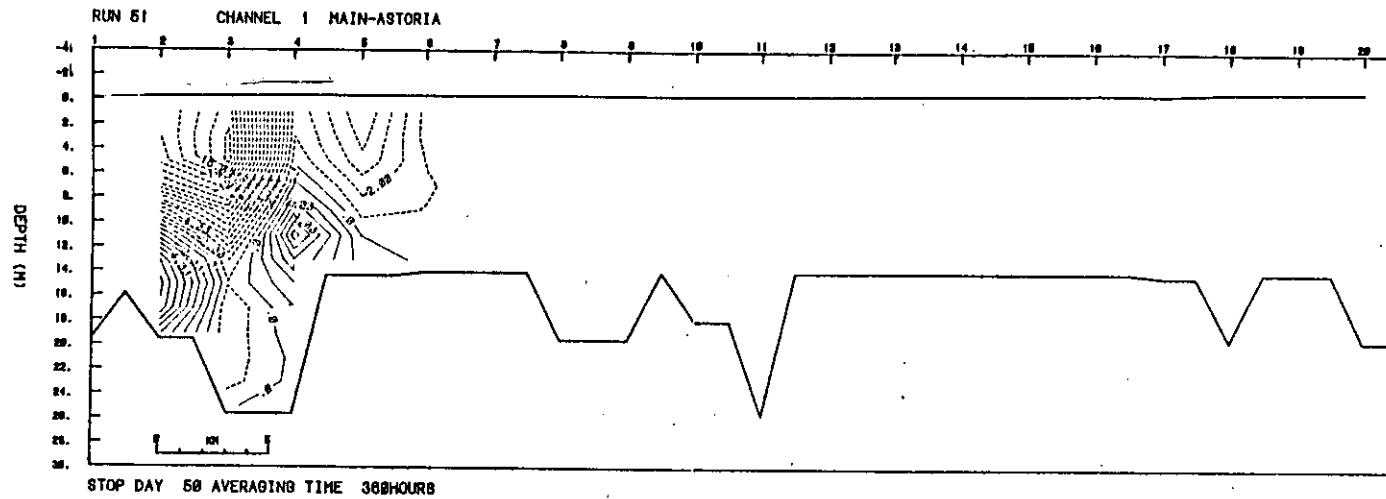


Figure 40b. Channel 1, 15-day mean. Salt flux ( $\text{kg/s} \cdot 10^3$ ).

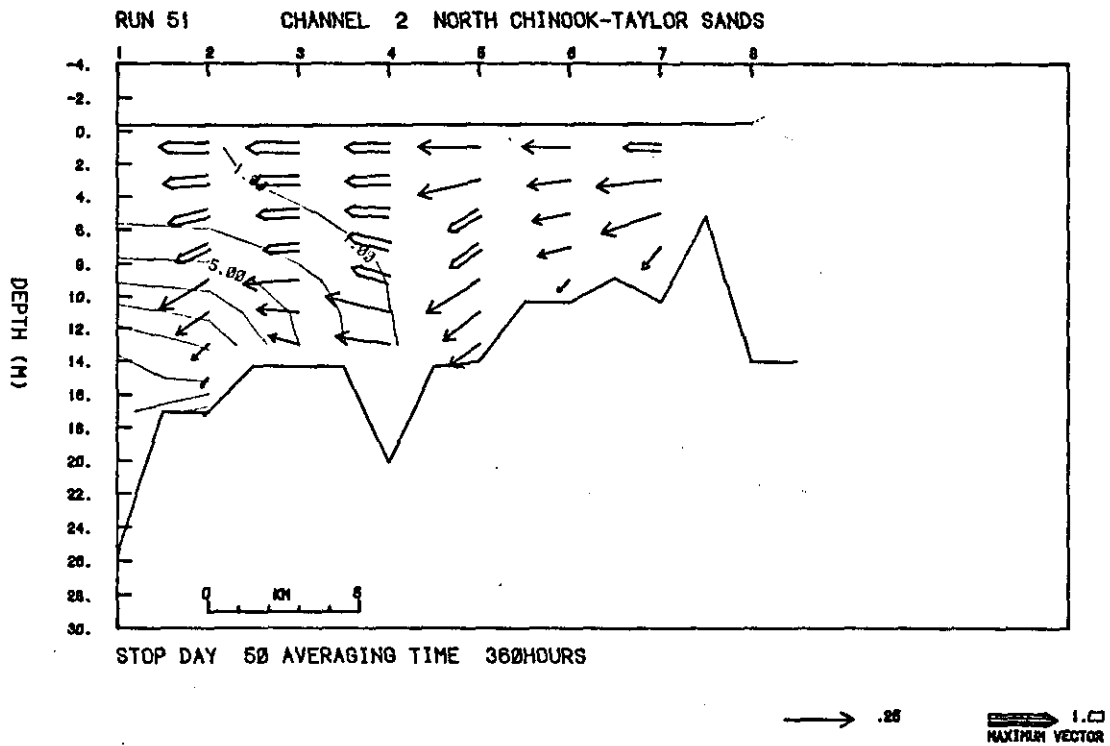


Figure 40c. Channel 2, 15-day mean. Mean currents and salinities (m/s and  $\sigma_{\theta}$ ).

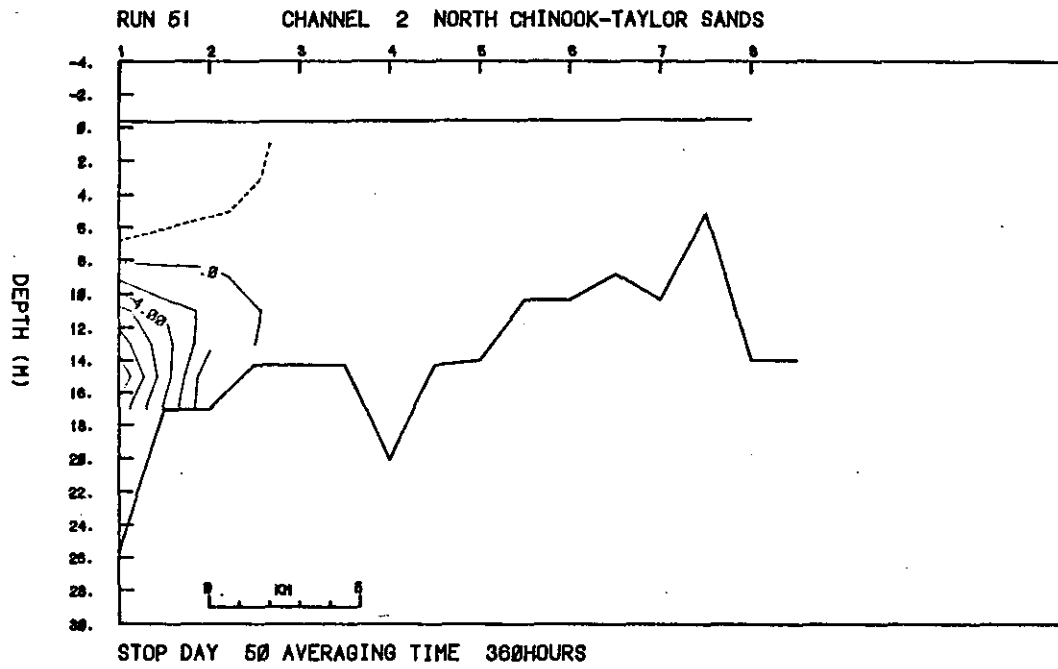


Figure 40d. Channel 2, 15-day mean. Salt flux ( $\text{kg/s} \cdot 10^3$ ).

The major forcing for the estuary is the oceanic tide and the majority of the results can be explained in terms of the interaction of the tide and the riverflow. The nature of the  $M_2$  and  $K_1$  tides is discussed in Volume I and Jay (1984). The semidiurnal tide in the lower estuary is a mixture of both progressive and standing waves which amplifies between the mouth and Tongue Point and then decays upstream. In the upper part of this estuary, upstream of Skamokawa, the wave becomes purely progressive. Tidal dispersion is the primary mechanism for maintaining the salt balance of the estuary against seaward advection by the riverflow. The frictional drag by the channel bed and sides on the tidal currents produces the energy for turbulent mixing; therefore, the strength of the tidal currents control the vertical mixing of salinity and momentum. The stratification, however, has the effect of dampening the turbulent fluctuations and the mixing which further reinforces the dependence of salinity field on the amplitude of the tidal currents. There is also dynamical connection between the time and space varying salinity field and the current field through the baroclinic pressure gradient. Thus the density field affects the profiles of the tidal currents generally producing a flood profile which is uniform or increases with depth and an ebb profile which is strongly sheared with maximum speeds at the surface. These tidal processes are well reproduced by the model and are the reason why successful simulation of the marked neap-spring differences in tidal excursion, salinity stratification and mean and extreme salt intrusion lengths were achieved for low flows. At high flows, the stratification is maintained against neap-spring changes in advection and mixing by the riverflow component of the circulation and marked differences in intrusion length and stratification were not observed in the data. Again the simulation reproduces these high flow observations successfully, which indicates that the simple semi-empirical eddy coefficient formulas adopted in Section 2.3.2. adequately determine the turbulent mixing under a range of tidal and riverflow conditions.

The discussion above could have equally well been made from the current meter and tide gauge observations alone (Jay 1984), though the model does help enormously in visualizing the tidal circulations. The model, however, does allow important conclusions to be drawn in the areas of tidal residual flows and the interaction of the main channels which would be difficult to obtain from observations limited in time or in spacial coverage. One of the principal conclusions is that non-linear effects combined with topographic changes such as shoals or channel constrictions can strongly modify the basic weak density current circulation. The results generally confirm the studies of non-linear tidal residual circulations of Ianniello (1979, 1981). Thus, non-linear effects in the deep hole seaward of the Hammond reach of the navigation channel weakens or eliminates residual upstream flow in that region, breaking the Navigation Channel into two distinct regions of upstream bottom flow. Similarly, in the North Channel there is almost non-existent bottom upstream mean flow west of the bridge, but moderate upstream flows due to the shoaling east of the bridge. The insistance of these cells of upstream near-bottom residual flows may have important implications for the transport and fate of organic and inorganic materials within the estuary.

The second area where the model is the main source of information is in the interaction of the channels and the relative distribution of flows and salinity between channels. The conclusions drawn from the model results are that the North Channel has relatively large tidal volume flows and a relatively larger proportion of the riverflows than the Navigation Channel west of Tongue Point. The mean flows in the North Channel are made up of flows diverted from the main Navigation Channels through Grays Bay and across Taylor and Desdemona Sands. At low flows, because of the larger tidal salt flux in the North Channel, salinity tends to intrude relatively farther east than in the Navigation Channel. At high flows there is a more even balance between tidal salt and mean salt fluxes in the two channels, so that the intrusion lengths are more similar. Biological implications are that the two major channels should not be treated separately and that the path of a small organism in the lower estuary over several tidal cycles is probably quite complicated with some probability of being carried from one channel to the other via the shallow cross-channels, across the sands, or due to exchange at the channels' junction at Clatsop Spit.

#### 3.1.5. Extreme Low Flow Simulations

The previous sections discussed the model simulations for periods when data for verification was available and forcing functions (tidal elevation and riverflow) were prescribed from observations. In this section, the model is used in a predictive mode for a very low riverflow situation, which was not observed during any of the data collection periods. A riverflow of approximately  $2,000 \text{ m}^3/\text{s}$  has been observed in historical records during the 1930s (Jay-personal communications), and though such a low flow is unlikely today because of storage and flow regulation by the hydroelectric schemes of the upper Columbia River, it is of interest to determine the salt intrusion characteristics under such low flow conditions. This is important for shallow productive regions such as Cathlamet and Grays Bays, which have a largely freshwater-based ecology. Thus, if in the future (due to severe drought) the Columbia River<sub>3</sub> flow falls to the minimum historically observed level of  $2,000 \text{ m}^3/\text{s}$ , an estimate of the salinity effects on the ecology of Cathlamet Bay may be made using the simulations presented in this section.

A 10-day period was simulated using the observed tide at Jetty A from May 25-June 4, 1981, which corresponds to days 21-30 of the spring 1981 simulations (Figure 7a). This tide was used because of the large amplitude difference between the neap and spring tides, the similarity of this 10-day period with the 10-day October 1980 tide at Jetty A (Figure 6), and because this tide was also used for the historical simulations in Section 3.2. Riverflow was held constant at  $2,000 \text{ m}^3/\text{s}$ , divided equally between the Main Channel and the Upriver-Tidal Channel. The salinity field was initialized to a high tide 29 hours after  $t = 0$ , and the same initial salinity field as the October 1980 simulation was used. Evidently this initial salinity field may underestimate the high tide intrusion length. Since there is no other basis for determining the initial salinity field, and based on previous

simulations the adjustment to the current intrusion length is expected to occur rapidly (less than 2 days), this initialization is reasonable.

The simulation results (Run 27) are presented as 50-hour means and extremes representative of neap tides (day 2:22h-day 4:24h) and spring tides (day 8:22h-day 10:24h). The neap and spring tidal ranges are 2.23 and 3.68 m, respectively. The sections should be compared directly with the results for the October 1980 simulations for channels 1, 2, 4 and 7 (Figures 19-26). The subsidiary channels, 4 and 7, are included, since they are the feeder channels for Cathlamet and Grays Bay, respectively. The results will be discussed by channel and compared directly with the October 1980 simulations.

#### Channel 1 (Figures 41, 45, 19 and 23)

For the neap tide, the main part of the mean salinity field has not intruded much farther than the October 1980 simulation. The 1 ‰ isohaline now reaches Altoona (14) rather than Rice Island (12); stratification is similar and the density current flow penetrates to grid number 12. Maximum salinities for the neap tide are less stratified than in October, particularly upstream of Rice Island (12). The low salinity tail of the intrusion penetrates to grid number 17 (Three Tree Point), partly due to the larger influx of salt from channels 2, 3 and 7 on the flood tide. Minimum salinities are similar, with slightly more stratification for this very low flow period.

The spring tide simulations (Figures 45 and 23) are again similar with the stronger mixing, weaker stratification, and weaker and more patchy residual currents. Downstream of Tongue Point, the isohaline patterns are similar except for higher salinity values. The low salinity tail of the intrusion is now much more saline and much longer than in October. This again is due to the greater influence of the other channels that connect with channel 1 between Tongue Point and Pillar Rock. This is even more clearly demonstrated by the maximum salinity sections, where the 5 ‰ and 1 ‰ isohalines reach to Jim Crow Sands (15) and to the northern tip of Puget Island (21), respectively. The extended low-salinity tail is also present in the salinity plots (Figure 45c).

#### Channel 2 (Figures 42, 46, 20 and 24)

The sections for the North Channel for the two periods have again similar patterns for the mean and extreme fields. The very low flow simulations indicate that the salinities have increased by 4-6 ‰ over the October simulations for the neap tide and by 6-8 ‰ for the spring tide. The increase in salt content between spring and neap tides for run 27 contrasts with a small decrease for the October simulations on run 26. The maximum salinities show much higher salinities and stronger horizontal gradients in the eastern end of the channel, which supports the interpretation that channel 2 has become a source of high salinity water for the upstream reaches of channel 1. This mechanism is not an important source of salt for channel 1 in October, since the higher riverflows keep the salinity intrusion downstream of the Tongue Point section for most of the tide.

#### Channel 4 (Figures 43, 47, 21 and 25)

In the October simulation (Figures 21 and 25), there was only a small penetration of salt at the Tongue Point end of the channel; and, evidently the salinity was controlled by the neap-spring changes of the salinity field in the Navigation Channel at Tongue Point. In the extreme low flow simulations (Figures 43 and 47), low salinities (1-5 ‰) are present throughout the channel with very weak horizontal gradients. The channel is evidently being fed with low salinity water, probably by tidal dispersion, from the Navigation Channel via both entrances (Tongue Point and Jim Crow Point) and the Woody Island Channel (Channel 6). As pointed out above, the source of the low salinity water upstream of Tongue Point is primarily the North Channel.

#### Channel 7 (Figures 44, 48, 22 and 26)

Channel 7 salinities are about 4 ‰ greater than in October. The distributions and differences between neap and spring have very similar patterns. The mouth of the channel (Knappton) has large horizontal gradients, particularly at the end of the spring flood, which is due to relatively higher salinities for the spring tide in channel 2.

The main conclusion from this predictive simulation is that lowering the riverflow from 4,000 m<sup>3</sup>/s increases the relative difference in salt content between channels 1 and 2 particularly on spring tides. There is now an increase in the number of sources of salinity for the main Navigation Channel upstream of Tongue Point. This promotes in this region an extended low gradient, relatively well-mixed low-salinity tail, which acts as a low salinity source for Cathlamet Bay via channels 4 and 6, and to a lesser extent the eastern end of Grays Bay. Thus, Cathlamet Bay is relatively uniformly flooded with low salinity water, which does not exceed 5 ‰ for spring floods and can fall below 1 ‰ on ebbs. Thus plants and animals that can tolerate 1-5 ‰ brackish conditions could survive very low river flow conditions, compared to the normally fresh habitats.

It is further noted that the spring-neap differences in the salinity fields which are so prominent for riverflows of 4,000 m<sup>3</sup>/s are not present at 2,000 m<sup>3</sup>/s. This implies that a riverflow of 2,000 m<sup>3</sup>/s is not able to maintain a highly stratified water column against weak tidal mixing on a neap tide, thus the salinity distribution resembles the spring tide situation since vertical mixing is relatively more important.

The above conclusion is based on a prediction using a model that has been calibrated and verified for existing low and high flow conditions. Thus even though the model is well proven for riverflows greater than 4,000 m<sup>3</sup>/s, the prediction should be used with caution and an awareness of the model's limitations. However, the simulation is the best quantitative estimate that can be made at this time of the effects of very low flows in the salinity region. The simulation is a good example of how a well-calibrated model can be used to make quantitative predictions concerning the hydrodynamics of the estuary caused by environmental changes (such as riverflow reductions, channel

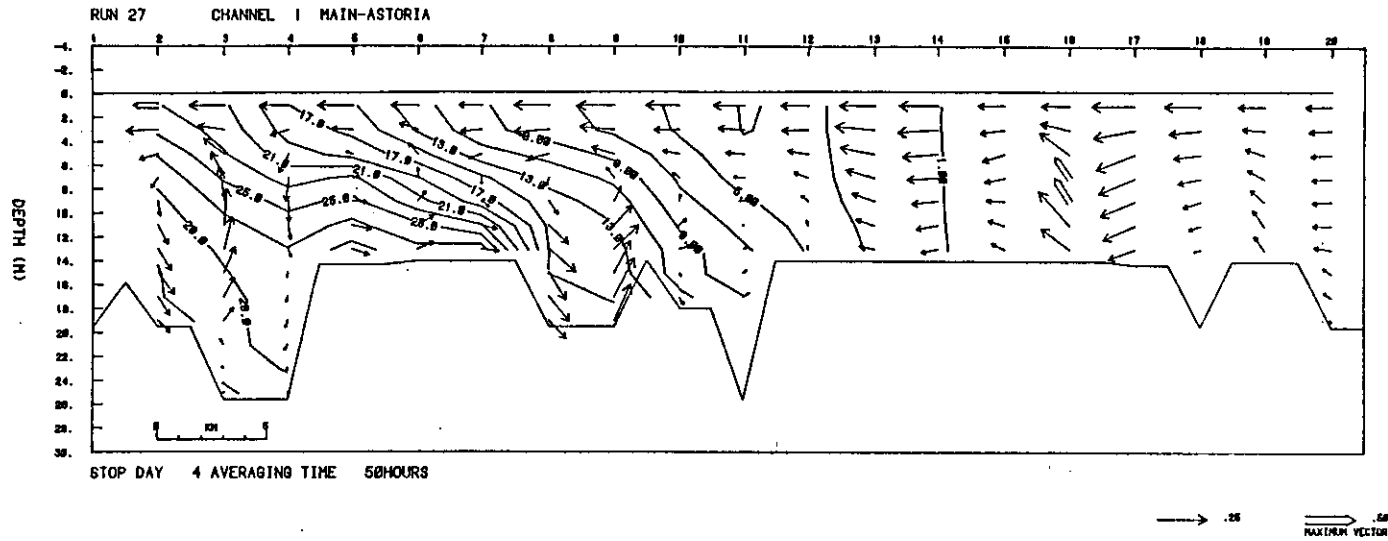


Figure 41a. Channel 1, neap tide period (constant riverflow =  $2000 \text{ m}^3/\text{s}$ ). Mean currents and salinities (m/s and ‰).

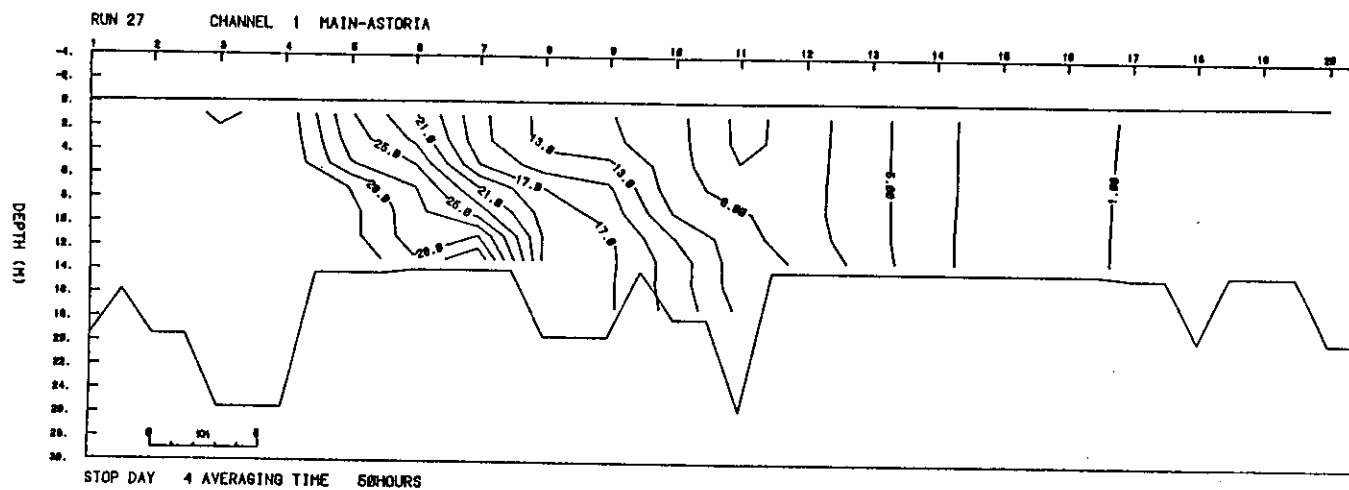


Figure 41b. Channel 1, neap tide period (constant riverflow =  $2000 \text{ m}^3/\text{s}$ ). Maximum salinities.

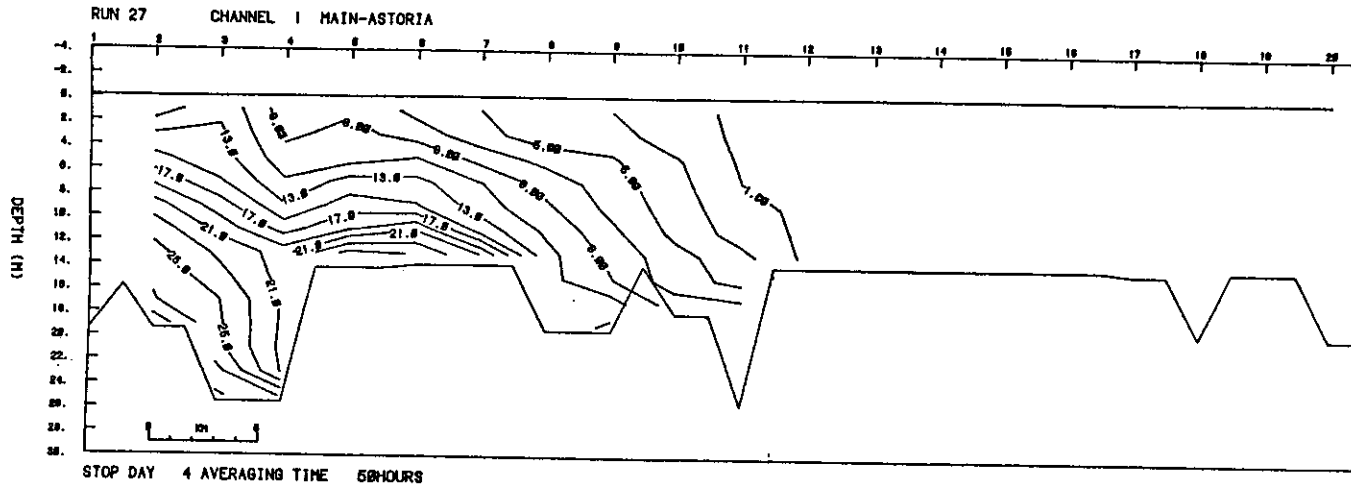


Figure 41c. Channel 1, neap tide period (constant riverflow =  $2000 \text{ m}^3/\text{s}$ ). Minimum salinities.

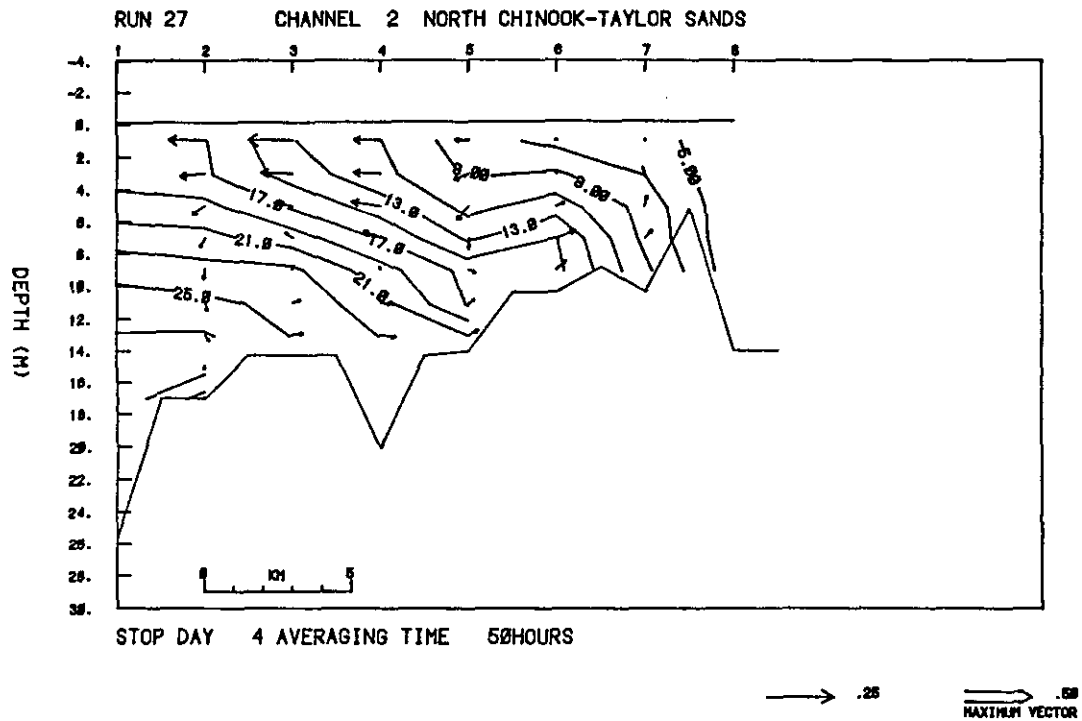


Figure 42a. Channel 2, neap tide period (constant riverflow =  $2000 \text{ m}^3/\text{s}$ ). Mean currents and salinities (m/s and  $^{\circ}/\text{oo}$ ).

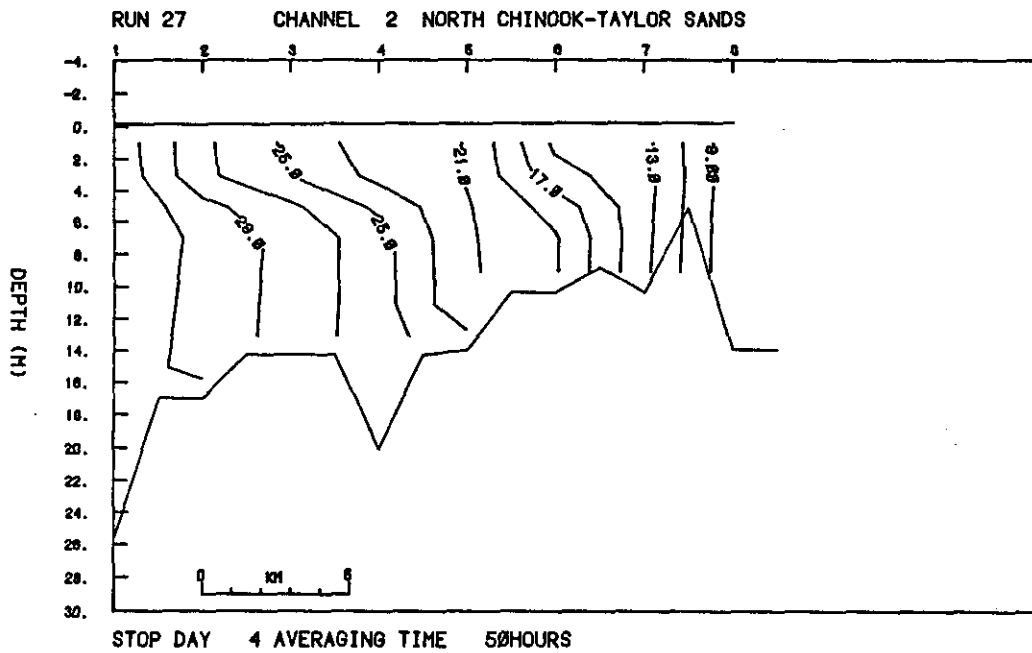


Figure 42b. Channel 2, neap tide period (constant riverflow =  $2000 \text{ m}^3/\text{s}$ ). Maximum salinities.

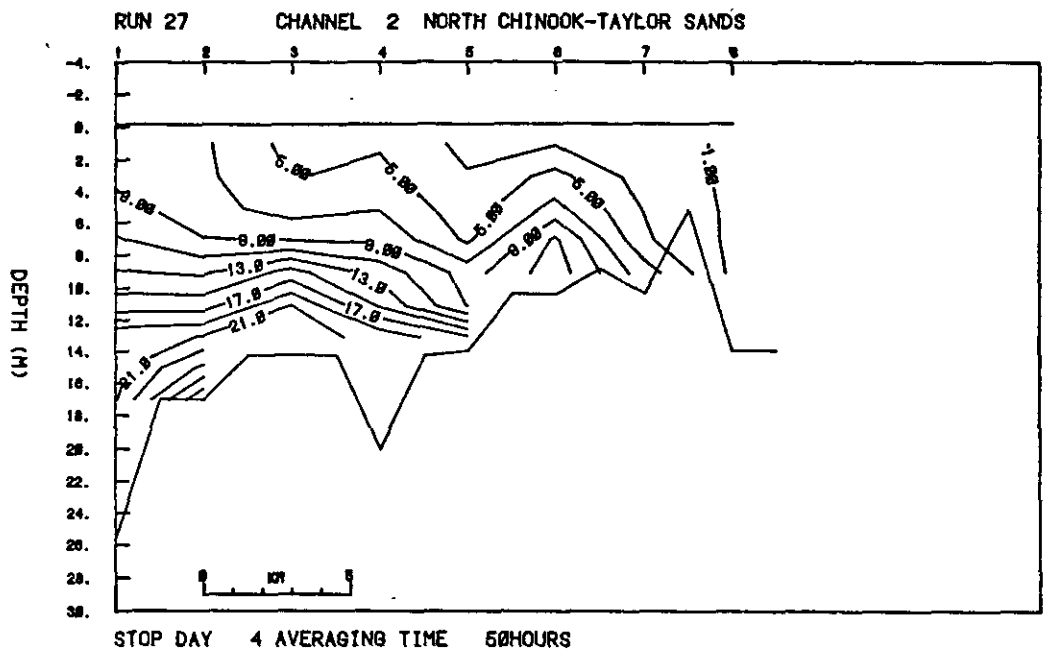


Figure 42c. Channel 2, neap tide period (constant riverflow = 2000 m<sup>3</sup>/s). Minimum salinities.

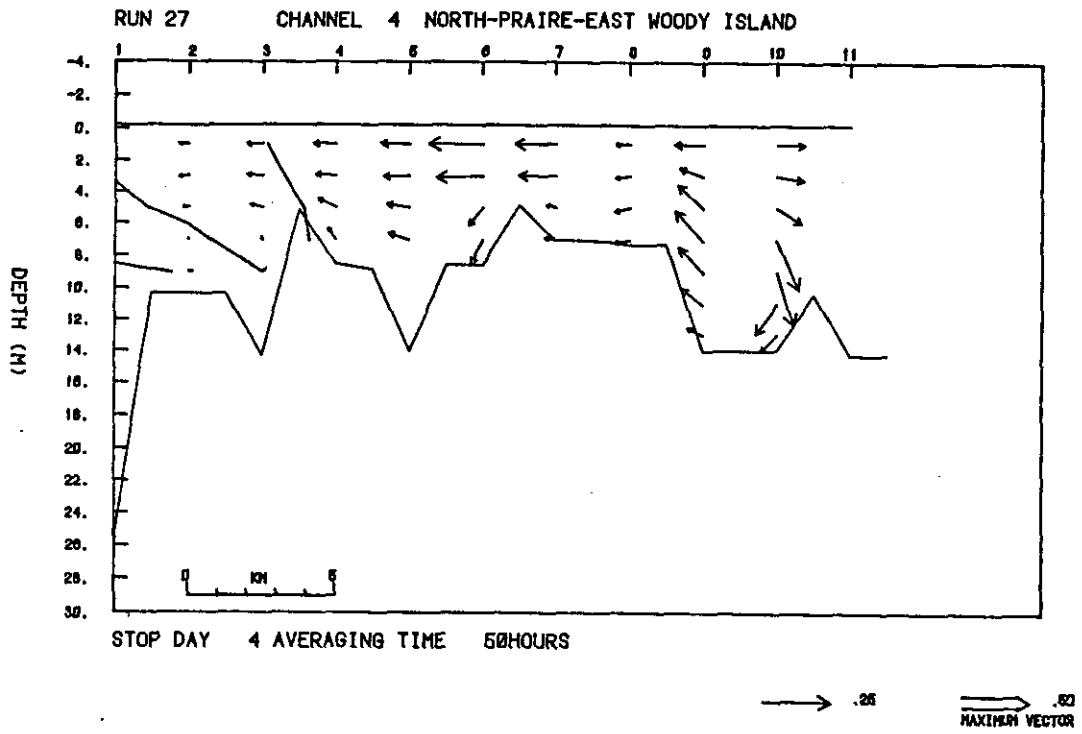


Figure 43a. Channel 4, neap tide period (constant riverflow =  $2000 \text{ m}^3/\text{s}$ ). Mean currents and salinities (m/s and  $^{\circ}/\text{oo}$ ).

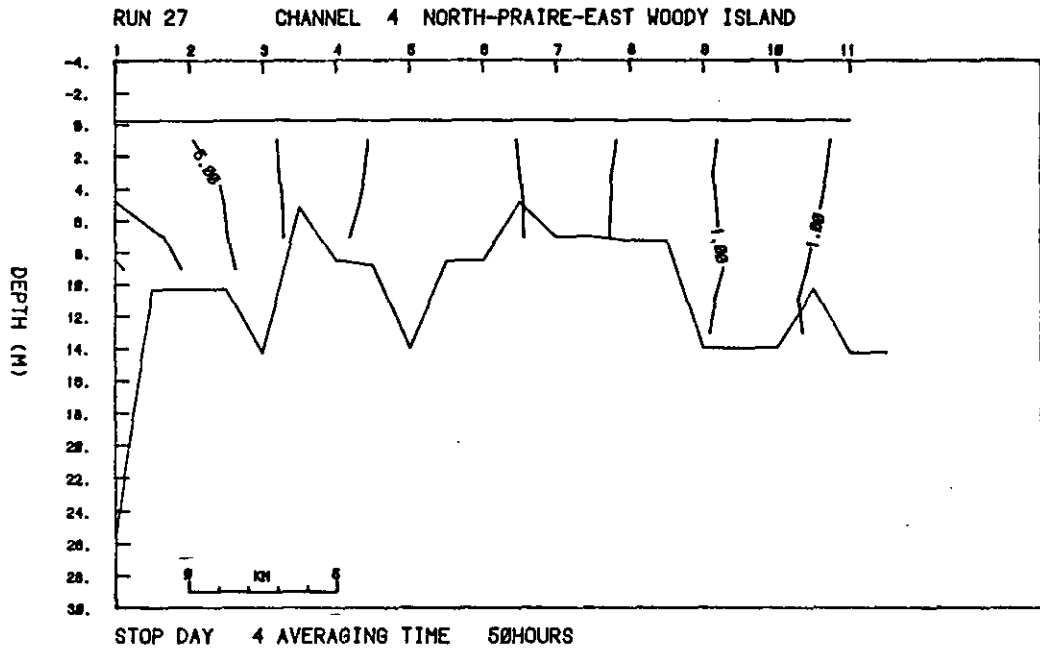


Figure 43b. Channel 4, neap tide period (constant riverflow = 2000 m<sup>3</sup>/s). Maximum salinities.

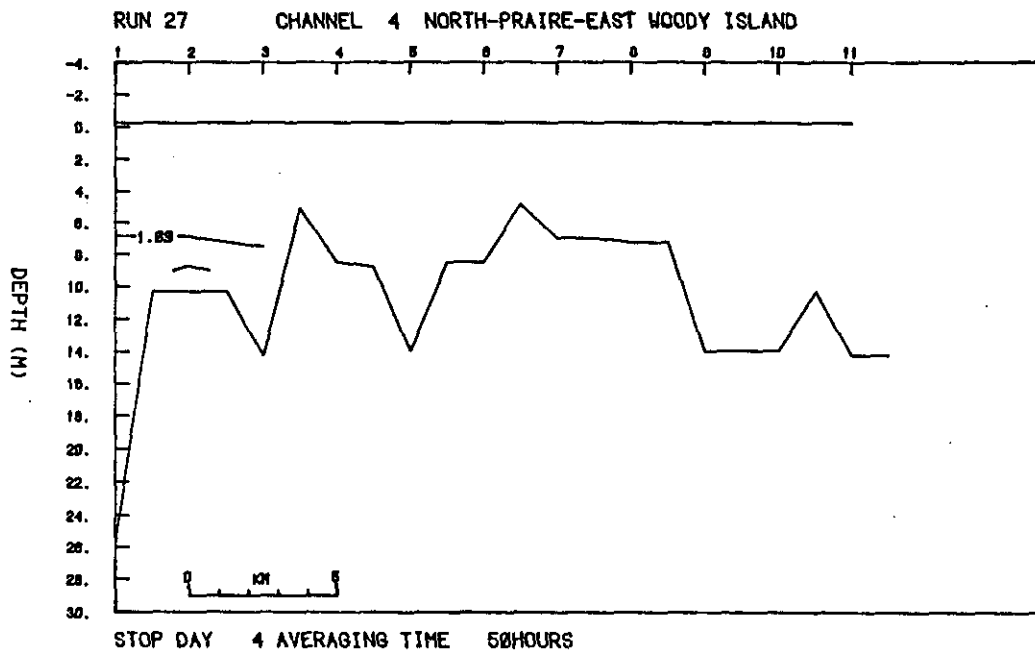


Figure 43c. Channel 4, neap tide period (constant riverflow = 2000  $m^3/s$ ). Minimum salinities.

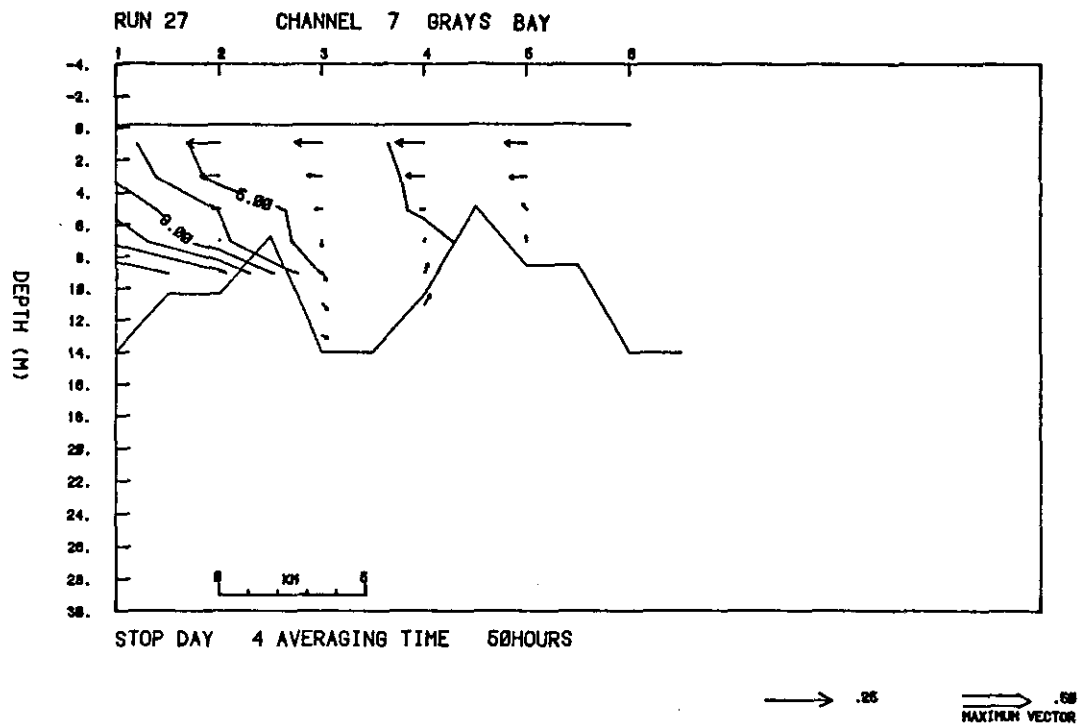


Figure 44a. Channel 7, neap tide period (constant riverflow = 2000 m<sup>3</sup>/s). Mean currents and salinities (m/s and ‰).

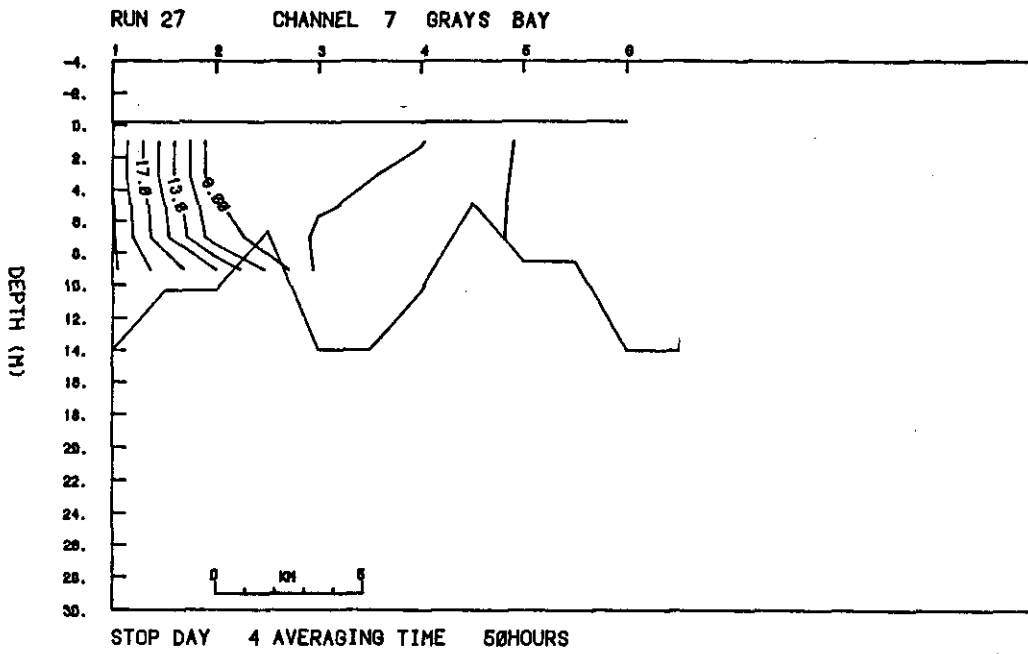


Figure 44b. Channel 7, neap tide period (constant riverflow = 2000 m<sup>3</sup>/s). Maximum salinities.

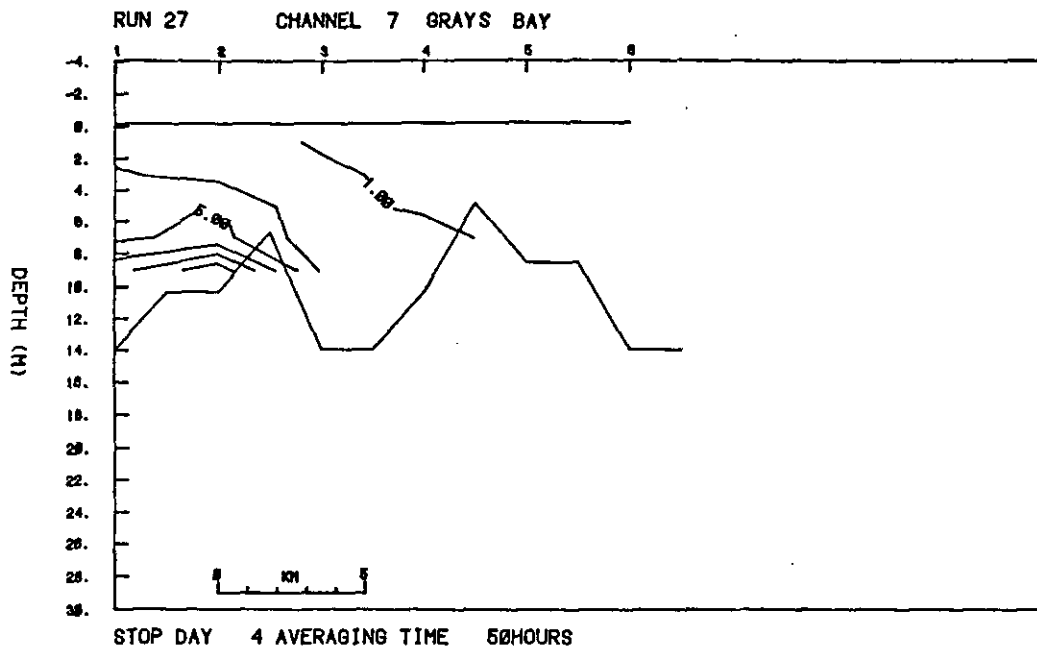


Figure 44c. Channel 7, neap tide period (constant riverflow = 2000 m<sup>3</sup>/s). Minimum salinities.

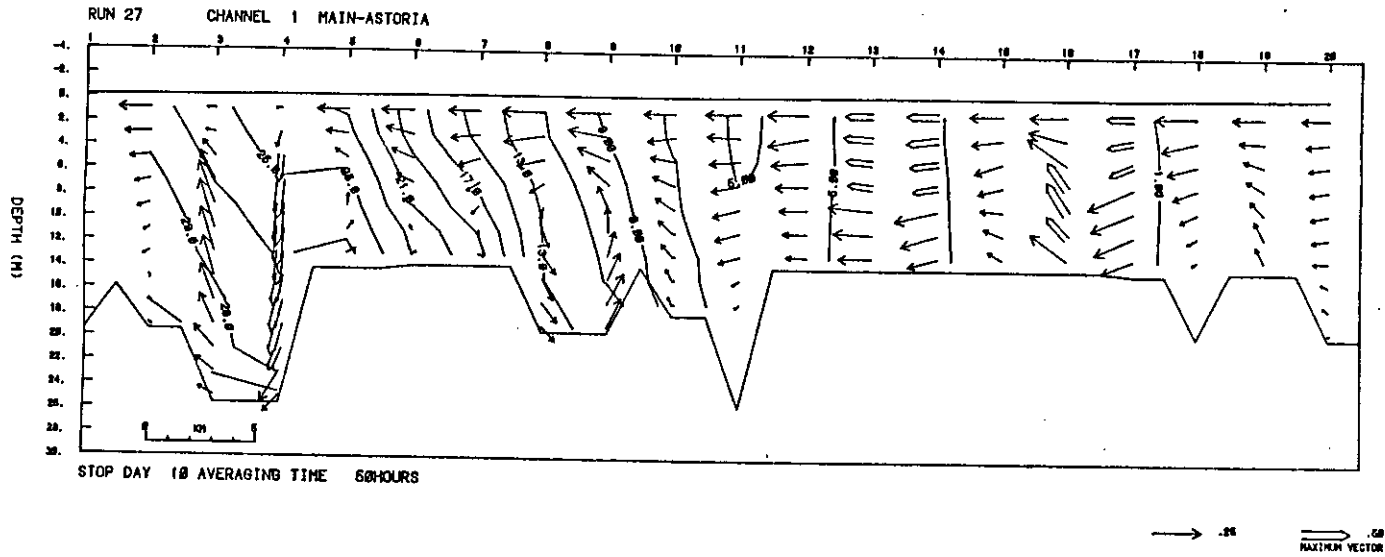
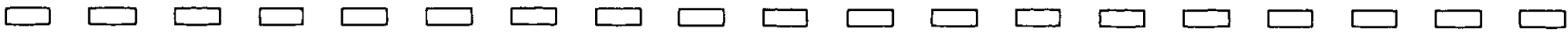


Figure 45a. Channel 1, spring tide period (constant riverflow =  $2000 \text{ m}^3/\text{s}$ ). Mean currents and salinities (m/s and ‰).



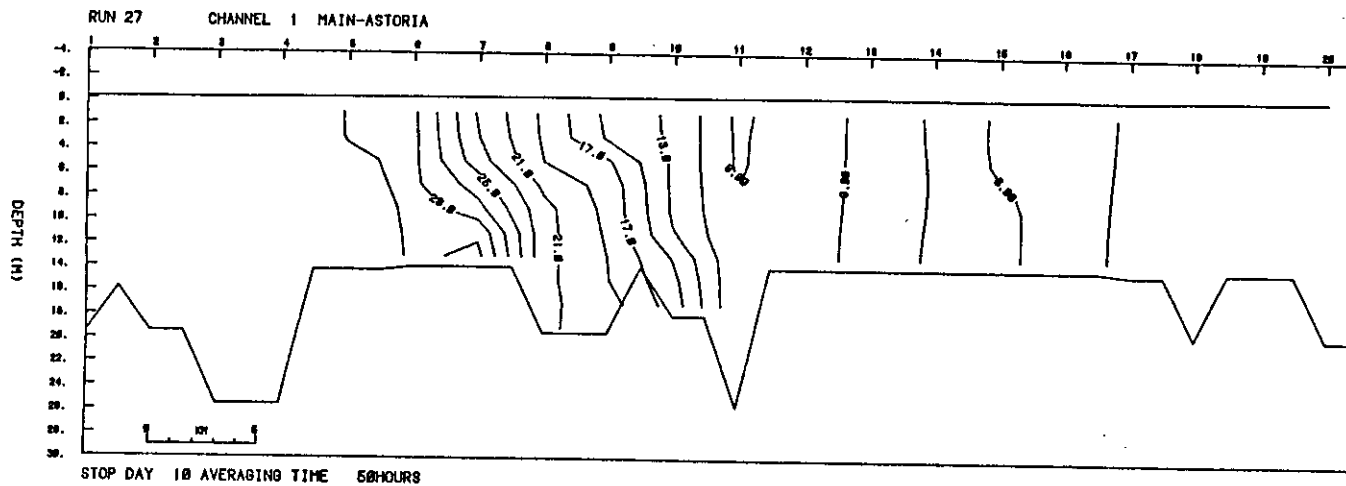


Figure 45b. Channel 1, spring tide period (constant riverflow =  $2000 \text{ m}^3/\text{s}$ ). Maximum salinities.

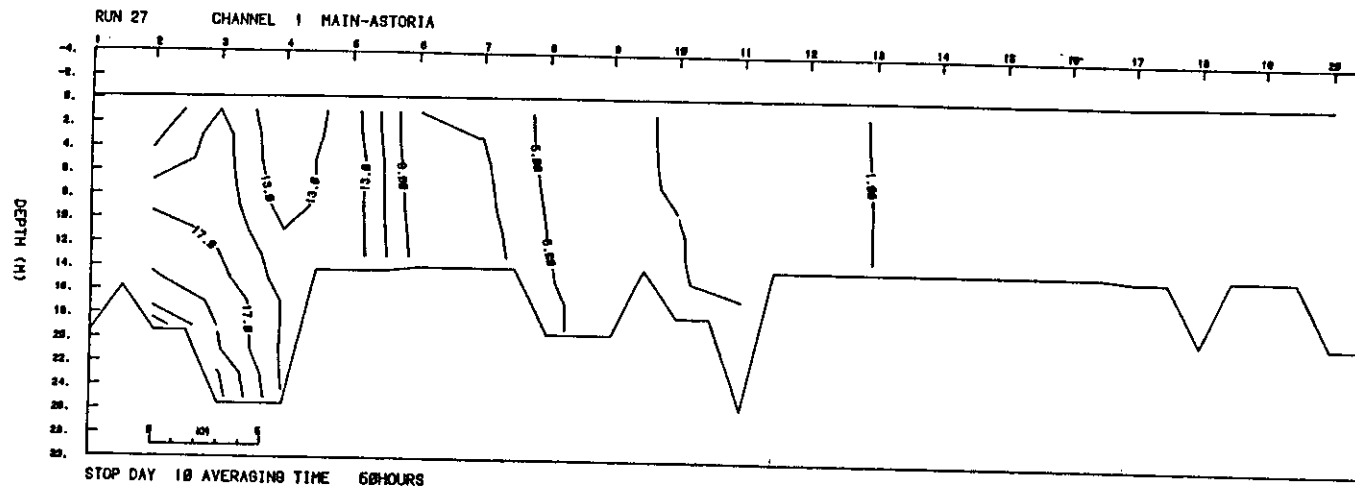


Figure 45c. Channel 1, spring tide period (constant riverflow =  $2000 \text{ m}^3/\text{s}$ ). Minimum salinities.

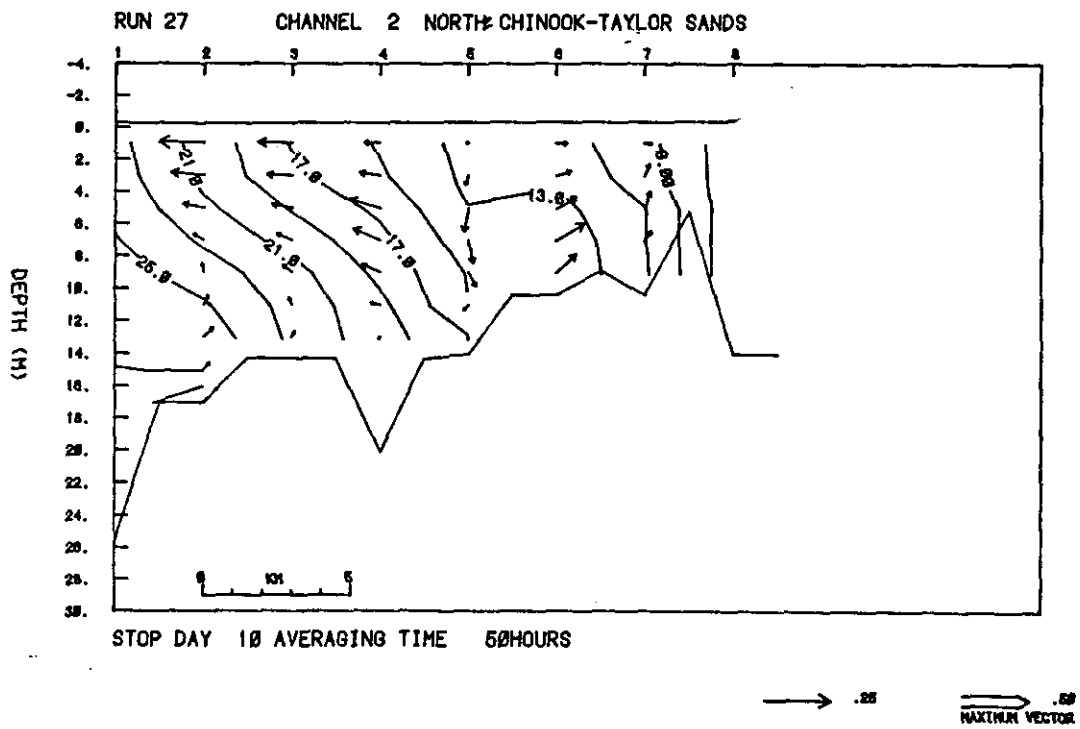


Figure 46a. Channel 2, spring tide period (constant riverflow = 2000  $m^3/s$ ). Mean currents and salinities (m/s and ‰).

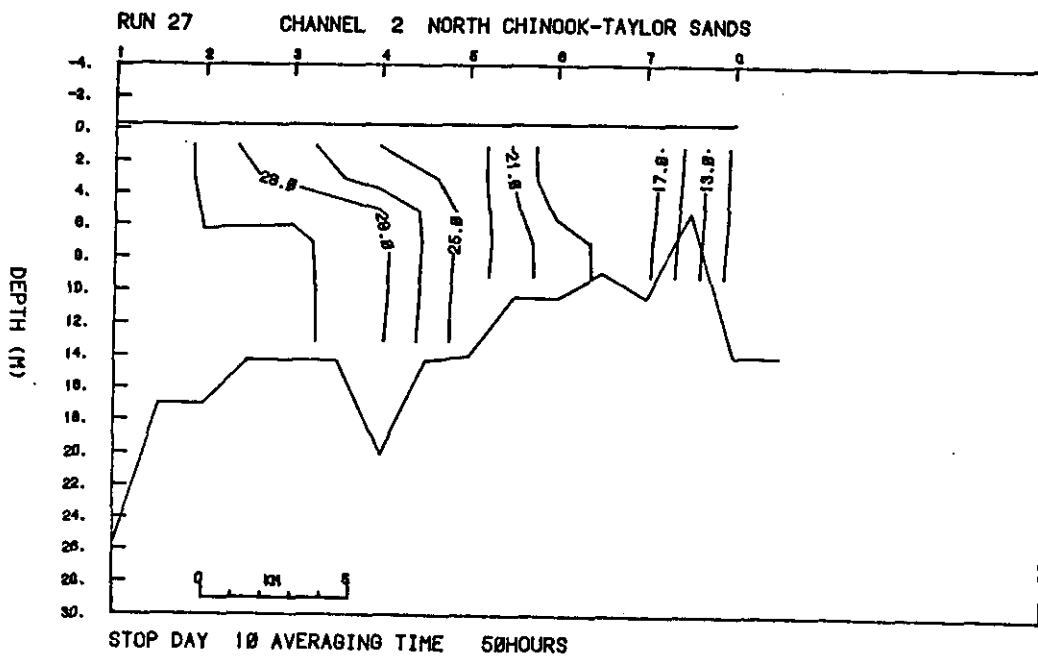


Figure 46b. Channel 2, spring tide period (constant riverflow = 2000 m<sup>3</sup>/s). Maximum salinities.

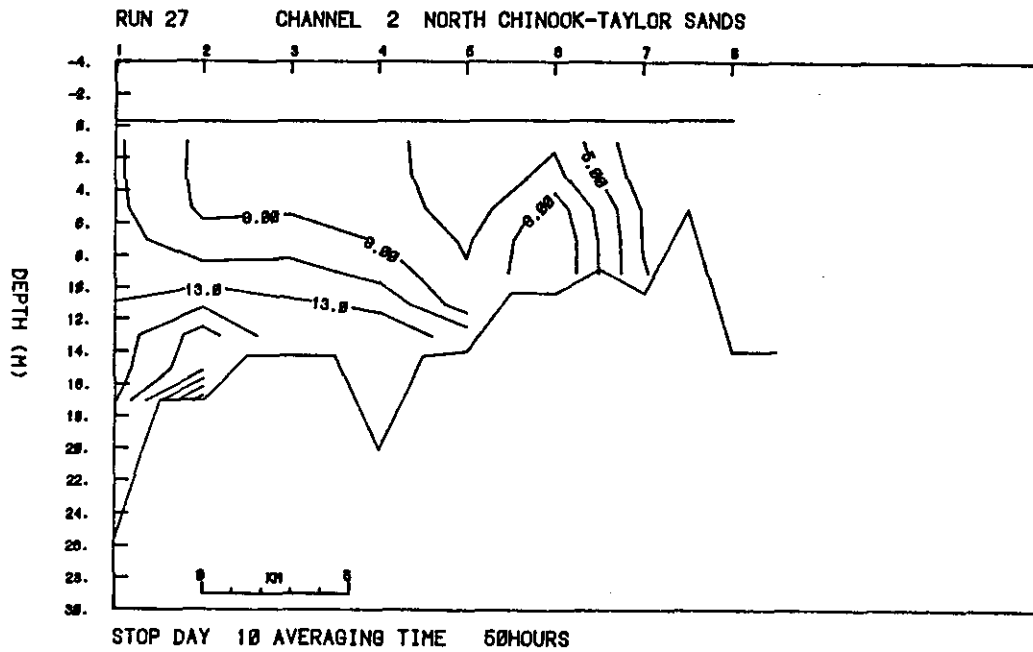


Figure 46c. Channel 2, spring tide period (constant riverflow = 2000  $\text{m}^3/\text{s}$ ). Minimum salinities.

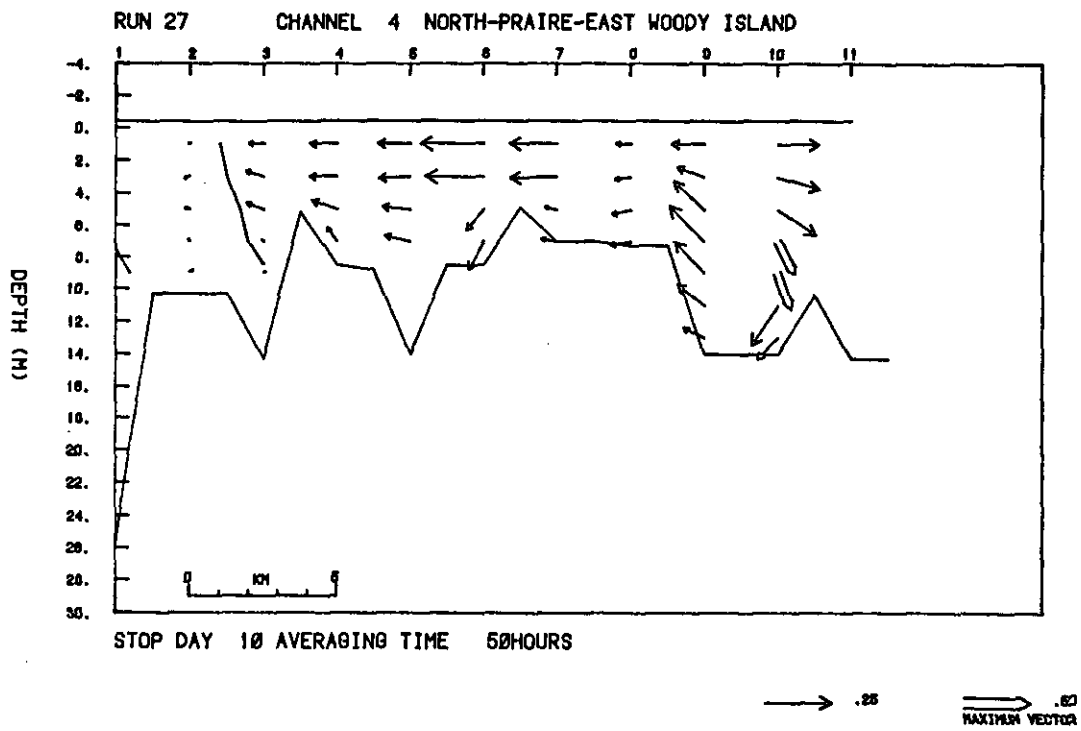


Figure 47a. Channel 4, spring tide period (constant riverflow = 2000 m<sup>3</sup>/s). Mean currents and salinities (m/s and ‰).

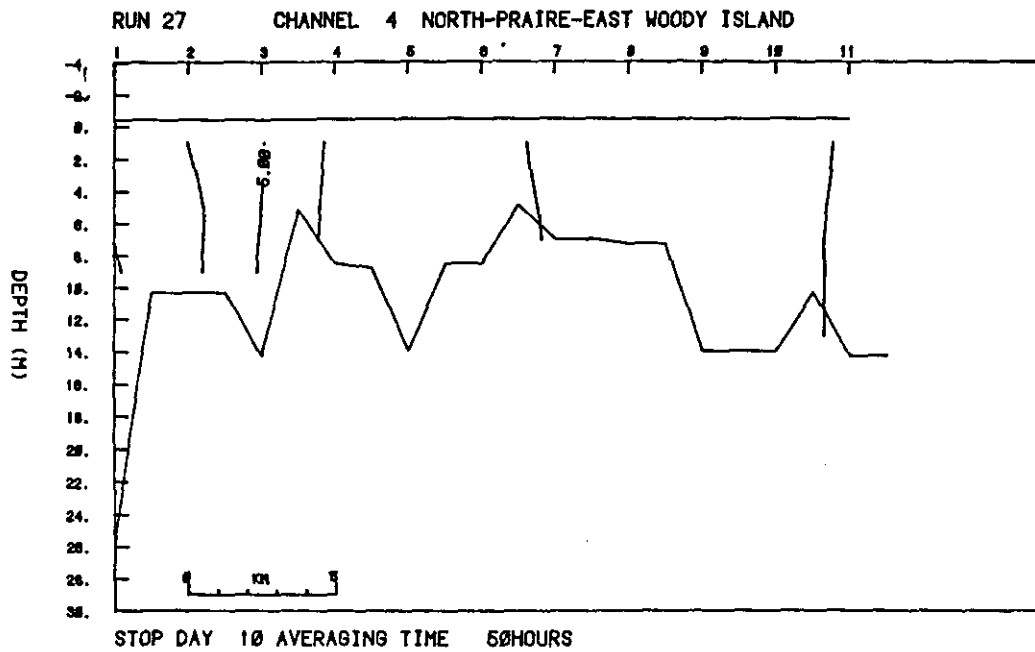


Figure 47b. Channel 4, spring tide period (constant riverflow = 2000 m<sup>3</sup>/s). Maximum salinities.

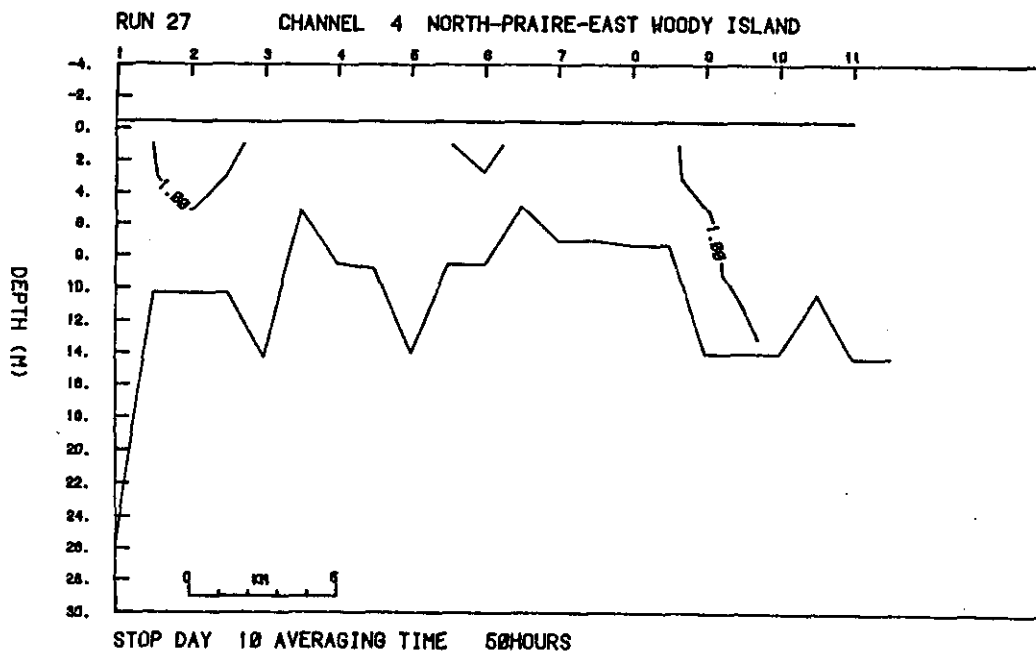


Figure 47c. Channel 4, spring tide period (constant riverflow = 2000 m<sup>3</sup>/s). Minimum salinities.

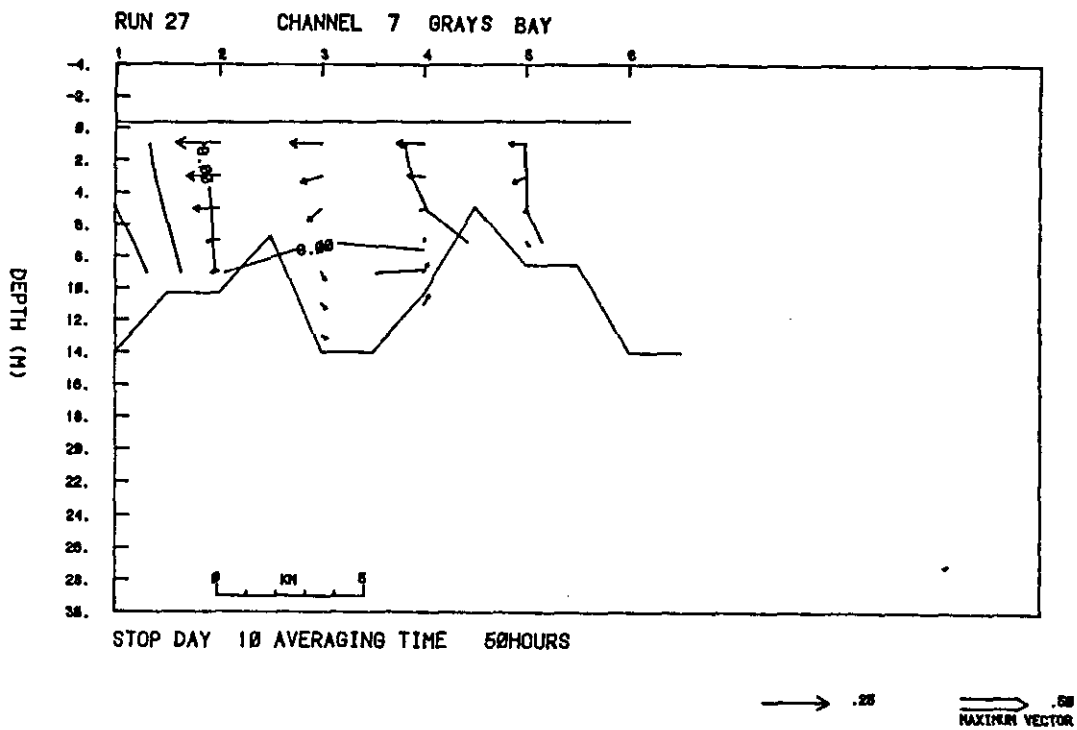


Figure 48a. Channel 7, spring tide period (constant riverflow = 2000 m<sup>3</sup>/s). Mean currents and salinities (m/s and ‰).

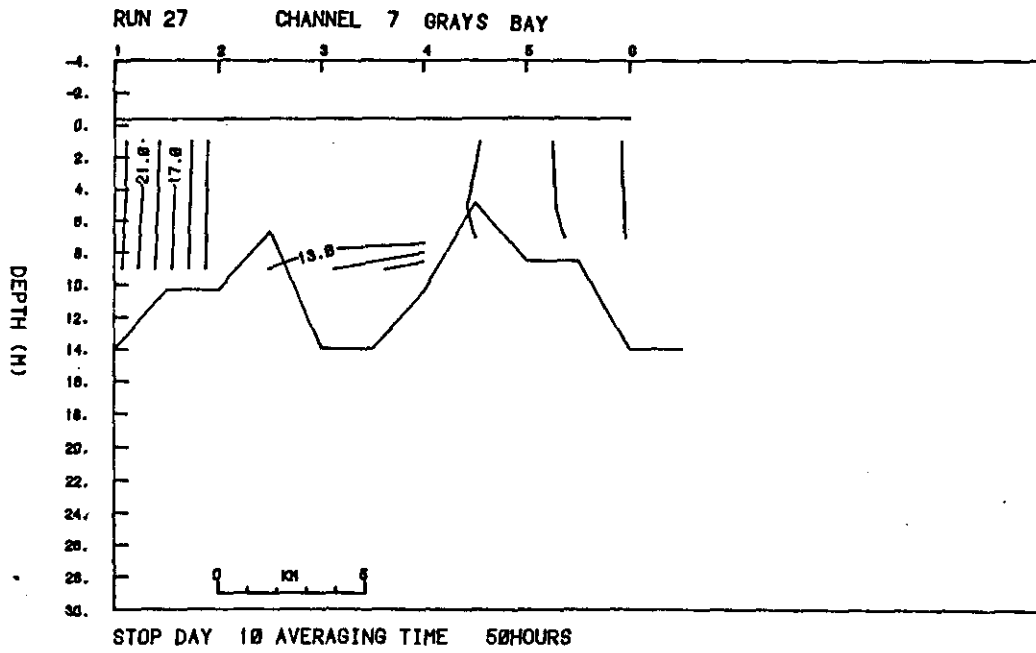


Figure 48b. Channel 7, spring tide period (constant riverflow = 2000 m<sup>3</sup>/s). Maximum salinities.

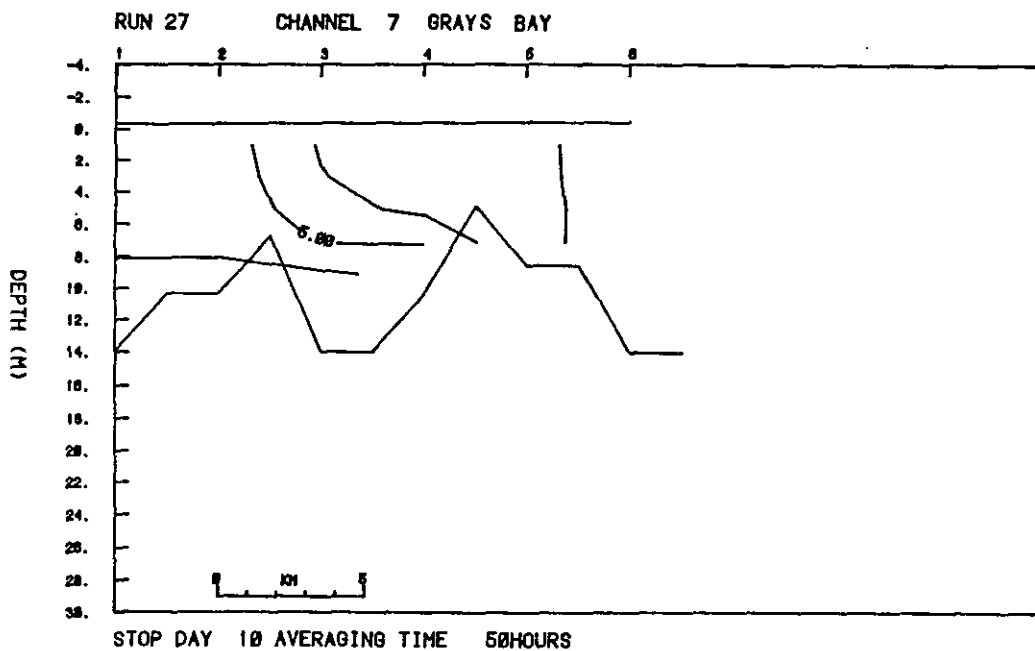


Figure 48c. Channel 7, spring tide period (constant riverflow = 2000 m<sup>3</sup>/s). Minimum salinities.

deepenings, etc.) that have not occurred yet or are extreme conditions that only have a small probability of occurring.

The effects of deepening the main Navigation Channel to 52 ft (15.9 m) between Clatsop Spit and Astoria and deepening the Entrance Channel to 67 ft (20.4 m) have been studied using an earlier version of the model (Hamilton 1983). The main results were an increase in the stratification<sub>3</sub> of the lower parts of the deepened channels for low flows (4,000 m<sup>3</sup>/s) and neap-tides. Upstream of Tongue Point there were negligible changes in salinity between base and plan.

### 3.2. SIMULATION OF THE 1868 ESTUARY

#### 3.2.1. Introduction

This section discusses the application of the channel model to the estuary using the bathymetry of 1868. The purpose is to simulate the circulation in the estuary prior to extensive dredging of the navigation channels and the Columbia River Bar and the construction of North and South Jetties. The hydrodynamic model is the only quantitative method that can provide estimates of the circulation in 1868, since the only physical oceanographic data available are some tidal height measurements. The tidal and subtidal distributions of current and salinity can be compared directly with the present day simulations previously discussed. Thus, the changes in the hydrodynamics brought about by a century of man's activities in the estuary can be estimated. The limitations of the model discussed in the previous sections will of course apply equally to the results of this section.

Bathymetric charts (1:20,000) from the 1868-1879 survey were supplied to this work unit by Northwest Cartography, Inc. A system of channels was set up for the estuary, using horizontal grid spacings similar to the 1980 model configuration. The channels and grid cells are shown in Figure 49 (compare with Figure 4), and channel names and statistics are given in Table 6. Only land areas that interfered with the channels have been removed from the chart. The islands and marsh areas in Cathlamet Bay were not quite as extensive in 1868 as in 1980; the estuary was more shallow except for the scour holes, which had similar depths; and shoal areas were less extensive and relatively deeper than at the present time. The most extensive changes have occurred at the mouth and in Cathlamet Bay. In 1868, the mouth was about twice as wide as at present, and there were two major entrance channels separated by a 12-ft deep shoal. Both entrance channels had an extensive bar positioned just seaward of the end of the present-day jetties (Grid Points #1, Channels 1 and 3), which had a depth of 24 ft below MLLW. The north entrance channel (Channel 3) occupied much of Baker Bay, and the Sand Islands did not exist. The cross-section in 1868 and 1982 between Cape Disappointment and Point Adams is shown in Figure 50. Proceeding upstream from the mouth to the Point Ellice-Astoria section, it can be seen from Figure 50 that the cross-sections are similar. The Desdemona Sands-Tongue Point Channel (4) of 1868 is also present in 1982, but it does not penetrate over the

Table 6. Channel Names for 1868 Bathymetry

<u>Channel Number</u>	<u>Name</u>	<u>Total No. Points</u>	<u>Horizontal Grid Spacing (km)</u>
1	South Main-Astoria	40	3
2	Chinook-Jim Crow Point	13	3
3	North Entrance-Baker Bay	6	3
4	Desdemona Sands-Tongue Point	5	3
5	Youngs Bay	5	3
6	North-Prairie-Clifton	14	2.5
7	Tongue Point Bar	4	2.5
8	Miller Sands	3	3
9	Prairie-Grassy Island	3	3
10	Grays Bay	6	3
11	Fitzpatrick Island	3	3.5
12	Cathlamet-East Puget Island	5	3.5
13	Upriver Tidal	<u>15</u>	3.5
	Total	122	

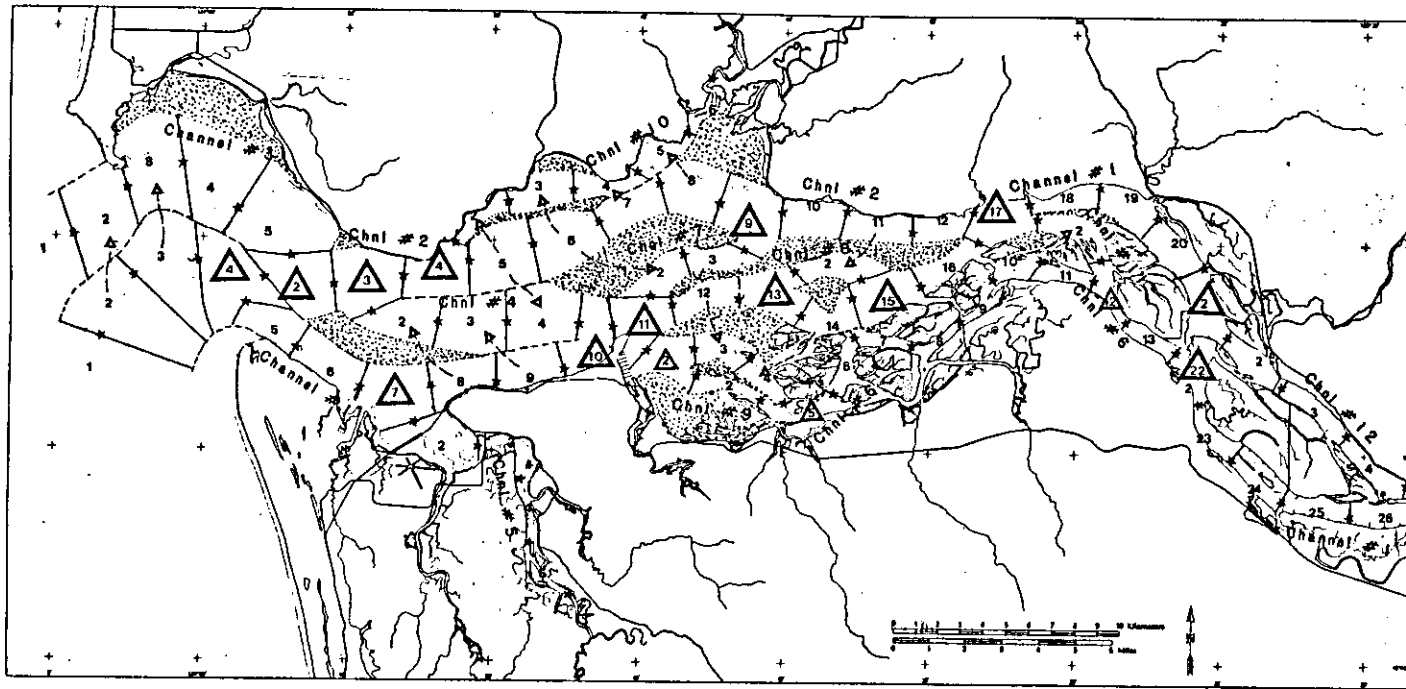


Figure 49. The channels and grid cells used for the schematization of the 1868 estuary. Grid cell number gives the position of elevation points, a star is the position of a transport point. Triangles denote channel junction grid points. Dashed arrows denote across barrier inter-channel connections.

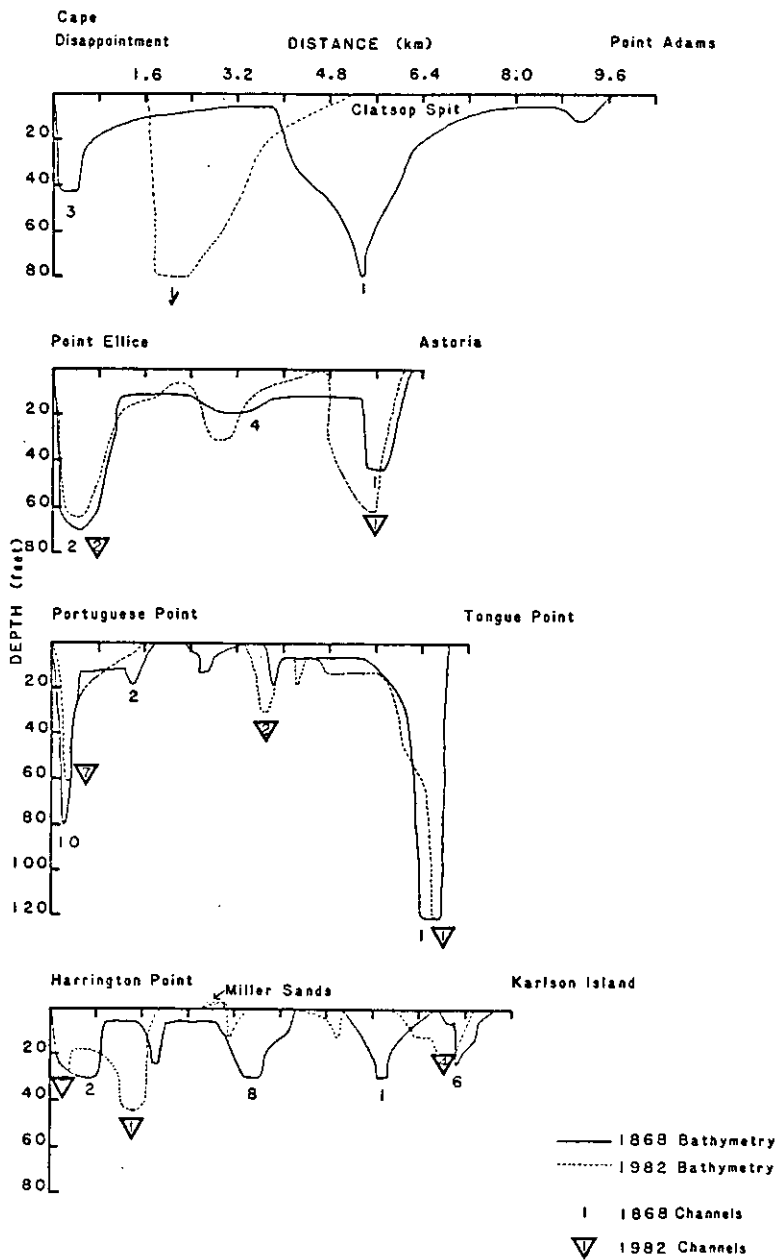


Figure 50. Cross-sections of bathymetry for 1982 and 1868 between indicated points (see Figure 5a).

shoals to connect with channel 1 as it did in 1868. The next section (Portugese Point-Tongue Point) is also quite similar for both periods, with the scour holes off both points still existing today. Upstream of Tongue Point, the major channels all shoal and their exact paths are sometimes difficult to determine. However Channels 1 and 2 remain separated on the north and south shores until they merge at Jim Crow Point. In 1868, channel 1 followed the approximate route of channels 6 and 4 in 1982, and channel 2 followed the present day route of channels 7 and 1. The section (Figure 50) between Harrington Point and Karlson Island shows the most change between the two dates. Except for the Main Navigation Channel, the subsidiary channels are much shallower today and the sandflats are less deep and more extensive than in 1868. It is also noted that in 1868 the Prairie Channel (Channel 6), which runs south of the islands in Cathlamet Bay, was much more isolated from the estuary north of the islands than it is at the present time. There was a barrier between channels 6 and 1 off Karlson Island, which is now no longer in existence (the junction of channels 4, 6, and 8, in Figure 4). Similarly in 1868, Lois Island did not exist and the marsh area in this southwest corner of Cathlamet Bay was crossed by a number of small channels, including the John Day Channel. Only the largest of these channels has been included as channel 9 for the 1868 model configuration.

The model was set up exactly as in the previous simulations. The channel cross sections corresponding to each grid point were digitized from the chart. The input tide was the same ten days as were used for the low flow run 27. Thus the input tide corresponding to 81/5/25-81/6/4 (days 20-30 of run 51) was used as a boundary condition for both channels 1 and 3. Riverflow was held constant for the ten-day period of the simulations. The neap and spring tide periods were taken to be day 2: 22h - day 4: 24h and day 8:22 h - day 10: 24h, respectively. The bottom friction coefficient (Table 2) was the same as before, and where the channels corresponded in the upper estuary, the slightly smaller adjusted values were also used. The eddy coefficient formulas were not changed. The main uncertainty is the initialization of the salinity field. Three 10-day simulations were performed for constant riverflows of 12,000 m<sup>3</sup>/s (run H1), 4,000 m<sup>3</sup>/s (run H2) and 2,000 m<sup>3</sup>/s (run H3) corresponding to high, low and very low flows simulated during runs 51, 26, and 27, respectively. Salinity was therefore initialized to similar distributions used for these latter present day runs and modified for the increased number of channels such that the salinity was at approximately the same value for each north-south cross section. The guiding principal was to make the stratification and intrusion length similar to the corresponding present day run. Since the salinity fields adapt rapidly to the tidal and riverflows (within one day), the initial salinity field quickly loses its influence on the numerical simulations.

The remainder of this section discusses the neap and spring tidal variability for the low flow run H2 and describes the differences between the mean and extreme fields for the three different riverflows as a function of neap and spring tide. Comparisons are made with the present day simulations of Section 3.1 where appropriate.

### 3.2.2. Neap and Spring Tides

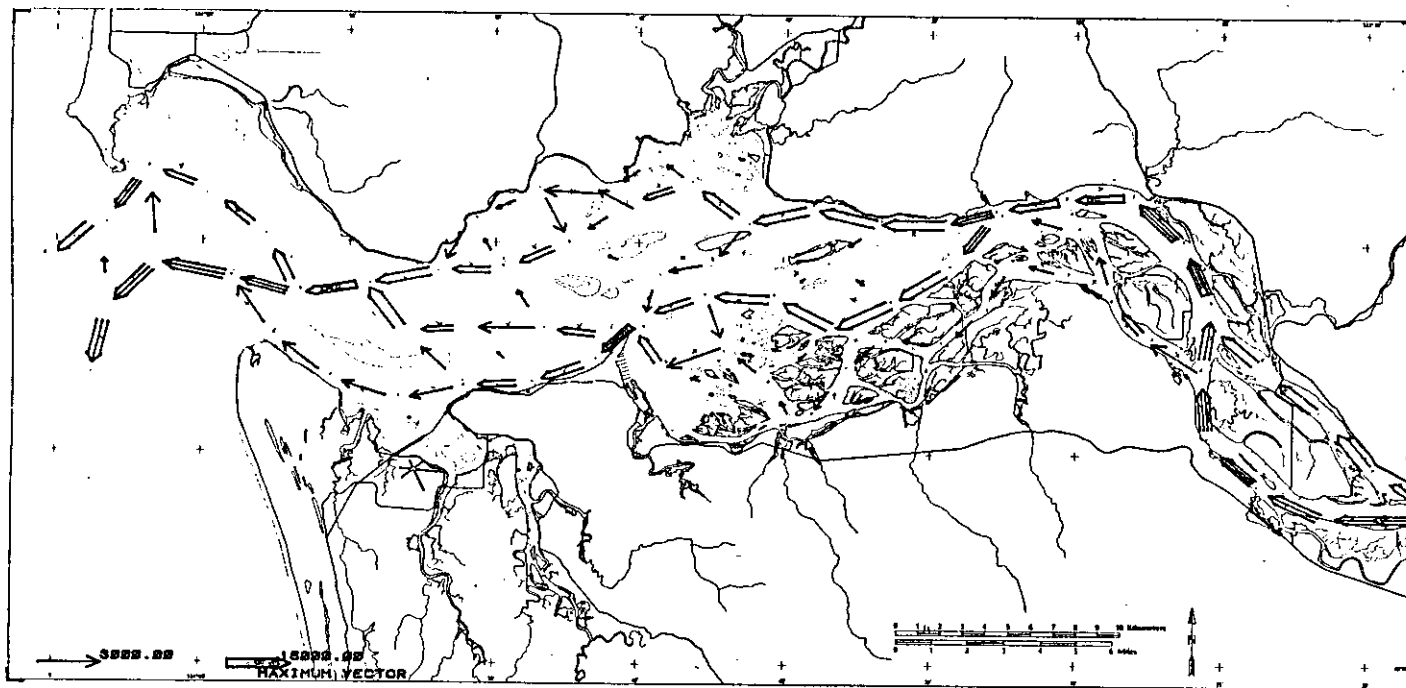
The distribution of volume flows in the channel network is more complex than for the present day. This is most clearly shown by the 50-hour average volume transports plotted on the map (Figure 51); these are equivalent to the present-day transports given in Figure 18. The volume transports split into two approximately equal parts between channels 1 and 2 at Jim Crow Point. The flows remain reasonably separate until Chinook Point, except for moderate flows from channel 2 to channel 1 across the Tongue Point Bar (present-day Navigation Channel). Flows between channels 2 and 10 off Grays Point become confused due to the shallow depths and the complex bathymetry. There is considerable exchange across relatively deep shoals (4 m) between channels 2 and 10. Similar to the present day, a number of flows join together at Tongue Point, producing a locally large volume transport. Between Tongue Point and Astoria, there are large flows from channel 1 to channel 2 via channel 4 and across sand bank flows. Average flow in channel 1 is much reduced over the present day (it is also much more narrow and shallow than today), and flow in channel 2 is relatively increased. At the entrance, the deeper and wider channel 1 carries more flow, but there is still a tendency for south to north across shoal exchange between the two entrance channels.

In the discussion of the sections that follow, the results for channels 1, 2, and 3 will be given: channel 1 can be compared directly with the present day results between the mouth and Tongue Point and upstream of Jim Crow Point. Channel 2 is the same as today up to grid point 6, after which it follows the approximate path of present-day channel 7. The Baker Bay entrance channel has no correspondence in the present-day estuary.

The 10-day simulated tidal elevations were compared with the observed present day water levels at the tide stations given in Figure 5c. The figures were almost identical to Figure 7 and therefore are not shown. There is apparently no systematic differences between the simulated tidal elevations for 1868 and 1982. This is probably due to the fact that the total channel lengths (particularly channel 1) are almost exactly the same for both dates, and the depths of channels 1 and 2 in the region, which contains a large part of the tidal prism between Point Adams and Astoria, are similar to the present day. The lack of change in the tidal elevations between 1868 and 1982 is borne out by analysis of historical tidal records (Jay-personnel communication).

The 9 neap-tide sections for channels 1, 2, and 3 (Figures 52-54) and the volume transport maps (Figure 55) follow the same sequence of high and low waters as Figures 13, 14, and 15. The riverflow is 4,000 m<sup>3</sup>/s, which is very similar to the riverflows of the October 1980 results presented above.

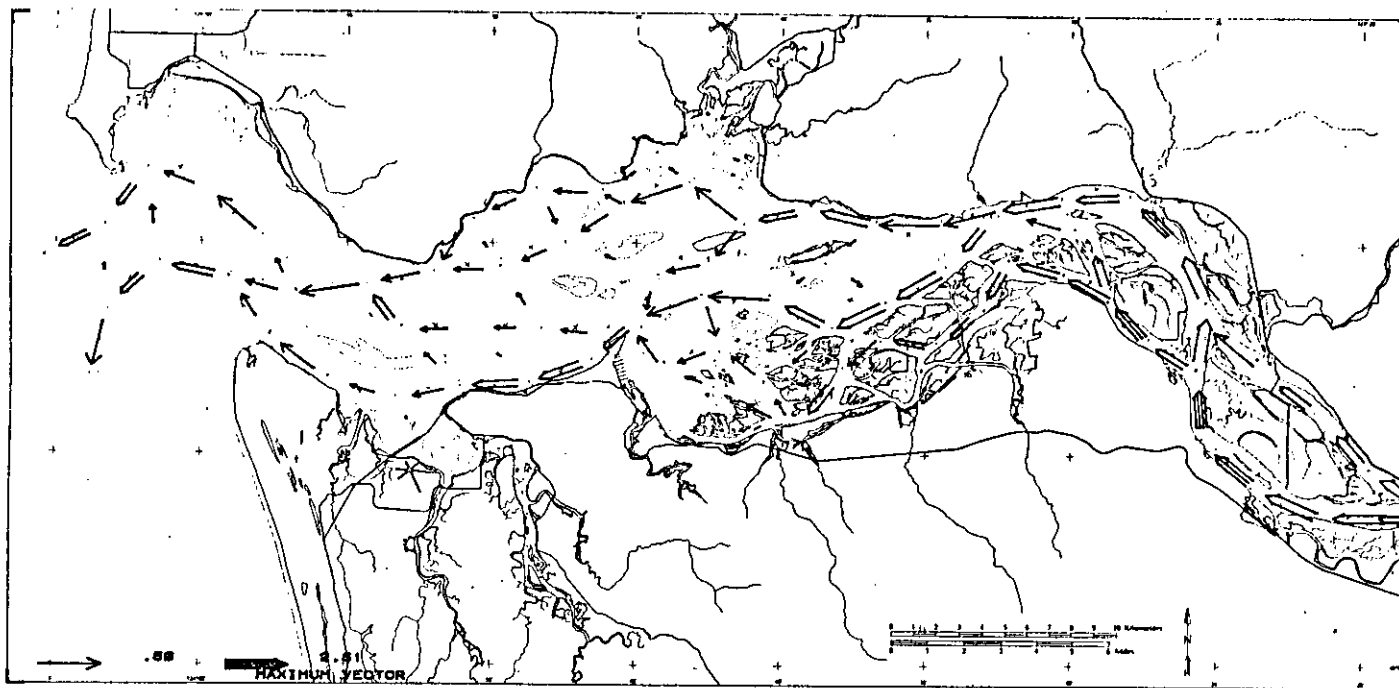
A study of the volume transport maps over the 25-hour tide (Figure 55) shows a number of important differences with Figure 15.



RUN HI 1863

STOP DAY 4 AVERAGING TIME 50HOURS

Figure 51a. Horizontal vectors averaged over a neap tide plotted on the 1868 estuary chart. Volume transports ( $m^3/s$ ).



RUN HI 1863

STOP DAY 4 AVERAGING TIME 50HOURS

Figure 51b. Horizontal vectors averaged over a neap tide plotted on the 1868 estuary chart. Surface velocities (m/s).

Immediately apparent are the relatively larger volume flows west of Tongue Point at practically all stages of the tide, indicating that a larger volume of water is exchanged over the tidal cycle. Jay (personal communication) has calculated a 10-15% reduction of the tidal prism between 1868 and 1982. This decrease is also confirmed by Thomas' (1983) estimates of the losses of inter-tidal areas based on analysis of the 1868 and modern bathymetric maps. Channel 2 transports are much stronger than channel 1 transports between Point Adams and Tongue Point. There is also considerable asymmetry between ebb and flood flows in channel 1 in the Astoria reach, with the ebb flow being relatively weaker than the flood. This occurs partly because there is preferential northward transport across the Desdemona Sands into channel 4. The asymmetry is vice-versa in channels 2 and 4, with ebb transports larger than flood transports. Note also the large across-shoal exchanges between channels 2 and 10 in the vicinity of Grays Point and the west side of Grays Bay. They may provide an explanation of why the Deep River Channel north of Rocky Point has almost completely filled in during the last century.

Turning to the channel sections, the effects of the larger volume transports at the entrance and the more marked ebb-flood asymmetries in channels 1 and 2 are apparent. The salinities at high tide are higher and the salt penetrates farther upstream in both channels 1 and 2. The stratification is smaller but less uniformly distributed along the channels with sharp vertical fronts over the shallow bars just downstream of Tongue Point in channel 1 and upstream of grid point 6 in channel 2. The vertical isohalines of the front reach only to about mid-depth over the channel 1 bar. The salt content of channels 1 and 2 remains greater than the present day at all points of the tide. It is noted that unlike the present day, the south channel (1) is generally saltier than the north channel (2) partly because of the relative decrease over the present day in the proportion of the freshwater flow through channel 1 downstream of Tongue Point and partly because of the asymmetry in the tidal flow that favor the influx of salt by stronger flood currents. Channel 2 is also more directly connected to the freshwater flow at Jim Crow Point in 1868 than in 1982.

Channel 3, however, has no equivalent in the present-day estuary. It is generally shallow except for a deep scour hole inside Cape Disappointment (grid point 3). The Baker Bay section of the channel remains horizontally stratified over the tidal period (Figure 54) presumably because of the influence of the upper part of the water column of channel 2 at the junction point. The mouth of the channel is horizontally stratified on the ebb but becomes homogeneous on the flood with evidence that mixing is caused by overturning of the water column (Figure 54e,h). A vertical front forms downstream of the scour hole between the mixed and stratified water masses.

The spring tide sequence of sections for channels 1, 2, and 3 are given in Figures 56, 57, and 58, respectively. The tidal sequence follows the same ordering as figures 16 and 17 starting at a high tide. Again the maps of volume transports are not presented as they have similar patterns to Figures 55.

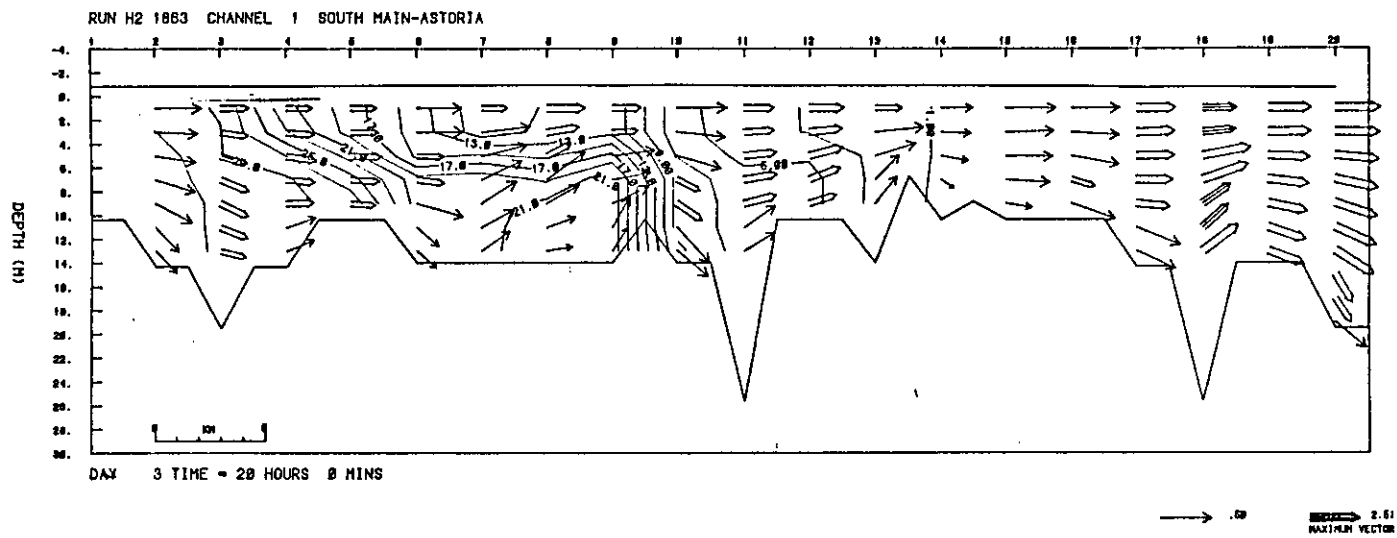


Figure 52a. Channel 1, neap tide period, currents and salinities (m/s and  $^{\circ}/\text{oo}$ ), low riverflow. High water.

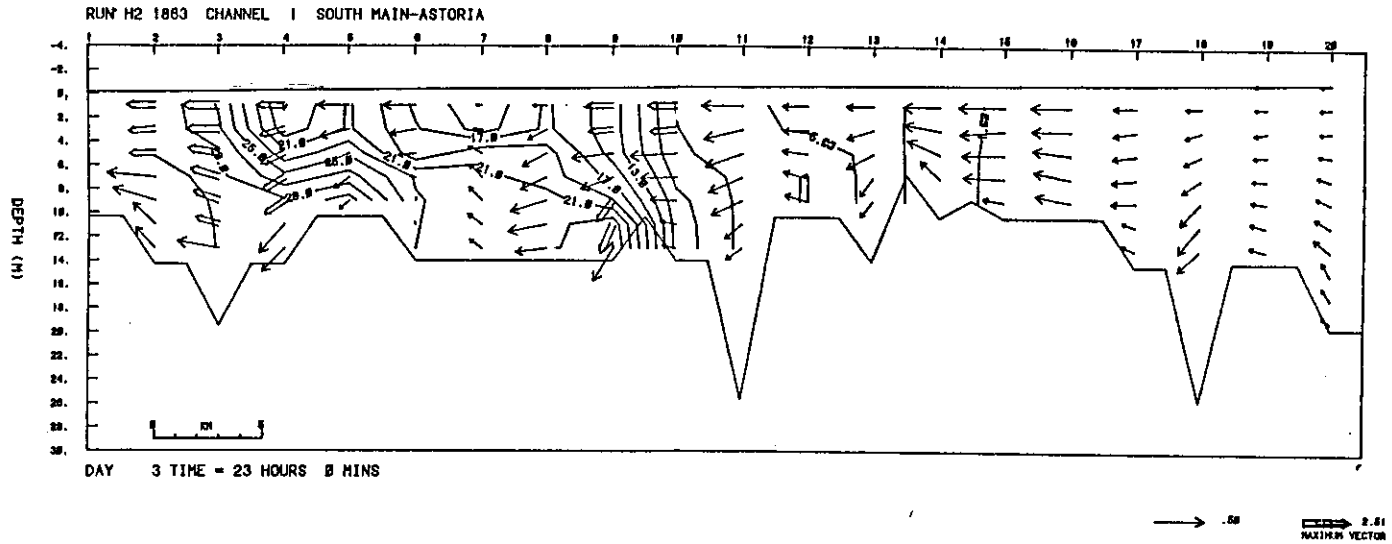


Figure 52b. Channel 1, neap tide period, currents and salinities (m/s and ‰), low riverflow. Half tide ebb.

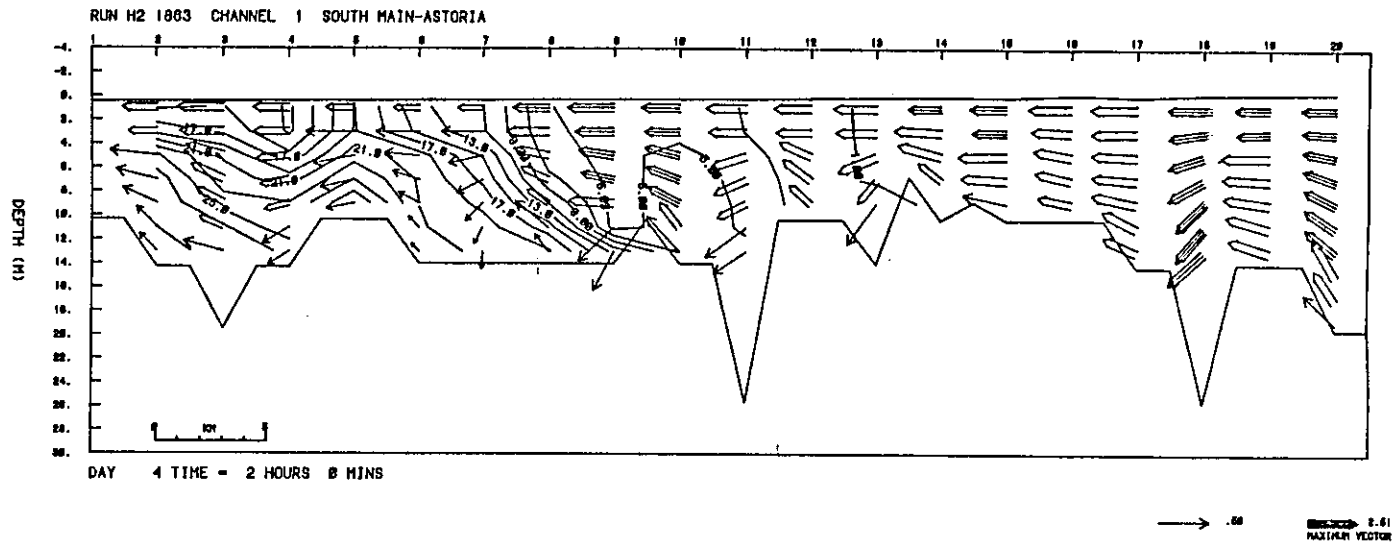


Figure 52c. Channel 1, neap tide period, currents and salinities (m/s and ‰), low riverflow. Low water.

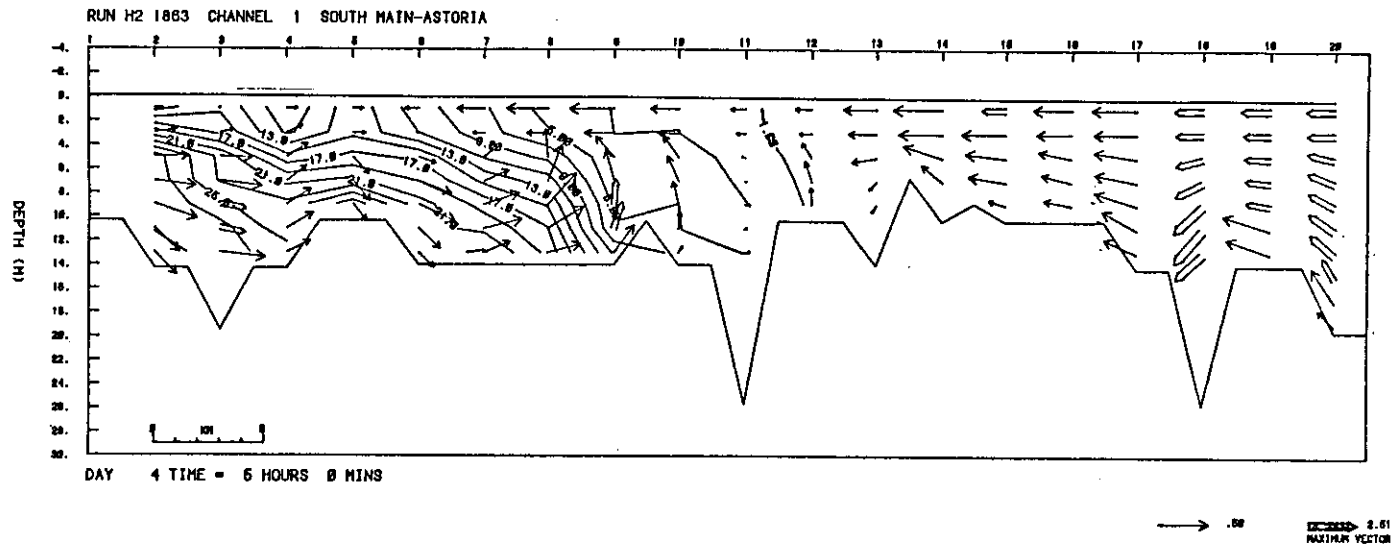


Figure 52d. Channel 1, neap tide period, currents and salinities (m/s and ‰), low riverflow. Half tide flood.

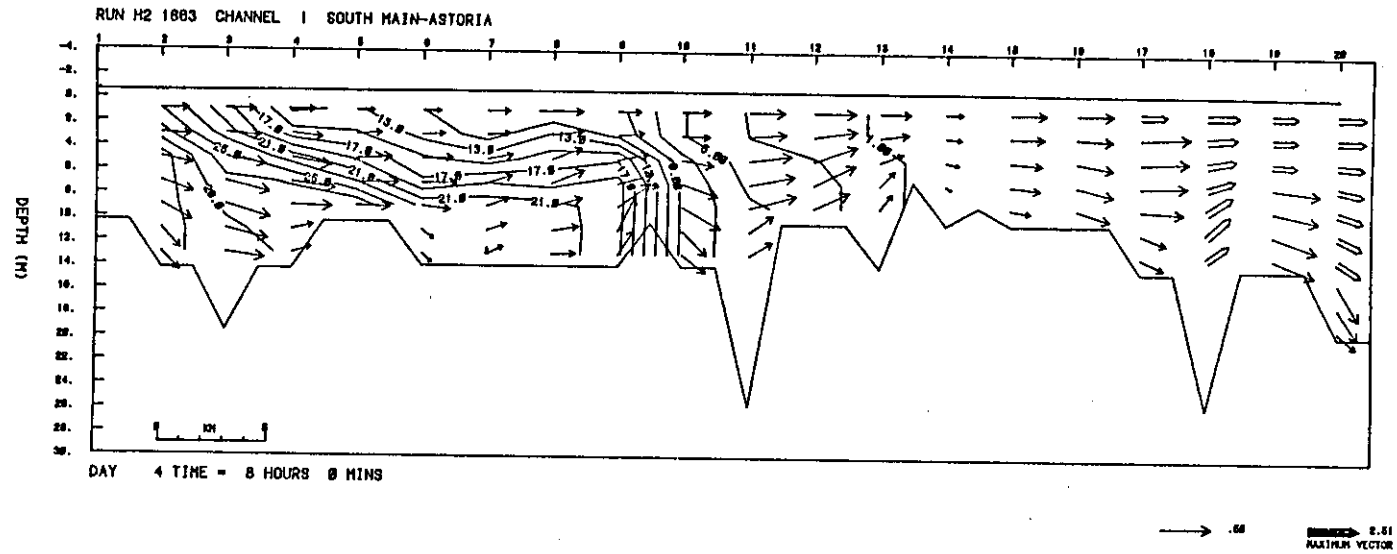


Figure 52e. Channel 1, neap tide period, currents and salinities (m/s and ‰), low riverflow. High water.

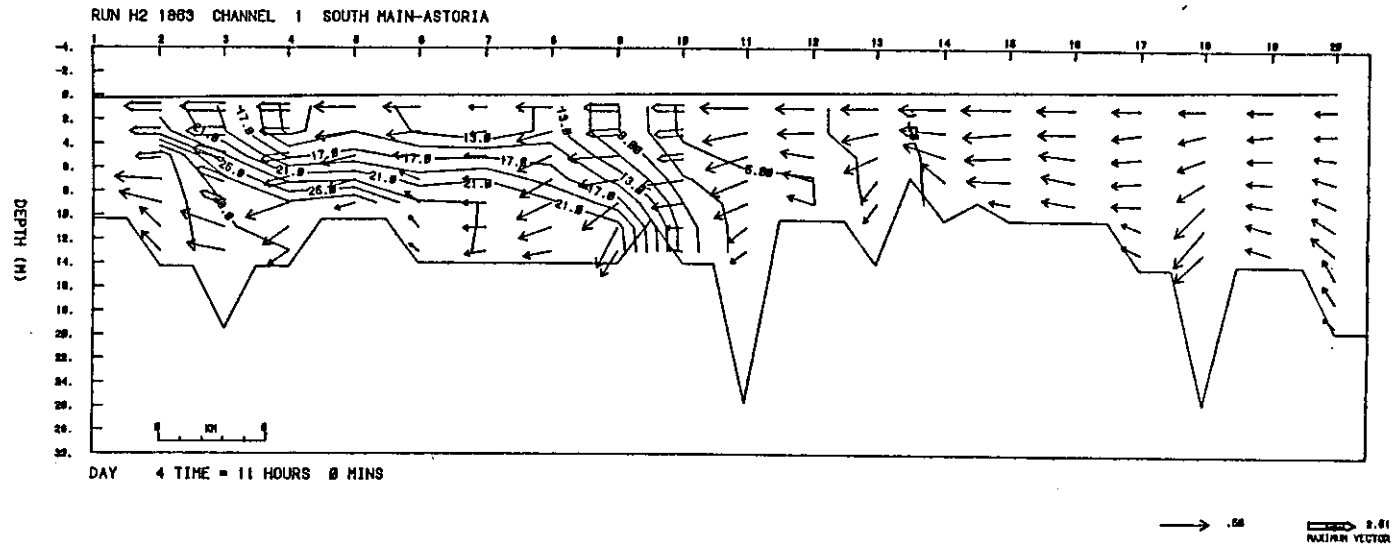


Figure 52f. Channel 1, neap tide period, currents and salinities (m/s and ‰), low riverflow. Half-tide ebb.

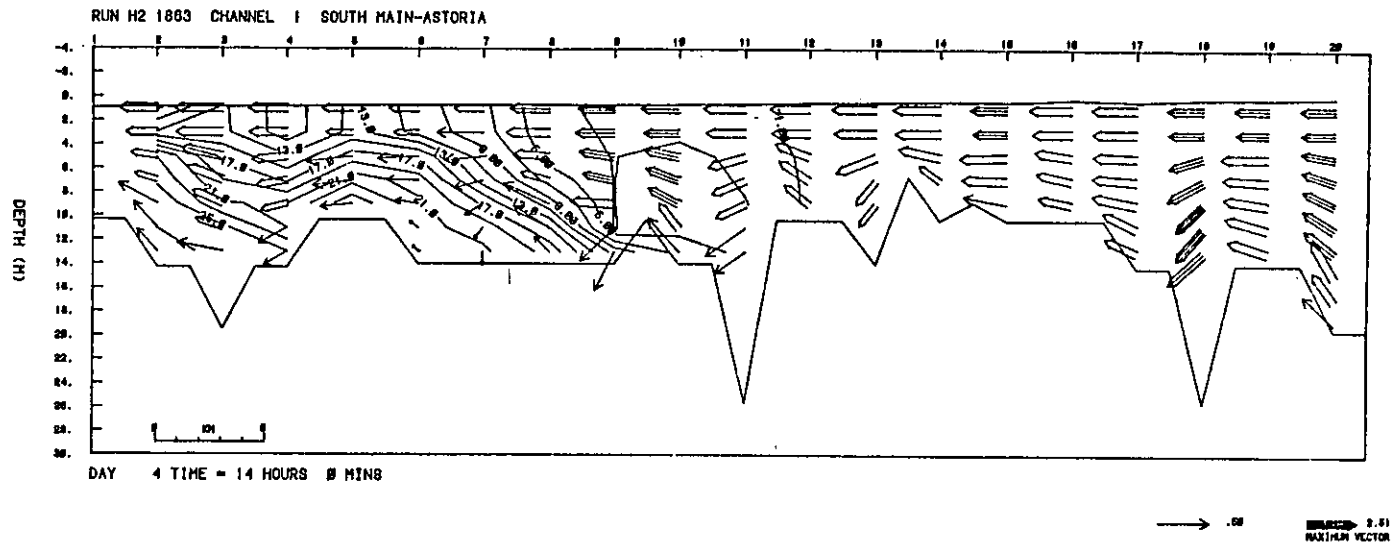


Figure 52g. Channel 1, neap tide period, currents and salinities (m/s and ‰), low riverflow. Low water.

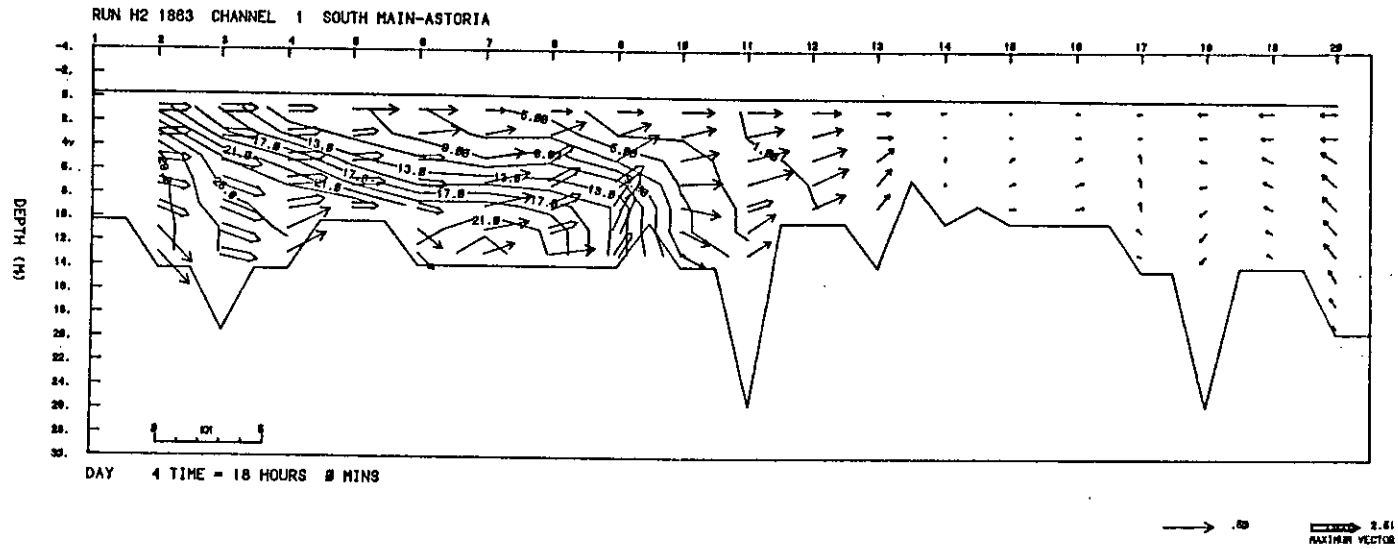


Figure 52h. Channel 1, neap tide period, currents and salinities (m/s and  $^{\circ}/\text{oo}$ ), low riverflow. Half-tide ebb.

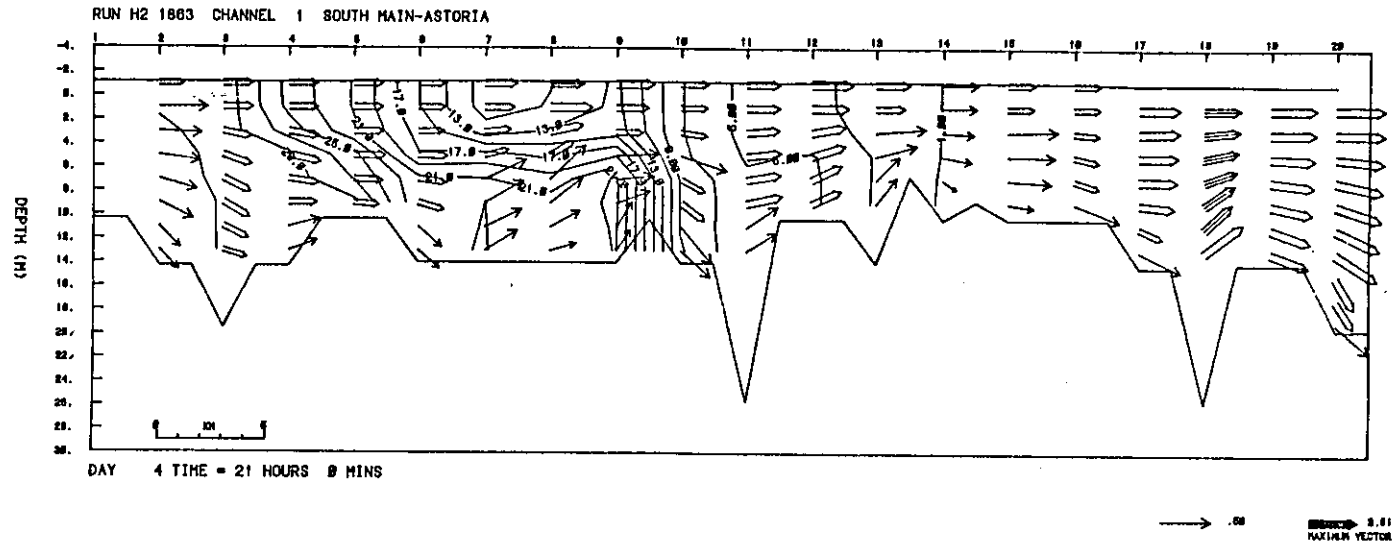


Figure 521. Channel 1, neap tide period, currents and salinities (m/s and ‰), low riverflow. High water.



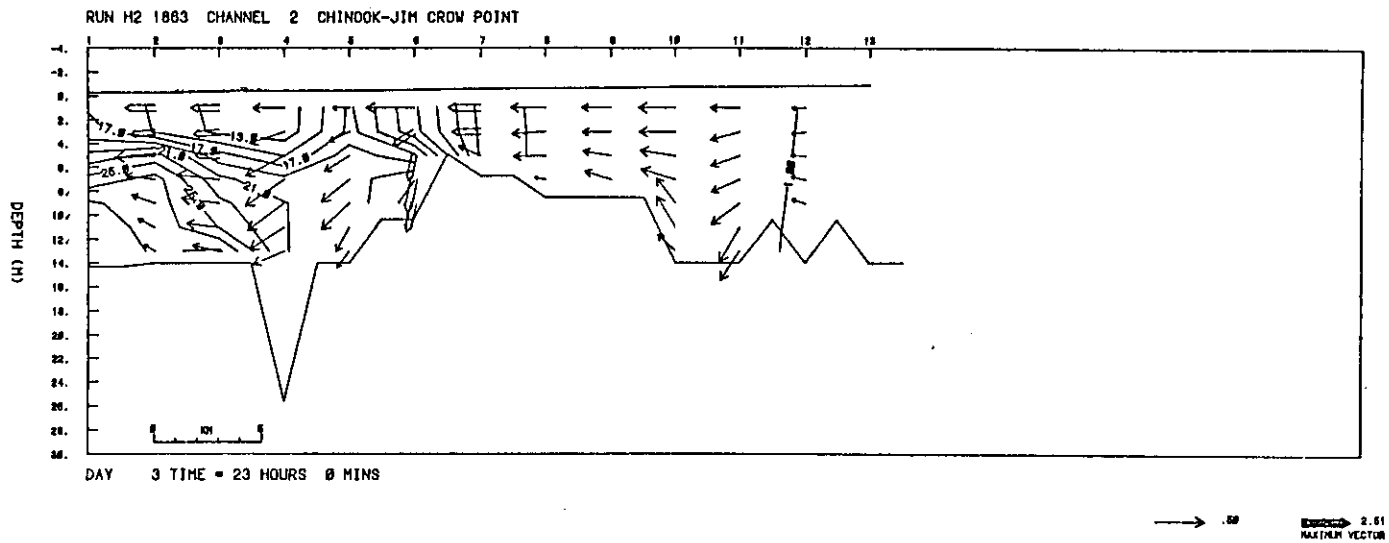


Figure 53b. Channel 2, neap tide period, currents and salinities (m/s and  $^{\circ}/\text{oo}$ ), low riverflow. Half-tide ebb.

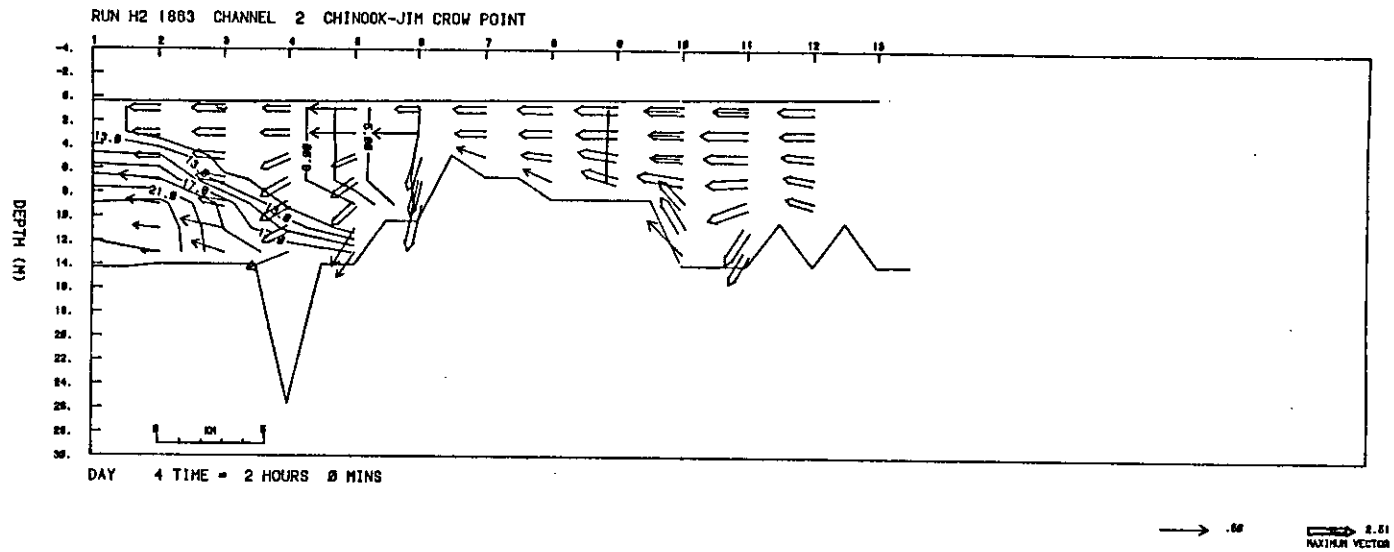


Figure 53c. Channel 2, neap tide period, currents and salinities (m/s and ‰), low riverflow. Low water.

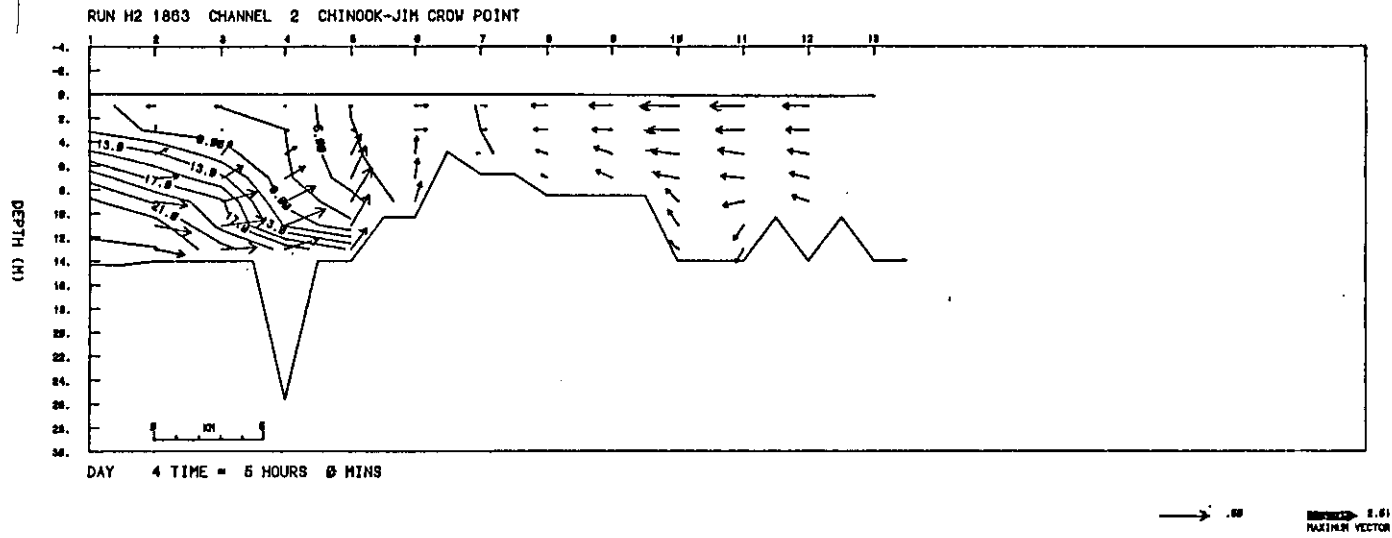


Figure 53d. Channel 2, neap tide period, currents and salinities (m/s and  $^{\circ}/\text{oo}$ ), low riverflow. Half tide flood.

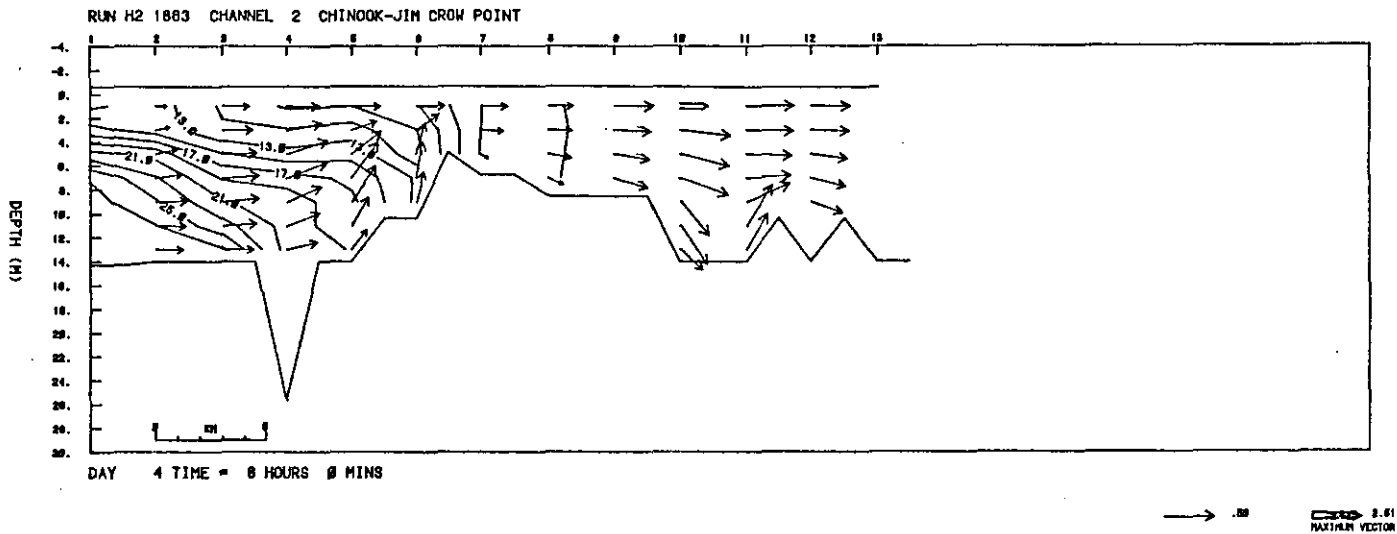


Figure 53e. Channel 2, neap tide period, currents and salinities (m/s and ‰), low riverflow. High water.

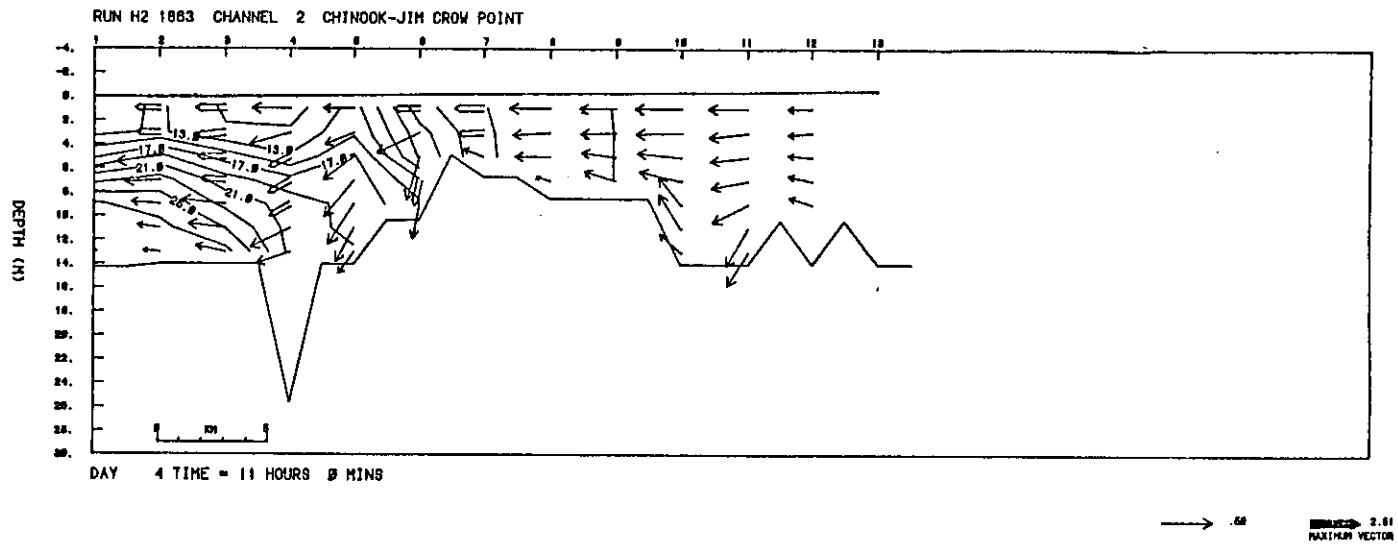


Figure 53f. Channel 2, neap tide period, currents and salinities (m/s and ‰), low riverflow. Half-tide ebb.

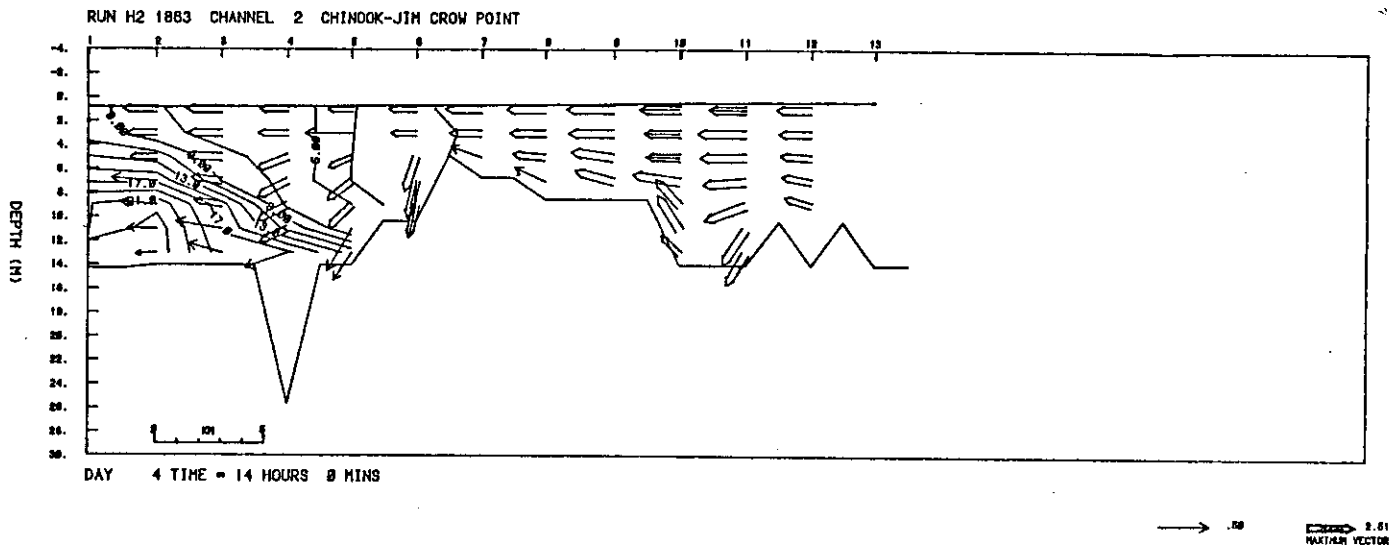


Figure 53g. Channel 2, neap tide period, currents and salinities (m/s and ‰), low riverflow. Low water.

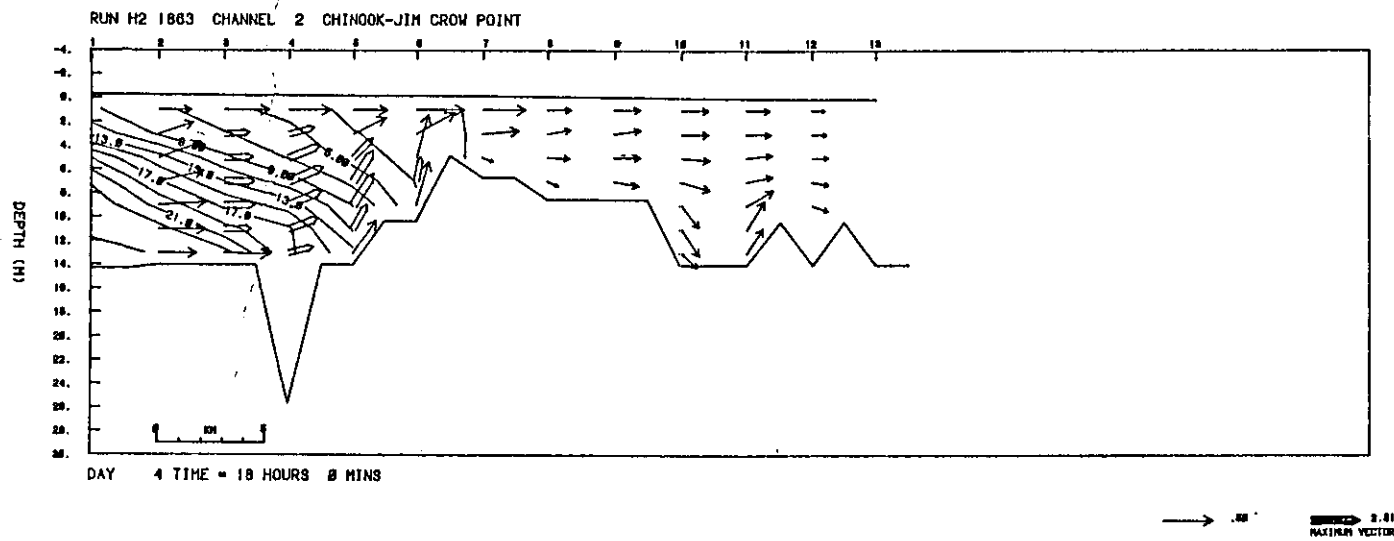


Figure 53h. Channel 2, neap tide period, currents and salinities (m/s and  $^{\circ}/\text{oo}$ ), low riverflow. Half-tide ebb.

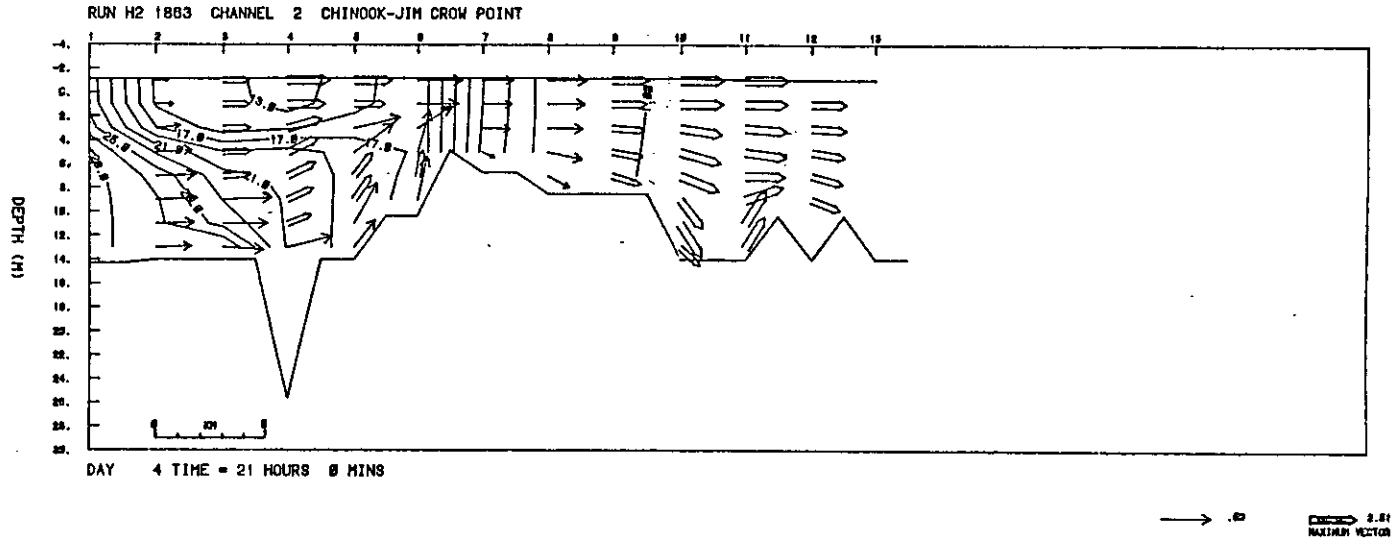


Figure 53i. Channel 2, neap tide period, currents and salinities (m/s and  $^{\circ}/_{\infty}$ ), low riverflow. High water.

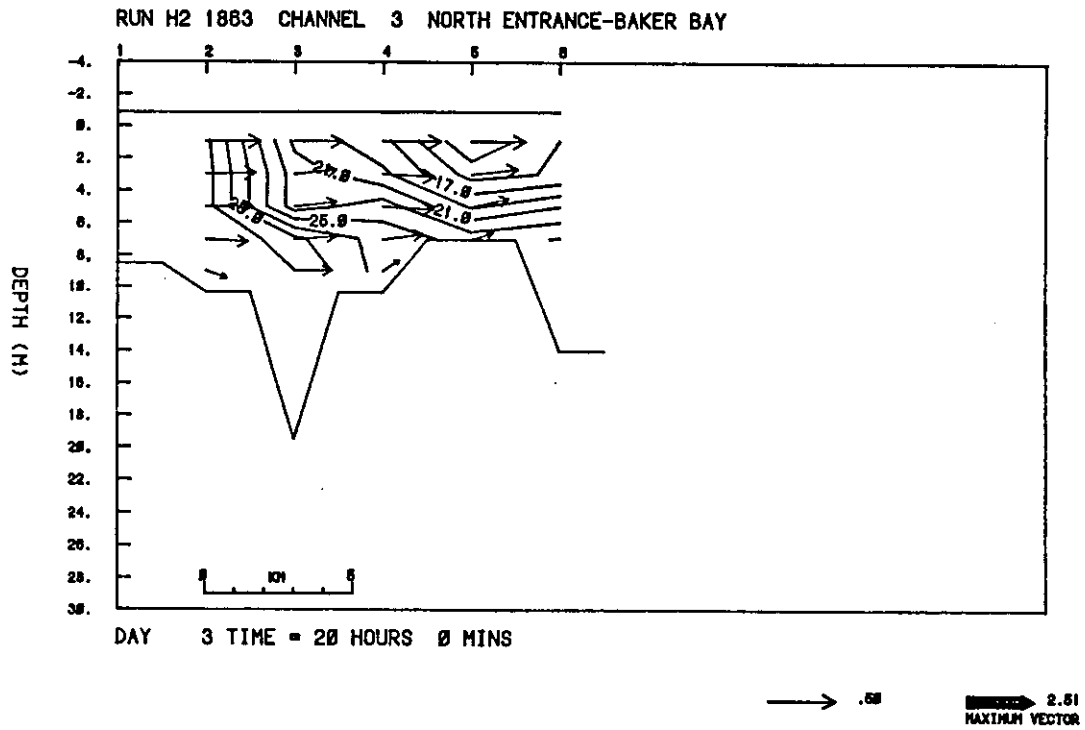


Figure 54a. Channel 3, neap tide period, currents and salinities (m/s and ‰), low riverflow. High water.

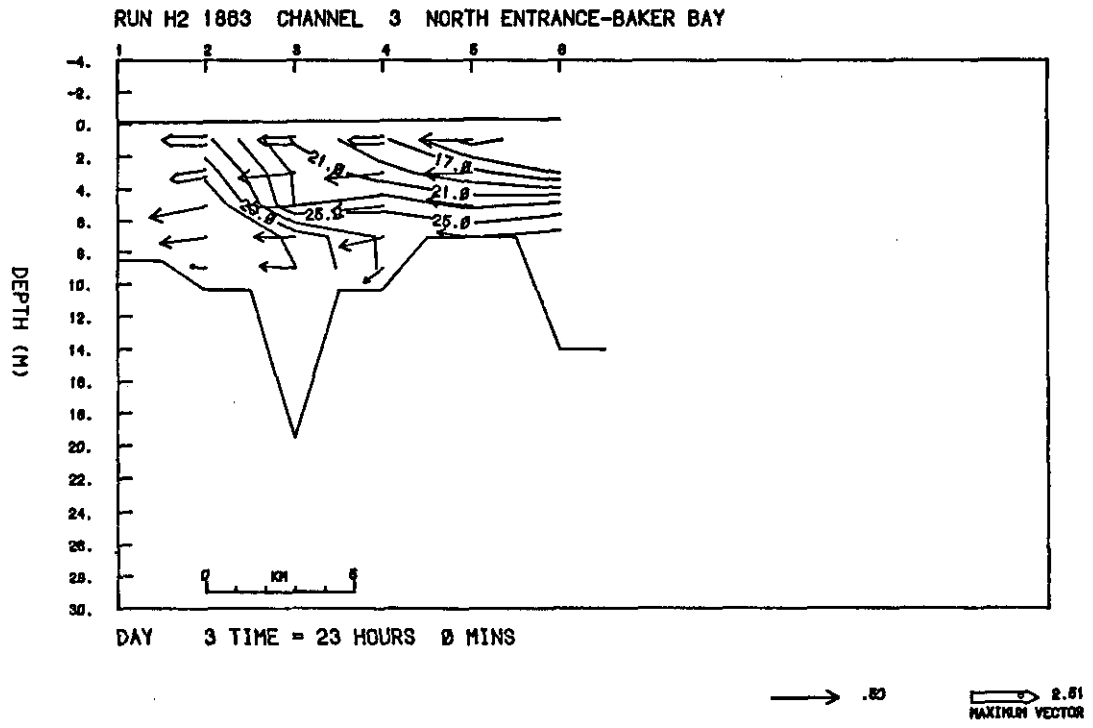


Figure 54b. Channel 3, neap tide period, currents and salinities (m/s and ‰), low riverflow. Half-tide ebb.

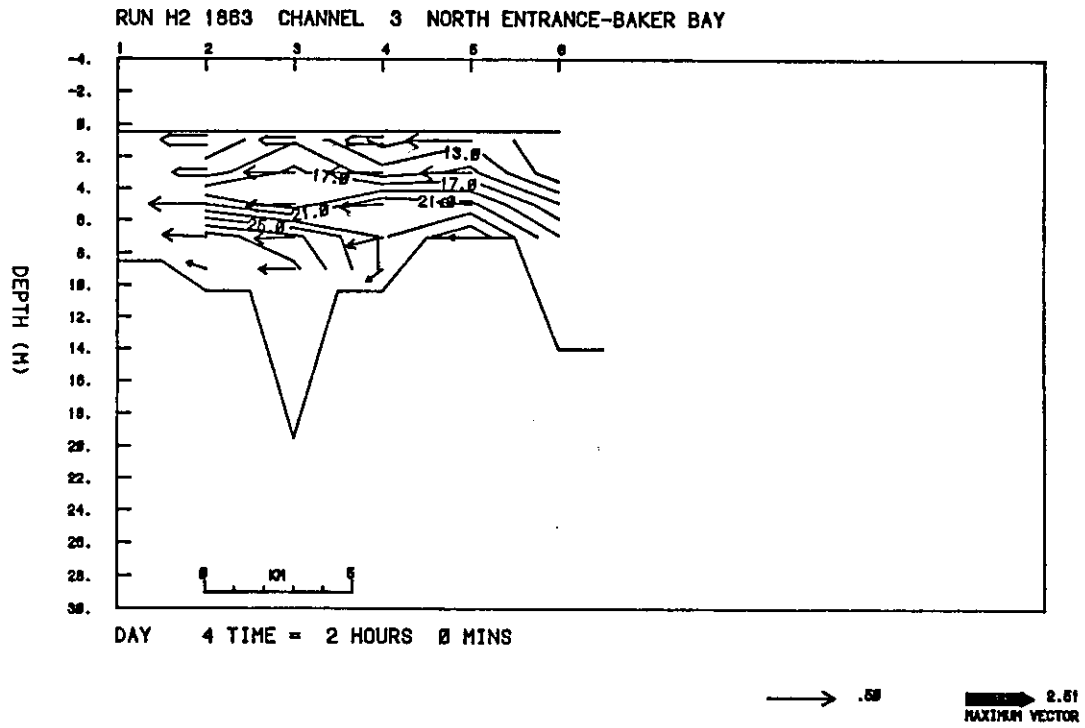


Figure 54c. Channel 3, neap tide period, currents and salinities (m/s and ‰), low riverflow. Low water.

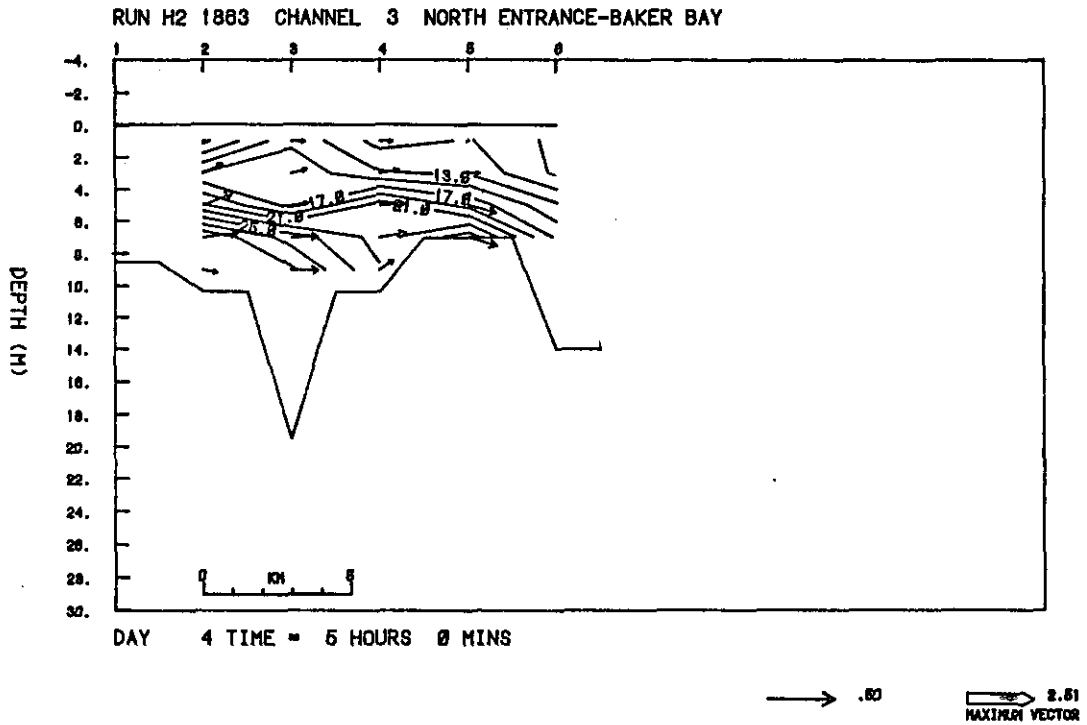


Figure 54d. Channel 3, neap tide period, currents and salinities (m/s and ‰), low riverflow. Half-tide flood.

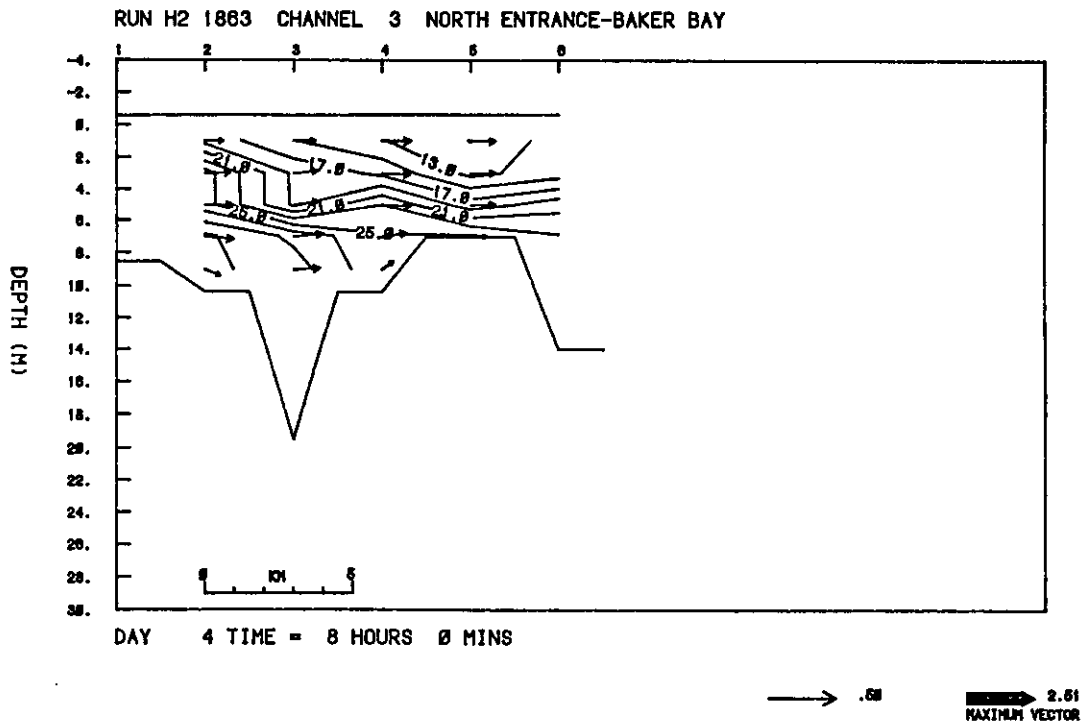


Figure 54e. Channel 3, neap tide period, currents and salinities (m/s and ‰), low riverflow. High water.

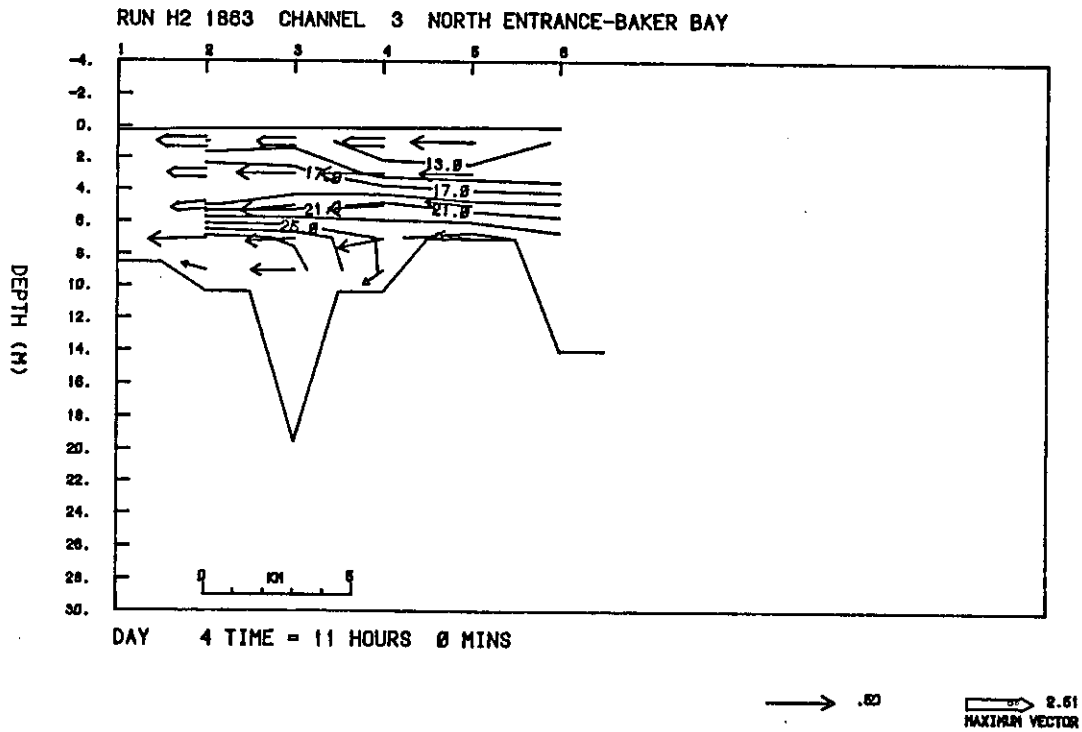


Figure 54f. Channel 3, neap tide period, currents and salinities (m/s and ‰), low riverflow. Half-tide ebb.

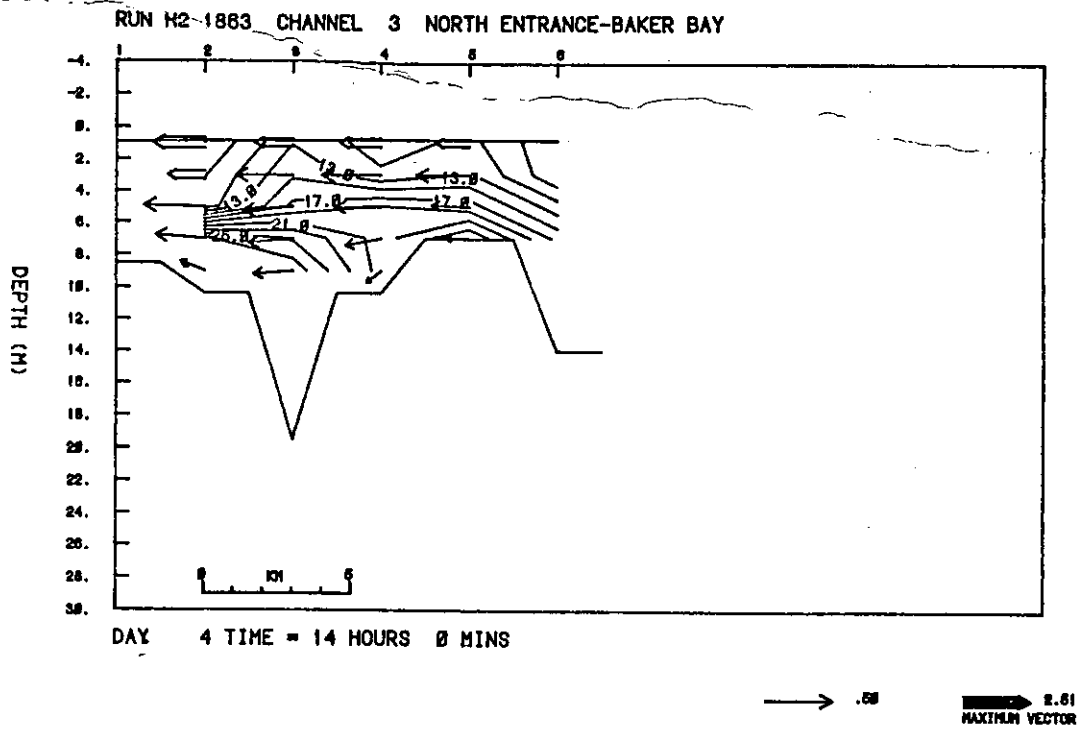


Figure 54g. Channel 3, neap tide period, currents and salinities (m/s and ‰), low riverflow. Low water.

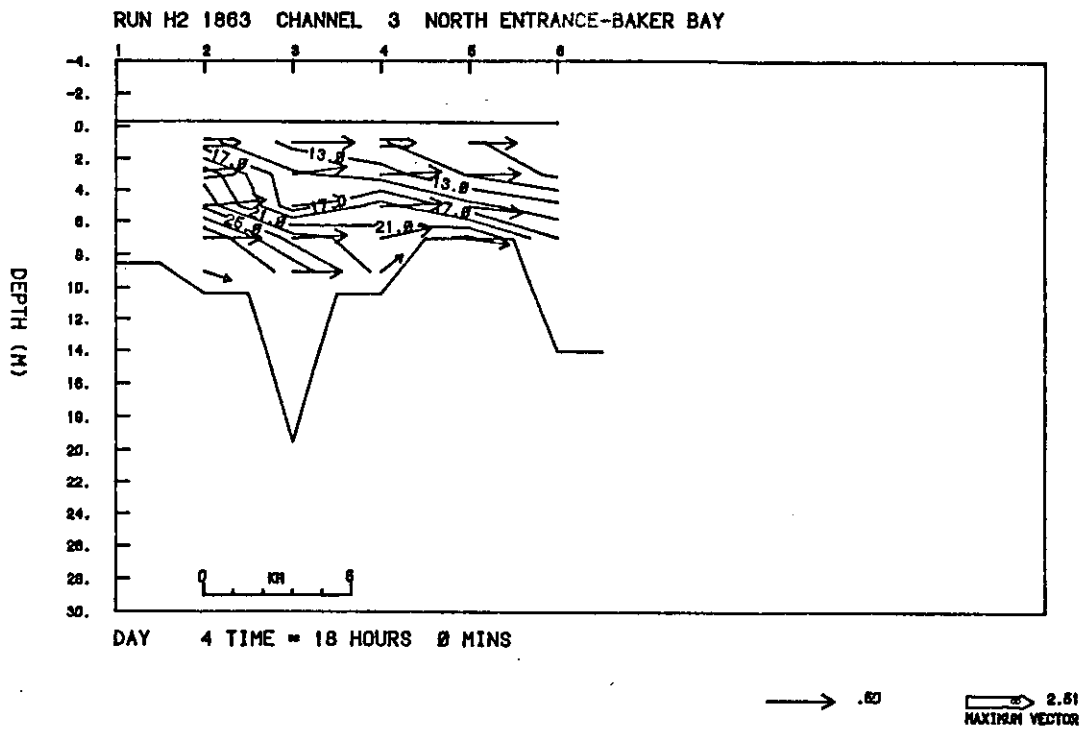


Figure 54h. Channel 3, neap tide period, currents and salinities (m/s and ‰), low riverflow. Half-tide flood.

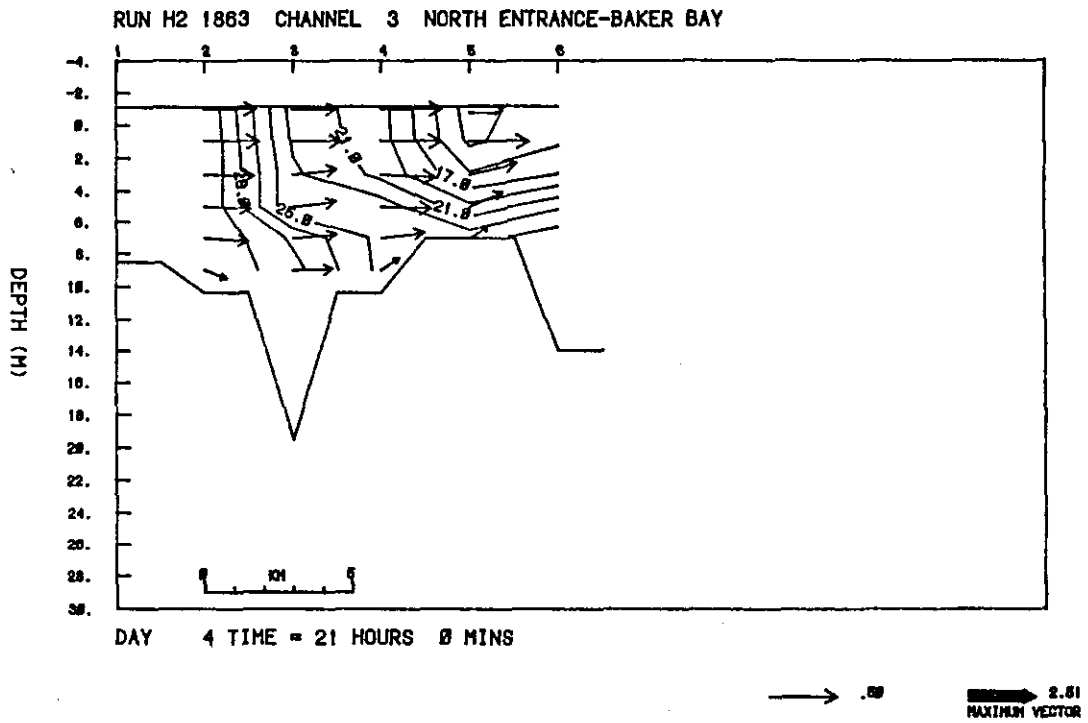
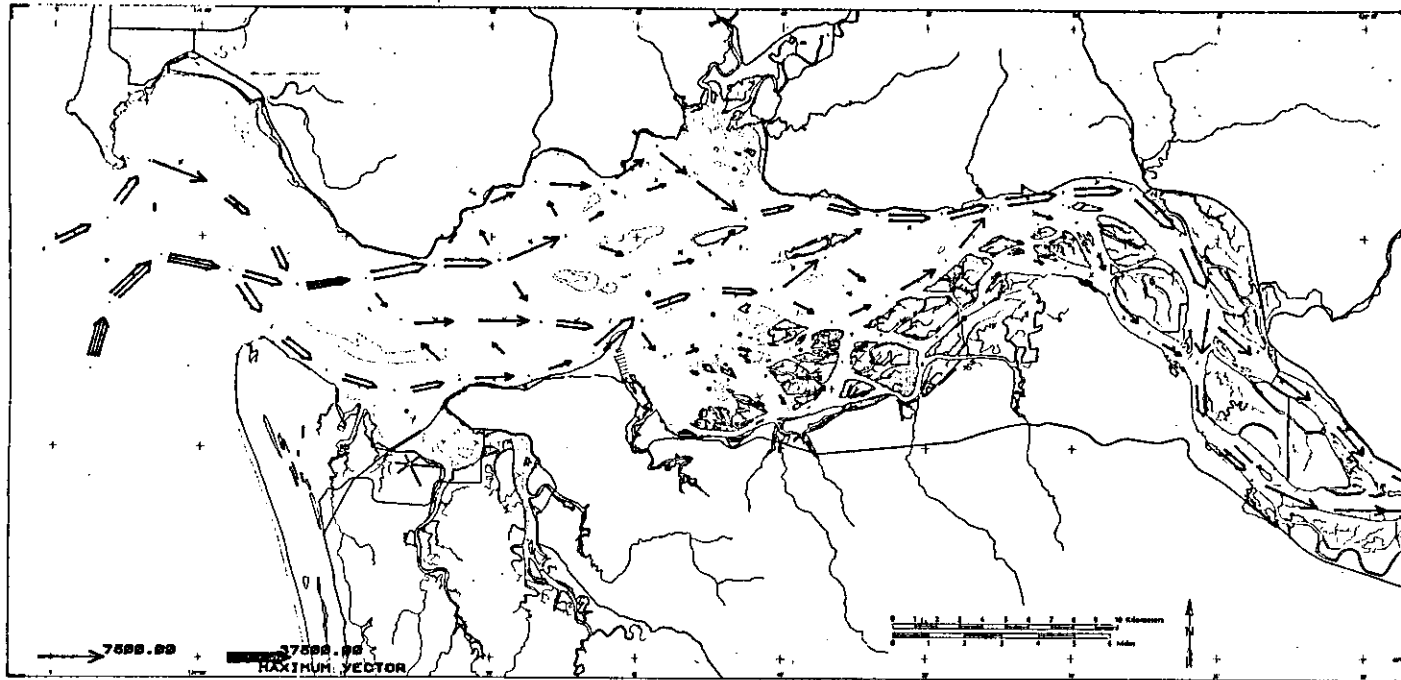


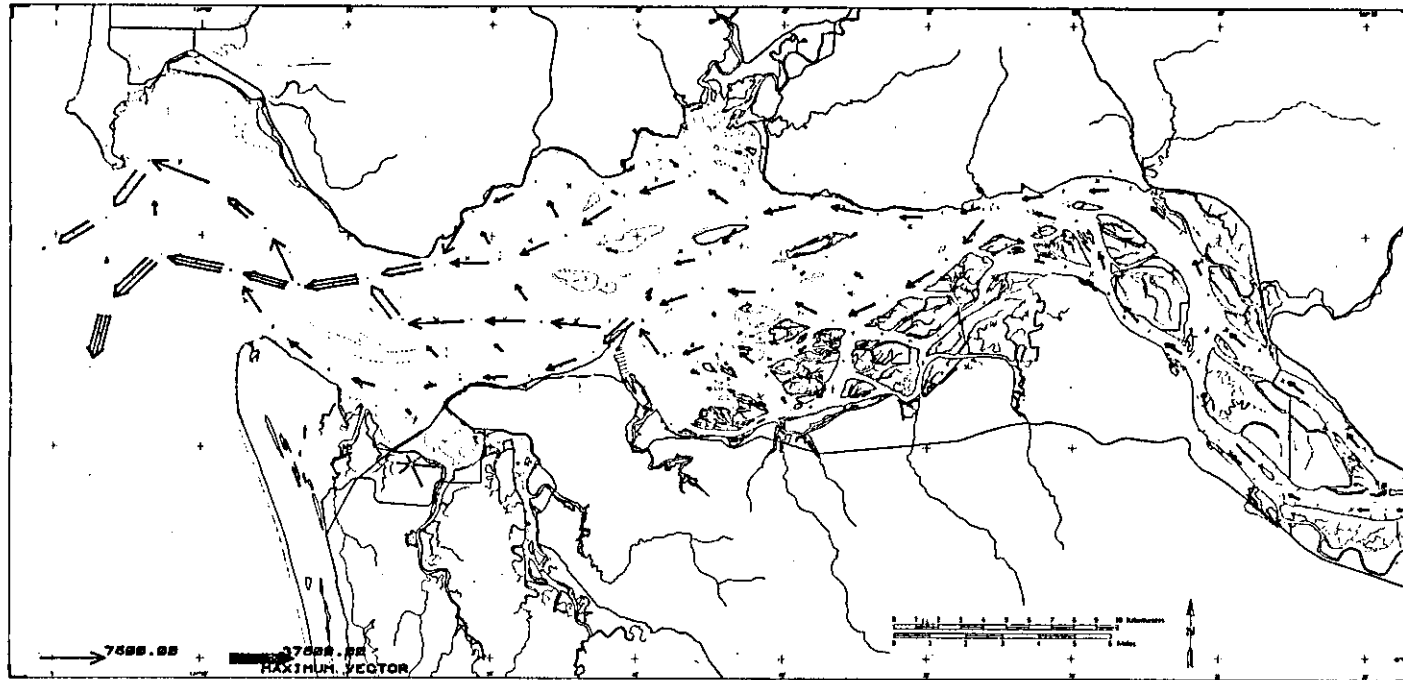
Figure 54i. Channel 3, neap tide period, currents and salinities (m/s and ‰), low riverflow. High water.



RUN H2 1863

DAY 3 TIME = 20 HOURS 0 MINS

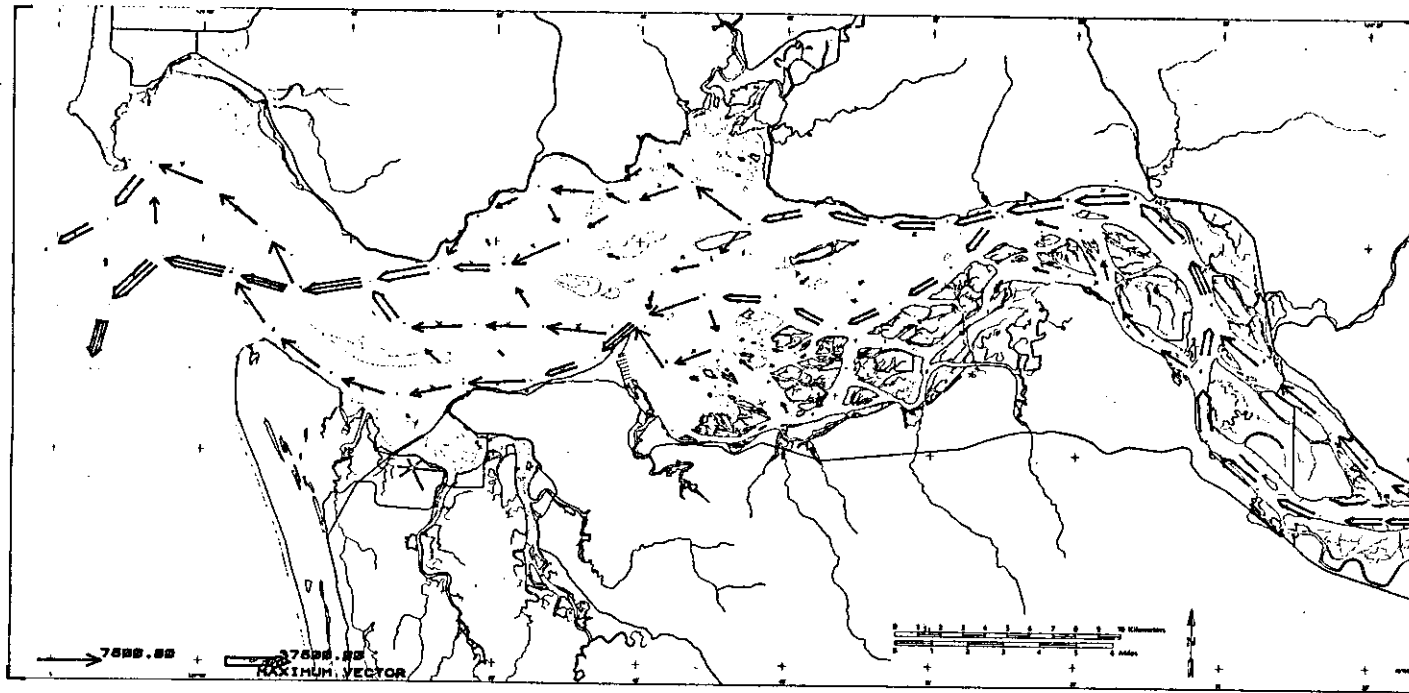
Figure 55a. Horizontal volume transport vectors ( $\text{m}^3/\text{s}$ ) for neap tide and low riverflow. High water.



RUN H2 1883

DAY 3 TIME = 23 HOURS 0 MINS

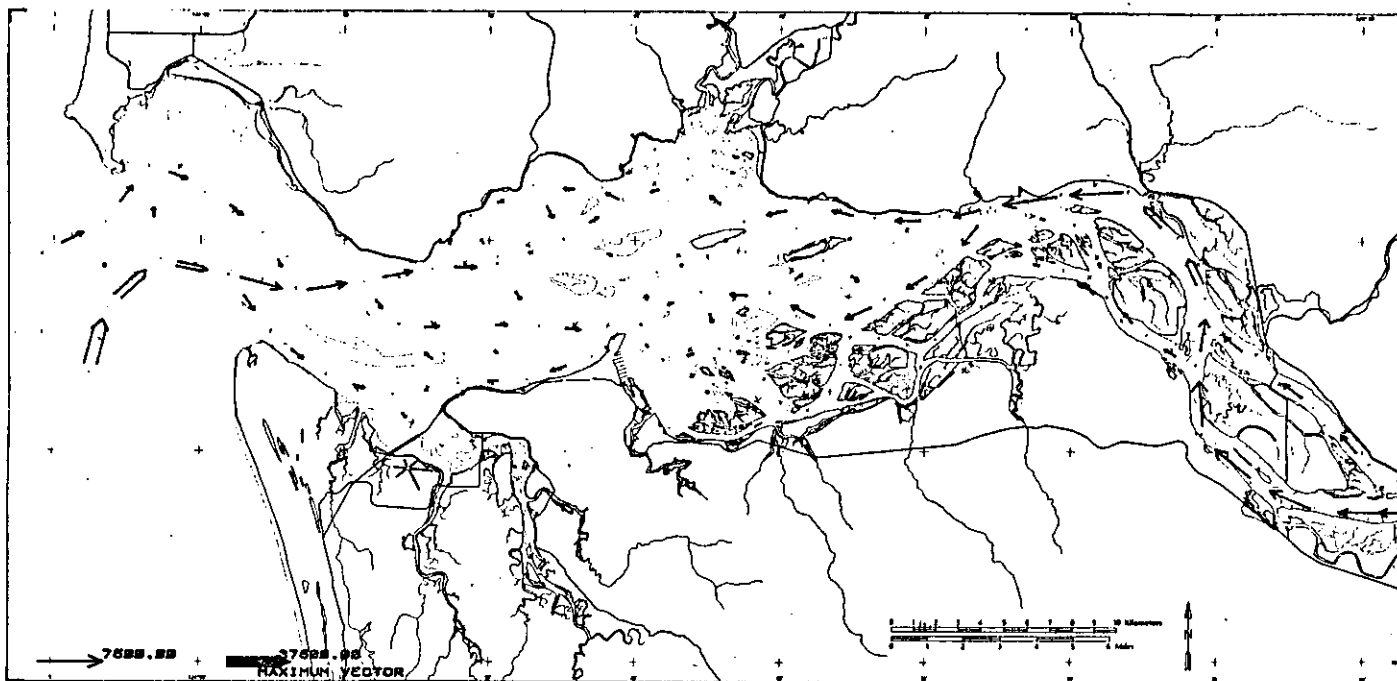
Figure 55b. Horizontal volume transport vectors ( $\text{m}^3/\text{s}$ ) for neap tide and low riverflow. Half-tide ebb.



RUN H2 1863

DAY 4 TIME = 2 HOURS 0 MINS

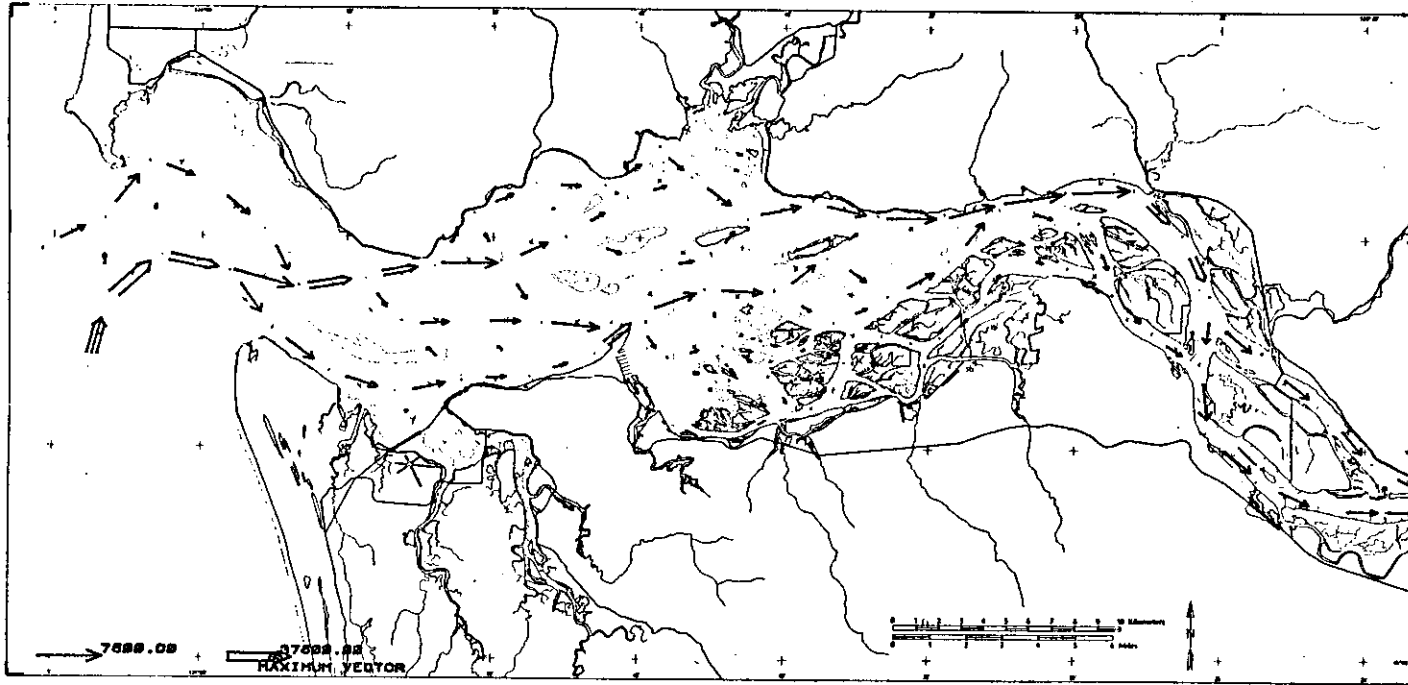
Figure 55c. Horizontal volume transport vectors ( $\text{m}^3/\text{s}$ ) for neap tide and low riverflow. Low water.



RUN H2 1863

DAY 4 TIME = 6 HOURS 0 MINS

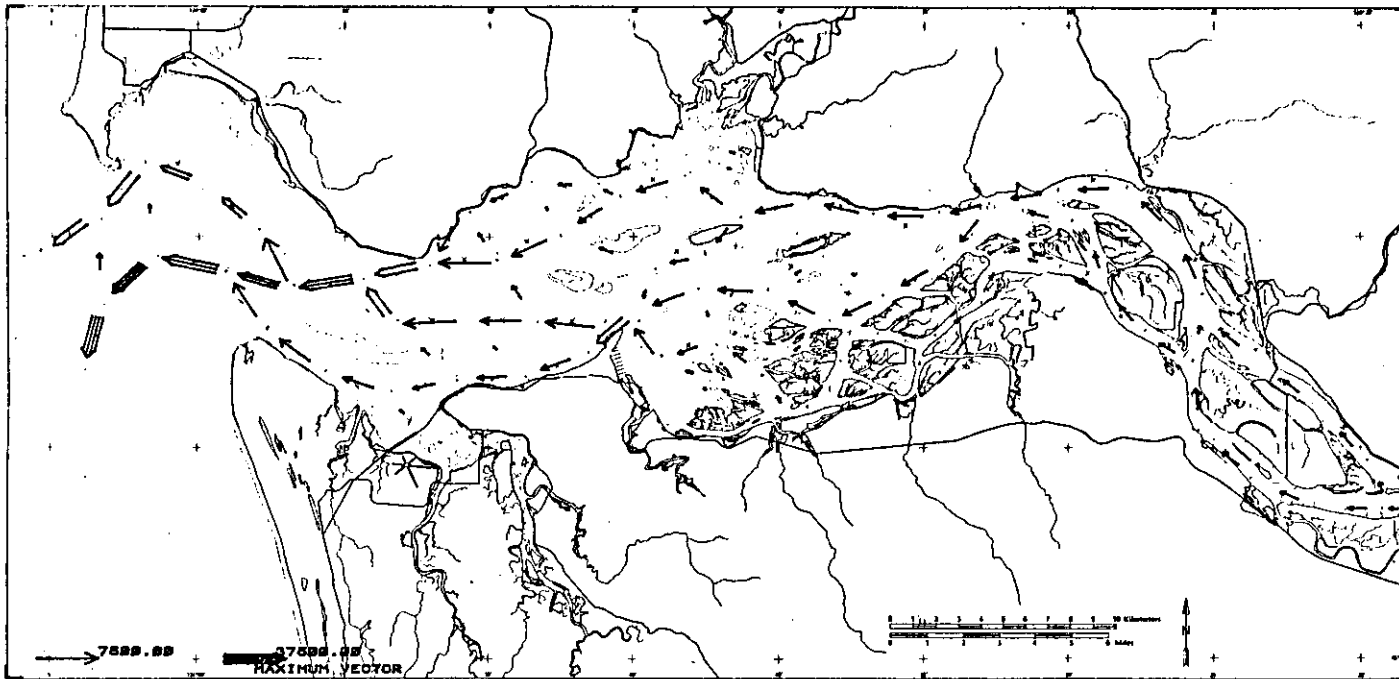
Figure 55d. Horizontal volume transport vectors ( $\text{m}^3/\text{s}$ ) for neap tide and low riverflow. Half-tide flood.



RUN H2 1863

DAY 4 TIME = 8 HOURS 0 MINS

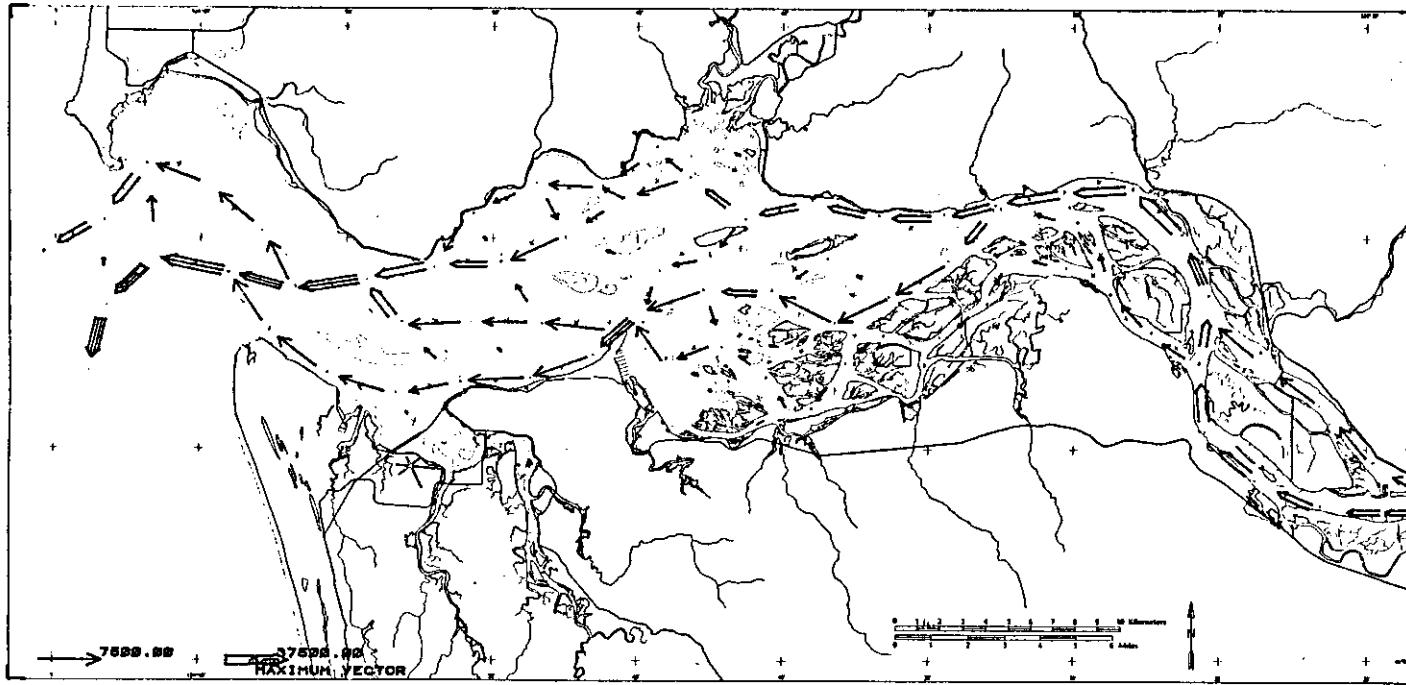
Figure 55e. Horizontal volume transport vectors ( $\text{m}^3/\text{s}$ ) for neap tide and low riverflow. High water.



RUN H2 1883

DAY 4 TIME = 11 HOURS 0 MINS

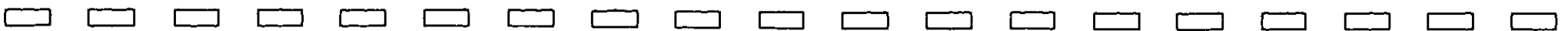
Figure 55f. Horizontal volume transport vectors ( $\text{m}^3/\text{s}$ ) for neap tide and low riverflow. Half-tide ebb.

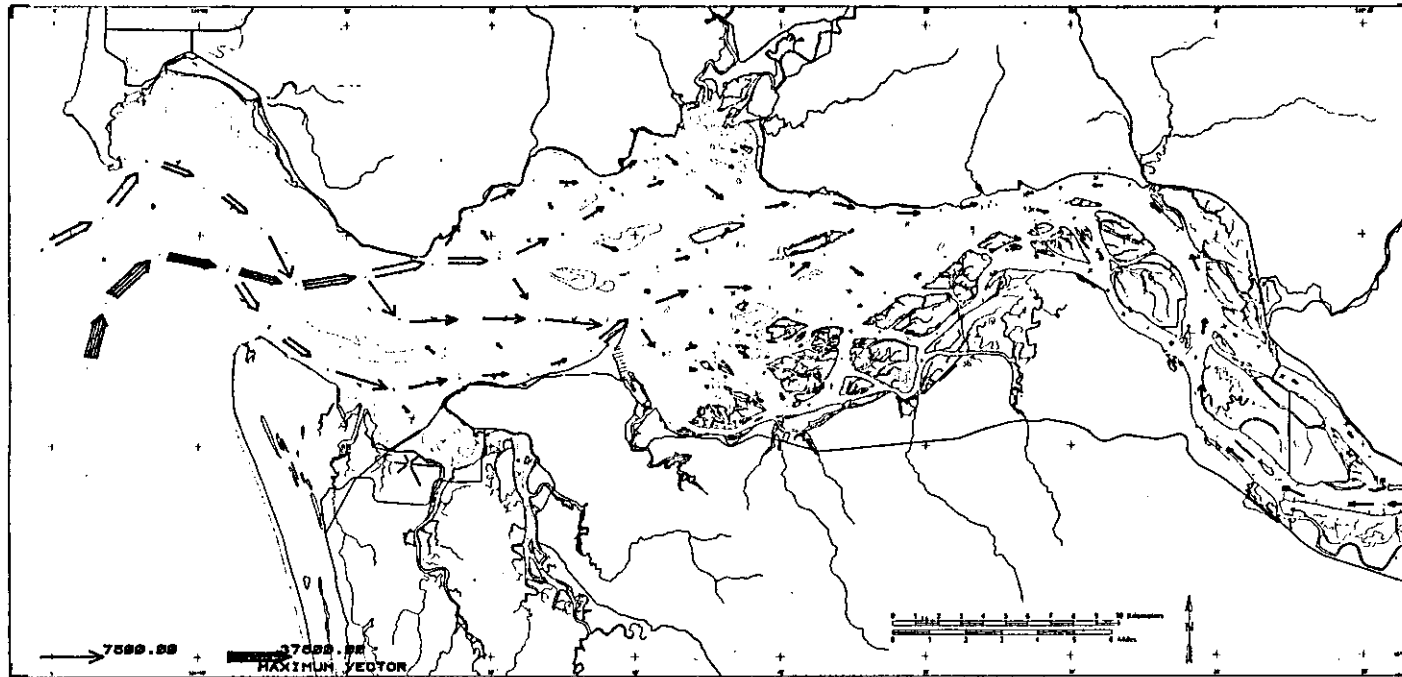


RUN H2 1863

DAY 4 TIME = 14 HOURS 0 MINS

Figure 55g. Horizontal volume transport vectors ( $m^3/s$ ) for neap tide and low riverflow. Low water.

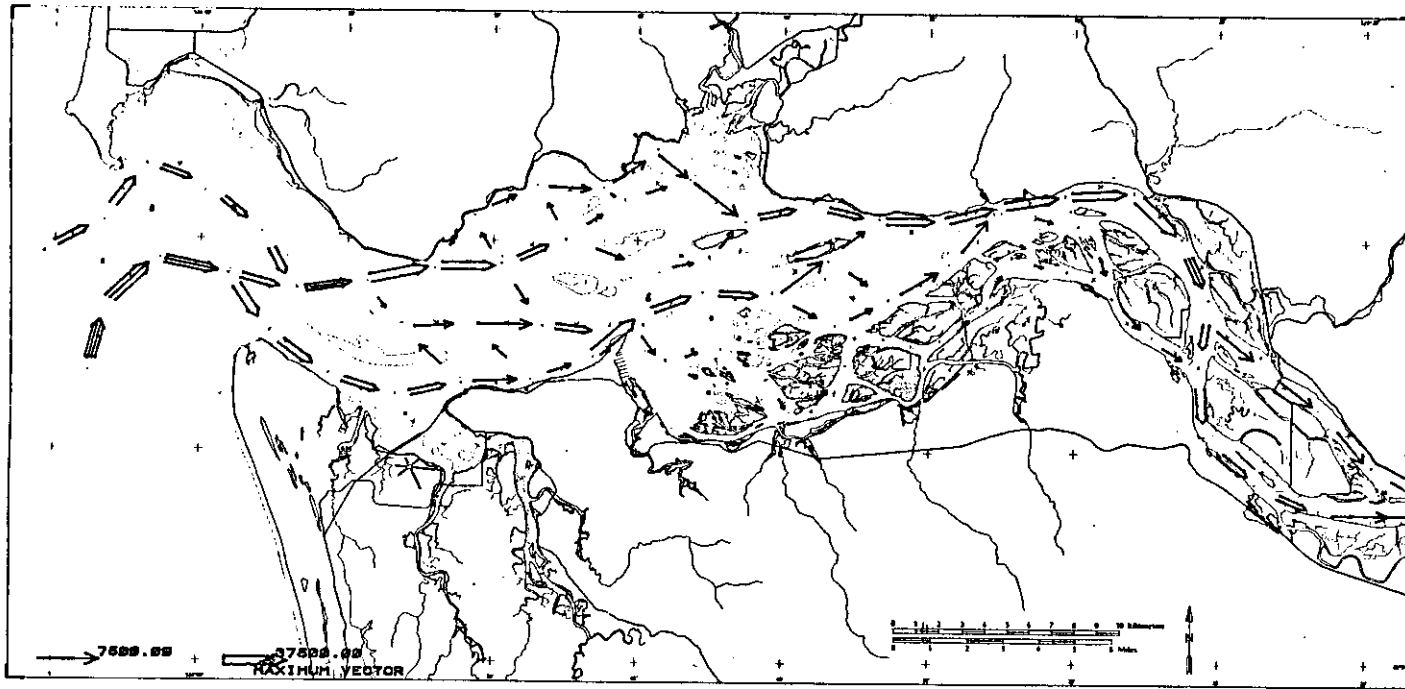




RUN H2 1863

DAY 4 TIME = 18 HOURS 0 MINS

Figure 55h. Horizontal volume transport vectors ( $\text{m}^3/\text{s}$ ) for neap tide and low riverflow. Half-tide flood.



RUN H2 1883

DAY 4 TIME = 21 HOURS 0 MINS

Figure 551. Horizontal volume transport vectors ( $m^3/s$ ) for neap tide and low riverflow. High water.



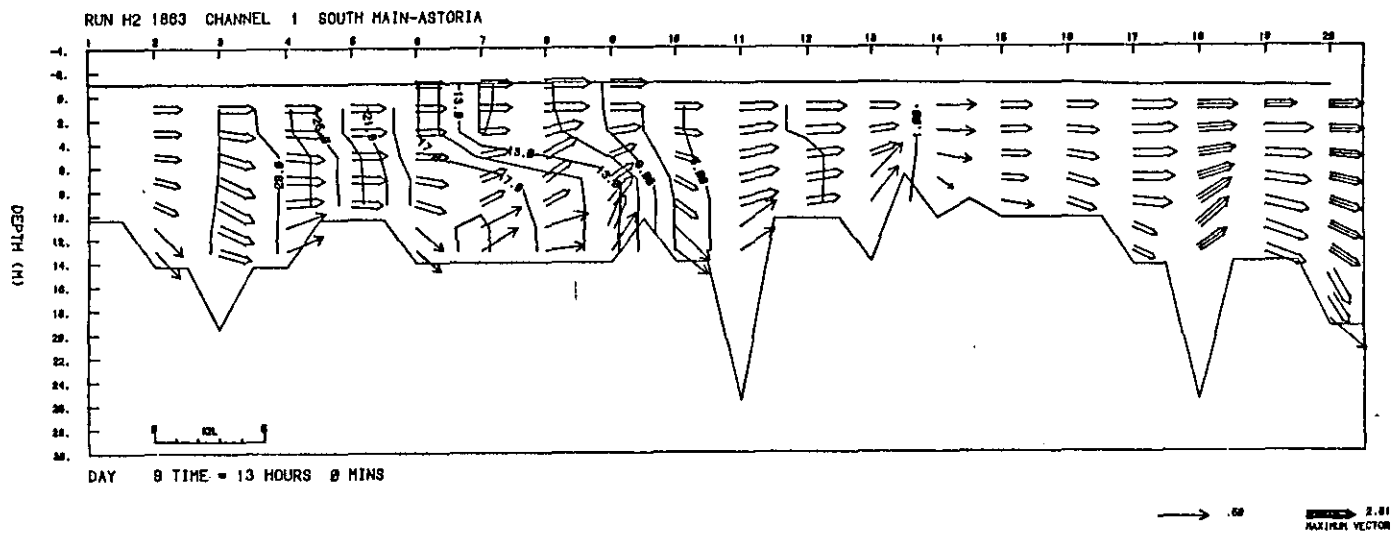


Figure 56a. Channel 1, spring tide period, currents and salinities (m/s and  $^{\circ}/\text{oo}$ ), low riverflow. High water.

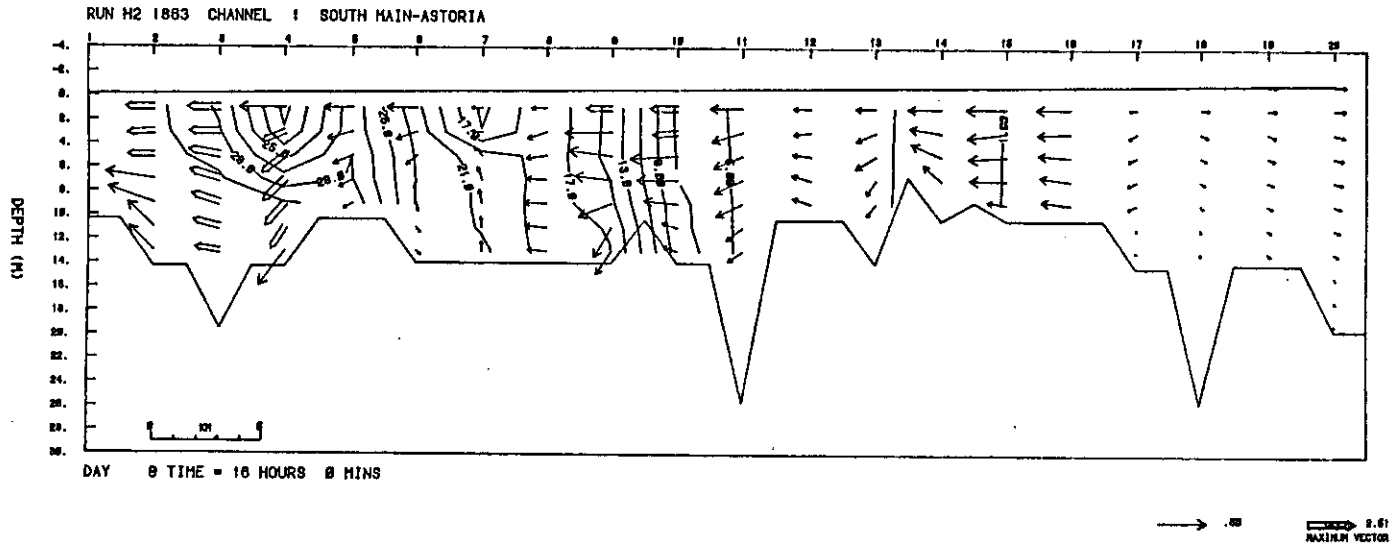


Figure 56b. Channel 1, spring tide period, currents and salinities (m/s and  $^{\circ}/\text{oo}$ ), low riverflow. Half-tide ebb.



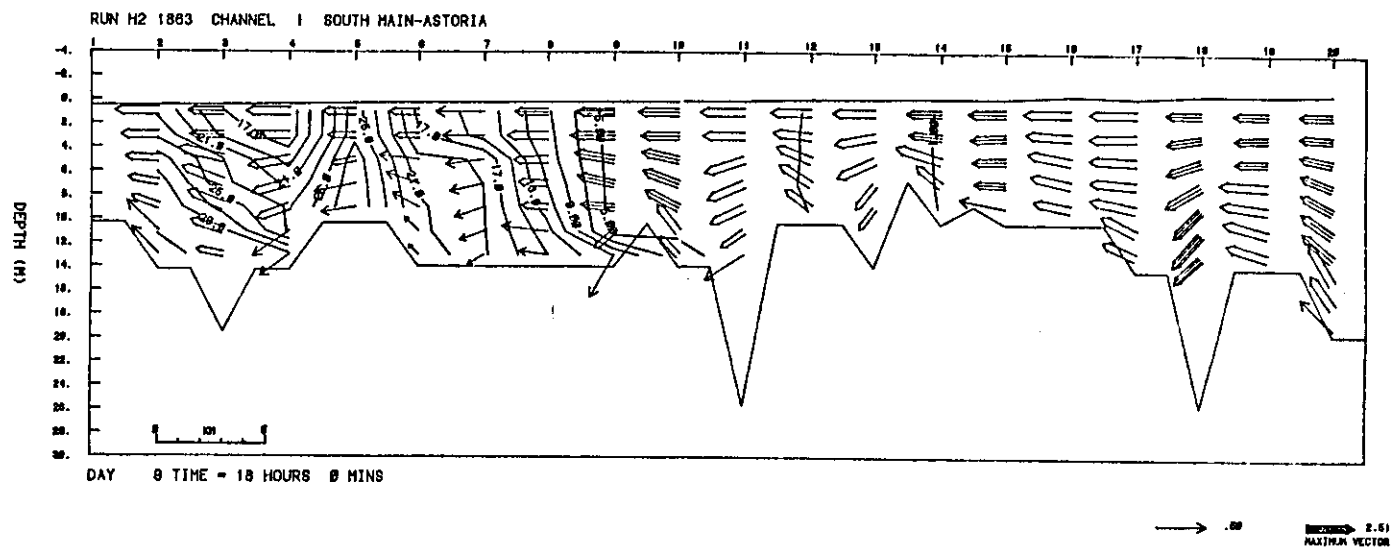


Figure 56c. Channel 1, spring tide period, currents and salinities (m/s and  $^{\circ}/\text{oo}$ ), low riverflow. Low water.

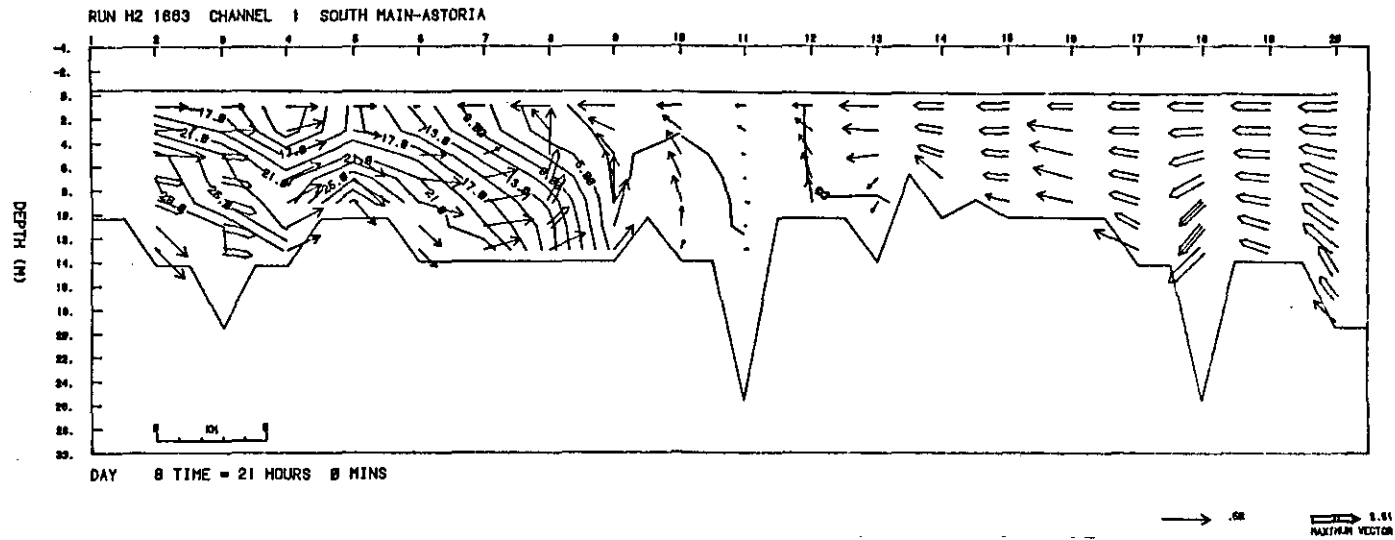


Figure 56d. Channel 1, spring tide period, currents and salinities (m/s and ‰), low riverflow. Half-tide flood.

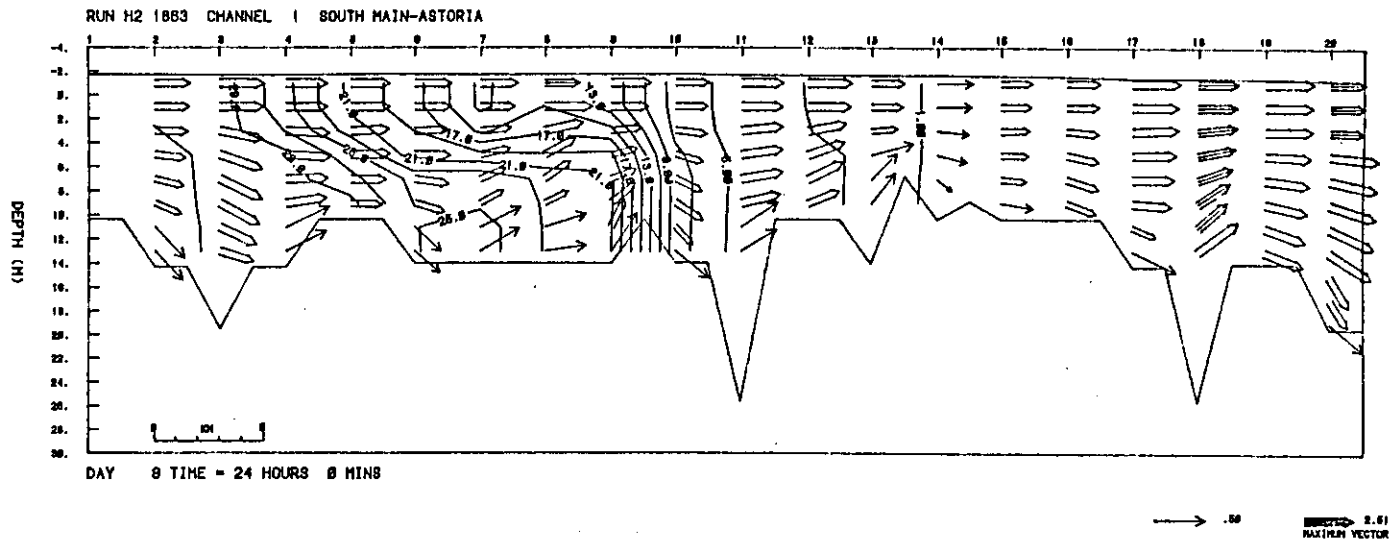


Figure 56e. Channel 1, spring tide period, currents and salinities (m/s and ‰), low riverflow. High water.

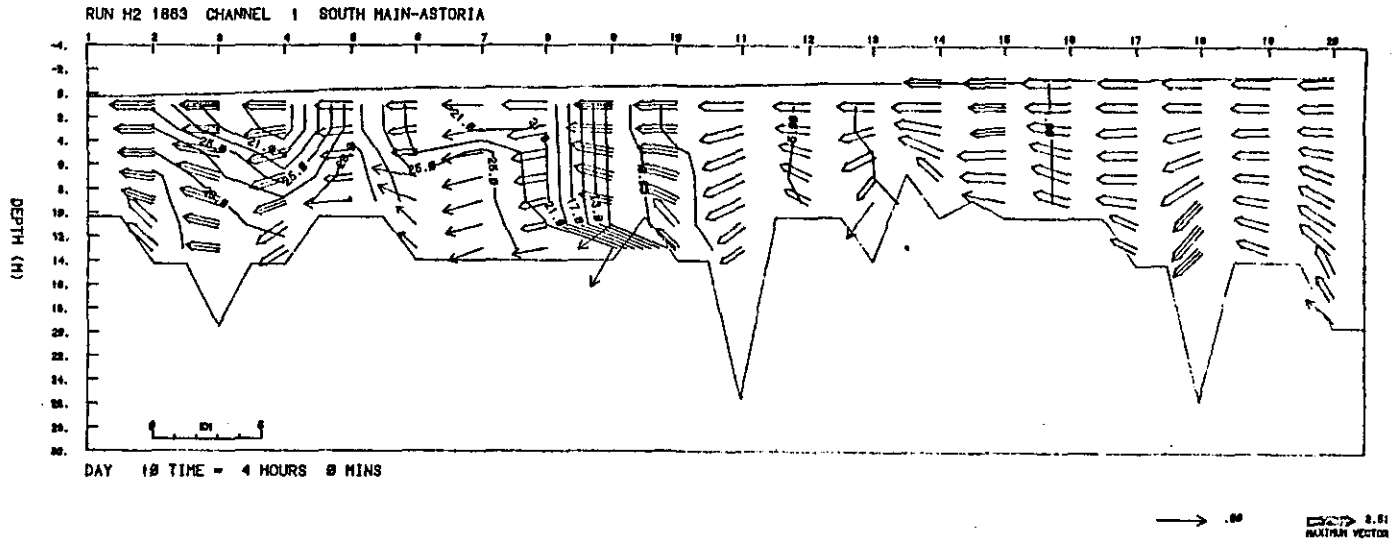


Figure 56f. Channel 1, spring tide period, currents and salinities (m/s and  $^{\circ}/\text{oo}$ ), low riverflow. Half-tide ebb.

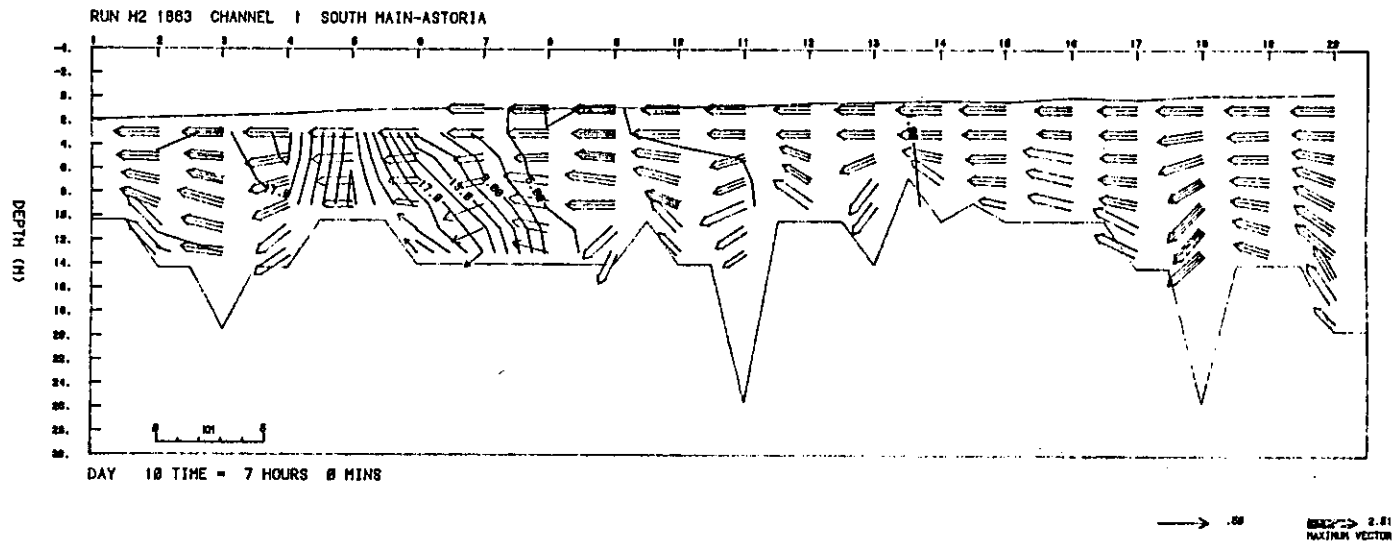


Figure 56g. Channel 1, spring tide period, currents and salinities (m/s and ‰), low riverflow. Low water.

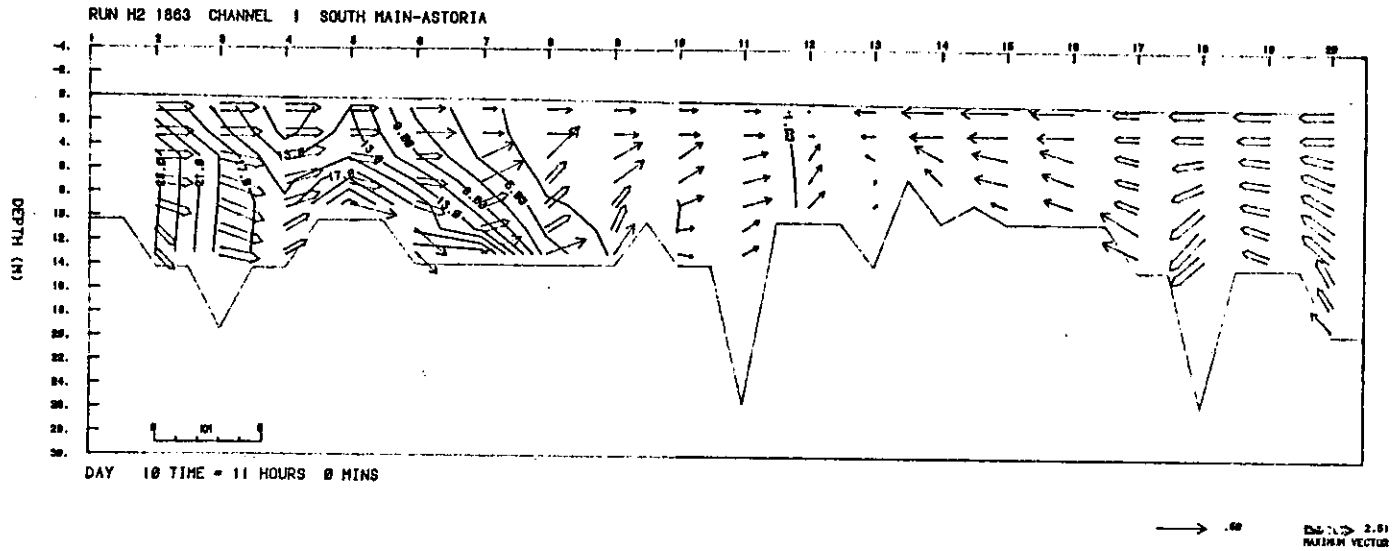


Figure 56h. Channel 1, spring tide period, currents and salinities (m/s and  $^{\circ}/\text{oo}$ ), low riverflow. Half-tide flood.

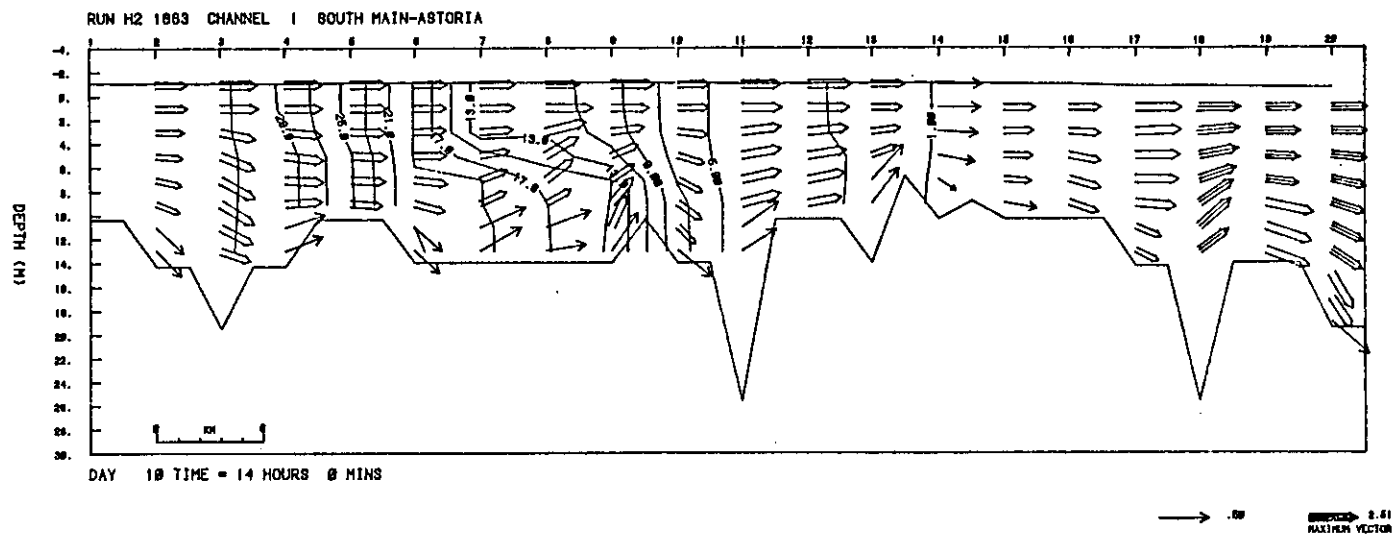


Figure 561. Channel 1, spring tide period, currents and salinities (m/s and ‰), low riverflow. High water.

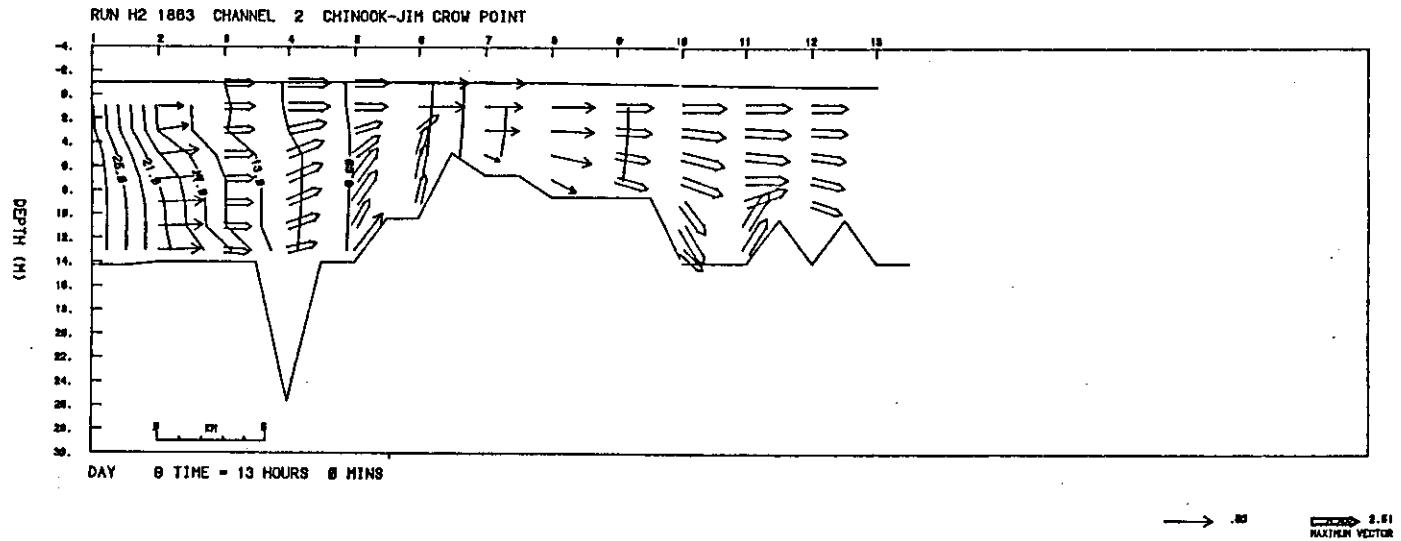


Figure 57a. Channel 2, spring tide period, currents and salinities (m/s and  $^{\circ}/_{oo}$ ), low riverflow. High water.

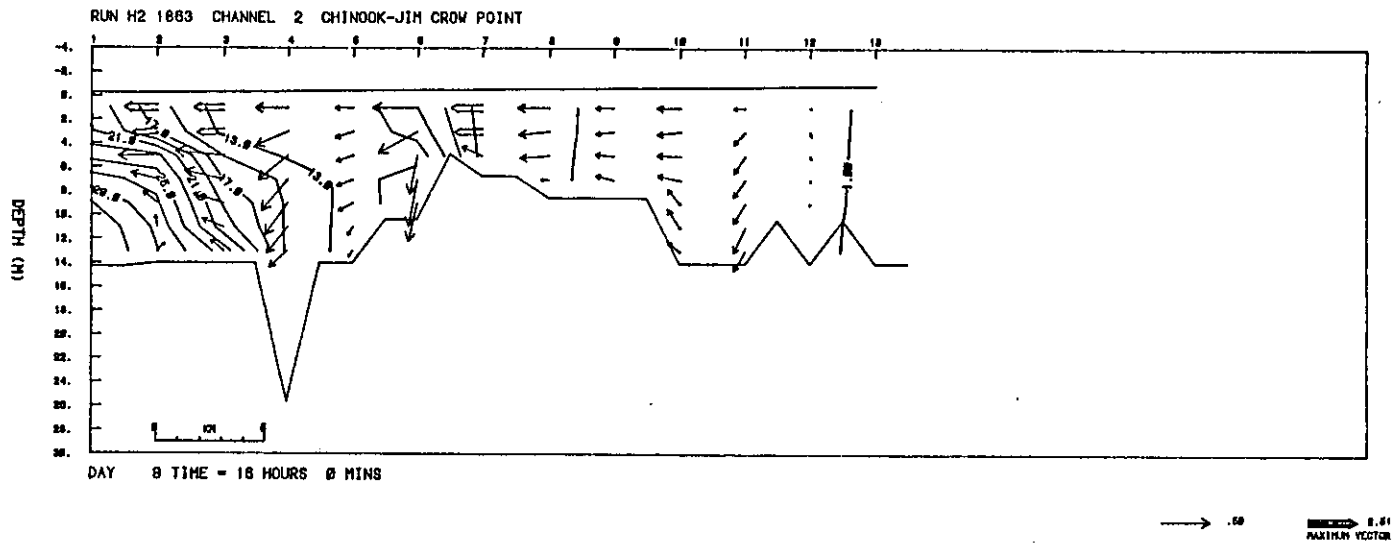


Figure 57b. Channel 2, spring tide period, currents and salinities (m/s and ‰), low riverflow. Half tide ebb.

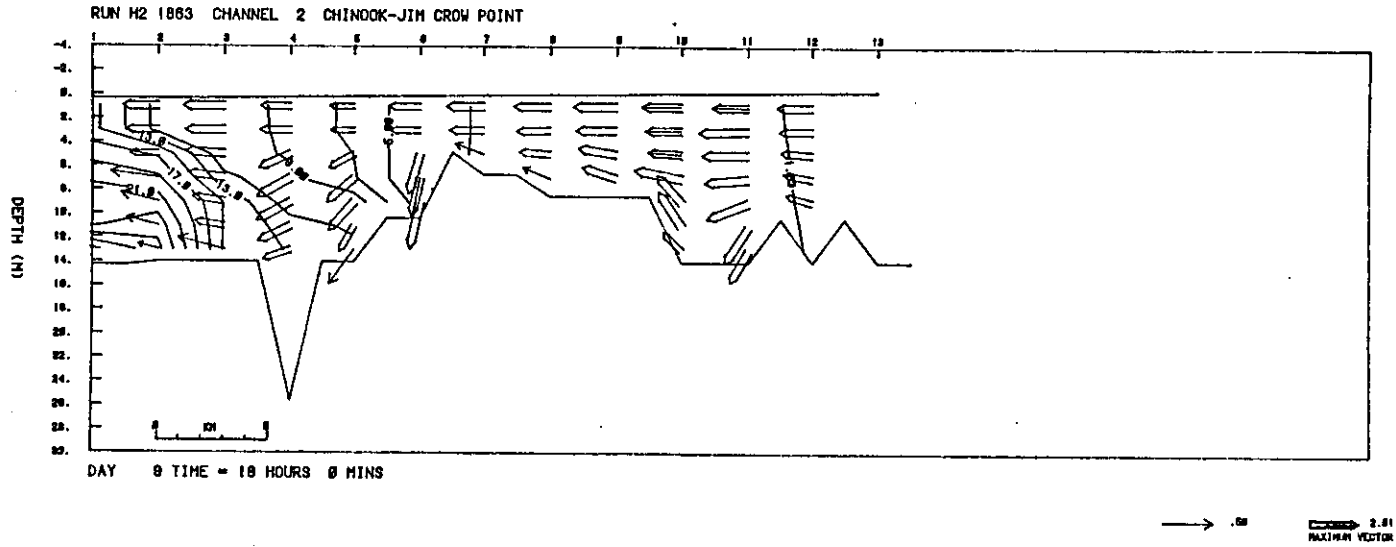


Figure 57c. Channel 2, spring tide period, currents and salinities (m/s and ‰), low riverflow. Low water.



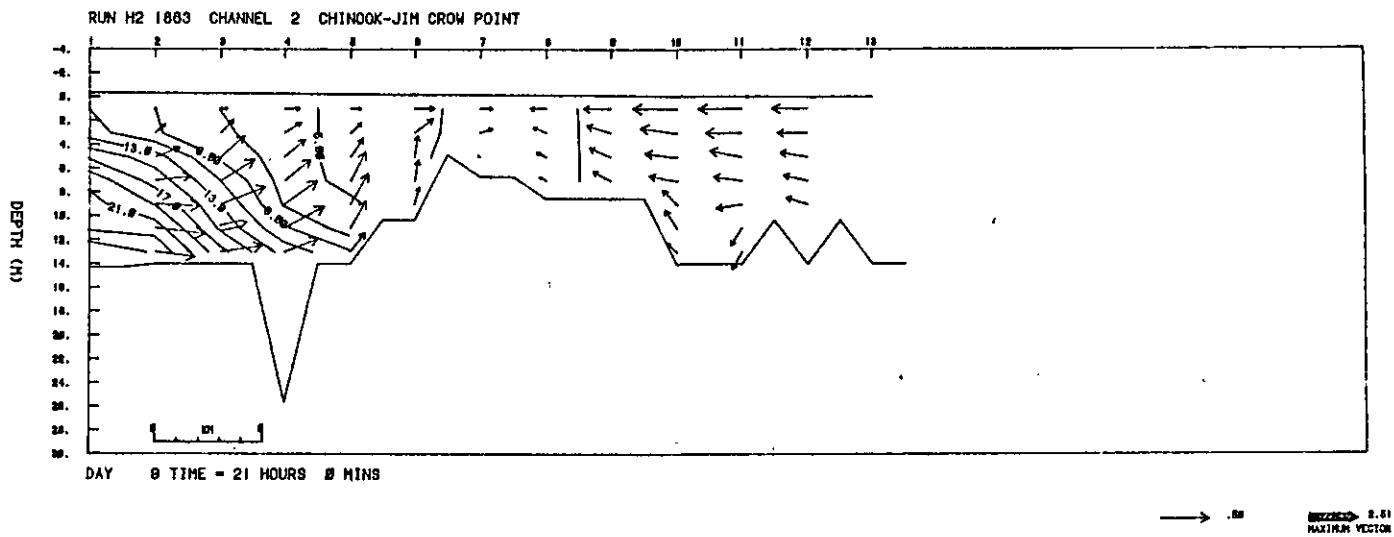


Figure 57d. Channel 2, spring tide period, currents and salinities (m/s and  $^{\circ}/\text{oo}$ ), low riverflow. Half-tide flood.

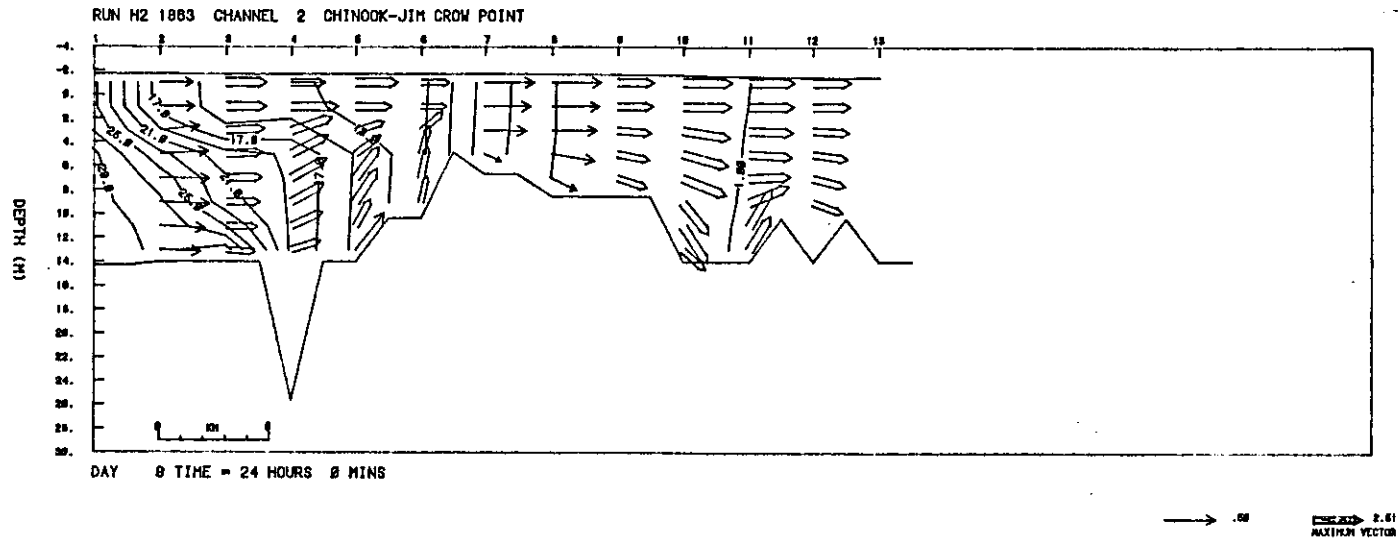


Figure 57e. Channel 2, spring tide period, currents and salinities (m/s and ‰), low riverflow. High water.

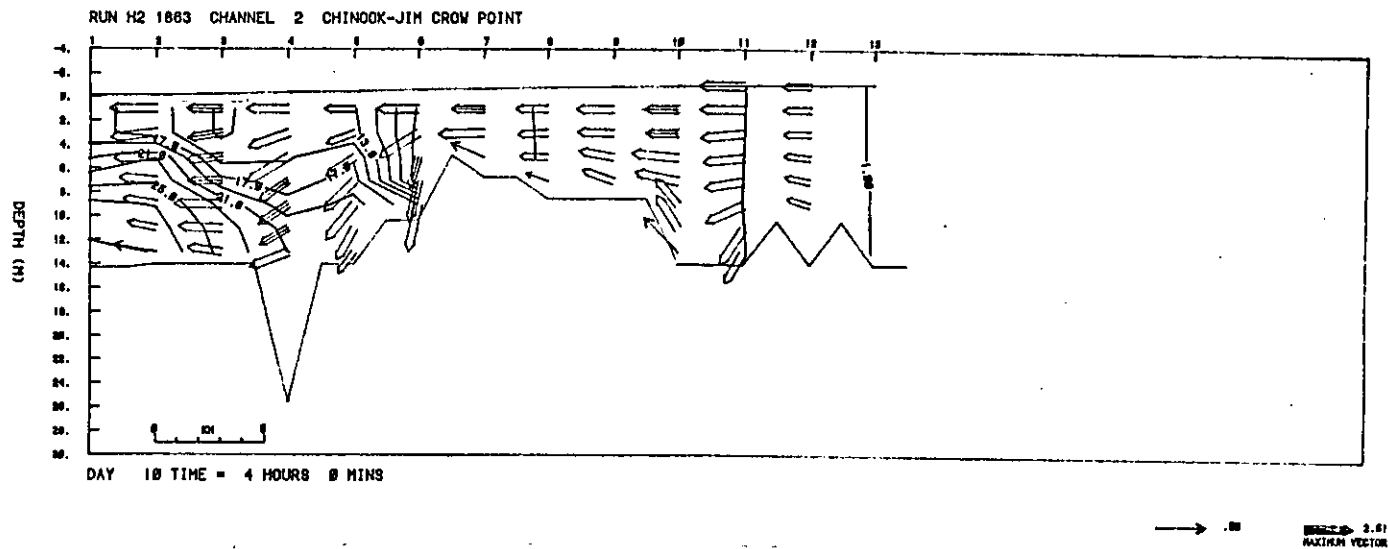


Figure 57f. Channel 2, spring tide period, currents and salinities (m/s and ‰), low riverflow. Half-tide ebb.

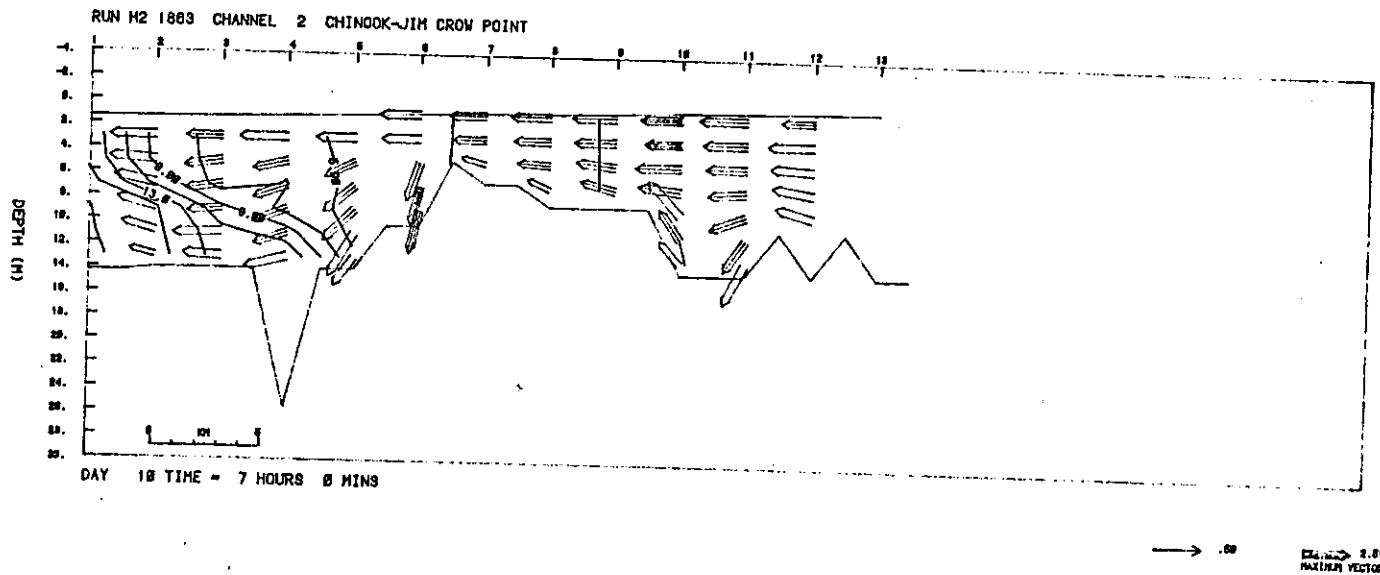


Figure 57g. Channel 2, spring tide period, currents and salinities (m/s and ‰), low riverflow. Low water.

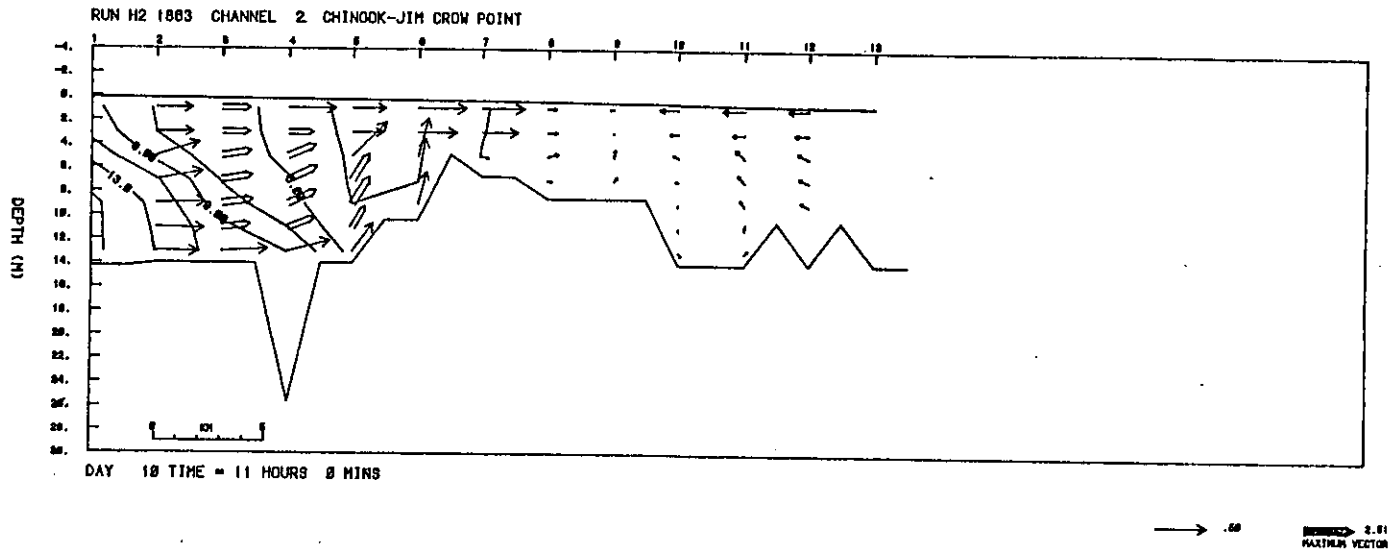


Figure 57h. Channel 2, spring tide period, currents and salinities (m/s and ‰), low riverflow. Half-tide flood.

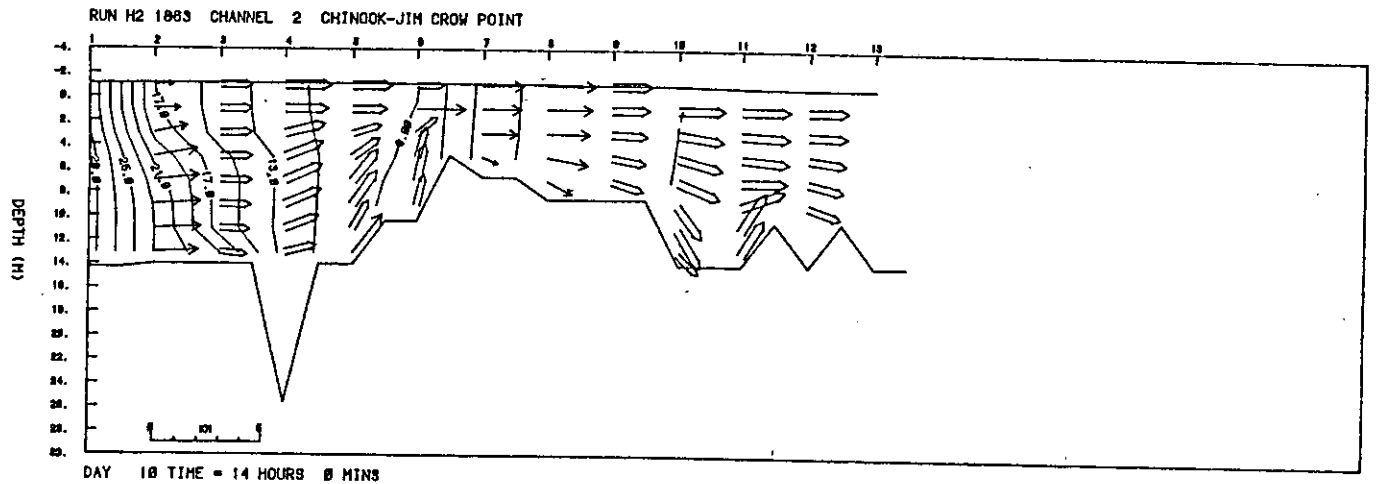


Figure 57i. Channel 2, spring tide period, currents and salinities (m/s and ‰), low riverflow. High water.

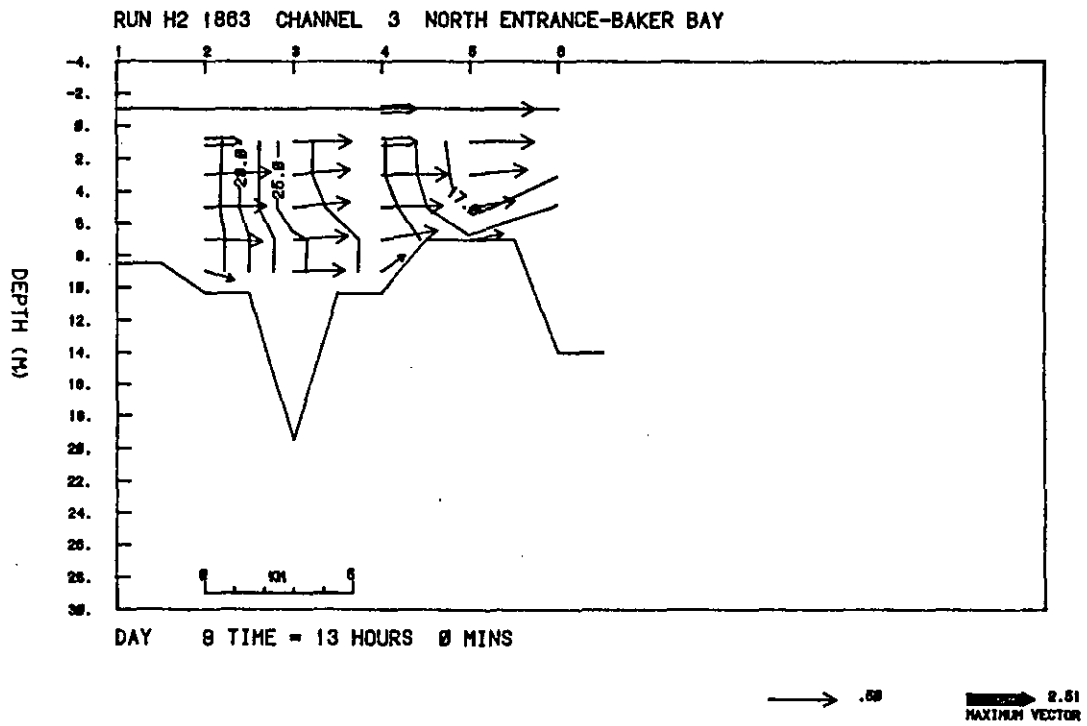


Figure 58a. Channel 3, spring tide period, currents and salinities (m/s and ‰), low riverflow. High water.

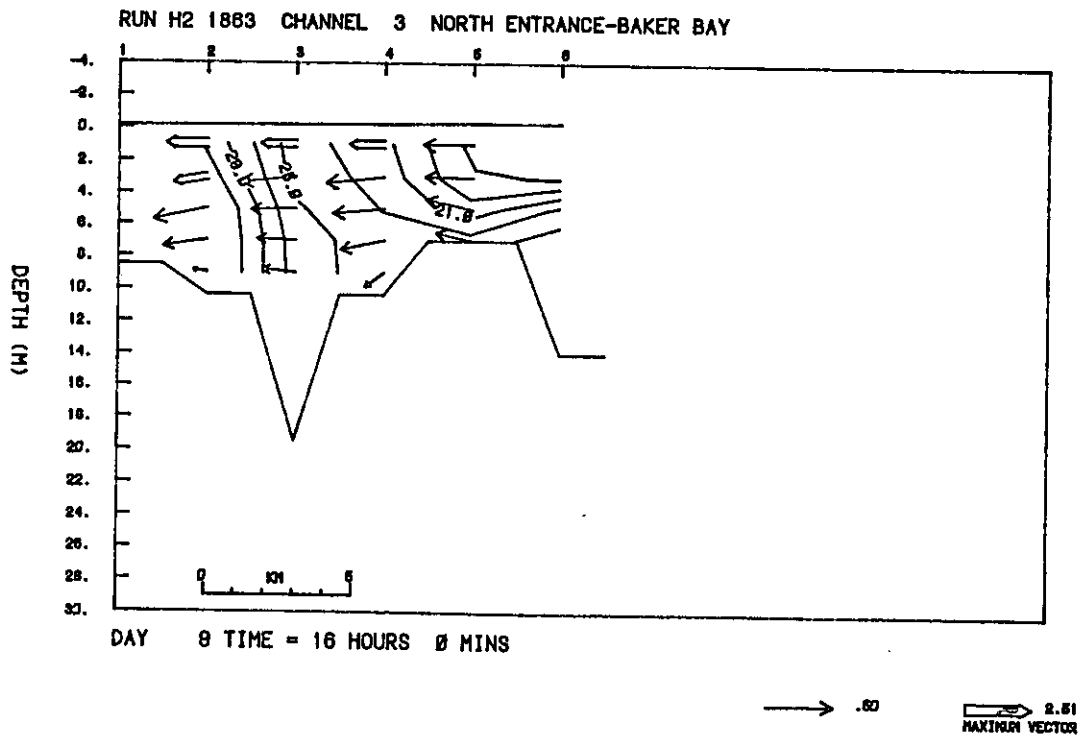


Figure 58b. Channel 3, spring tide period, currents and salinities (m/s and ‰), low riverflow. Half-tide ebb.

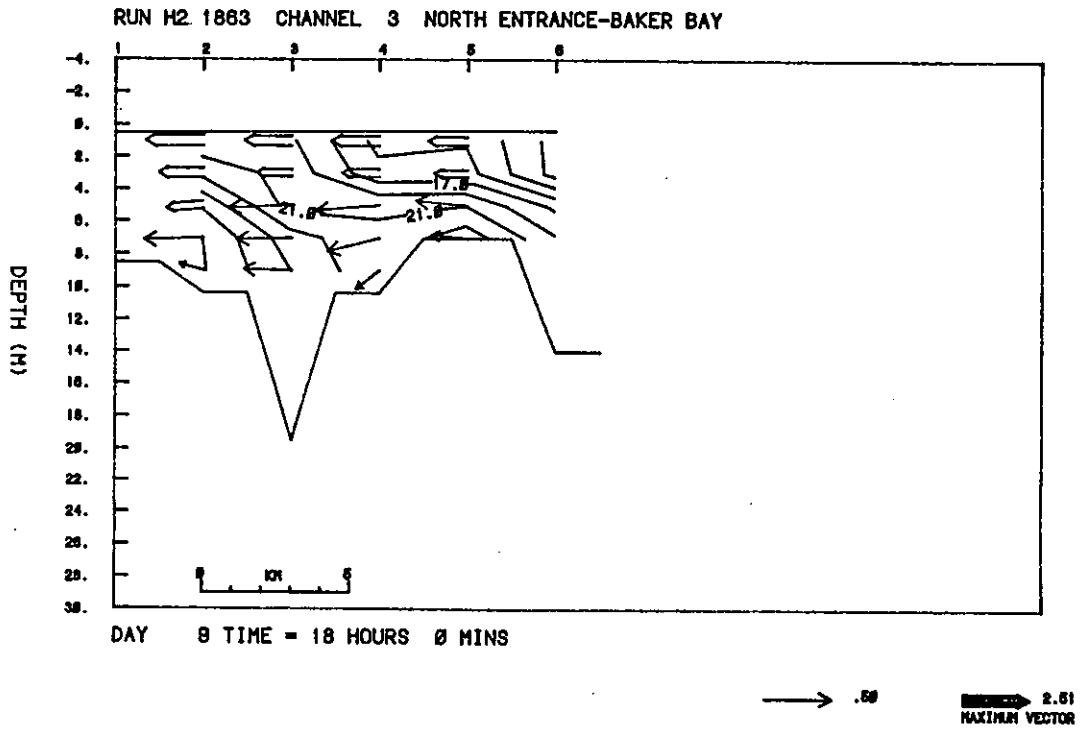


Figure 58c. Channel 3, spring tide period, currents and salinities (m/s and ‰), low riverflow. Low water.

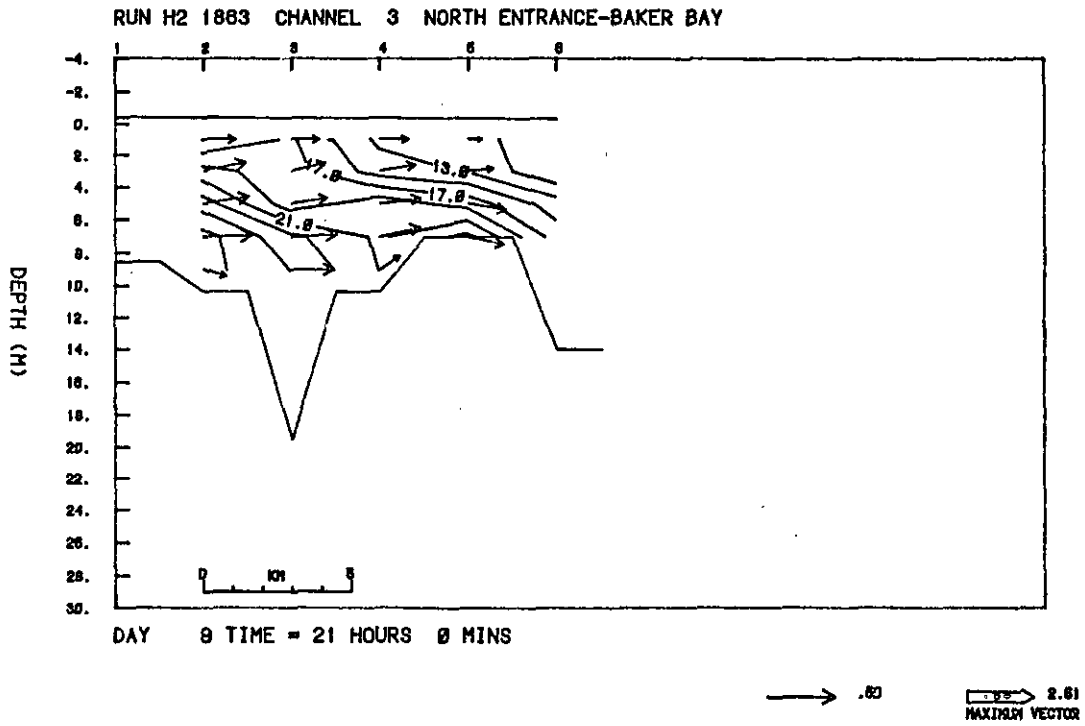


Figure 58d. Channel 3, spring tide period, currents and salinities (m/s and ‰), low riverflow. Half-tide flood.

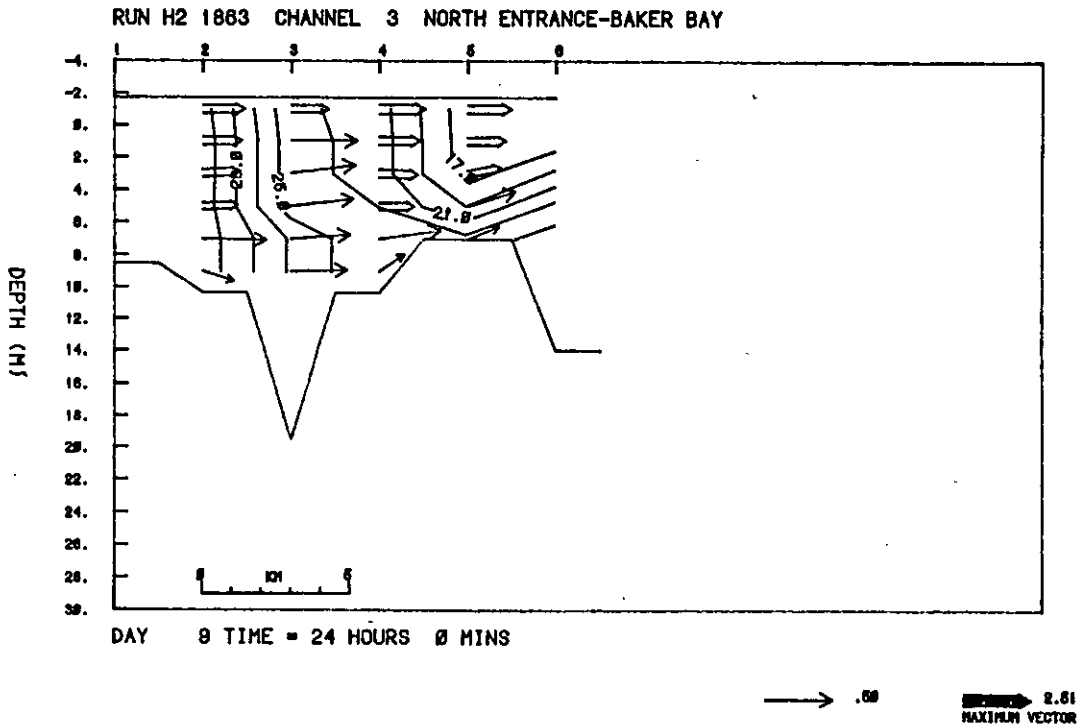


Figure 58e. Channel 3, spring tide period, currents and salinities (m/s and ‰), low riverflow. High water.

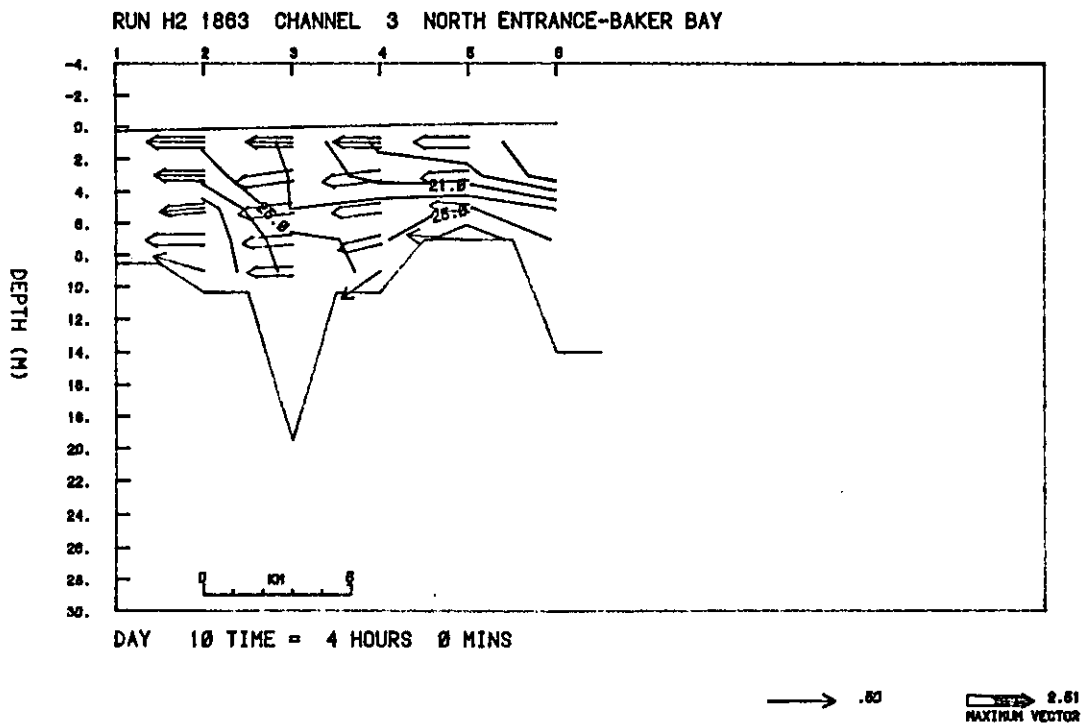


Figure 58f. Channel 3, spring tide period, currents and salinities (m/s and ‰), low riverflow. Half-tide ebb.

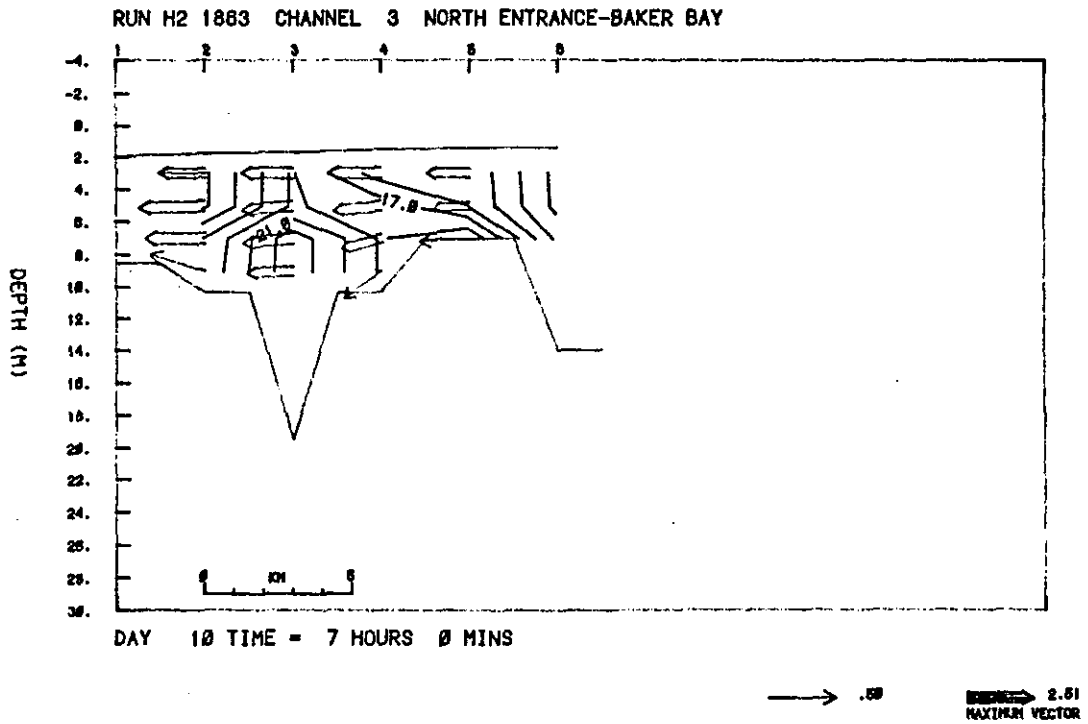


Figure 58g. Channel 3, spring tide period, currents and salinities (m/s and ‰), low riverflow. Low water.

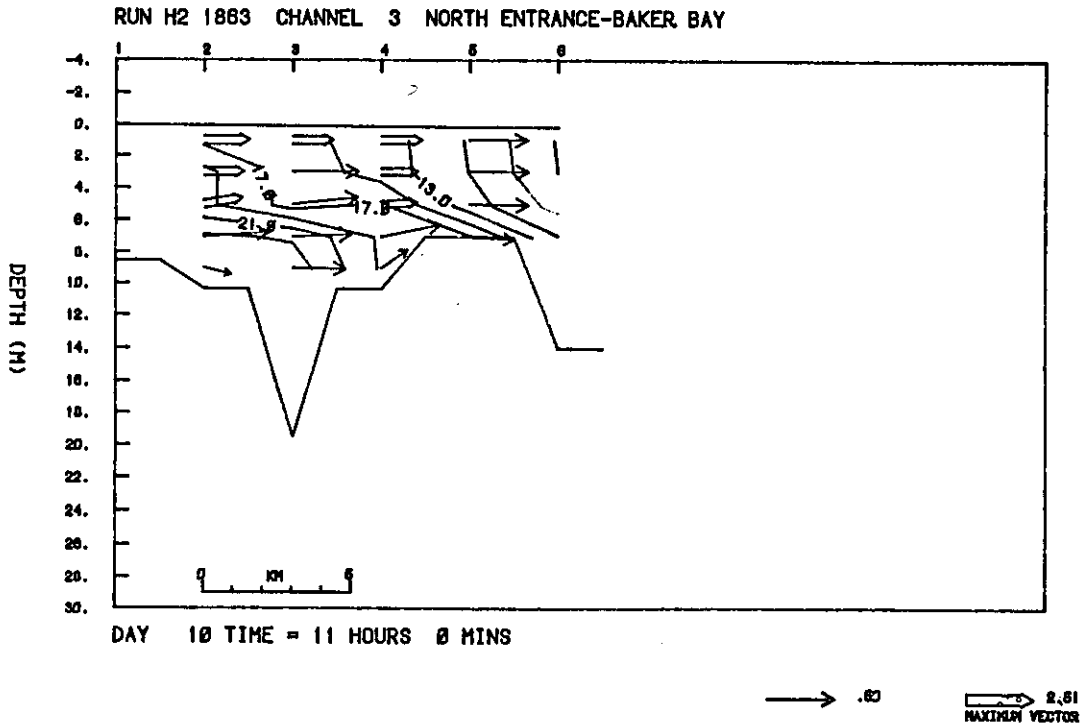


Figure 58h. Channel 3, spring tide period, currents and salinities (m/s and ‰), low riverflow. Half-tide flood.

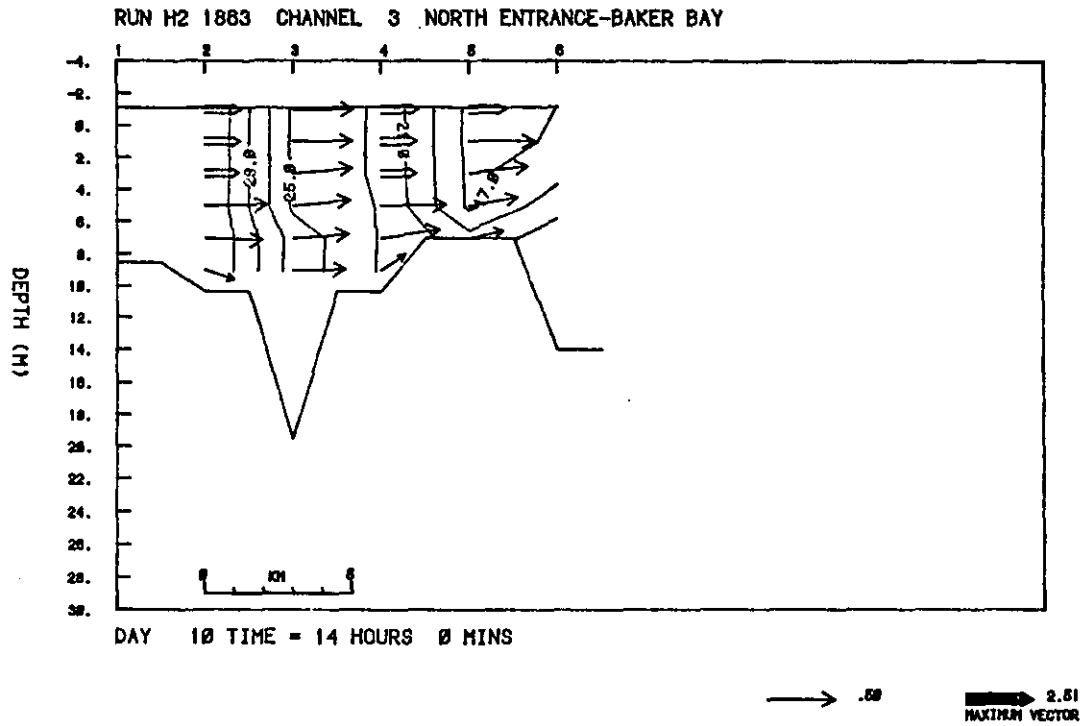


Figure 58i. Channel 3, spring tide period, currents and salinities (m/s and ‰), low riverflow. High water.

Some features of the sections for channels 1 and 2 are similar to the neap tide sections. The salinity of the north channel is lower than the south channel seaward of Tongue Point. The bars in both channels act as barriers to salt penetration through the vertical fronts are more diffuse particularly in channel 2. All three channels are much less stratified than at neap tide with smaller salt intrusion lengths in both channels. Also due to increased mixing the tidal extremes of salinity are not as large as the neap tide extremes. Except for this last point, the neap-spring differences are similar to the present day.

### 3.2.3. Riverflows

This section discusses the neap and spring tide means and extreme salinities for the three different riverflow runs. The high riverflow (12,000 m<sup>3</sup>/s) run (H1) results are given in Figures 59-64 for spring and neap tides in the form of sections for channels 1, 2, and 3. The equivalent present day results are given in Figures 31-34 for spring and neap #2 of Run 51.

The neap tide means show very weak upstream bottom flow at the entrances to channels 1 and 2 and rather more stratification than the present day high flow neap tide results. Salt intrusion lengths for both mean and maximum salinity fields are greater than in Figures 31 and 32 for both channels 1 and 2. Channel 3 is horizontally stratified with mean outflow at all depths.

The spring tide high flow sections (Figures 61-64) show less stratification than both the neap tide and spring #2 of Run 51. The mean currents show no evidence of upstream flow though magnitude of the bottom downstream flow shows considerable variation due to variations in channel widths and depths as well as due to density gradients. The minimum salinities show that salt is expelled almost completely from the estuary on the ebb tide which was not the case for the present day results even with the largest riverflows during the freshet of June 1981.

The low flow (4,000 m<sup>3</sup>/s) run (H2) results, in the form of sections of mean currents and salinities and contours of maximum and minimum salinities calculated at each grid point over the 50-hour period, are given in Figures 65-67 and 68-70 for neap and spring tides, respectively. These figures should be compared with Run 26 sections given in Figures 19-26.

The mean density current is better developed for the neap tide than in Run H1. The density current is particularly strong in the Hammond-Astoria reach of channel 1 where the freshwater outflow is reduced by divergent flows over Desdemona Sands. The salinity in both channels intrudes over the bars relatively further than in 1982. The difference in salt content between channels 1 and 2 is clearer with the spring tide mean and maximum fields. The maximum salinity plots show clearly, for both tides the strong vertical fronts which develop over

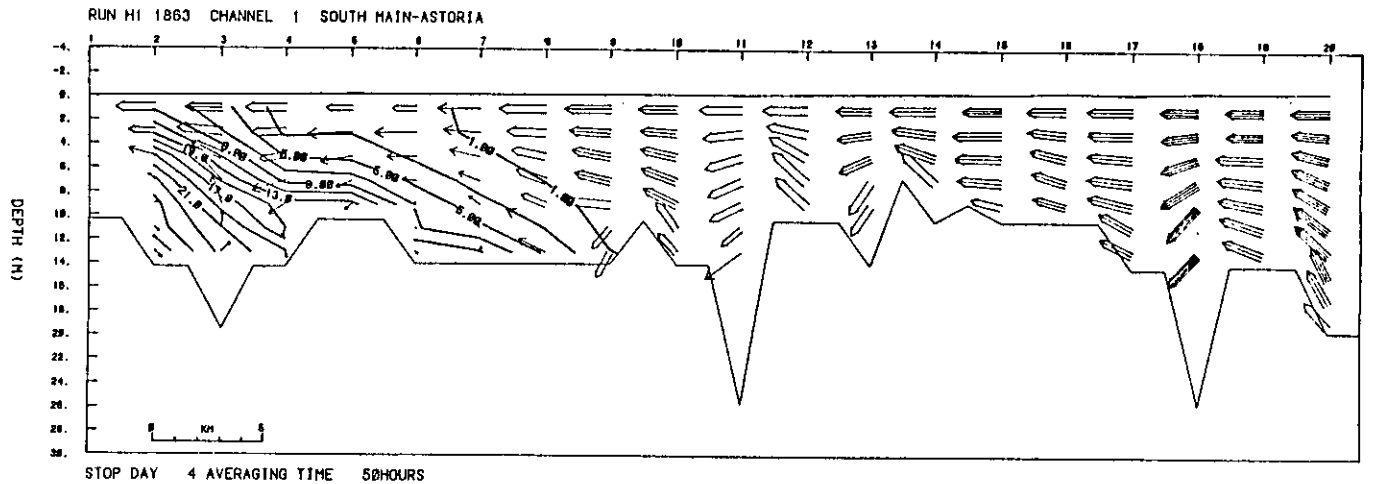


Figure 59a. Channel 1, neap tide period (historical bathymetry, riverflow =  $12000 \text{ m}^3/\text{s}$ ). Mean currents and salinities (m/s and ‰).

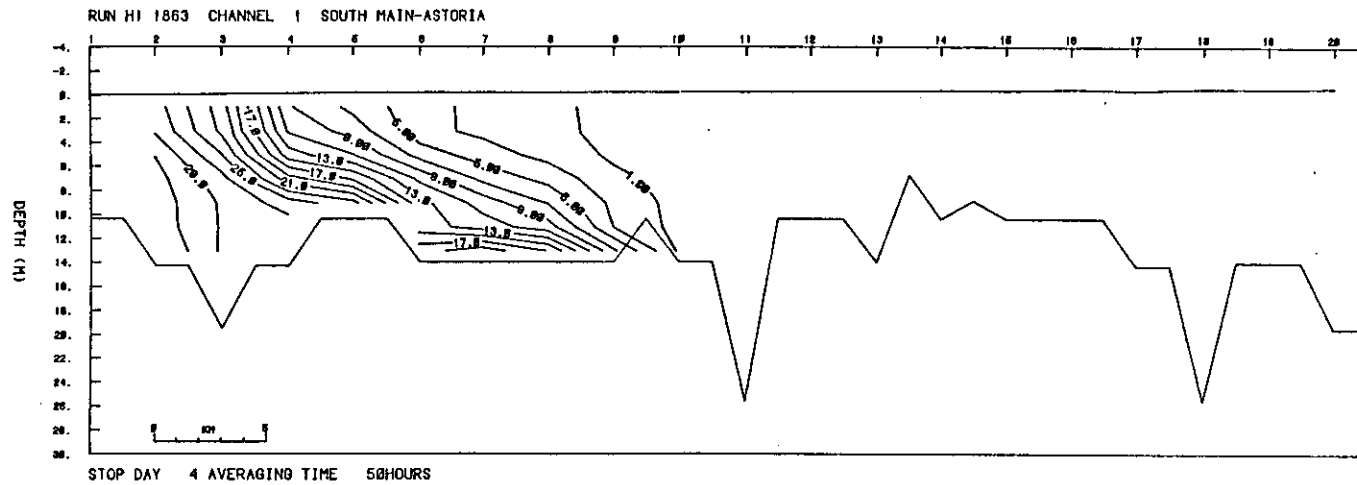


Figure 59b. Channel 1, neap tide period (historical bathymetry, riverflow =  $12000 \text{ m}^3/\text{s}$ ). Maximum salinities.

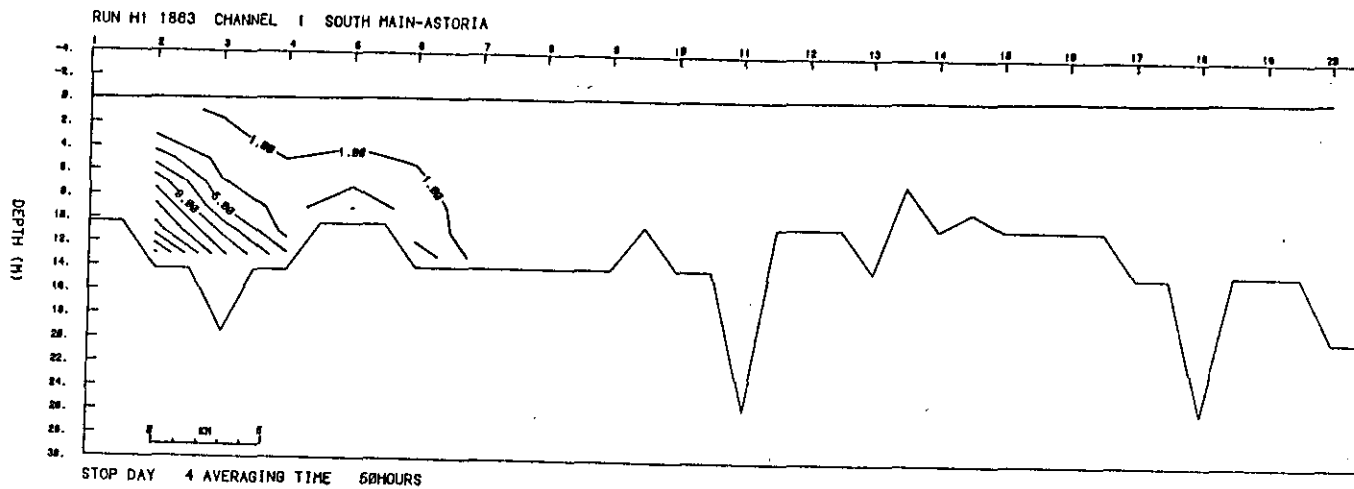


Figure 59c. Channel 1, neap tide period (historical bathymetry, riverflow =  $12000 \text{ m}^3/\text{s}$ ). Minimum salinities.

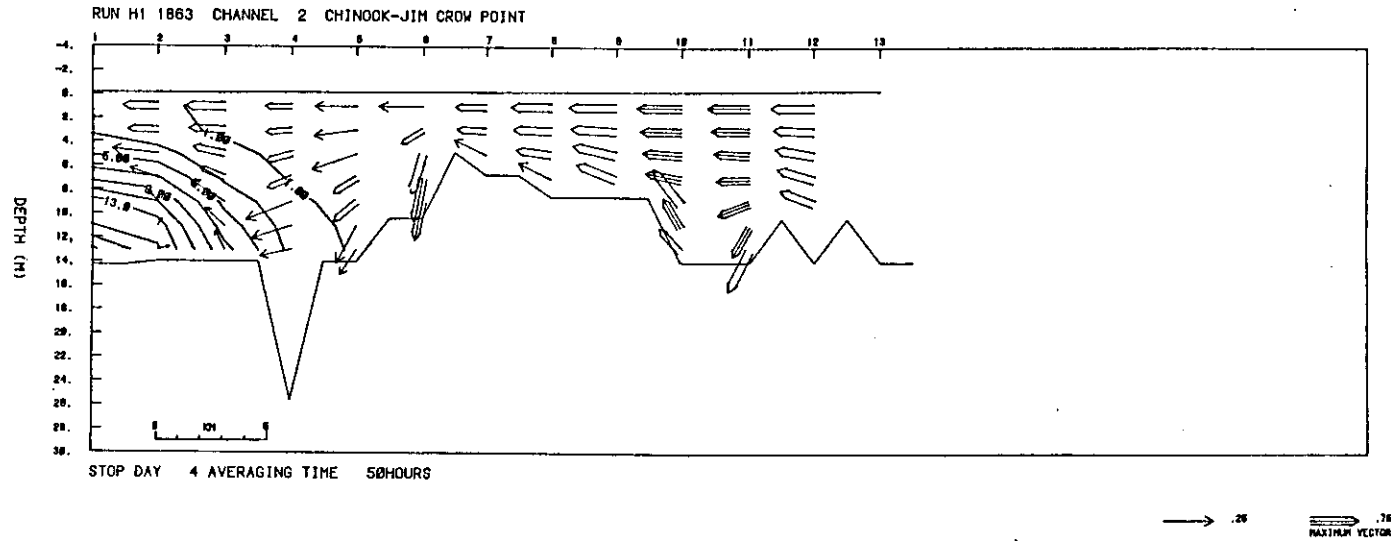


Figure 60a. Channel 2, neap tide period (historical bathymetry, riverflow =  $12000 \text{ m}^3/\text{s}$ ). Mean currents and salinities (m/s and ‰).



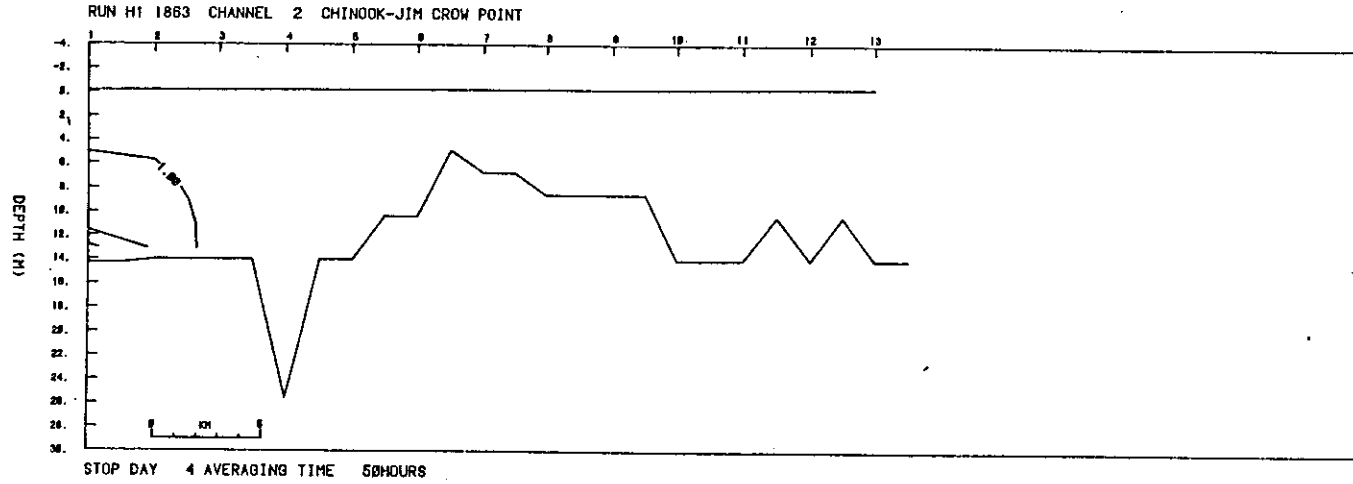


Figure 60c. Channel 2, neap tide period (historical bathymetry, riverflow =  $12000 \text{ m}^3/\text{s}$ ). Minimum salinities.

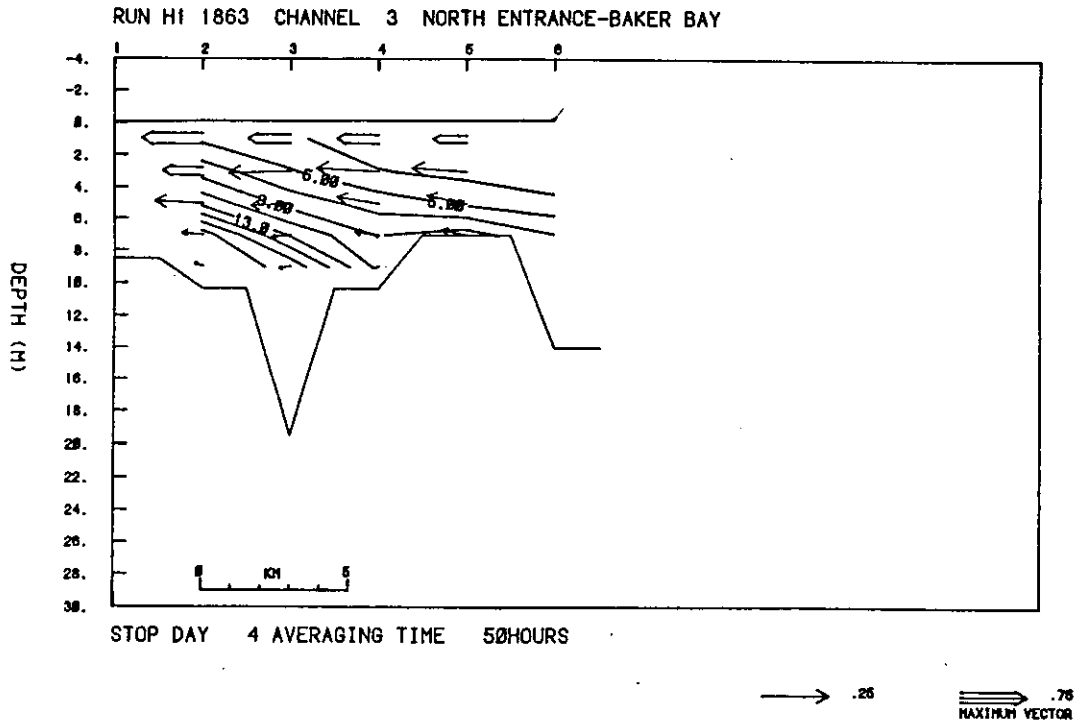


Figure 61a. Channel 3, neap tide period (historical bathymetry, riverflow = 12000 m<sup>3</sup>/s). Mean currents and salinities (m/s and ‰).

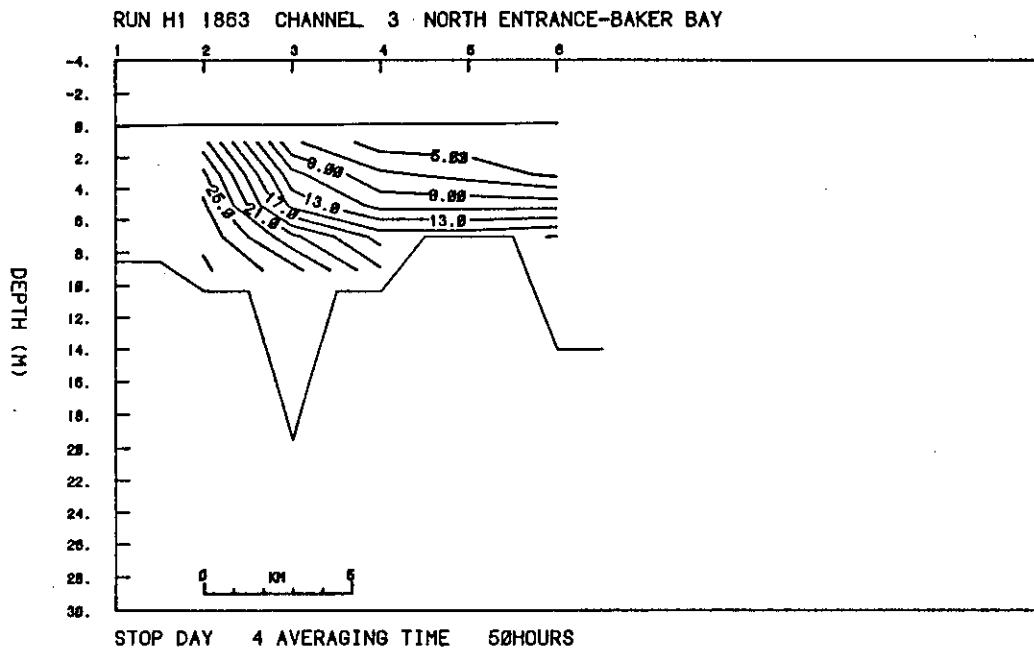


Figure 61b. Channel 3, neap tide period (historical bathymetry, riverflow = 12000 m<sup>3</sup>/s). Maximum salinities.

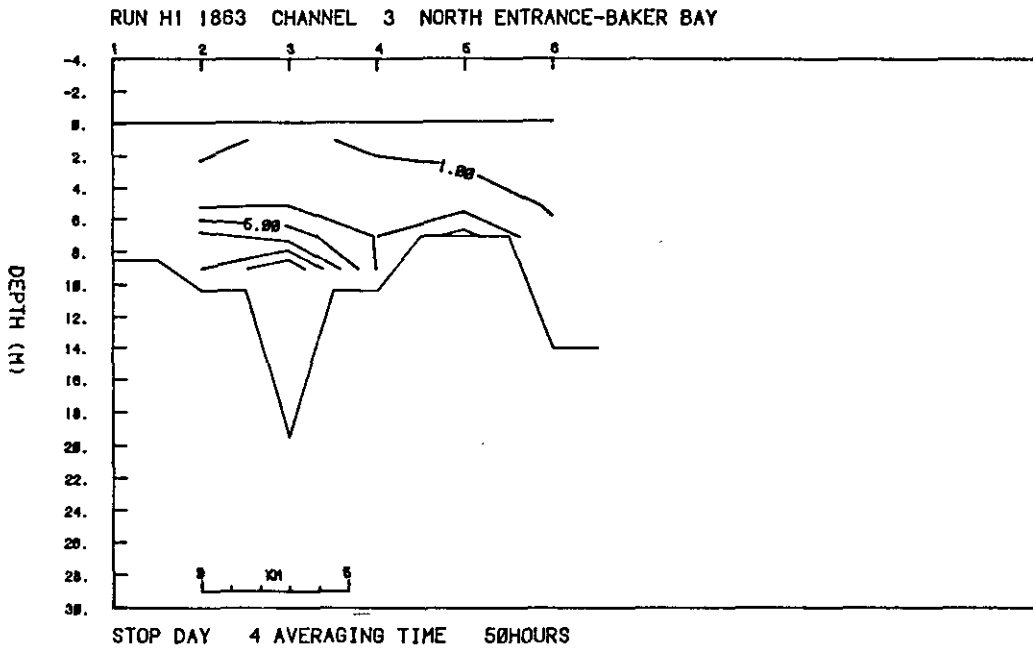


Figure 61c. Channel 3, neap tide period (historical bathymetry, riverflow = 12000 m<sup>3</sup>/s). Minimum salinities.

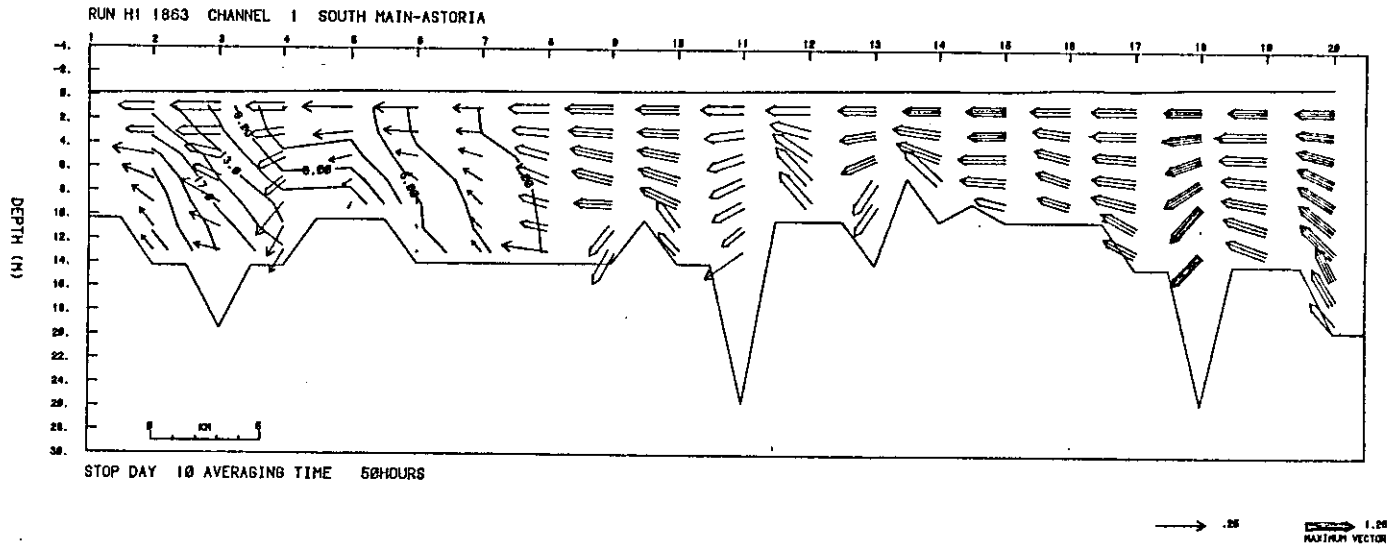


Figure 62a. Channel 1, spring tide period (historical bathymetry, riverflow =  $12000 \text{ m}^3/\text{s}$ ).  
Mean currents and salinities (m/s and ‰).

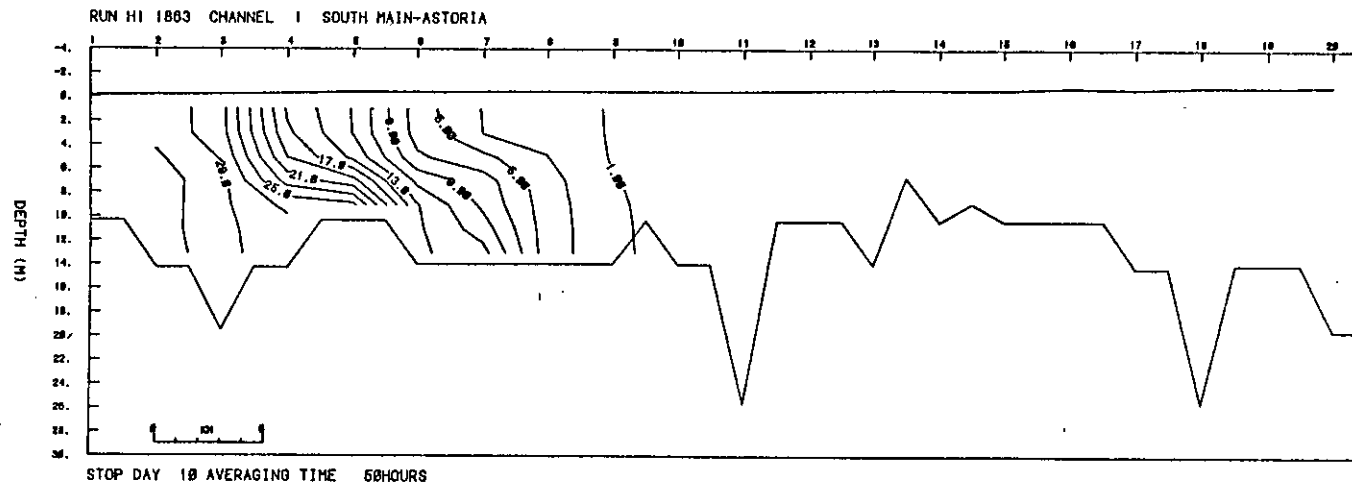


Figure 62b. Channel 1, spring tide period (historical bathymetry, riverflow =  $12000 \text{ m}^3/\text{s}$ ). Maximum salinities.

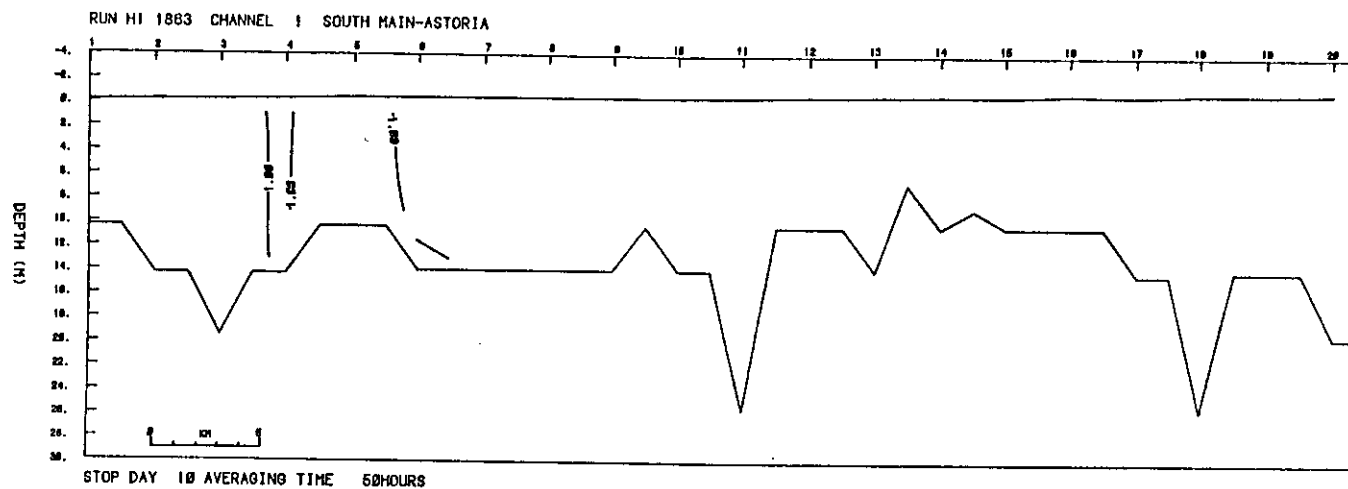


Figure 62c. Channel 1, spring tide period (historical bathymetry, riverflow =  $12000 \text{ m}^3/\text{s}$ ). Minimum salinities.

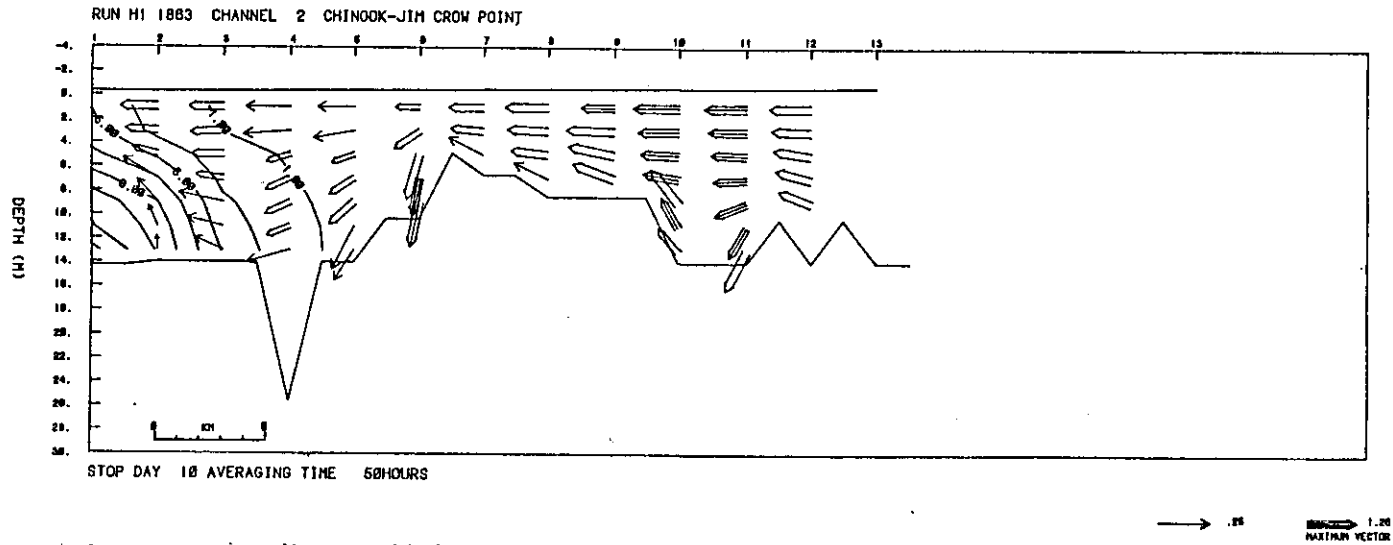


Figure 63a. Channel 2, spring tide period (historical bathymetry, riverflow =  $12000 \text{ m}^3/\text{s}$ ).  
 Mean currents and salinities (m/s and ‰).

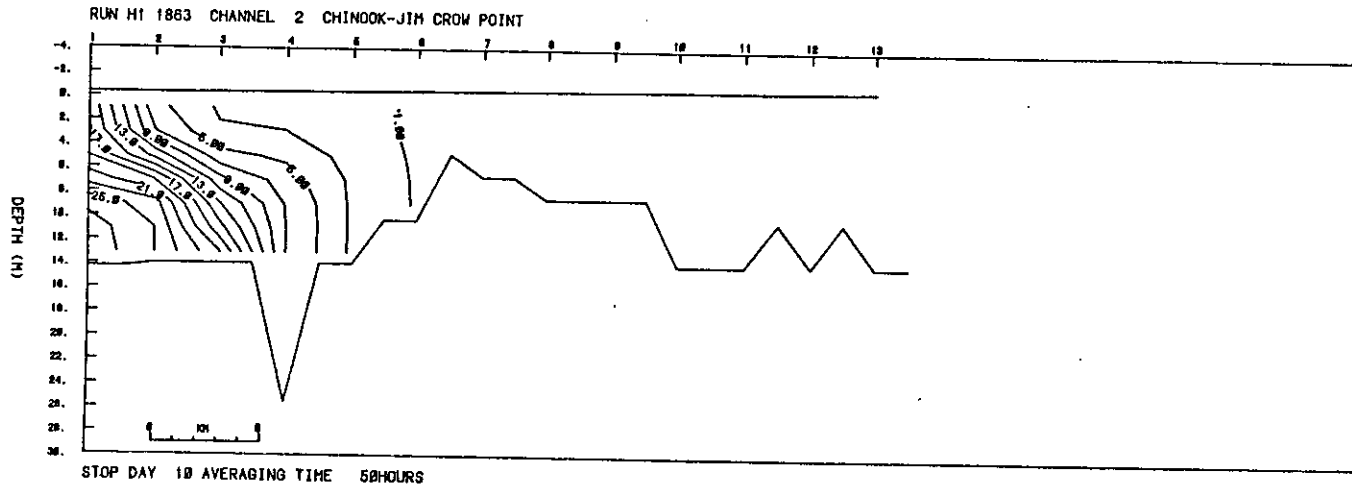


Figure 63b. Channel 2, spring tide period (historical bathymetry, riverflow =  $12000 \text{ m}^3/\text{s}$ ). Maximum salinities.

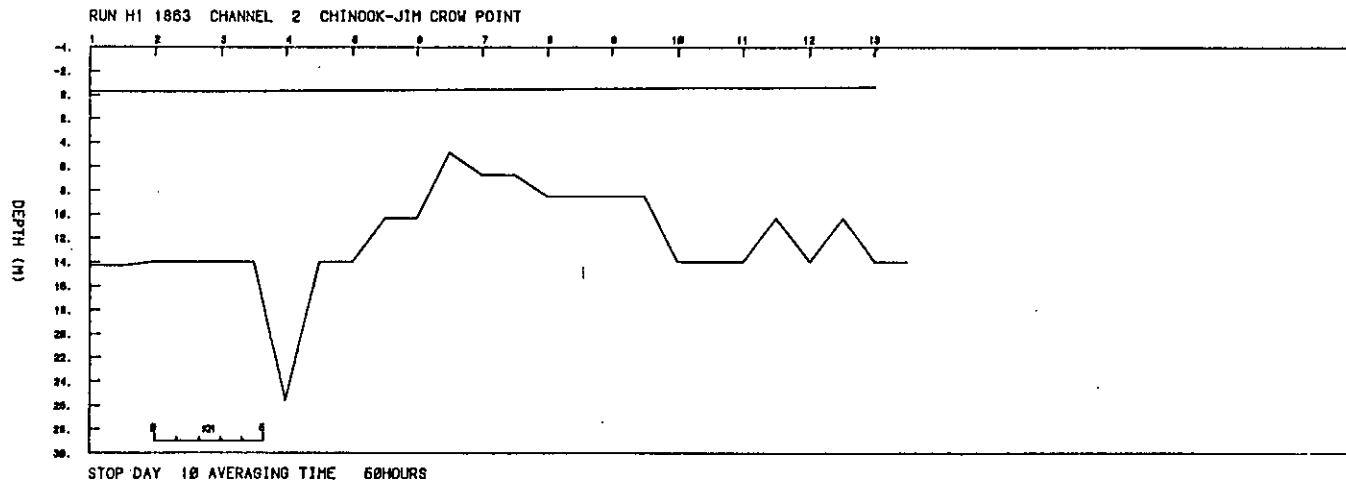


Figure 63c. Channel 2, spring tide period (historical bathymetry, riverflow =  $12000 \text{ m}^3/\text{s}$ ). Minimum salinities.

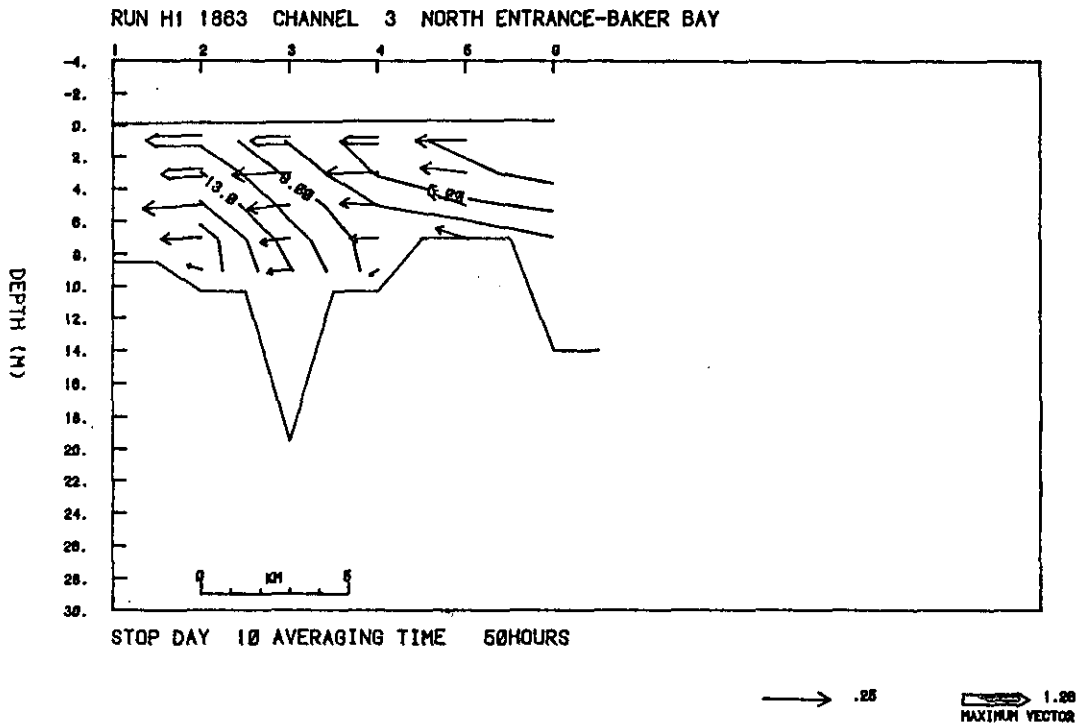


Figure 64a. Channel 3, spring tide period (historical bathymetry, riverflow = 12000 m<sup>3</sup>/s). Mean currents and salinities (m/s and ‰).

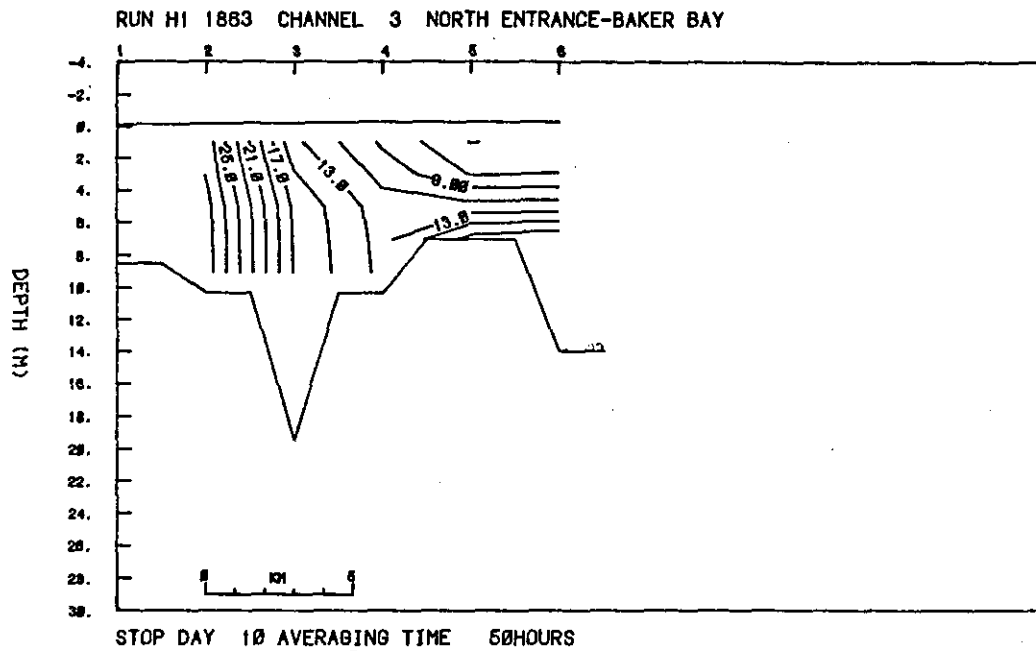


Figure 64b. Channel 3, spring tide period (historical bathymetry, riverflow =  $12000 \text{ m}^3/\text{s}$ ). Maximum salinities.

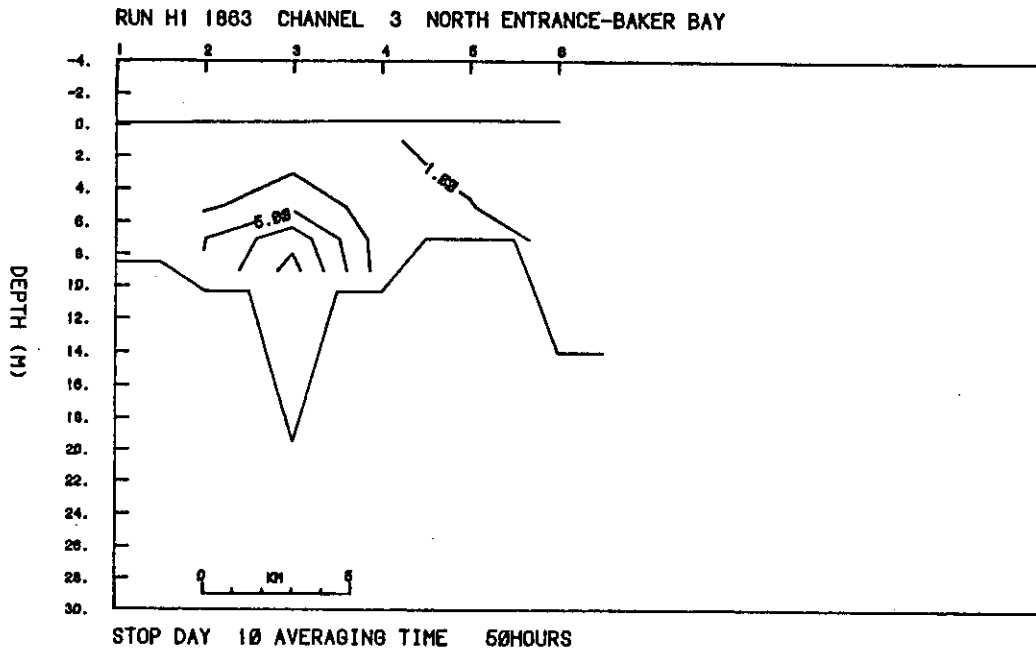


Figure 64c. Channel 3, spring tide period (historical bathymetry, riverflow =  $12000 \text{ m}^3/\text{s}$ ). Minimum salinities.

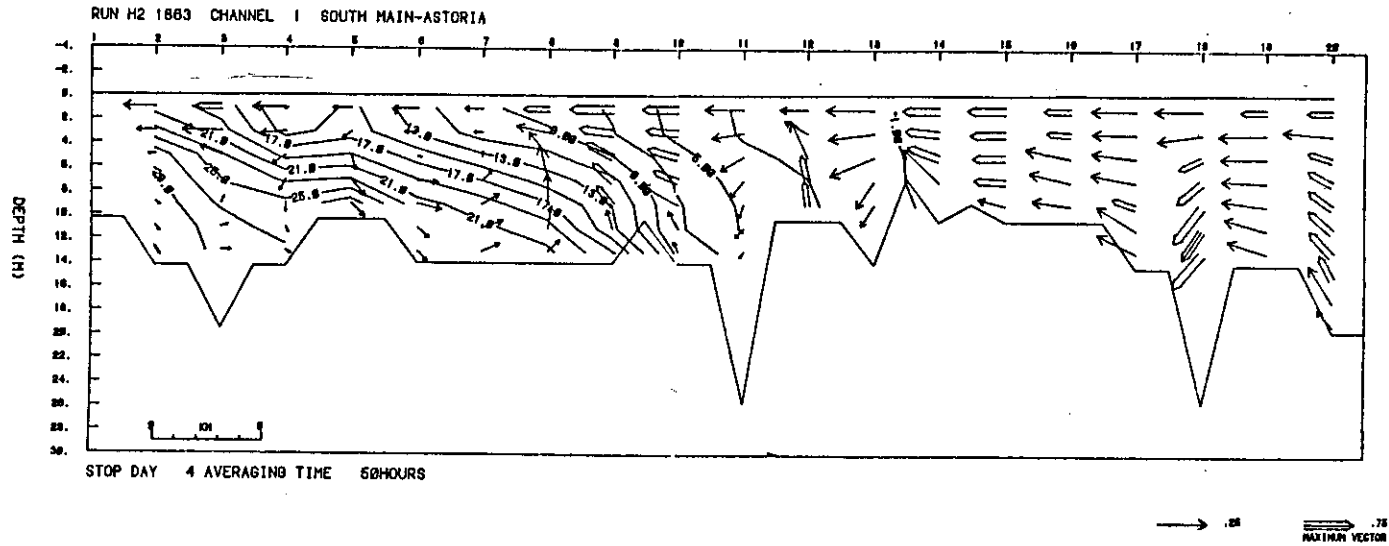


Figure 65a. Channel 1, neap tide period (historical bathymetry, riverflow =  $4000 \text{ m}^3/\text{s}$ ). Mean currents and salinities (m/s and ‰).

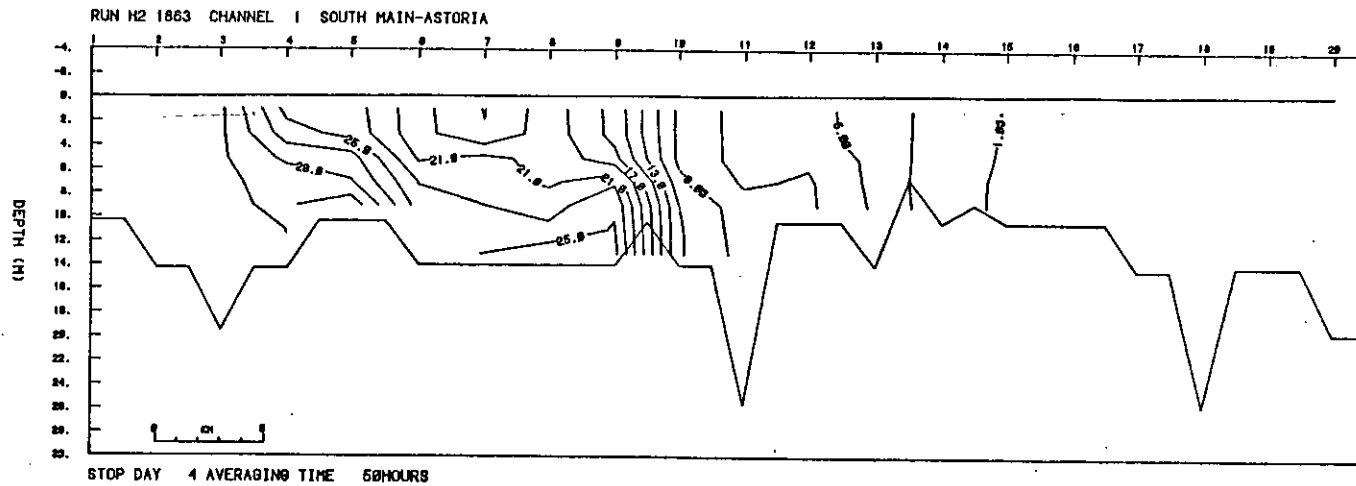


Figure 65b. Channel 1, neap tide period (historical bathymetry, riverflow =  $4000 \text{ m}^3/\text{s}$ ). Maximum salinities.

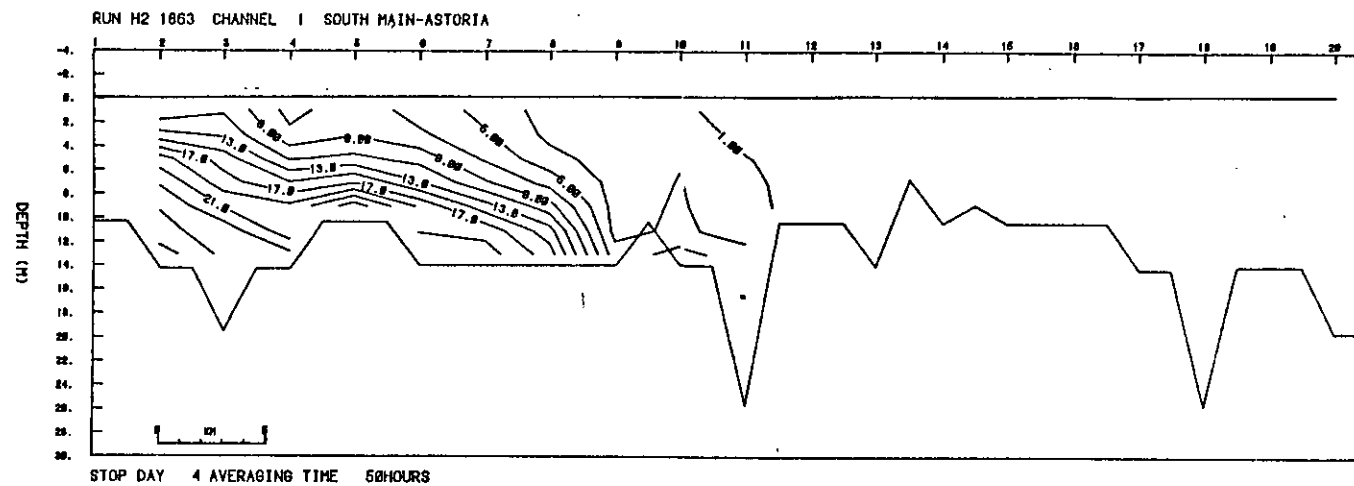


Figure 65c. Channel 1, neap tide period (historical bathymetry, riverflow =  $4000 \text{ m}^3/\text{s}$ ). Minimum salinities.

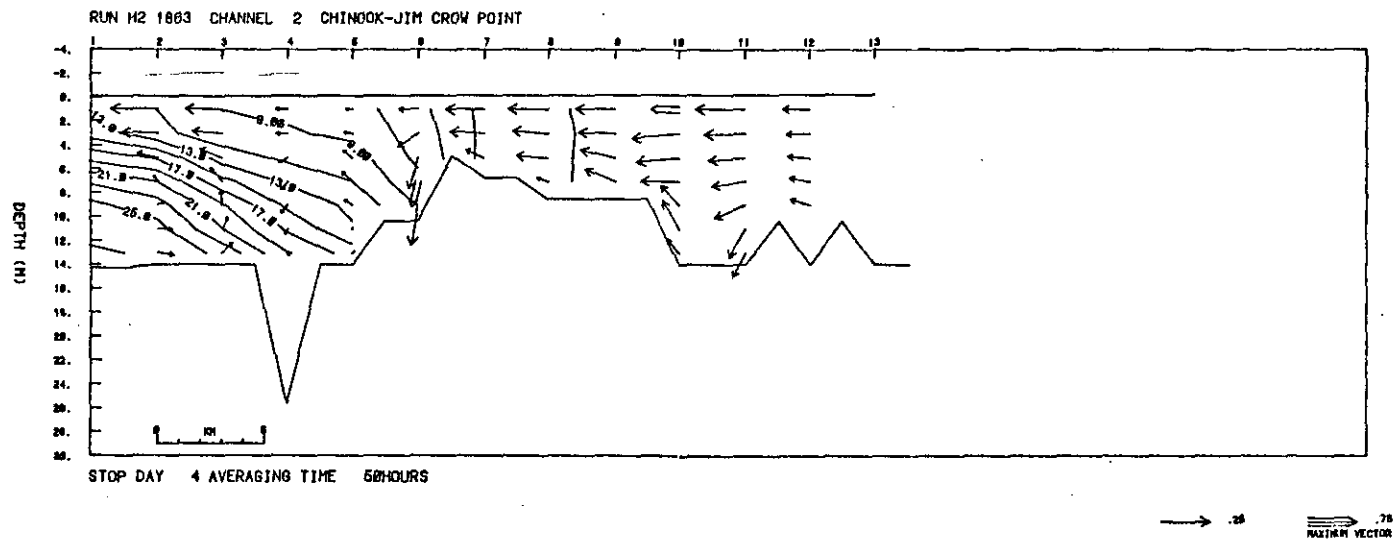


Figure 66a. Channel 2, neap tide period (historical bathymetry, riverflow =  $4000 \text{ m}^3/\text{s}$ ). Mean currents and salinities (m/s and ‰).

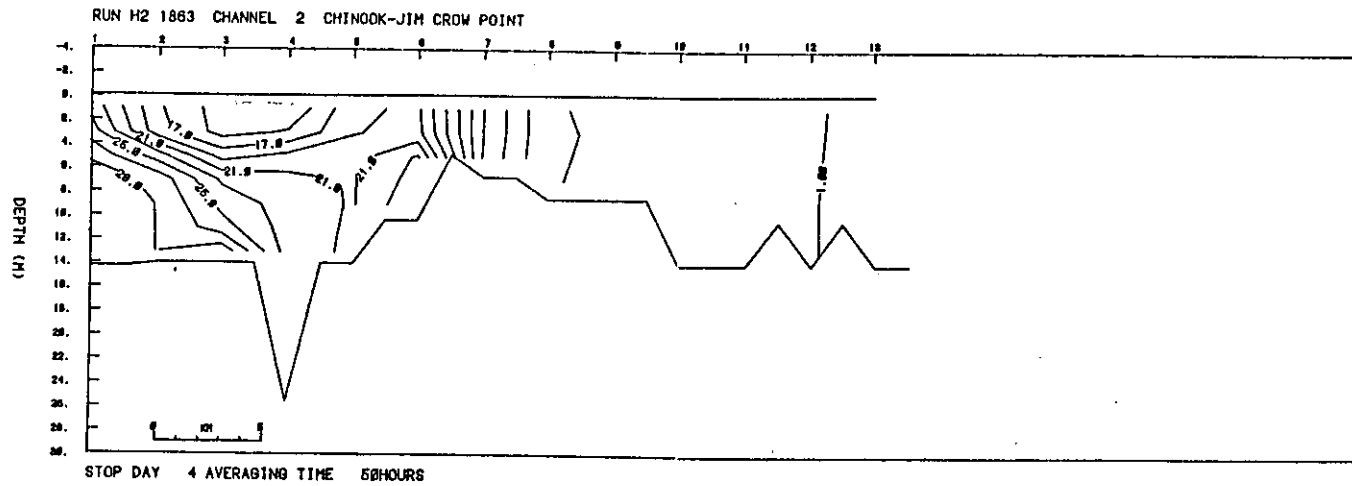


Figure 66b. Channel 2, neap-tide period (historical bathymetry, riverflow =  $4000 \text{ m}^3/\text{s}$ ). Maximum salinities.

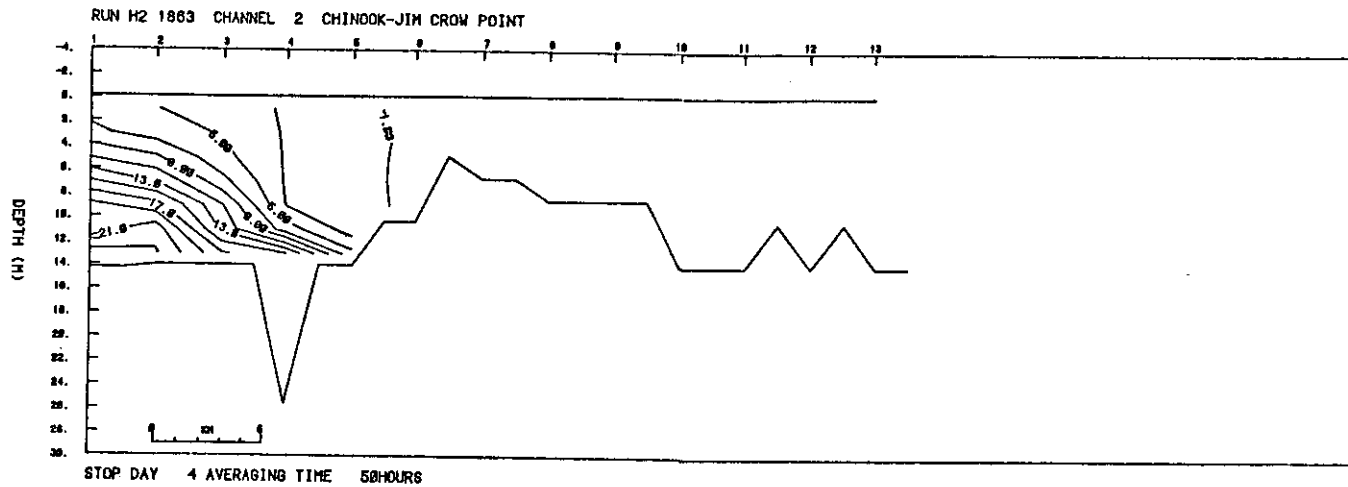


Figure 66c. Channel 2, neap tide period (historical bathymetry, riverflow =  $4000 \text{ m}^3/\text{s}$ ). Minimum salinities.

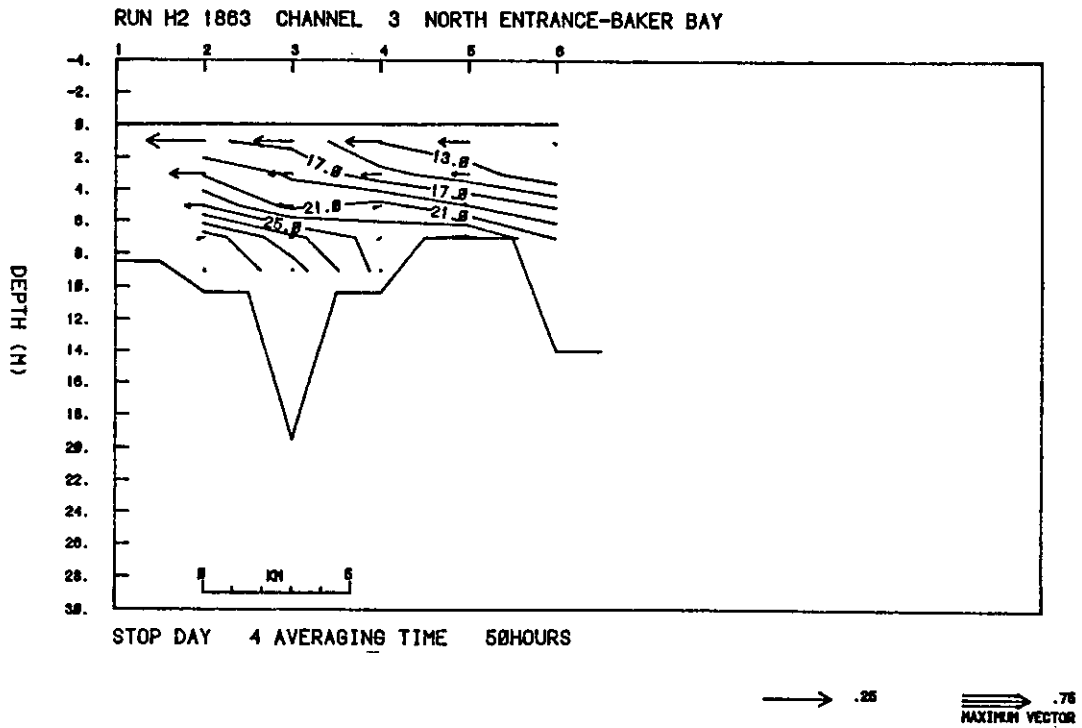


Figure 67a. Channel 3, neap tide period (historical bathymetry, riverflow =  $4000 \text{ m}^3/\text{s}$ ). Mean currents and salinities ( $\text{m/s}$  and  $^{\circ}/\text{oo}$ ).

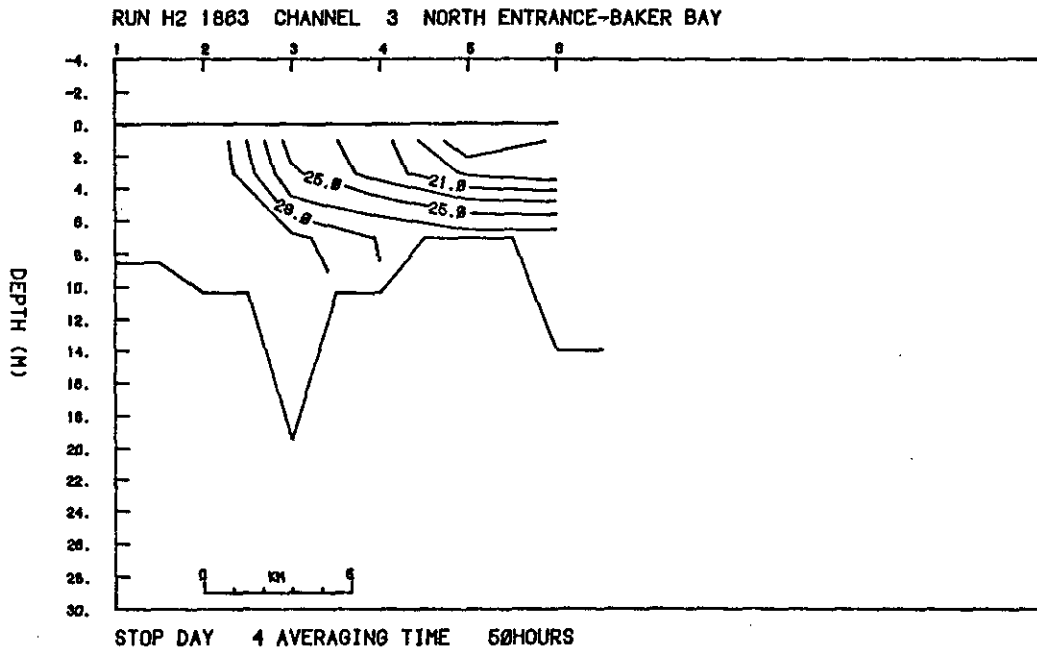


Figure 67b. Channel 3, neap tide period (historical bathymetry, riverflow =  $4000 \text{ m}^3/\text{s}$ ). Maximum salinities.

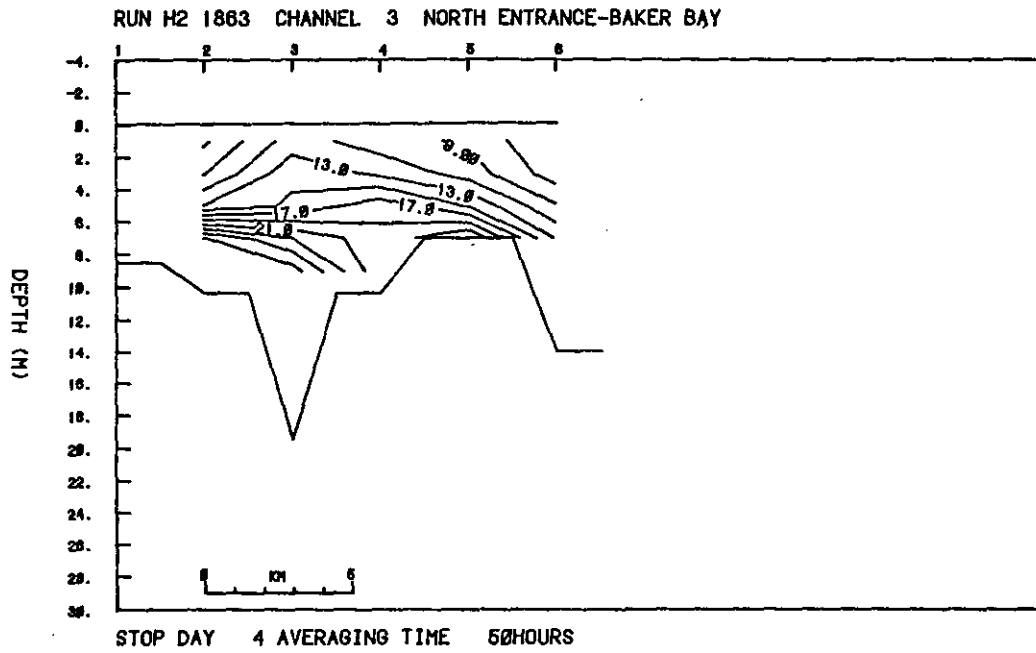


Figure 67c. Channel 3, neap tide period (historical bathymetry, riverflow = 4000 m<sup>3</sup>/s). Minimum salinities.

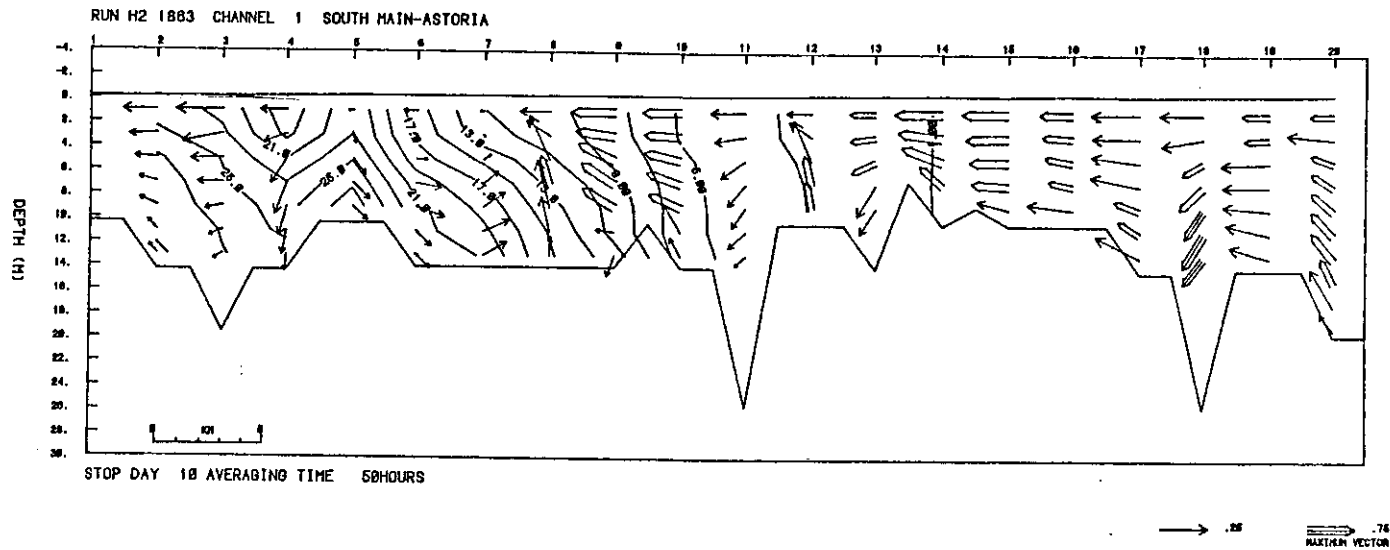


Figure 68a. Channel 1, spring tide period (historical bathymetry, riverflow =  $4000 \text{ m}^3/\text{s}$ ). Mean currents and salinities (m/s and ‰).

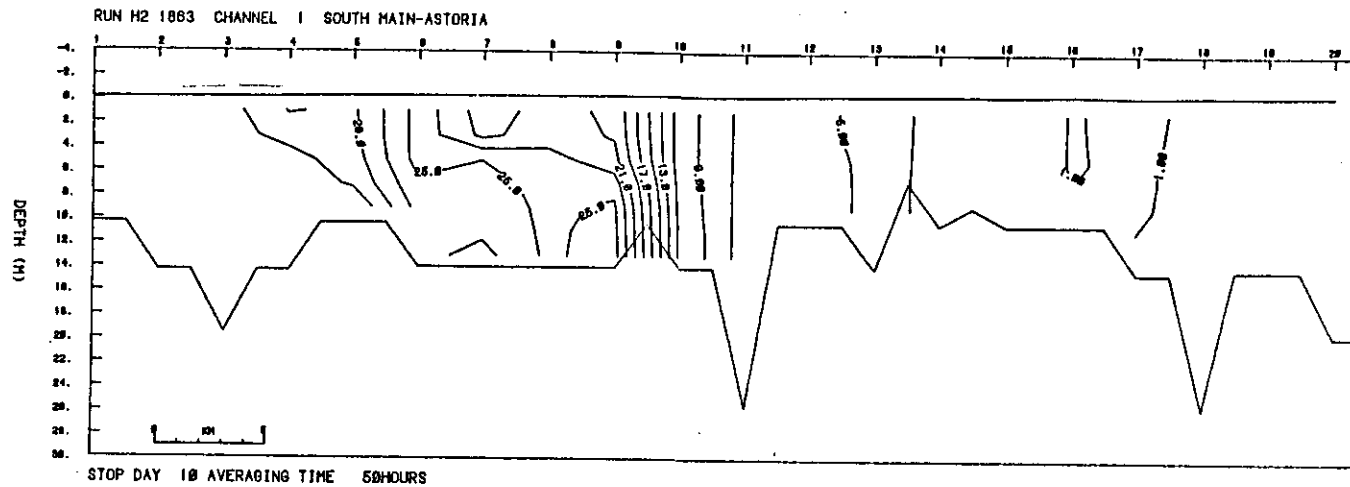


Figure 68b. Channel 1, spring tide period (historical bathymetry, riverflow =  $4000 \text{ m}^3/\text{s}$ ). Maximum salinities.

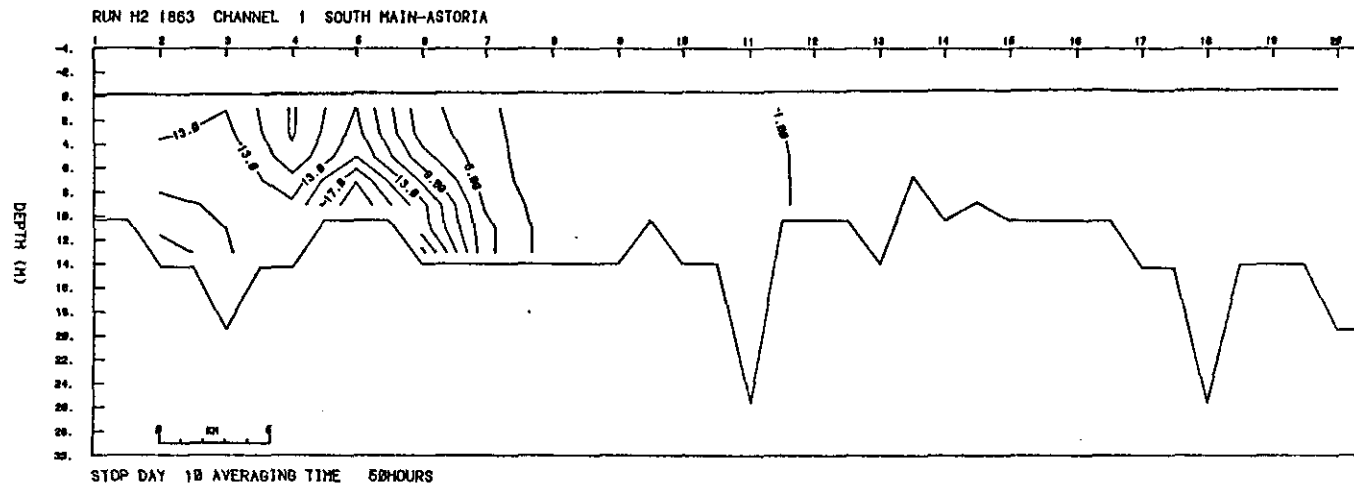


Figure 68c. Channel 1, spring tide period (historical bathymetry, riverflow =  $4000 \text{ m}^3/\text{s}$ ). Minimum salinities.

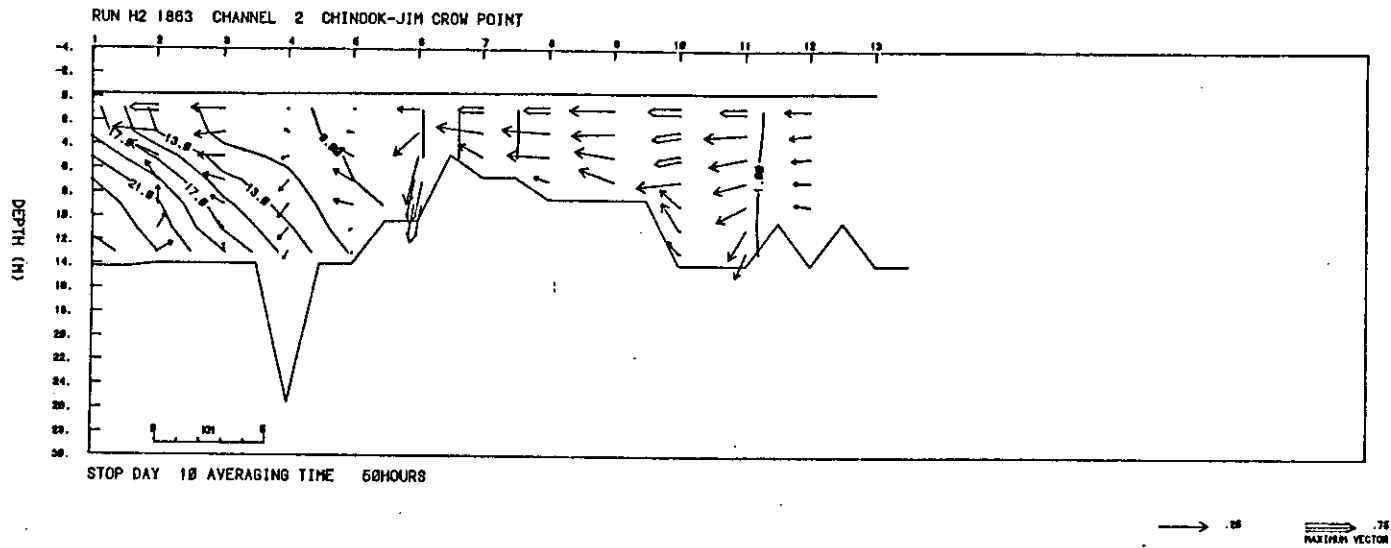


Figure 69a. Channel 2, spring tide period (historical bathymetry, riverflow =  $4000 \text{ m}^3/\text{s}$ ). Mean currents and salinities (m/s and ‰).

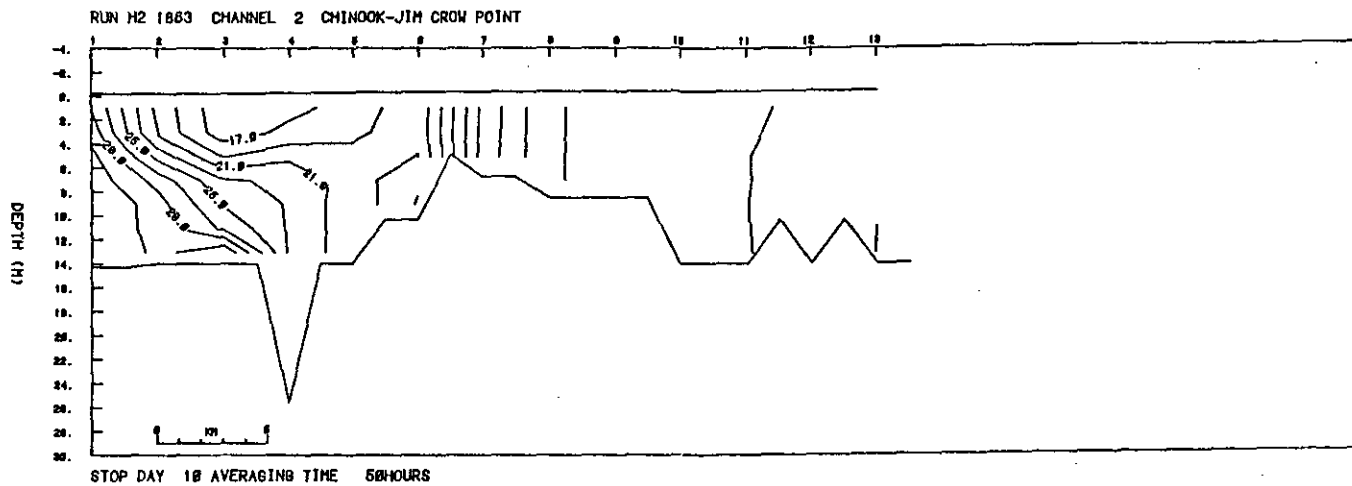


Figure 69b. Channel 2, spring tide period (historical bathymetry, riverflow =  $4000 \text{ m}^3/\text{s}$ ). Maximum salinities.

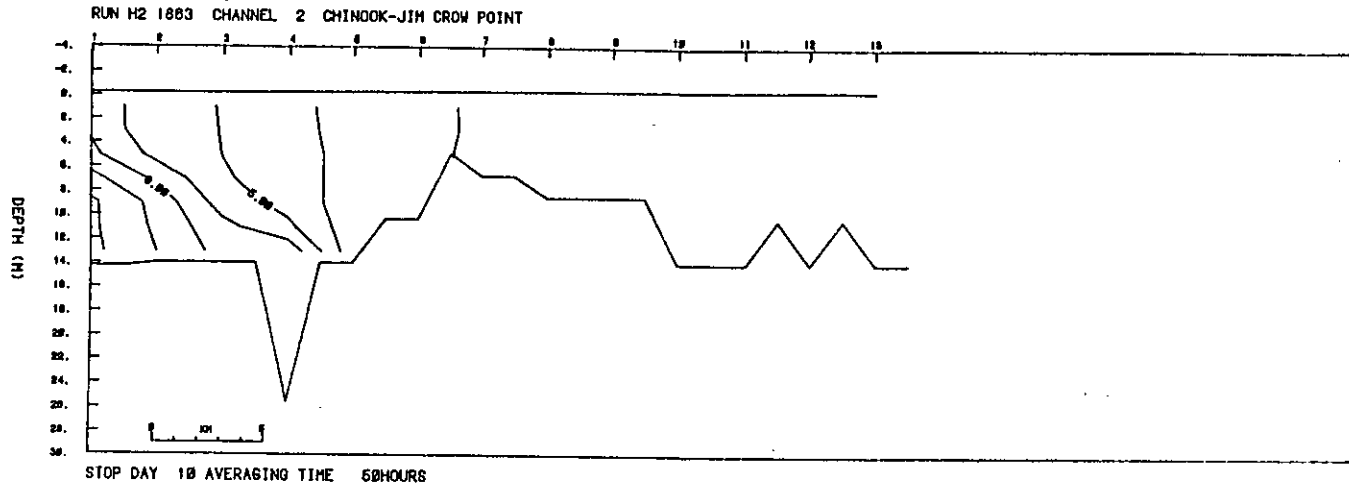


Figure 69c. Channel 2, spring tide period (historical bathymetry, riverflow =  $4000 \text{ m}^3/\text{s}$ ). Minimum salinities.

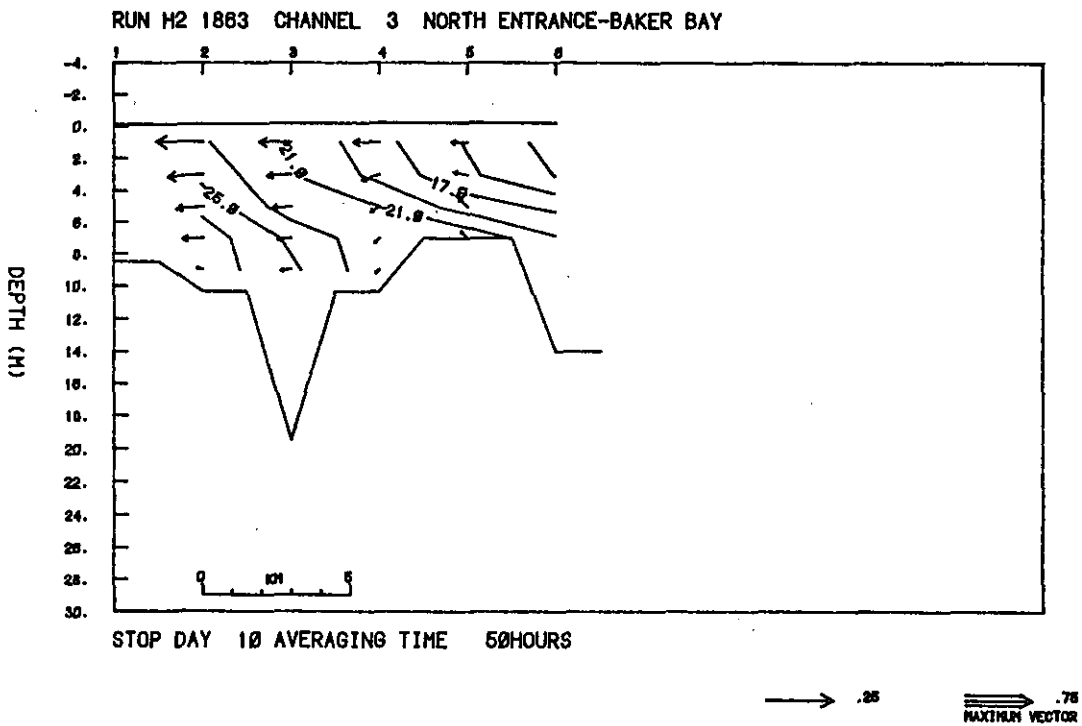


Figure 70a. Channel 3, spring tide period (historical bathymetry, riverflow =  $4000 \text{ m}^3/\text{s}$ ). Mean currents and salinities ( $\text{m/s}$  and  $^{\circ}/\text{oo}$ ).

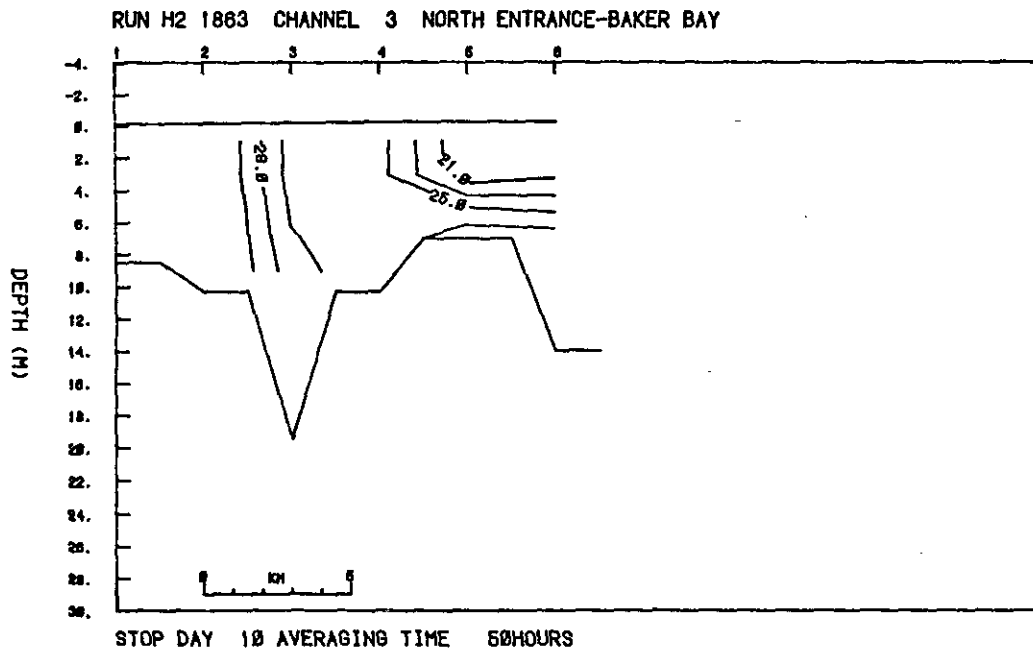


Figure 70b. Channel 3, spring tide period (historical bathymetry, riverflow =  $4000 \text{ m}^3/\text{s}$ ). Maximum salinities.

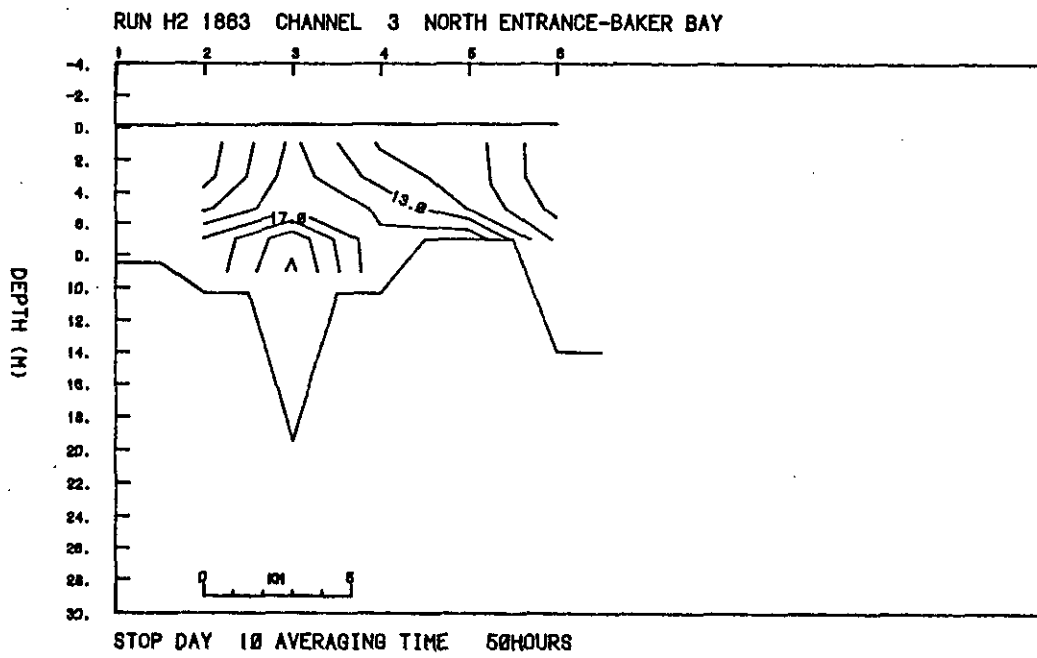


Figure 70c. Channel 3, spring tide period (historical bathymetry, riverflow =  $4000 \text{ m}^3/\text{s}$ ). Minimum salinities.

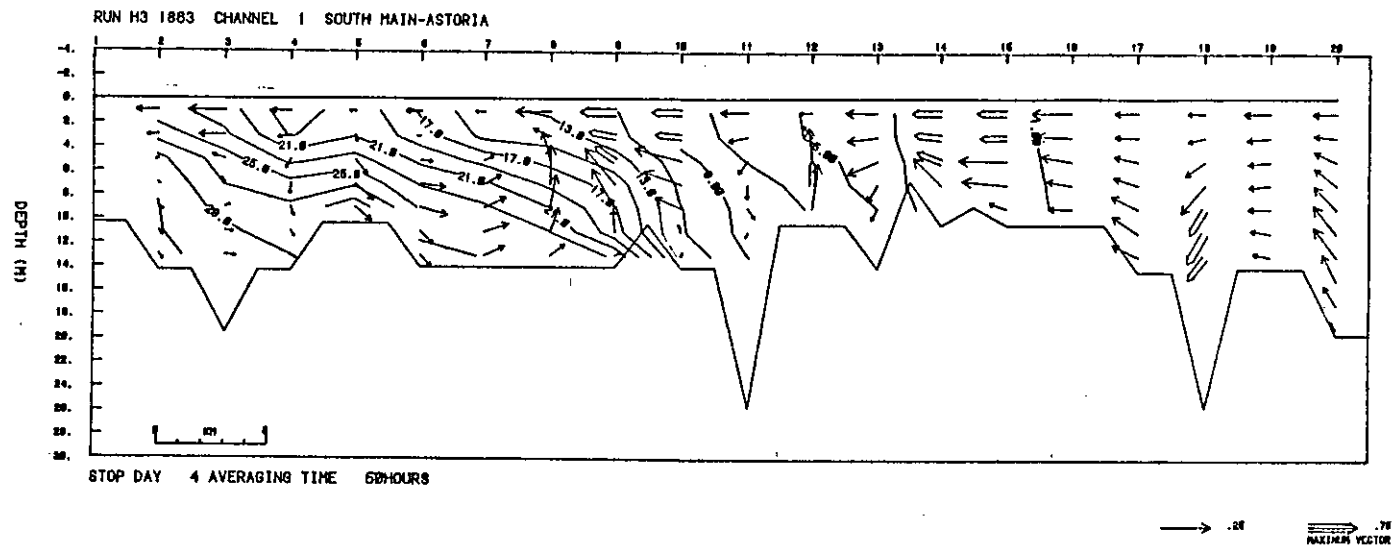


Figure 71a. Channel 1, neap tide period (historical bathymetry, riverflow =  $2000 \text{ m}^3/\text{s}$ ). Mean currents and salinities (m/s and ‰).

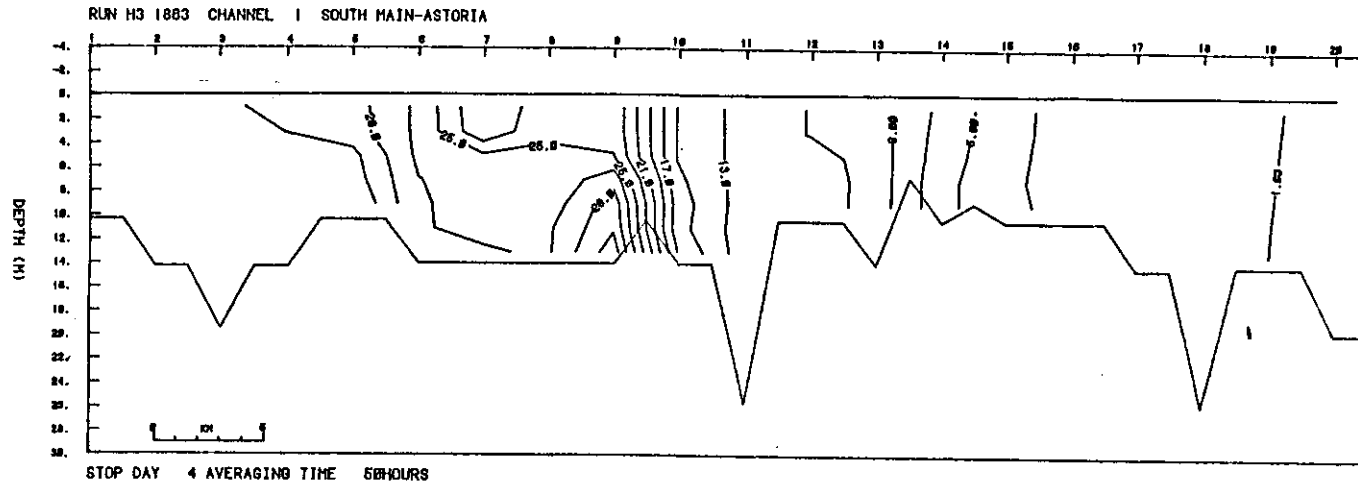


Figure 71b. Channel 1, neap tide period (historical bathymetry, riverflow = 2000 m<sup>3</sup>/s). Maximum salinities.

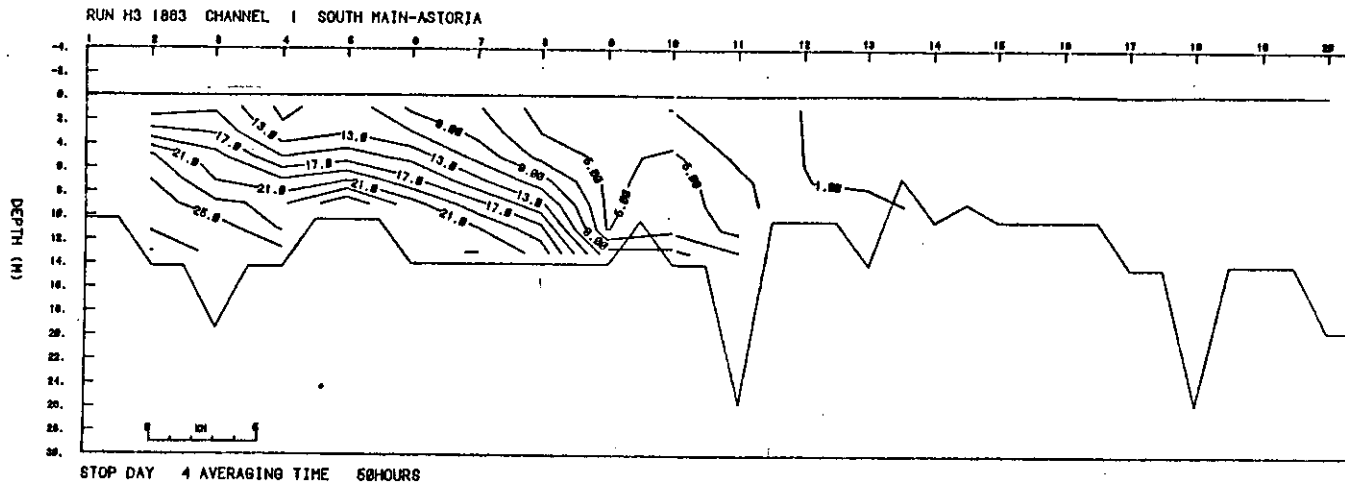


Figure 71c. Channel 1, neap tide period (historical bathymetry, riverflow =  $2000 \text{ m}^3/\text{s}$ ). Minimum salinities.

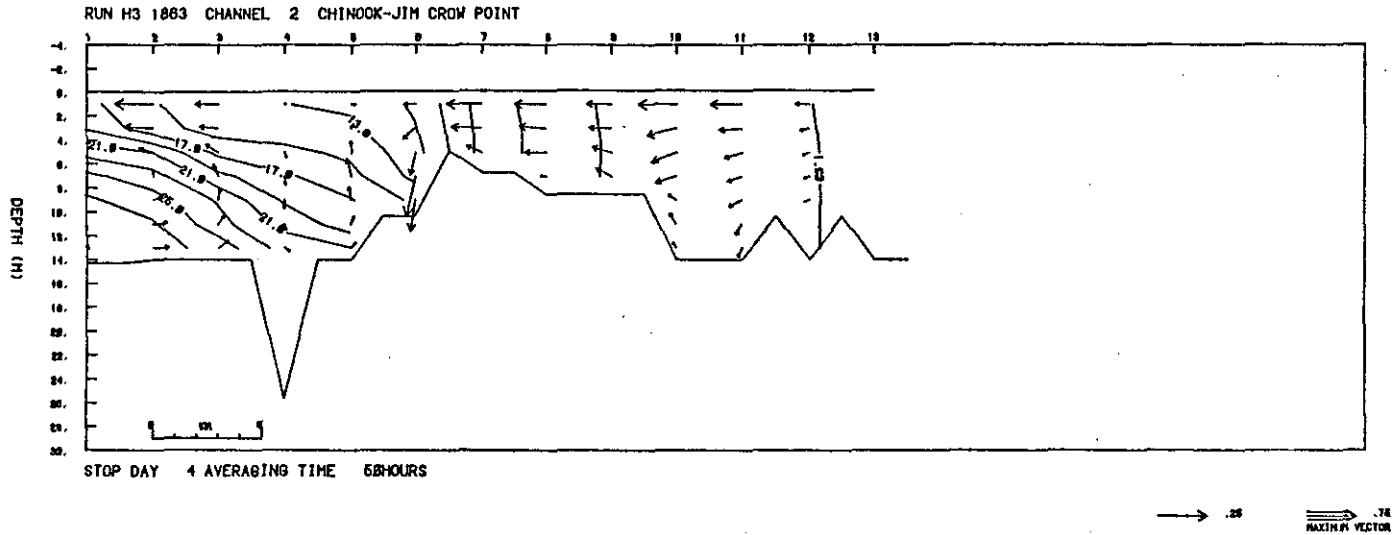


Figure 72a. Channel 2, neap tide period (historical bathymetry, riverflow =  $2000 \text{ m}^3/\text{s}$ ). Mean currents and salinities (m/s and ‰).

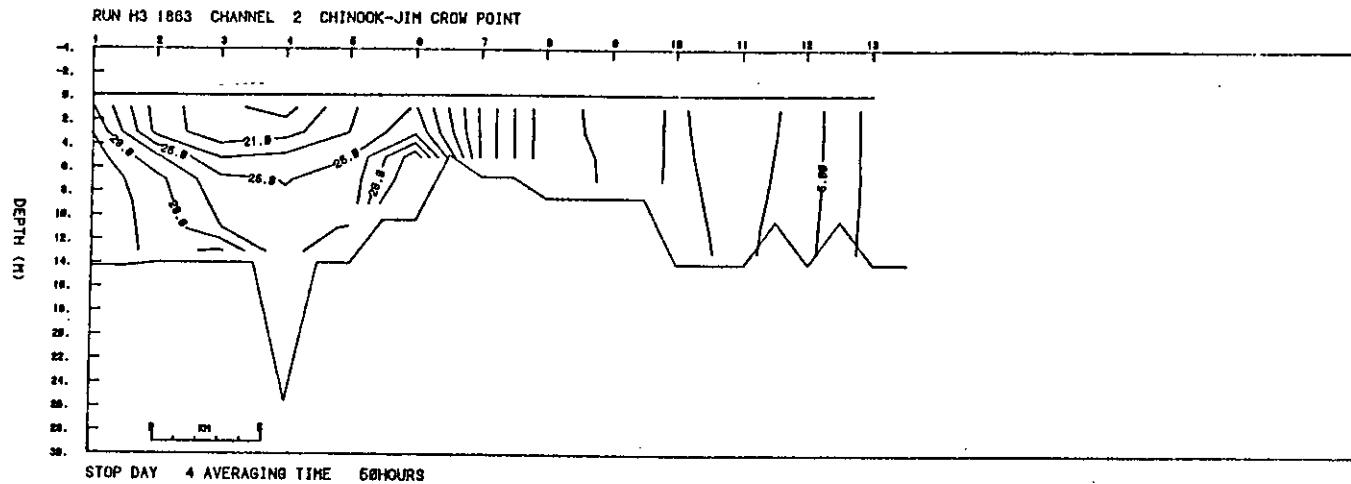


Figure 72b. Channel 2, neap tide period (historical bathymetry, riverflow =  $2000 \text{ m}^3/\text{s}$ ). Maximum salinities.

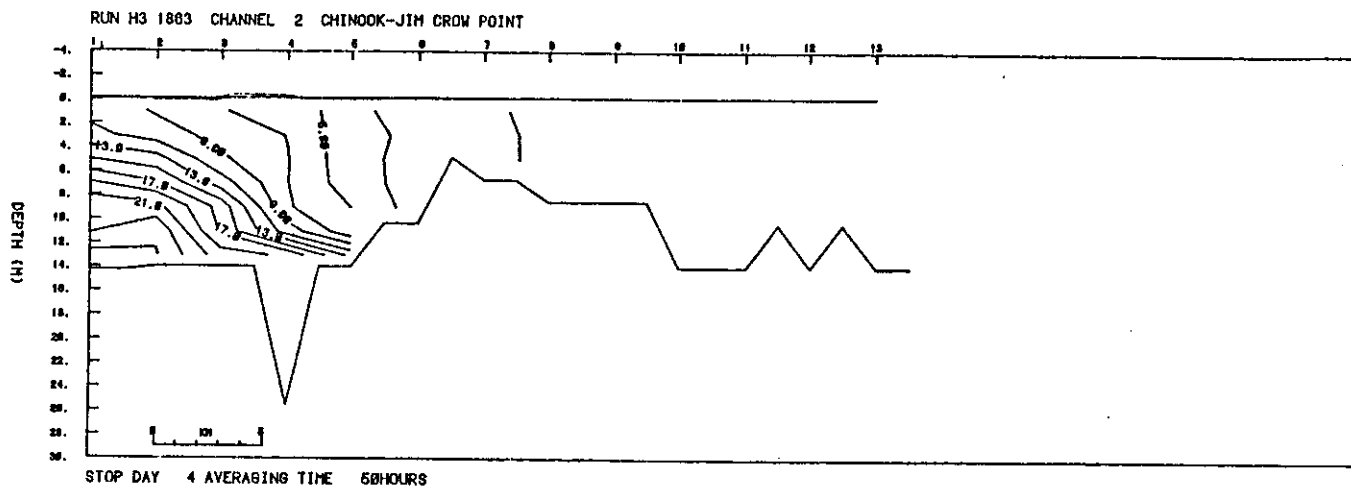


Figure 72c. Channel 2, neap tide period (historical bathymetry, riverflow =  $2000 \text{ m}^3/\text{s}$ ). Minimum salinities.

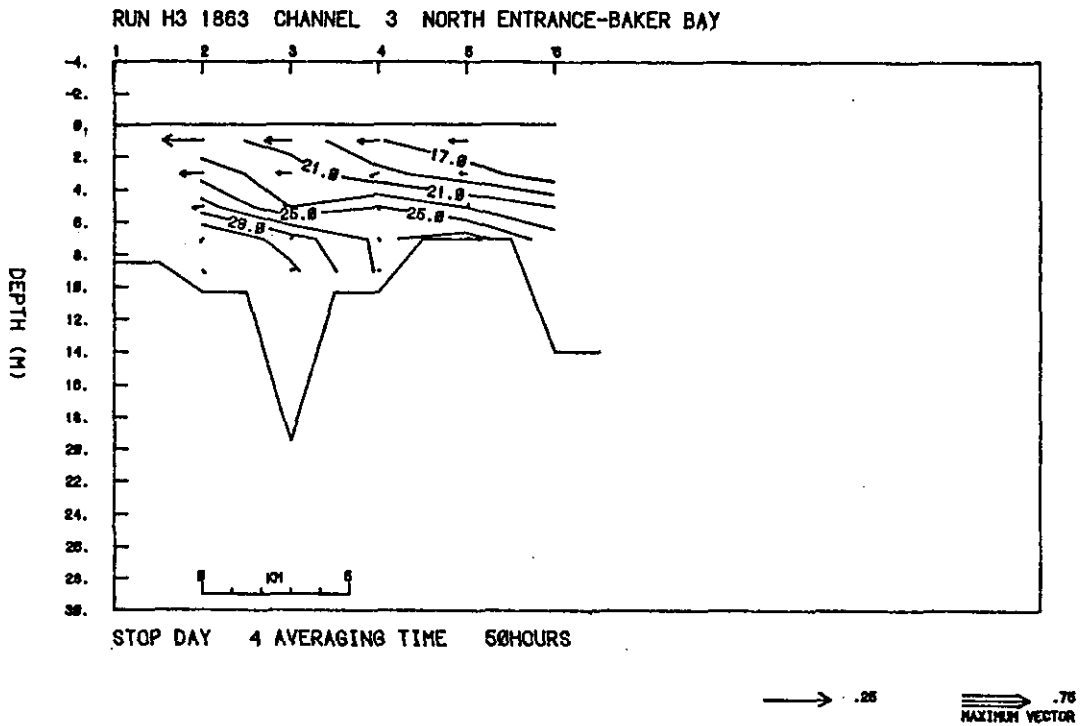


Figure 73a. Channel 3, neap tide period (historical bathymetry, riverflow =  $2000 \text{ m}^3/\text{s}$ ). Mean currents and salinities ( $\text{m/s}$  and  $^{\circ}/\text{oo}$ ).

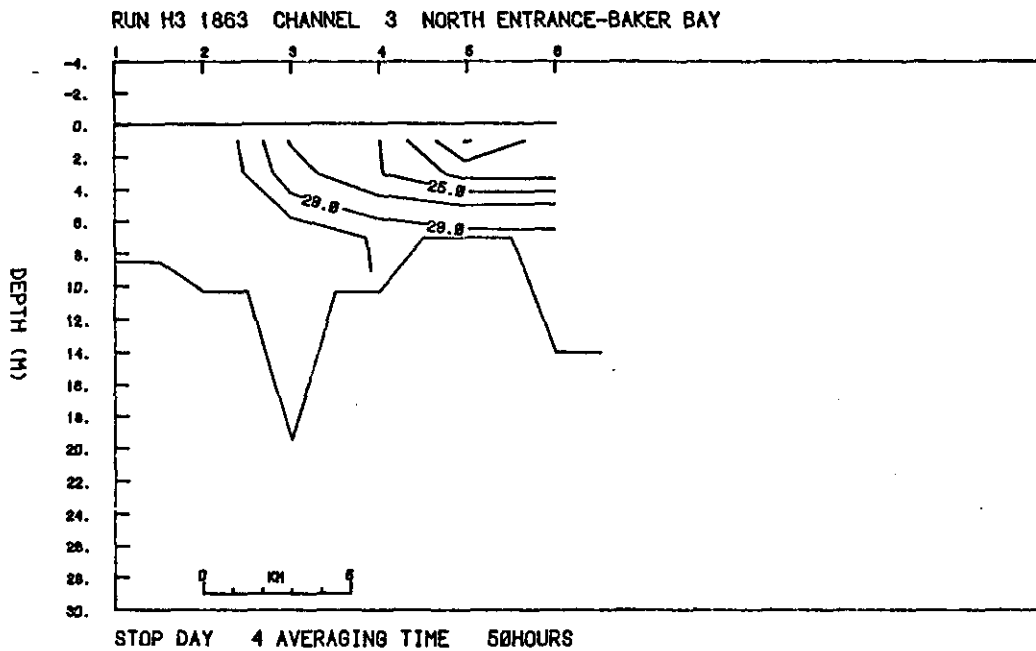


Figure 73b. Channel 3, neap tide period (historical bathymetry, riverflow =  $2000 \text{ m}^3/\text{s}$ ). Maximum salinities.

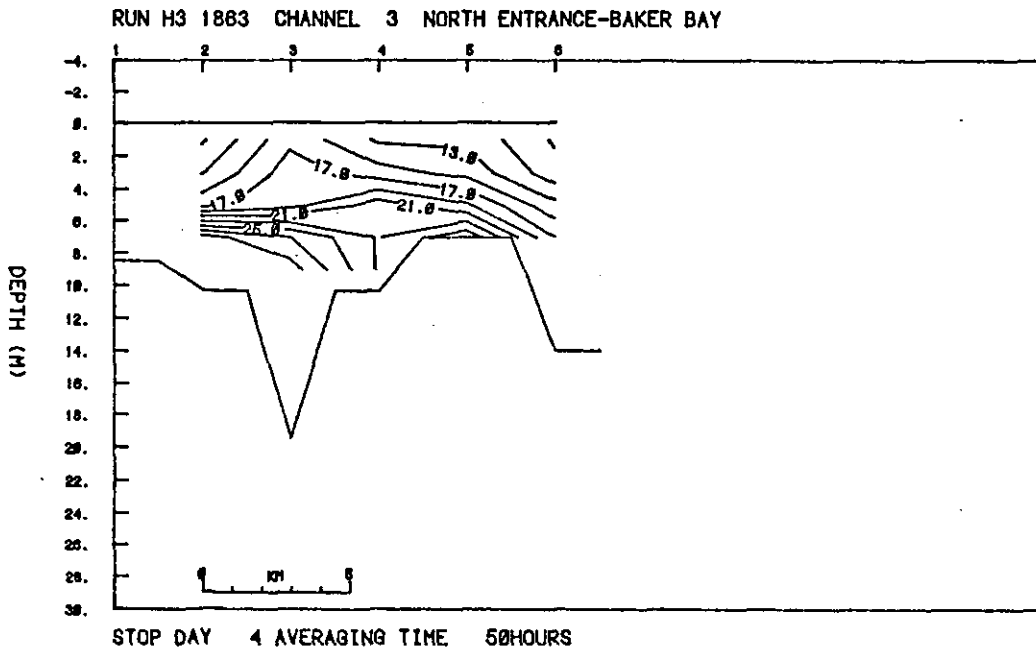


Figure 73c. Channel 3, neap tide period (historical bathymetry, riverflow = 2000 m<sup>3</sup>/s). Minimum salinities.

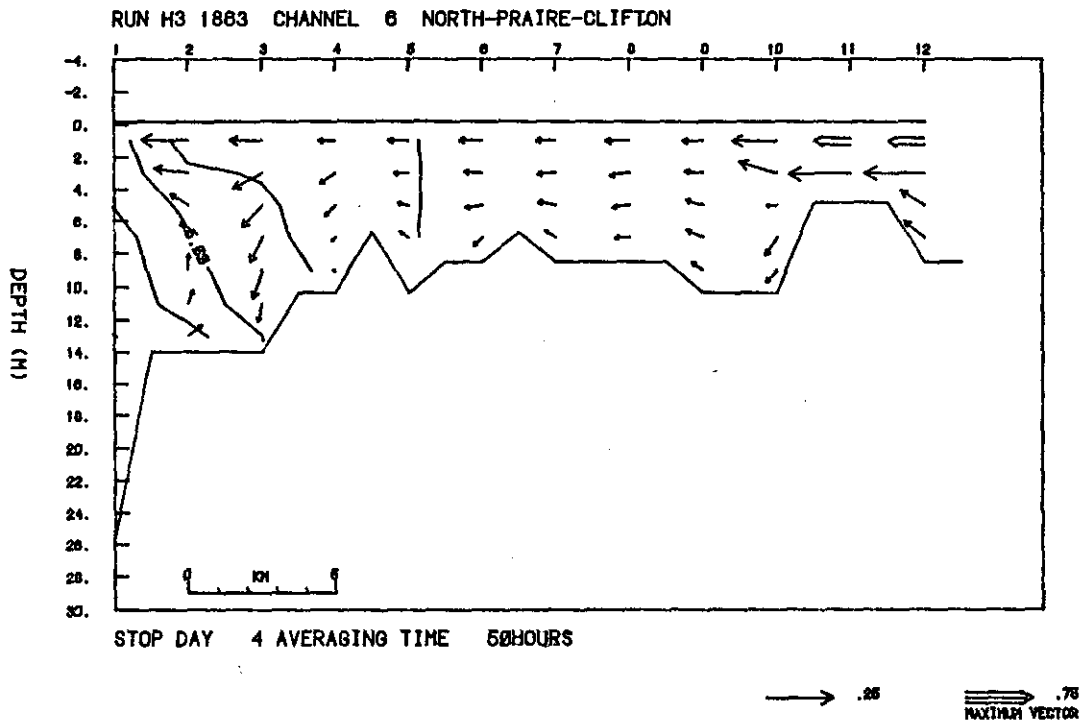


Figure 74a. Channel 6, neap tide period (historical bathymetry, riverflow = 2000 m<sup>3</sup>/s). Mean currents and salinities (m/s and ‰).

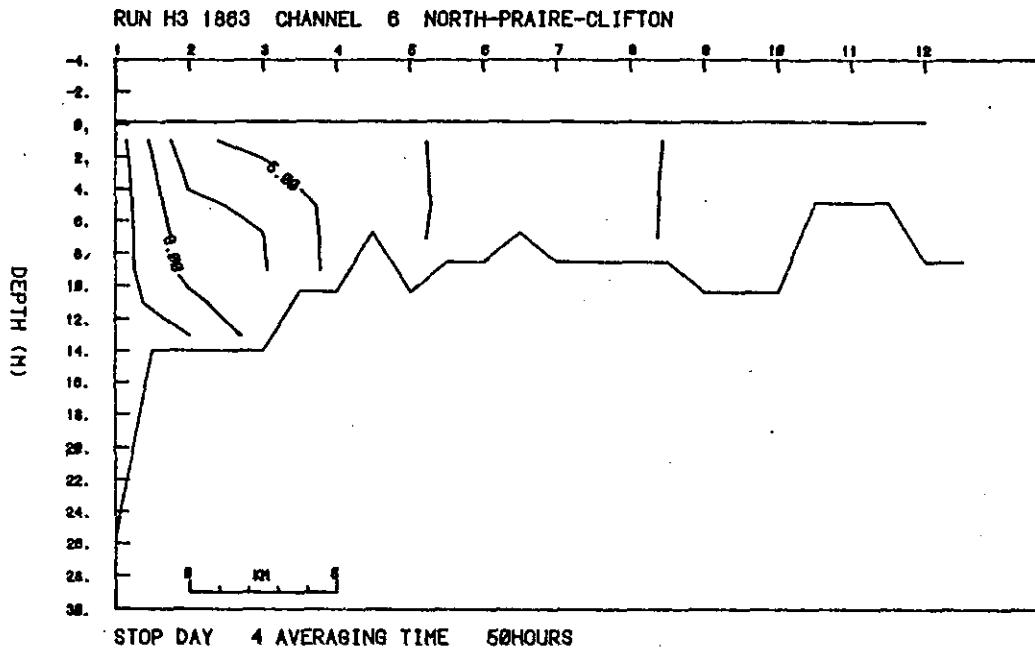


Figure 74b. Channel 6, neap tide period (historical bathymetry, riverflow = 2000 m<sup>3</sup>/s). Maximum salinities.

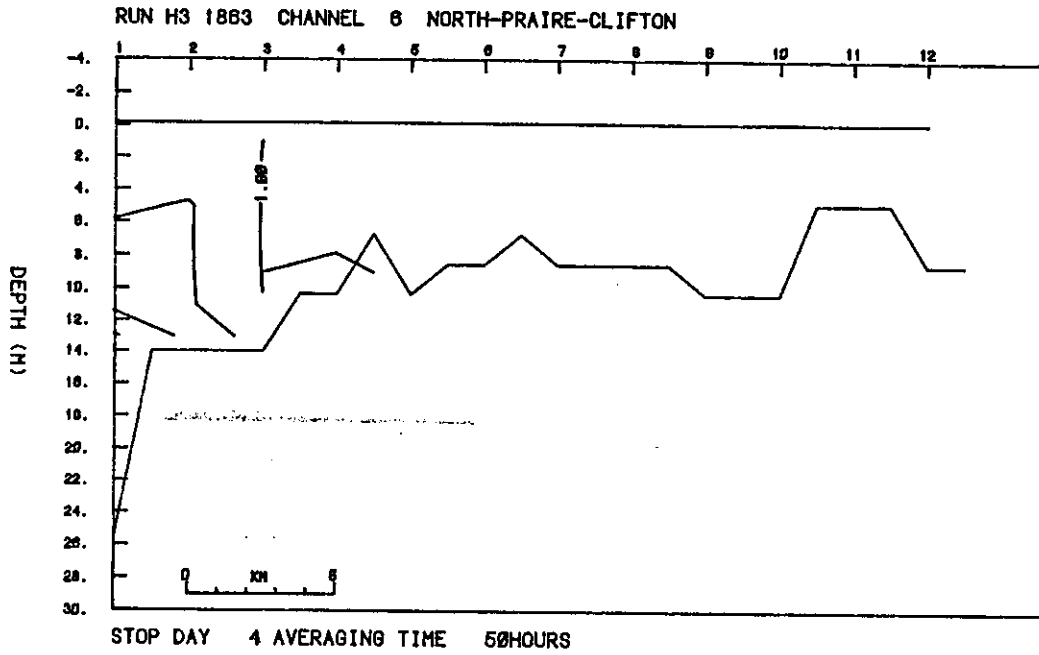


Figure 74c. Channel 6, neap tide period (historical bathymetry, riverflow = 2000 m<sup>3</sup>/s). Minimum salinities.

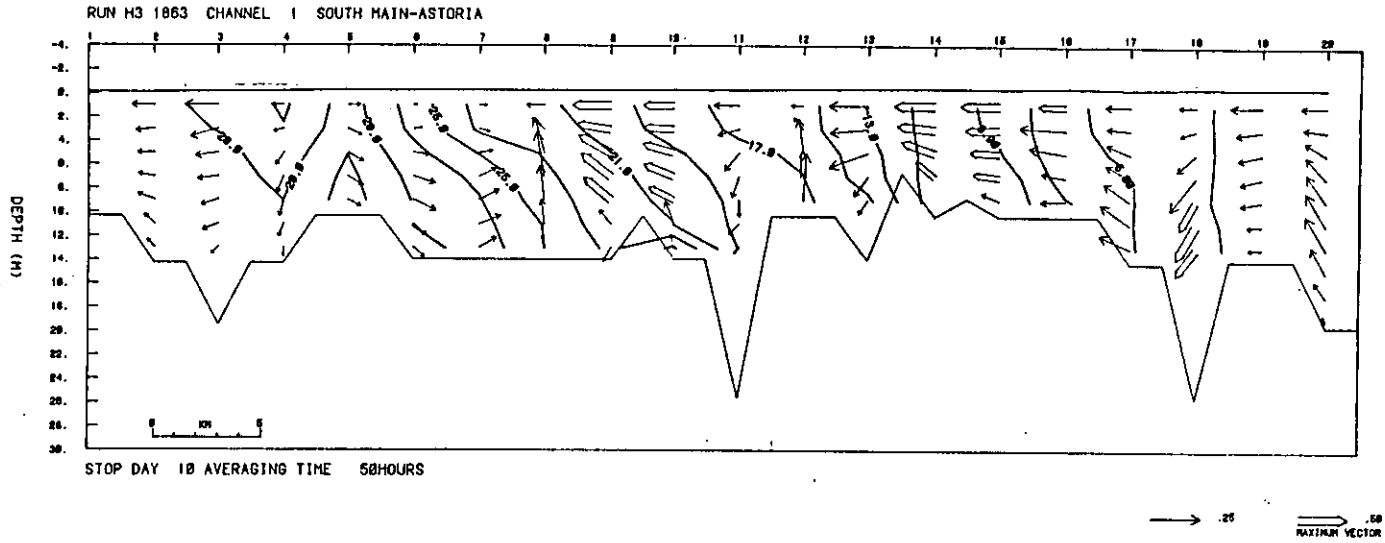


Figure 75a. Channel 1, spring tide period (historical bathymetry, riverflow =  $2000 \text{ m}^3/\text{s}$ ). Mean currents and salinities (m/s and ‰).

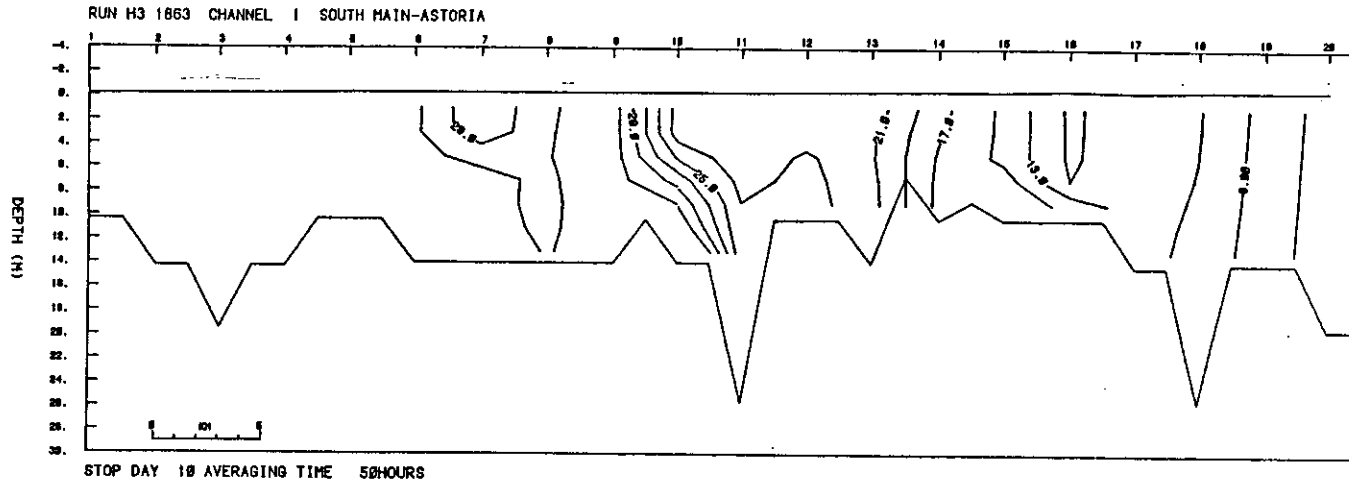


Figure 75b. Channel 1, spring tide period (historical bathymetry, riverflow =  $2000 \text{ m}^3/\text{s}$ ). Maximum salinities.

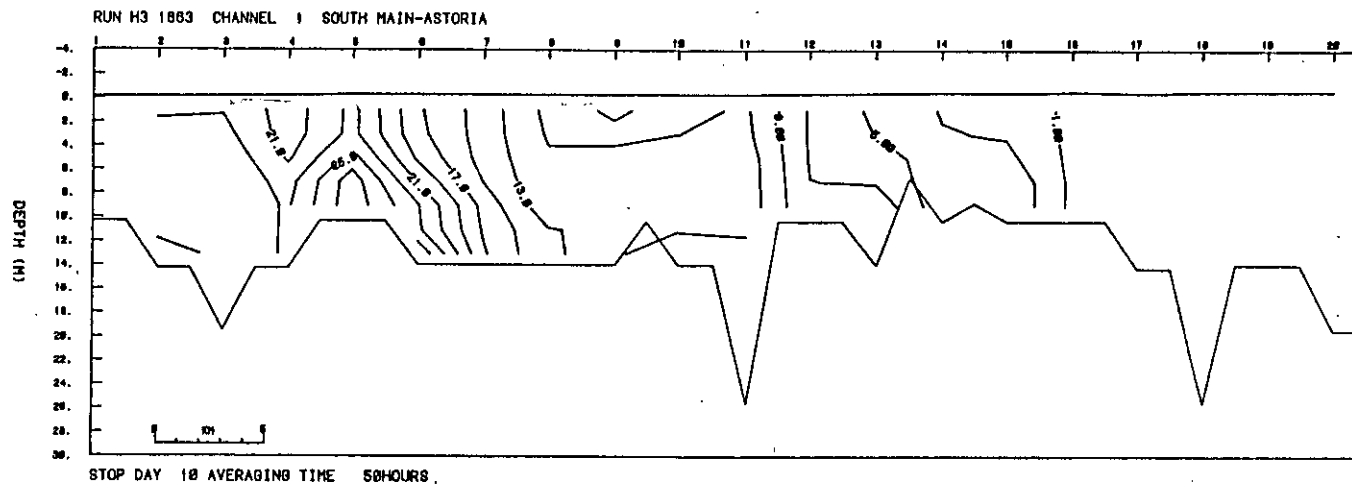


Figure 75c. Channel 1, spring tide period (historical bathymetry, riverflow =  $2000 \text{ m}^3/\text{s}$ ). Minimum salinities.

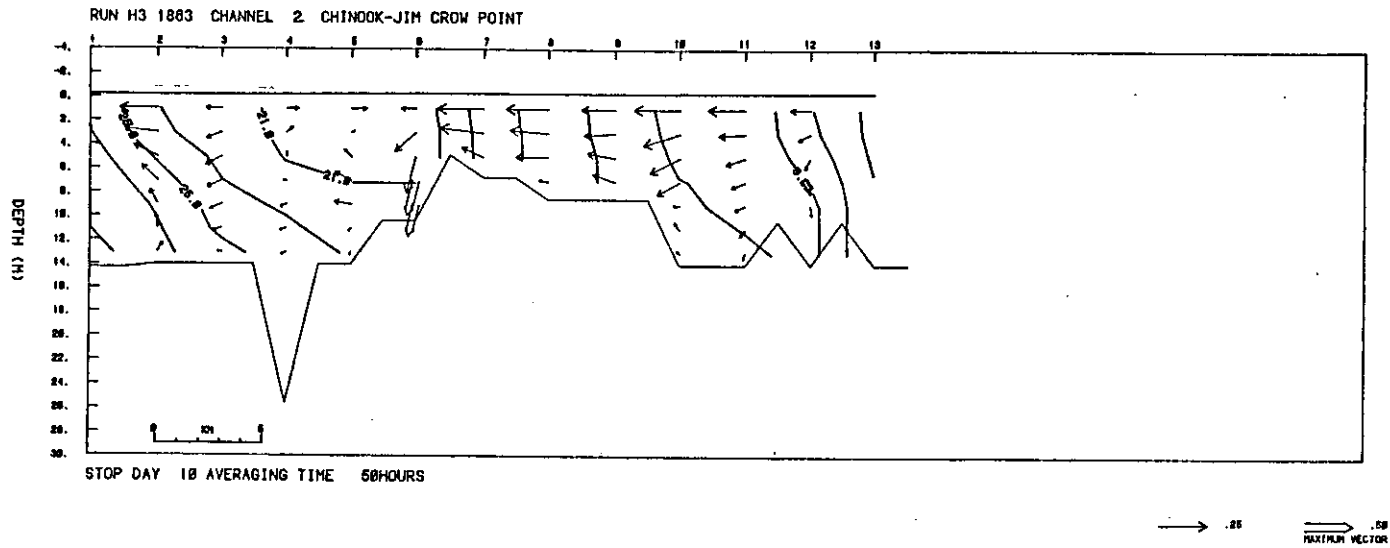


Figure 76a. Channel 2, spring tide period (historical bathymetry, riverflow =  $2000 \text{ m}^3/\text{s}$ ). Mean currents and salinities (m/s and ‰).

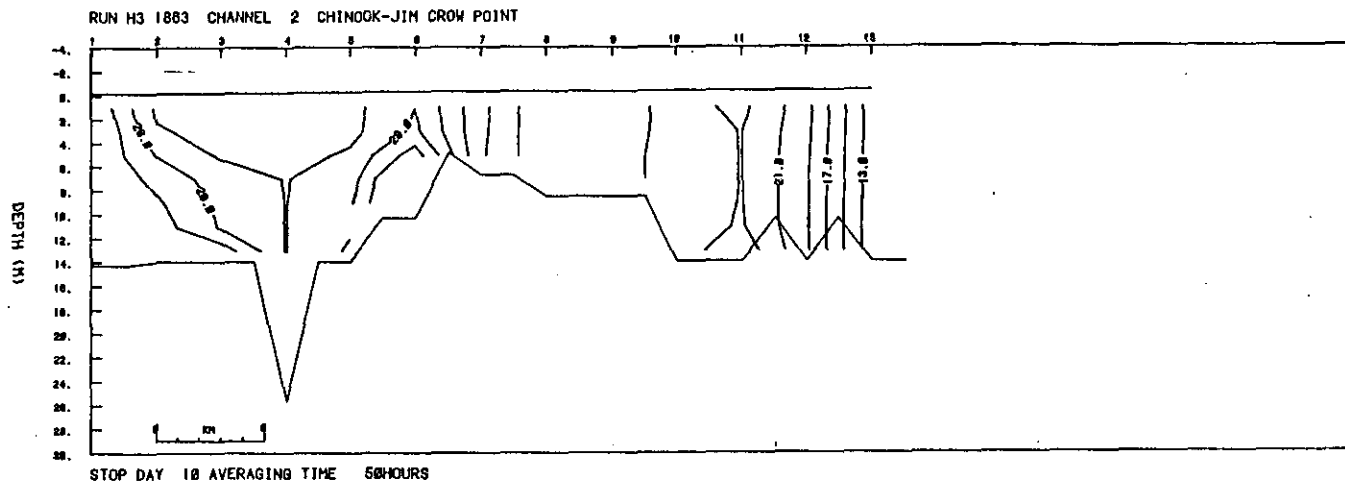


Figure 76b. Channel 2, spring tide period (historical bathymetry, riverflow =  $2000 \text{ m}^3/\text{s}$ ). Maximum salinities.

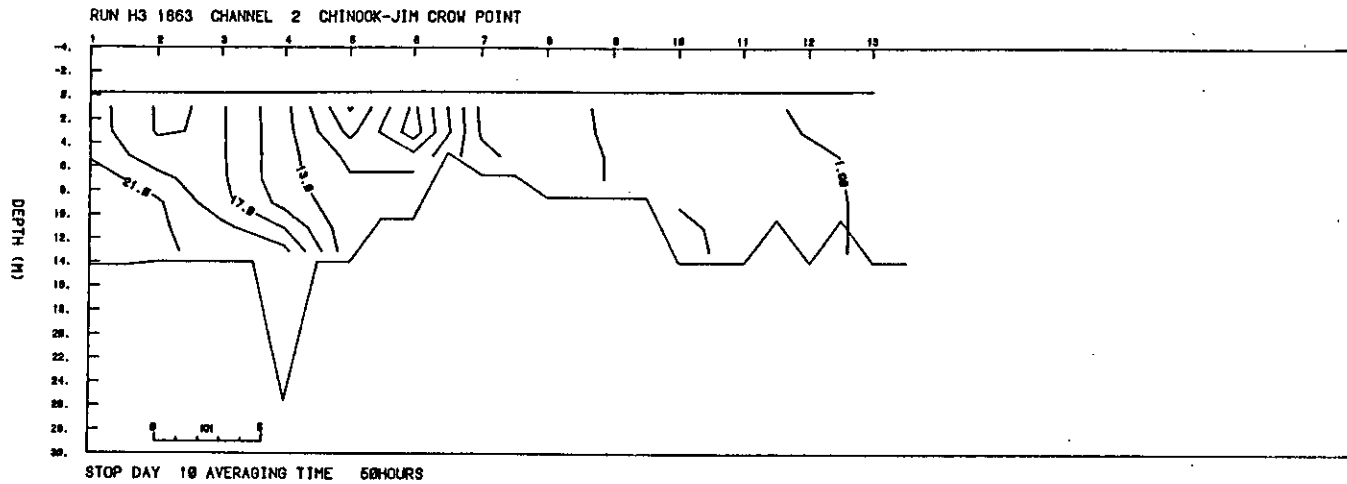


Figure 76c. Channel 2, spring tide period (historical bathymetry, riverflow =  $2000 \text{ m}^3/\text{s}$ ). Minimum salinities.

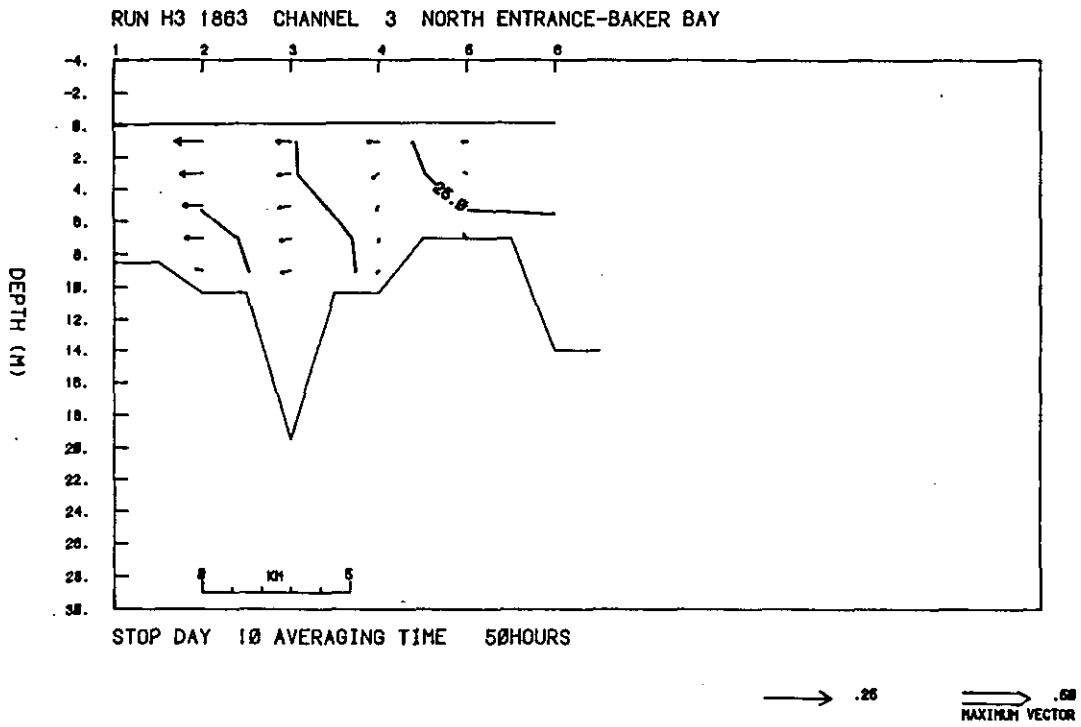


Figure 77a. Channel 3, spring tide period (historical bathymetry, riverflow =  $2000 \text{ m}^3/\text{s}$ ). Mean currents and salinities ( $\text{m/s}$  and  $^{\circ}/\text{oo}$ ).

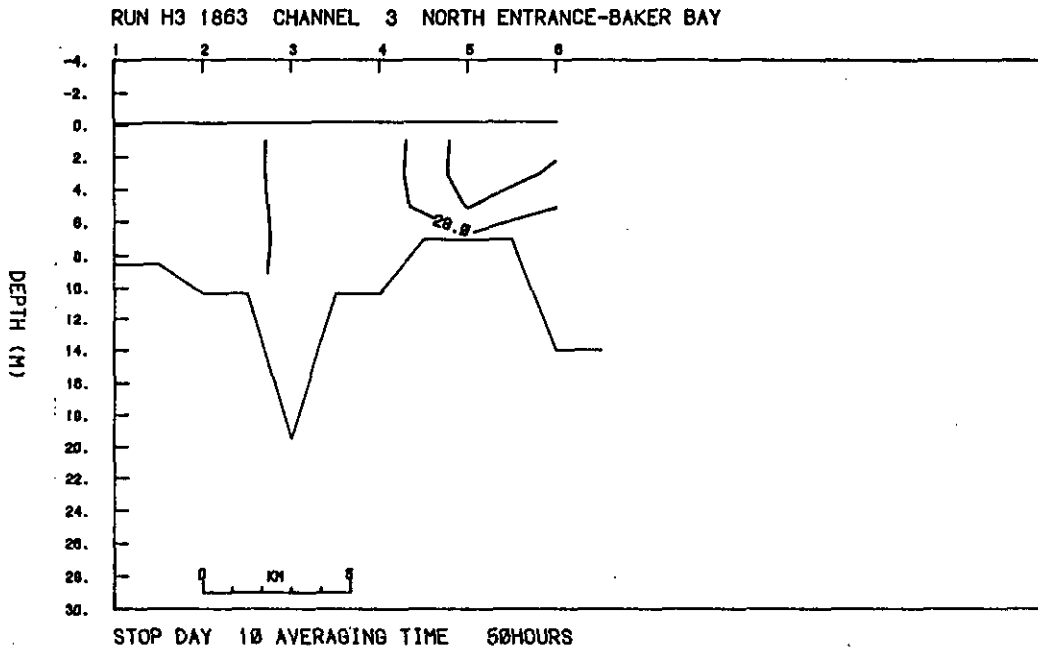


Figure 77b. Channel 3, spring tide period (historical bathymetry, riverflow = 2000 m<sup>3</sup>/s). Maximum salinities.

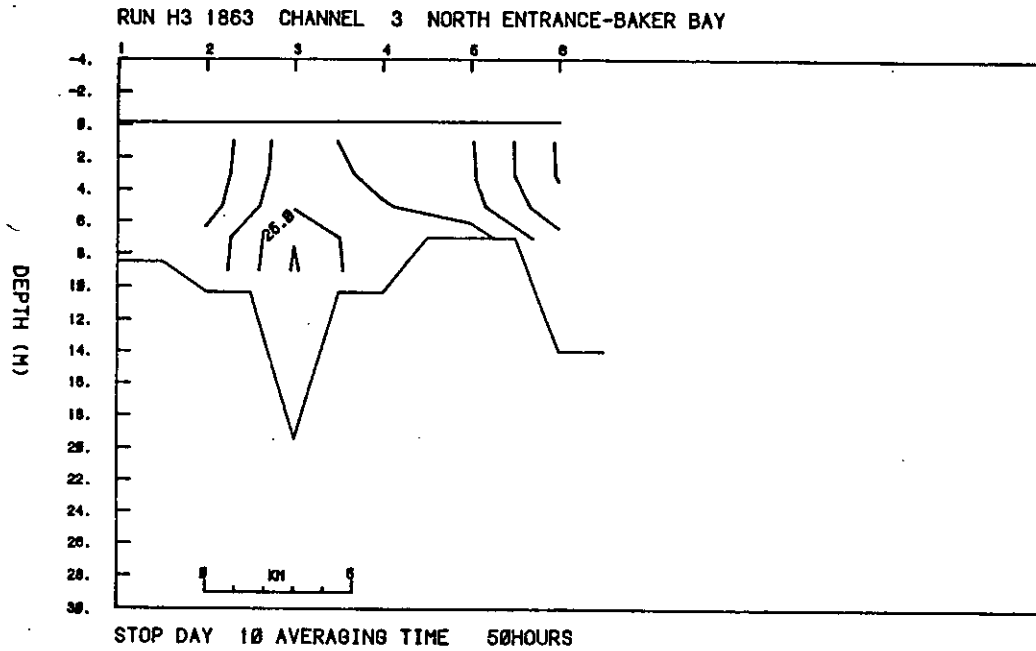


Figure 77c. Channel 3, spring tide period (historical bathymetry, riverflow =  $2000 \text{ m}^3/\text{s}$ ). Minimum salinities.

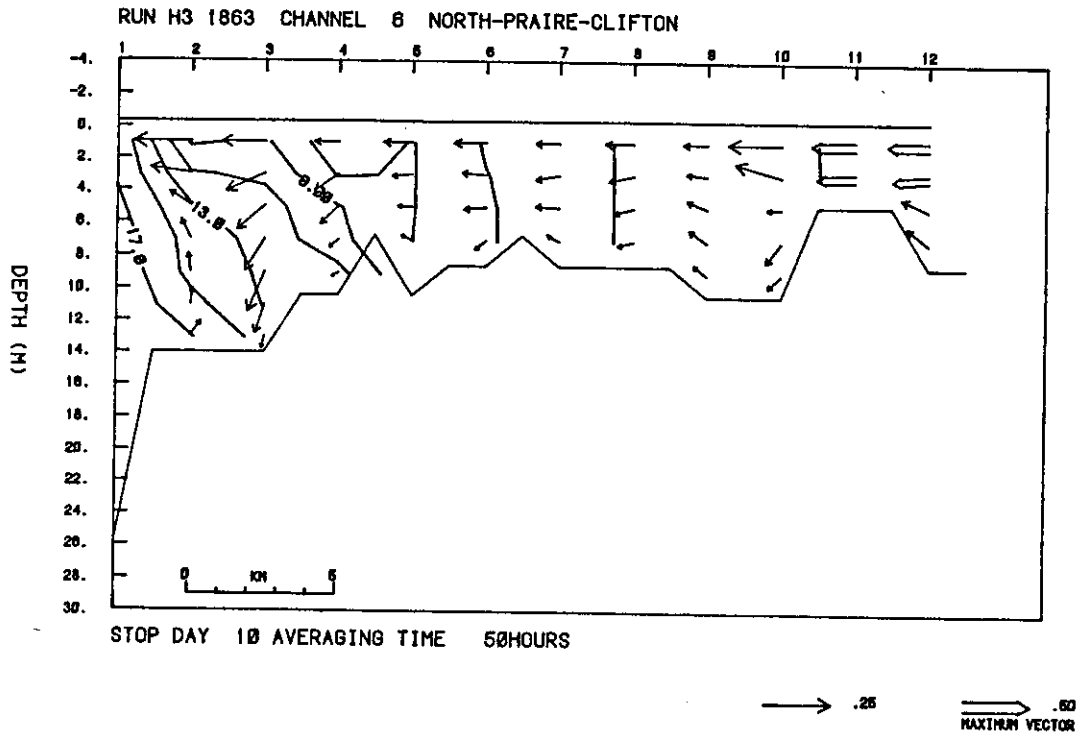


Figure 78a. Channel 6, spring tide period (historical bathymetry, riverflow =  $2000 \text{ m}^3/\text{s}$ ). Mean currents and salinities ( $\text{m/s}$  and  $^{\circ}/\text{oo}$ ).

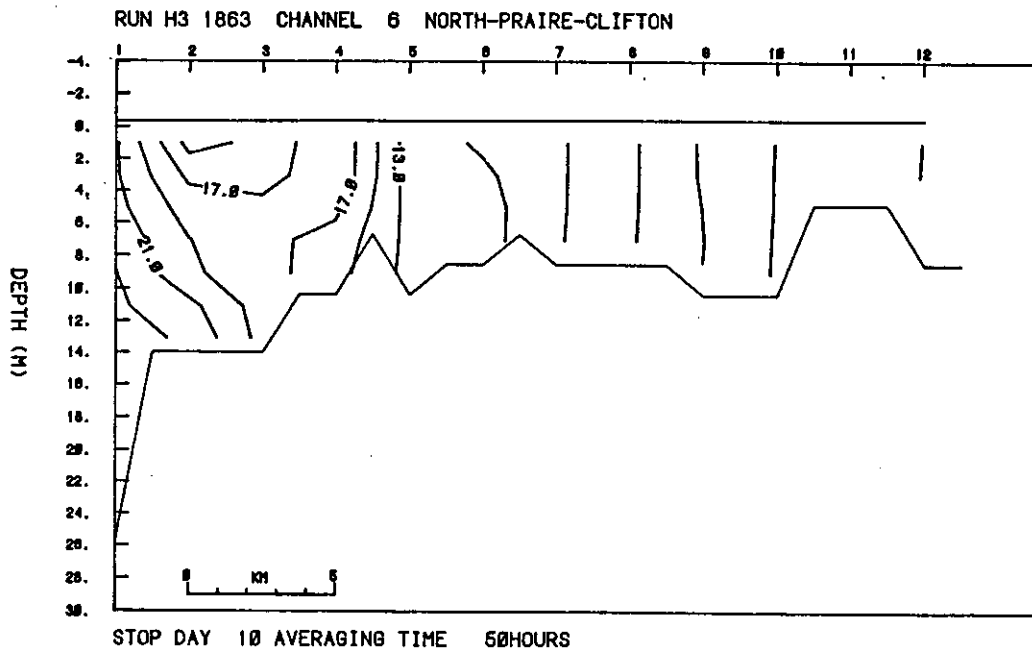


Figure 78b. Channel 6, spring tide period (historical bathymetry, riverflow =  $2000 \text{ m}^3/\text{s}$ ). Maximum salinities.

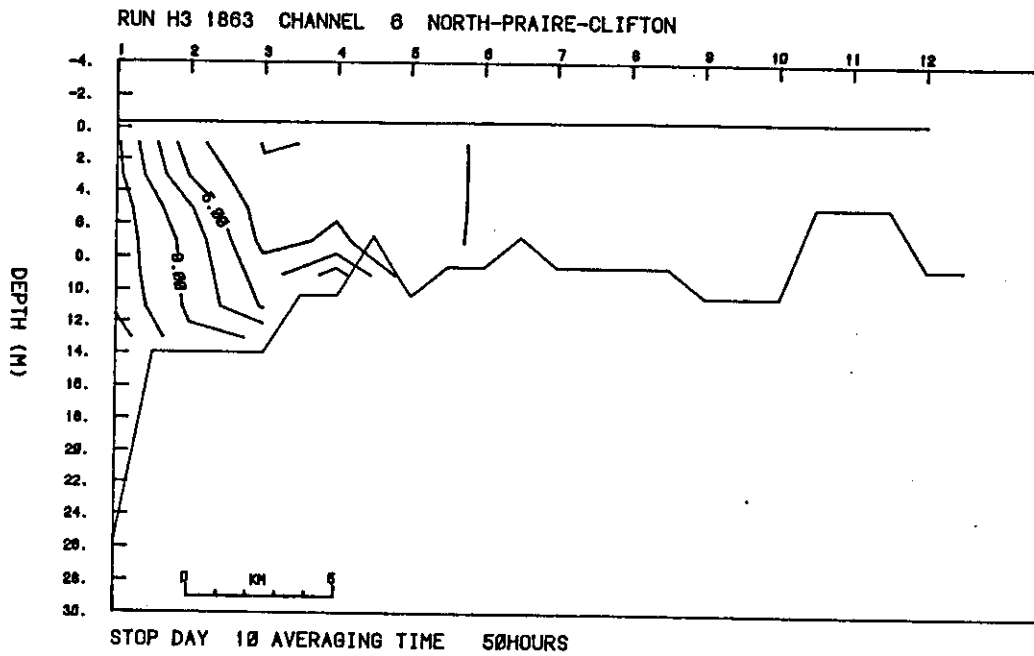


Figure 78c. Channel 6, spring tide period (historical bathymetry, riverflow =  $2000 \text{ m}^3/\text{s}$ ). Minimum salinities.

the bars at the foot of the major part of the salinity intrusion. Otherwise the differences in stratification between spring and neap are similar to the present day. Unlike the present-day, there are only small differences in the intrusion lengths in both North and South Channels between neap and spring tides. This indicates that either the neap-spring differences occur at higher riverflows than  $4,000 \text{ m}^3/\text{s}$  in the 1868 estuary or do not occur at all due to different advective and mixing patterns. Differences in intrusion length do not occur at riverflows of  $12,000 \text{ m}^3/\text{s}$  in run #1.

The very low flow period ( $2,000 \text{ m}^3/\text{s}$ ) run (H3) corresponds to run 27. The sections for channels 1, 2, 3, and 6 for neap and spring tides are given in Figures 71-74 and 75-78, respectively. The neap tide mean fields for channels 1 and 2 are very similar to the low flow period described above except for the relatively higher salinities. There are again sharp vertical fronts over the bars in channels 1 and 2 which separate the high salinity region from the well-mixed and diffuse low salinity tails. It is evident that channels 1 and 2 remain relatively isolated except possibly at high tide when the  $1 \text{ }^\circ/\text{oo}$  isohaline is upstream of the channel junction point at grid number 17, channel 1. Channel 6 shows some salinity intrusion from the Tongue Point region which shows higher salinities than the equivalent position in channel 4, run 27 (Figure 43).

The spring tide mean sections for channels 1 and 2 show considerably more effective horizontal dispersion of salt than on the neap tide. Thus, the salinity intrudes a considerable distance, with the mean position of the  $1 \text{ }^\circ/\text{oo}$  isohaline being at the northern tip of Puget Island. In the Astoria reach of Channel 1, the salinity is still a little higher than the equivalent position in channel 2. However, upstream of the bars, channel 2 is relatively more salty than channel 1. The high water maximum flood salinities in channel 1 show the  $5 \text{ }^\circ/\text{oo}$  isohaline reaching Puget Island. The  $5 \text{ }^\circ/\text{oo}$  isohaline reached only grid #15 (Pillar Rock) at the end of the spring flood in run 27. Weak vertical fronts are still present at high tide over the bars. The Cathlamet Bay channel (6) shows much higher salinities than the equivalent channel in run 27 due to high salinities at Tongue Point and the penetration of low salinity water at high tide to the other end of channel 6 at Puget Island. Therefore, one conclusion is that Cathlamet Bay may have infrequently experienced much higher salinities due to very low flows in the past, before channelization, than it does at the present time.

#### 3.2.4. Conclusions

The hydrodynamics of the 1868 estuary have been simulated using the depth-dependent multi-channel model. Compared to the present day, the 1868 bathymetry is shallower in the channels but deeper over the shoals with less land area in the form of islands, sandbanks and marshlands (Thomas 1983). The mouth region is much wider, with two entrance channels. The north entrance channel covers much of Baker Bay which today is mostly shoal. Upstream of Tongue Point, the channel network is more complex than today with many shoal areas which form bars to the flow.

The tidal wave is very little changed from today despite the large changes in bathymetry. However, due to the larger tidal prism, tidal volume transports were larger than today, particularly in the entrance and north channels. The ebb and flood flows also exhibit more asymmetry with the ebb dominating over the flood in channel 2 and vice-versa in channel 1. Channel 2, downstream of Tongue Point, carries a much larger proportion of the tidal transport than today.

As a result of the different distribution of tidal and residual flows, the salinity intrusion is much larger in channel 1 than channel 2 and generally the estuary is distinctly more saline than today for similar riverflows. This may seem like a contradiction considering the more deeply dredged main navigation channel of today, which superficially would be expected to increase the salt intrusion due to density current flows. However, the increased salt intrusion is due to increased tidal dispersion, i.e. the interaction of the tidal currents with the vertical and horizontal salinity gradients, which is due to the larger tidal currents and tidal current asymmetries than exist today.

The estuary shows similar relative neap-spring differences in stratification which exist also at high flows rather than just low flows. Stratification at low flows is generally less than it is today. The weaker stratification is due to the stronger tidal currents and shallower depths which promote more effective vertical mixing. It is noteworthy also that at low flows ( $4,000 \text{ m}^3/\text{s}$ ) there is no marked neap-spring change in salt intrusion length that occurs for low flows in the present-day estuary. This implies that the neap-spring change in intrusion length occurs at higher riverflows, which would be required to suppress the relatively stronger tidal mixing on a neap tide due to the larger tidal prism, or that the shallow topography with frequent bars and more effective vertical mixing does not allow the salt wedge to develop upstream of Tongue Point. Therefore, significantly larger intrusion lengths for highly stratified (neap-tide) conditions may not have existed in 1868. One aspect of the salinity fields, which has no equivalents at the present time is the existence of sharp vertical fronts over the bars, particularly the bar in channel 1 between Tongue Point and Astoria and the bar in channel 2, north of Taylor Sands. These fronts, which are probably formed by the convergences of the tidal currents over the shoals and through the constrictions, are prevalent at the end of the flood and show closely spaced vertical isohalines over the shoals. It is unlikely that these fronts were regions of enhanced productivity due to the light limitation of primary productivity in this estuary. However, they may have been regions of enhanced turbidity and sediment deposition due to increased vertical mixing and convergent residual currents.

The very low flow ( $2,000 \text{ m}^3/\text{s}$ ) simulation showed that the upper estuary and Cathlamet Bay would become considerably more saline than if a similar riverflow occurred in the present day estuary. The implication is that before regulation of the freshwater flows, the channelisation of the Navigation Channel and construction of the

Jetties, the estuarine habitants would experience much more variability of salinity both on tidal and tidal monthly time scales as well as due riverflow variability, than in the present-day estuary.

These predictions of the historical estuarine circulation are the first attempts to use models to determine the differences between an estuary as it existed in the past before man's intervention and the present day. The predictions may provide some explanations for ecological and geophysical changes observed over the last century. The accuracy of these historical predictions cannot be checked since no observations of currents and salinity are available for 1868. However, the accuracy is probably similar to that of the model for the present day estuary, which is quite good. Therefore the predictions can be considered to give the major features of the circulation in 1868 with a fairly high degree of certainty.

#### 4. SUMMARY

The depth-dependent tidal hydrodynamics of the Columbia River Estuary have been successfully simulated using an interconnecting-channel model. The model is an advanced development of the depth-dependent laterally averaged estuary models of Hamilton (1975, 1976), Blumberg (1975), Elliott (1976) and Wang and Kravitz (1980). Besides the channel connection scheme, features of the model include variable channel widths and depths; the provision for across-sandbank flows between channels, when the water level exceeds the height of the crest of the bank; and depth- and time-dependent formulas for the eddy coefficients. The model uses efficient semi-implicit finite-difference methods which allow large time steps; consequently, computer time is not a primary concern as it is with some three-dimensional models. The advection scheme is much more accurate than has previously been used in this type of model and considerably reduces the effects of spurious numerical dispersion which is important for this estuary. It is considered that the laterally averaged channel approximation includes the major physical processes responsible for the distribution of current, salinity, and water level throughout the estuary. Extensive comparisons of the model simulations with observations from CREDDP and NOS show good agreement for both high and low flow periods. The limitations of the model are primarily due to the semi-empirical formulae used for the eddy coefficients and neglect of cross-channel covariances, which may be an important contribution to the salt balance. Apart from experimenting with eddy coefficient formulations, major improvements in the simulations may be expected by reducing the horizontal grid spacing. Experiments performed for the Corps of Engineers have indicated that the salinity intrusion is particularly sensitive to the value of the bottom friction coefficient. The model was used to predict the salinity field for very low riverflows to determine the hydrodynamic effects of unlikely but possible reduction of riverflows to 2,000 m<sup>3</sup>/s.

The model simulations confirm many of the analysis results of Jay (1984), obtained from the CREDDP and NOS field data. Salt intrusion processes are dominated by tidal dispersion rather than by two-layer density currents. At low river flows, stratification and intrusion length are sensitive functions of the vertical mixing which is a function of tidal range. The ability of the model to simulate these neap-spring differences indicates that the interaction of vertical and horizontal gradients of salinity and current, along with vertical mixing which is a function of the local tidal current and stratification, controls the salinity field within the estuary. The neglect of cross-channel variability seems to be justified by these results. Tidal processes also dominate the residual mean flows. The model showed that the non-linear inertial terms and their interaction with topography had a strong influence on the residual currents. Density current circulations were generally weak, particularly at spring tides, despite large horizontal salinity gradients. The non-linear residual flows showed that bottom upstream currents are broken into cells in both the Navigation Channel and the North Channel. The model simulations are useful in showing the exchanges and

interactions between the channels. Stronger tidal dispersion in the North Channel causes higher salinities there than in the Navigation Channel at low freshwater flows. There is also a tendency of the tidal-residual flows and riverflows to be diverted from the Navigation Channel upstream of Astoria, and flow across Taylor and Desdemona Sands into the North Channel. The vertical section and horizontal plots of residual flows should be useful to investigators requiring knowledge of potential transport pathways within the estuary. The two cells of bottom upstream residual flow at the entrance and the Astoria reach may help to explain the different species of phytoplankton and zooplankton in these regions and their ability to maintain relatively distinct populations despite the strong tidal dispersion. Similarly, the plots of maximum and minimum salinities for neap and spring tides for various riverflows give a good indication of the tidal excursion, in the salt intrusion region of the estuary, of any passive solute, including fine sediment particles or phytoplankton if sinking is not important. These tidal excursions, illustrated by these salinity plots, may be useful for interpreting data taken at different tidal stages in the deep channels.

The simulation of the extensive low-flow case showed that neap-spring differences in intrusion length were much less important than for 4,000 m<sup>3</sup>/s riverflows. Stratification was weaker and the upper estuary was supplied with low salinity water by tidal dispersion from the North Channel via the shallow channels through Taylor Sands. Cathlamet Bay has fairly uniform salinities of between 1-5 ‰, whose source is the Navigation Channel upstream of Tongue Point. This general situation could have been deduced given that the salt intrusion is governed by riverflow and tidal dispersion. However, the details of the extreme low-flow salinity field could be predicted only from the model simulations, given the complexity of the circulation.

The model was reconfigured for the historical estuary of 1868. Neap and spring tides were simulated for riverflows of 12,000, 4,000, and 2,000 m<sup>3</sup>/s. Prior to channel dredging and the construction of the entrance jetties, the 1868 estuary had a larger tidal prism, shallower channels, deeper shoals, and a more complex system of channels, particularly in the upper estuary. The stronger tides resulted in larger salinity intrusions, weaker stratification and a more asymmetrical distribution of tidal currents and residual flows between North and South Channels compared with the same riverflows for the present-day estuary. At extreme low flows, which may have occurred quite frequently before regulation of the freshwater flow, Cathlamet Bay is predicted to have been quite brackish (5-20 ‰). Therefore, it may be speculated that the wetlands and shallow regions had a different ecology than that of today.

Further studies have been performed with this model for the Corps of Engineers. These studies involve the use of slightly more accurate bathymetry, the improvement of the October 1980 simulation of the salinity intrusion off Astoria by further adjustments of the bottom friction coefficients, and the inclusion of a channel representing Baker Bay. Recommendations for further studies with this model include:

1. Verification of the improved calibration using the NOS June 1981 data for high riverflows.
2. Calculation of the balance of forces at different sections of the estuary for different riverflows and tides, both on an instantaneous and tidal residual basis.
3. Further refinement of the model by the use of finer grids and the splitting of the entrance channel into two side-by-side channels to attempt to take into account the cross-channel variability which seems to be important there (Hughes and Rattray 1980).
4. Refinement of the equations of motion to account for channel curvature.
5. Experiments with eddy coefficient formulations for vertical mixing. The employment of a second order turbulent scheme to calculate the eddy coefficients would also be a useful research study.
6. Extension of the model seaward of the mouth by the use of a vertical shelf model (Hamilton and Rattray 1978) combined with the estuary model. This combined model could be used to study the interaction of the shelf and estuarine circulations.

#### LITERATURE CITED

- Blumberg, A.F., 1975. A Numerical Investigation into the Dynamics of Estuarine Circulation. Chesapeake Bay Institute, The Johns Hopkins University Tech. Report 91, 59 pp.
- Bowden, K.F. and P. Hamilton, 1975. Some experiments with a numerical Model of Circulation and Mixing in a Tidal Estuary. Estuarine and Coastal Marine Science, 3: 281-301.
- Butler, H.L., 1980. Evolution of a Numerical Model for Simulating Long-period Wave Behavior in Ocean-estuarine Systems. In Estuarine and Wetland Processes, Ed. P. Hamilton and K.B. Macdonald, Plenum Press N.Y. pp. 147-182.
- CREDDP, 1983. Map Series. Columbia River Estuary Data Development Program, Astoria, OR.
- Elliott, A.J., 1976. A Numerical Model of the Internal Circulation in a Branching Tidal Estuary Chesapeake Bay Institute Special Report 54, Ref. 76-7. The John Hopkins University, Baltimore, MD 85 pp.
- Foreman, M.G.G., 1979. Manual for Tidal Currents Analysis and Prediction. Institute of Ocean Sciences, Patricia Bay, Victoria, B.C., Pacific Marine Science Report 78-6.
- Gardner, G.B., A.R.M. Nowell and J. Dungan Smith, 1980. Turbulent Processes in Estuaries. In Estuarine and Wetland Processes, Ed. P. Hamilton and K.B. Macdonald, Plenum Press, N.Y., pp 1-34.
- Hamilton, P., 1975. A Numerical Model of the Vertical Circulation of Tidal Estuaries and its Application to the Rotterdam Waterway. Geophys. J. Roy Astr. Soc., 40: 1-21.
- Hamilton, P., 1976. On the Numerical Formulation of a Time-dependent, Multi-level Model of an Estuary with Particular Reference to Boundary Conditions. In ESTUARINE PROCESSES (ed. Martin Wiley) 347-364, Academic Press, New York.
- Hamilton, P. and M. Rattray, Jr., 1978. A Numerical Model of the Depth-dependent, Wind-driven Upwelling Circulation on a Continental Shelf. Journal of Physical Oceanography, 8(3): 437-457.
- Hamilton, P. and M. Rattray, Jr., 1978. Theoretical Aspects of Estuarine Circulation. In ESTUARINE TRANSPORT PROCESSES (ed B. Kjerfve) 37074, University of South Carolina Press.

- Hamilton, P., 1983. Numerical Modeling of the Depth Dependent Salinity Intrusion for the Coal Port Deepening Project in the Columbia River Estuary. Tech Report (Contract No. DACW47-83-M-1703) U. S. Army Engineer District, Portland, OR. 163 pp.
- Hansen, D.V. and M. Rattray, Jr. 1965. Gravitational Circulation in Straits and Estuaries. J. Mar. Res. 23: 104-122.
- Hughes, F.W. and M. Rattray, Jr. 1980. Salt Flux and Mixing in the Columbia River Estuary. Est. Coastal Marine Science 10, 479-493.
- Ianniello, J.P., 1979. Tidally Induced Residual Currents in Estuaries of Variable Breadth and Depth. J. Phys. Oceanogr., 9, 962-974.
- Ianniello, J.P., 1981. Comments on Tidally Induced Residual Currents in Estuaries: Dynamics and Near-Bottom Flow Characteristics. J. Phys. Oceanogr. 11, 126-134.
- Jay, D., 1984. Circulatory Processes in the Columbia River Estuary. Final CREDDP Report, CREST, Astoria OR.
- Mellor, G.L. and T. Yamada, 1982. Development of a Turbulence Closure Model for Geophysical Fluid Problems. Rev. Geophys. Space Phys. 20, 851-876.
- Munk, W.H., and E.R. Anderson, 1948. Note on the Theory of the Thermocline. J. Mar. Res. 7 276-295.
- Pritchard, D.W., 1960. The Mixing and Movement of Contaminants in Tidal Estuaries. Proceedings of the 1st International Conference on Waste Disposal in the Marine Environment. Univ. of CA at Berkeley. Pergamon Press.
- Roach, P.J., 1972. Computational Fluid Dynamics. Hermosa, Albuquerque, NM, 446 pp.
- Smolarkiewicz, P.K., 1982. The Multi-Dimensional Crowley Advection Scheme, Monthly Weather Revue 110, 1968-1983.
- Smolarkiewicz, P.K., 1983. A Simple Positive Definite Advection Scheme with Small Implicit Diffusion Monthly Weather Revue 111, 479-486
- Thomas, D.W., 1983. Changes in Columbia River Estuary. Habitat Types Over the Past Century. Final CREDDP Report, CREST, Astoria, OR
- Wang, D.P. and Kravitz, D.W., 1980. A Semi-Implicit Two-Dimensional Model of Estuarine Circulation. J. Phys. Oceanogr. 10, 441-454.
- Zalesak, S.T., 1979. Fully Multi-Dimensional Flux-Corrected Transport Algorithms for Fluids J. Comp. Phys. 31, 335-362.